

# IV. Applied Battery Research for Transportation

## IV.A. Introduction

The widespread adoption of electric vehicles remains critical to attaining the economic, energy security, and environmental goals that form the mandate of the Office of Renewable Energy and Energy Efficiency within the United States Department of Energy. Success requires U.S.-sourced and U.S.-developed technical innovation supporting and supported by a strong U.S.-based battery manufacturing sector. Inherent to the idea-to-societal benefit process is the translation of materials discovery and device innovation from the R&D community into commercially viable products and processes, often described as applied research. This critical R&D functionality requires input and effort from industry, national laboratories, and academia and such contributions are supported and leveraged by funding from the Vehicle Technologies Office.

The Applied Battery Research (ABR) for transportation program is comprised of high risk, high reward projects investigating issues and advances at the cell level. Success in ABR projects means electric drive vehicle energy storage products that can be realized (manufactured) and that lead to cost reduction. Such improvements will be accomplished through novel materials, particularly the active components of the cell, but also through innovative cell design and electrode composition. Also, materials production, electrode processing, and cell manufacture are important R&D areas within ABR. Completing the suite of project modalities is the Critical Barrier Focus (CBF). Applied research programs always contain and are often defined by a major barrier, a set of structurally and functionally interrelated problems that simultaneously appear intractable and absolutely require mitigation or adaptation in order to achieve a particular technical target. Solutions to critical barriers, if possible, require understanding across the dimensions of the problem, and such understanding occurs only through in-depth science practiced by a cross-disciplinary team—and a lot of data. In FY 2016, two CBF projects were active: Enabling High Energy, High Voltage lithium-ion Batteries, and Next Generation Anodes for Lithium-ion Batteries.

Two distinct campaigns comprise the 2016 ABR project portfolio: cell optimization activities and advanced processing R&D projects. Central to the cell optimization campaign is moving innovations from the laboratory bench to the production plant floor. These are advances in materials, components, and cell construction that have shown promise at the proof-of-concept level, demonstrating half-cell performance, preliminary full cell performance, and safety results that support their possible commercial development. For 2016, fourteen cell optimization projects were active which were typically team-based and included participants from eight national labs, three universities, and more than fifteen small, medium, and large commercial entities. Advanced processing research is relatively new to the VTO Energy Storage line-up with three initial projects at the national labs originally funded through the American Recovery and Reinvestment Act of 2009. Over the past six years, this campaign has grown to encompass six distinct projects at the national labs and thirteen projects at battery OEMs active in 2016. For thematic considerations and ease of access, the thirty three projects on these two campaigns are further categorized into five sections reflecting specific project goals and the funding vehicle utilized. This organizational rubric is briefly developed below.

**Core and Enabling Support Facilities.** Across several of the national laboratories, infrastructure has been created and resources grouped into facilities that support complex activities critical to ABR. This provides the U.S. energy storage research community a powerful tool to carry out scientific investigations by using, for example, state-of-the-art fabricated lithium-ion battery electrodes, commercially viable and high purity electrolyte additives, chemical and electrochemical analysis of cycled battery components, and component-level abuse response analysis. The services and products of these facilities are fully funded through the ABR program and are available hierarchically, with VTO funded projects first, followed by other DOE funded projects (BES, ARPA-E), then other government agencies down the line through to U.S. commercial entities. The anchor facility among ABR's support facilities is the Cell Analysis, Modeling, and Prototyping Facility (CAMP) based at the Argonne National Laboratory. The CAMP Facility is an integrated team effort designed to support the production of prototype electrodes and cells, including materials validation (benchmarking), modeling, and diagnostics. As in FY2015, the majority of the individual projects undertaken within CAMP this year centered on fabricating, testing, and characterizing silicon-based anodes.

**Critical Barrier Foci—Enabling High Energy & Next-Generation Anodes.** In 2016, two CBF projects have been active: “Enabling High Energy, High Voltage lithium-ion Batteries” and “Next-Generation Anodes for LiBs”, designated as the “HE/HV deep dive” and the “Si cell deep dive”, respectively. Both are consortium projects, each led by ANL, but involving researchers from several other national labs. The overall objective of the HE/HV deep dive, now in its last full year, is to understand the failure mechanisms that prevent state-of-the-art lithium-ion battery systems from achieving higher practical energy densities than currently obtainable with both automotive and consumer electronic commercial lithium-ion battery materials and cell configurations. The inability to delithiate commercially available cathode materials beyond ~4.3 V (vs. Li/Li<sup>+</sup>) without incurring excessive surface damage, electrolyte decomposition, and bulk structural instabilities is a significant challenge. The Si cell deep dive began in FY2016 as a result of a directed funding opportunity initiated in 2015 and competitively awarded to a team led by ANL but with substantial contributions proposed from LBNL, ORNL, NREL, and SNL. The central questions of the project deal with the industry-wide inability to achieve lifetime targets with Si-based cells demonstrating superior energy densities, e.g., why successful cells cannot be made, the underlying structural factors leading to failure at the atomic-to-sub-micron scale, etc.

**Next-Generation Lithium-ion Chemistries “Improvements in Cell Chemistry, Composition, and Processing”.** In September 2013, DOE VTO awarded six contracts to develop cells that met or exceeded performance targets for EV or PHEV batteries. Contracts were awarded to teams led by 3M Company, Envia Systems, Farasis, Penn State University, TIAX (now CAMX Power), and Argonne National Laboratory. Each development team has used next-generation anodes and cathodes. The active material in all cases for the anode was a carbon-Si (or silicon-based nanocomposite) blend. For the cathode, each development team has investigated either high voltage NMC-based cathodes with high Ni content or lithium rich, manganese rich oxide-based cathodes (or both).

**Process Development and Manufacturing R&D at National Laboratories.** Critical to establishing a U.S.-based battery manufacturing industry is the development of process-oriented intellectual property (IP). However, many of the opportunities to develop such IP have long lead times associated with process development, novel equipment design, and the time associated with technology learning. This often means there is a strategic financial barrier for for-profit entities. Too much business risk is associated with process technology development. Considering the potential reward to the US economy and to society in general, where possible and relevant, this risk could be assumed by the government. The reports contained in this section detail work across three national labs that not only has led to IP creation of its own, but the research teams have also leveraged EERE-funded work to partner with American companies developing proprietary processing technologies. A variety of U.S. companies have collaborated on those projects, ranging from multinational corporations to start-up small businesses. As new processing resources are developed, they are also made available to the U.S. energy storage research community via the support facilities described above.

**Process Development and Manufacturing R&D with US Industry.** The EERE-VTO advanced batteries R&D program, in addition to process R&D at the national labs, supports the development of manufacturing processes through funded agreements with for-profit entities, leveraging entrepreneurial investment and allowing private sector innovators to stretch resources through DOE funding. Over the past two fiscal years several high risk/high reward projects at commercial entities were funded. Four of the six projects reported deal with various approaches to or aspects of battery electrode or separator fabrication. Miltec International, for example, is developing a novel approach to introduce ceramic subcomponents into battery separators to dramatically improve thermal abuse prevention. An important aspect of battery electrode fabrication is solvent removal after electrode coating; Lambda Technologies is showing some success in reducing the drying residence time and energy used via a microwave-assisted drying approach. The other two industrial projects in this section deal with, respectively, an inventive and promising method to produce a potentially game-changing new active cathode material: Sila Nanotechnologies’ gas-phase synthesis of transition metal fluoride conversion cathode materials and with an innovation in cell design and architecture, Parthian Energy’s efforts to substantially increase energy density via a non-parallel plate full cell geometry, their S-cell design.

The remainder of this section provides technical highlights and progress reports on the Applied Battery Research program for FY 2016 organized by the project groups discussed above. Each report was prepared to capture the purpose, approach, major gains and setbacks (if any) of the project (or its component). For more technical detail, actual experimental methods, and data analytics, please see each report’s referenced scientific publications or contact the appropriate project lead.

## IV.B. Core and Enabling Support Facilities

### IV.B.1. Cell Analysis, Modeling, and Prototyping (CAMP) Facility Research Activities (Argonne National Laboratory)

**Andrew N. Jansen, Principal Investigator**

Argonne National Laboratory  
9700 South Cass Avenue, CSE-200  
Lemont, IL 60439  
Phone: 630-252-4956  
E-mail: [jansen@anl.gov](mailto:jansen@anl.gov)

**Peter Faguy, DOE Program Manager**

U.S. Department of Energy  
Vehicle Technologies Office  
1000 Independence Avenue, SW  
Washington, DC 20585  
Phone: 202-586-1022  
E-mail: [Peter.Faguy@ee.doe.gov](mailto:Peter.Faguy@ee.doe.gov)

Start Date: October 1, 2014  
End Date: September 30, 2017

#### Abstract

#### Objectives

The objective of this core-funded effort is to design, fabricate, and characterize high-quality prototype electrodes and cells that are based on the latest discoveries involving high energy anode and cathode battery materials. Using this multi-disciplined facility, analytical diagnostic results can be correlated with the electrochemical performance of advanced lithium-ion battery technologies for plug-in electric vehicle (PEV) applications.

- Link experimental efforts through electrochemical modeling studies.
- Identify performance limitations and aging mechanisms.
- Support lithium-ion battery projects within the DOE-EERE-VTO.

#### Accomplishments

- Fabricated silicon-graphite electrodes and pouch cells with 15% silicon and NMC622
  - Demonstrated that the choice of NMC cathode does not influence silicon capacity fade.
  - Initiated study of effects of calendar life versus cycle life for silicon-based cells.
- Determined the capacity, energy, and average voltage of a wide range of commercially available cathode materials as a function of upper cutoff voltage. NMC811 has superior capacity and energy for potentials up to 4.5 V vs. Li<sup>+</sup>/Li.
- Examined electrochemical performance of cells containing NMC532-based positive electrodes, 15 wt.% nanosilicon-bearing graphite-based negative electrodes, and 1.2 M LiFSI in EC:EMC (3:7 w/w) electrolytes in the 3.0-4.1 V range. Observations include the following:
  - The initial discharge capacity of LiFSI (only) cells is comparable to that of the LiFSI-VC and LiFSI-FEC cells. However, after 100 cycles, the LiFSI cells show a relatively low capacity (26 mAh/g), when compared to the LiFSI-VC (86 mAh/g) and LiFSI-FEC (79 mAh/g) cells. That is, the additives improve the cycle life of cells.
  - The LiFSI-VC cells displayed the best performance on cycling – lowest impedance rise and highest capacity retention – of all cells tested.

- The performance of LiFSI-FEC and LiPF<sub>6</sub>-FEC cells are very similar. This result, in conjunction with data from the other cells, indicates that these salts play a much smaller role in performance degradation than the electrolyte solvent. Therefore, future achievements to enhance cell life-times will focus on designing alternative solvent systems.
- Demonstrated that in carbonate electrolytes, LiTDI prevents anodic dissolution of Al current collectors, which places it into a select group of corrosion inhibitors.
  - Demonstrated that LiTDI becomes reduced on lithiated graphite, undergoing sequential defluorination and yielding a thick and resistive solid-electrolyte interphase (SEI), which increases impedance and lowers electrode capacity.
  - Showed that the negative effects of LiTDI reduction can be prevented by certain electrolyte additives, which include fluoroethylene carbonate, vinylene carbonate, and LiBoB.
- Fabricated silicon-graphite double-sided electrodes and matched NMC532 double-sided electrodes for SNL thermal abuse tests.
- Designed and fabricated numerous baseline electrodes and prototype electrodes and cells for:
  - High-Energy High-Voltage Project
  - Next Generation Anodes Project
  - Electrode Library users (national labs, universities, industry)
- Held numerous discussions with materials suppliers on their materials.
- Expanded electrochemical model for interfacial impedance and bulk transport.

### Future Achievements

- Fabricate new generation of silicon-graphite electrodes using larger silicon particles
  - 70-130 nm silicon from NanoAmor.
  - Move towards 30% silicon.
  - Study effect of calendar life versus cycle life.
  - Study effect of cell pressure and electrode porosity on lithium plating/cycle life.
- Master new Buhler mixer that will enable CMC-SBR (and other) aqueous binders.
- Install new 2 Ah pouch cell assembly equipment and upgraded 18650 winder.
- Continue study of performance of high-loading electrodes
  - Use reference electrodes to determine rate limiting electrode (anode or cathode).
  - Determine influence of segmented charge rates for low, medium, and high SOC.
- Collaborate with Next Generation Anodes Project on binder systems and electrolyte additives for silicon-based cells
- Continue support of High-Energy High-Voltage Project with emphasis on NMC811.
- Work with Post-Test Facility on determining failure mechanisms in silicon cells
  - Analyze multi-layer pouch cells for gas and electrolyte composition.
  - Analyze surface of cycled silicon electrodes.
- Continue development of Gr-Si electrode electrochemical model.
- Continue work with MERF on demonstrating performance of new materials, including new conductive binders for silicon (with LBNL).

## Technical Discussion

### Background

The CAMP Facility is designed to work closely with materials researchers across the many electrochemical energy storage programs throughout the DOE-EERE-VTO. In addition to its own yearly R&D tasks, it actively coordinates its efforts to provide support to other national lab teams: the High Energy High Voltage deep dive (Section IV.C), the Next Generation Anodes deep dive (Section IV.D.7-9), and the CAEBAT programs (Section III.C). The Materials Benchmarking Activities (Section IV.B.2) is a segment of the CAMP Facility. The CAMP Facility also complements the capabilities of other DOE support facilities such as: the Materials Engineering Research Facility (MERF - ANL), the Post-Test Facility (PTF - ANL), the Battery Abuse Testing Lab (BATLab - SNL), and the Battery Manufacturing Facility (BMF - ORNL).

Key team members within the CAMP Facility in FY16 include: Daniel Abraham, Dennis Dees, Alison Dunlop, James Gilbert, Manar Ishwait, Andrew Jansen, Matilda Klett, Wenquan Lu, Bryant Polzin, Yan Qin, Xin Su, Steve Trask, and Linghong Zhang.

### Introduction

The “valley of death” is a phrase often used to describe the path a new discovery must traverse to become a commercial product. This is especially true for novel battery materials invented in research laboratories around the world. Often researchers are resource limited and only able to make gram quantities of their new material. A few grams is enough for several coin cells to prove the concept, but never enough for a battery manufacturer to test in a realistic format. Consider that a typical coin cell has a capacity near 4 mAh, while a cell in a PEV battery has a capacity near 40 Ah – four orders of magnitude larger. An unwarranted amount of resources is gambled to make the tens of kilograms needed for a full-sized cell industrial demonstration.

The CAMP Facility is appropriately sized to enable the design, fabrication, and characterization of high-quality prototype cells using just a few hundred grams of the latest discoveries involving high energy battery materials. Prototype cells made in the CAMP Facility generally have near 400-mAh capacity, which straddles the gap between coin cells and full cells – two orders of magnitude from each end point. Thus, a realistic and consistent evaluation of candidate chemistries is enabled in a time-effective manner with practical quantities of novel materials in cell formats commonly used in industry.

The CAMP Facility is an integrated team effort designed to support the production of prototype electrodes and cells, and includes activities in materials validation (benchmarking), modeling, and diagnostics. It is not the aim of this facility to become a small battery manufacturer, but instead to be a laboratory research facility with cell production capabilities that adequately evaluate the merits and limitations of new lithium-ion chemistries in a close-to-realistic industrial format.

As new cell chemistries and systems progress, they reach the point where they are considered for further development in larger prototype cells. When this happens, a limited quantity of these materials, along with their preliminary data, are transferred from the inventor or originator to the CAMP Facility for materials validation to determine if they warrant further consideration. The source of these materials (anodes, cathodes, electrolytes, additives, separators, and binders) may originate from the ABR and BMR Programs, as well as from other domestic and foreign organizations such as universities, national labs, and industrial vendors. Electrochemical couples with high power and energy density are given extra priority. Lately, efforts have focused on silicon-based anodes, and nickel-manganese-cobalt (NMC) cathodes that are high in nickel and operating at higher potentials.

The CAMP Facility has the capability to make two prototype cell formats in a 45 m<sup>2</sup> dry room: pouch cells (xx3450 format, with capacity around 0.4 Ah) and 18650 cells (with capacity around 2 Ah). Pouch cells are generally easier to assemble, but they may suffer from bulging if gases are evolved during cell aging and cycling. 18650s, which include rigid containers, may be used if the pouch cell format is deemed unreliable due to gassing, or if higher capacity cells are needed (greater than 1 Ah). Central to this effort is a pilot-scale coating machine that operates with slurry sizes that range from 20 grams to a couple of kilograms. This key feature of the CAMP Facility enables a professional evaluation of small quantities of novel materials. If needed, the MERF is available for scaling up materials for these prototype cell builds.

In general, two types of modeling are employed within this effort. First, battery design modeling is a spreadsheet based simulation used to determine the impedance behavior, available capacity, and thermal effects for general and specific cell, battery module, and battery pack designs. The model is also capable of performing simulations on multiple battery designs for comparison and optimization. In addition, the battery design model includes a module that calculates battery costs by combining materials and components costs with manufacturing expenses based on a plant design. A publicly available version of this work referred to as the battery performance and cost (BatPaC) model, represents the only public domain model that captures the interplay between design and cost of lithium-ion batteries for transportation applications.

Electrochemical modeling is aimed at associating electrochemical performance measurements with diagnostic studies conducted on lithium-ion cells. The methodology for the electrochemical model is described in detail in the literature [1-4]. Essentially, continuum-based transport equations are combined with kinetic and thermodynamic expressions to allow the potential, concentration, and current distributions to be determined throughout the cell. Two versions of the cell electrochemical model with the same basis are utilized to fully examine the broad range of electrochemical studies. One version of the electrochemical cell model is used to simulate the cell response from Electrochemical Impedance Spectroscopy (EIS) studies, and the other model version is utilized for examining DC studies, such as controlled current or power cycling and diagnostic Hybrid Pulse Power Characterization (HPPC) tests.

## Approach

The general approach used in this effort is to start small and grow large in terms of cell size and amount of resources devoted to each novel battery material. At various points in the development process, decisions are made to either advance, modify, or terminate studies to maximize the utilization of available resources.

Coin cells (2032 size) are used for materials validation purposes with initial studies performed at room temperature or 30°C. After formation cycles, the coin cells go through rate capability testing, HPPC testing, and limited cycle life testing. Accelerated aging studies are also performed at 45°C to 55°C for promising materials to give a preliminary indication of life. Where appropriate, the thermal abuse response is studied using a differential scanning calorimeter (DSC) and accelerating rate calorimeter (ARC).

Using the results obtained by the materials validation of promising materials, single-sided electrodes are fabricated on the larger dry-room coater for diagnostic study. The new cell chemistries are studied in detail using advanced electrochemical and analytical techniques, including the employment of micro-reference electrode cells. Factors are identified that determine cell performance and performance degradation (capacity fade, impedance rise) on storage and on extensive deep-discharge cycling. The results of these tests are used to formulate data-driven recommendations to improve the electrochemical performance/life of materials and electrodes that will be incorporated in the prototype cells that are later fabricated in the dry room. This information also lays the foundation for electrochemical modeling focused on correlating the electrochemical and analytical studies, in order to identify performance limitations and aging mechanisms.

The approach for electrochemical modeling activities is to build on earlier successful characterization and modeling studies in extending efforts to new PEV technologies. The earlier studies involved developing a model based on the analytical diagnostic studies, establishing the model parameters, and conducting parametric studies with the model. The parametric studies were conducted to gain confidence with the model, examine degradation mechanisms, and analyze cell limitations.

In addition, the battery design spreadsheet model (BatPac) is used to determine the impact of advanced materials on current technology. The performance of the materials within the battery directly affects the end energy density and cost of the integrated battery pack. Both modeling efforts complement each other and are specifically aimed at supporting the CAMP Facility goals.

If the results from diagnostics and modeling still look promising, full cell builds are conducted using double-sided electrodes. The electrodes are then either punched in the case of pouch cells, or slit in the case of 18650 cells and assembled into full cells in the dry room using the semi-automated cell assembly equipment. Formation procedures are conducted on the cells to encourage electrolyte wetting and uniform solid-electrolyte-interface (SEI) formation. These cells undergo rigorous electrochemical evaluation and aging studies under the combined effort of the CAMP Facility team, and Argonne's Electrochemical Analysis and

Diagnostic Laboratory (EADL) and Post-Test Facility. After testing, select cells are destructively examined by the Post-Test Facility to elucidate failure mechanisms. This information is then used to further improve the new chemistry, as well as future electrode and cell builds. The results of these tests are shared with other members of the ABR and BMR Programs and to the materials origin, and to battery developers, if appropriate.

## Results

The ever-increasing demand for high energy density lithium-ion cells has led to efforts to increase the capacity of the cathode and the anode. On the cathode side, improvements in energy density are centered on stabilizing high-nickel NMC materials operating at high potentials ( $> 4.3$  V vs.  $\text{Li}^+/\text{Li}$ ). The main focus here is to minimize the cathode degradation, which leads to transition metal dissolution into the electrolyte, followed by deposition on the anode. On the anode side, there is a resurgence of interest in silicon-based negative electrodes. Unlike conventional graphite-based negative electrodes which have a theoretical capacity of 372 mAh/g-graphite, silicon-based negative electrodes can deliver capacities up to 3579 mAh/g-silicon, thus making possible the development of thinner, higher-capacity electrodes. However, the commercialization of silicon anodes has been limited by factors that include the following: (a) the relatively large amounts of conduction additives required to ensure good inter-particle electric conductivity because of silicon's semi-conducting nature; (b) the large volume expansion/contraction resulting from silicon lithiation-delithiation processes leading to excessive cracking and delamination from the current collector; (c) the development of binder-systems that can maintain cohesion between the coating components and adhesion to the current collector during electrochemical cycling; (d) the excessive solid electrolyte interphase (SEI) formation on the electrodes that irreversibly trap lithium leading to rapid capacity fade.

### Silicon-containing Negative Electrodes: xx3450 Pouch Cell Builds

The CAMP Facility assembled multilayer xx3450-format pouch cells utilizing a high energy-dense silicon-graphite composite (Si-Gr) negative electrode and a NMC622 positive electrode. All cells in this section used a baseline 25  $\mu\text{m}$  PP/PE/PP tri-layer separator and electrolyte consisting of 90 wt. % (1.2 M  $\text{LiPF}_6$  in EC:EMC (3:7 wt.%) + 10 wt.% FEC additive. The results from this cell build are summarized in Figure IV-1 to Figure IV-7, where previous data has been included to compare the performance differences. Previous pouch cell data generated by the CAMP Facility provide a valuable baseline containing NMC532 to mark changes in cell performance due to the cathode. The “10% nSi, MagE, LiPAA vs. NMC532” and “15% nSi, MagE, LiPAA vs. NMC622” series names were pouch cell builds fabricated and tested in FY16.

The Si-Gr//NMC622 electrode couple (Table IV-1) was used to examine both comparative performance to Si-Gr//NMC532 pouch cells and investigate a recent concern over the poor calendar life for cells containing silicon in general. Twelve pouch cells were fabricated for this study. All 12 pouch cells went through the same formation cycling protocol: 15 minute tap charge to 1.5 V, 24 hour rest for electrode wetting, 2 cycles at C/20 from 3.0 to 4.1 V, 5 cycles at C/10 discharge and C/10 charge (trickle to C/16) from 3.0 to 4.1 V, and a 48 hour open circuit voltage rest to monitor for any self-discharge (Figure IV-1). After the formation test, 0.5 mL of electrolyte was added to the cells and vacuumed sealed again to remove any gasses generated during the formation step. The 12 cells were then split into 3 sets of 4 cells to examine the performance differences when using 3 different cycling protocols. The 1<sup>st</sup> set followed the same testing scheme (Cycle Life) as the previously reported Si-Gr//NMC532 pouch cell data for appropriate comparison of performance. The 2<sup>nd</sup> set used the cycling protocol from the Next Generation Anodes project (“Silicon Deep Dive”). The 3<sup>rd</sup> set followed a protocol written to have minimal cycles with long rest periods (Calendar Life). These protocols are described more in Table IV-2.

**Table IV-1: Electrodes Fabricated by the CAMP Facility for Si-Gr //NMC622 in xx3450 Pouch Cell Format**

Negative Electrode: 15% nSi, MagE, LiPAA	Positive Electrode: NMC622
73 wt% Hitachi MagE	90 wt% ECOPRO NMC622
15 wt% Nano&Amor Silicon (50-70 nm)	5 wt% Timcal C45
2 wt% Timcal C45	5 wt% Solvey 5130 PVDF Binder
10 wt% LiPAA (LiOH titrate)	
Cu Foil Thickness: 10 μm	Al Foil Thickness: 20 μm
Total Electrode Thickness: 116 μm (DS)	Total Electrode Thickness: 174 μm (DS)
Coating Thickness: 53 μm (SS)	Coating Thickness: 77 μm (SS)
Porosity: 42.6%	Porosity: 34.7%
Total SS Coating Loading: 6.21 mg/cm <sup>2</sup>	Total SS Coating Loading: 20.59 mg/cm <sup>2</sup>
Total SS Coating Density: 1.17 g/cm <sup>3</sup>	Total SS Coating Density: 2.67 g/cm <sup>3</sup>
*Capacity: 700 mAh/g	**Capacity: 168 mAh/g
Capacity: 3.91 mAh/cm <sup>2</sup> (1.5 to 0.05 V vs. Li/Li <sup>+</sup> )	Capacity: 3.11 mAh/cm <sup>2</sup> (3.0 to 4.2 V vs. Li/Li <sup>+</sup> )
<i>N:P Ratio: 1.26, ~ 450 mAh</i>	
<i>*grams of active materials: silicon, graphite, carbon black, (C/10, 1.5 to 0.05 V vs. Li<sup>+</sup>/Li</i>	
<i>**grams of active material: NMC622, (C/10, 3.0 to 4.2 V vs. Li<sup>+</sup>/Li</i>	

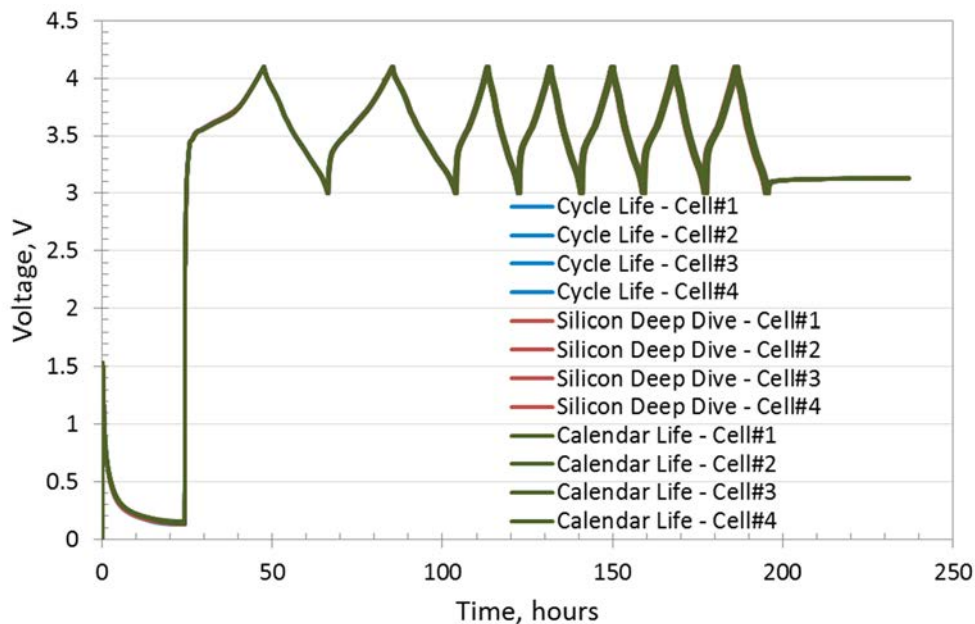


Figure IV-1: Voltage profile of the formation testing of the Si-Gr//NMC622 xx3450 pouch cells at 30 °C. The plot contains 12 individual cells formed under the same conditions (all voltage curves overlapped). The series names refer to the testing protocols to be used following the formation

**Table IV-2: Cycling Protocols for Si-Gr//NMC622 in xx3450 Pouch Cell Format**

Protocol	Description
Cycle Life	250 cycle at C/3 charge (trickle to C/20) and C/2 discharge, 3.0 to 4.1 V
Silicon Deep Dive	tap charge skipped (formation has already taken place), C/20 (no trickle charge) 3 cycles, HPPC (10 second 3C discharge and 2.25C charge pulses), 92 cycles at C/3 discharge and C/3 charge (no trickle charge), HPPC, 3 cycles at C/20 (no trickle), 3.0 to 4.1 V
Calendar Life	1.5 cycles at C/20 (no trickle charge), HPPC (10 second 3C discharge and 2.25C charge pulses), 2 cycles at C/3 charge (trickle to C/20) and C/2 discharge, C/20 charge to 3.9V, hold at 3.9V for 3 hours, rest at OCV for 168 hours (7 days), repeat until end of life, 3.0 to 4.1 V

All 12 Si-Gr//NMC622 pouch cells produced similar results for the formation protocol. The cells showed expected values for the 24 hour relaxation voltage after the tap charge (tap charge used to encourage wetting, while minimizing copper corrosion), similar charge and discharge voltage curves, and the expected capacity was observed. The Si-Gr//NMC622 formation data were similar to that of the Si-Gr//NMC532 pouch cells (not shown here). The formation test resulted in the 1st cycle average discharge capacity and coulombic efficiency being 149.8 mAh/g and 80.8%, respectively (Figure IV-2). All mAh/g values in this section refer to the grams of NMC622. The final cycle of the formation test (7th cycle) had an average discharge capacity and coulombic efficiency of 143.4 mAh/g of NMC 622 and 99.3%, respectively.

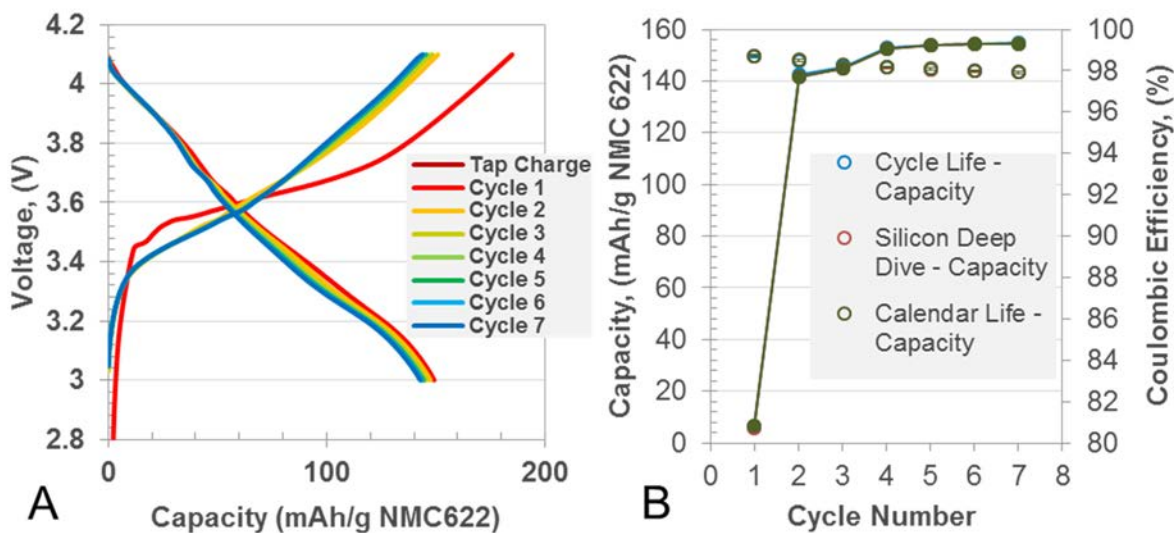


Figure IV-2: (A) Representative voltage profiles per cycle of the formation testing of the Si-Gr//NMC622 in xx3450 pouch cells at 30°C. (B) Average discharge capacities (hollow spheres) and corresponding coulombic efficiencies (solid spheres) per cycle for the formation testing of the Si-Gr//NMC622 in xx3450 pouch cells at 30°C. The plot contains 3 identically tested series for formation with a total of 12 cells represented. The series names refer to the future testing that will be performed. The error bars represent 2σ standard deviation

The overlay of the discharge capacities (mAh/g and mAh) as a function of total testing time for the Si-Gr//NMC622 pouch cells (Figure IV-3) suggests that while there is still significant capacity fade for each cycling protocol, the rate of the fade increased as the number of cycles increased within a given period of time. For this system, while resting at OCV after being charged to 3.9V, the Calendar Life test shows an average capacity retention of 93.8% (~C/2) from ~75 to 625 hours of total test time. Whereas the Cycle Life and Silicon Deep Dive protocols have markedly lower average capacity retentions of 31.7% (~C/2) from ~5 to 610 hours of total test time and 53.4% (~C/3) from ~155 to 610 hours of total test time, respectively.

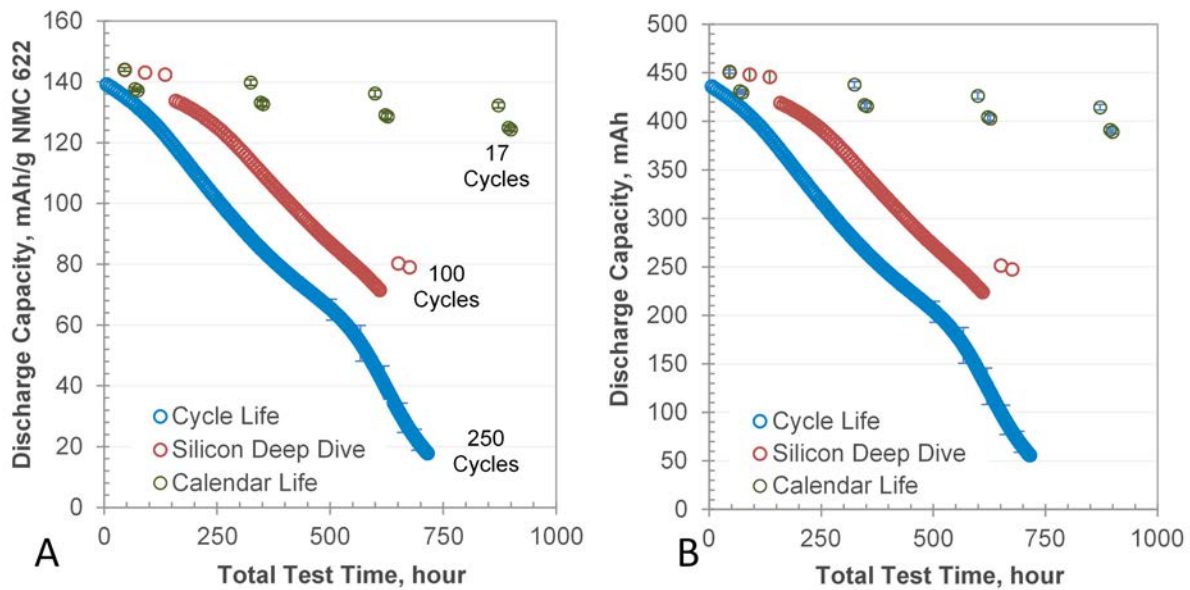


Figure IV-3: Average discharge capacities mAh/g of NMC622 (A) and mAh (B) as a function of total test time during the various cycling protocols of Cycle Life (blue), Silicon Deep Dive Protocol (red), and Calendar Life (green) for the Si-Gr//NMC622 in xx3450 pouch cells at 30 °C from 3.0 to 4.1 V. The formation data is not included here. The x-axis values were determined by the end of discharge per cycle. The plots shows average data from 4 pouch cells for each cycling protocol. A total of 12 cells were tested for this study. The error bars represent 2σ standard deviation for both the x and y axes

Furthermore, the overlay of the discharge capacity (mAh/g) and discharge energy density (mWh/g) as a function of cycle number for the Si-Gr//NMC622 pouch cells (Figure IV-4) suggest that the cells all fade similar to one another, regardless of the cycling rate and calendar rest period at an OCV of ~3.9 V. The average coulombic efficiencies (Figure IV-5) also track along each other with similar values and pattern of increasing up to ~99.5%, decreasing to ~99.0%, then increasing back up to ~99.3%. These results, along with Figure IV-3 suggest that calendar life at 3.9 V has less of an impact on the degradation of capacity retention than overall cycling. Further studies will be performed on these cells in the next fiscal year to continue to investigate the impact of various calendar conditions, such as voltage holds at multiple higher voltage limits.

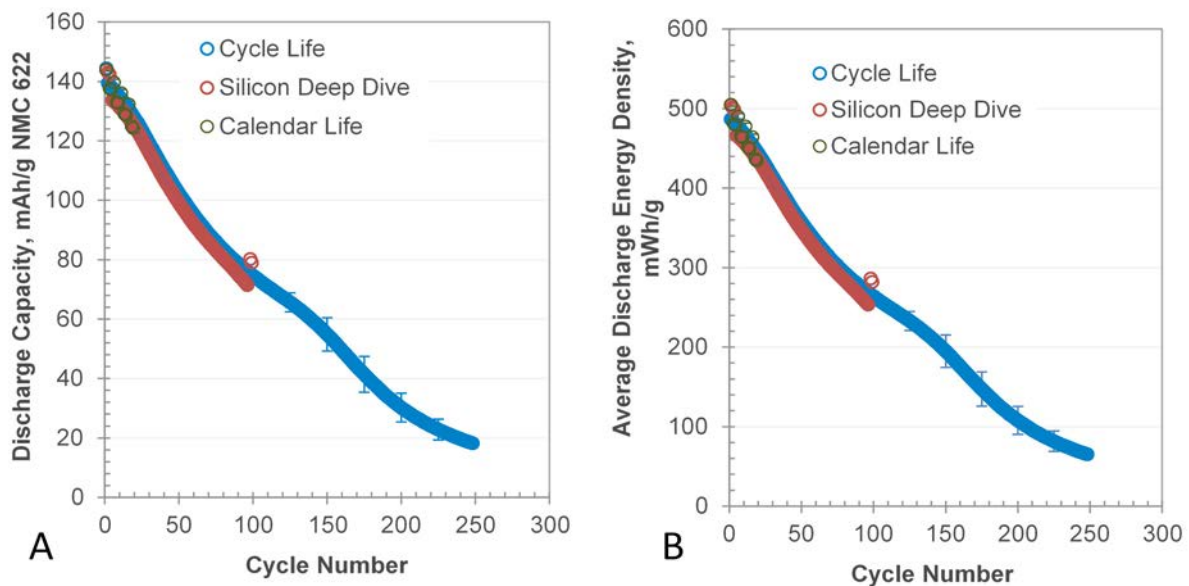


Figure IV-4: Average discharge capacity mAh/g of NMC622 (A) and energy density mWh/g of NMC622 (B) as a function of cycle number during the various cycling protocols of Cycle Life (blue), Silicon Deep Dive Protocol (red), and Calendar Life (green) for the Si-Gr//NMC622 in xx3450 pouch cells at 30 °C from 3.0 to 4.1 V. The formation data is not included here. The plots shows average data from 4 pouch cells for each cycling protocol. A total of 12 cells were tested for this study. The error bars represent 2σ standard deviation

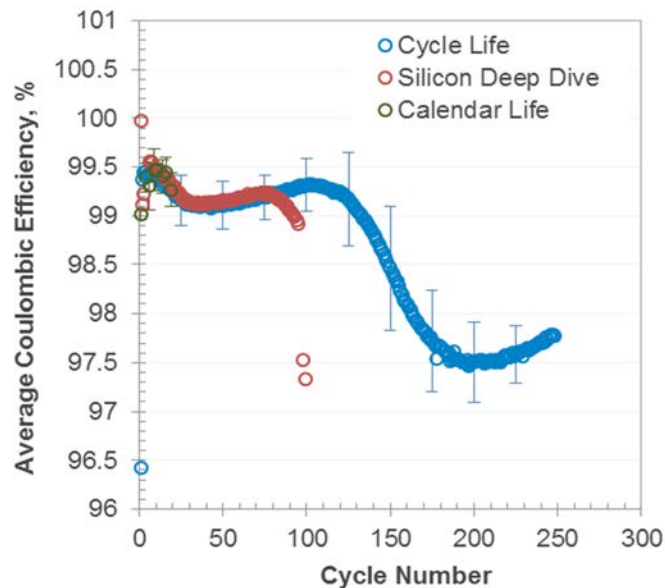


Figure IV-5: Average coulombic efficiency (%) as a function of cycle number during the various cycling protocols of Cycle Life (blue), Silicon Deep Dive (red), and Calendar Life (green) for the Si-Gr//NMC622 in xx3450 pouch cells at 30 °C from 3.0 to 4.1 V. The formation data is not included here. The plots shows average data from 4 pouch cells for each cycling protocol. A total of 12 cells were tested for this study. The error bars represent 2 $\sigma$  standard deviation.

Impedance measurements were also taken for the Silicon Deep Dive and Calendar Life protocols (Figure IV-6). The Silicon Deep Dive data series refers to the total test times of 134 and 650 hours, which corresponds to cycles 4 and 97, respectively. The Calendar Life data series refers to the total test times of 73, 351, 627, and 899 hours, which corresponds to cycles 2, 7, 12, and 17, respectively. The Calendar Life had an impedance rise from 22 to 25  $\Omega\text{-cm}^2$  at  $\sim 3.75$  V at the 627 hour mark. The Silicon Deep Dive had an impedance rise from 25 to 38  $\Omega\text{-cm}^2$  at  $\sim 3.75$  V at the 650 hour mark. While the Silicon Deep Dive protocol impedance has a statistically measurable increase, overall both testing protocols show a minimal rise if compared to a typical graphite//NMC system. However, the final 5 discharge pulses for the 97<sup>th</sup> cycle HPPC of the Silicon Deep Dive protocol could not fulfill the 10 second pulse time, thus there could be a significant impedance rise for the silicon since these pulses occur at the lower voltages of the full cell testing. This result, for the system and test conditions, suggests that calendar life is not detrimental to impedance. It even shows to be lower than a cycling protocol after a similar amount of time has passed, which could imply that the majority of the impedance rise is still coming from the positive electrode. As mentioned earlier, further studies will be performed on these cells, which are still on test at the time of this writing.

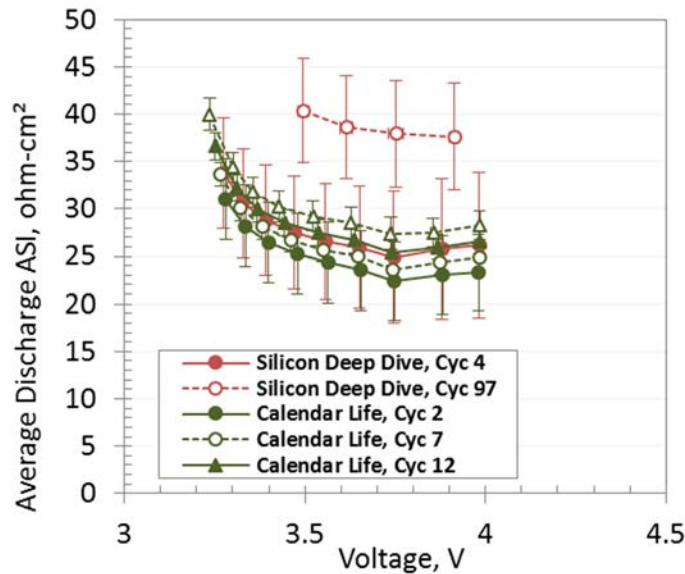


Figure IV-6: Average discharge ASI (area specific impedance) ohm-cm<sup>2</sup> as a function of OCV (open circuit voltage) before the discharge pulse during the various cycling protocols of Silicon Deep Dive (red) and Calendar Life (green) for the Si-Gr//NMC622 pouch cells at 30 °C. The plots shows average data from 4 pouch cells for each cycling protocol. A total of 8 cells were tested using the HPPC protocol. The error bars represent 2σ standard deviation

The Si-Gr//NMC622 pouch cells Cycle Life protocol allows for a comparison to the previous pouch cell builds using NMC532. Figure IV-7 shows the average discharge capacity of various silicon-graphite electrodes (0, 5, 10, and 15 wt.% silicon) matched against the baseline NMC532, and now the NMC622 (versus only 15 wt.% silicon). It is clear from this figure that the dominant cause of the rapid capacity fade is attributable to the silicon content. Switching to NCM622 as the cathode did not change the capacity fade rate.

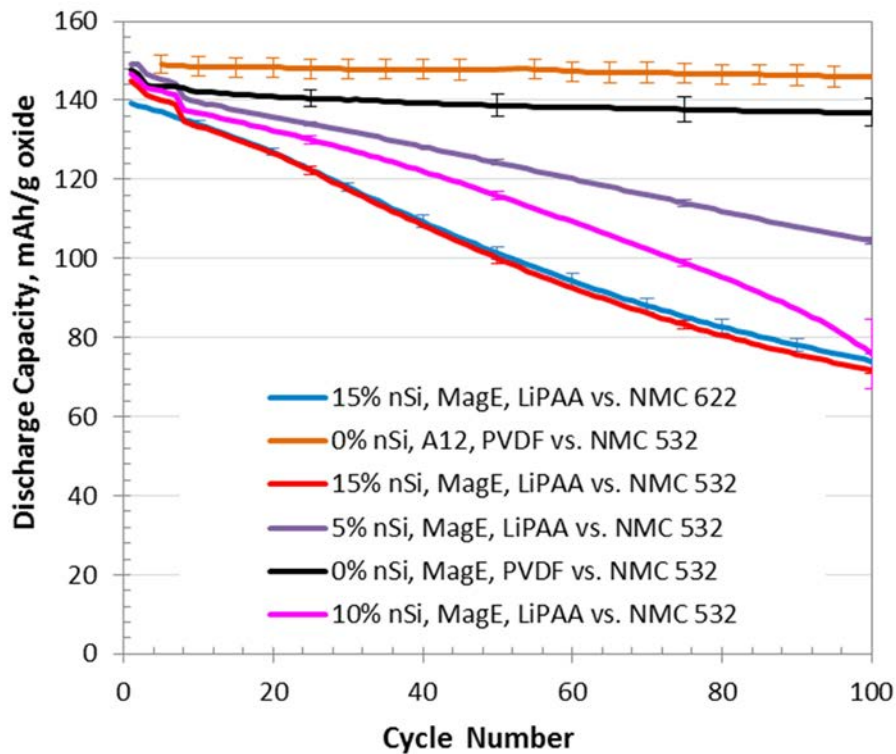


Figure IV-7: Average cycling performance of various generations of the Si-Gr//NMC532 & NCM622 in xx3450 pouch cells at 30 °C, with complementary Gr//NMC523 in xx3450 pouch cells representing baseline data, following the initial formation procedure. The cells were cycled using a C/3 charge and C/2 discharge rate. The error bars represent 2σ standard deviation. The error bars represent 2σ standard deviation

To support the efforts of the Next Generation Anodes (Silicon Deep Dive) Project, an excess of 10 meters of single-sided negative electrode containing 15wt.% silicon (NanoAmor 50-70nm), 73wt.% graphite (Hitachi MagE), 2wt.% Timcal C45 carbon, and 10wt.% LiPAA (LiOH titration) was delivered to the project team members and also made available to the Electrode Library. Other electrodes such as the 10 wt.% silicon, 5 wt.% silicon, and graphite-only single-side electrodes were also delivered upon request. The electrodes were designed to matching to the Electrode Library (~2 mAh/cm<sup>2</sup>) to enhance the versatility of the electrodes to be tested against a variety of cathode materials.

## Voltage Window Study

The CAMP Facility regularly adds electrodes comprising relevant battery materials to the Electrode Library that are capacity matched for various voltage windows, where all the anodes and cathodes are designed to have an n:p ratio of 1.05 to 1.20. In order to design the proper n:p ratio, appropriate half-cell testing (vs. Li<sup>+</sup>/Li) is required on cathodes in multiple voltage windows. In the case for the HEHV project, the anode is locked as a graphite electrode (Electrode ID: A-A002A), and these results are discussed in Section IV.C of this report. Additional cathodes were tested for comparison under the same voltage windows and are tabulated in Table IV-3.

**Table IV-3: Voltage Window Study Materials and Corresponding Electrode Details**

Material	Electrode ID	Composition, wt.%	Coating Loading, mg/cm <sup>2</sup>	Coating Thickness, μm	Porosity, %	Coating Density, g/cm <sup>3</sup>
Toda NCA	S-C002	86/4/2/8	11.59	45	30.8	2.73
BTR LCO	A-C010	94/2/4	14.53	49	35.0	2.97
Toda NMC 111	LN3032-13-2	90/5/5	11.18	40	32.0	2.80
Toda NMC 433	LN3061-25-2	90/5/5	12.57	45	31.5	2.79
Toda NMC 442	A-C014	90/5/5	11.76	43	33.0	2.73
Toda NMC 532	A-C013	90/5/5	11.33	42	33.5	2.70
ECOPRO NMC 622	A-C011	90/5/5	10.03	38	35.5	2.64
Targray NMC 811	LN2486-32-4	90/5/5	9.72	40	40.6	2.43
Toda HE5050	A-C006	92/4/4	6.4	26	36.1	2.46

Composition: Active Material/Timcal C45, Timcal Super P Li, Timcal SFG-6/Solvay 5130 PVDF

The voltage windows investigated were 3.0 to 4.2 V, 3.0 to 4.3 V, 3.0 to 4.4 V, 3.0 to 4.5 V, 3.0 to 4.6 V, and 3.0 to 4.7 V versus Li<sup>+</sup>/Li. Each cathode with each voltage window was evaluated using 4 coin cells. The total number of coin cells made per cathode was 24. All cells in this study used a baseline 25 μm PP/PE/PP tri-layer separator and electrolyte consisting of 1.2 M LiPF<sub>6</sub> in EC:EMC (3:7 wt.%). The cells were tested on a MACCOR Series 4000 cycler at 30°C with 3 formation cycles at a ~C/10 rate, 2 cycles at a ~C/24 rate, 3 cycles at a ~C/10 rate, 3 cycles at a ~C/5 rate, 3 cycles at a ~C/2 rate (C/5 charge), 3 cycles at a ~1C rate (C/5 charge), and 3 cycles at a ~2C rate (C/5 charge). The cells cycled for a total of 20 cycles. Cycle #1 charge (initial delithiation), cycle #5 discharge (reversible lithiation at C/24), and cycle #8 discharge (reversible lithiation at C/10) were evaluated. These results are summarized in Figure IV-8. (Cycle #17 (reversible lithiation at 1C rate) is also of interest for matching, but is not included in this report.)

The capacity values summarized in Figure IV-8 are used to design proper capacity matched negative-positive electrode pairs. It is clear from an inspection of this figure that the cathode HE5050 stands out as a high capacity material. However, this lithium-manganese-rich (LMR-NMC) cathode was investigated thoroughly in the Voltage Fade Project, and dropped as a baseline material due to the thermodynamically based voltage fade problem. While LCO shows a significant increase of capacity when  $>4.4$  V vs.  $\text{Li}^+/\text{Li}$  for the 1st delithiation Figure IV-8 (LEFT), there are known issues of “lattice defects, oxygen loss, transition metal dissolution, and/or structural degradation” at higher voltages [1]. The degradation of performance for LCO at higher voltages is observed during the 8th discharge Figure IV-8 (RIGHT), the corresponding voltage curve for the 4.7 V upper cutoff limit will be shown later in Figure IV-12. The plots above suggest the NMC811 material as the preferred cathode material when choosing a voltage limit of  $\leq 4.4$  V vs.  $\text{Li}^+/\text{Li}$ . The capacity data  $\geq 4.6$  V suggest that NMC622 and NMC811 are superior choices provided that cycle life and safety goals can be achieved at this high potential.

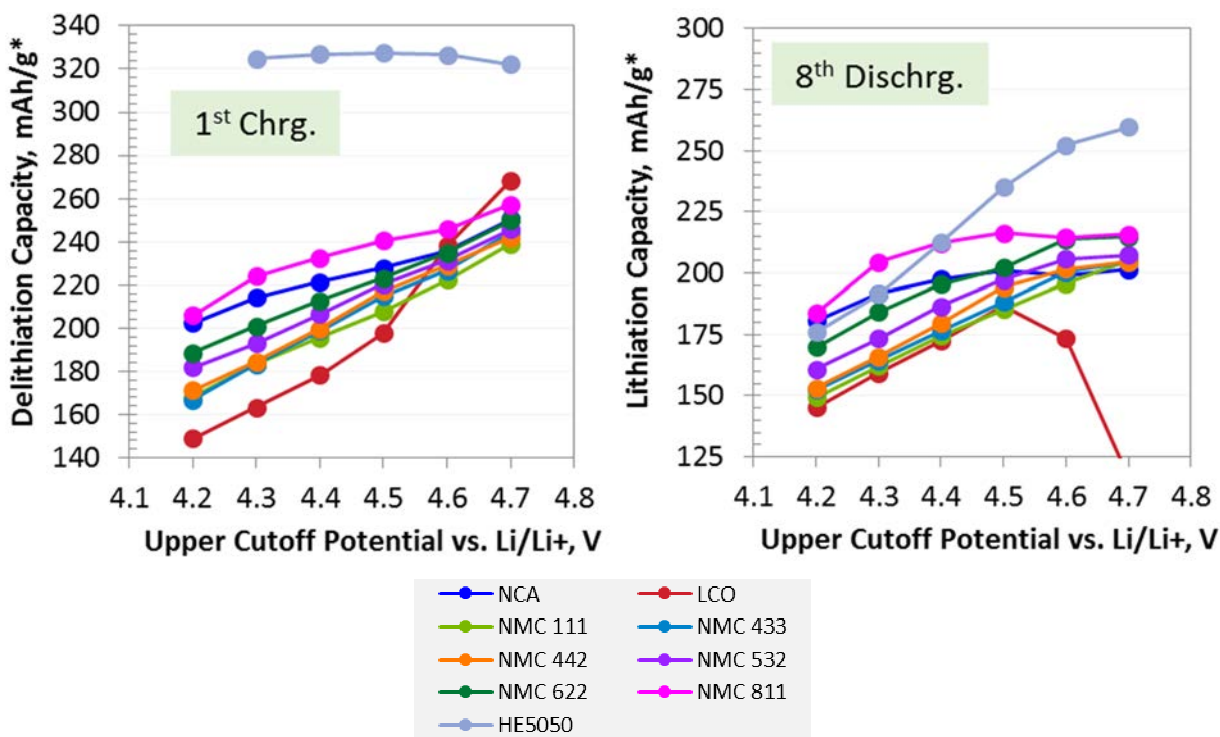


Figure IV-8: Average First Delithiation Capacity at C/10 Rate vs. Upper Cutoff Potential (LEFT) and Average Eighth Cycle Lithiation Capacity at C/10 Rate vs. Upper Cutoff Potential (RIGHT). All half-cell coin cells tested at 30 °C using 1.2M  $\text{LiPF}_6$  in EC:EMC (3:7 by wt.). Refer to the legend on the right to identify the series. \* weight of oxide

The energy density values in Figure IV-9 combine the impact of the operating voltage and achieved capacity. These values are critical for the evaluation of a material’s impact on a practical cell. As noted before, the degradation of performance for LCO at higher voltages is observed during the 8th discharge (RIGHT). The plots above suggest the NMC811 material as the preferred cathode material when choosing a voltage limit of  $\leq 4.5$  V vs.  $\text{Li}^+/\text{Li}$ . Likewise, the energy data  $\geq 4.6$  V suggest that NMC622 and NMC811 are superior choices provided that cycle life and safety goals can be achieved at this high potential.

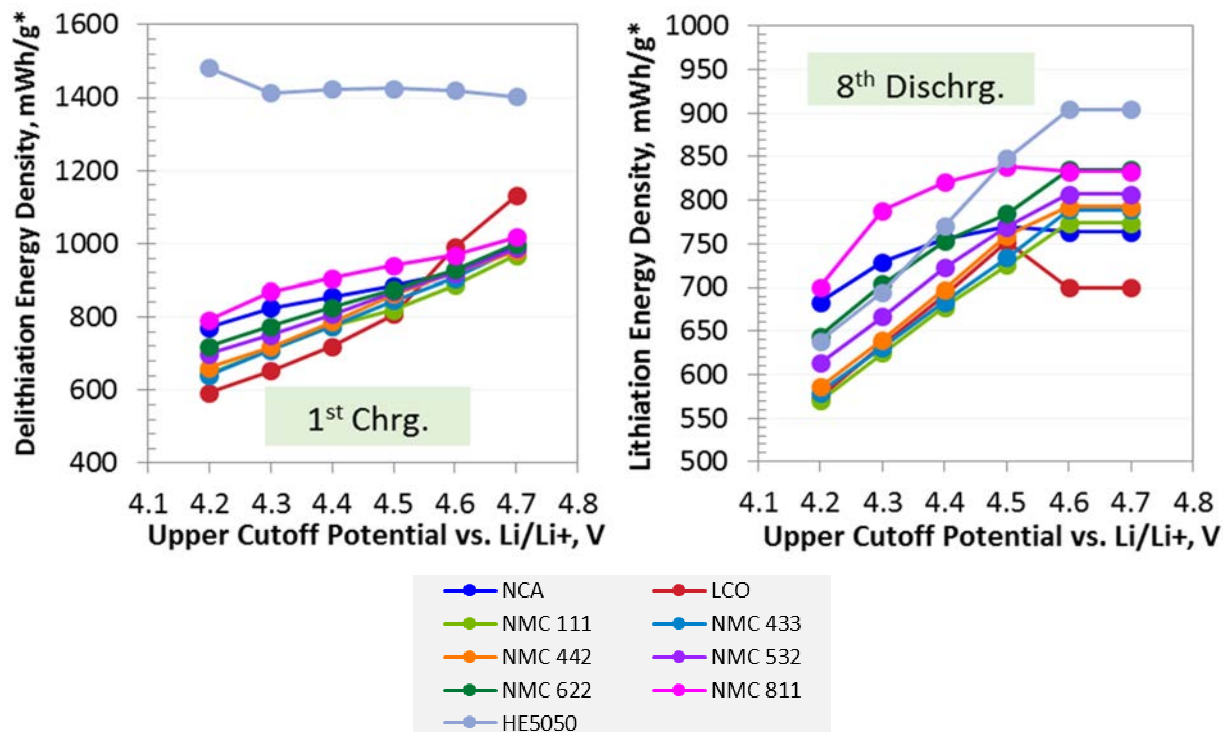


Figure IV-9: Average First Delithiation Energy Density at C/10 Rate vs. Upper Cutoff Potential (LEFT) and Average Eighth Cycle Lithiation Energy Density at C/10 Rate vs. Upper Cutoff Potential (RIGHT). All half-cell coin cells tested at 30 °C using 1.2M LiPF<sub>6</sub> in EC:EMC (3:7 by wt.). Refer to the legend on the right to identify the series. \* weight of oxide

The average charge average voltage (LEFT) and average discharge average voltage (RIGHT) for the 5<sup>th</sup> cycle at ~C/24 rate are reported for each of the cathode materials of interest in this study (Figure IV-10). The average voltages reported in these plots were calculated at end of charge (LEFT) and discharge (RIGHT) for the 5<sup>th</sup> cycle by calculating the total Wh ÷ total Ah, then taking the average of these values for each coin cell set.

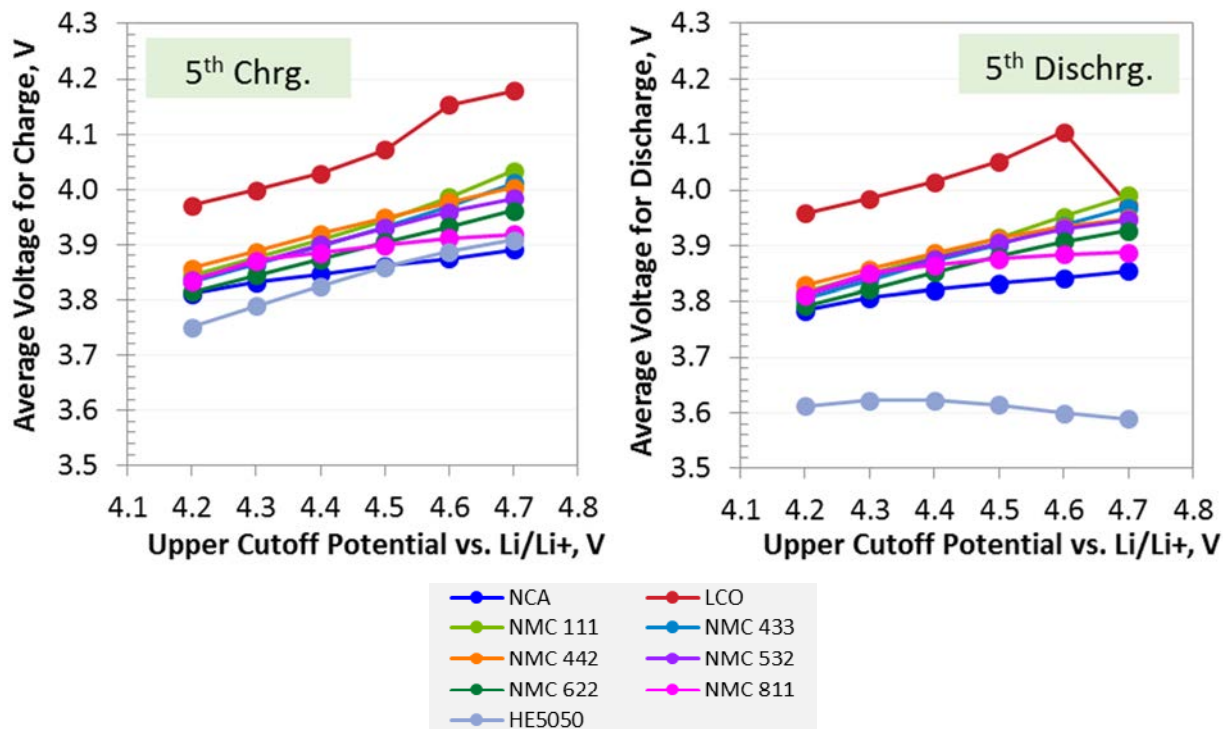


Figure IV-10: Average Charge Voltage at C/24 Rate vs. Upper Cutoff Potential (LEFT) and Average Discharge Voltage at C/24 Rate vs. Upper Cutoff Potential (RIGHT). All half-cell coin cells tested at 30 °C using 1.2M LiPF<sub>6</sub> in EC:EMC (3:7 by wt.). Refer to the legend on the right to identify the series.

Of particular interest to the BatPac modelers is the voltage at 50% depth of discharge (DOD) and at 50% state of charge (SOC). Figure IV-11 provides the charge voltage @ 50% SOC (LEFT) and discharge voltage @ 50% DOD (RIGHT) for the 5<sup>th</sup> cycle at ~C/24 rate for each of the materials of interest in this study. Voltages reported in these plots were determined by selecting the voltage value that was nearest the capacity at 50% DOD (on the discharge) and 50% SOC (on the charge) for each cell, then averaging these voltage values for each coin cell set. There are subtle differences between the voltage values of Figure IV-10 and Figure IV-11 for most of the materials. The one major exception is for the discharge voltages of HE5050.

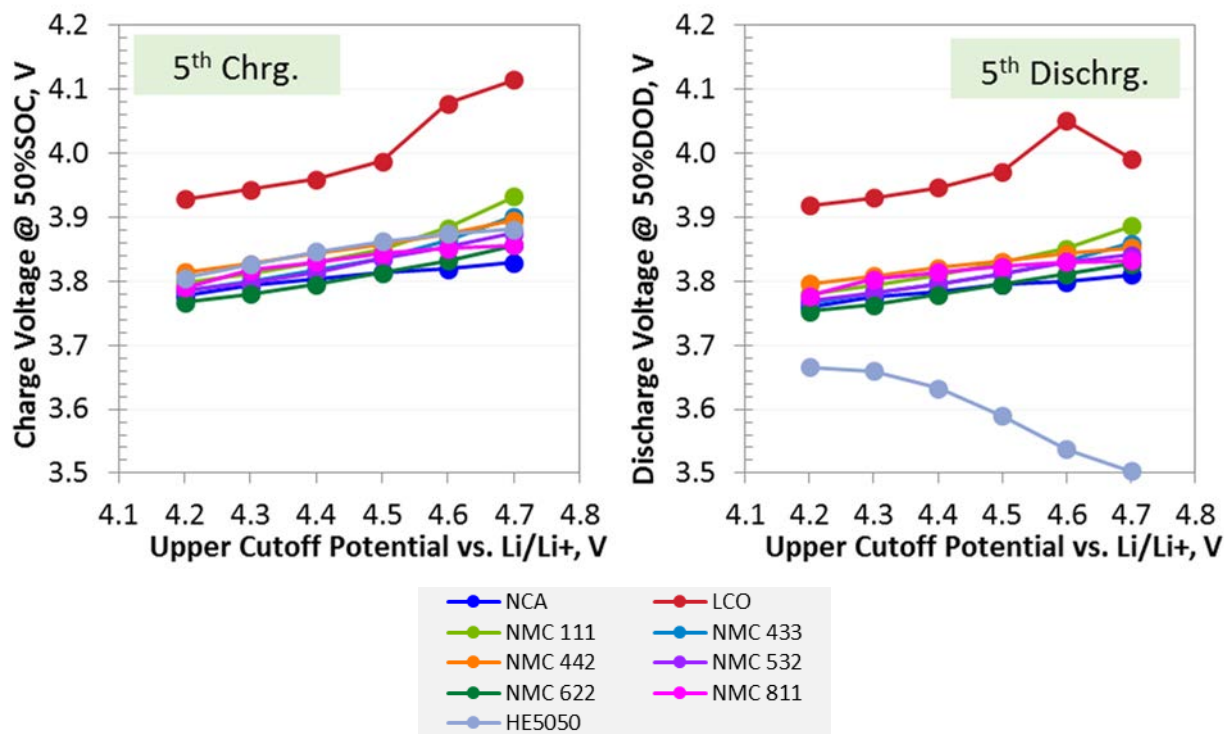


Figure IV-11: Charge Voltage at 50% SOC at C/24 Rate vs. Upper Cutoff Potential (LEFT) and Discharge Voltage at 50% DOD at C/24 Rate vs. Upper Cutoff Potential (RIGHT). All half-cell coin cells tested at 30 °C using 1.2M LiPF<sub>6</sub> in EC:EMC (3:7 by wt.). Refer to the legend on the right to identify the series

The plots in Figure Figure IV-12 show the representative performance for the 1<sup>st</sup> cycle (~C/10) and the 5<sup>th</sup> cycle (~C/24) of the various cathode materials when the upper cut off voltage was set to 4.7 V vs. Li/Li<sup>+</sup>. The voltage profile curves vs. energy density and dQ/dV curves help in the evaluation of the materials performance. They also highlight points of interest, such as the dQ/dV peak at~4.2 V for both NMC811 and NCA. The voltage window screening study over these various materials has already been helpful to the CAMP Facility in the design of NMC532, NMC622, NMC811, and NCA single-sided electrode pairings in the Electrode Library for both lower voltages and 4.4 V full cell cycling windows. The electrodes in Table IV-4 were added to the Electrode Library in FY16 to support the ABR High-Energy High-Voltage Project.

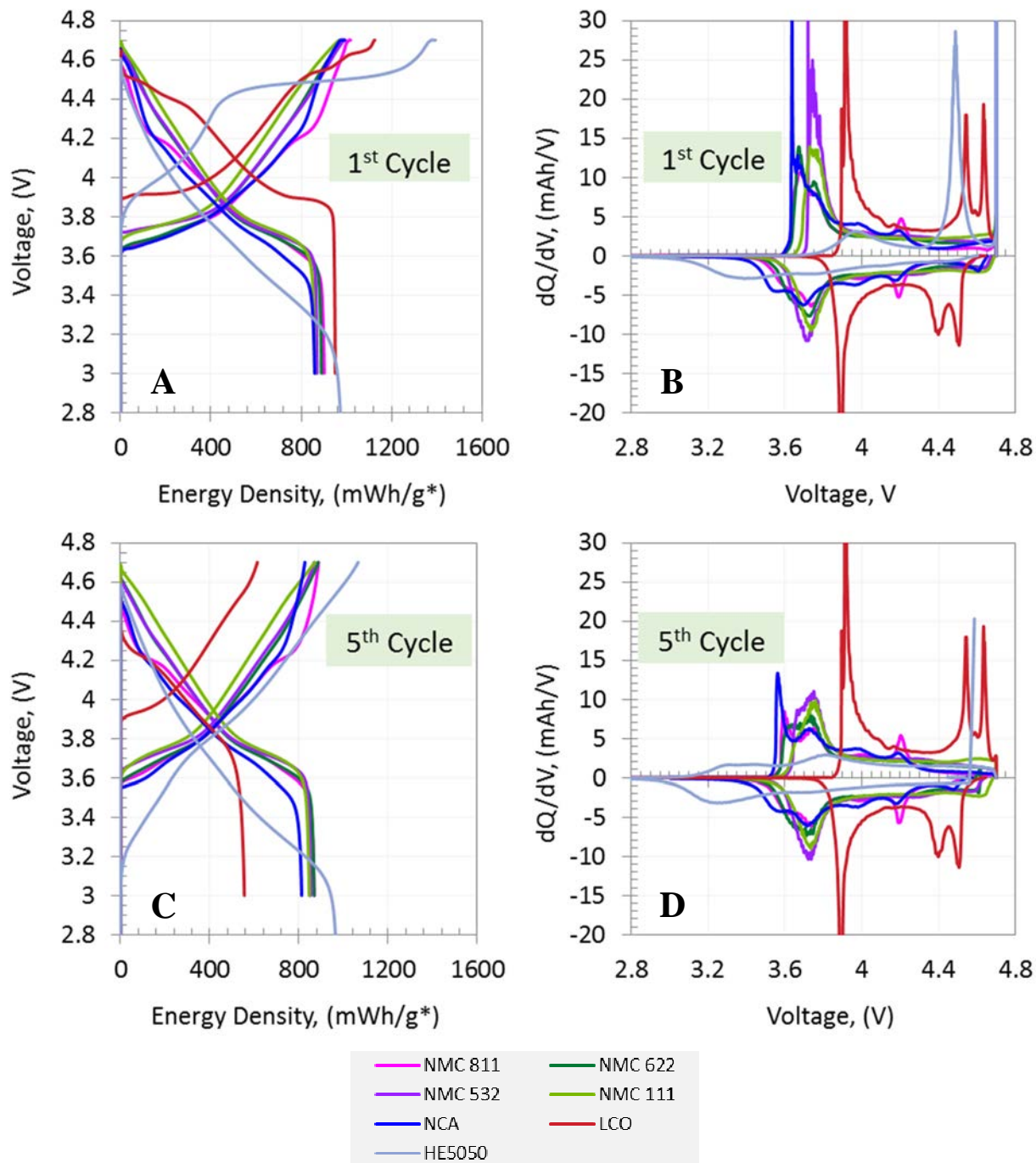


Figure IV-12: Representative energy density voltage profile curves for the 1<sup>st</sup> (A) and 5<sup>th</sup> (C) cycles. Representative dQ/dV curves for the 1<sup>st</sup> (B) and 5<sup>th</sup> (D) cycles. All half-cell coin cells tested from 3.0 to 4.7 V at 30 °C using 1.2M LiPF<sub>6</sub> in EC:EMC (3:7 by wt.). Refer to the legend on the right to identify the series. \* weight of oxide

**Table IV-4: Baseline Electrodes Developed for ABR High Energy-High Voltage Project**

Cathode: AC018	Cathode: A-C019	Cathode: A-C020
90% wt% ECOPRO NCM 622 5 wt% Timcal C45 5 wt% Solvay 5130 PVDF	90%wt% Targray NCM 811 5 wt% Timcal C45 5 wt% Solvay 5130 PVDF	90%wt% Targray NCM 811 5 wt% Timcal C45 5 wt% Solvay 5130 PVDF
<i>Matched for 4.4V full cell cycling</i> Al Foil Thickness: 20 $\mu\text{m}$ Al Foil Loading: 5.19 $\text{mg}/\text{cm}^2$ Total Electrode Thickness: 52 $\mu\text{m}$ Coating Thickness: 32 $\mu\text{m}$ Porosity: 32.7% Total Coating Loading: 8.82 $\text{mg}/\text{cm}^2$ Total Coating Density: 2.76 $\text{g}/\text{cm}^3$	<i>Matched for 4.4V full cell cycling</i> Al Foil Thickness: 20 $\mu\text{m}$ Al Foil Loading: 5.36 $\text{mg}/\text{cm}^2$ Total Electrode Thickness: 52 $\mu\text{m}$ Coating Thickness: 32 $\mu\text{m}$ Porosity: 36.3% Total Coating Loading: 8.34 $\text{mg}/\text{cm}^2$ Total Coating Density: 2.61 $\text{g}/\text{cm}^3$	<i>Matched for 4.2V full cell cycling</i> Al Foil Thickness: 20 $\mu\text{m}$ Al Foil Loading: 5.36 $\text{mg}/\text{cm}^2$ Total Electrode Thickness: 53 $\mu\text{m}$ Coating Thickness: 33 $\mu\text{m}$ Porosity: 32.5% Total Coating Loading: 9.12 $\text{mg}/\text{cm}^2$ Total Coating Density: 2.76 $\text{g}/\text{cm}^3$
Made by CAMP Facility	Made by CAMP Facility	Made by CAMP Facility

### Examine Performance of Lithium-ion Cells with LiFSI Salt Containing Electrolytes

Many approaches are being actively pursued at Argonne to accelerate the commercialization of silicon-based cells that are viable for use in batteries for vehicular applications. An important focus area is the development of electrolyte systems that enhance the stability of the silicon electrode-electrolyte interface. This interface is continually disrupted during silicon expansion and contraction often exposing fresh surfaces for SEI formation that trap additional lithium. Electrode and cell lifetimes are strongly dependent on the electrolyte solvents, salts and additives. For example, cells with electrolytes containing  $\text{LiPF}_6$  salt and conventional alkyl carbonate solvents display poor cycle life. However, the addition of fluoroethylene carbonate (FEC) and/or vinylene carbonate (VC) to these conventional systems cause remarkable improvements in cell lifetimes. An electrolyte salt that has generated significant interest in recent years is lithium bis(fluorosulfonyl)imide  $\text{Li}[\text{N}(\text{SO}_2\text{F})_2]$ , also known as LiFSI. This salt is reported to have higher ionic conductivity, better high temperature stability, and improved stability towards hydrolysis than the commonly used  $\text{LiPF}_6$  salt.

Research literature contains several studies of half-cells (Li-metal counter electrode) with the LiFSI salt. However, many of these studies containing electrodes with small mass loadings; the cyclability of electrodes with high mass loadings in a full-cell configuration is rarely described. Therefore, we examined the performance of full cells with LiFSI-bearing carbonate-based electrolytes, silicon-graphite negative electrode (also referred to as Si-Gr) and  $\text{Li}_{1.03}(\text{Ni}_{0.5}\text{Mn}_{0.3}\text{Co}_{0.2})_{0.97}\text{O}_2$ -based positive electrodes (also referred to either as oxide or NMC532). The silicon-graphite electrode was developed at CAMP as a drop-in replacement for conventional graphite-based electrodes; it is physically robust, highly uniform, and very flexible even at capacity loadings exceeding 3  $\text{mAh}/\text{cm}^2$ . The NMC532 electrode and the LiFSI-based electrolytes were prepared at Argonne from commercially-available constituents. The performance of the LiFSI-containing cells was compared to performance of our baseline  $\text{LiPF}_6$ -containing cells.

All electrodes used in these experiments were fabricated at the CAMP facility. The positive electrode contained 90 wt.% NMC532, 5 wt.% C45 carbon and 5 wt.% PVdF (polyvinylidene fluoride) binder. The negative electrode (Si-Gr) contained 73 wt.% graphite, 15 wt.% nanosilicon (50-70 nm), 2 wt.% carbons, and 10 wt.% LiPAA binder (450 kDa); the latter was introduced as an aqueous solution (9.4 wt.%) at pH 6.3 prepared by titration of PAA (polyacrylic acid) with lithium hydroxide. The main electrolyte used the 1.2 M LiFSI in EC:EMC (3:7 w/w) formulation. Electrolytes with 10 wt.% FEC or 10 wt.% VC was added to the main formulation were also prepared. The full cell tests were conducted in single-layer xx3450-type pouch cells assembled in a dedicated climate-controlled dry-room with a dew point less than  $-42^\circ\text{C}$  (<100 ppm moisture). These stack-type cells contained two manually-aligned electrode layers (one single-sided positive and one single-sided negative electrode) separated by a single sheet of Celgard 2325 (PP/PE/PP) separator. The positive electrode had an average coating area of 14.1  $\text{cm}^2$  and the negative electrode had an average coating area of 14.9  $\text{cm}^2$ ; the larger negative electrode area reduces the probability of lithium plating during electrochemical cycling. The electrolyte of interest was added by pipette to the single open edge of the pouch,

which was then subjected to two 18 s vacuum and air-refill stages in a vacuum sealer to minimize air pockets and enhance electrode wetting by the electrolyte. After these soak and degassing steps, the final side of the pouch was heat-sealed while the cell was under vacuum.

For the electrochemical tests, the cells were fixed to rigid, nonconductive boards with female banana plugs in 2 rows of 2 cells per fixture layer. Standard stainless steel plates, xx3450-sized acrylic sheets, springs, and wing nuts were used to apply added localized stack pressure to the cells; the initial stack pressure was estimated to be 15 kPa for each pouch cell. All cycling tests were performed at 30°C using a MACCOR Series 4000 Test System. The cycling was conducted in the 3.0-4.1 V range and included tests to obtain capacity retention and impedance rise information. The upper cutoff voltage (UCV) was limited to 4.1 V to minimize the likelihood of Al current-collector pitting that is known to occur at full cell voltages > 4.2 V. The lower cutoff voltage (LCV) was set at 3.0 V because prior experiments showed that lower voltages shorten cell life. The full cell data were complemented by half-cell capacity data obtained in 2032-type coin cells (1.6 cm<sup>2</sup> area electrodes). These cells contained the Si-Gr electrode, Celgard 2325 separator, and a Li-metal counter electrode. Each electrolyte was examined mainly to determine features associated with solid electrolyte interphase (SEI) formation. These cells were cycled in the 1.5-0.005 V vs. Li/Li<sup>+</sup> range with a 0.085 mA/cm<sup>2</sup> current at room temperature.

Figure IV-13 show differential capacity (dQ/dV) profiles calculated from the capacity-voltage data collected on the Li//Si-Gr cells containing the previously stated electrolytes; only data from the first Si-Gr lithiation cycle is shown. Figure IV-13 is divided into two panels for clarity; the upper panel shows data for the LiFSI and LiFSI-VC cells, and the lower panel shows data for the LiFSI-FEC and LiPF<sub>6</sub>-FEC cells. The data show that electrolyte reduction is initiated for the cells in the following order: LiFSI-FEC, LiPF<sub>6</sub>-FEC, LiFSI-VC and LiFSI, with peaks at ~1.2 V vs. Li<sup>+</sup>/Li, at ~1.04 V, at ~0.74 V, and at ~0.58 V, respectively.

Some observations from the data in Figure IV-13 are as follows: (i) the peak maxima for the cells containing VC and FEC are higher than that for the LiFSI cell without additives, which suggests that these compounds are reduced earlier than the carbonates in the LiFSI cell; (ii) the differences in peak maxima for the LiFSI-FEC and LiPF<sub>6</sub>-FEC suggest that the solvation structure of FEC varies with the electrolyte salt; (iii) the dQ/dV data for the LiPF<sub>6</sub>-FEC cell briefly changes sign, from negative to positive. This sign change could result from the breakdown of a resistive film formed during initial reduction reactions at the electrolyte-silicon interface; and (iv) additional peaks at 0.85 V and 0.92 V are seen in the LiFSI-FEC and LiPF<sub>6</sub>-FEC data, which suggests further solvent reduction.

The first cycle capacity-voltage profiles for the Si-Gr//NMC532 pouch cells containing the LiFSI, LiFSI-VC, LiFSI-FEC and LiPF<sub>6</sub>-FEC electrolytes are shown in Figure IV-14 (left panel). At first glance, the cycling behavior for the various cells appears similar. A closer look at the 1.8-3.4 V charge curve (see inset, Figure IV-14) reveals distinct inflections in the profiles, especially for the FEC-containing cells. More specifically, the LiPF<sub>6</sub>-FEC cell shows a brief drop in voltage at ~2.64 V before the voltage starts rising again. The LiFSI-FEC cell does not show this voltage drop; however, its profile deviates from that of the LiFSI cell around 2.4 V. The LiFSI-VC cell profile also shows a small deviation from that of the LiFSI cell around 2.8 V. The inset table shows that charge capacity of the LiFSI cells decreases slightly with VC and FEC addition. However, the discharge capacity and coulombic efficiency (CE) are marginally better for the LiFSI-VC cell. Note that the coulombic efficiencies for all cells are around 80%. Higher efficiencies, around 90%, are obtained when the LCV is lowered to 2.5 V; however, as indicated previously, cell lifetimes decrease when the LCV is reduced to 2.5 V.

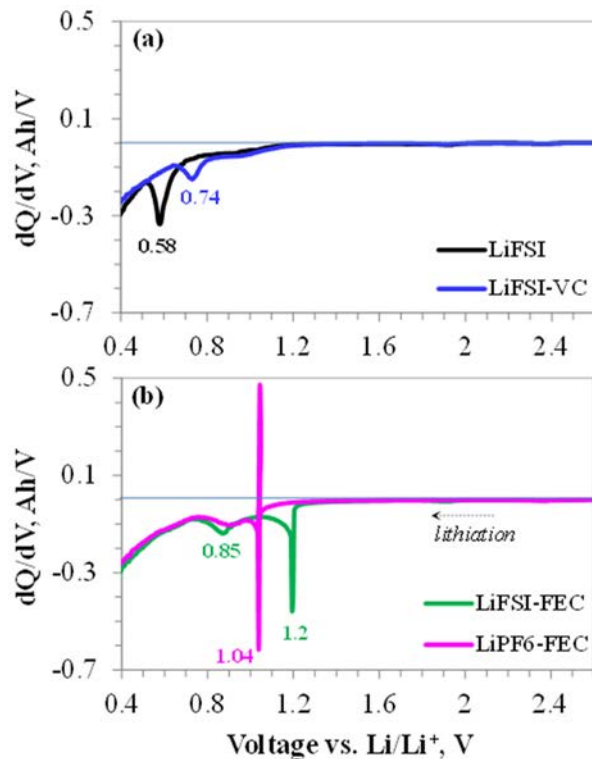


Figure IV-13: Differential capacity ( $dQ/dV$ ) vs. voltage profiles from Si-Gr//Li coin cells containing (a) LiFSI and LiFSI-VC and (b) LiFSI-FEC and LiPF<sub>6</sub>-FEC electrolytes, for the first lithiation cycle showing peaks associated with SEI formation. The peaks associated with active material lithiation, at voltages <0.4 V vs. Li/Li<sup>+</sup>, are not shown

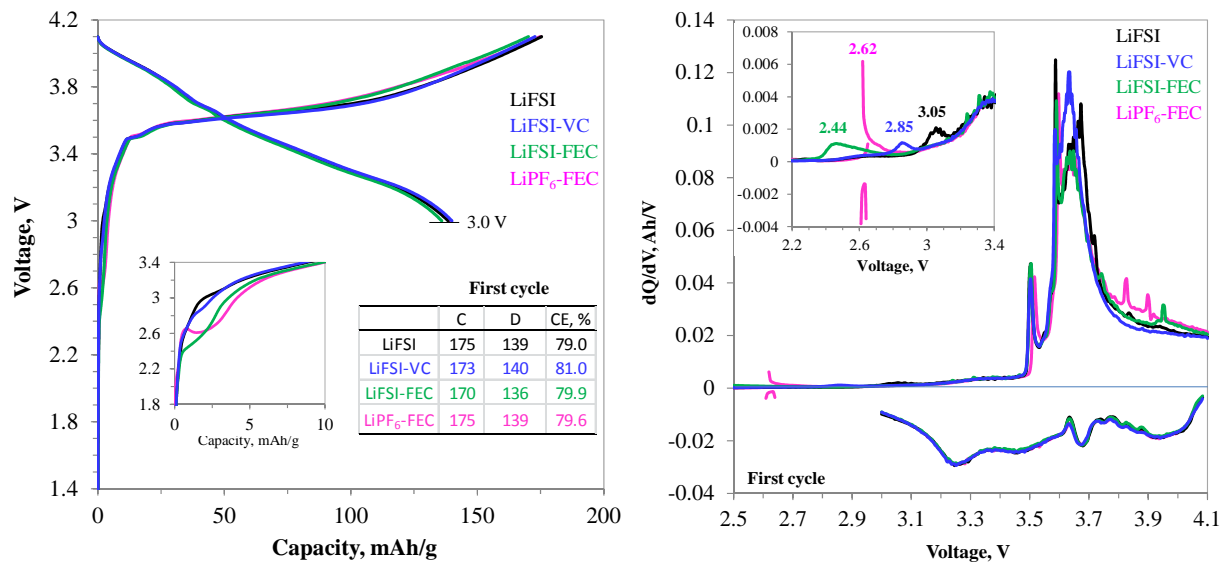


Figure IV-14: (Left panel) First cycle capacity-voltage profiles from Si-Gr//NMC532 pouch cells containing the LiFSI, LiFSI-VC, LiFSI-FEC, and LiPF<sub>6</sub>-FEC electrolytes. The data were obtained at a  $\sim C/20$  rate in the 3.0-4.1 V range at 30 °C. The inset figure is an expanded view of the 1.8-3.4 V range. The inset table shows the charge (C)/discharge (D) capacities (in mAh/g) and coulombic efficiencies (CE) of the cycle; the g in mAh/g refers to grams of oxide in the positive electrode

The right panel of Figure IV-14 shows differential capacity profiles calculated from the first cycle capacity-voltage profiles. The peaks observed in the 3.3-4.1 V range are mostly associated with lithiation and delithiation of the various electrode components in both the positive and negative electrodes. The peaks in the 2.2-3.2 V range (see inset) corresponds to the early onset voltage-profile inflections discussed in Figure IV-14

(left panel), and their peak shapes and locations differ based on the electrolyte composition. For the LiFSI cell the peak maximum is at 3.05 V, whereas for the LiFSI-VC and LiFSI-FEC cells the maxima are at 2.85 V and 2.44 V, respectively. The behavior of the LiPF<sub>6</sub>-FEC cell is distinctly different; after an initial increase, the dQ/dV values become negative around 2.64 V, and remains so for a brief period, before rising sharply and displaying a maxima at 2.62 V. This change in sign in the dQ/dV data directly results from the peak seen in the LiPF<sub>6</sub>-FEC initial charge data (inset, Figure IV-14), where the potential drops briefly before rising again. As such, it is a clear marker for this behavior, which can otherwise appear subtle in the voltage profiles themselves. The locations, shapes, and electrolyte composition dependence of peaks in the full cell data (Figure IV-14) are consistent with the electrochemical reduction reactions seen in the half-cell data of the Si-Gr electrodes (Figure IV-13).

The behavior of the Si-Gr//NMC532 full cells over 100 cycles is shown in Figure IV-15. In this figure cycles 1-3 and 97-100 are at a  $\sim C/20$  rate, whereas cycles 4-94 are at a  $\sim C/3$  rate. The initial discharge capacities of the various cells are similar; at the 3rd cycle, the capacities are between 136 (LiFSI-FEC) to 140 (LiFSI-VC) mAh/g, where g refers to the oxide content of the positive electrode. The coulombic efficiencies (CEs) at the 3rd cycle are 98.6% (LiFSI-VC), 98.4% (LiFSI-FEC), 98.3% (LiPF<sub>6</sub>-FEC data) and 97.1% (LiFSI); i.e., the efficiencies are lowest for LiFSI, but are in the same range for the other cells. On further C/3 cycling, the capacity of all cells decline (see Figure IV-15a). The fastest and slowest capacity decline is observed for the LiFSI and LiFSI-VC cells, respectively. The LiFSI-FEC and LiPF<sub>6</sub>-FEC cells show an intermediate capacity decline; the capacities for these cells at cycle 100 cycle are similar. The capacity retention at the 100th cycle (relative to the 1st cycle) decreases as follows: 61.4% (LiFSI-VC), 58.1% (LiFSI-FEC), 56.1% (LiPF<sub>6</sub>-FEC data), 18.7% (LiFSI), which is similar to the 3rd cycle CE trend shown above. The capacity retention is consistent with the CE values (at C/3 rate) with cycle number (see Figure IV-15b).

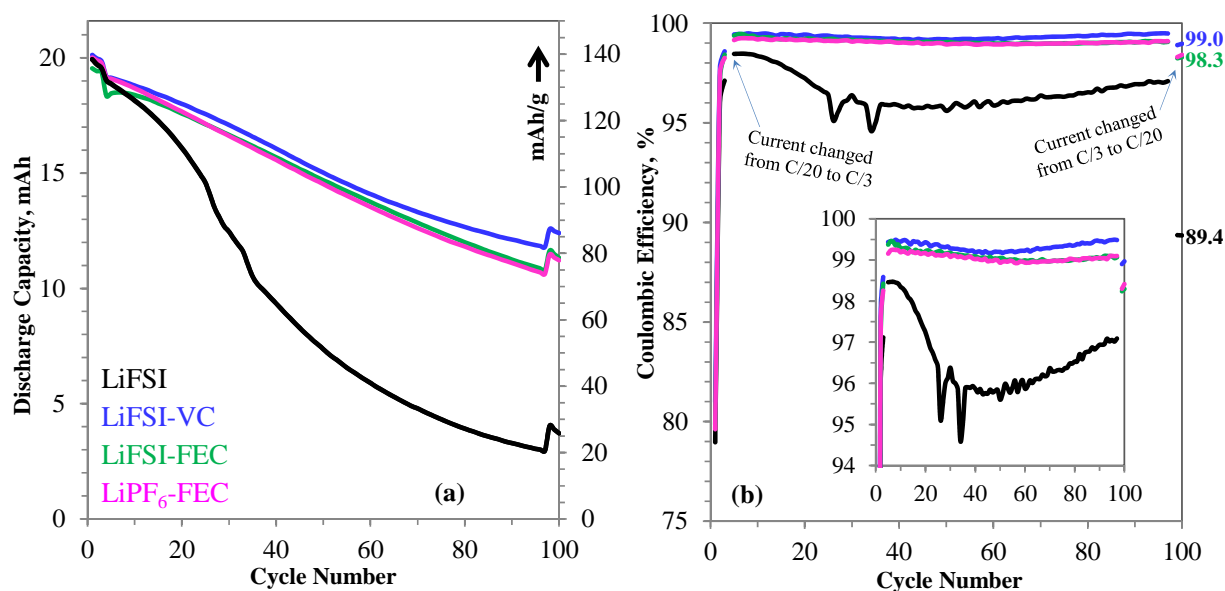


Figure IV-15: Discharge capacity (a) and Coulombic efficiency (b) vs. cycle number for Si-Gr//NMC532 pouch cells containing the LiFSI, LiFSI-VC, LiFSI-FEC, and LiPF<sub>6</sub>-FEC electrolytes. The data were obtained in the 3.0-4.1 V range at 30 °C; g refers to grams of oxide in the positive electrode. Cycles 1-3 and 97-100 are at a  $\sim C/20$  rate and cycles 4-94 are at a  $\sim C/3$  rate. The inset figure in (b) shows an expanded view of the C.E. axis, and highlights differences between the cells

In all cases, the CE is highest initially, shows a steady decrease, then rises again, i.e., it shows a “hammock” trend. For example, CE values for the LiFSI-VC cell are 99.5%, 99.2% and 99.5% at cycles 4, 50 and 97 respectively. The corresponding values for the LiFSI-FEC and LiPF<sub>6</sub>-FEC cells are 99.4%, 99.0%, 99.1% and 99.2%, 98.9% and 99.1% respectively. In contrast, the values for the LiFSI cell are 98.5%, 94.5% and 97%, consistent with its rapid capacity decline; the sharp peaks in this dataset, which indicates a higher charge-to-discharge ratio probably results from occasional fracturing and reformation of the negative electrode SEI layer. Finally, for all cells, the CE for the 100th cycle, which is at  $\sim C/20$  rate, is lower than the CE for the prior C/3 cycles, and is likely related to the longer measurement times for the C/20 cycles compared to that for the C/3 cycles.

For vehicular applications, in addition to excellent capacity retention, battery cells need to sustain high current pulses under rapid discharge and charge conditions without degrading significantly. This ability is often determined by the hybrid pulse power characterization (HPPC) tests, in which cell impedance is determined over its useable charge and voltage range. The area specific impedance (ASI) data for the various pouch cells, obtained by using the HPPC protocol, is shown in Figure IV-16. The initial ASI values are quite similar for all the cells, especially in the 3.4-4.0 V range. For example, at 3.7 V, the ASI values range from 29 (LiFSI) to 31 (LiFSI-VC); i.e., the values are the lowest for LiFSI and highest for the LiFSI-VC cell. Cell impedances are higher after the 100 charge-discharge cycles. We were unable to determine ASI values for the LiFSI cell because of its excessive capacity loss. For the other cells, however, the ASI values at 3.7 V are 42 (LiFSI-VC), 47 (LiFSI-FEC), 44 (LiPF<sub>6</sub>-FEC data). Although these data lie within a relatively narrow ASI band, the numbers indicate that the impedance increase is lowest for LiFSI-VC and highest for the LiFSI-FEC cell.

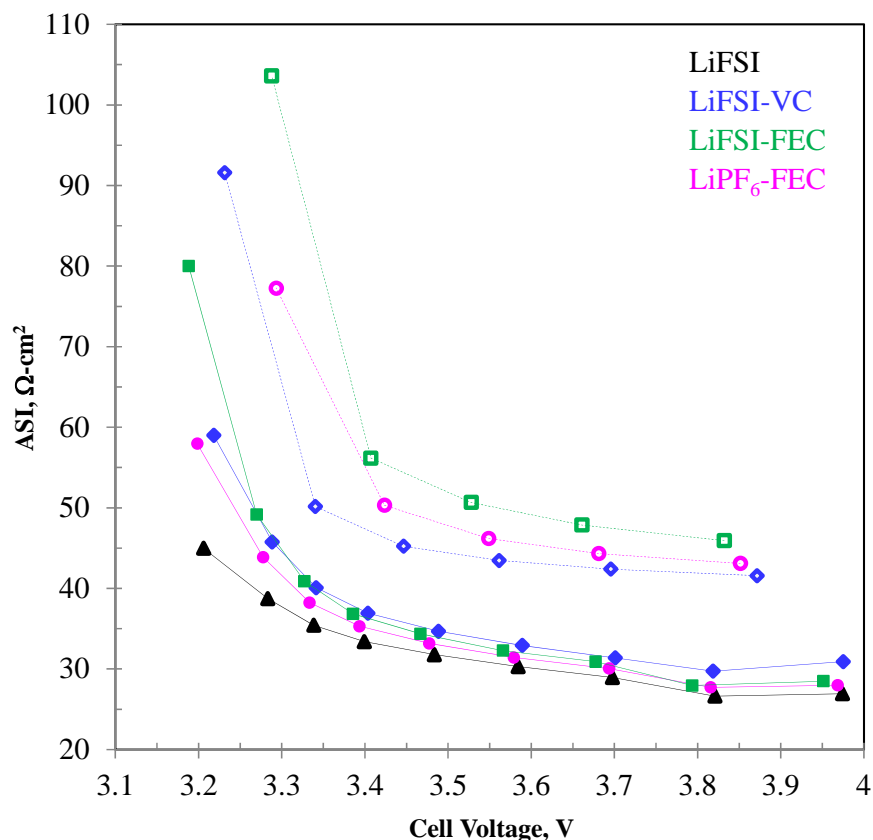


Figure IV-16: Area specific impedance (ASI) vs. cell voltage for Si-Gr//NMC532 pouch cells containing the LiFSI, LiFSI-VC, LiFSI-FEC, and LiPF<sub>6</sub>-FEC electrolytes, before (filled symbols) and after (open symbols) the aging cycles. The ASI data shown were obtained with a 3 C discharge pulse, where C refers to the initial C/1 capacity of the cells

### Assess Performance of Lithium-ion Cells with LiTDI Containing Electrolytes

Commercial lithium-ion batteries (LIBs) typically have liquid carbonate electrolytes containing molar concentration of lithium salts, of which the most common is LiPF<sub>6</sub>. Due to reversible dissociation to PF<sub>5</sub> and F<sup>-</sup>, the hexafluorophosphate anion is suboptimal, as the protonation of the fluoride and reactions of PF<sub>5</sub> yield hydrofluoric acid that corrodes positive electrodes and can react with components of the negatives electrode. Despite these well-known disadvantages, LiPF<sub>6</sub> remains the material of preference, as for the great majority of other lithium salts (that are more hydrolytically and solvolytically stable than LiPF<sub>6</sub>) there is rapid anodic dissolution and pitting corrosion of aluminum current collectors above a certain voltage (~ 4.0 V vs. Li<sup>+</sup>/Li). The very chemical and electrochemical stability of hard-to-oxidize anions (such as bistriflimide, TFSI-, and bis(fluorosulfonyl)imide, FSI-) becomes their downfall, as at the exposed aluminum surface, these anions combine with Al<sup>3+</sup> ions to form soluble complexes, which sustain pitting corrosion. In contrast, the poor chemical stability of PF<sub>6</sub><sup>-</sup> and BF<sub>4</sub><sup>-</sup> anions becomes beneficial, as the released fluoride combines with the aluminum oxide to yield a firm protective barrier. Because (from a practical standpoint) aluminum is the only cheap, light, conductive and malleable metal for a current collector, much effort has been invested into finding

new lithium salts that (i) inhibit this Al anodic dissolution, while (ii) being sufficiently stable chemically at high voltages on energized electrodes.

Lithium 4,5-dicyano-2-(trifluoromethyl)imidazolide (LiTDI) was developed by Niedzicki and co-workers for lithium-ion cells as an alternative to LiPF<sub>6</sub>. Imidazole is an N-heterocyclic base; electron withdrawing cyanide and trifluoromethyl groups are included to turn it into a strong acid, so the anion cannot be easily protonated. LiTDI can be produced conveniently and in high yield in a one-pot synthesis, and it is thermally stable to 250°C. This compound has begun to attract increasing attention, especially for high-energy/high-voltage batteries containing silicon (Li-Si) and graphite (Li-Gr) based negative electrodes. However, before it can be more widely used, its behavior on the negative electrode needs to be understood. In our study, we examined the chemical stability of LiTDI based electrolytes and suggest a rationale for the observed behavior. We first characterized anodic Al dissolution for LiTDI using a chronoamperometry method. We then compared the cycling behavior of Gr/Li cells containing LiPF<sub>6</sub> and LiTDI at different charging rates in solutions with and without electrolyte additives.

All electrochemical tests were conducted using a MACCOR Series 4000 test unit. Stainless steel based 2032-type coin cells were used, unless stated otherwise. To characterize the anodic oxidation of aluminum, the positive electrode casing of the coin cells was 304-stainless steel Ni-plated with aluminum cladding. The cells contained an Al foil positive electrode, Celgard 2325 separator and Li-metal counter electrode. The cells were operated at 55°C and held for an hour at the open circuit voltage before applying a 0.1 V increment step from 3.5 V to 5 V. The cells were held at each voltage step for 1 h, and the corresponding currents were measured during that time. The Li/Gr half cells contained either 0.5 M LiTDI or 1.2 M LiPF<sub>6</sub> salt. The graphite electrode was fabricated at Argonne's CAMP Facility and contained 91 wt.% Hitachi MAG-E graphite, 2 wt.% C45 conductive carbon black, 0.17 wt.% oxalic acid for improved adhesion to copper, and 6 wt.% KF-9300 Kureha PVdF polymer as the binder; these materials formed a ~40 micron thick composite coating on a 10 micron thick copper current collector. The electrolyte additives examined are as follows: 10 wt.% FEC (fluoroethylene carbonate), 5 wt.% VC (vinylene carbonate), or 2 wt.% LiBOB (lithium bis(oxalate)borate). Celgard 2325 was used as a microporous separator (25 micron thick, 28 nm pore, 40% porosity).

Potential and current response profiles during a typical electrochemical test for 0.5 M LiTDI electrolyte are shown in Figure IV-17a. Negligible currents were observed until ~22 h, when a small increase was observed (indicated with the arrow in the plot). Figure IV-17b demonstrates that, for 1.2 M LiTFSI, the rapid rise in current is observed at ~4.0 V, whereas no current is observed for 1.2 M LiPF<sub>6</sub> to 5.5 V. For LiTFSI, the current increased rapidly above 4.2 V reaching 1 mA, which indicates rapid dissolution (pitting corrosion) of the Al current collector. Smaller currents (< 0.1 μA) observed at lower potentials (< 3.6 V) indicates faradaic reactions at the positive electrode before this rapid current rise is observed. For LiTDI, the onset of the rise in the current is ~4.6 V; however, even at 5.0 V the current is only 1 μA, which is significantly smaller than that observed for LiTFSI at the peak of dissolution at 4.2 V. These data conclusively demonstrate that inhibition of Al dissolution is achieved not only transiently (i.e., on the time scale of cyclic voltammetry) but also under quasi-stationary regimes that are realistic approximations of electrochemical cycling conditions.

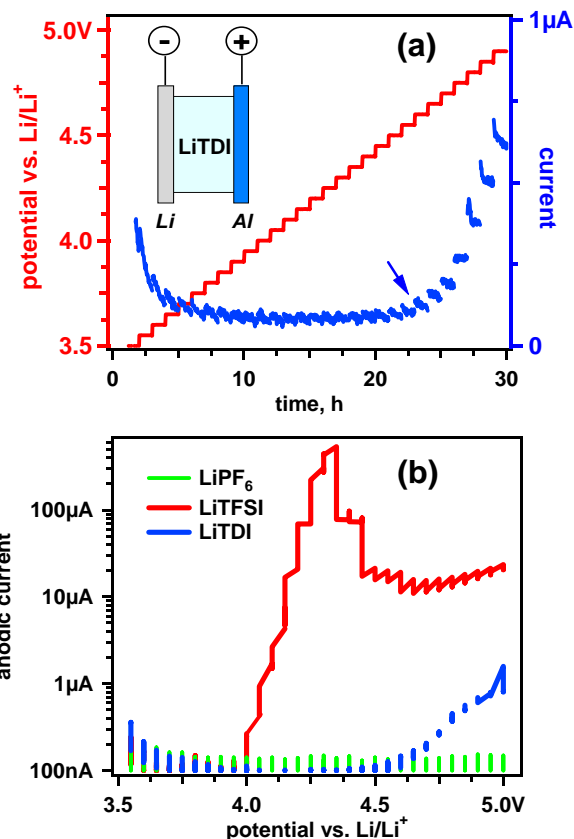


Figure IV-17: (a) Potential and current as a function of time for an Al/Li coin cell containing 0.5M LiTDI in EC:EMC (3:7 w/w) electrolyte. (b) Current versus potential plots for Al/Li cells containing 1.2 M LiTFSI, 0.5 M LiTDI or 1.2 M LiPF<sub>6</sub> salts

Figure IV-18 (left panel) shows potential vs. capacity plots for cycle 3 of Li/Gr cell tests. At this stage, the SEI is fully formed and the cells show stable cycling performance. As seen from this plot, cell A (containing the reference LiPF<sub>6</sub> electrolyte) and cells C to E (containing LiTDI with additives) show similar performances, and the same was observed when these cells were operated at higher charge rates. Without the additives, cell B shows inferior performance, which becomes increasingly worse at higher cycling rates. The cycling trends, and characteristic IR voltage polarization (Figure IV-18 Cell B), are consistent with increased resistance to Li<sup>+</sup> ion transport. The formation of a thick SEI would account for these results.

In order to gain more insight into electrode processes on the graphite, in Figure IV-18 (right panel) we plot  $dQ/dV$  vs. the potential for the same five cells during the first lithiation cycle when the SEI forms. For LiPF<sub>6</sub> containing cell A, the characteristic “twin” feature observed at 0.68-0.74 V corresponds to decomposition of EC. As the same electrolyte solvent is used in all of the tests, this feature is present in other traces shown in this figure, while the amplitude and the position of this feature vary between the systems. For FEC containing cell C, this feature is not observed; instead, there is a peak at 1.1 V corresponding to decomposition of FEC, which is known to be initiated by a defluorination reaction. Apparently, SEI formation in this cell is initiated by FEC decomposition that occurs at a higher potential than reduction of other electrolyte components, including LiTDI and EC; consequently, at the lower voltages (when these components can be directly reduced), the SEI is already formed, so further reduction of electrolyte is hindered. For LiBOB, there is a feature at 1.7 V, where the bis(oxalato)borate anion is reduced. This reduction, however, does not fully prevent further decomposition of the other electrolyte components. For LiTDI containing cell B (no additives), there is a large feature near 0.78-0.86 V. We attribute the larger feature to SEI formation initiated by the reduction of LiTDI. It is noteworthy that the corresponding potential is only slightly greater than the potential corresponding to EC reduction.

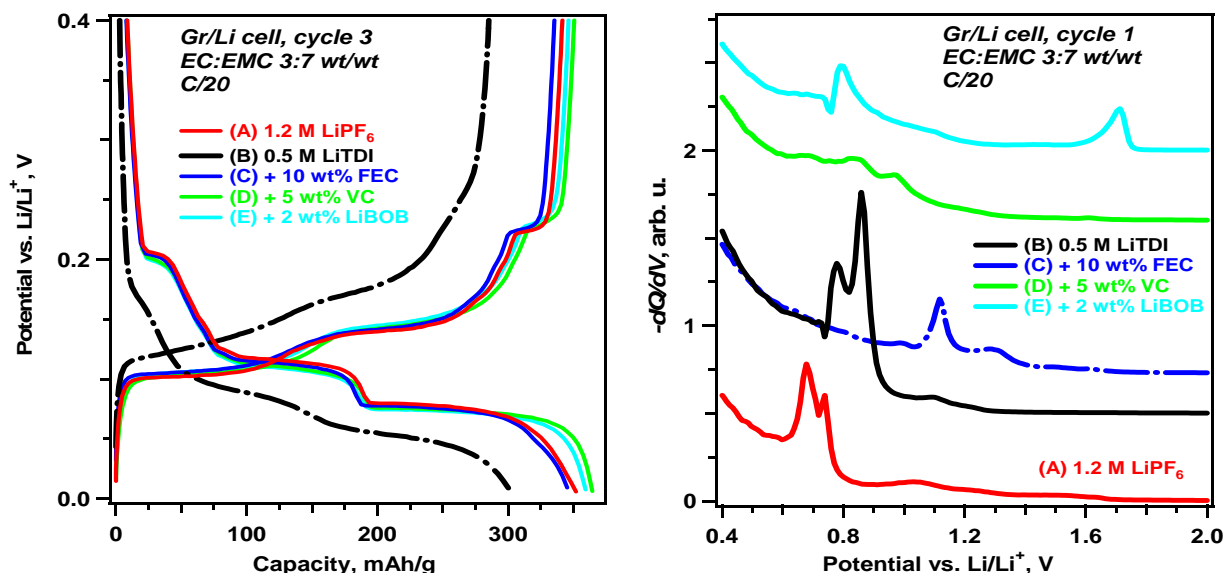


Figure IV-18: (Left panel) Potential versus specific capacity plots for cycle #3 of Li/Gr coin cells containing the electrolyte salt (shown in the legend) in EC:EMC (3:7 w/w) solvent. (Right panel) First cycle  $-dQ/dV$  vs. V during lithiation of Li/Gr coin cells at  $\sim C/20$  rate

## Electrochemical Modeling

This modeling effort focuses on the development of electrochemical models to describe advanced electrodes and cells. Work this year is part of an integrated effort with the Enabling High-Energy/Voltage Lithium-Ion Cells for Transportation Applications (HE-HV) program (see IV.C.1-3) to model cutting-edge NMC positives (e.g. LMR-NMC and high-nickel high-voltage NMC) for advanced lithium-ion battery technologies. The electrochemical modeling studies rely heavily on experimental analytical and electrochemical diagnostic and characterization studies conducted by the CAMP Facility and across the HE-HV program. Experimental data presented in this section are part of those efforts.

NMC532 is one of a series of high-nickel NMCs that are promising cathode active materials capable of delivering more than 200 mAh/g capacity as the electrode end-of-charge voltage is raised to greater than 4.5 volts vs lithium. This material is also one of the baseline active materials within the HE-HV program, tasked with pushing the lithium ion cell technology to higher voltages. Electrochemical modeling studies within this effort have focused on quantifying the lithium transport in the NMC532 electrode. The methodology for the electrochemical model is described in detail in the literature [2-5]. The model combines thermodynamic, kinetic, and interfacial effects with continuum based transport equations. The bulk transport model equations are given in Figure IV-19. Volume averaged transport equations account for the composite electrode geometry. Continuum based transport equations using concentrated solution theory describe the movement of salt in the electrolyte. The transport of ionic and electronic current throughout the cell is included, also the diffusion of lithium in the solid-state active materials.

**Transport through Cell Sandwich**

$$\varepsilon \frac{\partial c}{\partial t} = \frac{\varepsilon}{\tau} \nabla \cdot (D \nabla c) + \frac{\nabla \cdot [(1 - c \bar{V}_e)(1 - t_+^o) \vec{i}_2]}{z_+ v_+ F}$$

$$\vec{i}_2 = -\frac{\kappa \varepsilon}{\tau} \nabla \Phi_2 - v RT \frac{\kappa \varepsilon}{F \tau} \left( \frac{s_+}{n v_+} + \frac{t_+^o}{z_+ v_+} \right) \left( 1 + \frac{\partial \ln f_{\pm}}{\partial \ln c} \right) \nabla \ln c$$

$$\nabla \cdot \vec{i}_2 = F z_+ a j_n \quad \vec{i}_1 + \vec{i}_2 = \vec{I} \quad \vec{i}_1 = -\sigma_{eff} \nabla \Phi_1$$

**Bulk Solid-State Diffusion**

$$\frac{\partial c_s}{\partial t} = \nabla \cdot (D_s \nabla c_s)$$

Figure IV-19: Intercalation electrochemical model equations, grouped according to electronic and ionic transport through cell sandwich and solid-state diffusion in active material

Critical to quantifying the lithium transport in the NMC532 is determining the electrochemical model parameter set, which includes establishing the bulk lithium diffusion coefficient ( $D_S$ ) for the NMC532 active material as a function of lithium content. The diffusion coefficient can be extracted from fitting the model to a wide range of electrochemical studies, including electrochemical impedance spectroscopy (EIS) and DC current pulse/relaxation studies (e.g. HPPC and GITT). Ideally, reference electrode cell studies can provide the highest quality results because it is possible to eliminate effects from the counter electrode. Since quality reference electrodes cell studies can be a challenge, GITT studies on half-cells have been used to extract the diffusion coefficient of the active material. The issue with these studies is the stability and impact of the lithium counter electrode. In the half-cell studies, measurements on multiple cells were conducted and reproducibility between tests was the primary indicator of the quality of the data.

Initiated during the previous fiscal year, the electrochemical model presented in Figure IV-19 was applied to a wide range of NMC532 electrode electrochemical studies to obtain the lithium diffusion coefficient. The most consistent results between the studies were obtained using an intercalation model with three active material particle fractions, with a range of particle sizes. Shown in Figure IV-20, there is good agreement between the various experimental techniques, except at lithium content fractions ( $X_S$ ) above about 0.6. The challenge with fitting the GITT results is the slow relaxation after the current pulse. Close examination of NMC532 micro-reference electrode cells compared to other more common cathode materials (e.g. NCA and NMC333) confirms the slow relaxation after longer current pulses (e.g. several minutes). In general, the length of time is indicative of the penetration length of the cathode particles. The longer the time, the deeper the concentration gradient reaches into the particle. As an example, in micro-reference electrode cells, Figure IV-21 shows the relaxation after partial discharge before HPPC pulses for three different cathodes. Even with some degree of variation between experiments (e.g. active loading, current, state-of-charge, etc.), the slow relaxation of the NMC532 electrode when compared to the NCA and NMC333 electrodes is striking.

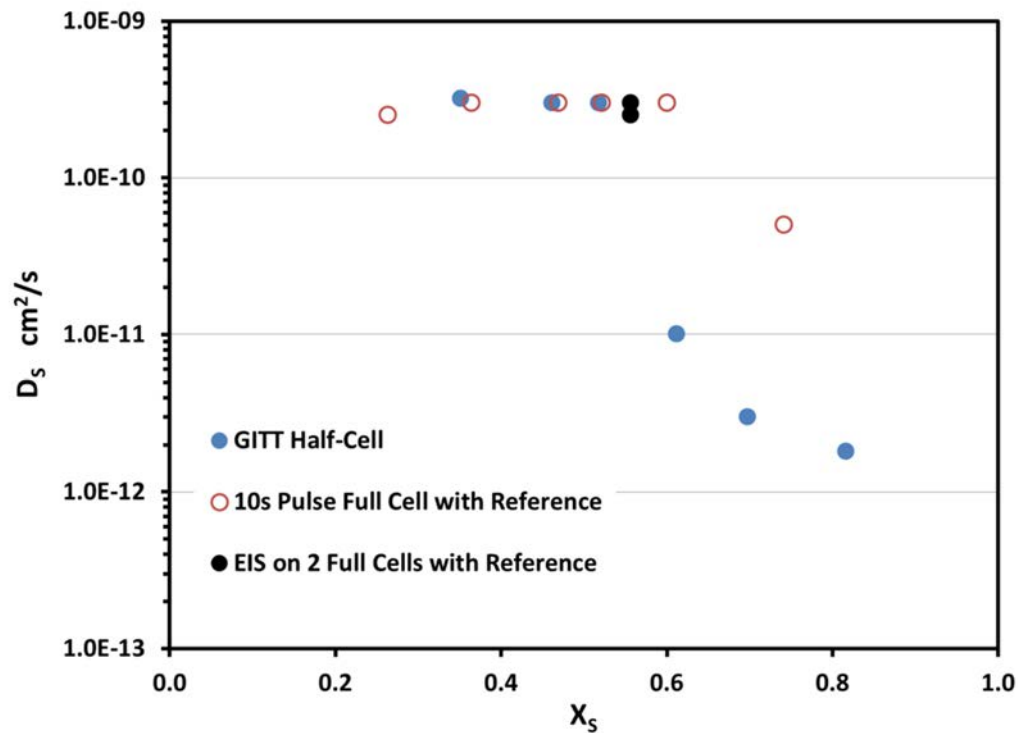


Figure IV-20: Lithium diffusion coefficient for NCM523 obtained from various studies using three particle fraction intercalation model

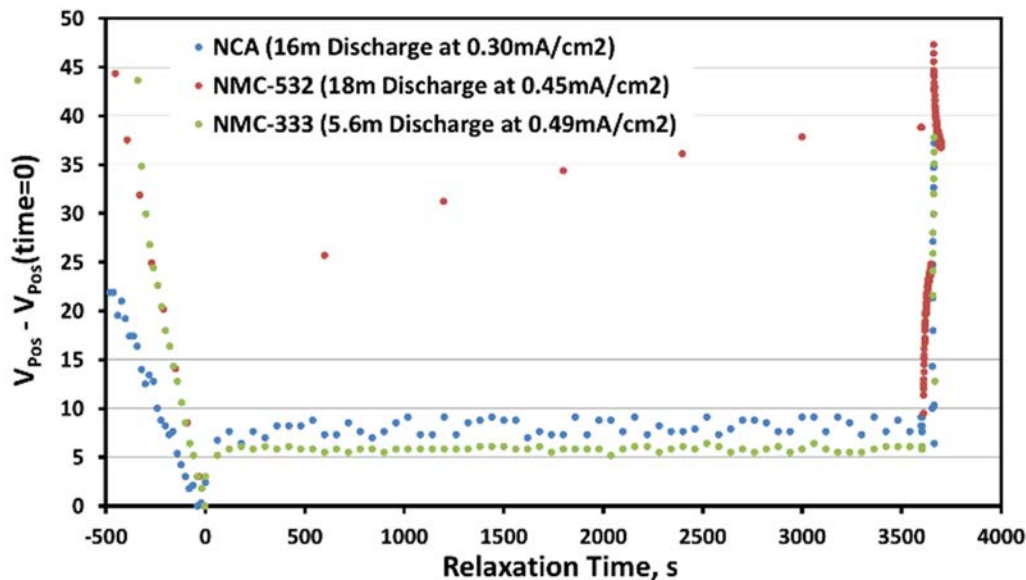


Figure IV-21: Relaxation of NCA, NMC532, and NMC333 electrodes in micro-reference electrode full cells with graphite negative after partial discharge before HPPC pulses. NCA active loading at 8.0 mg/cm<sup>2</sup>, full cell voltage (t=0) at 3.84 V, NMC532 active loading at 8.3 mg/cm<sup>2</sup>, full cell voltage (t=0) at 3.80 V, and NMC333 active loading at 10.4 mg/cm<sup>2</sup>, full cell voltage (t=0) at 3.85 V

The variation in diffusion coefficient (see Figure IV-20) at low SOCs (i.e., higher lithium content) correlates with the inflection in slope of the open circuit voltage (OCV) curve of NMC532, as shown in Figure IV-22. To account better for the inflection in the OCV curve, a concentrated solution electrochemical transport model for lithium diffusion through active material was applied to the present model, as outlined in Figure IV-23. In the model, the active material is considered an intercalation solid made of two components, a host component with a lithium and a host component with no lithium. Using the concentrated solution model for the NMC532 reduced the precipitous drop in the lithium diffusion coefficient at the OCV curve inflection point, but did not solve the variation and nor improve the fit.

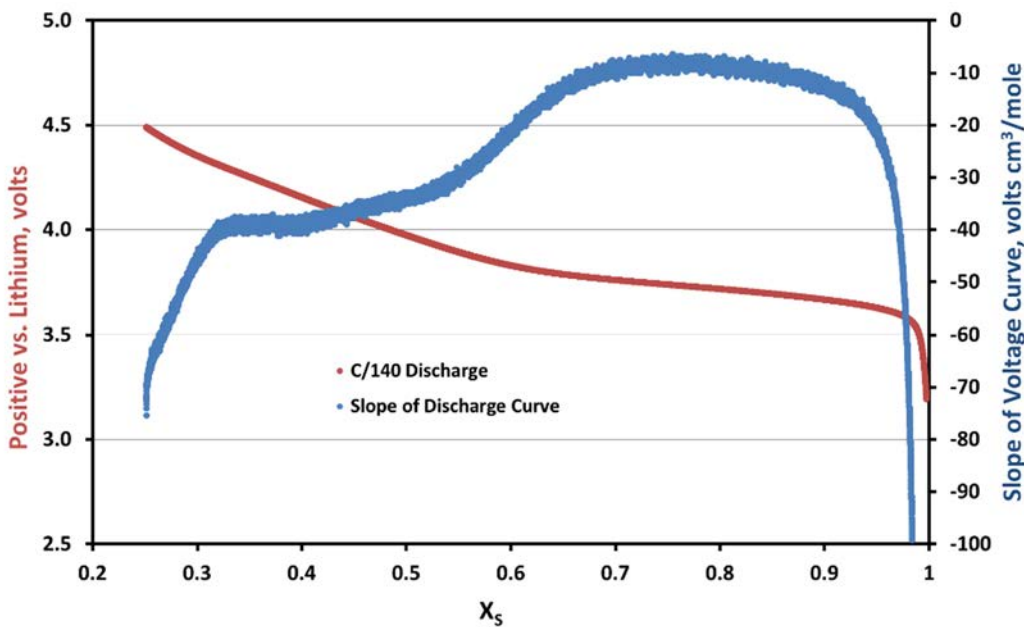


Figure IV-22: OCV curve for NMC532 and its slope obtained from slow discharge of half-cell

$$\begin{aligned}
 &Li^+ + e^- + Host \Leftrightarrow Li - Host \\
 &c_{Li} \nabla \mu_{Li} = \frac{RT}{D} \frac{c_H c_{Li}}{c_T} [v_H - v_{Li}] \\
 &N_{Li} = -\frac{D}{RT} c_{Li} \nabla \mu_{Li} + \frac{c_{Li}}{c_T} [N_H + N_{Li}] \\
 &N_{Li} = -D \frac{F}{RT} \left[ -\frac{dU}{dc_{Li}} \right] \left[ \frac{c_T - c_{Li}}{c_T} \right] c_{Li} \nabla c_{Li} + \frac{c_{Li}}{c_T} [N_H + N_{Li}] \\
 &D_S = D \frac{F}{RT} \left[ -\frac{dU}{dc_{Li}} \right] \left[ \frac{c_T - c_{Li}}{c_T} \right] c_{Li}
 \end{aligned}$$

Figure IV-23: Concentrated solution electrochemical transport model for lithium diffusion through active material

To help understand the complexity of NMC532 structure and how the lithium transport can be affected by the complexity, it will be helpful here to discuss these NMC materials. NMC-abc is a generic name that applies to a class of layered electrode materials that have a general formula of  $Li_{1+\delta}(Ni_xMn_yCo_{1-x-y})_{1-\delta}O_2$ , where abc refers proportionally to the x, y, and 1-x-y respectively and  $\delta$  is greater than zero, sometimes referred to as Li in the metal layer. More appropriately the formula can be written  $\Delta(Li_2MnO_3) \bullet (1-\Delta)(LiNi_qMn_rCo_{1-q-r}O_2)$  representing that the structure is actually made up of two different structures integrated on the nano-scale, which can be referred to as domains. The domains are not separate phases nor easily detected and may be better described as nano-regions, some rich in Mn and others poor in Mn. The  $Li_2MnO_3$  domains can be activated at higher voltages, generally done for larger  $\Delta$ s (say  $> 0.05$ ) along with a higher Mn content (i.e. so called LMR-NMC). Earlier work modeling LMR-NMC suggested that the slow relaxation could be associated with the  $Li_2MnO_3$  domains in the nanometer scale composite structure of the NMC [5]. However, modeling the NMC532 active material with a more complex dual-domain model, as given in Figure IV-24, did not result in any significant improvement, mostly because the amount of  $Li_2MnO_3$  domains is relatively small. The high-nickel NMC532 that is used in HE-HV program is only slightly above stoichiometric lithium,  $Li_{1.015}(Ni_{0.5}Mn_{0.3}Co_{0.2})_{0.985}O_2$  or  $0.03(Li_2MnO_3) \bullet 0.97(LiNi_{0.516}Mn_{0.278}Co_{0.206}O_2)$ .

$$\begin{aligned}
 \frac{\partial \varepsilon_{S1} c_{S1}}{\partial t} &= \nabla \cdot \left( \frac{\varepsilon_{S1} D_{S1}}{\tau_{S1}} \nabla c_{S1} \right) + a_{S21} N_{21} \\
 \frac{\partial \varepsilon_{S2} c_{S2}}{\partial t} &= \nabla \cdot \left( \frac{\varepsilon_{S2} D_{S2}}{\tau_{S2}} \nabla c_{S2} \right) - a_{S21} N_{21} \\
 N_{ij} &= k_{\mu ij} [\mu_{Li}(i) - \mu_{Li}(j)] = k_{\mu ij} F [U_j - U_i] \\
 k_{\mu ij} &= \frac{k_D D_{Si} k_{Dj} D_{Sj}}{(k_D D_{Si} + k_{Dj} D_{Sj})}
 \end{aligned}$$

Figure IV-24: Dual-domain LMR-NMC active material electrochemical model

DFT modeling within the HE-HV program suggests that the high-nickel NMCs are actually made up of nickel rich domains and domains of something like NMC333. This further structural complexity would also be suggested by assuming that the nickel can be either +2 or +3, while manganese and cobalt will be +4 and +3, respectively. While at present there is not a lot of evidence for this structural complexity, examining the OCV curves of NCA, NMC532, and NMC333, shown in Figure IV-25, is quite interesting. This rough comparison of the electrochemical signature for the three active materials suggest that the NMC532's OCV characteristics

are somewhere between NCA and NMC333, although clearly not a simple weighted average. As shown in Figure IV-26, adopting the dual-domain lithium diffusion model for the nickel rich and NMC333 domains within the NMC532 structure significantly reduces the change in lithium diffusion coefficient (i.e.  $1.5 \times 10^{-10}$  vs  $0.9 \times 10^{-10}$   $\text{cm}^2/\text{s}$ ) around the inflection in the OCV curve. Further, the quality of the fit is generally good without using multiple particle fractions. Of course, it also introduces several parameters that are difficult to determine independently.

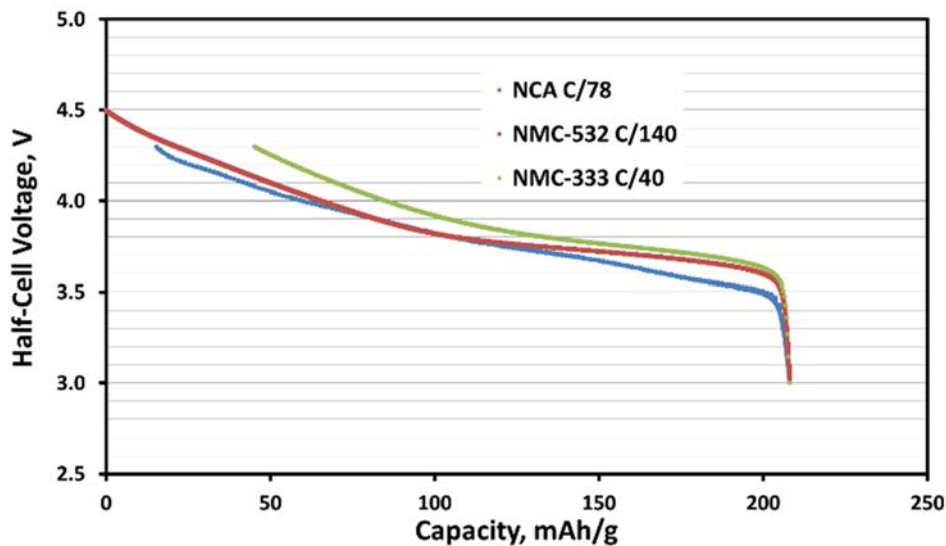


Figure IV-25: Slow discharge of NCA, NMC532, and NMC333 half-cells

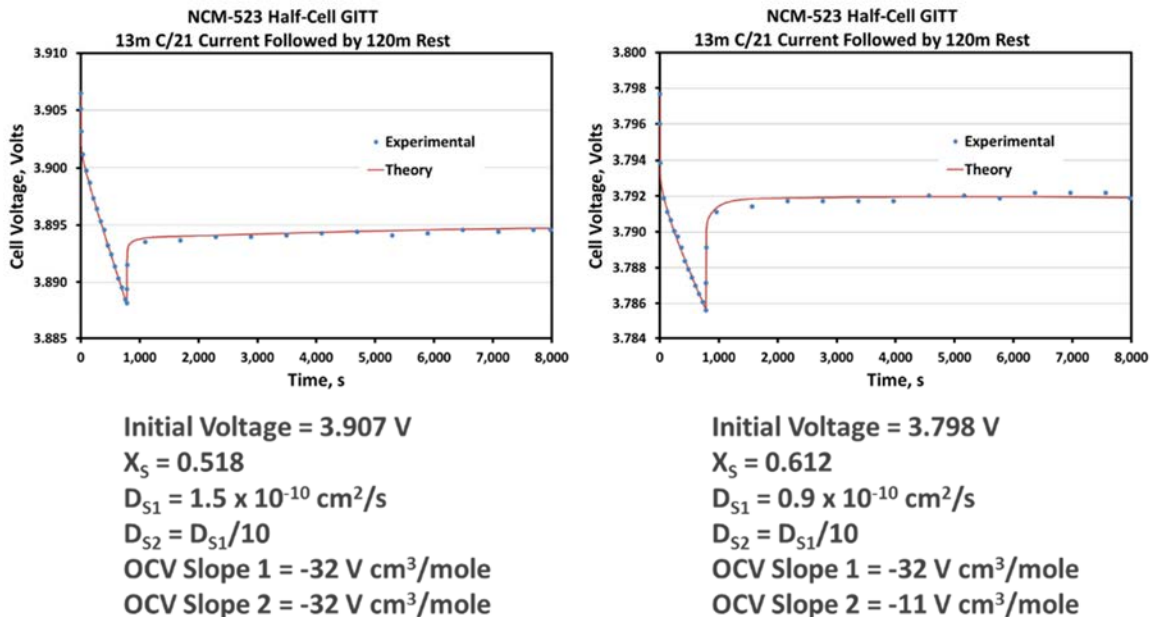


Figure IV-26: GITT modeling on NCM523 half-cell using dual-domain intercalation model for Ni-rich ( $\epsilon_{S1}=0.4$ ) and NMC333 ( $\epsilon_{S2}=0.6$ ) domains

### Electrode Builds for Silicon Thermal Abuse Study at Sandia National Laboratory

Silicon has been demonstrated to enhance the capacity of the negative electrode by over 100%. However, the safety implications of this relatively new active material are not fully understood. The CAMP Facility has teamed with the Battery Abuse Testing Lab (BATLab) at Sandia National Laboratory to begin assessing the thermal abuse response of silicon-graphite composite electrodes in lithium-ion cells (18650 format). This combined the electrode making expertise of the CAMP Facility with the thermal abuse testing expertise of the

BATLab. The CAMP Facility fabricated over 10 meters each of double-sided electrodes containing 0, 5, 10, and 15 wt. % of silicon, and over 25 meters of capacity-matched NMC532 double-sided electrode. These electrodes are described in more detail in Table IV-5 and shown in Figure IV-27.

**Table IV-5: Double Side Electrodes Fabricated for Thermal Abuse Studies at SNL**

	0% silicon-based anode	5% silicon-based anode	10% silicon-based anode	15% silicon-based anode	90% NMC 532 cathode
Electrode ID	LN3024-101-4&5	LN3024-89-6&7	LN3024-88-5&6	LN3024-87-3&4	LN3024-102-4 & 106-6
Silicon powder	-	NanoAmor, 50-70 nm particle size	NanoAmor, 50-70 nm particle size	NanoAmor, 50-70 nm particle size	-
Graphite / active material powder	Hitachi MagE	Hitachi MAGE	Hitachi MAGE	Hitachi MagE	Toda NMC 532
Binder	Kureha 9300 PVDF	Sigma Aldrich PAA 450,000 m.w., pre-titrated with LiOH•H2O	Sigma Aldrich PAA 450,000 m.w., pre-titrated with LiOH•H2O	Sigma Aldrich PAA 450,000 m.w., pre-titrated with LiOH•H2O	Solvay 5130 PVDF
Compositions (dry wt.%)	0 / 91.83 / 2 / 6 / 0.17 Gr / carbon black / PVDF / oxalic acid	5 / 83 / 2 / 10 Si / Gr / carbon black / LiPAA	10 / 78 / 2 / 10 Si / Gr / carbon black / LiPAA	15 / 73 / 2 / 10 Si / Gr / carbon black / LiPAA	90 / 5 / 5 NCM523 / carbon black / PVDF
Coating Thickness - Single Side (µm)	80	87	68	54	71
Porosity (%)	35.7	45.4	45.2	43.4	31.1
Coating Density (g/cm <sup>3</sup> )	1.40	1.11	1.12	1.16	2.80
Total Coating Loading (mg/cm <sup>2</sup> )	11.16	9.58	7.53	6.18	19.87
Estimated C/10 Capacity (mAh/cm <sup>2</sup> )	3.37	3.63	3.64	3.81	2.86
N:P ratio (based on reversible C/10 rate)	1.18	1.27	1.27	1.33	

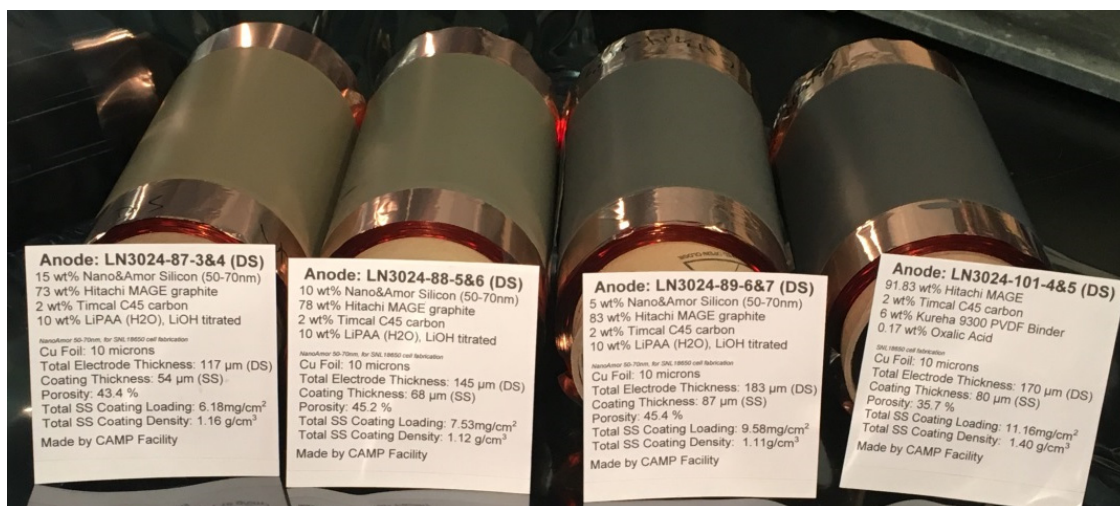


Figure IV-27: Rolls of double-sided silicon-graphite electrodes and double-sided NMC532 electrode fabricated by CAMP Facility for thermal abuse studies at the BATLab in Sandia National Laboratory

### Pouch Cell Build Using Miltec Cathode

The CAMP Facility was tasked to fabricate multilayer xx3450 pouch cells containing a double-sided cathode made via a novel coating method by Miltec. CAMP fabricated a capacity matched double side anode to the cathode provided by Miltec. Several ~100 mAh pouch cells were assembled and put through formation, rate, and HPPC characterization tests before being sent to Idaho National Laboratory for independent testing. These results are posted elsewhere in this annual report.

### Electrode Library

Table IV-6 shows the distribution of electrodes from the Electrode Library that is maintained by the CAMP Facility. In FY16, 2021 sheets of electrode were fabricated and distributed by the CAMP Facility, which is 49 square meters of electrodes. This amounted to ~20% more electrodes than were distributed in FY15. The main areas were more electrodes distributed this year in the Other Laboratories category. This is mainly due to the CAMP Facility's support of DOE's High-Energy High-Voltage Program as well as the Next Generation Anodes Program. Since these DOE programs are consortiums of the various national laboratories, the CAMP Facility is supplying all of the baseline electrodes for them. In addition to the electrodes, the CAMP Facility has distributed ~75 kg of active materials, carbon additives, binders and electrolytes. Figure IV-28 is a summary of the organizations that have benefited from collaboration with the CAMP Facility over the last several years.

Table IV-6: Summary of Electrode Library Distributions

Electrodes Delivered	FY13		FY14		FY15		FY16	
	Count	Percentage	Count	Percentage	Count	Percentage	Count	Percentage
Argonne	79	23.5%	116	13.3%	206	12.2%	174	8.6%
Other National Labs	102	30.4%	213	24.4%	373	22.0%	726	35.9%
Universities	56	16.7%	119	13.6%	83	4.9%	117	5.8%
Industry	98	29.2%	423	48.5%	1028	60.8%	1004	49.7%
<b>Total:</b>	<b>335</b>		<b>871</b>		<b>1690</b>		<b>2021</b>	



Figure IV-28: Organizations that have benefited from collaboration with the CAMP Facility over the last several years

## Conclusions

The main focus of the CAMP Facility is to support the numerous R&D battery programs taking place within the DOE’s Vehicle Technology Office. A common theme in many of these programs is to increase the energy density of lithium-ion batteries while maintaining good cycle life and thermal abuse response. Efforts this year for the CAMP Facility have been directed to three main areas: improving the capacity of the negative electrode with addition of silicon; increasing the energy of the positive electrode via higher nickel content and higher voltage; and enhancing life of these advanced anodes and cathodes with new electrolyte formulations. While many of the activities of the CAMP Facility are noted in this section, more results can be found distributed throughout other advanced batteries R&D sections in this annual report.

Silicon electrodes still do not meet the performance typical of graphite electrodes, with the main limitation in the area of cycle life. The problem lies in the poor coulombic efficiency, which is most likely due to the large volume expansion (~280%) of the silicon particle upon lithiation. What is needed is a flexible robust SEI layer on the silicon particle that will prevent or minimize the repeated loss of lithium upon each recharge. This will most likely be a combination of silicon surface modification, functionalized binder, and electrolyte additives.

Increasing the potential of commercially available cathode materials does result in increased capacity and energy up to a point. Beyond that potential, the capacity of the cathode material tends to level off and in some cases decrease as the cell voltage is raised. This is most likely due to decomposition of the cathode interface, cathode bulk, and/or electrolyte.

In the area of electrolytes, we examined the cycling of ~20 mAh pouch cells with LiFSI-containing carbonate-based electrolytes, silicon-graphite negative electrodes, and NMC532-based positive electrodes. The effect of fluoroethylene carbonate (FEC) and vinylene carbonate (VC) addition on cell performance was also examined

and compared to the performance of our baseline LiPF<sub>6</sub>-containing cells. Our data show that cells containing only the LiFSI salt show rapid loss of capacity, whereas additions of FEC and VC significantly improve cell capacity retention. Furthermore, the performance of LiFSI-FEC and LiPF<sub>6</sub>-FEC cells are very similar indicating that the electrolyte salts play a much smaller role in performance degradation than the electrolyte solvent. Future achievements to enhance longevity of cells with silicon-graphite negative electrodes will thereby focus on developing alternative solvent systems.

Our results suggest that LiTDI, like other lithium salts, has both advantages and disadvantages for use in lithium-ion cells. Among the disadvantages, we show that LiTDI alone in carbonate solvents degrades electrochemical performance, as it has a particular way of decomposition that disfavors radical polymerization of the solvent over anionic polymerization of the same solvent, causing low extent of cross linking and inferior, solvent-permeable outer SEI matrix. Among the advantages, by adding certain electrolyte additives, such as LiBOB, vinylene carbonate and, especially, fluoroethylene carbonate, this problem can be mitigated.

Another highly encouraging observation is the passivation of aluminum by LiTDI that prevents aluminum current collector dissolution to 5.0 V vs. Li<sup>+</sup>/Li. The mechanism for this beneficial action requires further elucidation. Taken together, our results suggest that with suitable modifications of the electrolyte, LiTDI can be a strong contender for lithium-ion cells, as it is hard-to-oxidize, hinders pitting corrosion of Al current collectors, and becomes noninterfering on the negative electrodes in the presence of the additives that are reduced above ~1.0 V vs. Li<sup>+</sup>/Li. Additional tests in full cells with layered-oxide based positive and graphite-based negative electrodes are underway to further evaluate the benefits of this novel salt.

Treating NMC532 as having multiple particle fractions, with a range of diffusion lengths, works relatively well at high SOC, but fails at low SOC where the material's OCV curve levels. Clearly, further work needs to be done. However, treating NMC532 as a nano-composite material made of two domains shows promise of unifying the diagnostic results, but adds a huge amount of complexity and is difficult to justify from our present level of knowledge. Efforts are ongoing to expand and improve the model's capabilities with the focus on NMC cathodes and silicon-graphite composite electrodes.

Multi-stack pouch cells of 0.5 Ah were fabricated with 15% silicon (50- 70 nm) in the anode and NMC622 in the cathode to establish a new baseline cell system. The study of the effects of cycle life protocols and calendar life was initiated with this cell build and will be used to direct future experiments.

## Products

### Presentations/Publications/Patents

1. Layered Oxide, Graphite and Silicon-Graphite Electrodes for Lithium-Ion Cells: Effect of Electrolyte Composition and Cycling Windows. Matilda Klett, James A. Gilbert, Krzysztof Z. Pupek, Stephen E. Trask, and Daniel P. Abraham. *Journal of The Electrochemical Society*, 164 (1) A6095-A6102 (2017). DOI: 10.1149/2.0131701jes.
2. Performance of Full Cells Containing Carbonate-Based LiFSI Electrolytes and Silicon-Graphite Negative Electrodes. Stephen E. Trask, Krzysztof Z. Pupek, James A. Gilbert, Matilda Klett, Bryant J. Polzin, Andrew N. Jansen, and Daniel P. Abraham. *Journal of The Electrochemical Society*, 163 (3) A345-A350 (2016), DOI: 10.1149/2.0981602jes.
3. Optimizing areal capacities through understanding the limitations of lithium-ion electrodes. Kevin G. Gallagher, Stephen E. Trask, Christoph Bauer, Thomas Woehle, Simon F. Lux, Matthias Tschech, Bryant J. Polzin, Seungbum Ha, Brandon Long, Qingliu Wu, Wenquan Lu, Dennis W. Dees, Andrew N. Jansen. *Journal of The Electrochemical Society*, 163 (2) A138-A149 (2016), DOI: 10.1149/2.0321602jes.
4. Electrode Behavior RE-Visited: Monitoring Potential Windows, Capacity Loss, and Impedance Changes in Li<sub>1.03</sub>(Ni<sub>0.5</sub>Co<sub>0.2</sub>Mn<sub>0.3</sub>)<sub>0.97</sub>O<sub>2</sub>/Silicon-Graphite Full Cells. Matilda Klett, James A. Gilbert, Stephen E. Trask, Bryant J. Polzin, Andrew N. Jansen, Dennis W. Dees, and Daniel P. Abraham, *Journal of The Electrochemical Society*, 163 (6) A875-A887 (2016), DOI: 10.1149/2.0271606jes.
5. Evaluation of Electrolyte Oxidation Stability on Charged LiNi<sub>0.5</sub>Co<sub>0.2</sub>Mn<sub>0.3</sub>O<sub>2</sub> Cathode Surface through Potentiostatic Holds. Adam Tornheim, Stephen E. Trask, Zhengcheng Zhang. *Journal of The Electrochemical Society*, 163(8):A1717-A1722 (2016). DOI: 10.1149/2.1051608jes.

6. Cycling Behavior of NCM523/Graphite Lithium-Ion Cells in the 3–4.4 V Range: Diagnostic Studies of Full Cells and Harvested Electrodes. James A. Gilbert, Javier Bareno, Timothy Spila, Stephen E. Trask, Dean J. Miller, Bryant J. Polzin, Andrew N. Jansen, and Daniel P. Abraham. *Journal of The Electrochemical Society*, 164(1):A6054–A6065 (2017). DOI: 10.1149/2.0081701jes.
7. Exploring Various Electrolytes in Silicon-Containing Lithium-Ion Batteries, S. Trask, K. Z. Pupek, J. Gilbert, M. Klett, B. Polzin, A. Jansen, D. Abraham, *33rd Annual International Battery Seminar & Exhibit* Fort Lauderdale, FL, March 22, 2016.
8. On the chemical stability of lithium 2-trifluoromethyl-4,5-dicyanoimidazolide (LiTDI), an electrolyte salt for Lithium-ion cells, I.A. Shkrob, K.Z. Pupek, J.A. Gilbert, S.E. Trask, D. P. Abraham, *J. Physical Chemistry C*, under review (2016).

## References

1. Extending the High-Voltage Capacity of LiCoO<sub>2</sub> Cathode by Direct Coating of the Composite Electrode with Li<sub>2</sub>CO<sub>3</sub> via Magnetron Sputtering, Xinyi Dai and et. al. *The Journal of Physical Chemistry*, 2016, DOI: 10.1021/acs.jpcc.5b10677
2. Alternating Current Impedance Electrochemical Modeling of Lithium-Ion Positive Electrodes. D. Dees, E. Gunen, D. Abraham, A. Jansen, and J. Prakash. 7, 2005, *J. Electrochem. Soc.*, Vol. 152, pp. A1409–A1417.
3. Electrochemical Modeling of Lithium-Ion Positive Electrodes during Hybrid Pulse Power Characterization Tests. D. Dees, E. Gunen, D. Abraham, A. Jansen, J. Prakash. 8, 2008, *J. Electrochem. Soc.*, Vol. 155, pp. A603–A613.
4. Analysis of the Galvanostatic Intermittent Titration Technique (GITT) as Applied to a Lithium-Ion Porous Electrode. D.W. Dees, S. Kawauchi, D.P. Abraham, J. Prakash. 2009, *J. Power Sources*, Vol. 189, pp. 263–268.
5. Electrochemical Modeling and Performance of a Lithium and Manganese-Rich Layered Transition-Metal Oxide Positive Electrode. D.W. Dees, D.P. Abraham, W. Lu, K.G. Gallagher, M. Bettge, A.N. Jansen. 4, 2015, *J. Electrochem. Soc.*, Vol. 162, pp. A559–A572.

## IV.B.2. Materials Benchmarking Activities for CAMP Facility (ANL)

### Wenquan Lu, Principal Investigator

Argonne National Laboratory  
9700 S. Cass Avenue  
Lemont, IL 60564  
Phone: 630-252-3704; Fax: 630-252-4176  
E-mail: [luw@anl.gov](mailto:luw@anl.gov)

### Peter Faguy, DOE Program Manager

U.S. Department of Energy  
Vehicle Technologies Office  
1000 Independence Avenue, SW  
Washington, DC 20585  
Phone: 202-586-1022  
E-mail: [Peter.Faguy@ee.doe.gov](mailto:Peter.Faguy@ee.doe.gov)

Start Date: October 2014

End Date: September 2017

### Abstract

#### Objectives

- The primary objective is to identify and evaluate low-cost materials and cell chemistries that can simultaneously meet the life, performance, and abuse tolerance goals for batteries used in PHEV and EV applications.
- A secondary objective is to enhance the understanding of the impact of advanced cell components and their processing on the electrochemical performance and safety of lithium-ion batteries.
- To support the CAMP Facility for prototyping cell and electrode library development, also the MERF facility for material scale up.

#### Accomplishments

- Studied lithium inventory effect on high energy, but low coulombic efficiency anode.
- Worked on advanced conductive additives to promote high energy and high power LIB.
- Explored high energy cathode materials and their thermal stability.
- Other cell components, such as electrolyte and additives, conductive additive, separators, binders, etc., have also been investigated.

#### Future Achievements

- High energy electrode materials
  - Continue to search and evaluate high energy density anode/cathode materials, as they become available.
  - Surface modification effect on electrochemical performance of high energy materials will be explored.
  - Continue the thermal investigation on high energy cathode materials.
- Electrode optimization:
  - Cabot carbon black has been requested and electrodes and pouch cells will be fabricated and tested at CAMP Facility.
  - SWCNT and graphene conductive additive will be explored to further improve the electrode performance.

- Continue to work closely with research institutions and industrial suppliers to enable the LIB technology for PHEV and EV applications.

## Technical Discussion

### Background

This benchmarking effort is conducted as part of the Cell Analysis, Modeling, and Prototyping (CAMP) Facility (Refer to IV.B.1) to identify and support promising new materials and components across the “valley of death”, which happens when pushing a new discovery towards a commercial product. The CAMP Facility is appropriately sized to enable the design, fabrication, and characterization of high-quality prototype cells with around 400-mAh capacity, which straddles the gap between coin cells and full cells nicely – two orders of magnitude from each end point. Thus, a realistic and consistent evaluation of candidate chemistries is enabled in a time-effective manner with practical quantities of novel materials.

However, the CAMP Facility is more than an arrangement of equipment, it is an integrated team effort designed to support the production of prototypes electrodes and cells. In order to utilize the facility more efficiently and economically, cell chemistries are validated internally to determine if they warrant further consideration.

High energy density electrode materials are required in order to achieve the 40-mile all electric range within the weight and volume constraints established by DOE and the USABC. One would need a combination of anode and cathode materials that provide 420mAh/g and 220mAh/g, respectively, as predicted by Argonne’s battery design model, if one uses a 20% margin for energy fade over the life of the battery assuming an average cell voltage of 3.6 volts. Therefore, the search for new high energy density materials is the focus of this project.

In addition to electrode materials, other cell components, such as separators, binders, current collectors, etc., are evaluated to establish their impact on electrochemical performance, thermal abuse, and cost.

### Introduction

Many anode materials, including hard carbon, tin, tin oxide, silicon, and silicon oxide, have high theoretical capacities (>550 mAh/g) but tend to exhibit a large first cycle irreversible capacity loss (ICL). This is an important issue for the commercial application of some types of high capacity anodes in full LIBs that overrides the true reversible capacity of the anode itself and reduce the energy of LIB as whole. The existing strategies employed to address this issue usually involve adding different lithium sources to the anode, such as, lithium powder or lithiated transition metal nitrides.[1-5] Unfortunately, these strategies may create safety issues in the practical application of LIBs. In order to overcome the large ICL of next generation LIB anodes, a new strategy is needed wherein a sacrificial lithium source additive, such as  $\text{Li}_5\text{FeO}_4$  (LFO) with theoretical capacity equal to 867 mAh/g is used on the cathode side, i.e., an additive that in theory could release up to 5 lithium cations per mole to the cell upon first charge.[6] As such, small amounts of LFO co-blended with the active cathode powder particles in conventional electrode laminate coatings could provide exactly what is needed to mitigate the ICL issues of hard carbon and related anode materials with high theoretical energy density.

Another way to improve the energy density of LIB is to reduce the usage of inactive materials, such as conductive additive and binder. In lithium-ion batteries, the active materials of the cathodes typically exhibit relatively high resistivity due to their intrinsically poor electronic conductivity and the limited point contacts between micro particles. To mitigate the poor electrical conductivity of the electrode, conductive powders, such as carbon black, carbon fiber, carbon nanotube, or graphene, are added to the electrode formulation. The binder usage is proportional to the usage of conductive additives due to its large surface area. Both conductive additive and additive are not electrochemically active and effectively reduced the energy density of the cathode electrode. Therefore, it is very rational to reduce the usage of conductive additive, such as carbon black, to increase the energy density of LIB. However, too little conductive additive will detrimentally affect the rate performance and cycle life. These two antagonistic requirements make high demands on optimizing conductive additives, which will be investigated in this report.

This work was carried out under CAMP under CAMP Facility and contributors are Xin Su, Linghong Zhang, Yan Qin, Manar Ishwait, SeonBaek Ha, Xiaoping Wang, Chi-Kai Lin, Christopher Johnson, Victor Maroni, Yang Ren, Andrew Jansen, Bryant Polzin, Steve Trask, and Dennis Dees from Argonne National Laboratory. Novel carbon black was provided by Hanwei Lei, Berislav Blizanac, and Miki Oljaca from Cabot Corporation.

## Approach

Lithium inventory effect of LFO on the full cell performance was investigated using LiCoO<sub>2</sub> (LCO) as the cathode and Hard carbon as anode due to their dramatically difference in first cycle coulombic efficiency, 97% for LCO and 80% for hard carbon, respectively. Without LFO in LCO cathode, the irreversible capacity loss of the full cell will be governed by the hard carbon, resulting less usage of LCO capacity. However, the capacity of LCO will be completely utilized by adding 7% LFO into the cathode. The details will be discussed in the results section.

The second part of this report will present the conductive additive effect on the energy density of LIB. The novel carbon black from Cabot (CBC) has been developed with a reduced number of functional groups and an increased degree of graphitization on the carbon black nanoparticles' surface. This novel carbon black has been investigated as the conductive additive in combination with LiNi<sub>0.5</sub>Mn<sub>0.3</sub>Co<sub>0.2</sub>O<sub>2</sub> (NMC532) and the commercial carbon black is used in the corresponding control experiments.

## Results

### Part one: lithium inventory for prelithiation - Li<sub>5</sub>FeO<sub>4</sub> (LFO)

The LFO powder used in this work was synthesized through the procedure developed in our laboratory and described in reference [6]. LFO powder synthesized in the lab was made into electrode and its first charge and discharge capacity is shown in Figure IV-29, at 700 mAh/g, which is equivalent to 4 mole of lithium cations per mole of LFO. The redox reaction is shown below.



It can also be seen that there is almost no discharge capacity during first cycle, which is perfect for this material to be used to compensate for the irreversible capacity loss (ICL) of the anode. Due to its high initial charge capacity, only a relatively small amount of LFO is needed to blend with the cathode material. In this work, 7 wt.% LFO powder was blended with LCO powder and fabricated into a conventional electrode laminate.

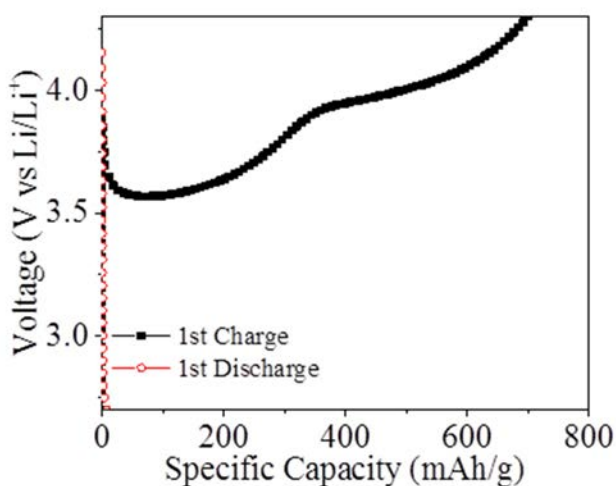


Figure IV-29: Voltage Profile of Li/LFO half-cell during 1st charge and discharge

Figure IV-30a and Figure IV-30b illustrate how the LFO additive affects the capacity usage of LCO in full cells with HC as anode. Figure IV-30a shows first charge/discharge voltage profiles of Li/HC (bottom black triangle curve) and Li/LCO half cells (top red square curve). Assuming that the capacity ratio of the negative (HC) electrode to the positive electrode (LCO) is equal to 1 ( $n/p = 1$ , determined by the first charge capacity), the HC/LCO full cell voltage profile, shown in Figure IV-30a (middle black star curve), was calculated from the Li/HC and Li/LCO half cells. The useable capacity of the LCO cathode is determined to be 121 mAh/g due to the large ICL of HC, which is much smaller than that of LCO in a half cell (160 mAh/g). However, for the HC/LCO-LFO full cell with the same  $n/p$  ratio, the voltage profile of HC/LCO-LFO full cell, shown in Figure IV-30b, is calculated from Li/HC (bottom black triangle curve) and Li/LCO-LFO (top red square curve) half cells. The reversible capacity of LCO-LFO cathode is determined to be 159 mAh/g (middle black star curve), since the extra lithium from the LFO can compensate the large ICL of the HC anode and all the capacity of the LCO can thereby be utilized.

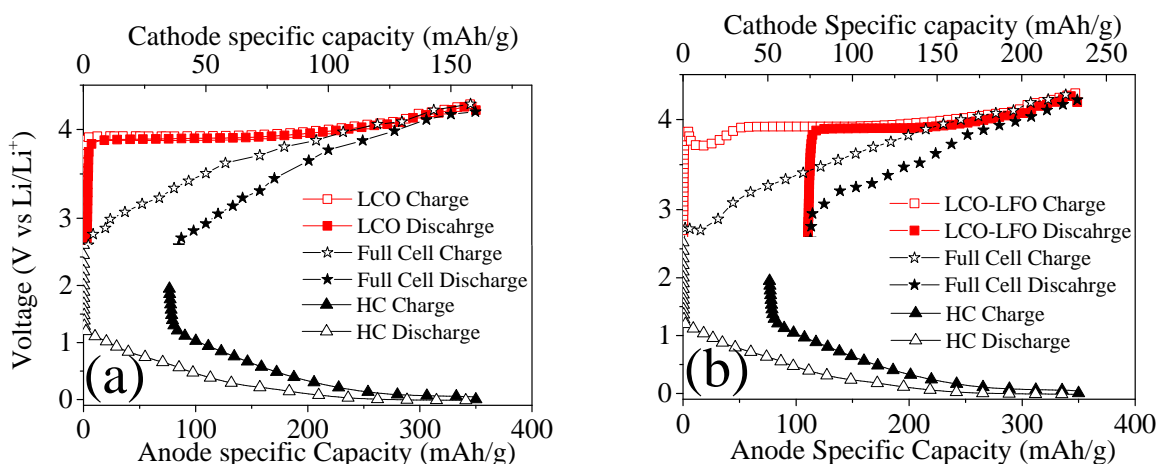


Figure IV-30: Voltage profiles for (a) the Li/HC half cell, the Li/LCO half cell, and the HC/LCO full cell, and (b) the Li/HC half cell, the Li/LCO-LFO half cell, and the HC/LCO-LFO full cell

The respective electrochemical performances of the full cells using the LCO-only cathode and the LCO-LFO cathode are shown in Figure IV-31. The reversible specific capacities of the LCO and LCO-LFO electrodes are 126 mAh/g and 144 mAh/g (which is actually equivalent to 156 mAh/g when normalized to the mass of LCO only), respectively, which are consistent with the calculation according to Figure IV-30a and Figure IV-30b. Therefore, the reversible specific capacity of the LCO-LFO cathode in the full cell can be increased by 14%, which is equivalent to a 10% increase in energy density. The energy density can be further improved by reducing the LFO content in the LCO-LFO electrode, since the 7 wt% LFO in LCO electrode results in a 31% ICL, which is more than enough to address the 22% ICL of HC electrode. Furthermore, the capacity retentions of the full cells during the 50 cycles of testing are also improved from <90% for LCO alone to  $\geq 95\%$  when the LFO is added. It is well accepted that one of the factors causing capacity fading in LIBs is the side reaction between electrolyte and anode, which tends to consume lithium ions leading to less available lithium. The extra lithium from LFO can behave as a lithium reservoir that provides lithium ions continuously during cycling to compensate for the lithium loss. Therefore, the LFO cathode additive not only mitigates ICL, but also improves cycle performance.

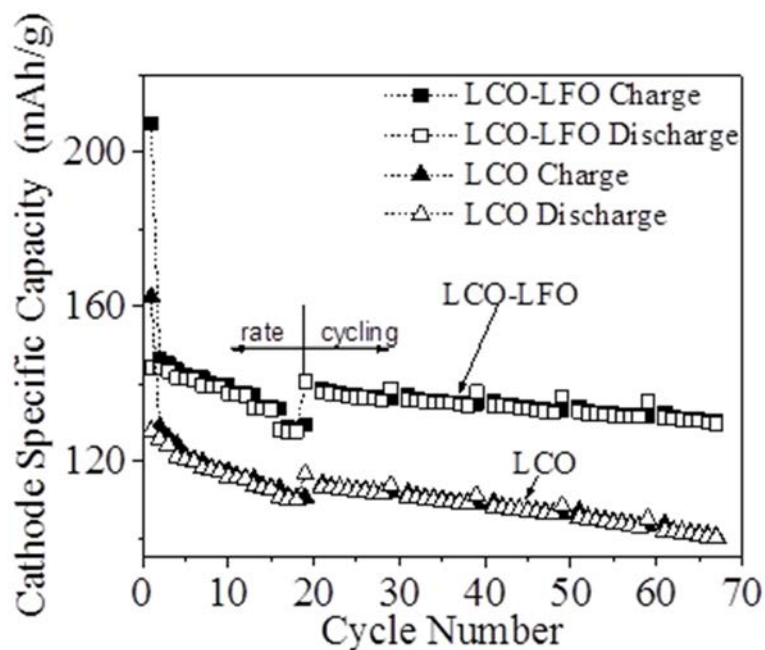


Figure IV-31: Cycling performance of the full cells using LCO-LFO blend (square (□)) and LCO-only and cathode and HC as the anode with the initial capacity of 350 mAh/g

## Part II: Conductive Additive Effect

The novel carbon black from Cabot (CBC) has been developed with a reduced number of functional groups and an increased degree of graphitization on the carbon black nanoparticles' surface. The NMC532 (NCM-04ST, TODA America, Inc.) electrodes were made using two different carbon blacks, standards and CBC. The final compositions of the electrodes were created in two groups. The first one was 90% NMC532, 5% PVDF, and 5% carbon black (standard or CBC). The second one was 98% NMC532, 1% PVDF, and 1% carbon black (standard or CBC). The coatings of the electrodes on Al foil were kept at  $\sim 10 \text{ mg/cm}^2$  with 30% porosity. From the SEM images, Figure IV-33, of the electrodes using 5% carbon black, the nanoparticles of standard carbon black appear more agglomerated than those of the CBC. The agglomeration issue becomes more apparent when the loading of carbon black is reduced from 5% to 1%.

The impact of carbon black's dispersion on the electrodes' resistance was evaluated by 4-point probe measurement under a series of currents. Surprisingly, nonlinear resistivity of the electrode was obtained, as shown in Figure IV-33a and Figure IV-33b, for NMC532 electrodes with both CBC and standard carbon black. The calculated resistance from the 4-probe measurement is relatively constant until the applied current is higher than certain value. After that, the electrode resistance will increase sharply. During the 4-probe measurements, since the current collector is more conductive than the coating, the majority of applied current through the outer two pins will go in depth through the coating and then the current collector. Little current will be conducted in parallel through the coating. Therefore, the resistance value obtained during the measurement cannot be simply defined as the electrode's or the coating's resistance because of the complication of current flow. However, the corresponding current, at which the electrode resistance starts to rise, is still representative. We hypothesize that the resistance rise in Figure IV-33a and Figure IV-33b is caused the saturation current, as is observed for the conductivity behavior of single carbon nanotube and graphene.

When the loading of carbon black is 5%, the resistance of the electrode jumps up at a saturation current of  $\sim 10 \text{ mA}$ , which is the same for both electrodes using standard carbon black and CBC. When reducing the loading of carbon black from 5% to 1%, the resistance of the electrode using 1% CBC is about  $0.02 \Omega$ , which is almost 10 times smaller than that using 1% standard carbon black ( $0.3 \Omega$ ). Furthermore, the resistance of the electrode using 1% CBC jumps up at the saturation current of  $\sim 2 \text{ mA}$ , which is reduced about 5 times, and is proportional to the reduction of the carbon black composition. However, the resistivity of the NMC532 electrode using 1% standard carbon black jumps at the saturation current of  $0.2 \text{ mA}$ , which is 10 times smaller than that of an electrode using CBC carbon black. The higher saturation current for the NMC532 electrode

using 1 wt.% CBC indicates good electronic conductivity, which explained the better high rate performance of NMC532 electrode with 1wt.% CBC, as shown in Figure IV-34b. However, no rate performance difference was observed for NMC532 electrode with 5wt.% carbon black (Figure IV-34a), regardless of standard or CMC. We believe that the saturation current of NMC532 electrode with 5% carbon black is higher than the highest rate applied to the electrodes.

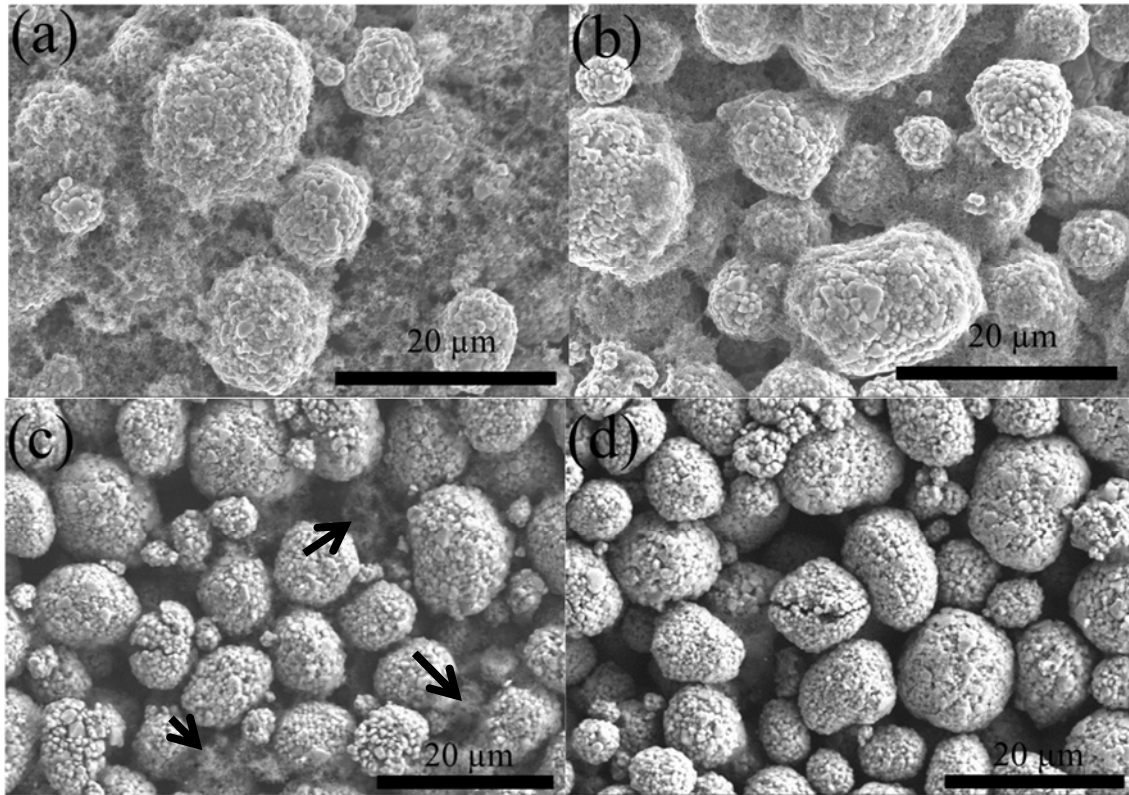


Figure IV-32: SEM images of NMC532 electrodes using a) 5% standard carbon black, b) 5% CBC, c) 1% standard carbon black, and d) 1% CBC

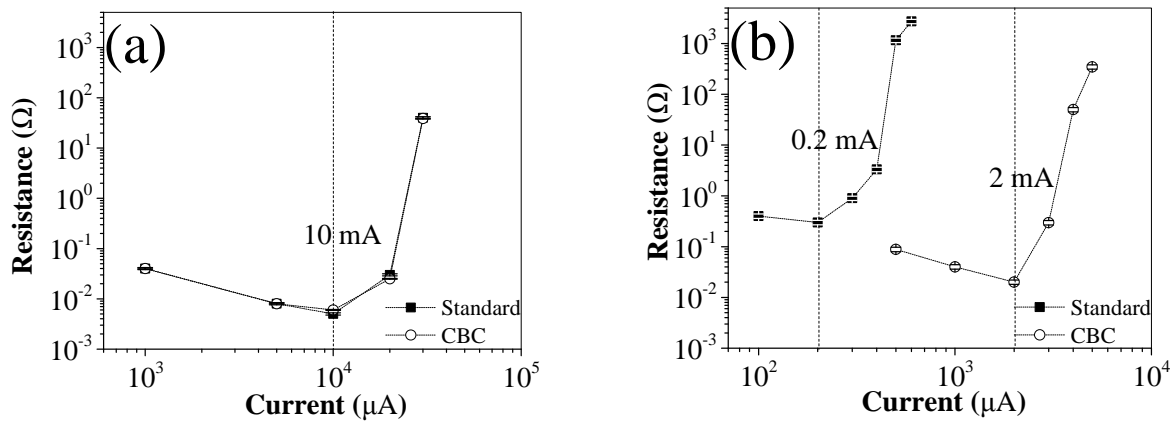


Figure IV-33: Resistance of NMC532 electrodes using a) 5% carbon black and b) 1% carbon black

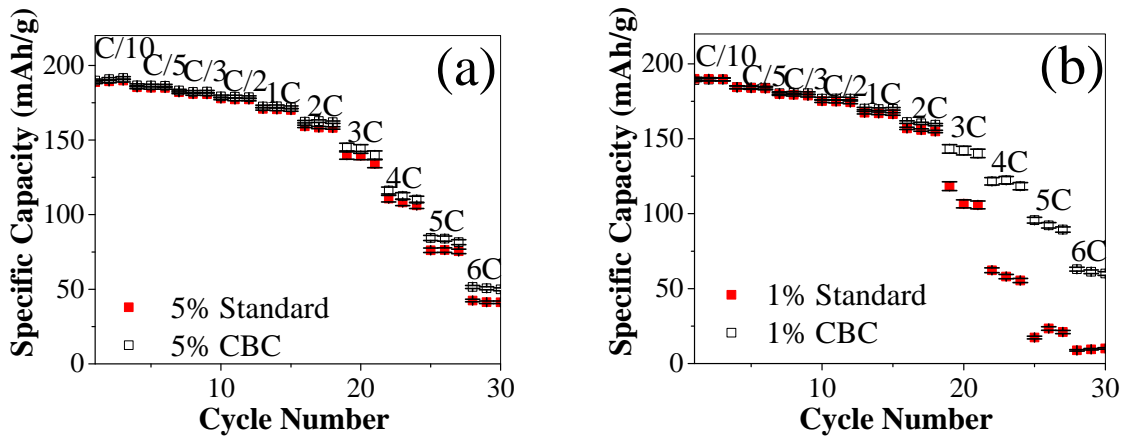


Figure IV-34: The rate performance of the NMC532 electrodes using a) 5% carbon black and b) 1% carbon black

Figure IV-35a and Figure IV-35b show the cycling performance of NMC532 electrode with 5% and 1%, respectively. The cycling performance of electrodes using 5% CBC and standard carbon black are very similar, as shown in Figure IV-35a. However when the loading of carbon black is reduced from 5% to 1%, the capacity retention of the electrode using CBC can be maintained at >95%, which is obviously better than that using standard carbon black with 91% capacity retention after 50 cycles, as shown in Figure IV-35b. The cell impedance could be a major factor for the different capacity retentions between the electrodes using 1% standard carbon black and CBC carbon black. At this low carbon content, the saturation current is very close to the operation current during the cycling test (including HPPC with high rate pulses), which will result in the higher impedance of the electrode locally. This higher local impedance will cause larger stress on the electrode due to the unavoidable local non-uniform carbon black distribution. In addition, the electrochemical stability difference of these two carbon blacks could be another reason for the difference in cycle life performance.

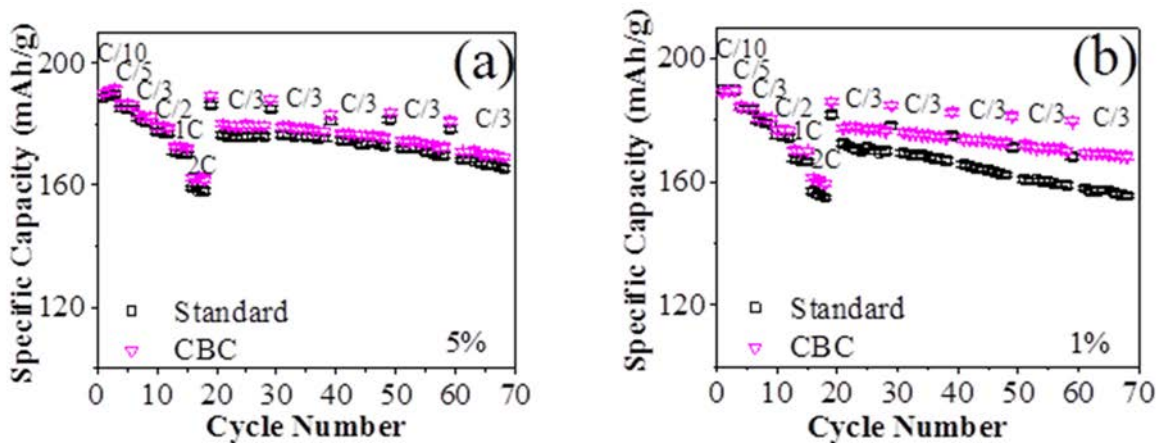


Figure IV-35: The cycling performances of NMC532 electrodes using a) 5% carbon black and b) 1 carbon black

### Conclusions

A new strategy has been developed to overcome the large ICL confronting HC type anodes in full cell LIB embodiments, wherein a sacrificial lithium source additive, e.g.,  $\text{Li}_3\text{FeO}_4$  (LFO), is used on the cathode side. Full cells using HC anodes and LCO cathodes without and with LFO additive were fabricated and subjected to detailed electrochemical testing. Comparison of full cells with LCO cathodes (without and with LFO additive) and HC anodes showed that with LFO additive the reversible specific capacity of the cathode increased by 14% and the corresponding capacity retention increased from <90% to >95% during 50 cycle charge/discharge testing. The extra lithium introduced to the full cells by adding only a small amount of LFO not only compensates for the ICL of HC, but also serves as a lithium reservoir that provides lithium ions continuously during cycling to compensate for lithium loss due to, e.g., side reactions. All of the results demonstrate an

effective strategy for overcoming the large initial capacity loss of anodes, like HC and also by implication tin, tin oxide, silicon, and silicon oxide as well; a problem that has hindered their commercial application.

A novel carbon black nanoparticle has been developed by Cabot. It has a reduced surface functional group and an increased level of surface graphitization, which can significantly improve the conductivities of the cathode electrodes. It is the first time that the nonlinear conductivity of cathode electrodes due to the tunneling saturation current has been discovered, which is dramatically impacted by the dispersion and surface crystalline quality of carbon black nanoparticles when the loading of carbon black is only 1 wt.%. The nonlinear conductivity of cathodes can dramatically affect their electrochemical performances at high rates. In addition, there is no discernable difference in terms of the rate and cycle performance for the NMC532 electrodes when reducing the loading of novel carbon black from 5 wt.% to 1 wt.% in the cathode. In summary, the total capacity of the electrode can be increased by 9% without sacrificing the capacity retention just by selecting 1% of the novel carbon nanoparticles as a carbon additive. The results offer an effective and affordable approach for improving the total capacity of the cathode electrode, just through optimizing the carbon additive.

## Products

### Presentations/Publications/Patents

1. A new strategy to mitigate the initial capacity loss of lithium-ion batteries, Xin Su, Chikai Lin, Xiaoping Wang, Victor A. Maroni, Yang Ren, Christopher S. Johnson, Wenquan Lu, *J Power Sources*, 324 (2016), 150-157.
2. Optimizing Areal Capacities through Understanding the Limitations of Lithium-Ion Electrodes, Kevin G. Gallagher, Stephen E. Trask, Christoph Bauer, Thomas Woehrle, Simon F. Lux, Matthias Tschech, Peter Lamp, Bryant J. Polzin, Seungbum Ha, Brandon Longa, *J. Electrochem. Soc.*, 163 (2), A138-A149 (2016).
3. Optimization of Inactive Material Content in Lithium Iron Phosphate Electrodes for High Power Applications, Seonbaek Ha, Vijay K. Ramani, Wenquan Lu, Jai Prakash, *Electrochimica Acta*, 191 (2016), 173-182.
4. High Energy Lithium Cobalt Oxide for Lithium Ion Batteries, Wenquan Lu, Xin Su, Yangxing Li, Frederic Aguesse, Javier Barenó, Ira Bloom, Chengjun Sun, Qi Liu, Yang Ren, Manar Ishwait, 18th IMLB Chicago, 2016.
5. A New Strategy to Mitigate the Initial Capacity Loss of Lithium Ion Batteries, Xin Su, Chi-Kai Lin, Xiaoping Wang, Victor A. Maroni, Yang Ren, Christopher Johnson, Wenquan Lu, 18th IMLB, Chicago, 2016.
6. Li-rich  $\text{Li}_3\text{FeO}_4$  (LFO) cathode material as pre-lithiation additive for enabling high-energy Si-C/NMC batteries, Chi-Kai Lin, Xiaoping Wang, Wenquan Lu, Xin, Su, Christopher S. Johnson, IBA Nantes, France, Mar. 20-25, 2016.
7. Toward high power density of lithium battery by balancing hard carbon and LFO/LCO electrodes, 11th Annual Knowledge Foundation Lithium Battery Power Conference, Baltimore, Nov. 17-20, 2015.
8. A New Process for Atomic Layer Deposition of  $\text{Al}_2\text{O}_3$  and Applications in Lithium-ion Batteries, Xiangbo Meng, Yanqiang Cao, Joseph A Libera, Wenquan Lu, Shaista Babar, and Jeffrey W. Elam, AVS 62nd Inter. Symp. & Exhibit. San Jose, Oct. 2015.

## References

1. J. Yang, Y. Takeda, N. Imanishi, O. Yamamoto, *J. Electrochem. Soc.*, 147 (2000) 1671-1676.
2. I.W. Seong, K.T. Kim, W.Y. Yoon, *J. Power Sources*, 189 (2009) 511-514.
3. I.W. Seong, W.Y. Yoon, *J. Power Sources*, 195 (2010) 6143-6147.
4. H. Sun, X.M. He, J.G. Ren, J.J. Li, C.Y. Jiang, C.R. Wan, *Electrochim. Acta*, 52 (2007) 4312-4316.
5. Y. Liu, Y. Takeda, T. Matsumura, J. Yang, N. Imanishi, A. Hirano, O. Yamamoto, *J. Electrochem. Soc.*, 153 (2006) A437-A444.
6. C.S. Johnson, S.H. Kang, J.T. Vaughey, S.V. Pol, M. Balasubramanian, M.M. Thackeray, *Chem. Mat.*, 22 (2010) 1263-1270.

## IV.B.3. Post-Test Diagnostic Facility Activities (ANL)

### **Ira Bloom, Principal Investigator**

### **Nancy Dietz Rago, Javier Bareño**

Argonne National Laboratory

9700 South Cass Avenue

Argonne, IL 60439

Phone: 630-252-4516

E-mail: [ira.bloom@anl.gov](mailto:ira.bloom@anl.gov)

### **Peter Faguy, DOE Program Manager**

U.S. Department of Energy

Vehicle Technologies Office

1000 Independence Avenue, SW

Washington, DC 20585

Phone: 202-586-1022

E-mail: [Peter.Faguy@ee.doe.gov](mailto:Peter.Faguy@ee.doe.gov)

Start Date: October 2015

End Date: September 2018

## Abstract

### Objectives

- The main objective of this project is to understand the materials-level effects of overcharging and overheating on the chemistry and physical properties of the cell components in small (~1.5 Ah) lithium-ion cells.
- Other objectives include characterizing the impact of electrode processing conditions on the performance and abuse response of lithium-ion cells.

### Accomplishments

- Cells based on NMC532/graphite chemistry (with NMP-soluble PVDF binder) were fabricated at Oak Ridge National Laboratory.
- Some of these cells were charged to 100, 120, 140, 160, 180 and 250% SOC at Sandia National Laboratories, with 250% SOC cells failing.
- The physical changes in these cells were thoroughly characterized by SEM, XPS, XRD, NMR, and HPLC methods. The results show that the SEI layer has a complex microstructure and changes in response to the extent of overcharge.
- On initial characterization, the overcharge response of the aqueous-processed cells (CMC binder) containing the same cell chemistry responded differently from the organic-processed. The electrodes in the former cells were not adhered to the separator. In the latter, they were.
- SEM, XPS, XRD, NMR, and HPLC characterization of the abused aqueous-processed CMC cells, similar to that reported here on the abused NMP-processed PVDF-based cells, is underway for the next reporting period.

### Future Achievements

- Complete characterization of the aqueous-processed cells to determine the SEI layer chemistry and structure. Characterize changes in the electrodes and separator and contrast them to those in the NMP-processed cells.
- Continue the collaborative effort to determine changes in cell components caused by changes in processing conditions and cell chemistry.

## Technical Discussion

### Background

This is a collaborative effort between Argonne (Ira Bloom, Nancy Dietz Rago and Javier Bareño), Oak Ridge (David L. Wood III, Jianlin Li, Zhija Du, Yangping Sheng) and Sandia National Laboratories (Kyle Fenton, Leigh Anna Steele, Josh Lamb, Scott Spangler and Chris Grosso). The collaboration leverages the unique facilities at each laboratory. Its purpose is to understand the abuse and performance response of lithium-ion cells and how this response change with changes in processing conditions and cell chemistry.

### Introduction

Battery technologies are routinely characterized by measuring the initial electrochemical performance and how it changes with age and use. These characterization methods and tests provide valuable information, from which degradation mechanisms can be inferred by modeling or curve fitting. However, these results do not have the benefit of direct, experimental observation of the underlying causes of the change in electrochemical behavior. There is much still left to be learned by the systematic investigation the effect of manufacturing variables on the materials changes in the cell responsible for aging. A materials-level understanding of these changes is necessary to develop new mitigation strategies that may lead to mass-produced, long-lived cells with minimal abuse response. And to confirm that the mechanistic hypotheses employed to develop these strategies correspond to the actual aging processes at operation.

With this information, battery developers may be able to improve the life and performance of batteries. Improved performance and life would be important to accelerate consumer acceptance of electric vehicles. In turn, with more electric vehicles on US roads, electricity generated from both renewable and domestic fossil fuel sources would imported oil as a source of energy for transportation, contributing to the nation's energy independence. Additionally, a decrease in air pollution due to automobile exhaust would be a direct result.

### Approach

Cell components harvested from abuse-tested cells will be characterized to determine the changes produced by differences in cell chemistry and processing variables. The characterization data will be compared to pristine materials to help delineate changes. The materials will be characterized, at first, by many techniques to determine which ones yield data that responds to the given perturbation of the system. Those techniques will then be the first ones used thereafter to track changes. The techniques available include EIS, SEM, XPS, XRD, NMR, Raman, FT-IR and HPLC methods.

### Results

Only the NMP-processed cells have been characterized fully. Here, the relationship between cell voltage and SOC is shown in Figure IV-36. Cell voltage increased linearly with SOC until 250% SOC. At that point, the cell voltage increased to the limiting voltage of the power supply. All cells, except that charged to 250% SOC, survived overcharging. The cell charged to 250% SOC went into thermal runaway and vented.

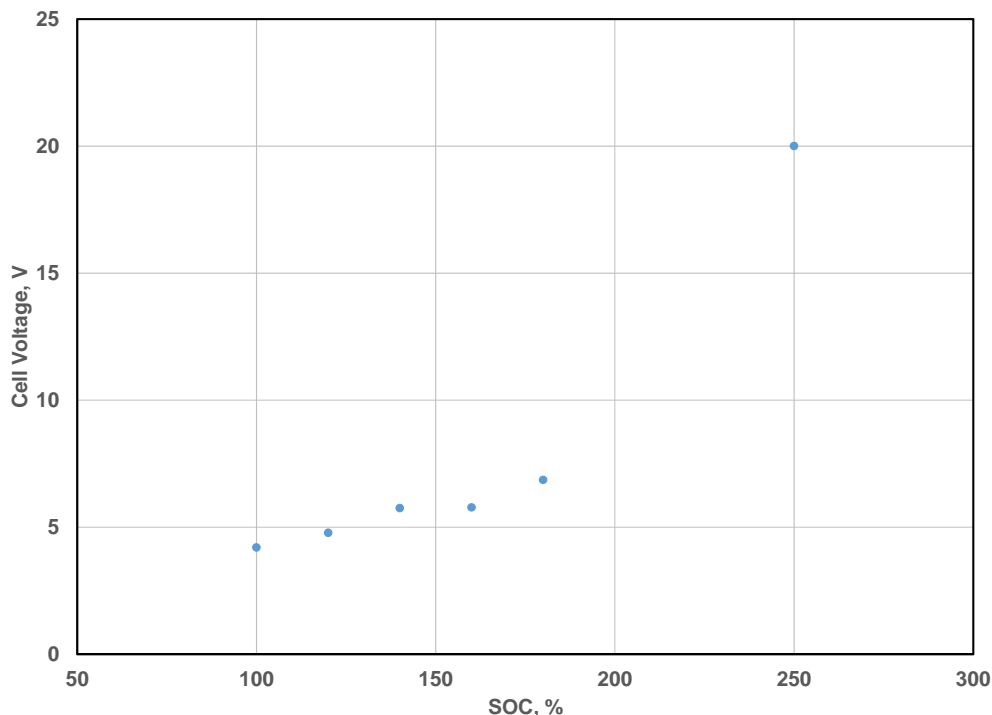


Figure IV-36: Cell voltage vs. state of charge

No obvious signs of physical damage were seen in the electrodes from the 100 and 120% SOC cells (see Figure IV-37). Observable changes were present in the anodes from cells charged to higher SOC and the extent of change increased with increasing SOC. In many cases, some of the anode material was stuck to the separator. It was interesting to note that the physical integrity of the cathode did not change with the extent of overcharge.

Examining cathode materials in the SEM showed that the microstructure did not change appreciably with extent of overcharge. On the other hand, microstructural changes in the anodes, starting with 120% SOC were evident (see Figure IV-38). Delamination of the anode coating from the copper collector was evident with increasing overcharge, starting at 140%.

Microstructures commonly referred to as “dendrites,” started to appear at 140% SOC, with dendrite concentration increasing with increasing SOC. It should be noted that, starting with 140% SOC, adherence of some electrode material to the separator was seen in all the cells. Throughout the anode surface, there were varying degrees of anode pull-away. Consequently, the microstructural representations of the surface have to be constructed by observing several areas on the anode and on the corresponding separator.

At 100% and 120% SOC, the anode surfaces appear unaltered and there did not appear to be any microstructural difference. Starting at 140% SOC, the anode surfaces were partially covered with dendrites that incorporated transition metals. Presumably, these islands of dendrites were what remained after pulling the separator away during disassembly. Observation of the separator confirmed the attachment of dendrite aggregates on the surface. Analysis of SEM images shows that the transition metals were distributed primarily in the dendrites.

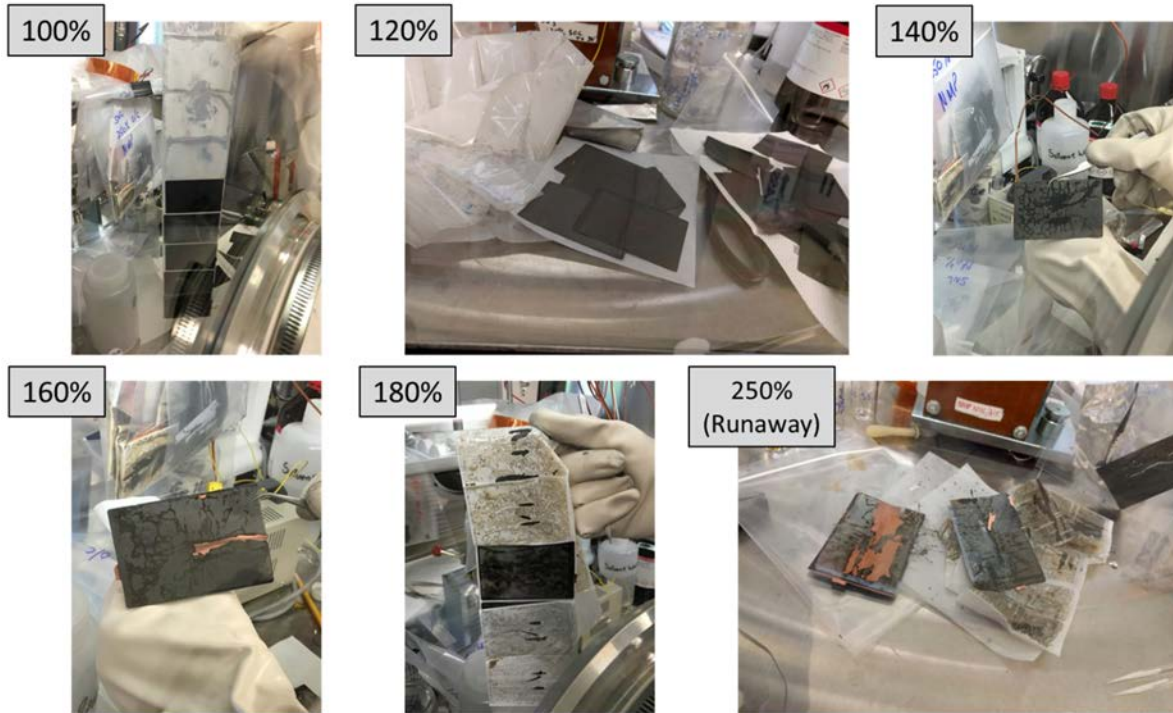


Figure IV-37: Optical photographs of initial cell disassembly. Damage to the anode laminate became obvious at 140% SOC and greater

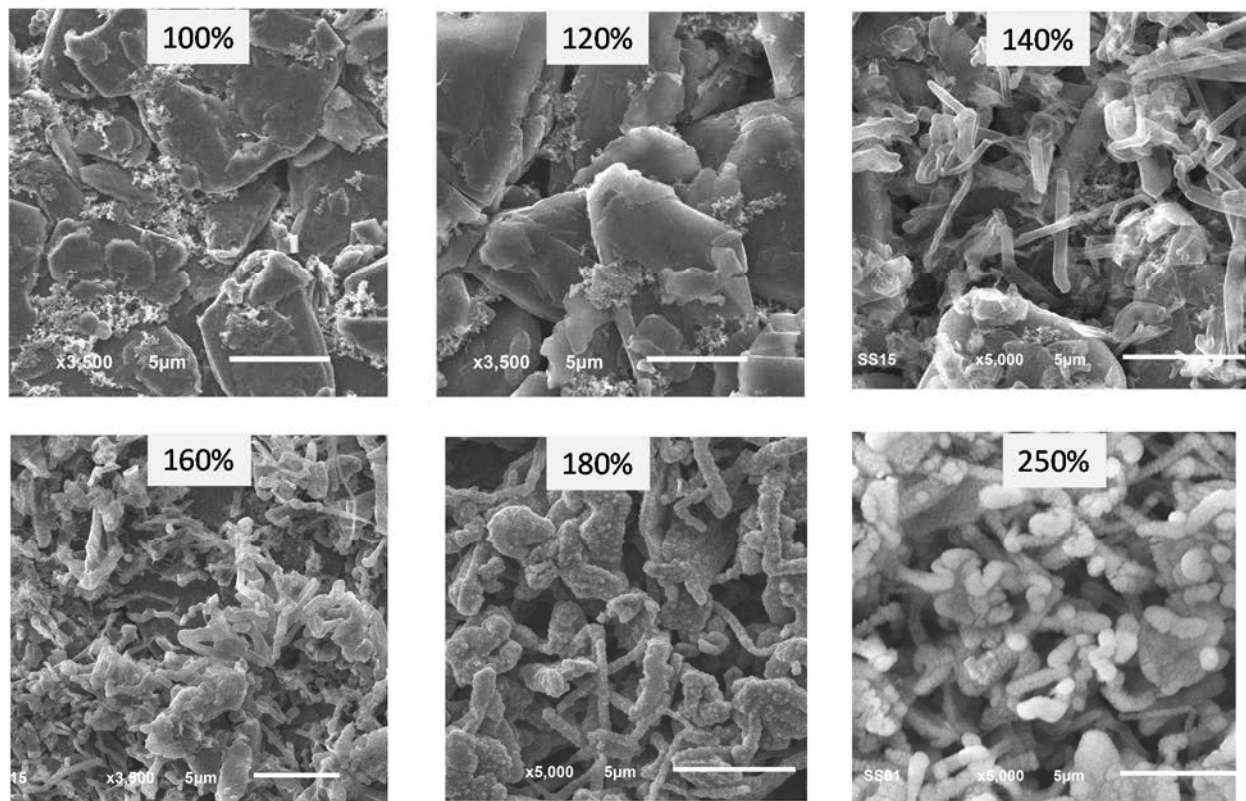
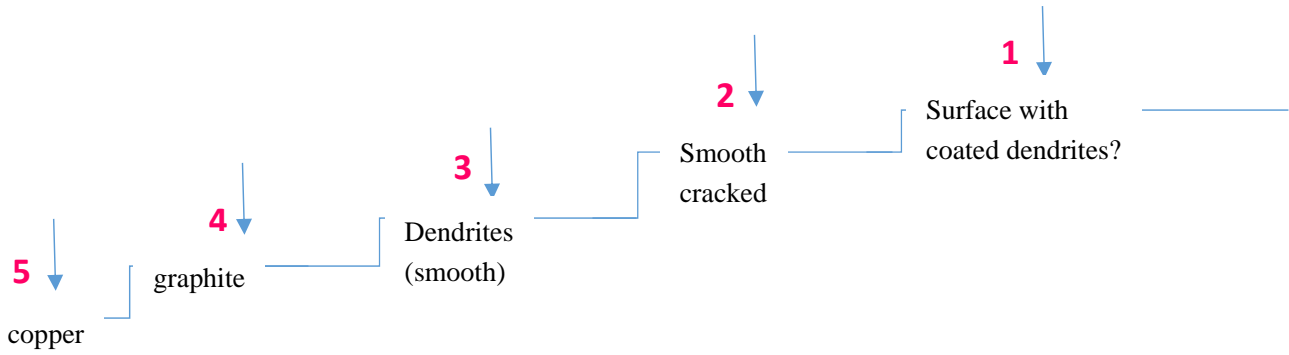
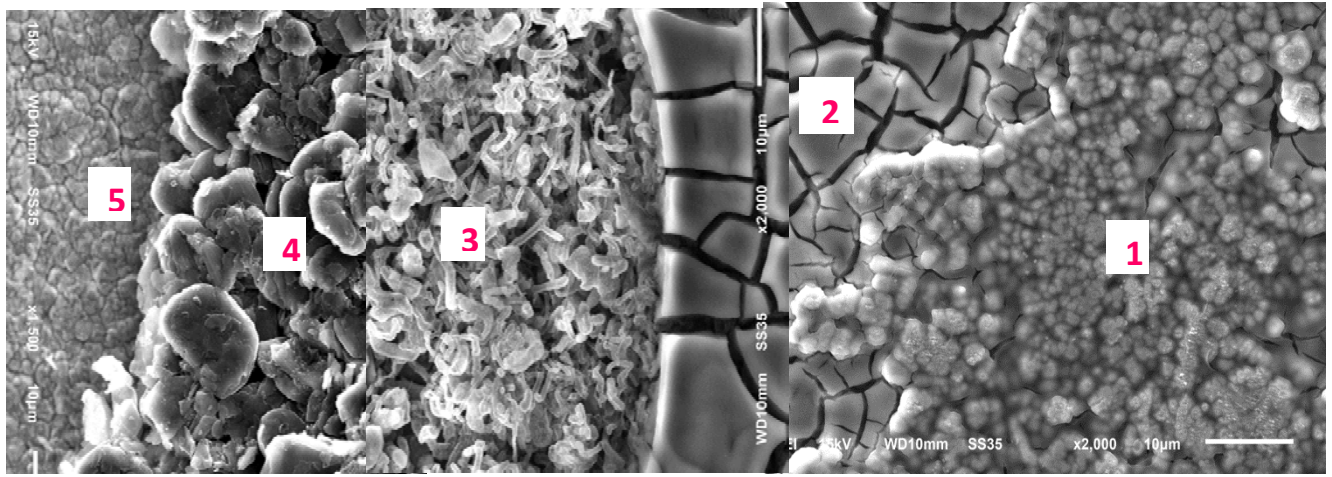


Figure IV-38: SEM images of the graphite surface vs. extent of overcharge

At 160% SOC, the anode had an “ashy” color. It appeared homogeneously covered with dendrites. It also had a smooth, but cracked layer. Similar to that seen in 160% SOC case, the 180% SOC anode surface had an “ashy” color. The smooth cracked surface layer seen in the 160% SOC cell was more extensive at 180% SOC (see Figure IV-39).

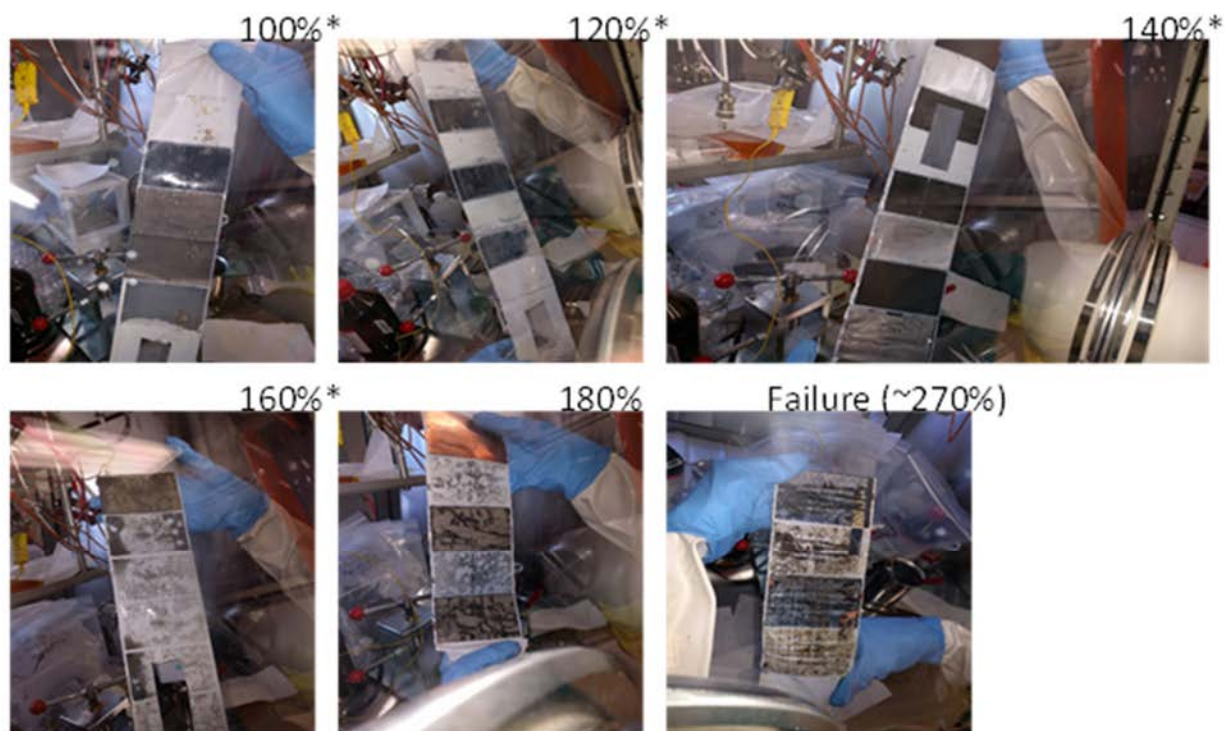


Area	1	2	3	4
C	42.25	23.63	45.09	89.41
O	32.48	14.44	32.48	5.57
F	11.45	54.37	9.50	4.75
P	2.06	6.06	1.65	0.21
S	0.13	0.33	0.17	
Mn	0.96	0.37	1.20	
Co	3.76	0.25	3.33	
Ni	6.69	0.70	6.28	
Cu				0.05
Total	100.00	100.00	100.00	

Figure IV-39: Layered structure and EDS data of 180% SOC anode surface

Examination of several areas along the anode surface made it possible to construct five layers of distinct microstructural differences between the copper collector and the anode surface. Transition metals were detected down to the dendrite layer. Their concentration decreased in the second layer and increased in the dendritic layer. It is not known if these five layers were homogeneously developed throughout the anode surface.

As a point of comparison, Figure IV-40 shows the response of the aqueous-processed cells to overcharging. Comparing Figure IV-37 and Figure IV-40 shows the impact of the binder/processing conditions. Unlike the cells containing the PVDF binder, there was no adhesion of the anode material to the separator until cell failure. The anode remained intact in all other cases. Characterization of these cells continues.



\*Hole = SEM sample of cell material

Figure IV-40: Optical photographs of initial disassembly of aqueous-processed cells that were overcharged to the extent shown

## Conclusions

The response of cells based on NMC532/graphite (PVDF binder) to overcharging is complex. The nature and structure of the deposited layer(s) depends on the extent of overcharge. Changing the binder to CMC (aqueous processing) had a profound effect on the abuse response of the cells. In general, anodes of the aqueous-processed cells tended to maintain their integrity through more of the overcharging.

## List of Abbreviations

NMC532:  $\text{LiNi}_{0.5}\text{Mn}_{0.3}\text{Co}_{0.2}\text{O}_2$   
 PVDF: poly(vinylidene difluoride)  
 NMP: N-methylpyrrolidone  
 SOC: state of charge  
 SEM: scanning electron microscopy  
 XPS: X-ray photoelectron spectroscopy  
 XRD: X-ray diffraction  
 NMR: nuclear magnetic resonance  
 HPLC: high-performance liquid chromatography  
 SEI: solid electrolyte interphase  
 CMC: carboxymethylcellulose  
 FT-IR: Fourier-transform infrared spectroscopy

## Products

### Presentations/Publications/Patents

1. "Effect of Fast Charging of Lithium-Ion Cells: Performance and Post-Test Results," Panos Prezas, Limhi Somerville, Paul Jennings, Andrew McGordon, John K. Basco, Tien Q. Duong, and Ira Bloom, SAE Technical Paper series, paper #2016-01-1194 (2016).
2. "The Effect of Pre-Analysis Washing on the Surface Film of Graphite Electrodes," Limhi Somerville, Javier Bareño, Paul Jennings, Andrew McGordon, Christopher Lyness, and Ira Bloom, *Electrochimica Acta*, 206 (2016) 70-76. doi:10.1016/j.electacta.2016.04.
3. "Experimental and Theoretical Investigations of Functionalized Boron Nitride as Electrode Materials for Lithium-ion Batteries," Fan Zhang, Károly Németh, Javier Bareño, Fulya Dogan, Ira D. Bloom, Leon L. Shaw, *RSC Advances*, 6 (2016) 27901-14.
4. "A High Power Rechargeable Non-aqueous Multivalent Zn/V<sub>2</sub>O<sub>5</sub> Battery," Premkumar Senguttuvan, Sang-Don Han, Soojeong Kim, Albert L. Lipson, Sanja Tepavcevic, Timothy T. Fister, Ira D. Bloom, Anthony K. Burrell, Christopher S. Johnson, *Advanced Energy Materials*, *Adv. Energy Materials* (2016); DOI:10.1002/aenm.201600826.
5. "New Insight into the Electrode Mechanism of Lithium Sulfur Batteries via Air-Free Post-Test Analysis," Lin Chen, Nancy L. Dietz Rago, Ira D. Bloom, Leon L. Shaw, *Chem. Commun.*, 52 (2016) 9913-16, DOI: 10.1039/C6CC04401H.
6. "The effect of charging rate on the graphite electrode of commercial lithium-ion cells: A post-mortem study," L. Somerville, J. Bareño, S. Trask, P. Jennings, A. McGordon, C. Lyness, I. Bloom, *J. Power Sources*, 335 (2016) 189-196. 10.1016/j.jpowsour.2016.10.002.

## IV.C. Critical Barrier Foci—Enabling High Energy and Next Generation Anodes

### IV.C.1. Enabling High-Energy, High-Voltage Lithium-Ion Cells for Transportation Applications – Part 1: Theory & Modeling: Surfaces & Reactivity (ANL, ORNL, LBNL, NREL)

**Hakim Iddir, Principal Investigator**

Argonne National Laboratory  
9700 South Cass Avenue  
Lemont, IL 60439  
Phone: 630-252-4505; Fax: 630-252-4176  
E-mail: [iddir@anl.gov](mailto:iddir@anl.gov)

**Peter Faguy, DOE Program Manager**

U.S. Department of Energy  
Vehicle Technologies Office  
1000 Independence Avenue, SW  
Washington, DC 20585  
Phone: 202-586-1022  
E-mail: [Peter.Faguy@ee.doe.gov](mailto:Peter.Faguy@ee.doe.gov)

Start Date: October 1, 2014  
End Date: September 30, 2018

#### Abstract

#### Objectives

Atomistic modeling to help provide fundamental understanding and prediction of  $\text{Li}(\text{Ni}_{1-x-y}\text{Mn}_x\text{Co}_y)\text{O}_2$  (NMC) bulk and surface structures, processes at surfaces and interfaces, and electrolyte-surface interactions to address the problems associated with “enabling” high-energy lithium-ion cells.

- Theoretical predictions of the low-energy surfaces of NMC particles and the effect of nickel content on particle shape and elemental segregation.
- Theoretical predictions of electrolyte- and additive-NMC surface interactions.

#### Accomplishments

- Cathode: Prediction of the crystal shape and surface morphology of  $\text{LiNi}_{1/3}\text{Mn}_{1/3}\text{Co}_{1/3}\text{O}_2$  (NMC-111) particles.
  - Established methodology to model NMC-111 polar and non-polar surfaces within the DFT+U framework.
  - Proposed models for reconstructions of polar surfaces.
  - Determination of surface energies of all low-index facets of the NMC-111 crystal.
  - Prediction of low surface-energies for Co-rich surfaces as a driving force for segregation.
  - Determination of the influence of the O and Li chemical potentials on the equilibrium particle shape of NMC-111.
  - Evaluation of voltage effect on the oxygen vacancy formation energy at different surfaces, providing insight into the relative stability of certain crystal facets with respect to oxygen loss.
- Electrolytes and additives
  - Prediction of the reaction energetics of an additive (TMSPi) with the fluorinated species in the electrolyte. Proposed a viable pathway toward the ability of the additive to scavenge HF in Gen2 electrolytes –  $\text{LiPF}_6$  in ethyl carbonate/ethyl methyl carbonate (EC/EMC).

- Computation of HOMO-LUMO gaps in Gen2 electrolytes.
- Proposed a new pathway for TMSPI decomposition in Gen2 electrolyte.
- Electrolyte - NMC-111 interaction
  - Investigated the binding of TTFP, FCP, FEC and DFEC on NMC-111 (010) surfaces in the pristine and charged states (See Chapter IV.C.3 – *Electrochemistry* for descriptions).
  - Predicted a weak binding of fluorinated species with NMC surfaces, even in the charged state.
  - Additive-additive interaction through F-F is not favorable to form a polymer-like SEI.
  - Prediction of a favorable hydrogen abstraction reaction (of EC, FCP) from NMC surfaces upon charge. Prediction of Mn reduction upon NMC surface hydroxylation (EC oxidation at NMC surface).
- Development of the spin-atom cluster expansion methodology (in collaboration with Eunseok Lee from the University of Alabama and Roy Benedek from CSE-ANL)
  - Development of a new cluster expansion method that incorporates spin within the expansion to account for the spin-dependence up-front and improve the accuracy and speed of the technique. Goal: model NMC atomic structures and apply the method to transition metal (TM) surface segregation.
  - Description of the effects from magnetic interactions as well as the effects from atomic arrangements.
  - Prediction of disproportionation:  $2\text{Ni}^{3+} \rightarrow \text{Ni}^{2+} + \text{Ni}^{4+}$
  - Prediction on the equilibrium Ni-antisite concentration in  $\text{LiNi}_{1-y}\text{Co}_y\text{O}_2$ : At 600 K, it is 8.3~11% for  $y < 0.28$  with a sudden decrease to 2.8%~3.9% in  $0.28 \leq y \leq 0.5$  and nearly 0 in  $y > 0.5$ .
  - Co-substitution can remove magnetic frustration similarly to  $\text{Ni}^{4+}$  but without the disproportionation.
  - $\text{LiCo}_4(\text{Ni}^{4+})_2$  clusters are observed at low  $y$  in  $\text{LiNi}_{1-y}\text{Co}_y\text{O}_2$ , which explains the existence of the chemical shift signal in nuclear magnetic resonance spectroscopy (NMR) at 0 ppm even in Co-dilute  $\text{LiNi}_{1-y}\text{Co}_y\text{O}_2$ .
  - Prediction of favorable Co-Co interlayer pairs when one Co becomes magnetic upon delithiation. Co-Co interlayer pairs are found to lead to phase transformation.

## Future Achievements

- Elucidate oxidation mechanisms of electrolyte molecules on pristine and delithiated NMC surfaces.
- Study the interaction of select additive decomposition products with NMC surfaces.
  - Predict the adsorption energies of several electrolyte and additive decomposition products on NMC surfaces.
  - Explore possible mechanisms of surface protection against metal dissolution.
- TM segregation to specific NMC surfaces.
  - Determination of the thermodynamic driving force for metal segregation to select NMC surfaces.
  - Investigate the relationship between surface segregation and reconstruction.
  - Establish the role of kinetic processes on the segregation of TMs to NMC surfaces.
- Cluster Expansion future work: Determine the nature of NMC phases (single phase vs. composite).
  - Extend the spin-atom cluster expansion method to NMC materials.
  - Determine thermodynamically favored phases.

## Technical Discussion

### Background

To better understand the atomic structures of NMC surfaces, electrolyte/NMC interfaces, and the fundamental processes behind the capacity fade of NMC-based cathodes, it is a prerequisite to determine the relevant NMC surfaces. Reliable atomic models can then be built to serve as a basis for further investigation on critical issues related to electrolyte/NMC interfaces and their reactivity under various conditions.

## Introduction

Energy storage devices with high energy densities are needed in order to meet the increasing demands of portable electronics and electric vehicles. Layered NMC oxides are promising cathode materials that are intrinsically capable of meeting many of these demands. However, in order to take advantage of these high, intrinsic energies, charging voltages of  $>4.2$  V (vs. graphite) are necessary. At such high voltages, surface degradation phenomena take place at untenable rates, thereby reducing the lifetime of cells. In order to take full advantage of NMC-based, lithium-ion cells, the mechanisms of these surface degradation processes must be more fully understood.

Atomistic simulations based on first-principles density functional theory at the GGA+U level, as well as at the hybrid HSE06 level, were performed to investigate the stability of several low-index surfaces of NMC-111 as a function of Li and O chemical potentials. A good agreement between predicted particle shapes and those of single-crystal NMCs synthesized under different conditions is obtained, hence, yielding valuable insight into not only the actual O and Li environment during synthesis, but also into the determination of the crystal facets and surface terminations most relevant for further studies. Preliminary results on elemental segregation of TMs to specific surfaces and on the reactivity of these surfaces toward electrolyte oxidation are presented.

## Approach

First-principles calculations based on density functional theory (DFT) at the GGA+U level, as well as the more computationally expensive hybrid functional (HSE06), were performed to investigate the stability of several low-index surfaces of NMC-111 as a function of Li and O chemical potentials. Single point calculations (no ionic relaxations) with HSE06 were needed to converge to the right electronic ground state, since the correct magnetic ground state of the TM is not always achievable with DFT+U. Implementation of this method was done using the VASP code. Computational cells including up to four hundred atoms in the periodic unit were employed. All surface calculations were performed using a periodically repeating slab separated by vacuum layers along the surface normal. A vacuum thickness of at least  $10 \text{ \AA}$  was adopted to remove interaction between the slab layers. The lattice parameter of the supercell was fixed at its bulk value. All the ions were allowed to be relaxed until the total energy differences were no more than  $0.003 \text{ eV}$ .

The layered NMC materials belong to the R-3m space group and are composed of alternate Li and TM layers with cations occupying octahedral sites. Large supercells (up to 400 atoms) were used in order to correctly depict the right symmetry of ion ordering in the TM layers of NMC-111 (see Figure IV-41). A k-point mesh of  $3 \times 3 \times 3$  was found sufficient to get accurate electronic energies for bulk calculations. Gamma point (mesh  $1 \times 1 \times 1$ ) calculations were used for surface and electrolyte/NMC interactions.

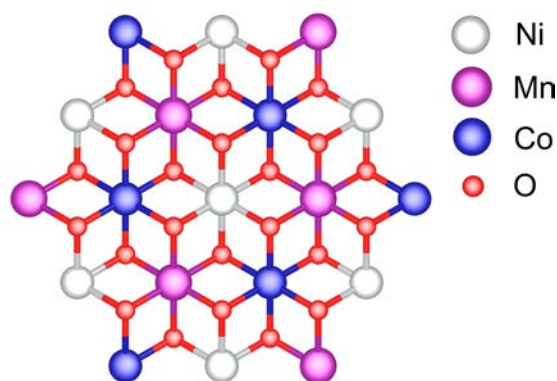


Figure IV-41: Schematic representation of the ions ordering in the TM layer of NMC-111

## Results

### 1. NMC Particle Shapes: Relevant Surfaces

The results of surface energy calculations for stoichiometric slabs are summarized in Table IV-7. The surface energy is an indication of the relative stability of different facets and terminations. The (104) surface is found to be the lowest surface energy among all the investigated surfaces, as it requires the least amount of bond breaking (one M-O bond). This surface is non-polar and each layer contains a stoichiometric amount of each component, making it less sensitive to changes in the O and Li chemical potentials. The flat, non-polar structure helps stabilize this facet. The second most stable surface is the reconstructed (110) surface. In this rearrangement, the surface forms a zigzag of (104) facets, such that the surface TMs are also fivefold coordinated. However, it is not clear from experimental images if this surface appears in the exposed surfaces of crystal particles. Kinetic processes can dominate the actual formation of this reconstruction. The (012) surface is another polar facet considered. This surface consists of alternating planes of cations and oxygen ions. Thus, there are two possible terminations for a dipole-free model of the slab; either a partially unoccupied, cation-terminated layer, or, a partially oxygen-terminated surface. The cation-terminated surface is found to be unstable; hence an oxygen-terminated surface is studied. For stoichiometric slabs, the (012) surface is less stable than the (001) surface. The stoichiometric ratio is achieved with half a monolayer of oxygen in the surface. The partial coverage of oxygen makes the (012) surface sensitive to changes in the oxygen chemical potential, and in fact becomes energetically favorable in an oxygen-rich environment (Figure IV-42). The non-polar (100) surface presents the highest energy among all the computed surfaces with a surface energy more than double the energy of the other non-polar, (104) surface. The TMs in the top layer are threefold coordinated. This produces a metal-oxygen coordination loss of three compared to one for the (104) surface.

**Table IV-7: Surface Energies for Low Miller Indices of Stoichiometric NMC-111**

Surface orientation	Surface Termination	Surface Energy (J/m <sup>2</sup> )
(104)	Ni, Mn, Co, O	0.83
(110)A*	Ni, Mn, Co, O	1.33
(001)	Ni, Mn, Co, O	1.45
(110)B*	Co, O	1.67
(110)B*	Ni, O	1.77
(110)B*	Mn, O	1.88
(012)	Ni, Mn, Co, O	2.10
(100)	Ni, Mn, Co, O	2.27

(\* ) A and B are different reconstructions that eliminate the overall dipole.

In order to predict the equilibrium particle shape of the crystal, it is necessary to take into account the conditions of the surrounding environment. Based on the possible surface compositions, there are two types of surfaces susceptible to changes with the synthesis conditions. Namely, the (012) surface is sensitive to changes in the oxygen chemical potential and the (001) is susceptible to changes in the Li chemical potential. Figure IV-42 shows the relationship between the surface energy and the oxygen chemical potential for 5 different oxygen coverage values on the (012) surface. The surface with a full monolayer of oxygen is favored at high oxygen chemical potentials (oxygen-rich environment). Highly oxidizing environments would lead to more stable (012) surfaces. It can be seen in Figure IV-42 that for those conditions, the (012) surface dominates energetically. In agreement with the experimental observations, about 80% of the exposed surfaces are (012) facets. The inset of Figure IV-42 shows an SEM image of particles synthesized using TM nitrate precursors, 1.1x LiNO<sub>3</sub>, CsCl flux, and 850°C for 8 h (See Chapter IV.C.2 - *Materials*). In contrast, in an oxygen-poor environment the predicted shape is dominated by the (104) surface, which is the most stable at stoichiometric conditions. The (001) surface appears in the particle at all the conditions at a practically constant proportion. However, this surface is covered by ½ of a monolayer of lithium and hence sensitive to variations in the chemical potential of Li.

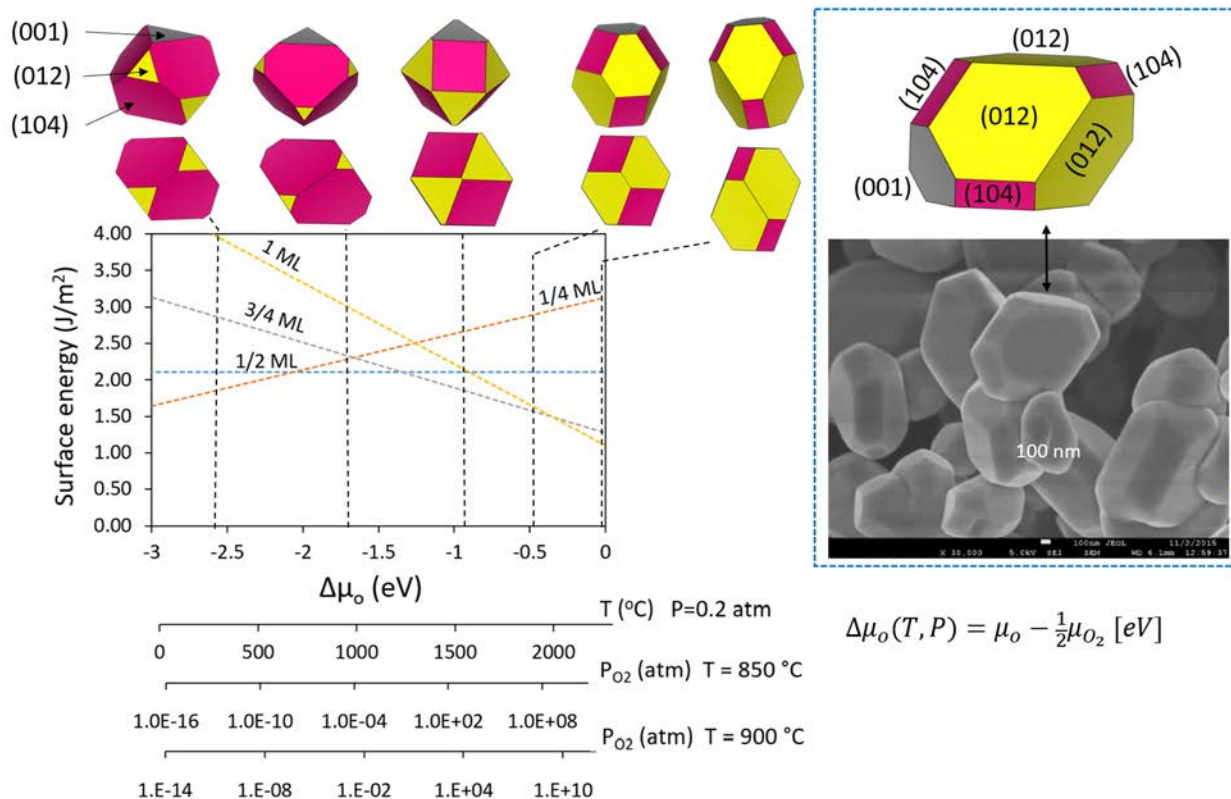


Figure IV-42: Surface energy of the (012) surface as a function of the oxygen chemical potential. The particle shape from the Wulff construction is shown at select conditions indicated by the vertical dotted lines. An SEM image of the synthesized particles is also shown

The chemical potential of lithium changes with the content of lithium during the synthesis of the material and during cycling. However, during cycling, kinetic barriers will impede changes in the particle shape. Figure IV-43 shows the (001) surface energy change with the chemical potential of Li for a value of oxygen chemical potential equal to -0.1 eV. This surface becomes predominant at  $\frac{3}{4}$  of a monolayer Li coverage on the surface, adopting a platelet shape. The inset in Figure IV-43 shows the conditions (high O and low Li chemical potentials) at which agreement is obtained with experimental results.

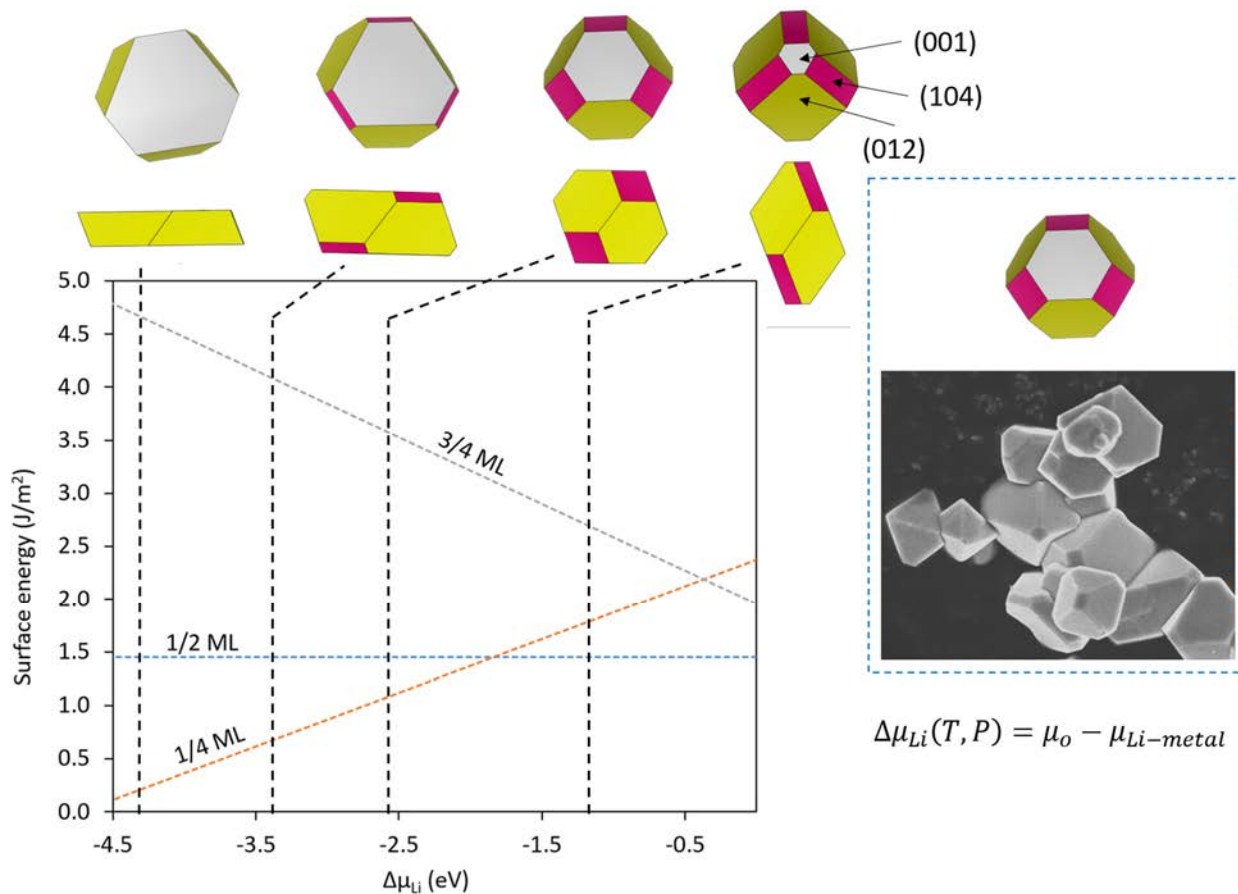


Figure IV-43: Surface energy of the (012) surface as a function of the Li chemical potential. The particle shape from the Wulff construction is shown at select conditions indicated by the vertical dotted lines. An SEM image of the synthesized particles is also shown

## 2. Electrolytes and Additives

In support of electrolyte and additive efforts within the project (See Chapter IV.C.3 – *Electrochemistry* for more details of additive molecules), the reactivity of TMSPi (Figure IV-44) with fluorinated molecules within the electrolyte was studied. A series of screening experiments revealed TMSPi to be an effective additive, acting on the cathode side of NMC/graphite full-cells, leading to better cycling performance versus TEPI as an alternative additive. One of the possible mechanisms of action is HF scavenging. Figure IV-44 shows the energetics of TMSPi transformations during reaction with fluorinated species. All the reactions are exothermic and the energy barriers are comparable, except for the interaction with LiF, where the reaction with HF is the most favored. TMSPi can react with both HF and LiPF<sub>6</sub>. In the electrolyte, LiPF<sub>6</sub> exists in equilibrium with LiF(s) and PF<sub>5</sub>(g). Additionally, LiPF<sub>6</sub> readily hydrolyzes in the presence of water to form HF, PF<sub>5</sub>, POF<sub>3</sub>, PO<sub>2</sub>F<sup>2-</sup>, and PO<sub>3</sub>F<sup>2-</sup>. TMSPi can act to significantly mitigate the formation of hydrolyzed LiPF<sub>6</sub> species.

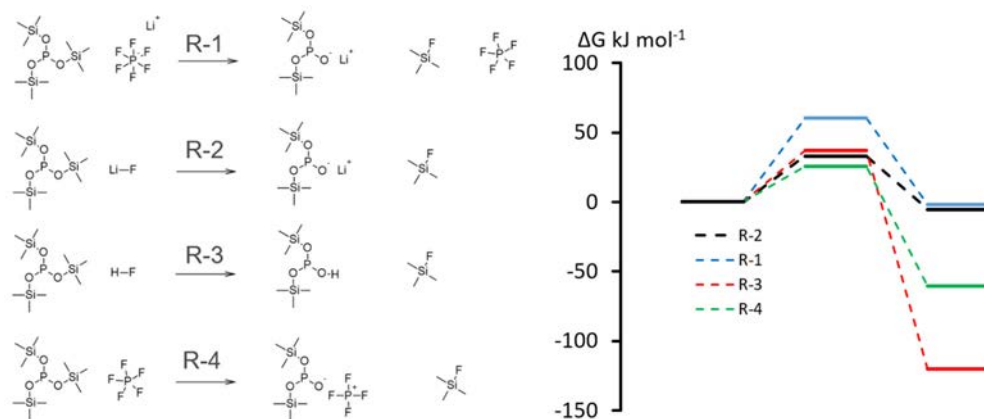


Figure IV-44: Free energies of the initial reactants, transition state, and final products for the reaction of TMSPI and fluorinated compounds present in the electrolyte

One of the significant outcomes of the electrolyte and additive work is the finding that fluorinated electrolytes produce much less TM dissolution from NMC cathode surfaces than conventional EC electrolytes. To gain some understanding on such experimental findings, the most relevant surface of NMC, (012), was chosen to investigate all possible outcomes of the interaction of EC, FEC, and DFEC with that surface. Modeling the interaction of electrolyte molecules and additives with the NMC surfaces is computationally demanding given the large supercells needed to accommodate the NMC surfaces and the relatively large molecules, without running into image-image interaction. Several initial configurations of the molecule/surface interaction are needed to determine the lowest energy state. It was found that adsorption of EC with its carbonyl group interacting on the (012) surface is thermodynamically favorable. The lowest energy configuration increases the coordination of the TM at the surface and the adsorption is preferred on Ni ions (Figure IV-45). On the contrary, the adsorption of the fluorinated molecules, FEC and DFEC, was found to be an endothermic process. In addition, it was found that EC oxidation at (012) NMC surfaces results in hydrogen abstraction and breaking of the C-H bond in EC. During this process a hydroxyl group is formed at the cathode surface and the EC ring opens. As a consequence, the surface is reduced. Preliminary data shows that the extra electron in the lattice tends to be localized on the Mn ions at the surface. This could be one of the initial steps in the dissolution of Mn into the electrolyte. The species formed at the surface upon EC oxidation is very reactive and would react with any other organic molecule in the electrolyte to form a polymer and carbonate species. The energy barrier for the hydrogen abstraction reaction from EC vanishes upon charge (80% delithiation). As expected, the reactivity of the surface increases when the cathode is charged. Contrary to EC, fluorinated electrolytes were found to interact weakly with the surface. The interaction of TTFP and TCP with NMC surfaces was also modeled and several configurations of these additive molecules were considered. Results indicate that TTFP can be oxidized at the cathode surface by bonding to an oxygen atom.

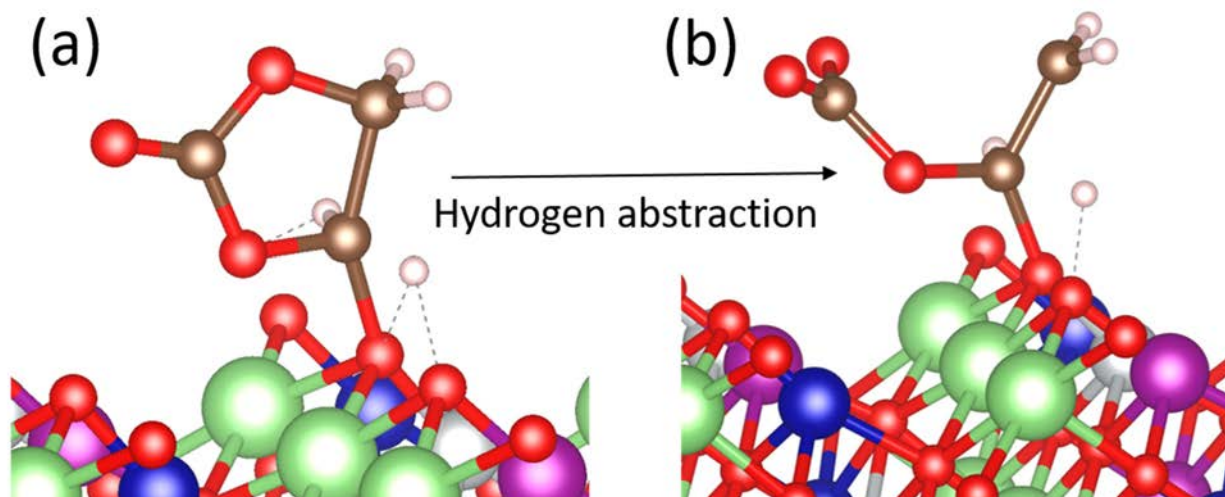


Figure IV-45: Configuration of EC on the NMC (012) surface. (a) Stable adsorption configuration. (b) Configuration after hydrogen abstraction.

### 3. Cluster Expansion Techniques and Spin States

The configuration space necessary to explore all the possible atomic arrangements needed to understand the bulk structure of NMC materials as well as TM segregation within these materials is too large to be explored solely by the relatively limited DFT models (a few hundred atoms). To be able to access larger systems (thousands of atoms) and expedite the calculations, a simpler model is needed to calculate the total energy. Cluster expansion (CE) techniques are usually used for such systems. In CE, the energy is expanded as a function of the occupancy of the ion sites and coefficients are obtained by fitting a few energies computed by first-principles. However, for NMCs the spin state (and magnetic moment) of TM ions can be degenerate. Hence, two identical atomic arrangements can have different thermodynamic energies due to distinct magnetic moment arrangements. Therefore, the inclusion of this effect is needed. Based on this idea, and in collaboration with Eunseok Lee (Alabama University) and Roy Benedek (ANL), a model was developed where the expansion basis function is a function of the coupled configuration of atomic arrangement and the spin state (magnetic moment). This model can describe the effects from magnetic interactions as well as the effects from atomic arrangements. This new model was tested with  $\text{LiNi}_{1-y}\text{Co}_y\text{O}_2$ . Figure IV-46 shows the predicted energies at different compositions. Predictions of the model include the disproportionation of Ni ( $2\text{Ni}^{3+} \rightarrow \text{Ni}^{2+} + \text{Ni}^{4+}$ ) in this system. Even though  $\text{Ni}^{4+}$  is unstable, the actual change in energy is only 9.2 (meV/f.u.) because the geometric frustration of anti-ferromagnetic ordering is removed with the disproportionation. JT distortion is removed with  $\text{Ni}^{2+}$ , and  $\text{Ni}^{2+}$ -containing structures are stable at finite temperature. JT distortion will be rare in stoichiometric  $\text{LiNiO}_2$ . Also, the model predicts at equilibrium that the Ni-antisite concentration at 600 K is 8.3~11% for  $y < 0.28$  but decreases to 2.8%~3.9% for  $0.28 \leq y \leq 0.5$  and to nearly 0 for  $y > 0.5$ . Co-substitution can remove magnetic frustration similarly to  $\text{Ni}^{4+}$  but without the disproportionation.

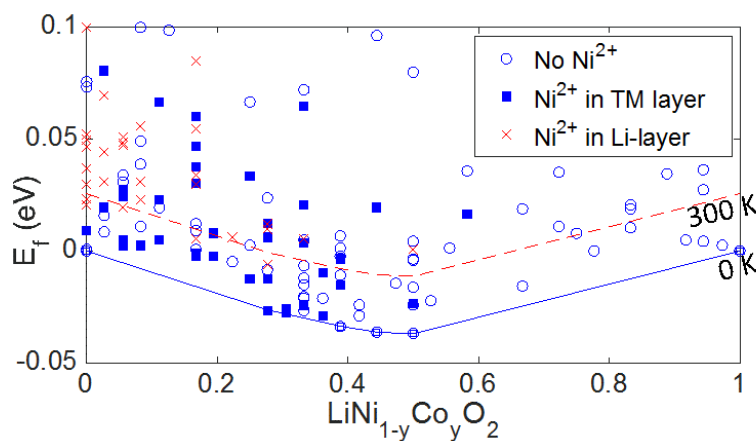


Figure IV-46: Display of Formation energy  $E_f(\text{LiNi}_{1-y}\text{Co}_y\text{O}_2) = E(\text{LiNi}_{1-y}\text{Co}_y\text{O}_2) - (1-y)E(\text{LiNiO}_2) - yE(\text{LiCoO}_2)$  as a function of the Co content. The continuous line and the dashed line indicate the convex hull at 0 K and its shift to 300 K (for comparison), respectively

### Conclusions

- Both modeling and experiment show that the NMC (012) surface is a major component in the overall mix of exposed surfaces interacting with the cell environment (electrolytes, additives, coatings, etc.) This surface is hence used as a model system for electrolyte/additive–NMC interactions.
- Modeling work on cathodes, additives, and electrolyte interactions with NMC surfaces (lithiated and delithiated), are helping to define new experiments, explain possible reaction mechanisms, and understand experimental results thus far obtained (See Chapter IV.C.2 – *Materials* and Chapter IV.C.3 – *Electrochemistry*).
- A rapidly convergent cluster expansion method was developed and tested for  $\text{LiNi}_{1-y}\text{Co}_y\text{O}_2$  systems. The extension of the technique to NMC is underway.
- The study of TM segregation to specific facets is currently in progress. Preliminary results suggest several phenomena play a role in the thermodynamic driving force of elemental segregation including

spine states and surface reconstructions. The effect of surface composition (resulting from TM segregation) on the electrolyte-NMC interactions will be the focus of future work.

## Acknowledgments

*Modeling of NMC Surfaces and Reactivity* - Hakim Iddir and Juan Garcia.

*Cluster Expansion Models* – Hakim Iddir, Roy Benedek, and Eunseok Lee.

*Synthesis and Characterization* – Guoying Chen, Javier Bareño, Fulya Dogan, Cameron Peebles, Adam Tornheim, and Ritu Sahore.

## Products

### Presentations/Publications/Patents

#### Publications

1. Fulya Dogan, John T. Vaughey, Hakim Iddir, and Baris Key, Direct Observation of Lattice Aluminum Environments in Li Ion Cathodes  $\text{LiNi}_{1-y-z}\text{Co}_y\text{Al}_z\text{O}_2$  and Al-Doped  $\text{LiNi}_x\text{Mn}_y\text{Co}_z\text{O}_2$  via  $^{27}\text{Al}$  MAS-NMR Spectroscopy, *ACS App. Mater. Interfaces*, **8**, 16708 (2016).
2. Hakim Iddir, Javier Barenó, and Roy Benedek, Stability of Li- and Mn-Rich Layered-Oxide Cathodes within the First-Charge Voltage Plateau, *J. Electrochem. Soc.*, **163**, A1 (2016).

#### Presentations

1. B. Key, F. Dogan, B. R. Long, J. R. Croy, K. G. Gallagher, H. Iddir, J. Russell, and M. Balasubramanian, *Re-Entrant Lithium Local Environments and Defect Driven Electrochemistry of Li- and Mn-Rich Lithium-ion Battery Cathodes*, 228th ECS Meeting, Phoenix, AZ, October 2015.
2. H. Iddir, J. Croy, K.G. Gallagher, C. Johnson, R. Benedek, and M. Balasubramanian, *Atomic Structure Evolution during First Charge of Layered-Layered Composite Lithium Ion Battery Cathode Materials*, 228th ECS Meeting, Phoenix, AZ, October 2015.
3. H. Iddir, *HE/HV Modeling Effort*, US Drive, Detroit MI, November 2105.
4. H Iddir, *Atomistic Models of LMRNMC Materials*, EMN Meeting on Batteries: Energy Materials Nanotechnology, Orlando, FL, February 2016 (Invited).
5. H Iddir, *Atomistic Models of Cathode Materials*, MSD Energy Storage Meeting, Argonne National Laboratory, Lemont, IL, April 2016.
6. F. Dogan, B. Key, H. Iddir, and J.T. Vaughey, *Investigation of Aluminum Environments in Lithium-ion Cathode NCA and Al-Doped NMC Via  $^{27}\text{Al}$  MAS-NMR Spectroscopy*, ECS 18<sup>th</sup> International Meeting on Lithium Batteries, Chicago, IL, June 2016.
7. E. Lee (University of Alabama), H. Iddir, and R. Benedek (ANL), *The Effects of Co-Substitution and Al-Doping on the Structural Stability of  $\text{LiNiO}_2$* , ECS 18<sup>th</sup> International Meeting on Lithium Batteries, Chicago, IL, June 2016.

## IV.C.2. Enabling High-Energy, High-Voltage Lithium-Ion Cells for Transportation Applications – Part 2: Materials (ANL, ORNL, LBNL, NREL)

### John T. Vaughey, Principal Investigator

Argonne National Laboratory  
9700 South Cass Avenue  
Lemont, IL 60439  
Phone: 630-252-8885; Fax: 630-252-4176  
E-mail: [vaughey@anl.gov](mailto:vaughey@anl.gov)

### Peter Faguy, DOE Program Manager

U.S. Department of Energy  
Vehicle Technologies Office  
1000 Independence Avenue, SW  
Washington, DC 20585  
Phone: 202-586-1022  
E-mail: [Peter.Faguy@ee.doe.gov](mailto:Peter.Faguy@ee.doe.gov)

Start Date: October 1, 2014  
End Date: September 30, 2018

### Abstract

### Objectives

- Develop surface-sensitive characterization tools to determine the inorganic and organic compounds that make up the electrochemically active surfaces of Ni-rich,  $\text{LiNi}_x\text{Mn}_y\text{Co}_z\text{O}_2$  (NMC-xyz) cathodes.
- Investigate the effect of cathode coating methodology including technique, annealing temperature, and coating thickness on electrochemical performance. Correlate electrochemical performance with changes in the composition and morphology of Ni-rich cathodes.
- Investigate and evaluate the role of cation ratio for pristine, Ni-rich cathodes with different compositions and study the correlations between electrochemical performance, composition, and structural changes upon cycling.
- Investigate the diffusion of coating and dopant constituents within  $\text{LiMO}_2$  (M=Ni, Mn, Co) structures.
- Investigate local structure and surface morphology via solid-state nuclear magnetic resonance spectroscopy (NMR) and electron microscopy techniques.
- Develop NMC-based, thin-film cathode materials for studies of surfaces and surface reactivity under various conditions (e.g., coatings, electrolytes, additives.)
- Synthesis of single-crystal NMCs having various, controlled compositions, sizes, and morphologies to couple experiment with theoretical predictions of surface composition, segregation, stability, and reactivity under various conditions (e.g., coatings, electrolytes, additives.)

### Accomplishments

- Evaluated the role of surface functionality by using a variety of ceramic coatings ( $\text{Al}_2\text{O}_3$ ,  $\text{Ga}_2\text{O}_3$ , and  $\text{SiO}_2$ ) on cathodes of different surface compositions including NMC-532 and  $\text{LiCoO}_2$  (LCO).
- Synthesized a series of aluminum (Al)-doped NMC, LCO, and NCA materials with varying transition metal (TM) and Al compositions to validate cation ordering models predicted by magic-angle spinning NMR efforts (MAS-NMR).
- Utilized microscopy techniques combined with multiple solid state NMR techniques to understand the surface morphologies, coating and bulk structures, and compositions for coated and doped materials.

- Determined the local lattice Al environments in pristine  $\text{LiNi}_{1-y-z}\text{Co}_y\text{Al}_z\text{O}_2$  (NCA) and Al “doped” NMC. Determined the TM-O-Al coordination environments, and the evolution of lattice Al sites on cycling, for NCA via solid-state NMR methods.
- Studied Al cation diffusion and its relationship to  $\text{LiAlO}_2/\text{Al}_2\text{O}_3$  solubility within  $\text{LiMO}_2$  by relating the  $\text{LiAlO}_2$  structural changes with coating performance.
- Evaluated the effect of calcination temperature on wet-coated NMC-532 and LCO and its effect on Al diffusion into the lattice, interfacial composition, electrochemical performance, and surface morphology.
- Evaluated ceramic coatings that did not form  $\text{LiMO}_2$  type structures (e.g.  $\text{SiO}_2$ ) and identified the importance of the  $\alpha \rightarrow \gamma$  phase transition of  $\text{LiAlO}_2$ .
- Synthesized and evaluated the electrochemical performance of polymeric, organosilane-coated NMC-532 as a way to study the role of water in the coating method.
- Synthesis of NMC-532 single-crystal particles with various sizes and morphologies.
- Synthesis of NMC, thin-film compositions with targeted stoichiometries and electrochemical performance.

### Future Achievements

- Understand the role of water in limiting the first-cycle efficiency of coated cathodes using structural (X-ray, electron microscopy, and NMR) and electrochemical characterization.
- Evaluate the coating conditions that lead to surface segregation and their relationship to the different NMC bulk compositions.
- GO/NO-GO decision on Al oxide as an effective coating, synthesized via wet-coating (aqueous) processes, for the baseline cathode systems.
- Evaluate the role of coating uniformity on cyclability and capacity retention.
- Develop a method for non-aqueous coatings and evaluate its effect on bulk lithium and capacity loss, formation of surface species, and overall electrochemical performance.
- Develop a new coating system with higher intrinsic lithium-ion conductivity for baseline cathodes (NMC-532, 622, and 811).
- Use MAS-NMR and electron microscopy methods to understand surface-electrolyte reactions with regard to surface cation reorganization.
- Probe surfaces and surface reactivity under various conditions utilizing well-defined, model, thin-film and single crystal NMC cathodes and couple the experimental results with theoretical calculations.

### Technical Discussion

#### Background

Many NMC-based, layered compounds of the form  $\text{LiNi}_x\text{Co}_y\text{Mn}_{1-x-y}\text{O}_2$  have been studied as promising high-energy density cathode materials. In general, NMCs possess better thermal characteristics, and are relatively lower in cost, when compared to traditional LCO-based cathodes. However, when charged to high voltages ( $\geq \sim 4.4$  V vs. graphite), NMC materials show cycling and structural instabilities that have been ascribed to surface reactions between charged electrodes and organic electrolytes as well as surface reconstructions triggered by oxygen release. The High-Energy/Voltage (HE/HV) program seeks to utilize a combination of spectroscopic tools, modeling, synthesis, and electrochemical testing to identify degradation mechanisms associated with NMC cathodes that preclude their use at higher voltages than currently utilized. By addressing materials failure mechanisms, understanding interfacial and bulk phenomena, and combining this information with new material/electrolyte designs, the underlying causes of cycling instabilities might be addressed with the view of enabling higher-energy, lithium-ion systems.

## Introduction

Various studies have shown that cycling NMC/graphite cells with an upper cutoff of ~4.2 V comes with minimal repercussions. However, above this voltage limit several issues have been identified including cation re-arrangement, increased electrolyte reactions, and TM dissolution. A common method to mitigate these phenomena has historically been ceramic coatings, a frequent choice being alumina ( $\text{Al}_2\text{O}_3$ ). However the literature has shown mixed results on this topic for NMC cathodes. In general,  $\text{Al}_2\text{O}_3$  coatings on NMCs have not consistently shown increased stability at higher-voltage cycling. The best results have been for aqueous (wet) coating methods, however, issues with thickness and uniformity are noted. In addition, atomic layer deposition (ALD) methods do not appear to provide adequate protection of NMC cathodes versus uncoated samples. Previous reports from the HE/HV team showed that one of the reasons for sub-par coatings associated with ALD was the proton-poor termination environment of NMC cathode surfaces. MAS-NMR indicated an approximate surface concentration of 15-20% hydroxyl groups, whereas the ALD method requires a more uniform coating to be effective. The Tenent group (HE/HV, NREL) has also noted similar results in attempts to get more uniform coatings. Attempts to increase the hydroxyl termination using weak organic acids were only partially successful and have led to ongoing efforts aimed at developing conformal coatings that are capable of spanning the random surface sites with the correct surface functionality.

To better understand the interaction mechanisms of surfaces and coatings, and their role in electrochemical performance, the HE/HV team has been evaluating the Ni-rich cathode materials NMC-532, 622, 811, and NCA. A systematic study of specific coating processes, correlated to cathode composition, has been carried out using a combination of spectroscopic tools, modeling, synthesis, and electrochemical testing methods (See also Chapter IV.C.1 – *Theory and Modeling* and Chapter IV.C.3 – *Electrochemistry*). Emphasis was placed on aqueous and ALD methods to synthesize a series of ceramic-coated ( $\text{Al}_2\text{O}_3$ ,  $\text{Ga}_2\text{O}_3$ , and  $\text{SiO}_2$ ) NMC-532 and LCO cathodes. The coated cathodes were treated at various post-annealing temperatures and fully characterized to understand the composition, homogeneity, and morphology of the coating layers. NMR and scanning/transmission electron microscopy (SEM and TEM) results revealed that the nature of the coating/cathode interface is highly dependent on the post heating temperature and initial cathode composition.

In addition to studies on baseline cathode powders, model NMC systems (single crystals and thin films) are being developed to better correlate theory with experiment and help to elucidate the mechanisms associated with surface-coating/surface-electrolyte interactions.

## Approach

In order to address the issues of surface instabilities, and explore the nature and efficacy of coating materials, the HE/HV project is utilizing a wide array of baseline NMC compositions and model systems including  $\text{Al}_2\text{O}_3$  coatings, single-crystal NMCs, and thin-film NMCs. These systems, coupled with theory and modeling (See Chapter IV.C.1 – *Theory and Modeling*), as well as characterization tools including diffraction, spectroscopy, and imaging, are being used to systematically probe the following, critical issues of interest:

- Description of bulk, local structures of pristine cathodes along with changes upon cycling for coated and uncoated materials.
- Characterization of cathode surfaces and cathode surface-speciation.
- Elucidating the interactions/modifications of coating materials on cathode surfaces.
- Assessing the structural and electrochemical differences between coated and doped cathode materials.
- Understanding of Al cation local environments and the composition of the interface between coating layers and the bulk of cathodes.
- Effect of sintering conditions on homogeneity, morphology, and thickness of coating layers.
- Understanding of how coating processes, cathode compositions, and surface speciation are correlated and affect interfacial chemistry and electrochemical performance.
- Developing methods to differentiate between surface and bulk Al-containing species.

## Results

During the last year, emphasis has been placed on 1) materials preparation and synthesis of both coated and doped cathodes; 2) detailed structural investigations involving bulk, local, and surface characterization techniques; and 3) electrochemical characterization. These efforts included several ceramic- ( $\text{Al}_2\text{O}_3$ ,  $\text{Ga}_2\text{O}_3$  and  $\text{SiO}_2$ ) and organic- (organosilanes, functionalized polymers) coated cathode materials as well as homogeneous materials, synthesized with the corresponding amount of dopant (relative to coated materials) as a component of the cathode structure, in order to assess the most thermodynamically stable states.

Al-cation based ceramic coating studies were performed on commercial NMC and LCO materials with varying compositions. Standardized samples were provided by Argonne's Cell Analysis, Modeling, and Prototyping Facility (CAMP). Wet-coated samples were synthesized by literature methods using an aqueous solution of Al nitrate as the source of Al cations. In a typical preparation, the cathode powder was added to a water solution of the appropriate amount of Al nitrate, stirred, and then heated at  $60^\circ\text{C}$  until nearly dry. The material was then vacuum dried, broken into batches of similar sizes, and annealed at various temperatures. The samples prepared were characterized with different techniques such as XRD, SEM/TEM, energy-dispersive X-ray spectroscopy (EDX), and solid state NMR to study the evolution of surface species, possible Al diffusion into the lattice, the changes in coating morphology and thickness, and the changes in the long-range order of coated materials upon high-temperature treatments. Electrochemical performances of all samples were tested in coin-cells in both half- (vs. Li anodes) and full-cell (vs. graphite anodes) configurations.

For the doped samples, three main aspects were studied: (i) the effect of nickel and cobalt content in NCA on bulk Al coordination and its evolution upon extended cycling, (ii) the effect of Mn on Al segregation in Al-doped NMC, (iii) the effect of Al content on the formation of secondary, diamagnetic, Al-bearing phases in NCA and Al-doped NMC. Solid state NMR has been used to qualitatively and quantitatively characterize lattice and non-lattice (i.e. surface, coatings, segregation, secondary phase etc.) Al coordination. The use of an Al specific local structural probe is crucial to effectively study the presence of lattice Al in Al-doped, layered oxides for specific Al contents and synthesis conditions, especially when the intended dopant is not always incorporated into the layered oxide structure but stays as a secondary species.

Organosilane and  $\text{SiO}_2$ -based coatings were studied on NMC-532 as a way to assess coating materials that either do not form structurally-related phases, or, do not require regular surface hydroxyl groups. NMC-532 coated with organosilanes, with varying coating contents and cathode surface pretreatment methods, were evaluated. The inorganic coatings were prepared with a wet-coating process using 2% silicic acid and  $\text{SiO}_3\text{H}_2$  ( $\text{SiO}_2 \cdot \text{H}_2\text{O}$ ) with annealing at 400 and  $800^\circ\text{C}$ . The organosilane coating process was performed with organosilanes containing various functional groups (as shown in Figure IV-47) and solvent mediums. The surface pretreatment of pristine cathode particles was critical to form surface proton groups which would affect the hydrolysis and polymerization of the organosilanes.

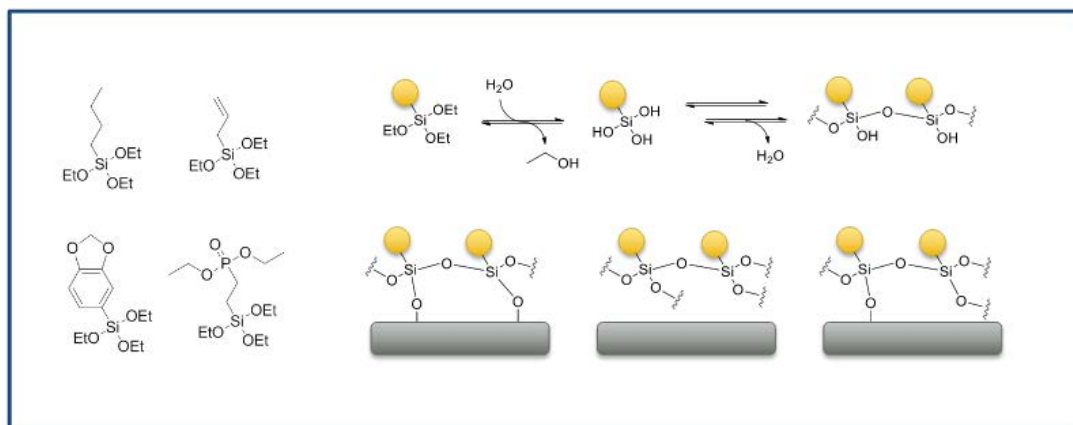


Figure IV-47: Surface coating of NMC-532 with organosilanes

## 1. Structural Characterization of Al<sub>2</sub>O<sub>3</sub>-Coated NMC-532 and LCO: Effect of Cathode Composition

Al oxide coated NMC-532 and LCO cathodes were prepared by a wet-coating process with 2 wt% Al<sub>2</sub>O<sub>3</sub> and annealing at various temperatures. The effect of cathode composition on surface and bulk structures was studied by solid state NMR. <sup>27</sup>Al MAS-NMR spectra from the NMC-532 sample annealed below 400°C (Figure IV-48, right) revealed only 6-coordinate Al peaks for surface Al<sub>2</sub>O<sub>3</sub> and/or Al(OH)<sub>6</sub>. Upon annealing to temperatures between 600-800°C the formation of lithium aluminate (LiAlO<sub>2</sub>) was observed with a new Al peak emerging at ~69 ppm. Formation of LiAlO<sub>2</sub> may indicate that lithium cations have been removed from the bulk, and/or surface, via ion exchange during the wet-coating process. Different from the Al<sub>2</sub>O<sub>3</sub>-coated NMC-532, prepared using the same conditions, coated LCO shows formation of new Al environments with annealing temperatures of 400°C (Figure IV-48, left). As the annealing temperature increased to 800°C for the LCO sample, formation of at least 6 different Al peaks are observed from 25 ppm to 60 ppm, each separated by ~7 ppm. These new peaks overlap with peaks observed for Al-doped Li(Al<sub>x</sub>Co<sub>1-x</sub>)O<sub>2</sub> and prove that Al-coated LCO gradually forms Al-doped LCO with increasing annealing temperatures; implying that Al from the Al<sub>2</sub>O<sub>3</sub> coating layer is diffusing into the bulk forming a solid solution of Li(AlCo)O<sub>2</sub>. Compared to the Al<sub>2</sub>O<sub>3</sub>-coated NMC-532 samples, Al diffusion from the surface coating layer to the bulk is much easier in LCO and leads to a homogenously-distributed, Al dopant in LCO cathodes (i.e., in the absence of Ni and Mn) above ~400°C.

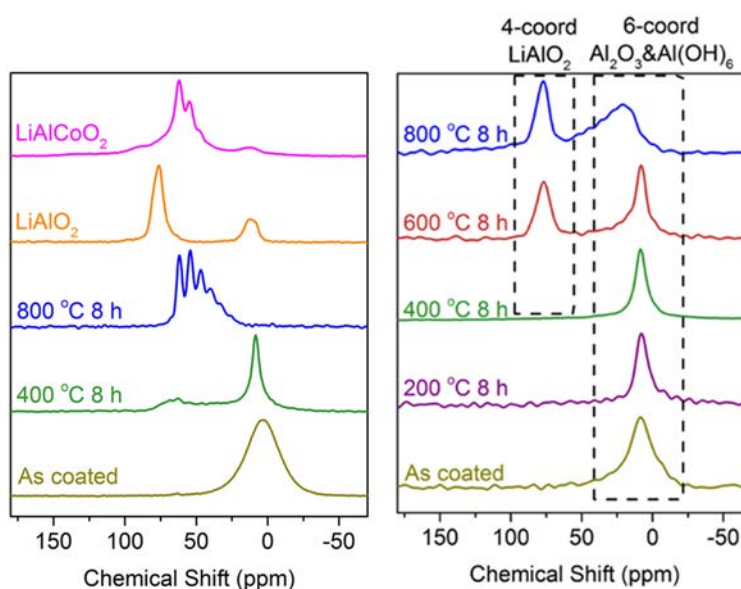


Figure IV-48: <sup>27</sup>Al MAS-NMR results of as-coated and annealed LCO samples compared to LiAlCoO<sub>2</sub> solid solution and LiAlO<sub>2</sub> reference samples (left). <sup>27</sup>Al MAS-NMR results of as-coated and annealed NMC-532 samples (right)

## 2. Surface Characterization of Al<sub>2</sub>O<sub>3</sub>-Coated NMC-532 and LCO

Using the 2 wt% coated samples of NMC-532 and LCO annealed at various temperatures, the effect on surface morphology and thickness was studied by SEM and TEM. Figure IV-49 shows SEM images of the pristine NMC-532 and Al-coated NMC-532 samples annealed at various temperatures. The pristine sample, Figure IV-49(a), consists of primary particles of ~500 nm with smooth surfaces and secondary particles of around 10 μm. The as-coated material, Figure IV-49(b), has a loose surface layer covering all secondary particles. As the material is heated from 200°C to 400°C, Figure IV-49(c)-(d), the loose surface layer appears more compact and closely attached to the surface. After annealing to 600°C, Figure IV-49(e), the surface Al<sub>2</sub>O<sub>3</sub> layer clearly transforms to a more uniform layer closely adhered to the surface of the NMC-532, better revealing again the primary particles underneath. On heating the coated sample to 800°C, Figure IV-49(f), the coating layer is better described as a hard shell uniformly covering the bulk NMC primary particles. There is no significant change observed in primary particle size with high temperature treatment. For both the 600°C and 800°C annealed samples, some small particles can be observed decorated on the surface. These particles may be due to excess Al<sub>2</sub>O<sub>3</sub> that has segregated under high temperatures.

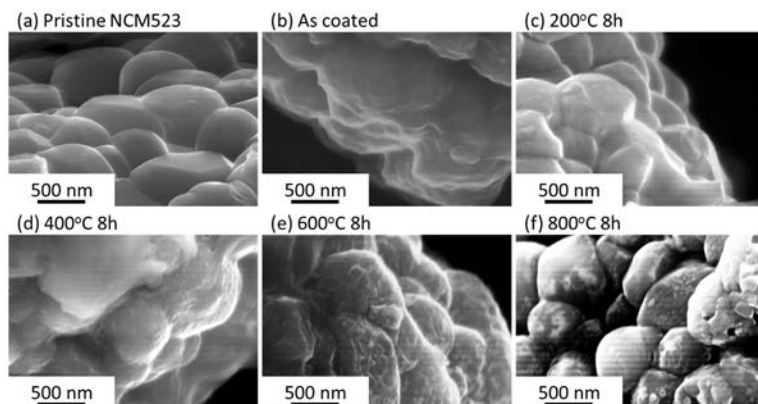


Figure IV-49: SEM images of (a) pristine NMC-532, (b) as-coated NMC-532, and (c)-(f)  $\text{Al}_2\text{O}_3$ -coated NMC-532 annealed at various temperatures for 8 h

In the case of  $\text{Al}_2\text{O}_3$ -coated LCO, due to the fast intercalation of Al into the bulk cathode after annealing, the morphological changes show a different trend from that of the coated NMC-532. Figure IV-50 shows SEM images of the pristine (a) and as coated LCO (b), and coated LCO samples annealed at 400°C (c) and 800°C (d). On annealing the sample to 400°C for 8 h, the coating becomes more uniform, covering the primary particles and resembling the coated NMC-532 primary particles that were annealed at 800°C. When the annealing temperature was increased to 800°C, the coated particle surface has no discernable surface layer that can be identified from the SEM images. This result may be due to the total insertion of the Al cations into the bulk as shown by the  $^{27}\text{Al}$  MAS-NMR data, Figure IV-48.

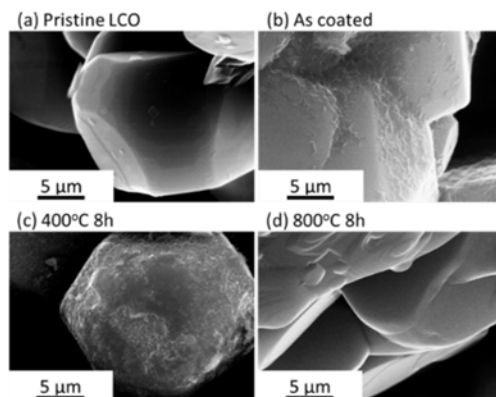


Figure IV-50: SEM images of (a) pristine LCO, (b) as-coated LCO, and (c)-(d)  $\text{Al}_2\text{O}_3$ -coated LCO annealed at various temperatures for 8 h

### 3. Electrochemical Testing

Preliminary electrochemical characterization of 2 wt%  $\text{Al}_2\text{O}_3$ -coated NMC samples annealed at various temperatures (200, 400, 600, and 800°C) indicated that the materials annealed at 800°C have the highest initial capacity and the best capacity retention. The initial capacities of all  $\text{Al}_2\text{O}_3$ -coated NMC-532 electrodes were lower than that of the pristine NMC-532 baseline. This effect may be attributable to the thickness of the coating layers creating high resistance for lithium transport through the cathode surfaces. The comparison of electrochemical performance for coated NMC-532 and LCO cathodes, Figure IV-51, shows that the latter has better performance after low-temperature annealing compared to high-temperature annealing, which may follow from solid-solution formation in the LCO cathodes.

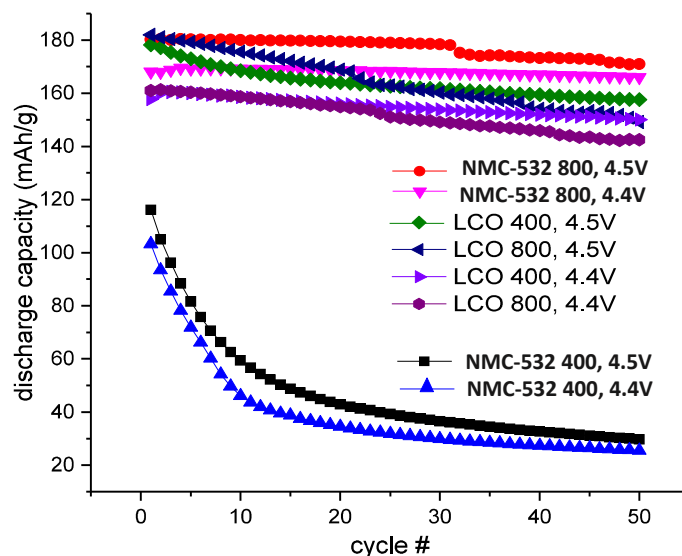


Figure IV-51: Electrochemical performance of  $\text{Al}_2\text{O}_3$ -coated NMC-532 and LCO

#### 4. Al Environments in NCA and Al-doped NMC

$^{27}\text{Al}$  solid state NMR was used to directly probe lattice (paramagnetic) and non-lattice (diamagnetic) Al environments for Al-doped NMC and NCA and to study the evolution of lattice Al sites upon cycling. The study focused on three main aspects: (i) the effect of nickel and cobalt content in NCA on bulk Al coordination and its evolution upon extended cycling; (ii) the effect of Mn on Al segregation in the Al-doped NMC structure; (iii) the effect of Al content on formation of secondary, diamagnetic Al-bearing phases in NCA and Al-doped NMC. Detailed synthesis and DFT structural modeling have shown direct evidence of lattice Al sites with non-preferential Ni/Co-O-Al ordering in NCA, and the lack of bulk lattice Al in “Al-doped” NMC. For NCA compositions with high nickel content, lattice Al prefers to occupy a position coordinated with 6Ni (thru oxygen) in honeycomb sites with a unique  $^{27}\text{Al}$  NMR peak at  $\sim -1200$  ppm, Figure IV-52. Increasing cobalt content increases Al site disorder, facilitating the formation of mixed coordination sites of the form  $[\text{3Ni3Co}]$  honeycomb sites. Increasing Al content forms large amounts of diamagnetic Al peaks that show segregation tendencies for aluminates (Al oxides, lithium aluminates, and Al oxynitrides), confirming that the maximum lattice Al occupancy in NCA is  $\sim 5\%$ . After extended cycling,  $^6\text{Li}$  and  $^{27}\text{Al}$  MAS-NMR data show Al local structure changes and lithium reordering, suggesting that Al environments are mostly in the vicinity of cobalt with Al-Co segregation and/or formation of nickel vacancies around Al. DFT calculations show that Ni vacancy formation is most favorable near Co and Al second nearest-neighbors, in other words when there is Al-Co clustering. On the other hand, Al-doped NMC has not shown lattice Al peaks or any evidence of Al substitution into the layered structure. DFT calculations have shown Al-Mn incompatibility and favored Al segregation in the presence of any significant concentration Mn within a Ni-rich matrix.  $^{27}\text{Al}$  solid state NMR studies have also shown formation of segregated Al species such as lithium aluminates, Al oxides, and Al oxynitrides acting as more of a coating/composite rather than a dopant in NMC.

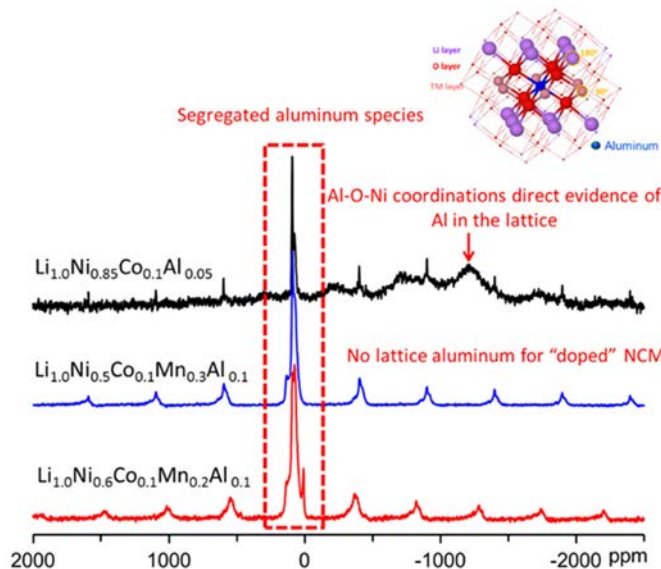


Figure IV-52: Effect of metal composition on Al local structure:  $^{27}\text{Al}$  MAS-NMR for Al-doped NMC and NCA

### 5. Ceramic and Organic Silicon Based Coatings on NMC-532: Structural and Electrochemical Characterization of $\text{SiO}_2$ -Coated NMC-532

NMC-532 cathodes were coated by 2 wt%  $\text{SiO}_2$  and annealed at 400 and 800°C. SEM images and EDX analysis of the samples, Figure IV-53(a) and (b), show a homogeneous distribution of the coating layer on particles and surface morphology changes with changes in annealing temperature. As shown in Figure IV-53 (a), more uniform, film-like surface morphology was observed for samples annealed at high temperature (800°C). However,  $^{29}\text{Si}$  solid state NMR studies revealed that high temperature treatments with the wet-coating process resulted in formation of lithium silicates with lithium removal from the bulk, Figure IV-53(c). The loss of lithium and corresponding surface-silicate formation resulted in decreased capacity and poor electrochemical performance in comparison to the uncoated cathode material, Figure IV-53(d).

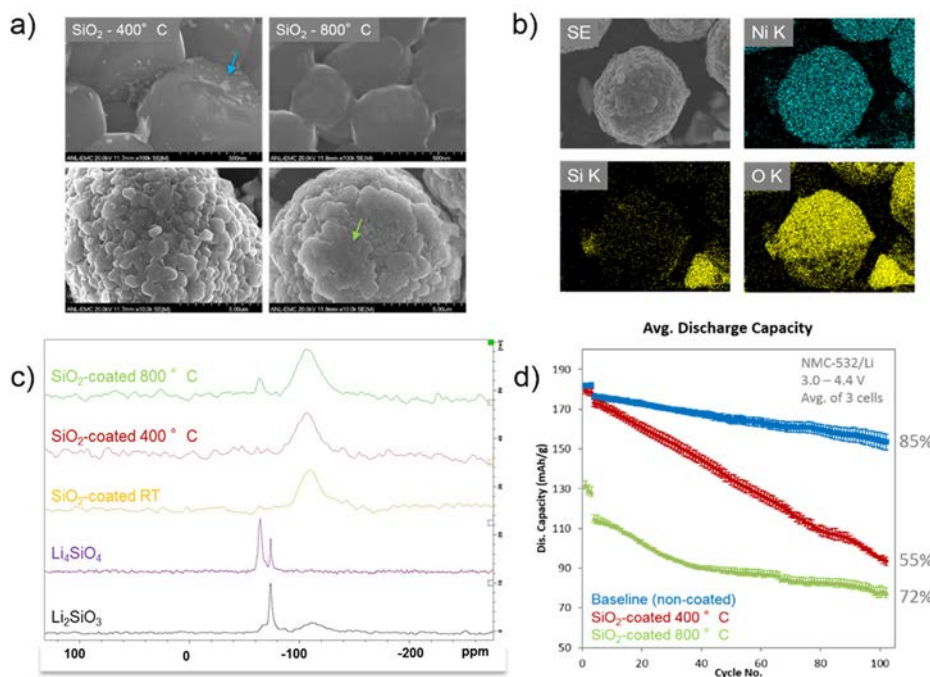


Figure IV-53: a) SEM images, b) EDX analysis, c)  $^{29}\text{Si}$  MAS-NMR, and d) electrochemical performance of  $\text{SiO}_2$ -coated and pristine NMC-532

## 6. Structural and Electrochemical Characterization of Organosilane-coated NMC-532

Organic coating of NMC-532 particles was performed in solutions of 95:5 water:EtOH and toluene followed by heating to 100°C. Fourier transform infrared spectroscopy (FTIR) studies on coated samples, Figure IV-54 (left), showed organosilane monomer polymerization on the NMC-532 particles and EDX analysis showed a homogeneous dispersion of silicon species. Electrochemical impedance spectroscopy on cycled cells (not shown) showed slightly higher impedance rise for coated samples compared to uncoated samples. Electrochemical cycling of the samples prepared in the water/EtOH environment showed slightly lower capacities compared to pristine materials, Figure IV-54 (right), with comparable capacity retention. Coating performed in toluene showed similar performance with the non-coated baseline material (not shown).

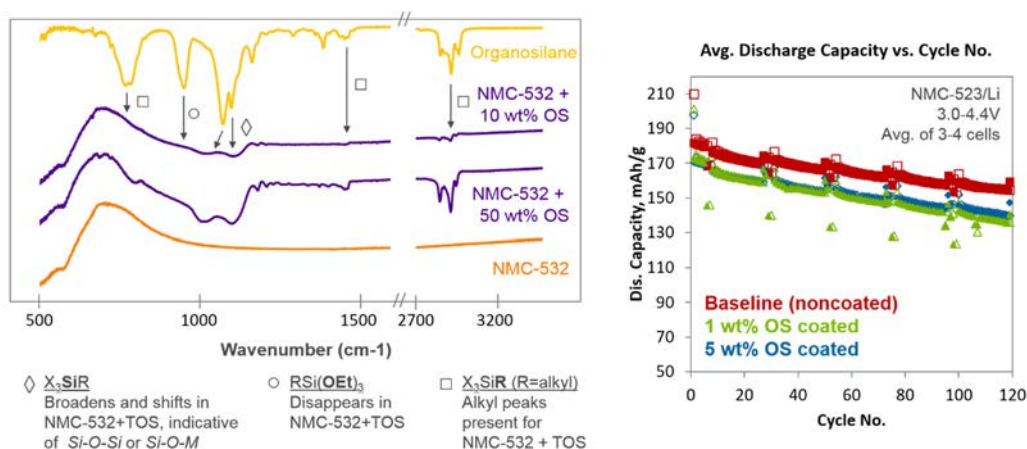


Figure IV-54: FTIR data (left) and electrochemical performance (right) of organosilane-coated NMC-532

## 7. Model Systems: Single-Crystal NMCs

Model-system based studies are effective in gaining fundamental understanding of structure-property-electrochemical relationships needed for materials optimization. In collaboration with the modeling effort (Chapter IV.C.1 – *Theory and Modeling*), Ni-rich NMC single-crystal samples with well-defined particle size and morphology were prepared by a molten-salt method. Several synthesis parameters, including the chemical nature of the precursors and the flux, the ratio between the TMs and the flux, as well as the soaking temperature and time, were adjusted to influence the uniformity and physical characteristics of the synthesized crystals. Figure IV-55 shows a series of well-formed NMC-532 crystal samples with particle sizes ranging from 10  $\mu\text{m}$ , Figure IV-55(a), to 50 nm, Figure IV-55(e). Depending on the conditions used, the samples adopted three different morphologies, namely octahedron, truncated-octahedron, and polyhedron. In all cases, the (012) family of planes dominate crystal surfaces with more than 70% coverage.

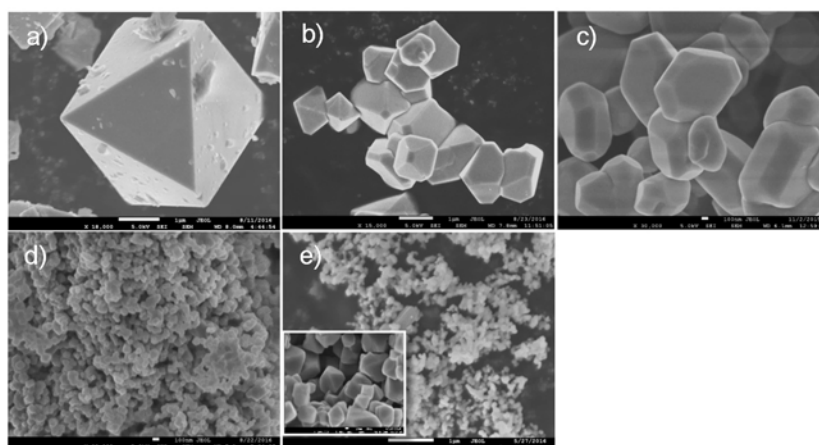


Figure IV-55: NMC-532 crystal samples with various particle sizes and morphologies: a) 10  $\mu\text{m}$ , b) 1  $\mu\text{m}$ , c) 1  $\mu\text{m}$ , d) 100 nm, and e) 50 nm

Ni-rich NMC crystal samples with other TM ratios and morphologies, especially those with metastable surface facets, are being synthesized. Characterization of the pristine and cycled crystals will be carried out in detail to determine the effects of particle size, surface faceting, Ni content, and Mn/Co ratio on cycling-induced surface changes as well as morphological, structural, and cycling instabilities.

## 8. Model Systems: Thin-Film NMCs

Thin film cathodes provide a simple structure that is well suited for advanced characterization of electrochemical reactions. The cathode structure is a thin platinum current collector (~100 nm) covered by about a micron of active cathode material. Unlike conventional slurry-cast composite cathodes, the thin-film cathode has a single phase at the outer interface that can be readily characterized by surface techniques. In addition, a barrier layer can be deposited on top of the cathode so that the effect of barrier layers on diffusion, reaction, or decomposition under different cathode conditions, can be determined on a simple geometry.

Magnetron sputtering is being used to produce thin-film cathode structures of NMCs. NMCs have a complex crystal structure with many atomic species. While the TM contents of NMC-sputtered films have been easy to achieve, the lithium content has been very sensitive to the sputtering conditions. The compositions of sputtered thin films for several NMCs have been measured by inductively coupled plasma mass spectroscopy (ICP-MS). Figure IV-56 gives an example the nickel content (a) and the lithium content (b) of sputtered NMCs as a function of the working pressure of deposition.

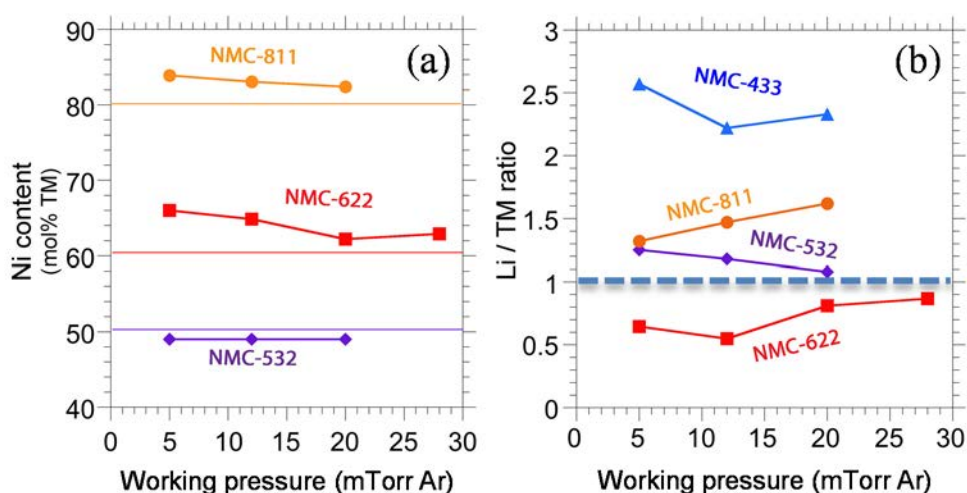


Figure IV-56: (a) Nickel content and (b) lithium content of sputtered NMC films as a function of working pressure of deposition

With the right sputtering conditions and heat-treatment temperatures, NMC cathodes have been produced that electrochemically behave like their slurry-cast counterparts. As might be expected, the discharge and cycling performance of the sputtered NMC films are very sensitive to the working pressure. For NMC-532 thin-film cathodes, films sputtered at 20 mTorr (argon), and heat-treated at 700°C, achieved over 150 mAh/g of cycling capacity, but films sputtered at 5 mTorr achieved less than 100 mAh/g. For NMC-622 thin-film cathodes, samples sputtered at 20 mTorr, and heat-treated at 700°C, resulted in 127 mAh/g compared to 64 mAh/g at 5 mTorr. The processing conditions for thin-film cathodes of other NMCs (and NCA) are being developed.

## Conclusions

Detailed analyses of several NMCs and LCO cathode materials have shown that the evolution of surface Al<sub>2</sub>O<sub>3</sub> coating layers, after heat treatment, is highly dependent on the chemistry of the underlying bulk cathode materials. Based on XRD, NMR, and electron microscopy results, two different models for the evolution of surface Al<sub>2</sub>O<sub>3</sub> coatings on NMC-532 and LCO, after different sintering conditions, are proposed. The models can be used to understand the influence of annealing temperature on the electrochemical performance of coated electrode materials. For Mn-containing NMC-532, after annealing at higher temperatures, the Al<sub>2</sub>O<sub>3</sub> surface layers became denser, more closely attached to the surface, and more uniformly distributed over both primary and secondary particles. In addition, a new LiAlO<sub>2</sub> phase is formed. However, no solid solution forms by Al

intercalation into the bulk, even after annealing at high temperatures (up to 800°C), for Al<sub>2</sub>O<sub>3</sub>-coated NMC-532 cathodes. In contrast, for Al<sub>2</sub>O<sub>3</sub>-coated LCO, a transition from an Al<sub>2</sub>O<sub>3</sub> coating to an Al dopant can be observed even at relatively low temperatures (~400°C) where Al can totally diffuse into the bulk at higher temperatures (~800°C). Electrochemical characterization studies have shown that the initial capacities of Al<sub>2</sub>O<sub>3</sub>-coated NMC-532, prepared with a wet-coating process, are lower than pristine samples when the coating content is 2 wt%. Preliminary studies have shown that decreasing coating content down to 0.5 wt% results in thinner coatings as well as improved initial capacities and capacity retention. Detailed synthesis and characterization studies on Al-doped systems (NCA and NMC) highlight Al-Mn incompatibility and the favored segregation of Al in the presence of any significant concentration Mn in a Ni rich matrix. <sup>27</sup>Al solid state NMR studies have shown the formation of segregated Al species such as lithium aluminates, Al oxides, and Al oxynitrides acting as more of a coating/composite rather than a dopant. Future studies will focus on non-aqueous methods, new coating methods, and Go/No-Go studies on Al<sub>2</sub>O<sub>3</sub> as a coating on NMCs. Spectroscopic investigations will continue and focus on surface reactivity of coated and uncoated particles in combination with detailed electrochemical investigations already in progress (See Chapter IV.C.3 – *Electrochemistry*) involving new electrolyte and additive formulations.

In addition to the detailed studies of coating materials, model systems are being successfully developed in order to better correlate experimental findings with theoretical predictions. In particular, thin-film NMCs as well as single-crystal NMCs with controlled composition, size, and morphology have been successfully synthesized.

## Acknowledgments

*Synthesis and characterization of coatings* – John T. Vaughey, Fulya Dogan, Binghong Han, Cameron Peebles, Chen Liao, Steve Trask, Bryant Polzin, and Andrew Jansen.

*Synthesis of single-crystal NMCs* – Guoying Chen, Terry Yan, and Saravanan Kuppan.

*Synthesis of thin-film NMCs* – Andrew Kercher and Gabriel Veith.

## Products

## Presentations/Publications/Patents

### Publications

1. F. Dogan, J. T. Vaughey, H. Iddir, and B. Key, Direct Observation of Lattice Aluminum Environments in Li Ion Cathodes LiNi<sub>1-y-z</sub>Co<sub>y</sub>Al<sub>z</sub>O<sub>2</sub> and Al-Doped LiNi<sub>x</sub>Mn<sub>y</sub>Co<sub>z</sub>O<sub>2</sub> via <sup>27</sup>Al MAS-NMR Spectroscopy, *App. Mater. Interfaces*, **8**, 16708 (2016).

### Presentations

1. F. Dogan, J. - S. Park, J. Croy, B. Key, and J. T. Vaughey, Investigation of Al Environments in Al<sub>2</sub>O<sub>3</sub> coated cathodes: The Effect of Cathode Composition on Electrochemical Performance and Al Local Environments, Gordon Conference on Batteries, Ventura, CA, February 2016.
2. Hubaud, F. Dogan, C. Peebles, C. Liao, and J. T. Vaughey, *Interfacial Stability of Ni-rich Layered Oxide Cathodes*, IBA2016, Nantes, France, March 2016.
3. F. Dogan, D. Proffit, A. Hubaud, D. J. Schroeder, B. Key, and J. T. Vaughey, *Materials Development for Energy Storage Applications*, Gordon Conference on Solid State Chemistry, New London, NH, July 2014.
4. C. Peebles, M. He, F. Dogan, A. A. Hubaud, and J. T. Vaughey, C. Liao, *Organosilane Cathode Coatings for High-Voltage Lithium Ion Batteries*, 18th International Meeting on Lithium Batteries, Chicago, IL, USA, June 2016.
5. C. Peebles, F. Dogan, A. A. Hubaud, and J. T. Vaughey, C. Liao, *Organosilane Coatings for Ni-Rich High-Voltage Lithium Ion Batteries*, 229th Meeting of the Electrochemical Society, San Diego, CA June 2016.

## IV.C.3. Enabling High-Energy, High-Voltage Lithium-Ion Cells for Transportation Applications – Part 3: Electrochemistry (ANL, ORNL, LBNL, NREL)

### Daniel P. Abraham, Principal Investigator

Argonne National Laboratory  
9700 South Cass Avenue  
Lemont, IL 60439  
Phone: 630-252-4332; Fax: 630-252-4176  
E-mail: [abraham@anl.gov](mailto:abraham@anl.gov)

### Peter Faguy, DOE Program Manager

U.S. Department of Energy  
Vehicle Technologies Office  
1000 Independence Avenue, SW  
Washington, DC 20585  
Phone: 202-586-1022  
E-mail: [Peter.Faguy@ee.doe.gov](mailto:Peter.Faguy@ee.doe.gov)

Start Date: October 1, 2014  
End Date: September 30, 2018

## Abstract

### Objectives

- Determine the effect of upper cutoff potential (UCP) on the specific capacity, specific energy density, and average voltage values for  $\text{LiNi}_{0.8}\text{Co}_{0.15}\text{Al}_{0.05}\text{O}_2$  (NCA) and  $\text{LiNi}_{0.5}\text{Mn}_{0.3}\text{Co}_{0.2}\text{O}_2$  (NMC-532) oxides.
- Conduct *in operando* X-ray diffraction (XRD) studies of NCA and NMC-532 electrodes to examine the phase transformation behavior of the oxides.
- Investigate electrochemically driven decomposition reactions of the electrolyte on Ni-rich oxides by examining gas evolution during high-voltage cycling.
- Determine the sources of capacity fade and impedance rise in NMC-532/graphite (Gr) full-cells during cycling at high voltages.
- Demonstrate the use of ethyl methyl carbonate (EMC) -based electrolyte solvents in high-voltage lithium-ion batteries and investigate EMC transesterification as a function of additive selection.
- Demonstrate the use of tricoordinate boron-based electrolyte additives for high-voltage lithium-ion battery operation.
- Evaluate degradation of the electrolyte/cathode interface with the baseline electrolyte, 1.2 M  $\text{LiPF}_6$  in EC:EMC (3:7 w/w) (GEN2), and determine (i) decomposition current at the electrolyte/cathode interface, and (ii) effect of electrolyte decomposition on battery performance.
- Use of potentiostatic holds to determine (i) the effect of additives in the baseline electrolyte on electrolyte oxidation rates, and (ii) effectiveness of inert coatings on cathode surfaces.

### Accomplishments

- Characterized the specific capacities and energy densities of NCA and NMC-532 electrodes at low and high UCPs. NCA values are higher than those of NMC-532 electrodes for potentials <4.5 V vs. Li. Above 4.5 V, the NMC-532 has a higher capacity and energy density. The average voltage of NMC-532 cells is higher than that of NCA cells at all UCPs studied.

- *In operando* XRD characterization – All XRD peaks of NCA and NMC-532 could be indexed by a rhombohedral phase. Splitting of the (110) peak, and appearance of the (440) peak, was observed above 4.5 V vs. Li. This new peak merged back into the (110) peak when the cell was discharged back to 2.5 V. This peak indicates the formation of a “pseudo spinel structure” in the oxides.
- Determined that  $\text{LiNi}_{0.6}\text{Mn}_{0.2}\text{Ni}_{0.2}\text{O}_2$  (NMC-622) electrodes cycled versus Li anodes show gas (mostly  $\text{CO}_2$ ) evolution at oxide potentials  $>4.4$  V vs.  $\text{Li/Li}^+$ , whereas NCA electrodes show gas evolution at oxide potentials  $>4.55$  V vs.  $\text{Li/Li}^+$ .
- Showed that the capacity fade in NMC-532/Gr full-cells, cycled in the 3–4.4 V range, results from  $\text{Li}^+$  trapping in the solid electrolyte interphase (SEI) of the graphite electrode. In contrast, cell impedance rise stems from impedance increases at the NMC-532 positive electrode.
- Determined that NMC-532/Gr cells with EMC-based electrolytes have lower capacity retentions, lower coulombic efficiencies, and higher impedance compared to the Gen2 electrolyte under program cycling protocols. Determined that ethyl carbonate (EC) addition leads to the formation of EMC-transesterification products; no such products are observed when vinylene carbonate (VC) or (4R,5S)-4,5-Difluoro-1,3-dioxolan-2-one (DFEC) are used as additives in EMC-based electrolytes.
- Three boron-based additives were investigated and of the additives tested, tris(trimethylsilyl) borate (TMSB) resulted in slightly better capacity retention, and TMSB and tris(dimethylvinyl silyl) borate (VDSMB) gave significantly lower impedance rise compared to the baseline (Gen2) electrolyte.
- Developed potentiostatic hold tests to evaluate the baseline (Gen2) electrolyte oxidation rate at high voltages with both NMC-532 and  $\text{LiMn}_{1.5}\text{Ni}_{0.5}\text{O}_4$  cathodes with  $\text{Li}_4\text{Ti}_5\text{O}_{12}$  (LTO) electrodes as anode/reference electrodes, and evaluated performance of a fluorinated electrolyte.
- Evaluated five additives across multiple metrics including cycling capacity, coulombic efficiency, and side-reaction rate, using the potentiostatic hold protocol.
- Measured effect of inert coatings on the cathode surface on initial cycling performance, side-reaction rates, and cell impedance.

### Future Achievements

- Conduct magnetic susceptibility and transmission electron microscopy (TEM) imaging investigations on the Ni-rich oxides and correlate the information with XRD data.
- Identify gas evolution reactions during electrochemical cycling as a function of electrolyte additives, test protocols, and Ni-rich oxide composition.
- Develop electrolyte systems that improve the performance of full-cells, containing Ni-rich oxides as positive electrodes, cycled at high voltages.
- Using the potentiostatic hold technique, design fluorinated electrolyte formulations for both efficient passivation of the anode and stability on the NMC-532 cathode at high voltages.
- Evaluate coulombic efficiencies and decomposition currents at the cathode/electrolyte interface for various fluorinated electrolyte components.
- Determine the effect of electrolyte formulation on transition metal (TM) ion dissolution from the positive electrode at high voltages.

### Technical Discussion

#### Background

The pursuit of high energy density lithium-ion batteries for transportation applications continues in order to increase the driving range of vehicles on a single charge. Because graphite (Gr) remains the active material of choice in the negative electrode, the search mainly revolves around layered oxides for the positive electrode. In recent years there has been immense interest in the lithium and manganese-rich layered oxides which are capable of delivering high energy density cells. This interest has ebbed somewhat because the voltage fade exhibited by these oxides lowers the usable energy and complicates state-of-charge determination of battery cells. As research to combat voltage fade continues, interest in the lithium-stoichiometric, manganese-bearing,

nickel-rich, layered oxides ( $\text{Li}_{1-x}\text{Ni}_x\text{Mn}_y\text{Co}_z\text{O}_2$ ,  $x$  typically  $<0.05$ ) has been rekindled. Oxides such as NMC-532, 622, and 811 are among the many candidates being studied as part of the Applied Battery Research (ABR) for Transportation program. These materials exhibit oxide-specific charge- and energy- densities exceeding 200 Ah/kg and 700 Wh/kg when cycled between 3-4.5 V vs. Li/Li<sup>+</sup> at low rates.

## Introduction

In this report the baseline positive electrode contains the layered oxide NMC-532 (from TODA America), the baseline negative electrode contains the A12 Gr (from Phillips 66), and the baseline electrolyte formulation (also known as Gen2) is 1.2 M LiPF<sub>6</sub> in EC:EMC (3:7 w/w) solvent. The studies reported here include tests in half-cells with lithium-metal counter electrodes and in full-cells with NMC-532 positive electrodes and capacity-matched, graphite-based negative electrodes. The ultimate objective of these studies is to enable full-cells, containing layered-oxide positive and graphite-based negative electrodes, which are able to deliver high energy densities when cycled at high voltages. With that objective in mind we describe the following experiments.

- Voltage window studies on NCA and NMC-532 electrodes to determine parameters that include discharge capacities, energy densities, and average voltages, as a function of cell (UCP).
- *In operando* XRD studies to determine crystal structure transformation and phase evolution during high-voltage cycling of NCA and NMC-532 electrodes.
- Initial studies describing gas evolution during high-voltage cycling of NMC-532 electrodes.
- Aging behavior of NMC-532/Gr full-cells cycled in the 3-4.4 V range for ~400 cycles.
- Behavior of NMC-532/Gr full-cells containing EMC-based electrolytes with SEI forming additives.
- Use of boron-based electrolyte additives to examine performance of NMC-532/Gr full-cells during high-voltage operation.
- Development of a ‘potentiostatic hold’ protocol to determine interactions at the cathode/electrolyte interface.

Studies of this nature are crucial to understanding the performance of these high-energy cells at high voltages, and for mitigating performance degradation, which is crucial to extending calendar and cycle life.

## Approach

The approaches for the various studies conducted as part of the High-Energy/Voltage (HE/HV) program are described below.

### Voltage Window Study for NCA and NMC-532 electrodes

Electrochemical performance of the oxides NCA and NMC-532 was investigated as a function of cell UCP. The voltage windows used in this study were 3.0V to 4.2V, 4.3V, 4.4V, 4.5V, 4.6V, and 4.7V vs. Li/Li<sup>+</sup>. For each cathode, 4 coin cells were examined per voltage window; hence, the total number of coin cells made per cathode was 24. All cells examined here used a baseline 25 μm, PP/PE/PP, trilayer, Celgard separator and GEN2 electrolyte consisting of 1.2 M LiPF<sub>6</sub> in EC:EMC (3:7 w/w). The cells were tested on a MACCOR Series 4000 cycler at 30°C with the following procedure: 3 formation cycles at a ~C/10 rate, 2 cycles at a ~C/24 rate, 3 cycles at a ~C/10 rate, 3 cycles at a ~C/5 rate, 3 cycles at a ~C/2 rate (C/5 charge), 3 cycles at a ~1C rate (C/5 charge), and 3 cycles at a ~2C rate (C/5 charge), for a total of 20 cycles. Particular attention was paid to Cycle #1 charge (initial delithiation capacity), cycle #5 discharge (reversible lithiation capacity at C/24 rate), and cycle #8 discharge (reversible lithiation capacity at C/10 rate).

### Gas evolution during high-voltage cycling of Ni-rich oxides

To investigate electrolyte decomposition reactions over electrode surfaces, studies were performed on electrodes cycled in a half-cell configuration (3-4.6 V vs. Li/Li<sup>+</sup>) in specially constructed electrochemical cells with gas sampling capabilities. In these cells, 2 mL/min of He are flown across the electrode to capture the evolved gases. This gas stream is then constantly sampled using an in-line mass spectrometer. In these

experiments, a 13 mm working electrode is combined with a lithium-metal anode separated with a glass fiber/Celgard-2325 separator stack infiltrated with 200  $\mu\text{L}$  of the Gen2 electrolyte. Electrodes were obtained either from Argonne National Laboratory's Cell Analysis, Modeling, and Prototyping Facility (CAMP), or Oak Ridge National Laboratory's Battery Manufacturing Facility (BMF).

### **Aging behavior of NMC-532/Gr lithium-ion cells cycled in the 3-4.4 V range**

All electrodes examined in this study were from Argonne's CAMP Facility. The positive electrode was comprised of a coating of NMC-532, C45 carbon black, and PVdF binder on an Al current collector. The negative electrode was comprised of a coating of A12 graphite (Phillips 66), C45 carbon black, and PVdF binder on a Cu current collector. All cells contained the Gen2-based electrolyte and Celgard 2325 trilayer separators. Electrochemical tests were conducted on 2032-type coin cells assembled in an argon-atmosphere glovebox. The cells were tested in a constant-temperature chamber held at 30°C. Long-term cycling tests were conducted in the 3.0-4.4 V range. The tests included four formation cycles at a  $\sim\text{C}/10$  rate, followed by aging cycles at a  $\sim\text{C}/3$  rate that included a 3-h constant voltage hold at 4.4 V. This constant current-constant voltage (CC-CV) cycling test was interrupted periodically to obtain reference performance data, which included impedance measurements using a modified hybrid pulse power characterization (HPPC) protocol and capacity measurements at low rates ( $\sim\text{C}/20$ ) to determine the true loss of cyclable lithium. Throughout the tests, selected coin cells were removed at predetermined intervals for detailed diagnostic evaluation. Before disassembly the cells were cycled between 3.0-4.4 V at a very slow rate (typically  $<\text{C}/50$ ), then held at 3.0 V for at least 12 h. To determine the effect of aging, coin cells were assembled with the harvested electrodes and cycled as appropriate to obtain the desired comparisons.

### **Examining EMC-based electrolyte with SEI forming additives for NMC-532/Gr full-cell cycling**

The idea of this research is to remove EC from the baseline carbonate-based electrolyte leaving a predominantly EMC-based electrolyte. The addition of small amounts ( $<5.0$  wt%) of SEI formers (or additives that have been shown to passivate the graphite electrode) to the EMC-based system should prevent severe electrolyte decomposition on the graphite electrode. The low concentrations of these additives ensure that once an SEI is formed, continual oxidation of these components at the positive electrode is suppressed. The SEI former additives used in this study include EC, vinylene carbonate (VC), and (4R,5S)-4,5-Difluoro-1,3-dioxolan-2-one (DFEC) which have all been previously shown to passivate the graphite electrode.

### **Use of boron-based electrolyte additives as cathode protection agents for high-voltage lithium-ion operation**

The idea of this research is to explore the impact of the branched functionality of tricoordinate boron-based electrolyte additives. The functionalities explored include tris(trimethylsilyl) borate (TMSB), boric acid tris(hexafluoroisopropyl) ester (THFIPB), and tris(dimethylvinyl silyl) borate (VDSMB). The role of the trisubstituted silyl groups are to act as scavengers for protic species (HF, acids) which are thought to be corrosive to the cathode surface. While two of the studied additives have these functionalities (VDSMB and TMSB), the other additive (THFIPB) does not. Full 2032-type coin cells (NMC-532/Gr) were assembled containing the baseline electrolyte with and without 1.0 wt% of the boron additives (the data shows the average of three cells) and their electrochemistry was observed.

### **Developing a 'potentiostatic hold' protocol to determine cathode-electrolyte interactions**

For this work NMC-532 cathodes were coupled with LTO anodes (both made by the CAMP Facility), cycled to confirm cell behavior, then charged to a high voltage and held there for 60 h. For cells with a stable electrolyte, the voltage will be maintained until the battery is discharged. For cells with 'unstable' electrolytes, oxidation reactions at the cathode/electrolyte interface will tend to lower the voltage. In order to maintain the cell voltage, a current that is equal and opposite to the side-reaction current must be provided; this current serves as a measure of electrolyte instability. Finding an electrolyte formulation, electrolyte additive, or electrode surface treatment that decreases this side-reaction current is necessary to enable high-performing, high-voltage, lithium-ion electrodes; however, in order to do so, a baseline test protocol is needed. The test protocol developed includes the following steps: (i) cells undergo a single, slow cycle followed by ten faster cycles at room temperature (RT). Cells are then placed in a constant-temperature chamber and allowed to come to thermal equilibrium; (ii) cells are slow charged to the hold voltage (for example, 4.6 V vs.  $\text{Li}^+/\text{Li}$ ),

then held at the hold voltage for 60 h; (iii) cells are then removed from the chamber and cycled at RT, one slow cycle and ten faster cycles, as in (i); (iv) The cells are then held at an intermediate voltage for impedance measurements. This ‘potentiostatic hold’ protocol has been used to examine the behavior and effectiveness of various electrolyte additives and cathode coatings.

## Results

### 1. Voltage Window Study for NCA and NMC-532

The data in Figure IV-57 are useful to evaluate capacities in the various voltage windows and also to design properly capacity-matched electrode (negative-positive) pairs. The cycle-8 delithiation capacity plots in Figure IV-57 (right) indicate that the NCA electrode has significantly higher capacity than NMC-532 for potentials <4.5 V vs. Li/Li<sup>+</sup>. Above 4.5 V, the NMC-532 has a slightly higher capacity.

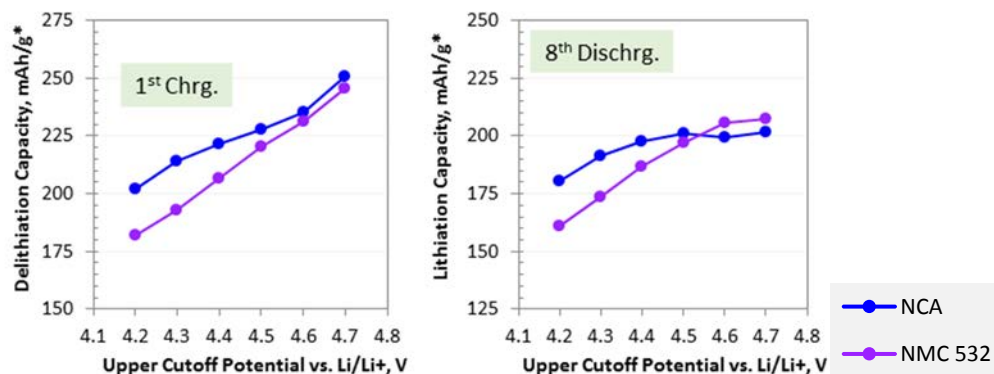


Figure IV-57: Average first delithiation capacity at a C/10 rate vs. UCP (left) and average eighth-cycle lithiation capacity at a C/10 rate vs. UCP (right). All cells were tested at 30°C. \* Weight of oxide in grams

Although capacities are useful to design properly balanced electrodes, the practical energy density of the cathode is of greater importance because it impacts the performance specifications of practical cells. Energy densities of the NCA and NMC-532 electrodes are shown in Figure IV-58 as a function of UCP. As observed for the capacity plots, the NCA cathode has significantly higher specific energy density than NMC-532 when the potential is limited to 4.5 V versus Li/Li<sup>+</sup>. Above 4.5 V, the NMC-532 has a higher specific energy density.

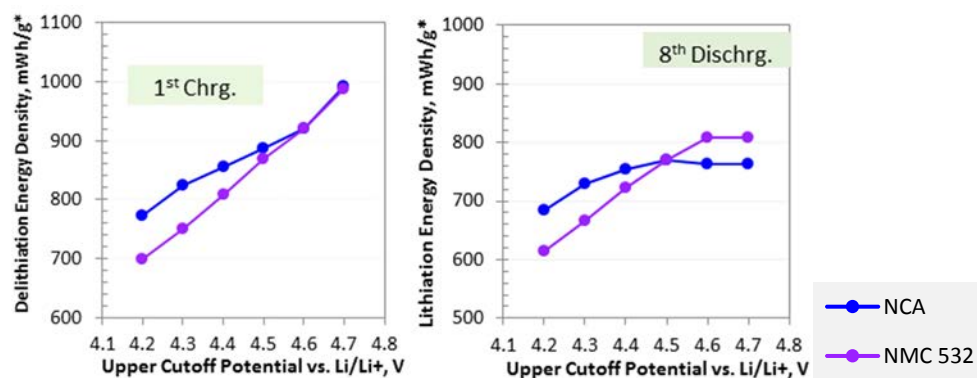


Figure IV-58: Average first delithiation energy density at a C/10 rate vs. UCP (left) and average eighth-cycle lithiation energy density at a C/10 rate vs. UCP (right). All cells were tested at 30 °C. \* Weight of oxide in grams

The energy-capacity relationship was investigated further by calculating the average voltage of the NCA and NMC-532 during charge and discharge. Figure IV-59 depicts the average charge voltage (left) and average discharge voltage (right) for the 5<sup>th</sup> cycle at a ~C/24 rate for the two oxide electrodes. The average voltages reported in these plots were calculated at the end of charge (left) and discharge (right) for the 5<sup>th</sup> cycle of each cell by dividing the total Wh by the total Ah, then taking the average from each set of coin cells. The study shows that the average voltages for NMC-532 are higher than those of NCA at all UCP values, i.e., the NMC-532 oxide operates at a higher potential than the NCA oxide.

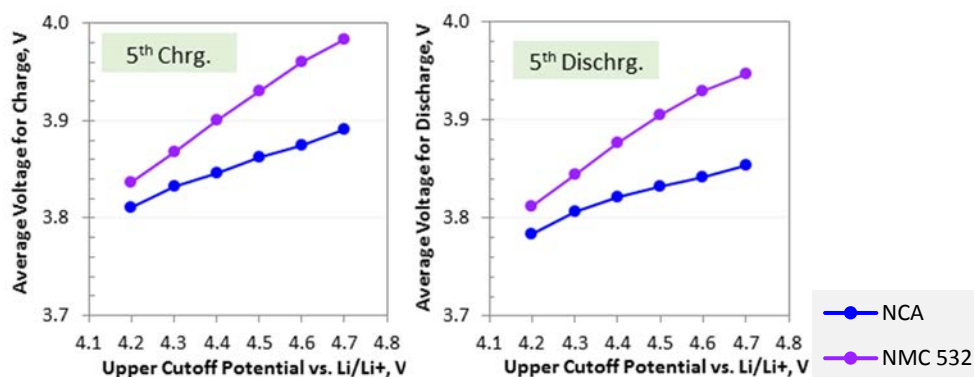


Figure IV-59: Average charge voltage at a C/24 rate vs. UCP (left) and average discharge voltage at a C/24 rate vs. UCP (right). All cells were tested at 30 °C. \* Weight of oxide

## 2. *In operando* X-ray Studies of NCA and NMC-532 Electrodes

In order to understand the mechanism of capacity fade, phase transformations in the NMC-532 and NCA electrodes were followed using *in operando* XRD. The electrodes were monitored during the first charge-discharge-charge cycles between 2.5 and 4.75 V vs. Li/Li<sup>+</sup> with a current rate of C/20 (Figure IV-60). The experiments were performed in a specially modified 2032 coin cell. All the characteristic peaks associated with the rhombohedral phase were indexed. To study these diffraction patterns in detail, magnified spectra of (003), (101), (012), (108), and (110) Bragg reflections along with time resolved isoplots of (003), (101), (012), (104), and (113) Bragg reflections were used, Figure IV-60.

Only the NCA data are shown in Figure IV-60, but similar trends were observed for NMC-532. Splitting of the (110) peak with appearance of the (440) peak was observed above 4.5 V. This new peak merged back into the (110) peak when the cell was discharged back to 2.5 V. This peak can be assigned to a spinel structure. However, since there is no appearance of the (220) peak, this transformation is often termed as a “pseudo spinel structure”. During charging, the  $2\theta$  value of the (003) peak decreased slightly up to ~4.5 V. The gradual c-axis expansion is due to oxygen layer repulsion as lithium ions are removed from the lithium layer. Upon further charging to 4.75 V the (003) peak shifted significantly to higher angle, indicating that the interlayer distance suddenly decreased. This suggests that the optimum UCP for NCA is ~4.5 V vs. a graphite anode. Further investigations into the behavior of these Ni-rich cathodes are being carried out using magnetic susceptibility and TEM imaging techniques.

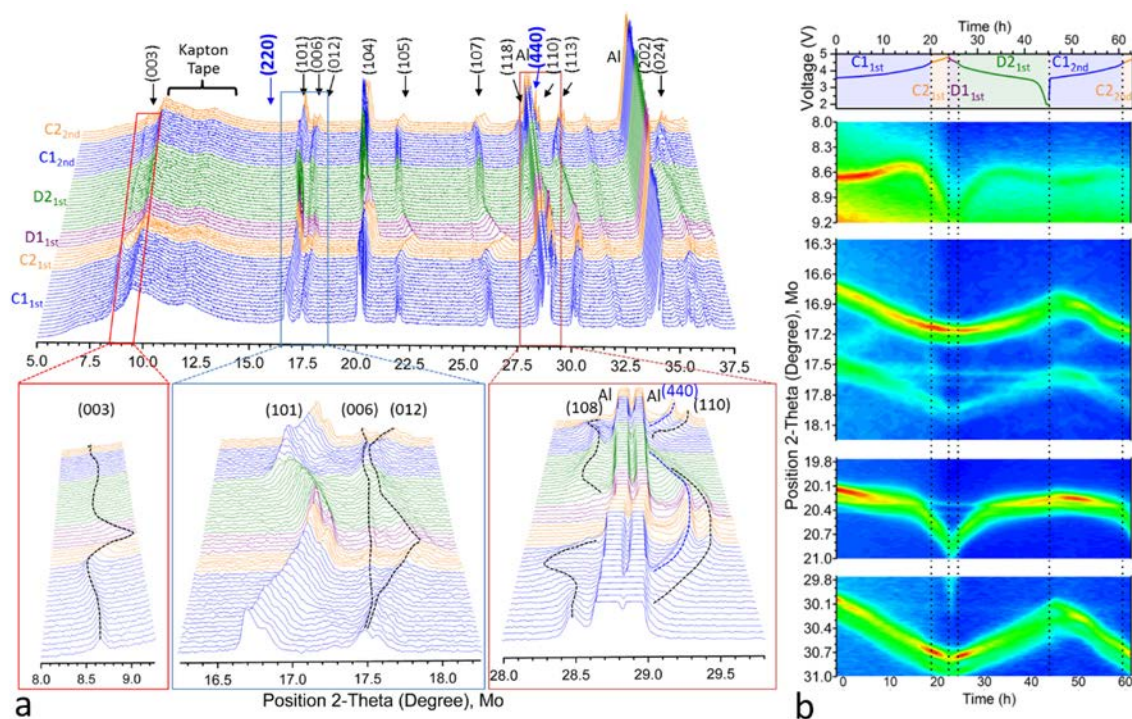


Figure IV-60: (a) *In operando* XRD of NCA showing the appearance of the (440) peak from the (110) peak at high voltages, which can be attributed to conversion of the layered structure to a pseudo-spinel structure when the cells are cycled to high UCP. (b) Isoplots of the *in operando* XRD data to better illustrate the shift in peak position as the cell is cycled

### 3. Gas Evolution during High-Voltage Cycling of Ni-Rich Oxides

The gas evolution experiments were conducted on electrodes obtained from either the Argonne CAMP facility or ORNL's BMF. In these measurements there are several effects going on at the same time. First, the linear carbonate solvent in Gen2 electrolyte is slightly volatile and contributes a background gas pressure/mass spectrometer signal. The intensity of this signal is related to the evaporation of the solvent which is assumed to be constant; the additional signal intensities are from catalytic decomposition of the electrolyte over the electrode surfaces. This effect is highlighted in Figure IV-61 which shows mass spectrometry data collected from a NMC-532/Li cell (left); Gr/Li cell (middle), and a NMC-532/Gr cell (right).

**Background keeps getting higher from more gas evolution (from left to right)**

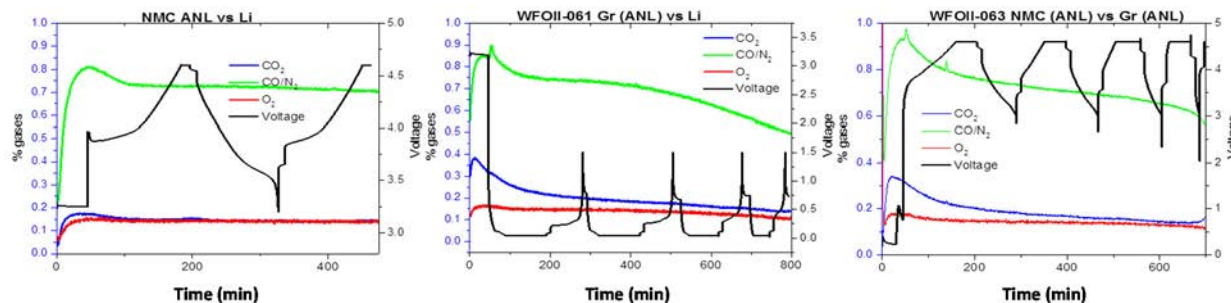


Figure IV-61: Mass spectrometry data collected as a function of potential from cells with NMC-532 vs. Li (left), graphite vs. Li (middle), and NMC-532 vs. graphite (right). The higher CO and CO<sub>2</sub> signals from left to right correspond to more intrinsic catalytic decomposition of the electrolyte.

The second gas evolution is caused by electrochemical decomposition of the electrolyte. This is demonstrated in Figure IV-62 (left) for a NMC-622 electrode cycled versus lithium metal. In this dataset there is no gas evolution until the cell is charged to 4.4 V (vs. Li/Li<sup>+</sup>). At this point there is a clear evolution of CO<sub>2</sub>, presumably from electrolyte solvent oxidation. Similarly, the NCA electrode, shown in Figure IV-62 (right),

also exhibits a significant gas evolution event, but at 4.55 V (vs. Li/Li<sup>+</sup>). The reaction mechanisms leading to gas generation are unclear at this time and will be the subject of future investigations.

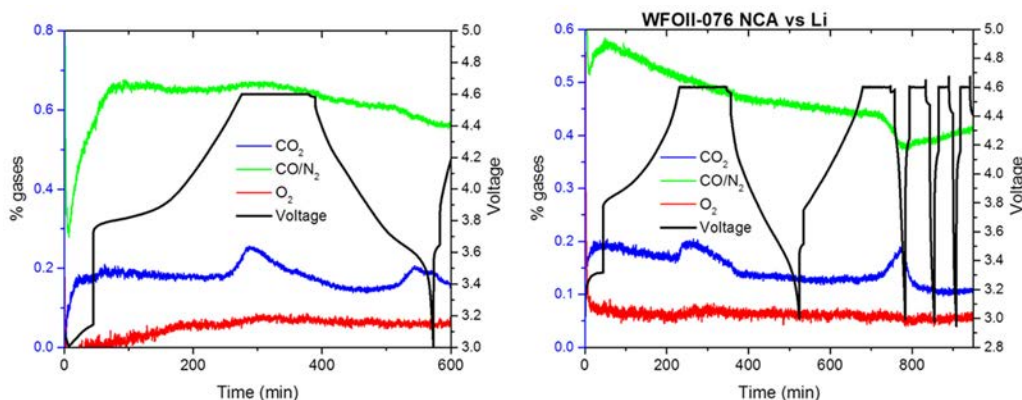


Figure IV-62: Gas evolution in a cell containing a NMC-622 electrode (left) and a NCA electrode (right)

#### 4. Aging Behavior of NMC-532/Gr Lithium-Ion Cells Cycled In the 3-4.4 V Range

A representative example of capacity-voltage plots from the NMC-532/Gr full-cells, cycled in the 3-4.4 V range at 30°C, is shown in Figure IV-63(a). For the first cycle, the charge and discharge capacities are 217.6 and 189.2 mAh/g respectively, yielding a Coulombic efficiency of 87.0%. At cycle 404, values of the discharge capacity, capacity fade, and coulombic efficiency are 112.5 mAh/g, 40.5%, and 99.4%, respectively; the corresponding values of the discharge energy, energy fade, and energy efficiency are 433 mWh/g, 39.4%, and 97.7%, respectively. The loss in cell capacity, calculated at two cycling currents (18 mA/g and 180 mA/g), is shown in Figure IV-63(b). The values are the average of multiple cells tested under the same conditions and the error bars reflect variations in the data obtained from multiple cells. Note that the capacity variation between cells at the low current is small. At higher currents, the variation is small initially but increases on cycling and is significant beyond ~200 cycles. The percent capacity loss measured with the lower current is linear, ~40% capacity loss after 404 cycles. Because this value roughly reflects the amount of cyclable lithium, the data indicates that the lithium loss is a linear function of the cycle number. At the higher current, the measured percent capacity loss is not linear, indicating a greater influence of cell impedance, especially beyond ~200 cycles.

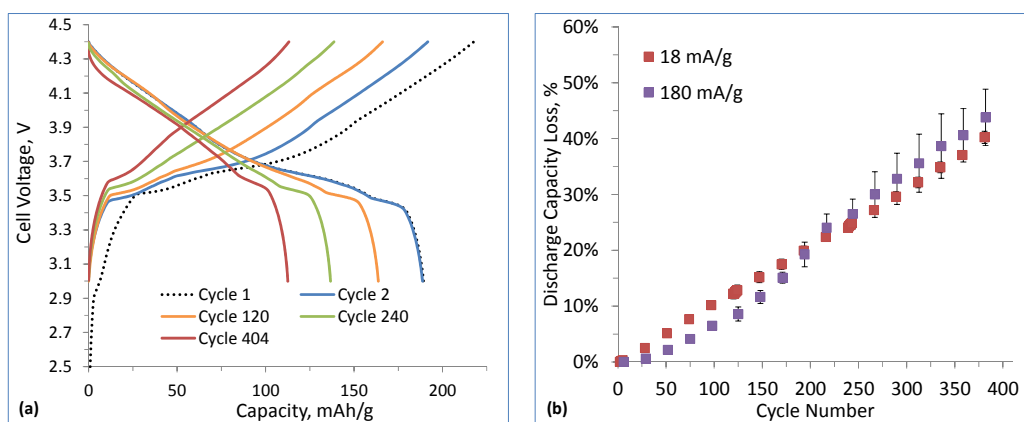


Figure IV-63: (a) Capacity-voltage profiles for NMC-532/Gr cells as a function of cycling (3.0-4.4 V, 30 °C). (b) Average discharge capacity loss measured with two cycling currents, 18 mA/g and 180 mA/g

In order to determine electrode contributions to cell capacity fade, capacity data on electrodes harvested from cells, after formation cycles and after extended cycling, was obtained. Because of the very low currents, the effect of impedance can be neglected and capacities measured can be assumed to reflect the true capacity of the electrodes. Figure IV-64(a) and Figure IV-64(b) show data from the positive and negative electrodes, respectively. The discharge capacity of the positive electrodes harvested from cells after formation cycling, 120 cycles, 240 cycles, and 404 cycles are 202, 199, 197, and 189 mAh/g-oxide, respectively; the corresponding values for the harvested negative electrodes are 354, 345, 344, and 330 mAh/g-graphite,

respectively. These data indicate that both positive and negative electrodes lose some capacity after extended cycling – these losses may arise from various factors that include particle isolation resulting from fracture and/or loss of electronic connectivity, loss of electrode active material through dissolution into the electrolyte, and reductions in specific capacity because of phase changes in the active materials.

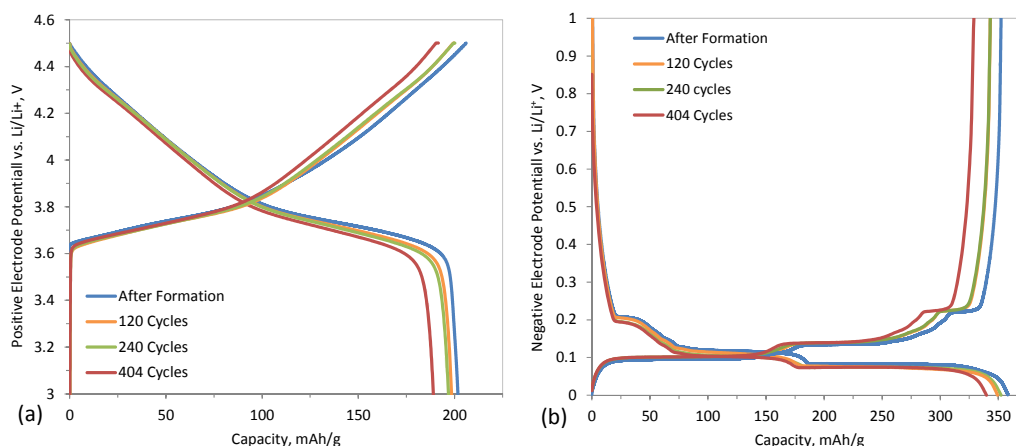


Figure IV-64: (a) Cell voltage profiles (<math>C/50, 30\text{ }^\circ\text{C}</math>) for the NMC-532/Li cell cycled between 3.0 and 4.5 V and (b) the Gr/Li cells cycled between 1.5 and 0.0 V. The electrodes were harvested from full-cells after formation, 120, 240, and 404 cycles

Cell impedance is an importance measure for transportation applications because batteries may be discharged rapidly during vehicle acceleration or charged rapidly during vehicle (regenerative) braking. Because both acceleration and braking demand high current bursts during short time periods, impedance was determined by HPPC tests which measure the cells' ability to withstand high discharge or charge current pulses without significant degradation. A representative example of area specific impedance (ASI) values ( $\Omega\text{-cm}^2$ ), during the discharge pulse from a NMC-532/Gr cell, as a function of cell voltage and cycle number is shown in Figure IV-65(a). It is evident that cell impedance increases on cycling; furthermore, the impedance rise is non-uniform across the voltage range and is higher for cell voltages  $>4.0$  V. Note that the actual voltages of the current pulse are indicated by the markers. After formation cycling (e.g., after cycle 6), data from nine discharge pulses covering the entire voltage range are obtained during the measurement. As cycling progresses, and cell impedance rises, fewer and fewer data points are obtainable as the cell becomes unable to complete the high current pulses due to the lower voltage limit (2.5 V) set to prevent over-discharge. Thus after 126, 245, and 383 cycles, the ASI values are only obtained at 8, 7, and 5 voltage locations, respectively.

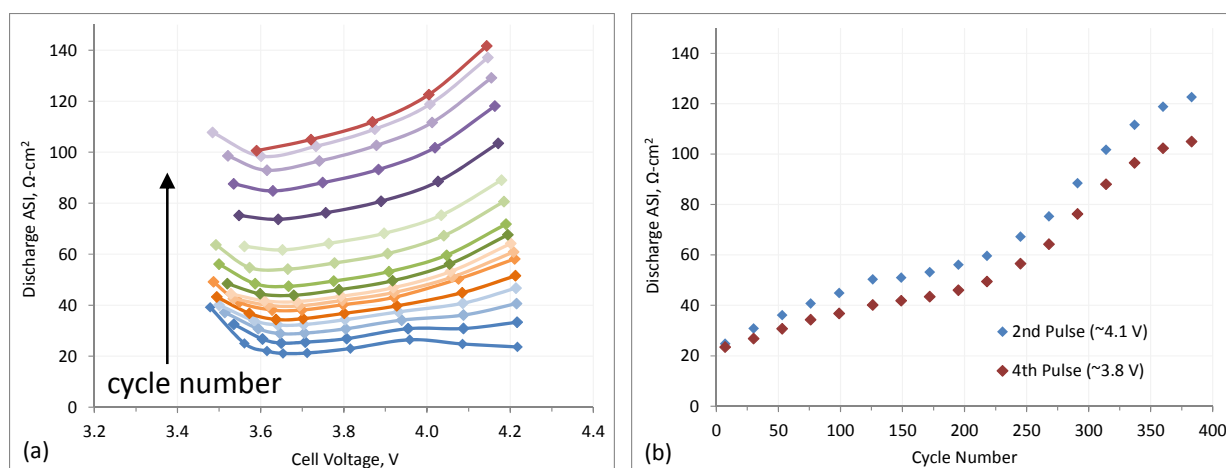


Figure IV-65: a) ASI calculated from HPPC tests as a function of cell voltage and cycle number. (b) ASI as a function of cycle number for the 2<sup>nd</sup> (~4.1 V) and 4<sup>th</sup> (~3.8 V) pulses

The ASI values at the 2<sup>nd</sup> and 4<sup>th</sup> discharge pulses, as a function of cycle number, are shown in Figure IV-65(b). The nominal cell voltages at these pulse locations are ~4.1 V and ~3.8 V, respectively. Some relevant features from the plots are as follows: (i) the ASI increases at both pulse locations are not linear – the rise is gradual initially (up to ~220 cycles), then relatively rapid, then gradual again. Such a trend in impedance rise

has been observed previously for NCA/Gr cells; (ii) although similar initially, the ASI values at the 2<sup>nd</sup> discharge pulse (the higher of the two full-cell voltages plotted) increase faster and always remain higher than the values at the 4<sup>th</sup> discharge pulse.

To determine the source of cell impedance rise on aging, data from the harvested electrodes was obtained. Representative examples are shown in Figure IV-66, which contains data from HPPC, Figure IV-66(a), and AC impedance, Figure IV-66(b), experiments. Figure IV-66(a) shows that the Formed(+)/Formed(-) cell, which contains positive (+) and negative (-) electrodes harvested from cells after formation cycling, shows the lowest impedance. The Aged(+)/Aged(-) cell, which contains positive and negative electrodes harvested from cells after 400 cycles, shows the highest impedance. In between are profiles from the “hybrid” cells. It is evident that the impedance of the Aged(+)/Formed(-) cell, which contains a positive electrode harvested after 400 cycles and negative electrode harvested from a cell after formation cycling, has higher impedance than a Formed(+)/Aged(-) cell, which contains a positive electrode harvested from a cell after formation cycling and negative electrode harvested from cell after 400 cycles. Similar impedance trends are also seen in Figure IV-66(b). Hence, it can be concluded that during cell aging, the positive electrode is the main contributor to cell impedance rise; the negative electrode impedance does increase but its contribution to the full-cell impedance is smaller.

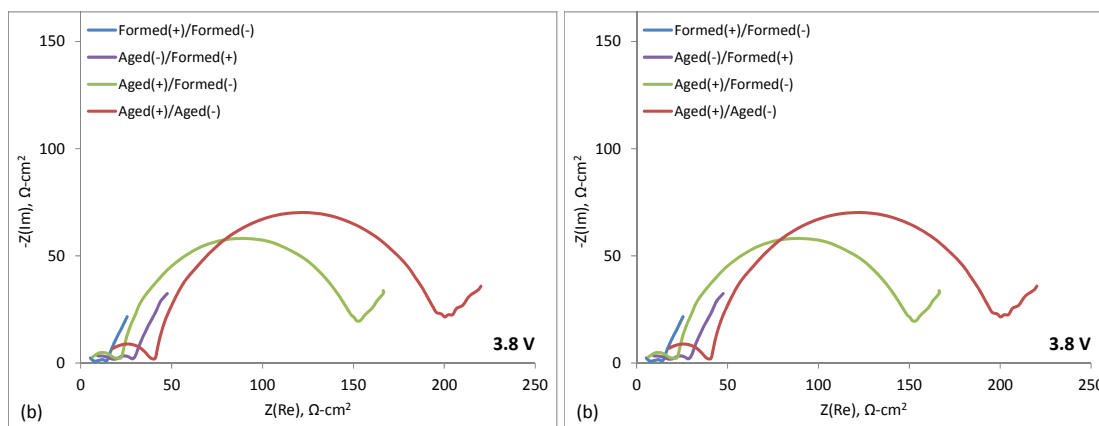


Figure IV-66: (a) ASI data obtained from HPPC tests. (b) ASI data obtained from AC impedance (3.8 V, 100 kHz - 0.005 Hz, 30°C) experiments. Electrodes were harvested from formed (4 cycles, 3-4.4 V) and aged (400 cycles, 3-4.4 V) cells

## 5. Examining EMC-Based Electrolyte with SEI Forming Additives for NMC-532/Gr Full-Cell Cycling

The four electrolyte systems investigated were 100% EMC, 2.0 wt% EC in EMC, 2.0 wt% VC in EMC and 5.0 wt% DFEC in EMC, all with 1.0 M LiPF<sub>6</sub>. The discharge capacities versus time for the electrolytes studied are shown in Figure IV-67(a). The baseline Gen2 electrolyte (gray) shows the best capacity retention of the five systems investigated (~90%). While the initial discharge capacity of the 2.0 wt% EC electrolyte is slightly higher than the baseline, the DFEC and VC cells both take a larger initial capacity loss compared to the baseline electrolyte. The capacity fade of the EC, VC, and DFEC-based cells are all linear with no significant drops. The 100% EMC electrolyte (no SEI former) cells show dramatic capacity fade. The coulombic efficiencies of the cells are shown in Figure IV-67(b). The 100% EMC-based cell shows significantly lower efficiencies compared to the other cells, consistent with continual electrolyte decomposition during cycling.

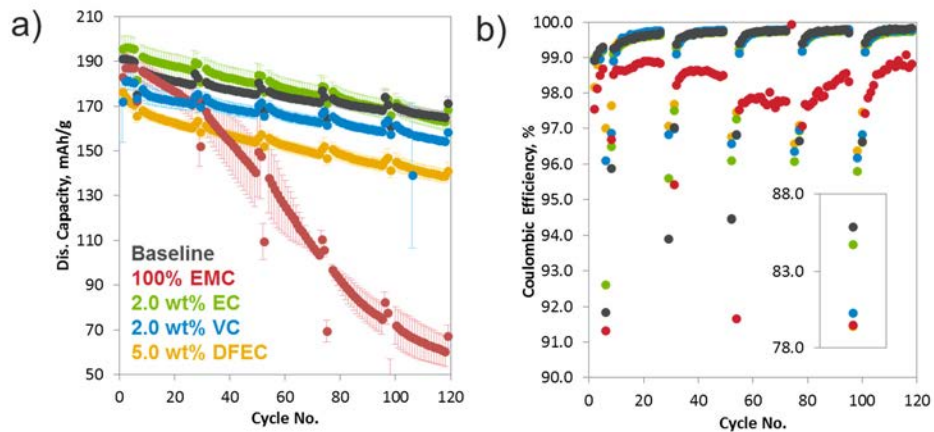


Figure IV-67: (a) Discharge capacity versus cycle number for the baseline and EMC-based electrolytes and (b) coulombic efficiency versus cycle number for the baseline and EMC-based electrolytes (the inset shows the first-cycle efficiency)

Figure IV-68(a)-(d) compare the ASI plots from the HPPC tests between the baseline electrolyte and the four EMC-based systems. In all plots, the baseline electrolyte ASI is plotted as a series of gray lines with HPPC 1 (Cycle 7) tests represented as the bottom line and HPPC 5 (Cycle 99) tests represented as the top line, with the middle lines following order from bottom to top (Cycles 30, 53, 76). The 100% EMC electrolyte, Figure IV-68(a), shows significant impedance right after initial cycling (Cycle 7, red line) and significant impedance growth during cycling. In contrast, the other three EMC-based systems look more reasonable with the 2.0 wt% VC system, Figure IV-68(c), actually showing both a smaller initial impedance and a smaller overall impedance growth compared to the baseline system.

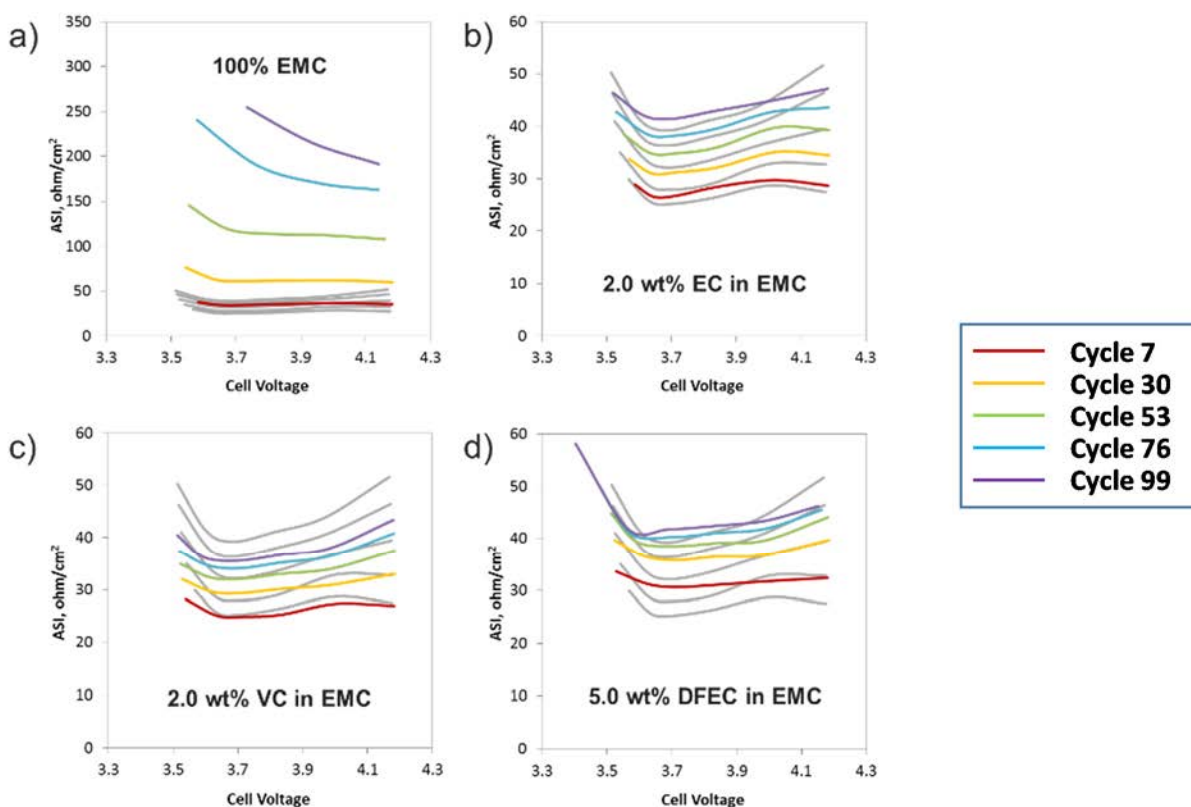


Figure IV-68: (a) ASI values for the 100% EMC, (b) 2.0 wt% EC in EMC, (c) 2.0 wt% VC in EMC, and (d) 5.0 wt% DFEC in EMC cells. Values were calculated from HPPC tests performed on NMC-532/Gr full-cells at 30 °C as a function of cycle number and cell voltage. The baseline electrolyte data is shown as gray lines. (Cycle 7 – red, Cycle 30 – yellow, Cycle 53 – green, Cycle 76 – blue, Cycle 99 – purple). Note the scale for the 100% EMC electrolyte is much larger

To observe how much of the SEI former was being consumed during the initial (formation) cycles, electrolyte was harvested from freshly assembled cells after four C/10 cycles. The harvested electrolyte was evaluated using solution-state  $^1\text{H}$  NMR analysis (Figure IV-69). The non-cycled baseline electrolyte (black line) shows three peaks in the region of interest highlighted, corresponding to EC (4.46 ppm) and EMC (4.13 and 3.71 ppm). The 2.0 wt% EC cell shows the presence of EMC transesterification products (DEC @ 4.13 ppm and DMC @ 3.72 ppm) which are typically observed for the baseline system after formation and full cycling (data not shown). The cell also shows a small EC peak (@ 4.46 ppm) indicating that EC is still present in the electrolyte (not entirely consumed) after the formation cycles. On the other hand, the cells containing 2.0 wt% VC and 5.0 wt% DFEC do not show any EMC transesterification products. This may allude to the requirement of EC, or EC decomposition products, as reagents to facilitate the EMC transesterification process. The presence of both VC and DFEC in the cells after the formation cycles indicates that not all of the SEI former is consumed during the formation cycles.

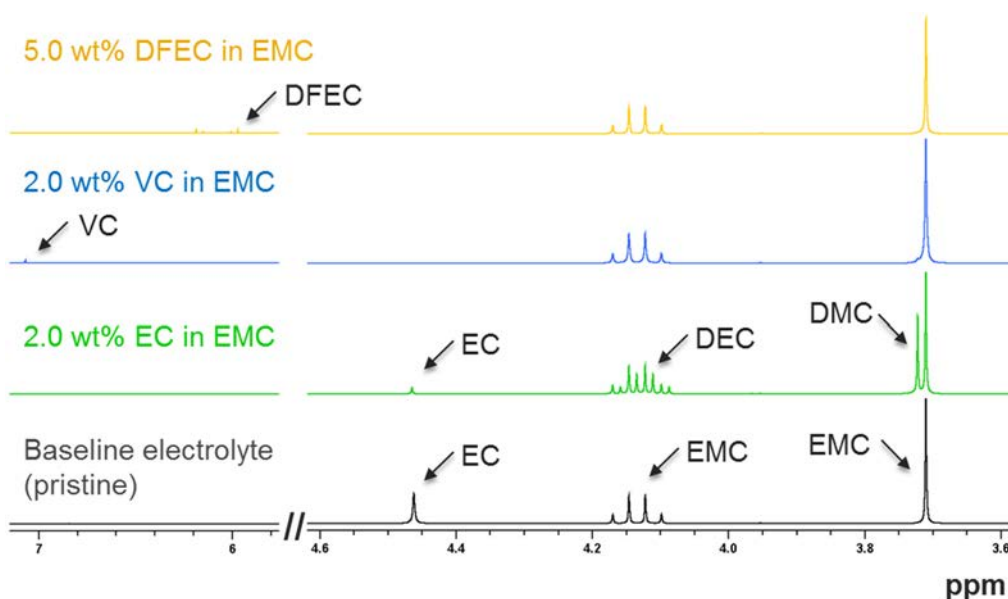


Figure IV-69:  $^1\text{H}$  NMR of the pristine baseline electrolyte (non-cycled) and harvested electrolytes from the EMC-based solutions after formation (4x C/10) cycles. Known components are identified in the figure

## 6. Use of Boron-Based Electrolyte Additives as Cathode Protection Agents for High-Voltage Lithium-Ion Battery Operation

The molecular structures of three boron-based additives are shown in Figure IV-70. The discharge capacities versus time for the electrolytes studied are shown in Figure IV-71(a). The baseline electrolyte (gray) shows high initial capacity and a roughly 85% capacity retention over the cycling protocol. Both VDSMB and THFIPB show larger capacity fade compared to the baseline, however, the capacity fade of the TMSB cell is less than the baseline electrolyte (~90%), albeit having a lower initial capacity. The coulombic efficiencies of the cells are shown in Figure IV-71(b). Besides the slightly lower efficiency of the THFIPB cells, there are no significant differences in efficiency between the additives and the baseline electrolyte.

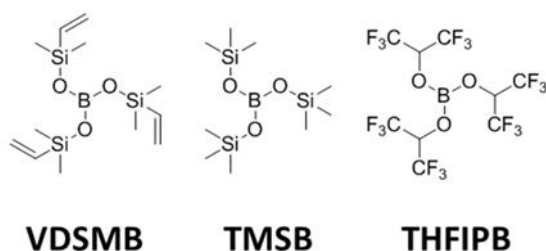


Figure IV-70: Molecular structures of the three boron-based additives tested in the study

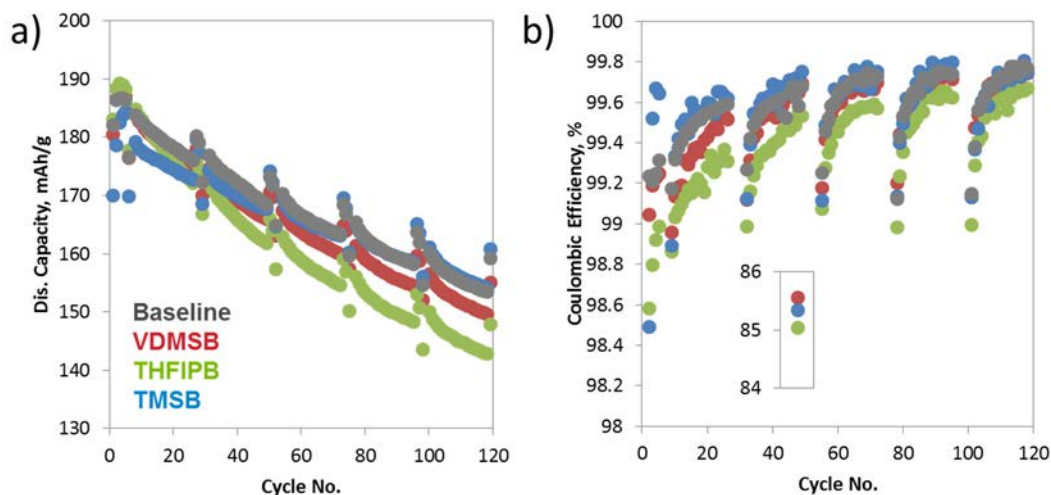


Figure IV-71: (a) Discharge capacity versus cycle number for the baseline electrolyte with and without additives (1.0 wt%) and (b) coulombic efficiency versus cycle number for the baseline electrolyte with and without additives (the inset shows the 1st cycle efficiency)

Figure IV-72(a)-(c) compare the ASI plots from the HPPC tests between the baseline electrolyte and the three boron-based additive-containing cells. In all plots the baseline electrolyte ASI is plotted as a series of gray lines with HPPC 1 (Cycle 7) tests represented as the bottom line and HPPC 5 (Cycle 99) tests represented as the top line with the middle lines following order from bottom to top (Cycles 30, 53, 76). For the cell containing TMSB, the impedance is initially lower compared to the baseline, Figure IV-72(a), and the impedance rise roughly half as much as the baseline over the course of a full cycling protocol. The VDMSB electrolyte shows a significantly lower initial impedance (Cycle 7, red line) and significantly lower impedance growth during cycling compared to the baseline electrolyte Figure IV-72(b). In contrast, the non silyl-containing additive, THFIPB, shows a much higher impedance rise over time compared to the baseline electrolyte, Figure IV-72(c).

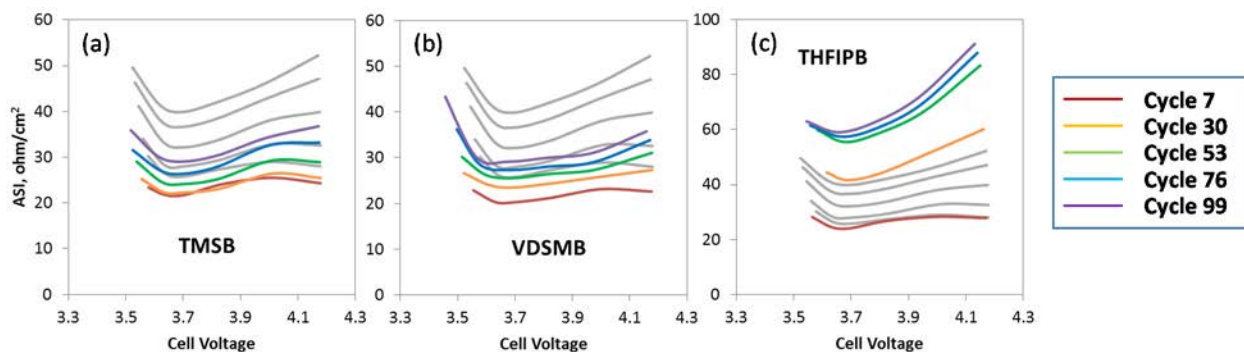


Figure IV-72: (a) ASI values for the 1.0 wt% TMSB, (b) 1.0 wt% VDMSB, and (c) 1.0 wt% THFIPB cells. Values were calculated from HPPC tests performed on NMC-532/Gr full-cells at 30 °C as a function of cycle number and cell voltage. The baseline electrolyte data are shown as gray lines (Cycle 7 – red, Cycle 30 – orange, Cycle 53 – green, Cycle 76 – blue, Cycle 99 – purple). Note the scale for the THFIPB electrolyte is much larger

## 7. Developing a ‘Potentiostatic Hold’ Protocol to Determine Cathode-Electrolyte Interactions

The behavior of cells containing the baseline (Gen2) electrolyte is shown in Figure IV-73. Here, 3 cells aged at different temperatures (as labeled) were charged and held at high voltage (4.6 V vs. Li/Li+). It is evident that the measured side reaction current increases with increasing temperature. At 55°C, Figure IV-73(d), there is an additional parasitic process observed that causes the current to increase substantially. With the exception of the 55°C high-voltage holds, the current behaviors at all temperatures tested are similar.



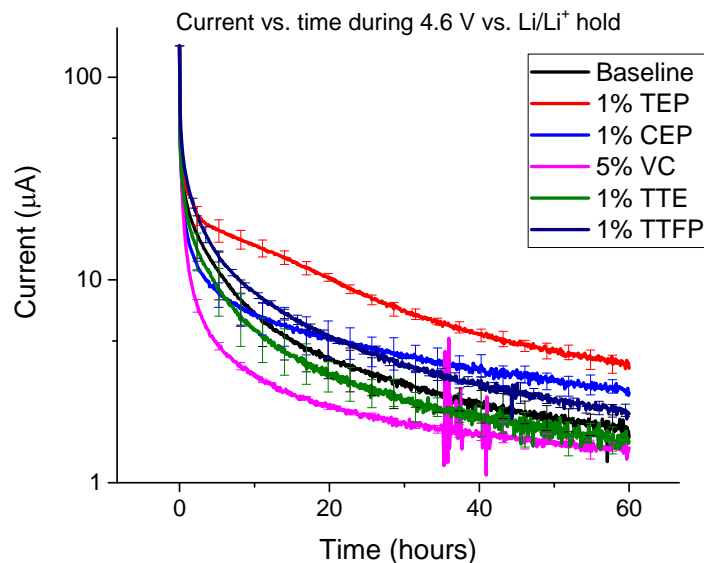


Figure IV-75: Current vs. time during the potentiostatic hold at 4.6 V vs. Li/Li<sup>+</sup> at 45 °C

Figure IV-76 shows the initial capacity of cells before the potentiostatic hold, (a), and the final capacities after the potentiostatic hold, (b). Before the hold, the capacities are mostly independent on electrolyte formulation. After the hold, there is a much larger range in capacities, with 5% VC showing the lowest, and 1% TEP showing the highest, capacities.

In this way, the effect of the additive in the normal operation of the battery, i.e., below the high voltage of the potentiostatic hold, as well as the effect of the high-voltage hold on the subsequent capacity of the battery, can be observed. AC impedance measurements, Figure IV-77, also showed that the 5% VC cell had the highest impedance, indicating that a stable interface was formed, but with a lowering of cell performance.

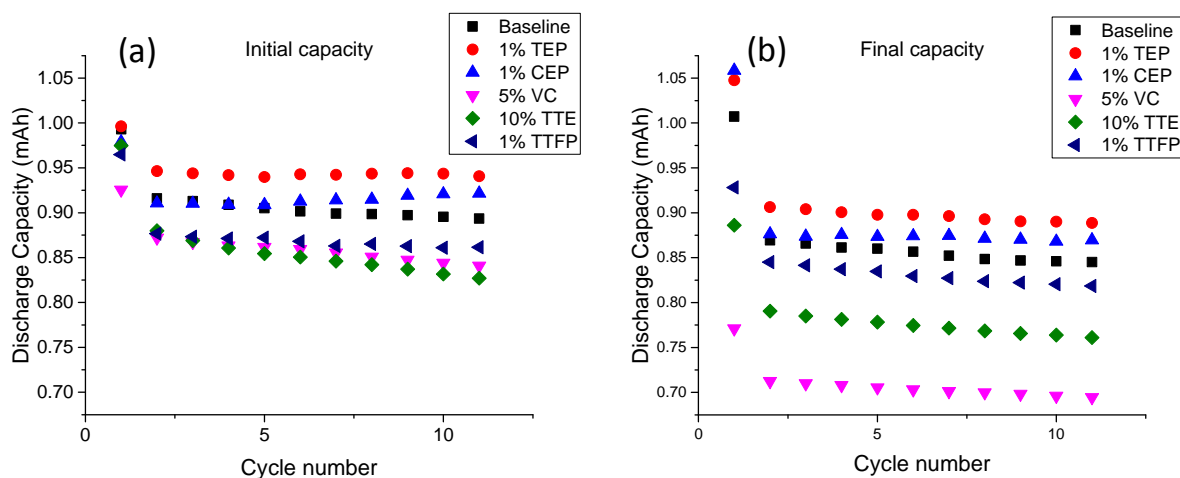


Figure IV-76: (a) Discharge capacity both before (initial) and (b) after (final) the potentiostatic hold. All cycling tests were performed at RT, and the potentiostatic hold was performed at 45 °C

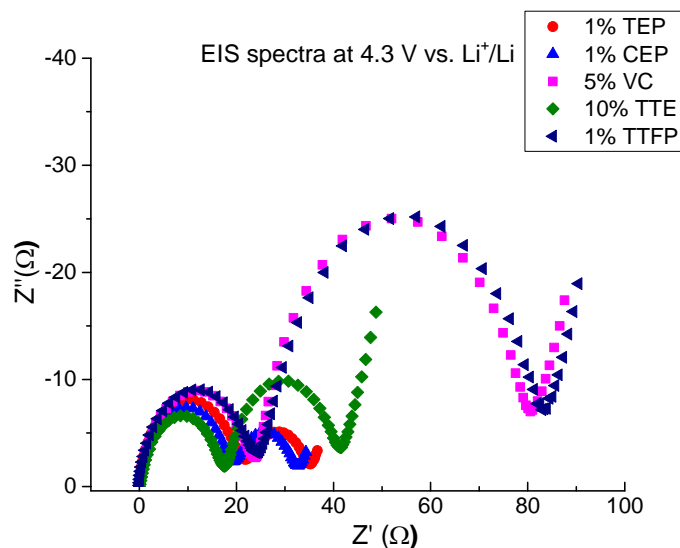


Figure IV-77: RT Impedance spectra from cells with the various additive formulations after the potentiostatic hold

Another strategy of stabilizing the interface is through a coating on the cathode particles that limits electrical contact with the electrolyte (See Chapter IV.C.2 – *Materials*). This strategy was tested using atomic layer deposition (ALD) of  $\text{Al}_2\text{O}_3$  on the cathode, with treatments of 9 and 80 ALD cycles, corresponding to approximately 1 nm and 10 nm coating thicknesses, respectively. As shown in Figure IV-78, these coatings cause a decrease in cell discharge capacity, (a), and show no benefits in the coulombic efficiency, (b).

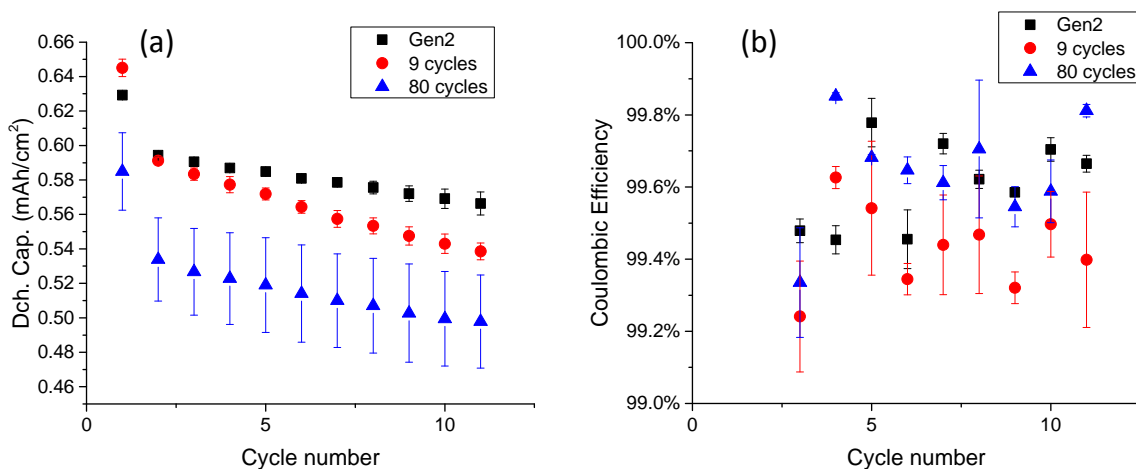


Figure IV-78: Discharge capacity and coulombic efficiency for uncoated (GEN2) and ALD-coated (9 and 80 cycles) NMC-532

Figure IV-79(a) shows current vs. time for the potentiostatic hold using the baseline electrolyte and 0 cycles (bare cathode), 9 ALD cycles, and 80 ALD cycles. Although the 9-cycle ALD cell showed slightly lower current, the coating did not significantly decrease the side-reaction current, nor was there any significant differences between the two coating thicknesses. However, when cell impedance was measured, Figure IV-79(b), the 80-cycle ALD cells showed significantly higher impedance than the 9-cycle ALD cells, consistent with the lower discharge capacity seen for the thicker coatings. The data from Figure IV-79 indicate that this ALD coating did not appreciably mitigate electrolyte degradation at the cathode/electrolyte interface, although the thicker coating does interfere with battery cycling performance (See also Chapter IV.C.2 – *Materials*).

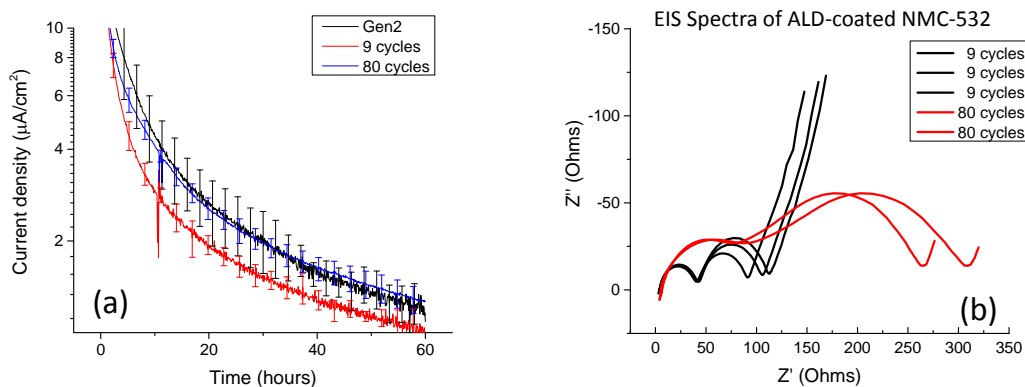


Figure IV-79: (a) Current vs. time for the potentiostatic holds for uncoated (Gen2) and ALD-coated (9 and 80 cycles) NMC-532. (b) AC Impedance spectra for the two different ALD coating thicknesses on the cathode.

## Conclusions

- NCA electrodes deliver significantly higher capacities than NMC-532 electrodes for potentials  $<4.5$  V vs.  $\text{Li}/\text{Li}^+$ . Above 4.5 V, NMC-532 delivers slightly higher capacities. Similar trends are also seen for the specific energy densities. The average voltages, however, are higher for NMC-532 than for NCA in all potential ranges studied.
- NMC-532/Gr and NCA/Gr cells tested using the HE/HV protocol in the 3-4.4 V range show capacity loss and impedance rise. Data from harvested electrodes show that Li-trapping in the negative electrode SEI is the main contributor to capacity fade. Data from reference electrode cells show that (i) the positive electrode is the main contributor to impedance rise, and (ii) electrode potential-window shifts during cycling reduce utilization of electrode active material.
- The capacity retention of NMC-532/Gr cells containing EMC-based electrolytes with SEI formers (EC, VC, and DFEC) is inferior to that of cells with the Gen2 electrolyte. The impedance rise of the EMC-based electrolytes is also higher than that of the Gen2 cells. Interestingly, EMC-transesterification products were observed in the EC-containing cells, but not in cells with VC and DFEC, indicating that EC must be involved in this reaction process.
- Three boron-based electrolyte additives were investigated in NMC-532/Gr full-cells. While the capacity fade of the TMSB cell was better than the baseline electrolyte, the other two additives (VDSMB and THFIPB) showed worse capacity retention. Importantly, both initial impedance and overall impedance rise were significantly lower for the TMSB and VDSMB containing cells compared to the Gen2 electrolyte. The data indicate that TMSB (and other additives containing silyl functionalities) should be further explored as electrolyte additives for lithium-ion battery systems operating at high voltages.
- The Gen2 electrolyte stability was characterized both in terms of decomposition rate and effect on cathode capacity for a range of temperatures. Higher temperatures led to greater decomposition and worse battery performance. In contrast, fluorinated electrolytes showed better stability at higher voltages.
- Multiple additives, with very different chemical structures, were tested to determine their ability to stabilize the electrolyte/cathode interface. Of the additives evaluated, only VC and TTE lowered the side-reaction current. However, both of these additives also lowered the discharge capacity of the cells.
- The effect of  $\text{Al}_2\text{O}_3$  coatings on the NMC-532 cathode was studied using the potentiostatic hold protocol. The ALD coatings did not stabilize the interface, and the thicker coating significantly decreased cell capacity and increased cell impedance. These results are in agreement with parallel studies on  $\text{Al}_2\text{O}_3$  coatings prepared by alternative routes (See Chapter IV.C.2 – *Materials*).
- Potentiostatic holds, coupled with cycling and impedance measurements, provide a useful diagnostic method to quantitatively describe the stability of electrolyte/cathode interfaces.

## Acknowledgments

*Electrochemistry and Characterization* – Daniel P. Abraham, James Gilbert, Adam Tornheim, Cameron Peebles, Rose Ruther, Lamuel David, John Zhang, Ritu Sahore, Javier Bareño, Ira Bloom, Gabriel Veith, Chen Liao, Stephen Trask, Bryant Polzin, Andrew Jansen, and David Wood.

## Products

## Presentations/Publications/Patents

### Publications

1. J. A. Gilbert, J. Bareño, T. Spila, S. E. Trask, D. J. Miller, B. J. Polzin, A. N. Jansen, and D. P. Abraham, *Cycling behavior of NCM523//Graphite lithium-ion cells in the 3-4.4 V Range – Diagnostic studies of Full-cells and Harvested Electrodes*, *J. Electrochem. Soc.*, **164**, A6054 (2017).
2. A. Tornheim, S. E. Trask, and Z. Zhang, *Evaluation of Electrolyte Oxidation Stability on Charged  $\text{LiNi}_{0.5}\text{Co}_{0.2}\text{Mn}_{0.3}\text{O}_2$  Cathode Surface through Potentiostatic Holds*, *J. Electrochem. Soc.*, **163**, A1717 (2016).
3. B. R. Long, S. G. Rinaldo, K. G. Gallagher, D. W. Dees, S. E. Trask, B. J. Polzin, A. N. Jansen, D. P. Abraham, I. Bloom, J. Bareno, and J. R. Croy, *Enabling High-Energy, High-Voltage Lithium-Ion Cells: Standardization of Coin-Cell Assembly, Electrochemical Testing, and Evaluation of Full-cells*, *J. Electrochem. Soc.*, **163**, A2999 (2016).
4. I. A. Shkrob and D. P. Abraham, *Electrocatalysis Paradigm for Protection of Cathode Materials in High-Voltage Lithium-Ion Batteries*, *J. Phys. Chem. C*, **120**, 15119 (2016).

### Presentations

1. C. C. Su, M. He, C. Peebles, and Z. Zhang, *The Impact of Different Substituents in Fluorinated Cyclic Carbonates in the Performance of High-voltage lithium-ion Battery Electrolyte*, Abstract, International Meeting of Lithium Batteries, Chicago, IL, June 2016.
2. M. He, C. C. Su, Y. Wang, Z. Zhang, and C. Peebles, *Mechanistic Studies of Fluorinated Electrolyte for High-voltage lithium-ion Battery*, Abstract, International Meeting of Lithium Batteries, Chicago, IL, June 2016.
3. J. A. Gilbert, M. Klett, J. Bareno, D. Miller, V. A. Maroni, and D. P. Abraham, *Performance Changes in NCM523/Graphite Cells Resulting from High-Voltage Cycling*, Abstract, International Meeting of Lithium Batteries, Chicago, IL, June 2016.

## IV.C.4. Next Generation Anodes for Lithium-Ion Batteries: Overview (ANL)

### Dennis Dees, Point-of-Contact

Argonne National Laboratory  
9700 South Cass Avenue  
Argonne, IL 60439  
Phone: 630-252-7349  
E-mail: [dees@anl.gov](mailto:dees@anl.gov)

### Peter Faguy, DOE Program Manager

U.S. Department of Energy  
Vehicle Technologies Office  
1000 Independence Avenue, SW  
Washington, DC 20585  
Phone: 202-586-1022  
E-mail: [Peter.Faguy@ee.doe.gov](mailto:Peter.Faguy@ee.doe.gov)

Start Date: October 1, 2015, Kickoff: January, 2016

End Date: September 30, 2018

### Abstract

### Objectives

- Understand and overcome the science and technology barriers to the use of silicon-based anodes in high-energy density lithium-ion batteries for transportation applications.
  - Stabilize the SEI
  - Stabilize the electrode
- Demonstrate functional prototype lithium-ion cell chemistries which meet the DOE/USABC performance targets.

### Accomplishments

- Large highly integrated program stood-up, based on expertise and past accomplishments.
  - Develop technical targets.
  - Assigned individual responsibilities.
  - Initiated work.
  - Established communications.
- Battery Performance and Cost (BatPaC) Model (see page 315). BatPaC model utilized to establish program relevance by connecting transportation battery pack DOE/USABC goals to anode targets.
- Baseline Materials, Electrodes, and Cells (see page 316)
  - Established silicon-containing baseline materials and anodes, including pouch cell builds.
    - Impact on performance of increasing silicon weight % in anode.
  - Examined replacement silicon baseline active material.
- Trial Coating of Si/C Anode with New Baseline Silicon Powder (see page 320). Successfully coated and examined 25 ft of Si/C anode with 3.39 mg/cm<sup>2</sup> areal loading.
- Thermodynamic Understanding and Abuse Performance (see page 321)
  - Double sided electrodes (for cylindrical cells) were fabricated and evaluated to show comparable response to baseline materials used throughout the program.
  - Materials level thermal runaway was conducted on baseline materials through DSC, TGA, MS, and ARC bomb evaluations.
  - Larger format cylindrical cells (18650) were constructed and tested for electrochemical and thermal abuse response.

- A smaller capacity cell platform was developed for quantification of runaway enthalpy using ARC techniques.
- Full Cell Testing Protocol (see page 323). Adopted a standard testing protocol for program shown to work well for lithium-ion cells with silicon containing anodes.
- Fundamental Studies of Si-C Model Systems. See section IV.D.8 of this annual report.
- Characteristics of Half and Full Cells containing Layered Oxide, Graphite and Silicon-Graphite Electrodes (see page 325)
  - Showed that voltage profiles of the blended SiGr electrode are a superposition of graphite potential plateaus on a sloped Si profile with a large potential hysteresis.
  - Noted the effect of voltage-hysteresis in the full cell voltage versus impedance data, which are distinctly different for the charge and discharge cycles.
  - Capacity retention improves when compounds, such as vinylene carbonate (VC) and fluoroethylene carbonate (FEC), are added to the baseline Gen 2 electrolyte (1.2 M LiPF<sub>6</sub> in EC:EMC, 3:7 w/w); better retention is seen at higher additive contents (up to 10 wt%).
  - Noted the spontaneous aggregation of Li<sup>+</sup> ion coordination polymers in FEC-containing electrolytes with > 0.8 M LiPF<sub>6</sub> and determined that the compounds have the Li(FEC)<sub>3</sub>PF<sub>6</sub> crystal structure.
- NMR Studies of Composite Silicon Electrodes (see page 330)
  - Developed a method to monitor and optimize silicon to silicon oxide composition in bulk commercial powders. Findings suggest that small particle sizes result in large compositions of silicon oxide type order that could be significantly detrimental in electrochemical performance.
  - Identified preliminary key reactions of electrolyte and additive components after extended cycling for baseline electrodes.
- Advanced Characterization of Silicon/Graphite Composite Electrodes (see page 332)
  - Micro-Raman mapping of 100 X cycled 15 wt. % - Si composite electrodes showed presence of isolated crystalline Si along with regular amorphous Si.
  - Observed cracking event associated with Si for the first time in Si-graphite-NMC pouch cells using *in situ* electrochemical acoustic ToF measurements.
- Gas Evolution from Silicon Anodes (see page 334)
  - Examined gas evolution of baseline silicon-graphite electrode.
  - Compared gas evolution of silicon-graphite and graphite only electrodes.
- The Effect of Oxidation on the Electrochemical Performance of Silicon Electrodes (see page 335)
  - Established a relationship between the grown thickness and the oxidation temperature under experimental conditions of silicon anode materials.
  - Demonstrated improved cycle performance when the silicon anode material is treated under mild oxidation conditions.
- Development of High Energy Metals (see page 337)
  - Synthesis and performance of Si-Sn and Si-Sn-C nanocomposites via mechanical milling explored.
  - Identified issues with development of nanocomposites using mechanical milling.
- Interfacial Modifications: MLD Surface Coatings (see page 338)
  - Developed MLD alucone coatings for the baseline Si anodes. Molecular layer deposition has been performed via sequential reactions of trimethylaluminium and glycerol, to develop surface coating for silicon laminated electrodes.
  - Demonstrated the electrochemical behavior for the MLD coated Si anodes.
    - No major impact on the electrochemical cycling performance was observed for the electrodes fabricated with LiPAA and CMC binders.
    - Significantly improved cycling performance has been obtained for the electrodes fabricated by using PVDF binder.

- Investigated the impact of MLD coating on the mechanical properties of Si electrodes. Nanoindentation and scratch techniques were used to characterize the effect of MLD coating on the mechanical properties.
- Evaluated the electrode thickness effects on the electrochemical performance of Si-CB-PVDF electrodes.
  - Stable cycling performance was demonstrated in the uncoated Si electrodes with low mass loading; but very fast capacity decay was observed for the bare electrodes with medium and high mass loading.
  - Improved capacity retention has been achieved for all of coated electrodes regardless of mass loading, which confirms the positive impact of coating on the cycling performance.
- Interfacial Modification of Si Anode – Electrochemical/Chemical Approach through Electrolyte/Additive (see page 343)
  - TEM utilized for fundamental study of SEI formation on silicon anode particles.
  - Detailed impedance and cycling studies helps quantify impact of Silazane additive.
- Exploring Lithium Inventory Strategies (see page 346)
  - LFO pre-lithiation additive successfully works to improve the cycling of full cells with cathode of LCO and anode of hard carbon.
  - LFO pre-lithiation additive was tested in a physical blend with NMC532 (commercial) and the electrochemical performance in Li half-cells was not adversely affected.
- Polymer Binder for Silicon Anode (see page 348)
  - Polyacrylic acid (PAA) polymers were obtained and their molecular weight and molecular weight distribution (PDI) was measured by GPC after methylation of the polymers. The electrochemical performance of these binders was examined using Si/Carbon composite electrode half cells. High molecular weight PAA is beneficial to the initial capacity and capacity retention of the Si anode.
  - A Chitosan-backbone multiphase graft copolymer containing lithium polyacrylate (Chitosan-graft-PAA) was synthesized via a controlled radical polymerization (RAFT polymerization). Initial cell results using the 15% silicon showed that lithium Chitosan-graft-PAA exhibited better cycling performance than that of lithiated PAA due to the good mechanical property of the chitosan backbone and high density of lithium polyacrylate side chains, which provide better contact with the active material.
  - A series of polysiloxane comb-polymers were designed and synthesized with glycidyl ether (AGE) and oligo(ethylene glycol) (APEO3) side chains. Initial electrochemical testing was performed on the Si anode fabricated by a “wet” method. Comb-polymer with AGE was cross-linked at the presence of the diamine crosslinking agent and showed much better performance than its non-crosslinked counterpart.
  - Quantification of the reactivity and stability of poly(1-pyrenemethyl methacrylate) (PPy) binder at low potential was performed.
    - The higher utilization of Si for PPy based electrode has been proved through the voltage/capacity profiles, and lithiated electrode morphologies.
    - The degree of lithium doping was further quantified to be 1 Li<sup>+</sup>/pyrene through the comparison of first cycle charge quantity between PAALi and PPy based electrode.
    - The improved mechanical strength and stability of PPy to PAALi is demonstrated through SEM and post FTIR analyses.
  - One class of “self-healing” co-polymer based on acrylamide (AAM) and N-[3-(Dimethylamino)propyl] acrylamide (DMAPA) were synthesized and through a systematic variation of the monomer ratios and molecular weights. A library of polymer binders is being built, which will then be tested in a number of ways to determine their effectiveness as binders for producing silicon anode laminates that are stable, have high capacities, and are stable to lithiation/delithiation cycling.

## Future Achievements

- Continue search for improved silicon baseline materials.
- Fabricate advanced baseline silicon-graphite composite electrodes using improved silicon materials.
- Complete evaluation of cylindrical cells during abuse conditions and compare with baseline materials (both from this program and with historical data).
- Refine the understanding of materials level changes and how they contribute to runaway energy, full cell safety, gas generation during runaway, and overall enthalpy released during runaway.
- Continue advanced diagnostic studies on baseline and advanced materials and electrodes in half, full, and reference electrode cells, using a broad range of electrochemical and analytical studies.
- Determine effect of prelithiation, either of the positive or negative electrode, on cell performance and longevity. Prelithiation could be conducted either in a chemical or electrochemical manner.
- *In situ* NMR studies of composite electrodes are in progress to study highly reactive phases and their interaction with electrolyte components.
- Model lithium silicates have been synthesized and characterization of their interaction with electrolyte and additive species is in progress.
- Identification of key interfacial reactions and formation of surface and bulk species governing electrochemical efficiency is in progress.
- Continue NMR studies on the role of modified surfaces, new electrolytes and additives on interface and electrochemical performance.
- Understand the mechanism on the improvement of cycle performance after mild oxidation of silicon anode materials.
- Study the effect of oxidation on the thermal properties of silicon anode materials.
- Develop interfacial modification for Si particles designed to stabilize the SEI.
  - Coating directly on the Si particles and laminated electrodes.
  - Explore new coating techniques and materials, including hybrid and pure polymer coatings.
- Investigate the relationship between the surface/interface chemistry and the mechanical properties.
- Evaluate the chemical compatibility and interaction between the coating materials, binder materials and electrolyte additives.
- Further study the effectiveness of silazane (Si-N) compounds as electrolyte additives and synthesize/characterize the first generation silane-based artificial SEI.
- Demonstrate and scale-up the LFO to 50-100g batch sizes for making prototype pouch cells with the LFO additive co-blended NMC type cathodes. Further, support the electrode design of the prototype LFO-NMC cathodes.
- Examine newly synthesized LFO and its modifications thereof using electrochemical, structural, and physical characterization.
- Prepare amorphous Si-Sn phase using splat quenching method, which is a commonly used method in metallurgy and well suited for preparation of metal/alloy materials that are near-amorphous, non-crystalline.
- Synthesize a range of promising polymer binder candidates and evaluate their physical, chemical, and electrochemical properties to understand and narrow classes of polymers for consideration.

## Technical Discussion

### Background

Silicon has received significant attention as a viable alternative to graphitic carbon as the negative electrode in lithium-ion batteries due to its high capacity and availability [1]. Elemental silicon can theoretically store >3500 mAh/g, nearly an order of magnitude higher than graphite (372 mAh/g and 818 mAh/mL, respectively). However, several problems have been identified that limit its utility including large crystallographic expansion (~320%) upon lithiation which translates to particle cracking, particle isolation, and electrode delamination issues. Further, there are fundamental and volume change related SEI stability issues, which affect cycling efficiency. The wealth of previous studies in this area is both a testament to its potential and the size of the challenge that must be overcome, requiring a great amount of innovation on multiple fronts.

### Introduction

Next Generation Anodes for Lithium-Ion Batteries, also referred to as the Silicon Deep Dive Program, is a five National Laboratory consortium assembled to tackle the barriers associated with development of an advanced lithium-ion negative electrode based upon silicon as the active material. This research program baselines promising silicon materials that can be developed or obtained in quantities sufficient for electrode preparation within the consortium facilities. Composite electrode and full cell development leverages recent investments made by DOE-EERE-VTO in electrode materials and characterization. The primary objective of this program is to understand and eliminate the barriers to implementation of a silicon based anode in lithium-ion cells. The Labs are focused on a single program with continuous interaction, clear protocols for analysis, and targets for developing both the understanding and cell chemistry associated with advanced negative electrodes for lithium-ion cells. First and foremost, this undertaking is a full electrode/full cell chemistry project leveraging baseline electrodes prepared at the consortium facilities. All efforts are directed to understanding and developing the chemistry needed for advancing silicon-based anodes operating in full cells. Materials development efforts include active material development, binder synthesis, coatings, safety, and electrolyte additives. Efforts include diagnostic research from all partners, which span a wide range of electrochemical, chemical and structural characterization of the system across length- and time-scales. Specialized characterization techniques developed with DOE-EERE-VTO funding, include neutrons, NMR, optical, and X-ray techniques being employed to understand operation and failure mechanisms in silicon-based anodes. In addition, several strategies to mitigate lithium loss is being assessed. The project is managed as a single team effort spanning the Labs, with consensus decisions driving research directions and toward development of high-energy density lithium-ion batteries. A detailed list of participants is given in Figure IV-80.

## Research Facilities

- Post-Test Facility (PTF)
- Materials Engineering Research Facility (MERF)
- Cell Analysis, Modeling, and Prototyping (CAMP)
- Battery Manufacturing Facility (BMF)
- Battery Abuse Testing Laboratory (BATLab)

## Contributors

- |   |   |  |
|---|---|--|
| <ul style="list-style-type: none"> <li>▪ Daniel Abraham</li> <li>▪ Eric Allcorn</li> <li>▪ Chunmei Ban</li> <li>▪ Javier Bareno</li> <li>▪ Ira Bloom</li> <li>▪ Anthony Burrell</li> <li>▪ Yang-Tse Cheng</li> <li>▪ James Ciszewski</li> <li>▪ Claus Daniel</li> <li>▪ Dennis Dees</li> <li>▪ Fulya Dogan Key</li> <li>▪ Zhijia Du</li> <li>▪ Alison Dunlop</li> <li>▪ Trevor Dzwiniel</li> <li>▪ Kyle Fenton</li> <li>▪ Kevin Gallagher</li> <li>▪ Steve George</li> <li>▪ James Gilbert</li> </ul> | <ul style="list-style-type: none"> <li>▪ Jinghua Guo</li> <li>▪ Atetegeb Meazah Haregewoin</li> <li>▪ Kevin Hays</li> <li>▪ Bin Hu</li> <li>▪ Aude Hubaud</li> <li>▪ Andrew Jansen</li> <li>▪ Christopher Johnson</li> <li>▪ Baris Key</li> <li>▪ Robert Kostecki</li> <li>▪ Gregory Krumdick</li> <li>▪ Jianlin Li</li> <li>▪ Min Ling</li> <li>▪ Gao Liu</li> <li>▪ Wenquan Lu</li> <li>▪ Jagjit Nanda</li> <li>▪ Kaigi Nie</li> <li>▪ Ganesan Nagasubramanian</li> <li>▪ Christopher Orendorff</li> <li>▪ Bryant Polzin</li> </ul> | <ul style="list-style-type: none"> <li>▪ Krzysztof Pupek</li> <li>▪ Philip Ross</li> <li>▪ Tomonori Saito</li> <li>▪ Yangping Sheng</li> <li>▪ Seoung-Bum Son</li> <li>▪ Robert Tenent</li> <li>▪ Lydia Terborg</li> <li>▪ Wei Tong</li> <li>▪ Stephen Trask</li> <li>▪ Jack Vaughey</li> <li>▪ Gabriel Veith</li> <li>▪ David Wood</li> <li>▪ Jing Xu</li> <li>▪ Liang Zhang</li> <li>▪ Linghong Zhang</li> <li>▪ Lu Zhang</li> <li>▪ Shuo Zhang</li> <li>▪ Zhengcheng Zhang</li> </ul> |
|---|---|--|

Figure IV-80: Program participants including Laboratories, research facilities, and individual contributors

## Approach

Sandia National Laboratories (SNL), Oak Ridge National Laboratory (ORNL), National Renewable Energy laboratory (NREL), Lawrence Berkeley National Laboratory (LBNL), and Argonne National Laboratory (ANL) have teamed together to form an integrated program. Technical targets have been developed and regular communications have been established. Throughout the program, there is a planned focus on understanding, insights into, and advancement of silicon-based materials, electrodes, and cells. All anode advancements will be verified based on life and performance of full cells. Toward that end, baseline silicon-based materials, electrodes, and cells have been adopted, along with full cell testing protocols. As the program matures, materials developments will be incorporated into baseline silicon-based materials, electrodes, and cells. Scale-up of materials, incorporation of materials advancements into electrodes and prototype cells, and characterization and testing of cells, as well as evaluation of safety and abuse tolerance are part of a wide range of integrated studies supported by battery research facilities at the National Labs working closely with the program. These research facilities include the Battery Abuse Testing Laboratory (BATLab), the Battery Manufacturing Facility (BMF), the Cell Analysis, Modeling, and Prototyping (CAMP), the Materials Engineering Research Facility (MERF), and the Post-Test Facility (PTF).

The fundamental understanding of silicon-based electrode active materials is based on extensive electrochemical and analytical diagnostic studies on components, electrodes, and cells conducted within the program. This effort includes *in situ* and *ex situ* studies, as well as the development and characterization of model systems. The model system studies (see IV.D.8 Next-Generation Anodes for lithium-ion Batteries: Fundamental Studies of Si-C Model Systems) are generally thin-film well-defined active area electrodes on which it is easier to extract fundamental information on lithium-silicon phase formation, lithium transport, and interfacial phenomena (e.g. SEI formation and growth). Overall, the diagnostic studies are intended to help establish structure-composition-property relationships, including lithium-alloying surface and bulk transport and kinetic phenomena. Further, they should form the basis for accurately assessing component and electrode failure modes and lay a path for advancements.

Supported by the diagnostic studies, materials development on silicon-based materials, electrodes, and cells is being conducted to enhance interfacial stability, accommodate intermetallic volume changes, and improve overall performance and life. Key to this effort is the development and testing of coatings and additives designed to modify and stabilize the dynamic silicon-electrolyte interface. Further, functional polymer binders designed to accommodate volume changes, increase conductivity, and improve adherence are being developed and analyzed. Finally, the program is exploring active material development. Alternative high-energy silicon-alloy/composite materials are being considered. Also, strategies for introducing additional lithium inventory into the cell are being developed.

Communication of programmatic progress to battery community is critical. This will generally be accomplished through publications, presentations, reports, and reviews. Further, the program is open to industrial participation and/or collaboration that does not limit program innovation or the free flow of information. Programmatic changes are expected as the program moves forward. The promise of the model systems studies have instigated a major change in the program for fiscal year 2017. As shown in Figure IV-81, the model systems studies will be significantly expanded, along with support from the diagnostic effort. The result will be a separate, but integrated, program. The new program will focus on the SEI-Stabilization, called SEI-Sta for short.

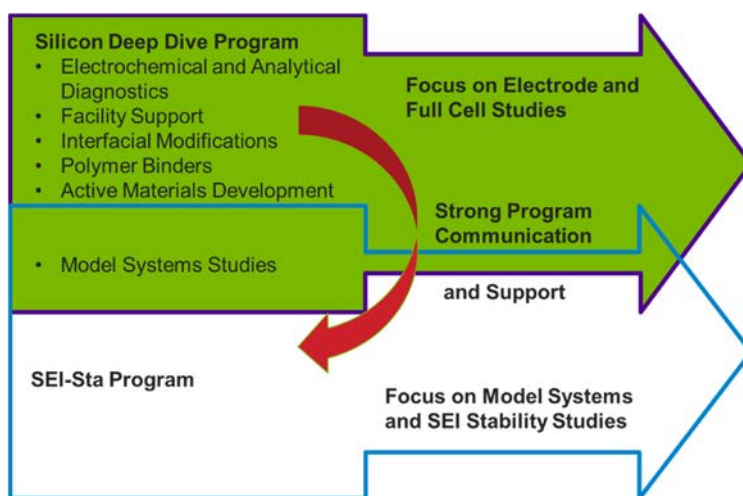


Figure IV-81: FY17 changes in Silicon Deep Dive Program

## Results

### Battery Performance and Cost (BatPaC) Model (ANL)

BatPaC [2], a techno-economic program designed to model lithium-ion battery performance and cost, was utilized to establish program relevance by connecting DOE/USABC pack performance targets to anode targets. Generally, research with silicon containing anodes is focused on improving the specific capacity of graphite. However, this simple metric requires a more detailed analysis with factors such as the impact on average cell voltage, and volumetric capacity. It is notoriously difficult to select appropriate metrics that will enable an accurate calculation of the energy of a single electrode. Most methods estimate the volumetric energy density of active materials with the simplistic assumption that bulk density of the electrode does not undergo change in volume during cycling. While this serves well for most cathodes where the voltage can be fixed against lithium it is inappropriate for electrodes such as silicon.

As shown in Figure IV-82 (left frame), BatPaC calculations indicate anode volumetric capacities greater than  $1000 \text{ mAh/cm}^3$  ( $= \rho \cdot \epsilon \cdot Q$  [ $\text{g/cm}^3_{\text{act}} \cdot \text{cm}^3_{\text{act}}/\text{cm}^3_{\text{elect}} \cdot \text{mAh/g}$ ]) generally minimizes battery cost with an advanced NMC cathode. Note that higher capacities result in diminishing savings in cost. The analysis (right frame) also predicts that silicon-graphite electrodes with less than 75 wt% graphite can achieve the target. Finally, alloys of inactive metals (not shown) with silicon (or tin) can meet the volumetric capacity target as long as the metal choice is inexpensive (e.g. iron rather than nickel or cobalt).

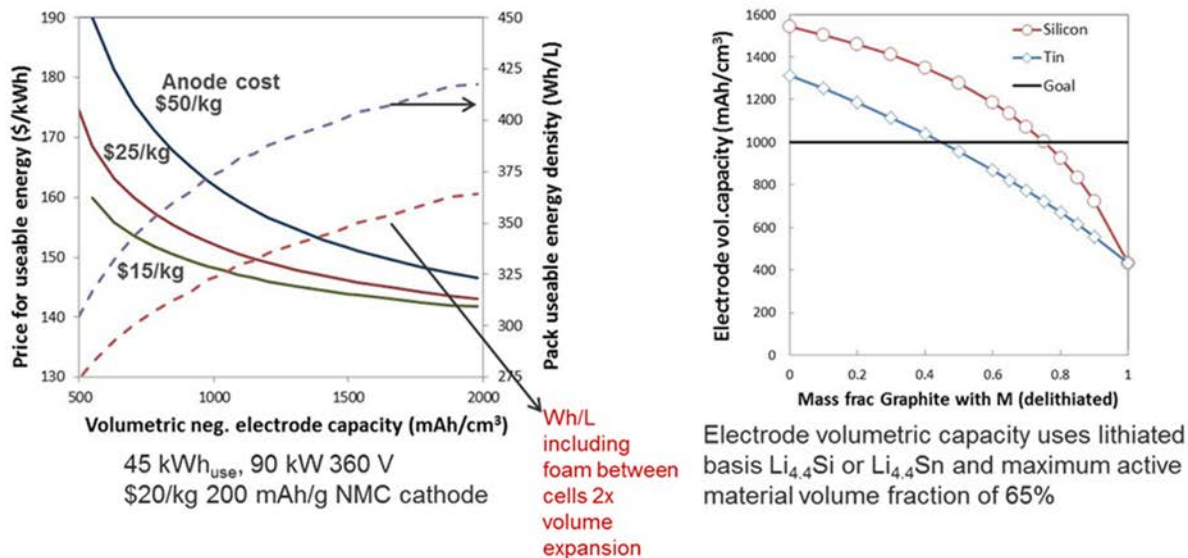


Figure IV-82: Battery Performance and Cost (BatPaC) model utilized to establish relevance by connecting pack to anode targets

### Baseline Materials, Electrodes, and Cells (ANL)

As with all R&D projects a benchmark must be set at the beginning of the project to gauge the significance of later successes. Fortunately for this project, the CAMP Facility at ANL had been developing silicon-based electrodes in the previous years. The CAMP Facility had developed silicon-based graphite composite electrodes that used lithiated polyacrylic acid (Li-PAA) as the aqueous binder. While this is not an ideal binder due to its hydrophilic nature and brittleness, it is one of the best available binder systems that enables a couple hundred cycles to be obtained with silicon. More information on the development of this composite electrode system is available in the CAMP Facility's FY15 annual report section. Four electrodes were selected as the baseline anodes, which consisted of 0, 5, 10, and 15 wt. % silicon (50-70 nm from NanoAmor) balanced with Hitachi Mag-E graphite. A capacity-balanced NMC532 cathode was also selected as the baseline counter electrode. The physical and electrochemical properties of these electrodes are depicted in Figure IV-83 and Figure IV-84, respectively. Note that for the 0 wt. % silicon, PVDF was used as the binder because the Li-PAA binder proved to be too brittle with very low silicon content.

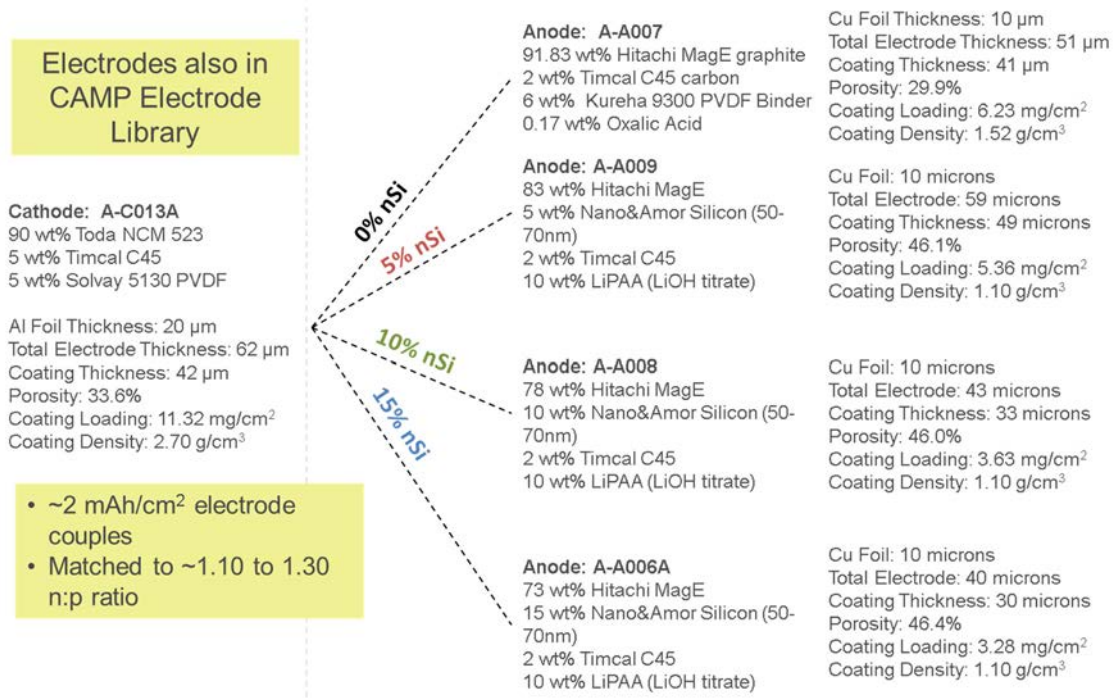


Figure IV-83: Baseline silicon-graphite composite electrodes selected for the next generation anode project with capacity-matched NMC532 cathode as counter electrode. Electrodes developed and provided by CAMP Facility

Two observations are clear from the data shown in Figure IV-84. Firstly, increasing the amount of silicon dramatically improves the specific capacity of the total active material (graphite + silicon), and secondly, that more effort is needed to improve the cycle life performance of silicon-based electrodes. While over a thousand cycles is typical for graphite-only negative electrodes, cells with as little as 5 wt. % silicon are only able to achieve a couple hundred cycles before excessive capacity loss. Similar results were seen in the CAMP Facility for these electrode compositions in 0.5 Ah pouch cells. As discussed in the FY15 annual report from the CAMP Facility, the main failure mechanism is poor coulombic efficiency caused by lack of formation of a robust SEI layer.

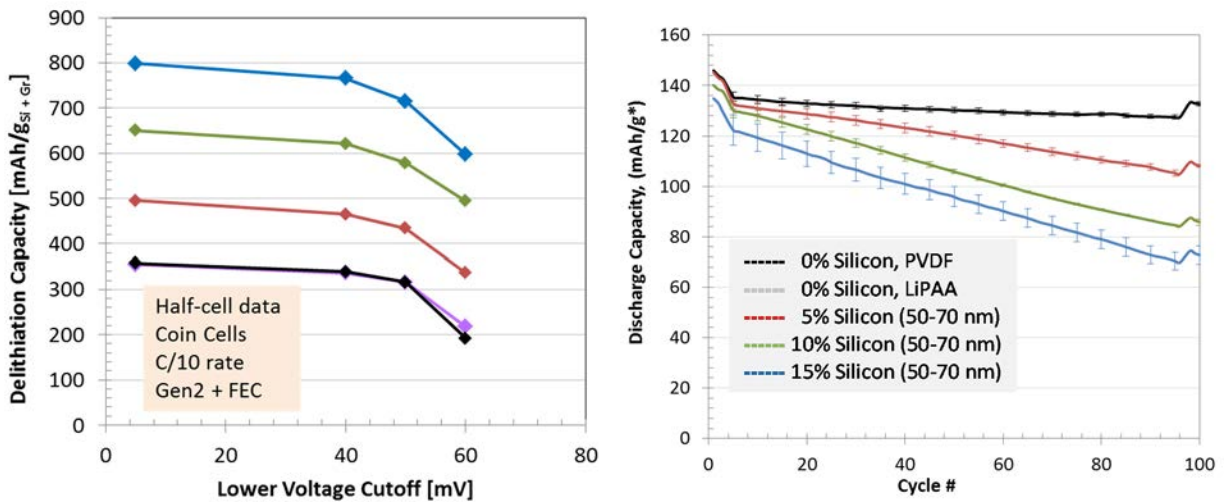


Figure IV-84: Electrochemical performance of baseline silicon-graphite composite electrodes. (LEFT) Delithiation capacity as a function of silicon content and lower cutoff voltage (vs.  $\text{Li}^+/\text{Li}$  half cells), and (RIGHT) discharge capacity versus cycle life as a function of silicon content in coin cells with baseline NMC532 electrode as the counter electrode. Voltage window of 3.0 to 4.1 V was used for full cells. Electrolyte was 1.2 M  $\text{LiPF}_6$  in EC:EMC (3:7 by wt.) with 10 wt. % FEC. Graphite only data (0% Si) with LiPAA and PVDF binders are nearly identical. The error bars represent  $2\sigma$  standard deviation. (\*weight of the NMC 532)

These electrodes have served well as initial baselines, but unfortunately, production of the 50-70 nm silicon from NanoAmor was discontinued in the fall of 2015. Initial experiments with the 30-50 nm silicon from NanoAmor as a replacement baseline were initially successful. The smaller silicon particles coated well on the CAMP Facility's pilot scale coater using a formula very similar to that used for the 50-70 nm silicon. The resulting capacity and cycle life were also acceptable. Some concern existed about switching to a smaller particle. During this selection time period, initial results of the SEI layer thickness were becoming available from other members of the team. These results (XPS and FTIR) were indicating that the SEI film thickness was on the order of 6 nm. It was now possible to calculate the impact of the SEI film volume on electrode energy density.

The SEI volume on a silicon particle that is swollen 300% (full lithiation) was calculated as a function of initial (before lithiation) particle diameter assuming a 6 nm SEI film thickness. These results are shown in Figure IV-85. From these results it is clear that going to a smaller silicon particle was detrimental to the energy density of the electrode. These calculations assumed that the silicon surface was pristine, but there is ample evidence that indicates these silicon particles have a SiO<sub>2</sub> layer on the surface, which would also lower the energy density of the silicon particle in a manner similar to the SEI film. Thus, it is clear, that a larger silicon particle is desirable. As further confirmation of this decision, preliminary results from thermal abuse tests at SNL suggest excessive thermal events for smaller silicon particles.

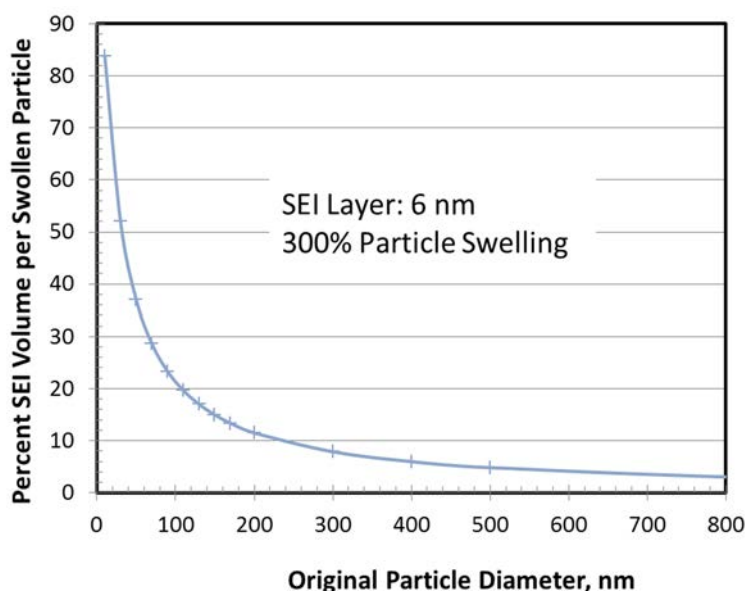
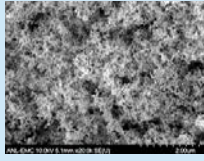
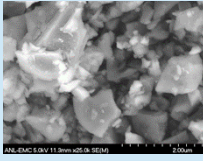
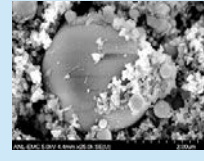
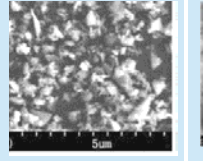
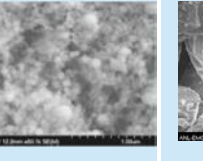
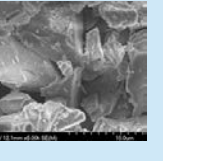


Figure IV-85: Percent SEI volume on swollen silicon particle as a function of original silicon particle diameter. The SEI film was assumed to be 6 nm based on recent FTIR and XPS results. Volume of SEI film calculated after particle was assumed to swell to 300%. Thickness of SiO<sub>2</sub> layer on surface of original silicon particle was not taken into account in these calculations

Search for larger silicon particles was initiated with the same limitation that the silicon powder must be open to the public and available to all members of the team without restrictions. A preference for particles in the 100 to 200 nm was made. Particles larger than 200 nm are much more likely to suffer from particle cracking due to volume expansion upon lithiation. Commercial materials available in this size range are shown in Table IV-8. A SiO sample from Aldrich was also included in this study, despite its large particle size. Samples were obtained from these sources and initial screening and electrode development were undertaken. None of the choices were ideal, but a decision was made to select the 70-130 nm silicon from NanoAmor due to its more uniform particle distribution (based on sample SEM images). A large order (6 kg) of the 70-130 nm silicon was procured from NanoAmor and distributed among the team labs. Searches for better silicon materials are still active. In addition, the DOE-EERE-VTO has initiated a program to develop silicon sources in-house. In addition to the silicon, graphite, electrolyte, a FEC additive was purchased and distributed to the team.

**Table IV-8: Silicon Materials Evaluated at the CAMP Facility for Use as New Baseline. The Respective Manufacturer’s Reported Average Particle Size is Listed. Assumed Product Processing Method and SEM Images Provided by ANL Team Members**

NanoAmor	NanoAmor	American Elements	American Elements	Hydro-Quebec	Aldrich
30-50 nm Si	70-130 nm Si	150 nm Si	500 nm Si	80 nm Si	40 μm SiO
Grown	Milled	Grown	Milled	Grown	Grown
					

Future work in silicon will include fabricating advanced silicon-graphite composite electrode using the newly obtained silicon and graphite materials: 70-130 nm Si from Nanostructured and Amorphous Materials (NanoAmor) and MagE3 from Hitachi. Trial electrodes have been made using typical approaches for slurry making and coating for silicon-graphite composites that were used in the previous electrode development, and are tabulated in Table IV-9. The goal is to achieve quality coatings with 30 wt. % silicon at the Electrode Library loading level (~2 mAh/cm<sup>2</sup>) for the team members to use as the new baseline. Preliminary results indicate that this should be reached in early FY16.

**Table IV-9: Electrode Fabrication – Trial Runs with 70-130 nm Silicon**

Idea	Electrode ID	Silicon, Nano-Amor, 70 to 130 nm, %	Graphite, Hitachi MagE3, %	Carbon, Timcal C45, %	Binder, %	Result
Replicate baseline electrode processing	LN302 4-139-2	15	73	2	10 (450k LiPAA)	High stresses observed after drying
Premix of LN3024-139	LN302 4-140-2	55.6	0	7.4	37.0 (450k LiPAA)	Thin, OK
Graphite only w/ PVDF	LN302 4-141-2	0	91.83	2	6 (PVDF) + 0.17 oxalic acid	Good
Increase surface area	LN302 4-142-2	30	58	2	10 (450k LiPAA)	Minimal improvement
Decrease binder	LN302 4-143-2	15	75	2	8 (450k LiPAA)	High stresses
Try 250k LiPAA	LN302 4-147	15	75	2	10 (250k LiPAA)	Less stresses, but still present
250k LiPAA w/ higher Si and less binder	LN302 4-149	30	62	2	6 (250k LiPAA)	Less stresses, but still present
250k LiPAA w/ less binder	LN302 4-150	15	77	2	6 (250k LiPAA)	Less stresses, but still present
250k LiPAA w/ even less binder	LN302 4-151	15	79	2	4 (250k LiPAA)	Noticeable decrease in adhesion properties

## Trial Coating of Si/C Anode with New Baseline Silicon Powder (ORNL)

BMF researchers have successfully coated 25 ft of Si/C anode with  $3.39 \text{ mg/cm}^2$  areal loading. The anode consists of 73wt% graphite (MAGE3, Hitachi), 15wt% Silicon(70-130 nm, Nano and Amor Silicon), 2 wt% carbon black (C-ENERGY Super C45, Imerys Graphite and Carbon), 10 wt% LiPAA (pH=7, 7.4 wt% in DI-water, PAA MW 250,000 g/mol). LiPAA solution was prepared by adding LiOH•H<sub>2</sub>O to the PAA solution until the pH=7. Si and carbon black were dry mixed followed by ball milling overnight. The mixed suspension was transferred to a planetary mixer (Ross, DPM ½) and mixed with graphite powder at 2000 RPM/25 RPM for ½ hour. The desired amount of LiPAA solution was added to the mixed suspension and mixed at 600 RPM/25 RPM for 1 hour. Additional water was added to adjust the solid loading to ~35wt%. Degassing was performed at 600 RPM for ½ hour before electrode coating. The as-coated anode was 58 μm thick including 9 μm from the Cu foil. The coating density is  $0.69 \text{ g/cm}^3$  with 66.4% porosity. Figure IV-86 shows the wet and dry coating, respectively.

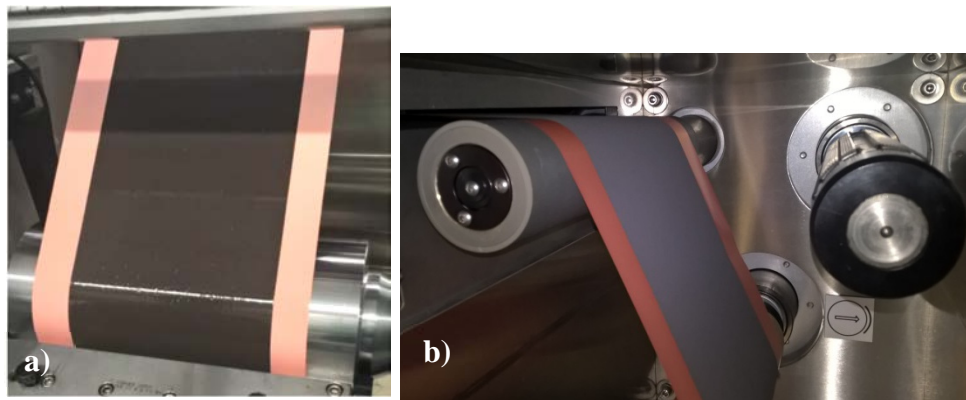


Figure IV-86: Si/C composite anodes a) wet coating and b) dry coating

## Preliminary electrochemical testing

½” diameter samples were punched out from the coating and used for half and full coin cell testing. Electrodes utilized Celgard 2325 separator and LiPF<sub>6</sub> in EC/EMC (3/7 wt) (ANL, Gen 2) with 10% FEC. Full cells were paired with  $12.5 \text{ mg/cm}^2$  NMC-532 cathodes. Half cells produced a first and second cycle capacity of 655 and 600 mAh/g respectively, with a first and second Coulombic efficiency of 92% (Cycled at ~C/8.6). The voltage profile of the Si-graphite half cells are shown in Figure IV-87.

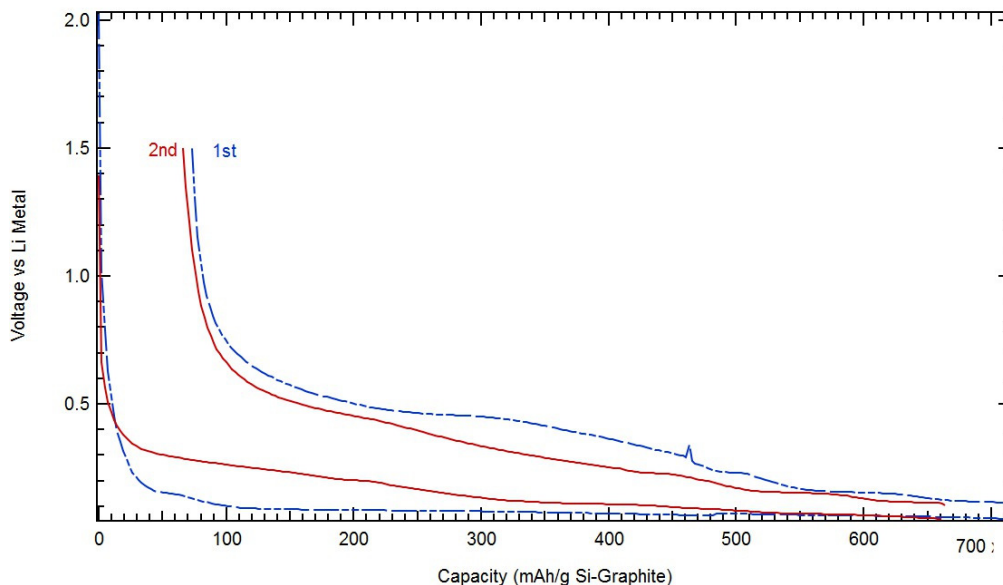


Figure IV-87: Voltage profile of 15%Si-Graphite half cells, cycled from 0.05 – 1.5 V vs Li metal at 30 °C. First cycle represented by blue dashed line, Second cycle represented by red solid line

The full cell was cycled from 3 to 4.1V at C/20 based upon a capacity 145 mAh/g of NMC-532 cathode. This resulted in the full cell initial capacity of 140 mAh/g (based on the cathode) followed by capacities of 135 and 131 on the following second and third cycles. Coulombic efficiencies of the first three cycles are as follows: 81%, 96%, and 96%. Full cell voltage profiles can be seen in Figure IV-88. Half cells and full cells are under continued cycling to obtain long term cycling data.

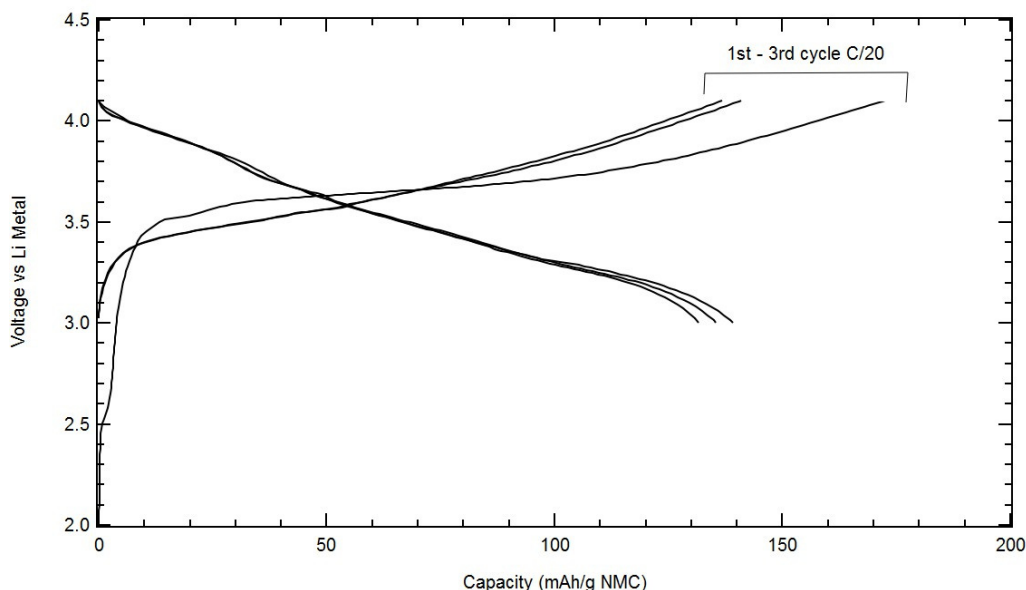


Figure IV-88: Voltage profile of NMC532/Si-C full cells (3-4.1 V, 30 °C, C/20, cycles 1-3)

### Thermodynamic Understanding and Abuse Performance (SNL)

As we develop new materials to increase performance of lithium-ion batteries for electric vehicles, the impact of potential safety and reliability issues become increasingly important. In addition to electrochemical performance increases (capacity, energy, cycle life, etc.), there are a variety of materials advancements that can be made to improve lithium-ion battery safety. Issues including energetic thermal runaway, electrolyte decomposition and flammability, anode SEI stability, and cell-level abuse tolerance behavior. Introduction of a next generation material, such as silicon based anode, requires a full understanding of the abuse response and degradation mechanisms for these anodes. This work aims to understand the breakdown of these materials during abuse conditions in order to develop an inherently safe power source for our next generation electric vehicles.

The effect of material level changes (electrolytes, additives, silicon particle size, silicon loading, etc.) to cell level abuse response and runaway reactions will be determined using several techniques. Experimentation will start with base material evaluations in coin cells and overall runaway energy will be evaluated using techniques such as differential scanning calorimetry (DSC), thermogravimetric analysis (TGA), and accelerating rate calorimetry (ARC). The goal is to understand the effect of materials parameters on the runaway reactions, which can then be correlated to the response seen on larger cells (18650). Cylindrical cells were fabricated using a variety of baseline materials with varying silicon loading to understand full cell response. Our approach that spans from the materials level through large cells aims to understand both properties and scale effects that will be important in the development of an inherently safe power source utilizing next generation silicon based anodes.

Initial efforts for the program focused on the fabrication and electrochemical evaluation of double-sided electrodes that showed identical performance to the CAMP developed materials. Electrode evaluations were conducted in 2032 coin cells to validate electrode performance is comparable across the program and across laboratories, as seen in Figure IV-89.

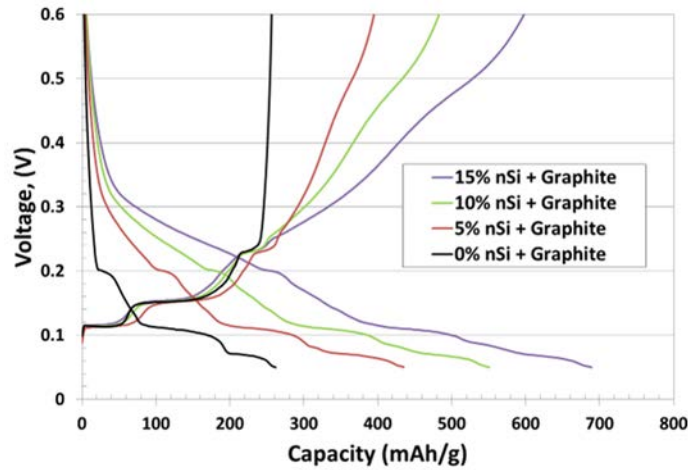


Figure IV-89: Example cycling data for electrodes used to evaluate abuse response. Varying silicon amounts are shown, all using gen 2 electrolyte with 10% FEC by weight. The materials used and cells fabricated were evaluated to ensure that all program data generated was comparable through the multi laboratory collaboration

Material level evaluations were conducted to understand the effect of several different materials properties on the overall energy output during a runaway or abuse event. DSC experiments were conducted to investigate the effect of silicon active material particle size and silicon loading in the electrode. ARC bomb evaluations were conducted in a step wise fashion to understand the contribution of each electrode component to gas generation for the materials only. The ARC evaluations do not immediately show the effect of these interactions in a full cell, since they exclude the lithium silicon alloying reactions and any catalytic effects from those reaction products. Figure IV-90 shows a summary of experimentation performed on the silicon electrodes for this program.

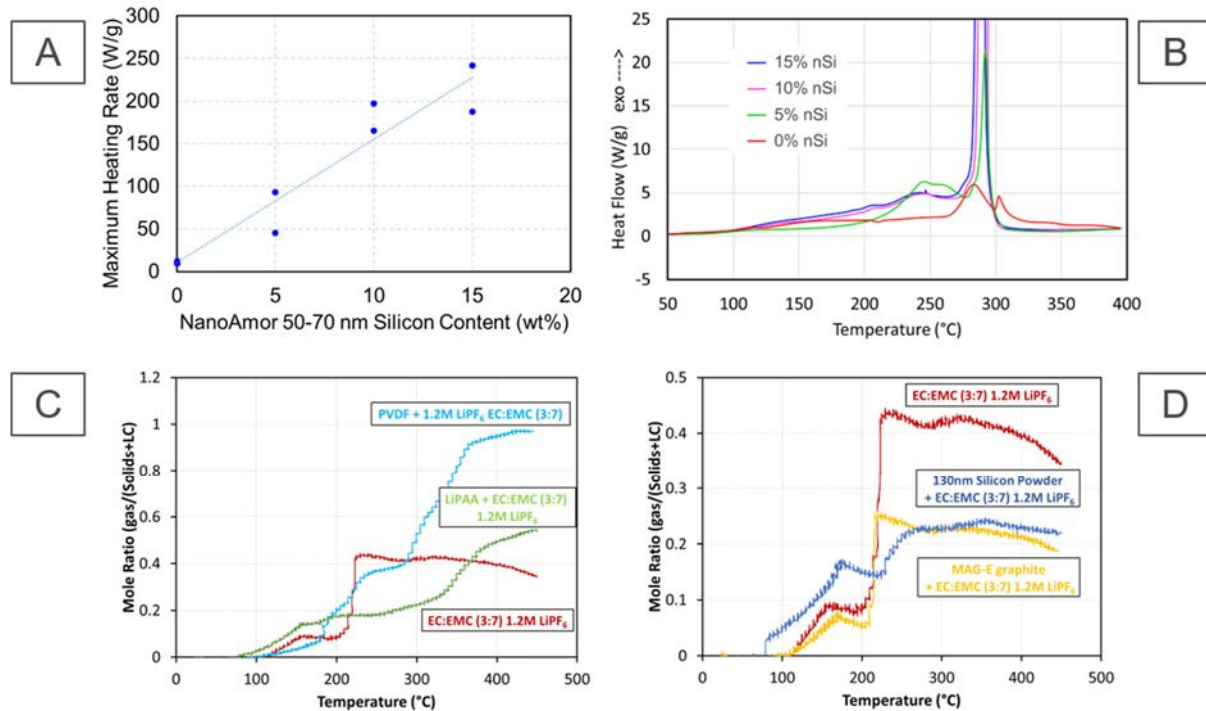


Figure IV-90: Selected material level evaluations for next generation anodes. Panels show the effect of silicon content on heating rate (A) and material decomposition (B), and gas generation based on electrolytes and binder (C) and with the addition of active electrode materials (D)

Panel A of Figure IV-90 shows that there is a dependence in energy output that varies with silicon content, which is indicative of the silicon material being a prime participant in the energetic decomposition of these materials. Panel B shows that this increase in energy during decomposition is primarily in the high rate output between 250 and 300 °C, using electrolyte containing 10 wt% FEC. Panel C shows the ARC response to the stepwise addition of binder materials to electrolytes to show that there is only minimal overall effect on abuse response. Panel D indicates that the addition of silicon or graphite powder to baseline electrolyte does not dramatically increase the gas generation. Panels C and D indicate that any increased response from silicon based anodes cannot be directly contributed to interactions of the materials only. Any response clearly requires the interactions that only occur once lithium silicon alloy reactions are present within the cell.

Full cells were built using the 0, 5, 10, and 15 wt% silicon electrodes and built into 18650 format cells for larger cell evaluation of decomposition and abuse response. Starting with the anticipated highest overall enthalpy output, the 15 and 10% silicon content cells were formed and put on ARC testing at 100% SOC (4.1V vs. a NMC532). Pictures of the result are showing in Figure IV-91.



Figure IV-91: ARC conditions from attempted evaluation of 18650 cells using NCM523 vs. 10 and 15 wt% nanosilicon

The overall cell response was sufficient to cause several failures within the ARC experimental setup, which is normally able to handle both research and commercial grade 18650 cells. The exact failure mechanism is not obvious and more testing is underway to identify the issue that was observed. It is evident that there was a good amount of gas and heat generated during this experiment. The immediate priority for this research is to understand and quantify exactly what is occurring within the nanoscale lithium silicon electrode system.

### Full Cell Testing Protocol (ANL)

All anode advancements will ultimately be verified based on life and performance of full cells against baseline materials, electrodes, and cells. In examining improvements, changes to the baseline cell technology will be minimized. As an example, silicon active material coating improvements will be verified on baseline silicon materials in electrodes fabricated by the battery research facilities. All other components in the prototype cells (i.e. positive electrode, separator, electrolyte, etc.) will be from the baseline technology. There are many testing protocols that can be utilized to benchmark the baseline technology. This program has adopted a testing protocol from literature [3] that has worked well for lithium-ion cells with silicon containing anodes. Shown pictorially in Figure IV-92 and in more detail in Table IV-10, the test starts with three slow ( $C/20$ ) formation cycles, an HPPC cycle, and then the  $C/3$  aging cycles. The test ends with another HPPC cycle and three more slow ( $C/20$ ) cycles. All constant current cycling is symmetric between charge and discharge rates. The tests are run at 30°C. If there is little or no aging in the first 100 cycles, the protocol can be repeated. However, as can be seen from Figure IV-84 above at present all the baseline silicon containing electrodes show significant signs of aging. Because wetting can vary according to cell format, the initial tap charge varies as described in Table IV-10. This protocol effectively examines capacity, impedance, and aging effects in about a month's worth of testing.

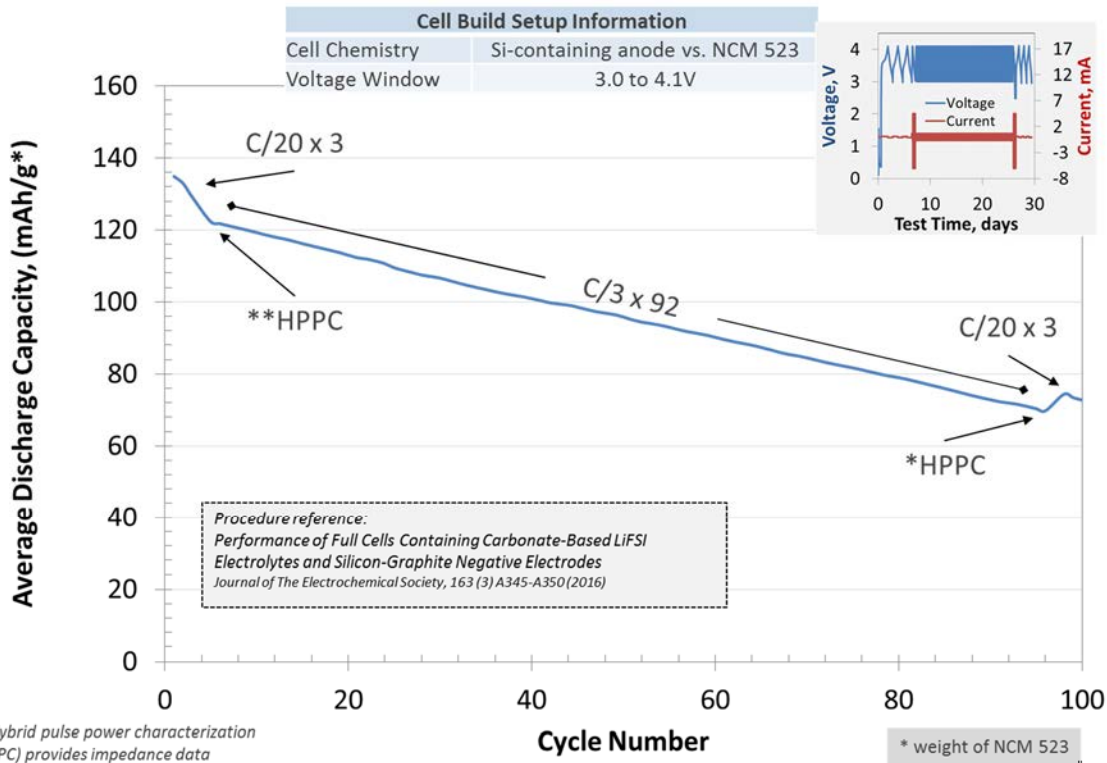


Figure IV-92: Full cell testing protocol

**Table IV-10: Full Cell Testing Protocol**

Test Parameters				
	Multi-layer Pouch Cell Protocol	Single-layer Pouch Cell Protocol	Coin Cell Protocol	
<b>Protocol Name</b>	NGA_Cyc_3-41_mpc_v1	NGA_Cyc_3-41_spc_v1	NGA_Cyc_3-41_cc_v1	<b>Purpose:</b>
Rest	2 min	2 min	2 min	Test setup rest
Tap Charge	C/10 to 1.5 V, then 15 min voltage hold at 1.5 V	C/10 to 1.5 V, then 15 min voltage hold at 1.5 V	No tap charge	Minimize Cu corrosion during wetting rest step
Rest	Open circuit, 24 hr	Open circuit, 12 hr	Open circuit, 2 hr	Time allowed for electrodes to wet
Initial Cycles	3 cycles, 3.0-4.1 V, C/20	"	"	Formation, Initial Slow Cycle Data
Initial Impedance	**HPPC – 10s pulses, 3C discharge, 2.25C charge, at each 10% DOD	"	"	
Aging Cycles	92 cycles, 3.0-4.1 V, C/3, HPPC – 10s pulses, 3C discharge, 2.25C charge	"	"	
Final Impedance				
Final Cycles	3 cycles, 3.0-4.1 V, C/20	"	"	Final Slow Cycle Data

### Fundamental Studies of Si-C Model Systems

Program efforts on the development of thin-film Si, Si/C, and Si/binder electrodes, as well as the wide range of fundamental characterization studies conducted on these electrodes are discussed in section IV.D.8 of this report (i.e. Next-Generation Anodes for Lithium-ion Batteries: Fundamental Studies of Si-C Model Systems).

## Characteristics of Half and Full Cells containing Layered Oxide, Graphite and Silicon-Graphite Electrodes (ANL)

The development of new high-energy electrochemical couples is important in reducing the overall cost and weight per kWh of lithium-ion batteries. Silicon and silicon-containing blended electrodes have been a focus of much recent research as an alternative to the commercial graphite-based negative electrode because of the substantially higher theoretical capacity of silicon (3579 mAh/g,  $\text{Li}_{15}\text{Si}_4$ ) compared to that of graphite (372 mAh/g,  $\text{LiC}_6$ ); the higher capacity enables reduction of the negative electrode weight, thereby increasing energy density of the cell. However, concerns including electrode integrity and durability related to the substantial volume expansion/contraction (~300%) of silicon during lithiation/delithiation reactions have hampered the use of silicon as a direct substitute for graphite.

Several strategies to overcome durability problems target design of the composite electrode and its components. For example, purposely-designed silicon particle morphologies and the use of graphene are reported to improve the cycle life of electrodes in cells with a Li-metal counter electrode (half-cells). The choice of binders also greatly influences electrode coherence; for example lithiated polyacrylic acid (LiPAA) has been shown to increase cycle life compared to e.g. polyvinylidene fluoride (PVDF). Direct incorporation and mixing of silicon particles into standard graphite slurries also provides a means of incrementally improving electrode capacity, while retaining the higher durability of graphite electrodes. In addition to variations in electrode constitution, alternative electrolytes are being studied to improve cell cycling stability by tuning the electrochemical interfaces. The use of electrolyte additives is especially common as small amounts can have large impact on the interfacial chemistry of both positive and negative electrodes. Fluoroethylene carbonate (FEC) specifically, and to some extent vinylene carbonate (VC), added to Si-containing cells has been shown to improve cycle life compared to cells containing the standard carbonate mixtures of ethylene carbonate (EC), ethyl methyl carbonate (EMC), and diethyl carbonate (DEC).

Our approach was to examine performance of half-cells, and longevity of full cells, prepared using electrodes fabricated (with commercially available materials) by the Cell Analysis, Modeling, and Prototyping (CAMP) facility of Argonne. We first examined the performance of half-cells with a layered oxide NMC532 ( $\text{Li}_{1.03}(\text{Ni}_{0.5}\text{Mn}_{0.3}\text{Co}_{0.2})_{0.97}\text{O}_2$ ), graphite (Gr), or blended 15 wt% Si- 85 wt% graphite (SiGr) electrodes. We then tested full cells containing NCM532-based positive and the SiGr-based negative electrodes. Such full cell studies are needed to capture crosstalk between the electrodes and to gauge durability of the lithium-limited cells. Of particular interest was the effect of voltage hysteresis introduced by the silicon on full-cell performance benchmarks, such as DC and AC power characterization tests, which are especially important for transportation applications. With the full cells we examined the effect of electrolyte composition, by adding various amounts of VC and FEC to our baseline (Gen2) electrolyte. Studies of this nature are the initial steps towards increasing the performance and durability of high-energy, silicon-containing, lithium-ion cells.

### Half Cell data for Graphite (Gr), and 15wt% Si-Gr (SiGr) electrodes

The first two cycles of Gr, and SiGr electrodes, in a cell with a Li-metal counter electrode and 10% FEC added to Gen2 electrolyte, are shown in Figure IV-93 a–f. Note that the Gr electrode profiles are similar for the two cycles, while the SiGr electrode lithiation profiles are distinctly different. The 15 wt% Si addition clearly increases electrode specific (delithiation) capacity displaying a value of 816 mAh/g compared to 362 mAh/g for the Gr electrode (for the second 1.5-0.0 V cycle); this specific capacity calculation includes the Si, graphite, and C45 carbon weight. The coulombic efficiencies of both first and second cycles are lower for the SiGr electrode; the first cycle efficiency is 90.4% compared to 93.6%, and the second cycle efficiency is 98.0% for the second cycle compared to 99.0% for the Gr electrode. Features associated with FEC reduction are seen in both the Gr/Li (Figure IV-93b, ~1.2 V) and SiGr/Li (Figure IV-93d, ~1.1 V) cells; this FEC reduction minimizes reduction of the EC component, which is typically observed at ~0.7 V for cells with the Gen2 electrolyte.

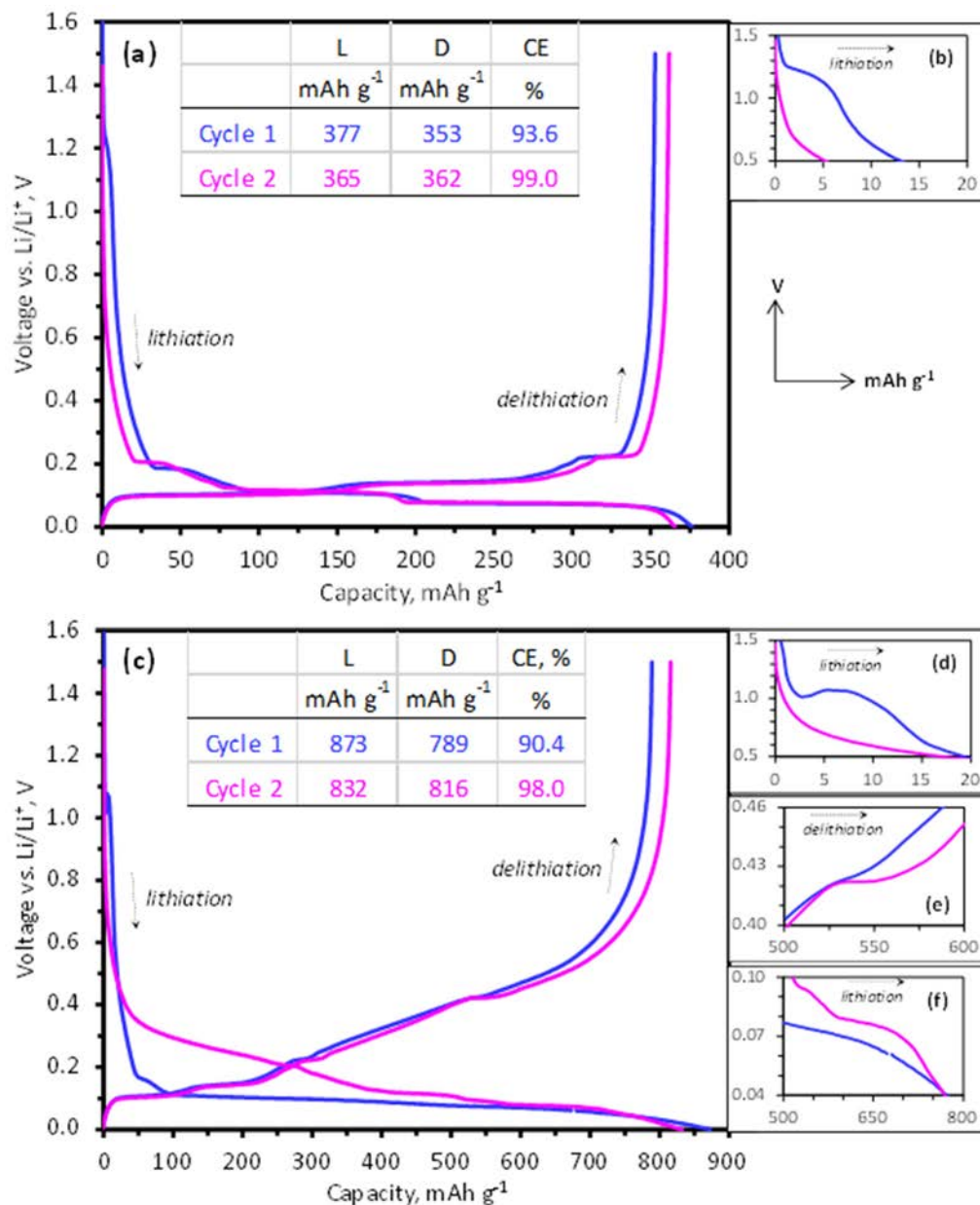


Figure IV-93: 1st and 2nd cycle capacity-voltage profiles from Gr/Li (a) and SiGr/Li cells (c) with Gen 2 + 10 wt% FEC electrolyte cycled at a  $\sim C/25$  rate in the 1.5-0.0 V range at 30 °C. The inset tables show lithiation (L) and delithiation (D) capacities and coulombic efficiencies (CE). Expanded views of specific sections are shown adjacent to the plots in (b) for Gr/Li, and (d) - (f) for SiGr/Li. For all figures the X and Y axes show capacity ( $\text{mAh g}^{-1}$ ) and voltages vs.  $\text{Li/Li}^+$  (V), respectively. Figures (b), (d), and (f) show lithiation cycles, whereas (e) shows delithiation cycles

The Gr electrode (Figure IV-93a) displays distinct plateaus during the lithium-ion intercalation/deintercalation reactions; the voltage profiles are altered by silicon addition. During first lithiation of the SiGr electrode (Figure IV-93c), the first graphite lithiation plateau is still visible ( $\sim 0.16$  V) before the characteristic low voltage gently-sloping plateau (around 0.1 V), associated with the initial lithiation and alloying of Si becomes dominant. The 0.16 V plateau is at a lower potential than that typically expected for graphite (0.21 V). However, the plateau is not observed in the Si-only (no graphite) electrode data and must, therefore, arise from the graphite component; the lower potential may be a consequence of higher ohmic polarization (higher electrode impedance) during the first cycle. Also, no obvious plateau associated with the  $\text{Li}_{15}\text{Si}_4$  phase is observed; this plateau may be shifted to values below our lower cutoff potential because of stresses remaining in the nanosilicon particles. Following the first lithiation, the addition of silicon increases the average voltage over the electrode capacity compared to the graphite electrode, as expected, both for lithiation and delithiation. A clear contrast between the sharp plateaus of the graphite electrode and the sloping profile of amorphous silicon is observed. Furthermore, a large voltage hysteresis between lithiation and delithiation results from Si

introduction. This hysteresis is clearly evident in Figure IV-94, which compares the lithiation and delithiation curves of the Gr and the SiGr electrodes obtained at a very slow ( $< C/100$ ) rate; the capacity values shown are normalized to graphite content in the electrodes. The data are from the fifth cycle, which provides features related to structural changes in the active material while minimizing features arising from electrolyte reduction. Two plots are shown for the SiGr electrodes; the lower cut-off potential (LCP) for the plots are 0.075 V (magenta) and 0.0 V (blue), respectively.

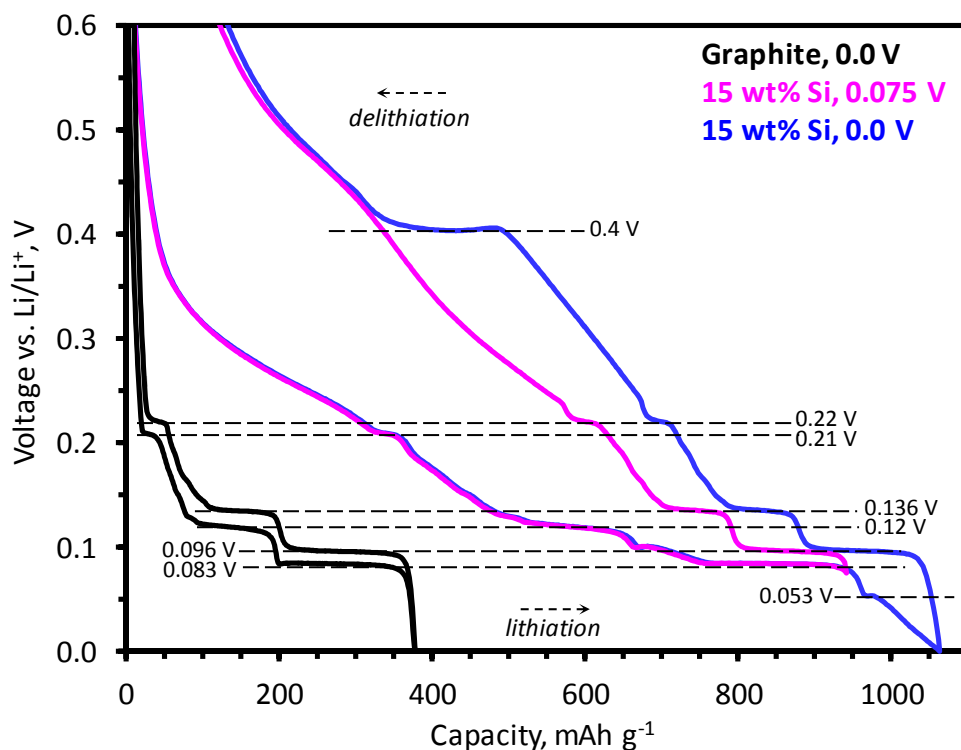


Figure IV-94: Capacity-voltage profiles of electrodes with graphite (black) and 15 wt% Si in graphite, with cut-off potentials at 0.0 V (blue) and 0.075 V (magenta). The graphite electrode was cycled at  $\sim C/120$  rate, and the silicon-bearing electrode at  $\sim C/140$  rate, in coin cells with a Li-metal counter electrode and 10 wt% FEC in the baseline electrolyte. The data are normalized to the graphite content in each electrode. The dashed lines mark plateaus and key features in the figure

During lithiation of the Gr electrode, distinct plateaus are observed at 0.21 V, 0.12 V, and 0.083 V (Figure IV-94). The SiGr electrode lithiated to 0.075 V also contains these features, and additional capacity in broad features above 0.21 V. On delithiation, the Gr electrode shows features at 0.096 V, 0.136 V, and 0.22 V; these features are also observed for the SiGr electrode. On lithiation down to 0.0 V, the SiGr electrode shows a feature at 0.053 V (blue curve, Figure IV-94), and another feature at approximately 0.4 V vs Li/Li<sup>+</sup> in the subsequent delithiation cycle. These features are indicative of the crystalline Li<sub>15</sub>Si<sub>4</sub> phase. The onset of the crystalline phase is believed to negatively impact the cycling behavior of Si electrodes, and limiting the capacity to avoid its formation is often suggested as a viable strategy to enhance cycle life. Note that the 0.4 V feature during delithiation does not appear when the lower cut-off potential is restricted to 0.075 V (magenta curve, Figure IV-94).

### Full Cell impedance data from NMC532/Gr and NMC532/SiGr cells

The initial impedance (after formation cycling) as a function of cell voltage is shown in Figure IV-95 for full cells containing the Gen2 + 10 wt% FEC electrolyte: data from a NMC532/Gr cell are compared with those obtained from a NMC532/SiGr cell. The DC impedance data were obtained with 10s 3C pulses during both charge and discharge cycles. Figure IV-95a (upper) contains data from charge pulses, during which Li<sup>+</sup> ions are extracted from the positive and inserted into the negative electrode. Figure IV-95b (lower) contains data from discharge pulses, during which Li<sup>+</sup> ions are extracted from the negative and inserted into the positive electrode.

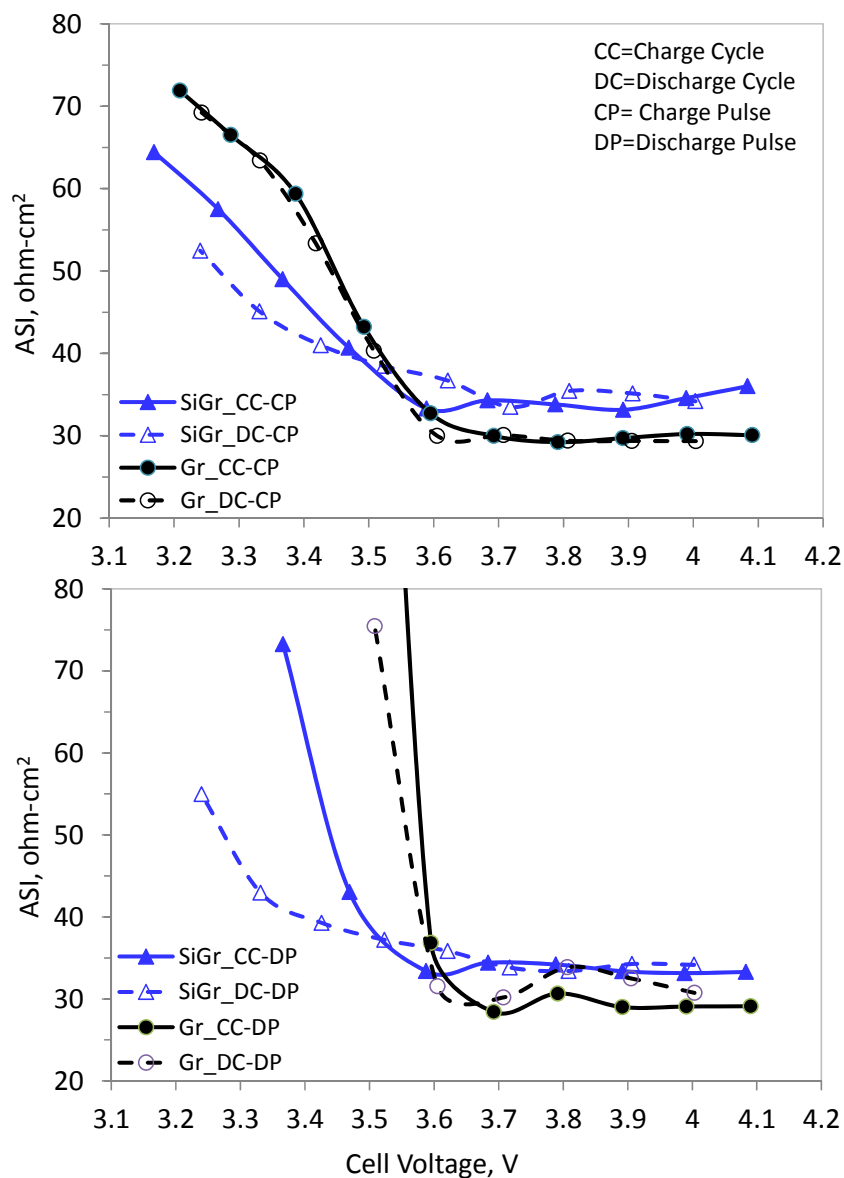


Figure IV-95: Area specific impedance (ASI) as a function of cell voltage for NMC532/Gr (Gr, black) and NMC532/SiGr (SiGr, blue) cells in the 2.5-4.1 V range. The data were obtained in the charge and discharge cycles with a 10 s, 3 C pulse, after the cells were charged to 3.2, 3.3, 3.4, 3.5, 3.6, 3.7, 3.8, 3.9, 4.0 and 4.1 V and allowed to rest (no current) for 1h. During this rest period, the cell voltage decreases some during the charge cycle and increases some during the discharge cycle. The cells could not successfully sustain the 3C pulses beyond the data values shown

The presence of silicon induces hysteresis in the voltage profile, which results in impedance differences between the charge and discharge cycle at the same cell voltage. For example the charge-pulse impedance data for the NMC532/Gr cell (Figure IV-95a) are very similar during the full cell charge and discharge cycles. The area specific impedance (ASI) values are ~29 ohm-cm<sup>2</sup> between 4.1 and 3.6 V, and then rise almost linearly to ~70 ohm-cm<sup>2</sup> at around 3.2 V; the increase at low cell voltages reflects the difficulty of extracting Li<sup>+</sup> ions from the relatively-full NMC532 oxide. The increases at the lower cell voltages is also seen for the NMC532/SiGr cell; however, this cell also shows bigger differences between the values during charge and discharge cycles resulting from the larger difference in electrode state-of-charge (SOC) at the lower cell voltages. The larger differences at low cell voltages for the NMC532/SiGr cell are also seen in Figure IV-95b, which contains impedance data from the discharge pulses.

#### Cycling data from NMC532/SiGr cells - effect of electrolyte compositions

Full-cell data from NMC532/SiGr coin cells with different electrolyte compositions, cycled in the 2.5-4.1 V range, are presented in Figure IV-96. Note that the electrolytes can be grouped into three categories: Gen 2,

Gen2 + 5 wt% additive (5 wt % VC, or 5 wt% FEC, or 2.5+2.5 wt % of VC and FEC), and Gen 2 + 10(or) 20 wt% (FEC or VC) additives. Figure IV-96a shows discharge capacity vs. cycle number of representative cells. The cell capacities are bunched together initially but then start diverging. The first cell to show faster capacity fade (around 15 cycles) is the one containing the Gen2 electrolyte; the cells containing the 5 wt% additives are the next to show accelerated fade (between 40 and 50 cycles). The cells with the 10 and 20 wt% additives show similar behavior up to the 100 cycles.

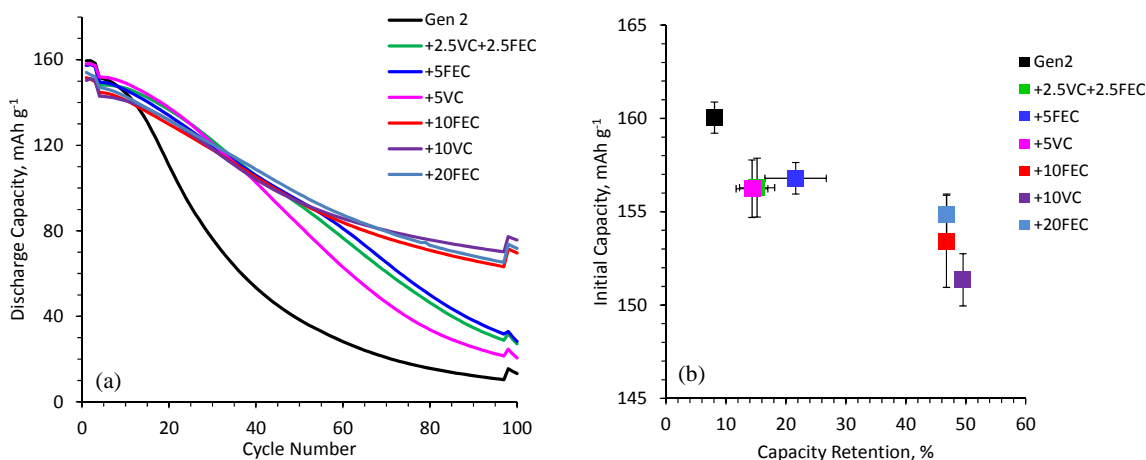


**Figure IV-96: Effect of electrolyte composition on (a) discharge capacity over cycle life, and (b) first cycle discharge capacity correlated to capacity retention after 100 cycles. The data are from NMC532/SiGr cells cycled at 30 °C in the 2.5-4.1 V range. The cycling protocol contained 3 initial ~C/20 cycles, 94 ~C/3 aging cycles and 3 final ~C/20 cycles**

Another representation of the cycling data is shown in Figure IV-96b, which displays the initial discharge capacity (cycle 1) of cells plotted as a function of capacity retention (comparing cycles 3 and 100 capacities, obtained at low rates); the data point and error bars represent the average and 2 standard deviations from multiple cells. Ideally, for each cell, the initial discharge capacity and capacity retention should be as high as possible. However, Figure IV-96b shows that the initial discharge capacity decreases when the additive content is increased. For example, the initial discharge capacity is lower (than that of the Gen2 cell) by ~3 mAh/g at 5 wt% additive content, and ~5-9 mAh/g at 10 and 20 wt% additive contents. Note that g (grams) refers to oxide content in the positive electrode. The lower initial capacity suggests that Li<sup>+</sup> ions are trapped in SEI formation products and hence unavailable for further cycling. On the other hand, capacity retention is enhanced by the additives: the retention improves from 8% for Gen2, to ~15-20% at 5 wt% additive content, and further to ~46-50% at 10 and 20 wt% additive contents.

Both Figure IV-96a and b suggest that cell capacity retention depends on additive content – the higher the additive content, the better the retention. However, capacity retention does not improve when the FEC content is increased from 10 to 20 wt%. This result may indicate that the 10% FEC is not depleted from the electrolyte during the 100 cycles; further cycling may deplete the FEC and accelerate capacity fade. That is, cycling differences between the 10 to 20 wt% FEC electrolyte cells could become prominent on extended cycling. If FEC is indeed consumed then even higher amounts could further delay capacity fade. Therefore, we inquired whether cells containing 1.2M LiPF<sub>6</sub> in FEC electrolyte would show superior behavior; these cells, however, did not cycle even when the temperature was increased to 55°C to reduce electrolyte viscosity.

To determine reasons for this poor cycling behavior we studied various fluorinated carbonate electrolytes containing LiPF<sub>6</sub> and compared their behavior with those of non-fluorinated carbonate solvents, such as PC and EC. Dilute LiPF<sub>6</sub> solutions in FEC (0.1-0.5 M) exhibited the same <sup>7</sup>Li NMR spectra as Li<sup>+</sup> ions in LiPF<sub>6</sub>-PC suggesting a similar mode of Li<sup>+</sup> solvation in the two solutions. However, as the concentration of LiPF<sub>6</sub> exceeded 0.8-0.9 M in FEC, the solutions displayed opalescence at room-temperature. After several days of standing at 25°C, there was sufficient Ostwald ripening in a 1.35 M LiPF<sub>6</sub> solution for phase separation to occur. The solid precipitate was separated by centrifugation and analyzed using <sup>19</sup>F NMR; the data indicated that the mole ratio of LiPF<sub>6</sub> to FEC in this precipitate was 3:1, suggesting a Li(FEC)<sub>3</sub>PF<sub>6</sub> solvate.

Further experiments on a 1 M LiPF<sub>6</sub> in 4:1 w/w BFEC:FEC electrolyte (where BFEC and FEC are abbreviations for bis(2,2,2-trifluoroethyl) carbonate and fluoroethylene carbonate, respectively) yielded high-

quality crystals that were separated, multiply washed with anhydrous toluene and analyzed. Using  $^{19}\text{F}$  NMR we established that this material contained no BFEC, while  $\text{LiPF}_6$  and FEC were again present in 1:3 mole ratio, suggesting that this compound was also  $\text{Li}(\text{FEC})_3\text{PF}_6$ . X-ray diffraction data on a single crystal, followed by single crystal refinement, yielded the structure shown in Figure IV-97. Comparisons with previously known crystal structures indicated several unusual features, which are as follows: (i) the  $\text{Li}^+$  ions are octahedrally rather than tetrahedrally coordinated, and (ii) the  $\text{Li}^+$  ions are shared by the carbonyl oxygens in the  $\text{Li}^+(\text{FEC})_3$  chains resulting in longer Li-O distances. In  $\text{Li}(\text{EC})_3\text{TFSI}$  (which has the same stoichiometry as  $\text{Li}(\text{FEC})_3\text{PF}_6$ ) no oxygen sharing occurs, and the  $\text{Li}^+(\text{EC})_3$  ions are bridged through the anions; for FEC, the anions occupy voids between the polymer chains, as shown in Figure IV-97.

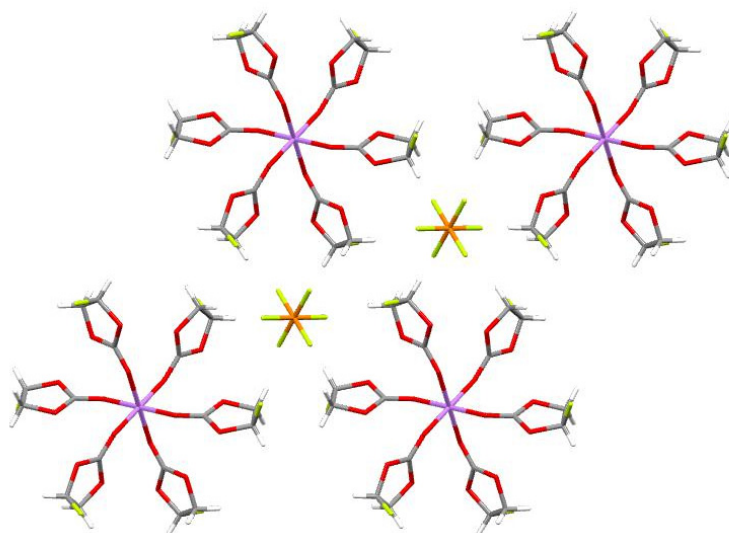


Figure IV-97: View of  $[\text{Li}(\text{FEC})_3]\text{PF}_6$  crystal lattice with crystallographic axis  $c$  perpendicular to the plane of the figure. The color scheme is as follows: Li (purple), C (grey), O (red), F (bright green), P (orange), H (white)

### NMR Studies of Composite Silicon Electrodes (ANL)

Solid state (NMR) has been instrumental in understanding lithiation and delithiation mechanism and SEI composition of silicon electrodes over the last decade [4-8]. The summarized results indicate formation of complex amorphous phase compositions upon lithiation of silicon and local formations of reactive overlithiated phases that lead to significant and complex side reactions in the electrolyte. The extent of these reactions, coupled with large volume changes, is believed to be responsible for poor cyclability of silicon electrodes.

The type of local order determines key electrochemical performance metrics in intermetallic anode systems such as silicon anodes. In the first year, this study has focused on characterization of the baseline commercial materials and their evolution and degradation on extended electrochemical cycling. Correlations between structure and activity relationships are drawn to help the team to optimize powders used in composite electrodes as well as detailed characterization of cycled electrodes to identify key reactions.

A multinuclear solid state NMR method has been used on pristine commercial silicon powders and large batch Si-Gr composite electrodes manufactured and cycled by CAMP. Local  $^{29}\text{Si}$ ,  $^{13}\text{C}$ ,  $^1\text{H}$ ,  $^7\text{Li}$  and  $^{19}\text{F}$  order is probed to gain comprehensive insights into pristine commercial powder composition, lithiation mechanism, Li-loss, SEI build-up and SEI composition, as well as side reactions due to electrolyte decomposition.

Figure IV-98 shows  $^{29}\text{Si}$  Magic Angle Spinning (MAS) of commercial silicon powders. The results mainly show two sets of silicon local order in the bulk ensemble. The peak at  $-80\text{ppm}$  is due to elemental Si and the peak at  $-110\text{ppm}$  is due to  $\text{SiO}_2$ . The area under the peaks indicate quantitative contribution of these two local orders in the bulk and relative ratios are reported in red. A large portion of the sample for 30-50nm commercial sample is found to be  $\text{SiO}_2$ . As the particle size is increased the relative ratio of  $\text{SiO}_2$  peak decreases to 50% for commercial sample with 70-130nm particles. As for much larger particle sized batches such as 325 mesh ( $<40$  microns and below, with average particle size of 100nm), only about 10%  $\text{SiO}_2$  order is found. Furthermore, exposure in ambient environment is also found to increase  $\text{SiO}_2$  peak intensity, shown in August and October

runs of the 70-130nm powder. It can be basically suggested that Si-batch, particle size, synthesis and exposure determines how much elemental Si to use in the formulation and SiO<sub>2</sub> shell thickness can be up to 15nm as suggested in literature [6-8].

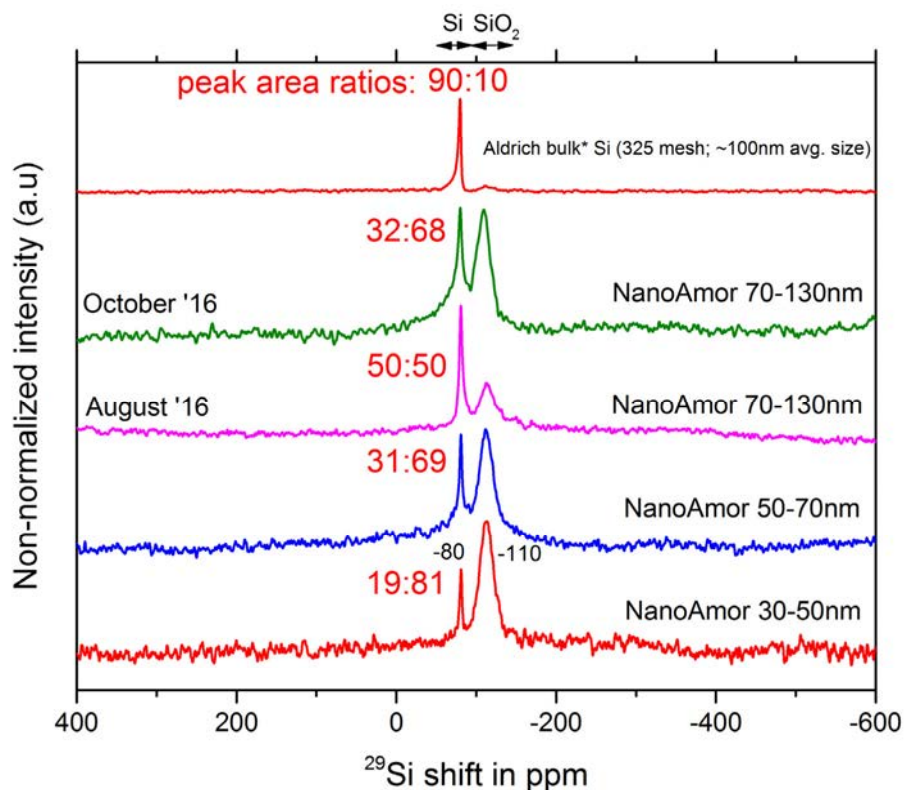


Figure IV-98: <sup>29</sup>Si MAS NMR of various commercial silicon powders

ANL, unpublished work

Figure IV-99 shows multinuclear NMR study of a 15% Si (50-70nm)- 73% Gr (Hitachi MagE Graphite) full cell composite anode with 10% LiPAA binder and 2% Timcal C45 carbon cycled vs. TODA NMC532 cathode in 1.2M LiPF<sub>6</sub> 3:7 EC:EMC Gen2 + 10wt. and then charged to 4.1V at the end of 250 cycles. Direct excitation and 1H-13C cross polarization 13C MAS NMR shows (Figure IV-99a) semi-quantitative representation of carbon containing species present in the sample (excluding graphite and conducting carbon, therefore including only SEI/decomposition species). The majority of the speciation is composed of FEC decomposition, PAA binder, EC (trapped), EMC (trapped) and EC decomposition species. Also some minor ether decomposition has been observed. 1H MAS NMR (Figure IV-99b) confirms the EC trapping and also shows aliphatic decomposition products, due to EC and EMC decomposition. <sup>7</sup>Li MAS NMR (Figure IV-99c) on the other hand, shows little Li<sub>x</sub>Si species (also confirmed by <sup>29</sup>Si MAS NMR, data not shown), but primarily Li in SEI, i.e. Li lost to side reactions based on literature work [7, 8] via the formation of Li-semicarbonates etc., and Li in graphite as LiC<sub>18</sub>, LiC<sub>27</sub>, and LiC<sub>36</sub> phases. Further confirmation of Li loss is observed in <sup>19</sup>F NMR (Figure IV-99d), due to complete consumption of FEC (likely within first cycles) where significant LiF have been observed. It must be noted that the cell had no Si capacity left at the end of extended cycling, which agrees well with Li loss and significant accumulation of degradation species. The amount of trapped electrolyte components is consistent with literature [6, 7] and likely points to increasing tortuosity and buildup of SEI.

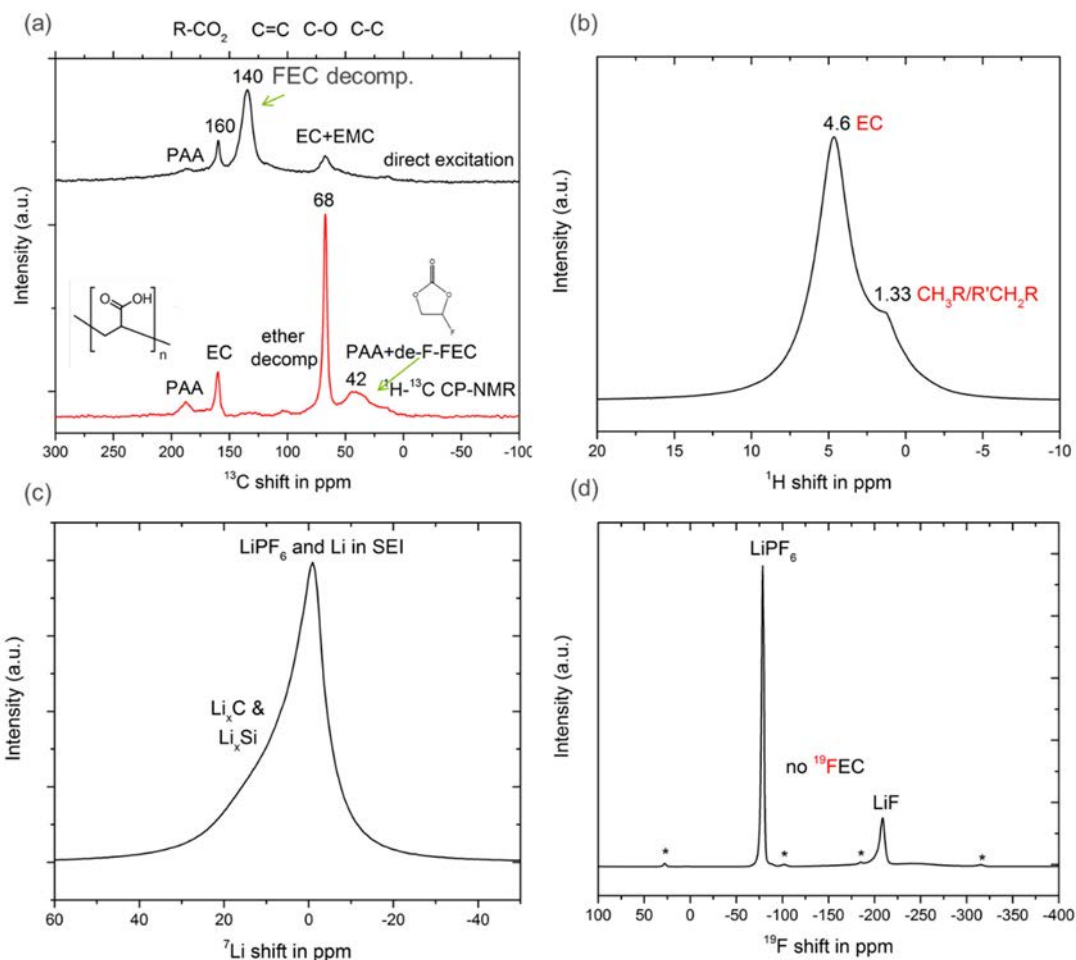


Figure IV-99: (a)  $^{13}\text{C}$  MAS NMR of charged Gr-Si electrode (b)  $^1\text{H}$  MAS NMR of charged Gr-Si electrode (c)  $^7\text{Li}$  MAS NMR of charged Gr-Si electrode (d)  $^{19}\text{F}$  MAS NMR of charged Gr-Si electrode  
ANL, unpublished work

## Advanced Characterization of Silicon/Graphite Composite Electrodes (ORNL)

At ORNL we are employing various multiscale characterization techniques towards understanding factors that determine local lithation-delithiation (alloying) events both inside the nano-silicon (as well as oxides of silicon) and the binder-silicon-carbon interfaces. The techniques include but are not limited to micro-Raman, FT-IR, *in situ* acoustic time of flight (ToF) and X-ray spectroscopy techniques. The overall goal is directed towards understanding the fundamental factors related to capacity loss and degradation associated with silicon composite electrodes cycled in full cell configuration. Electrodes and cells for this study are fabricated at ORNL and ANL.

Figure IV-100 shows the micro-Raman images of 15 wt.% Si-graphite electrodes of pristine as well and 100X cycled electrodes. The electrodes were harvested from Si-graphite-NMC full pouch cells cycled between 3- 4.1 V at C/3 rate after undergoing the formation cycle. The Raman maps show the blue regions as c-Si-rich with carbon black and LiPAA (binder) and red regions are primarily graphite-rich. The pristine electrode has a relatively uniform distribution of graphite and silicon, and silicon is mainly in the crystalline form. The D, G, and 2D bands of graphite appear at  $1356$ ,  $1585$ , and  $2720\text{ cm}^{-1}$ . Crystalline silicon shows a strong, sharp band at  $520\text{ cm}^{-1}$ , whereas amorphous silicon shows several broad, overlapping modes shifted to lower frequency. The most distinct peak for LiPAA binder is at  $2933\text{ cm}^{-1}$ . We observe a large fluorescence background signal from the 100X cycled Si-graphite electrode. The background-subtracted spectra are shown in the bottom panel. The red graphite-rich regions have relatively lower fluorescence signal compared to blue. The cycled Si-electrode shows a-Si rich regions as shown by the broad peaks near  $485\text{ cm}^{-1}$  but interestingly it still has c-Si Raman peak implying the possibility of some Si-regions that did not participate in the electrochemical reaction. There formation of crystalline silicon peak partly could be due to local laser power heating although we performed the experiment at the least possible power. Further Raman studies are underway to map the evolution of silicon-carbon regions at intermediate states of charge and cycle number.

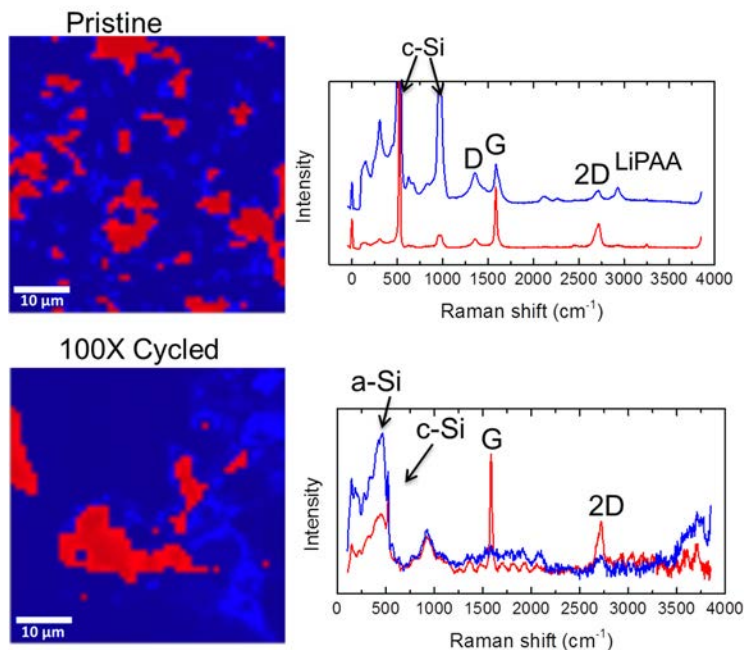


Figure IV-100: Top – Raman images of pristine 15 wt%- Si-graphite electrodes. Bottom: 100X cycled Si-graphite electrodes

Figure IV-101 shows the acoustic time of flight (ToF) signature of a Si-graphite-NMC pouch cell. The goal here is to measure the acoustic signal sensitive to the changes in density and modulus as the silicon composite electrode undergoes changes in its microstructure and density. The transmitted and reflected acoustic ToF maps measured in-operando helps to monitor the changes in microstructure during formation and lithiation (delithiation). Preliminary results (Figure IV-101) shows what appears to be cracking in first “formation” step of cell, consistent with literature on Si Anodes where initial rate is too high (C/5 formation rate). Very low coulombic efficiency is likely due to gas formation which clearly diminishes acoustic signal in 2nd cycle and beyond. The cell stopped functioning after the 1<sup>st</sup> cycle due to overcharging and experiments are in progress to collect data beyond the 1<sup>st</sup> cycle.

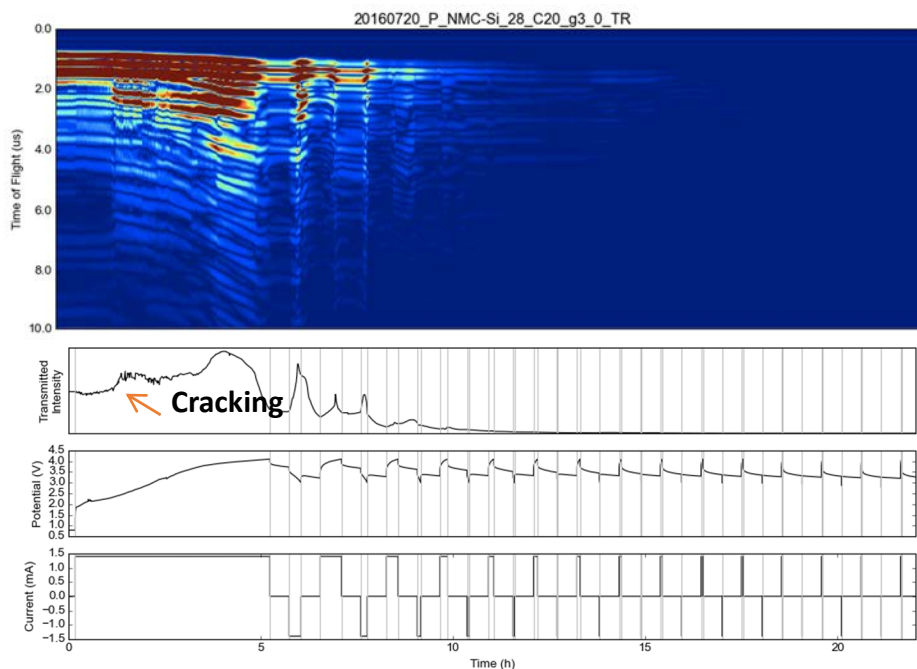


Figure IV-101: In operando Electrochemical Acoustic Time of Flight (EAToF) to monitor lithiation (delithiation) in silicon as a function of SOC (in collaboration with Dan Steingart, Princeton)

## Gas Evolution from Silicon Anodes (ORNL)

One of the challenges of the silicon anode chemistry we have observed is the propensity of the materials to cause extensive gassing. This is evident during cell cycling where pouch cells swell with time. The current hypothesis is that surface hydroxides, originating from the oxide passivation layer, cause acid-base type catalytic decomposition of organic electrolyte. To investigate this effect studies were performed where electrodes were cycled in half-cell type configurations (3-0.05 V vs. Li/Li<sup>+</sup>) in specially constructed electrochemical cells with gas sampling capabilities (Figure IV-102).

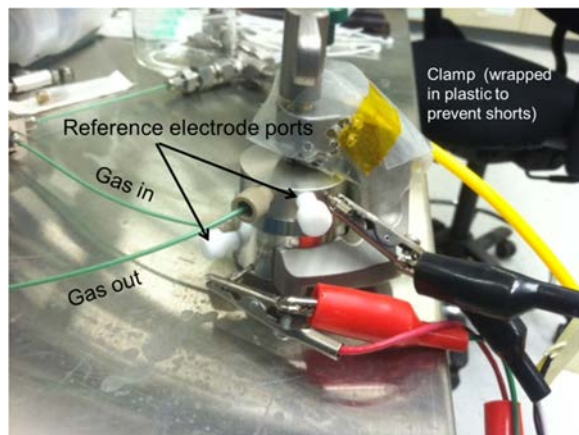


Figure IV-102: Picture of gas cell used in these measurements. Gas enters the cell, flows through the cell and collects evolved gas, and exits the top of the cell where it is analyzed with a mass spectrometer

In these cells 2 mL of He are flown across the electrode to capture the evolved gases. This gas stream is then constantly sampled using an in-line mass spectrometer. In these experiments a 13 mm working electrode obtained from either the CAMP facility or the ORNL BMF were combined with a Li metal anode separated with a glass fiber/celgard 2325 separator stack which was infiltrated with 200  $\mu$ L of GEN 2 electrolyte.

In these measurements, there are several effects going on at the same time. First the DEC in the GEN 2 electrolyte is slightly volatile and contributes a background gas pressure/mass spectrometer signal. The intensity of this signal is related to the evaporation of the DEC, which is assumed to be constant, and the additional signal from the baseline catalytic decomposition of the electrolyte over the electrode surfaces. This effect is highlighted in Figure IV-103 which shows the mass spectrometry data collected for a silicon anode (left), and two different graphite anodes (middle and right). The right plot is a reference for an electrode where there is little to no catalytic decomposition as evident by the low CO and CO<sub>2</sub> signals.

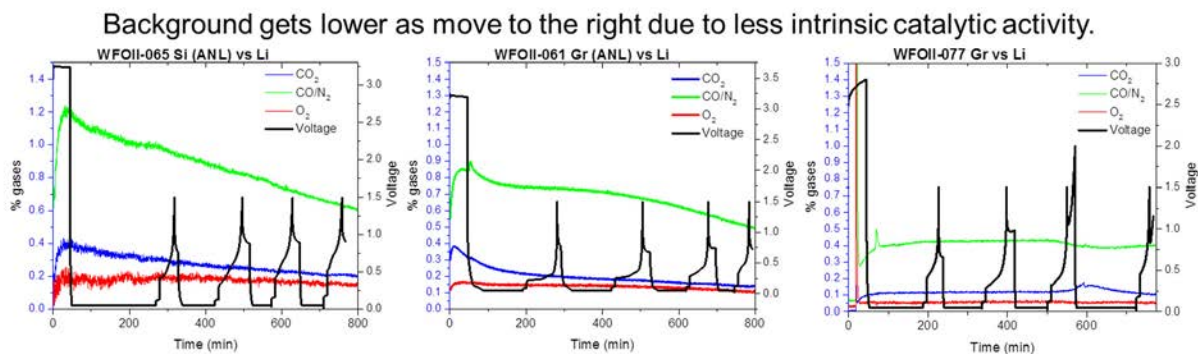


Figure IV-103: Plots show the mass spectrometry data collected as a function of potential for Si vs Li (left); graphite versus Li (middle and right). The higher CO and CO<sub>2</sub> signals from left to right correspond to more intrinsic catalytic decomposition of electrolyte

In comparison the CO and CO<sub>2</sub> signals go up significantly for the other anode materials. This is particularly clear for the silicon anode which has the highest CO and CO<sub>2</sub> background signal recorded. This means that the silicon electrode has a high intrinsic activity towards the decomposition of electrolyte solvent molecules leading to gassing and swelling. Upon cycling there is no evidence for electrochemically promoted

decomposition of the electrolyte as the cell cycles. This is evident by the lack of peaks in the mass spectrometer data with time. In addition there is no evidence for H<sub>2</sub> evolution from this sample which is good from a flammability perspective, Figure IV-104.

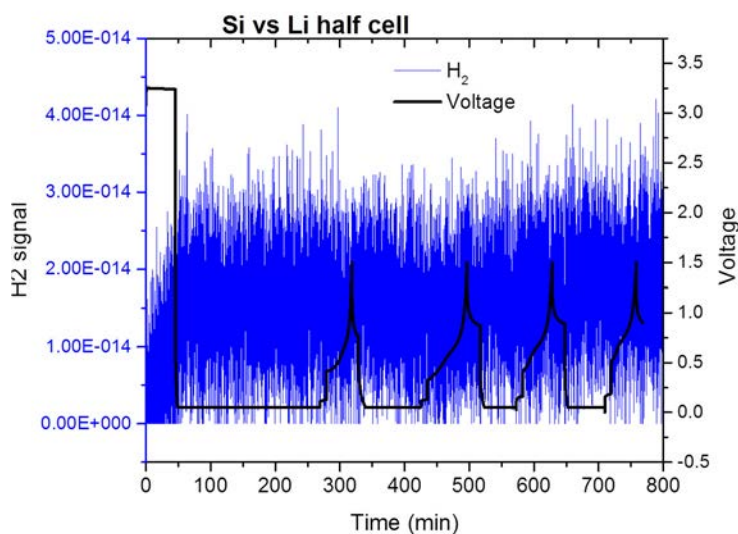


Figure IV-104: H<sub>2</sub> evolution data for silicon electrode during cycling

In other studies, the anode was subjected to a wider cycling window (0.05- 2 V (vs. Li/Li<sup>+</sup>)), Figure IV-103 (right). In this case there was no evidence of an electrochemically promoted decomposition reaction when cycled from (0.05- 1.5 V (vs. Li/Li<sup>+</sup>)). However, with an upper voltage limit of 2 V there is clearly an increase in the CO<sub>2</sub> signal due to electrochemical decomposition of the SEI or solvents. A subsequent cycle to a limit of 1.5 V reveals a much larger discharge capacity than the previous cycles. This indicates the reformation of an SEI layer and that the gas evolved comes from the decomposition of the SEI.

At this point we don't understand all the reactions that are taking place or the mechanisms. Studies are being performed to evaluate the gassing during electrode processing and the surface chemistry of the silicon anode materials. Particular effort will focus on identifying additives or treatment protocols that would prevent the intrinsic decomposition of the electrolyte.

### The Effect of Oxidation on the Electrochemical Performance of Silicon Electrodes (ANL)

When silicon is in contact with air, a native oxide layer of several nanometers will form. The actual thickness of the oxide layer may also vary due to the manufacturing processes and storage history. As the size of the silicon particle becomes smaller, this oxide layer plays a more important role as it takes up a larger volume and weight percentage. It has been reported that the presence of oxide layer harms the initial performance of the silicon anodes in a non-aqueous system [9-11]. However, the effect of the oxide layer on the long term cycling performance of the electrodes has not been well studied. Furthermore, with the current trend going towards water-based laminate making processes due to both electrode performance and economic reasons, the presence of an oxide layer in the silicon electrodes is inevitable. Thus, it is very important to understand how the existence of an oxide layer affects the electrochemical performance of silicon electrodes and furthermore optimize the electrodes based on that understanding.

We investigated the effect of the oxide layer on the electrochemical performance of silicon anodes by growing the oxide layer of Si nanoparticles in a controlled manner. Si particles from Hydro-Quebec with an average size of 80 nm were used. LiPAA and carbon black were used to fabricate the electrodes. Brunauer-Emmett-Teller (BET) surface analysis, transmission electron microscopy as well as Fourier-transform infrared spectroscopy were performed to characterize the silicon nanoparticles. The electrochemical performance of the silicon electrodes of different thicknesses was analyzed and compared.

Figure IV-105a shows a TEM image of the as-received Si nanoparticles. An approximately two nanometer oxide layer is estimated from the oxygen mapping. A more accurate estimation of the thickness of the oxide layer is yet to be determined. In order to oxidize the Si nanoparticles in a controlled manner, the Si

nanoparticles were placed into an air-convection oven for a fixed time period (15 hours) at different temperatures (300°C, 400°C, 500°C, 600°C, and 700°C). The mass change of the particles was recorded after each heat treatment. Figure IV-105b shows the mass change of silicon particles after heat treatment at different temperatures. As the heating temperature increases, the mass change increases in an exponential manner, showing that the oxidation process is kinetically-controlled.

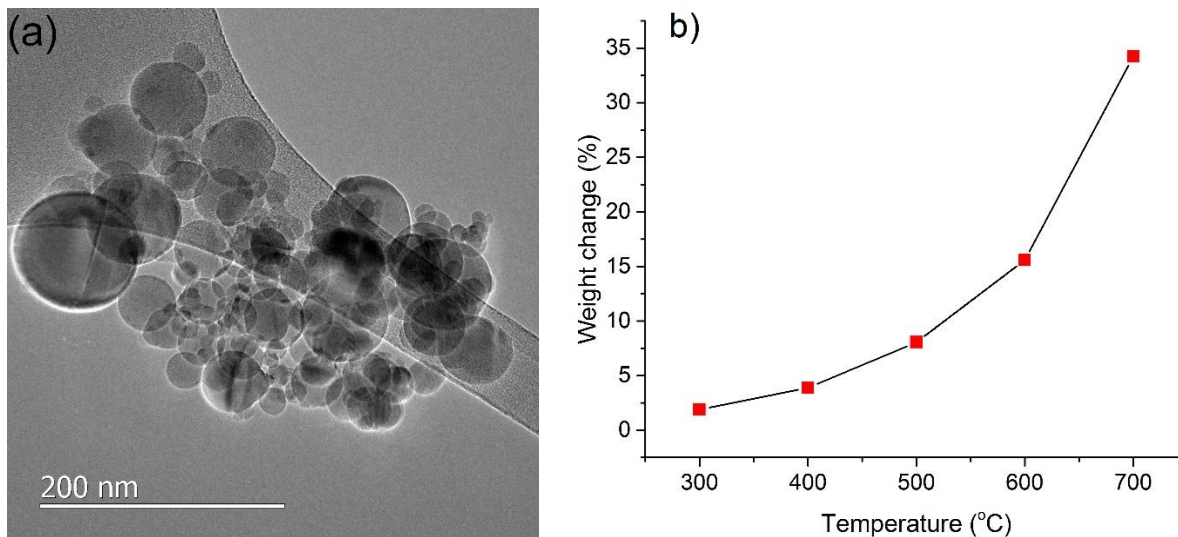


**Figure IV-105: (a) TEM image of the as-received Si nanoparticles (b) Weight change of the Si nanoparticles after heat treatment**

TEM was conducted by Yuzi Liu/Center for Nano-Materials, Argonne National Laboratory

Figure IV-106 compares the electrochemical performance of the initial formation cycles of the Si electrodes after different treatments. Si nanoparticles treated at 700°C did not show any reversible capacity from silicon and is therefore not shown in the figure. Si nanoparticles treated at 500°C and 600°C showed decreased specific capacity and coulombic efficiency compared to the non-treated anode, which is likely due to the significant decrease of the active Si and the parasitic reactions caused by the irreversible reaction between SiO<sub>2</sub> and lithium ions. The Si anodes after 300°C and 400°C heat treatment, however, showed comparable initial specific capacity and coulombic efficiency to the non-treated anode. It is known that the native oxide is not thick enough to prevent the reaction of water with inner silicon core. Therefore, it is likely that the increased oxide thickness resulted from the 300°C and 400°C heat treatment to some extent prevented the reaction between water and the inner silicon core, resulting in an overall thinner oxide layer, thus maintaining good initial specific capacity and coulombic efficiency.

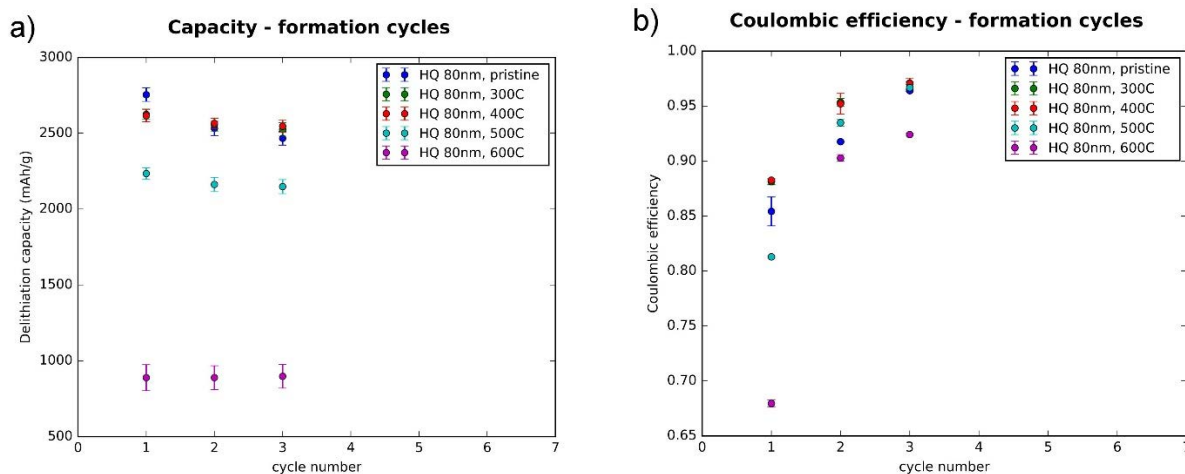


**Figure IV-106: a) Delithiation capacity and b) coulombic efficiency during initial formation cycles of silicon anodes after different treatments**

Since the 400°C-treated Si anode showed comparable initial performance to the non-treated anodes, their cycling performance was further compared. Figure IV-107 shows the cycling performance of the non-treated and 400°C-treated Si anode. After 50 cycles, 400°C-treated Si anode showed an 83.6% capacity retention whereas the non-treated Si anode showed a 61.4% capacity retention. Therefore, a significantly better capacity retention was observed for the 400°C-treated Si anode.

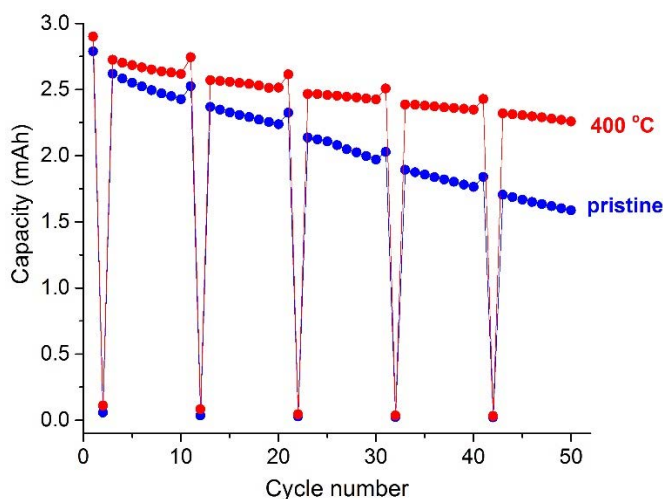


Figure IV-107: Cycling performance of the non-treated and 400 °C-treated Si anodes

### Development of High Energy Metals (LBNL)

Dahn's group identified amorphous Si-Sn films with Sn content lower than 40 mol% as the ideal compositions in thin film batteries, for example,  $\text{Si}_{0.64}\text{Sn}_{0.36}$  showed a large reversible capacity of ~ 1900 mAh/g and low irreversible capacity of ~ 100 mAh/g during the 1<sup>st</sup> cycle [12]. Ahn et al. later confirmed amorphous Si-Sn nanocomposite electrode films produced by magnetron co-sputtering method demonstrated improved cycling performance compared to amorphous Si film at a similar thickness [13]. Sputtered films with phase separated amorphous Si embedded in the Sn matrix also delivered a reversible capacity of 1400 mAh/g with good cycling stability at Si/Sn ratio close to 1 [14]. Attempts to prepare nanocomposites of Si/Sn-based nanoparticles enwrapped in porous carbon nanofibers led to an initial specific capacity of 1347 mAh/g and 1073 mAh/g was retained at the 50<sup>th</sup> cycle [15]. Kwon et al. reported a sophisticated synthesis of carbon-coated  $\text{Si}_{70}\text{Sn}_{30}$ , the composite electrode exhibiting a high reversible capacity of 2032 mAh/g and excellent capacity retention (97% after 60 cycles) [16]. All the previous work showed the promising electrochemical performance within Si-Sn system, it would be interesting to apply a facile and scalable method to capitalize on the large theoretical capacity of Si, high electrical conductivity of Sn, as well as potential improvement in structural stability of the host electrode [17].

The synthesis of Si-Sn nanocomposites was explored via mechanical milling method that is cost-effective, facile, and scalable. Using the base  $\text{Si}_{0.66}\text{Sn}_{0.34}$  composition identified from the previous work [12], we investigated the effect of milling energy and milling time on the phase formation and electrochemical properties. In addition, we introduced the graphite during the synthesis and studied the electrochemistry of Si-Sn-C nanocomposites to alleviate the Sn agglomeration effect that is likely due to its low melting point (232°C) [18].

The synthesis of Si-Sn nanocomposites was first explored on both Retsch planetary and Spex shaker mill. Several representative XRD patterns of Si-Sn nanocomposites are presented in Figure IV-108(a) and (b). Overall, no mechanochemical reaction occurred between Si and Sn due to the immiscibility between Si and Sn. The intensity of the Si diffraction peaks started to decrease even after milling for 3 hours, suggesting Si phase tended to loose crystallinity during the high energy milling process. And Si ultimately became amorphous after milling for an extended period of time. A slight difference in Si crystallinity was observed in the final products when they were prepared by different mills even for the same period of time because the precursors that were subjected to a planetary mill experienced a lower milling energy compared to those using a Spex mill. On the contrary, we observed very little change in Sn, which remained as a high crystalline phase. This phenomenon appeared to be independent of milling energy and milling time. Additionally, Sn phase agglomeration was

observed and it became even more severe at a higher energy and longer milling time. To overcome the Sn agglomeration problem, graphite was introduced during the high energy milling process because it can largely improve the electronic conductivity, and the high surface area of carbon could potentially alleviate the material agglomeration. Meanwhile, milled Si was used as the precursor along with Sn and graphite (15 wt%) in order to minimize the milling time for the preparation of Si-Sn-C nanocomposites. Overall, no agglomeration was noticeable even after the precursors were milled for up to 12 hours. But, it did not bring an appreciable effect on reducing the crystallinity of Sn. The XRD patterns of as-prepared Si-Sn-C nanocomposites were very close, and no pronounced changes were observed with increasing milling time (Figure IV-108 (c)).

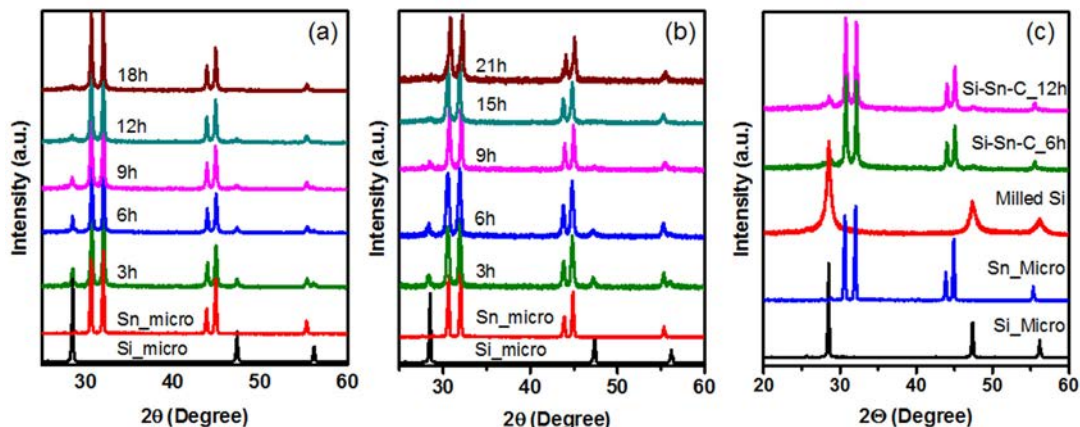


Figure IV-108: X-ray diffraction patterns of (a) Si-Sn nanocomposites by planetary mill, (b) Si-Sn nanocomposites by Spex mill, and (c) Si-Sn-C nanocomposites by Spex mill for designated periods of time

The as-prepared Si-Sn (Spex mill, 15h) and Si-Sn-C (Spex mill, 12h) samples were selected for the electrochemical studies and the performance is presented in Figure IV-109. As shown in Figure IV-109 (a), milled Si (Spex mill, 15h) was tested as a control sample and it delivered an initial capacity of 2270 mAh/g as a result of significantly reduced particle size. Si-Sn nanocomposites delivered an initial reversible capacity of about 650 mAh/g with the 1st cycle coulombic efficiency of 77.8%. Variation in electrode mass and capacity was observed due to the inhomogeneity of the as-prepared sample. Addition of carbon improved the reversible capacity to about 1000 mAh/g and the 1st cycle coulombic efficiency of the as-prepared Si-Sn-C nanocomposites was increased to 80.2%. Meanwhile, milled Si showed a very fast capacity decay even in the early cycles (Figure IV-109 (b, c)) due to the lack of buffering matrix (e.g., carbon) and possible side reactions with electrolyte. The capacity retention of Si-Sn-C nanocomposites was about 80% at Cycle 50, very close to that of Si-Sn nanocomposites. Such improvement could be ascribed to the following positive effects by adding carbon: (1) an increase in electronic conductivity, (2) a minimal loss of electronic contact, and (3) its buffering effect. Additionally, this could be an indication of the mutual buffering effect between Si and Sn as their lithiation/delithiation occurs at slightly different potentials.

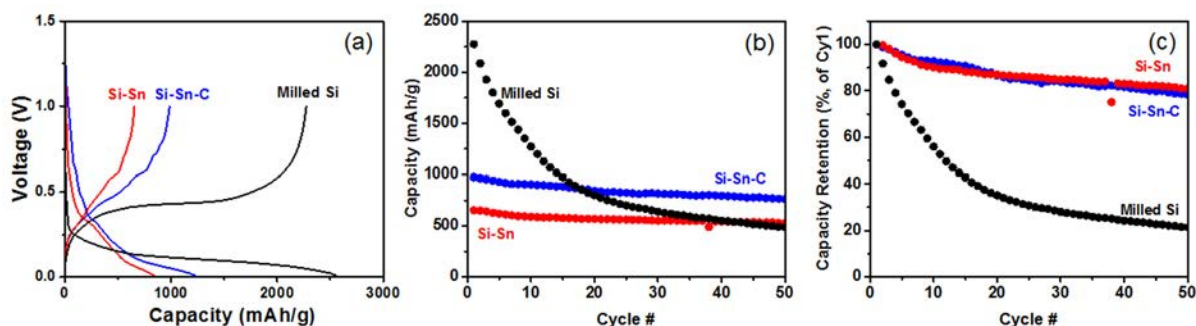


Figure IV-109: (a) Voltage profiles and (b, c) cycling performance of milled Si, Si-Sn, and Si-Sn-C nanocomposites

### Interfacial Modifications: MLD Surface Coatings (NREL)

The overall goal of this project is to develop sustainable high-energy density of Si-based nanocomposite electrodes for use in vehicular applications. In this work, surface modifications, which chemically or physically change the surface of electrode components, has been applied to improve the interphase chemistry,

conductivity, and mechanical integration in Si-based electrodes. It is the nanostructured architecture that greatly increases the overall capacity; however, decreasing the particle size also increases both the surface area and electrolyte-reduction reactions resulting in the formation of solid-electrolyte-interphase (SEI) layer and the associated irreversible loss of Li. Surface modifications on both active particles and laminated electrodes have the capability to modify the solid-electrolyte-interphase (SEI) through the control of composition, thickness and mechanical properties [19, 20]. Unlike other electrode materials, Si particles are covered by an insulating oxide layer, but also suffer from the morphological changes during Li cycling. Therefore, besides the requirement for the chemical stability, a functional coating is required with the control of thickness and mechanical properties. Molecular layer deposition (MLD) will be used to produce a conformal surface coating composed of an elastic aluminum alkoxide polymer with a tunable elastic modulus and chemical reactivity, depending on composition. Based on low-temperature, sequential and self-limiting surface reactions, MLD can also apply to the laminate electrodes, resulting in conformal coatings with atomic-level control of film thickness while maintaining the electrode architecture and inter-particle electronic path.

ALD technique has proven itself to be the *best method to deposit continuous, conformal and pinhole-free films*. Our recent work has proven ALD as an important tool in mitigate the parasitic side reactions between the liquid electrolyte and electrode surface, leading to the improved performance of LIBs electrodes [21]. But the rigid inorganic coatings, such as Al<sub>2</sub>O<sub>3</sub> coating, are not robust enough to provide structural support when applied to large-volume-expansion materials such as Si. In order to address the challenge of Si's dramatic volumetric change, NREL have utilized MLD to grow a mechanically robust, flexible coating as a surface modification for high capacity Si nanocomposite anodes. Based on the similar mechanism of ALD, MLD method allows for the integrating the organic fragments into metal oxide matrix, leading to the formation of hybrid organic-inorganic materials. The thin, conformal, and flexible MLD coating is able to penetrate the electrode's porous structure and covalently bind to available surfaces. This creates a strong, flexible network within the electrode that binds the materials and ensures sufficient contact area throughout cycling.

### **Molecular Layer Deposition**

Alumium alkoxide (AIGL) films were grown directly on the laminated electrodes using trimethylaluminum and glycerol precursors at 150°C. The typical growth rate for the AIGL chemistry is 2.5 Å per cycle. The AIGL reaction sequence was: i) Dose trimethylaluminum for 2 seconds, ii) hold trimethylaluminum pressure static for 90 seconds, iii) flow purge for 180 seconds, iv) 5 cycles of argon static purge, v) dose glycerol for 2 seconds, vi) hold glycerol pressure static for 120 seconds, vii) flow purge for 240 seconds, viii) 7 cycles of argon static purge. Flow purge is performed by pumping out excess precursors and reaction byproducts while flowing argon through the reactor. Argon static purge is performed by dosing argon for 20 seconds, holding argon pressure static for 5 seconds, pumping for 45 seconds, and flow purging for 20 seconds. This sequence constitutes of one AB cycle of AIGL. The electrodes were coated with 10 cycles of AIGL.

### **Preparation of electrodes and coin cells**

Standard types of 2032 half coin cells with Li metal foil as counter electrodes were prepared for these experiments. The anode mixture was composed of Si, carbon black and Polyvinylidene fluoride (pvdf) binder with a wt % ratio of 60%-20%-20%, and mixed with a 1-methyl-2-pyrrolidinone (NMP) solution. The mixture was coated on Cu foil and then dried under air. Before assembling the cells the 1.4 cm punched electrodes were dried overnight (120°C) in a vacuum oven. 1.5 M LiPF<sub>6</sub> in ethylene carbonate, diethyl carbonate and fluoroethylene carbonate (5:70:25) was used as the electrolyte. Cells were assembled in an Ar filled glove box and tested at room temperature. Constant current (CC) is applied during discharge and charge between the voltage range of 0.01 V and 1.0 V. Electrochemical measurements were carried out using an Arbin<sup>TM</sup> 2000 battery test station.

### **Electrochemical performance of the MLD coated Si-Graphite-LiPAA electrodes and Si-C-CMC electrodes**

The Si-Gra.-PAA electrodes provided by ANL is composed of 73 wt% graphite, 15 wt% Si (Nano and Amor, 50-70nm), 10 wt% lithiated poly acrylic acid (LiPAA) and 2 wt% Timcal C45. The electrodes have been coated with ~2 nm MLD AIGL film and ~1nm ALD Al<sub>2</sub>O<sub>3</sub> film. Based on the electrochemical cycling data, there is no major difference between the as-received electrode and the coated electrodes, except for the improved CE for the coated electrodes, as shown in Figure IV-110. The MLD coating has been also applied to the electrodes made with the carboxymethyl cellulose binder. Interestingly, the MLD coating has no major

impact on the performance. In both cases, PAA and CMC have been considered as a surface modifier, which greatly enhance the binding strength between the active materials and the conductive matrix. We believe that the polymer binders have covered the surface of Si particles in both electrodes, thereby, blocking the MLD coating directly on the surface of active materials. In contrast to the cycling performance of the coated Si-Gra-PAA and Si-C-CMC electrodes, significant improvements have been achieved in the MLD coated Si-C-PVDF electrode (made with polyvinylidene difluoride). Due to the weak interaction between PVDF binder and Si active particles, the MLD coating can reach the surface of Si particles and result in forming MLD coating on the Si active materials.

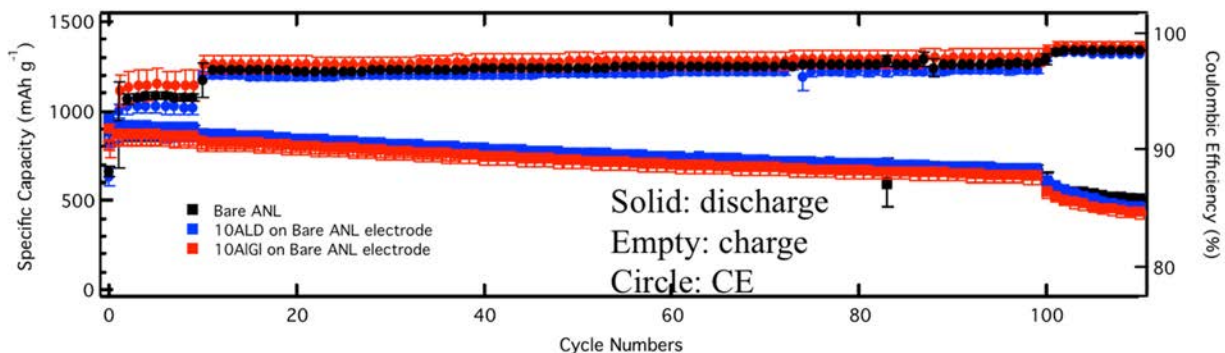


Figure IV-110: Specific capacity of uncoated and ALD/MLD coated Si-Gra-PAA electrodes (provided by ANL) versus cycle numbers. Specific charge (delithiation) capacity was considered for the comparison. Multiple cells have been tested in each condition to confirm the electrochemical cycling performance and presented here using the error bar

### Electrode thickness effects on the electrochemical performance of Si-C-PVDF electrodes

Previous work has demonstrated the success in utilizing MLD to grow mechanically robust and flexible surface coatings to address the challenges associated with Si's dramatic volume changes [22-24]. The presence of MLD coating on the electrodes increases the mechanical properties such as elastic modulus and hardness, which makes electrode robust and resistant to volume changes. In this work, Si electrodes with 3 different mass loading were prepared and represented as  $\tau 1$ ,  $\tau 2$  and  $\tau 3$ , respectively. FEC has been used as an electrolyte additive to enhance the cyclability. PVDF was used as a baseline binder for this study, while new functional polymeric binders are still under development within the program. Although aqueous binders such as CMC and LiPAA show some improvement in cycling performance, however, the aqueous binders also introduce extra oxidation for silicon particles during process. Silicon particles purchased from Alfa chemicals were used for this study, while other Si particles (e.g. Si particles from NanoAmor) are under investigation. All of the cells were tested in a half-cell configuration by using Si nanoparticles (Alfa)-carbon black(C)-PVDF electrodes as the work electrode and lithium metal as the counter electrode. Details of specification of the each electrode can be found in Table IV-11.

Table IV-11: Detail Specification of Electrodes

Electrodes	Composition	Mass of Si (mg cm <sup>-2</sup> )	Thickness (μm)
$\tau 1$	Si (alfa 50nm) 60 wt%, Super P 20 wt%, PVDF 20 wt%	0.35	12
$\tau 2$	Same as above	0.60	17
$\tau 3$	Same as above	0.79	25

Figure IV-111 presents the cross-sectional scanning electron microscopy (SEM) images prepared by using focused ion beam (FIB) operation and energy dispersive x-ray spectroscopy (EDS) line scanning of AIGL-MLD coated  $\tau 1$ ,  $\tau 2$  and  $\tau 3$  electrodes. Pt was deposited on the electrodes during FIB operation to protect the electrode surface from Ga<sup>+</sup> ion. As shown in Figure IV-111, Al signal, which only can be achieved from AIGL, is detected along the whole electrodes. Even for the thicker electrode ( $\tau 3$ ), the vapor precursors for

AIGL-MLD coating can penetrate the electrodes reaching to the bottom of the electrode, leading to MLD coating for the whole electrode. It further confirms the capability of MLD coating technique for surface modification of 3-D tortuous architecture.

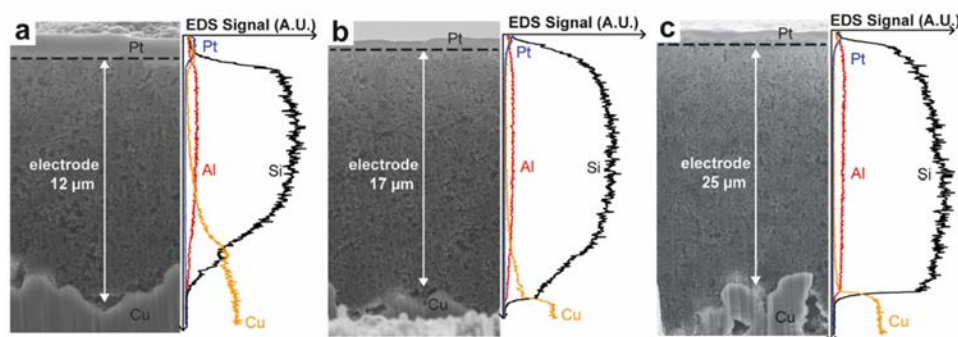


Figure IV-111: Cross-sectional SEM observation on MLD coated electrodes with EDS line scanning. (a) AIGL-MLD coating on  $\tau$  1 electrode. (b) AIGL-MLD coating on  $\tau$  2 electrode. (c) AIGL-MLD coating on  $\tau$  3 electrode

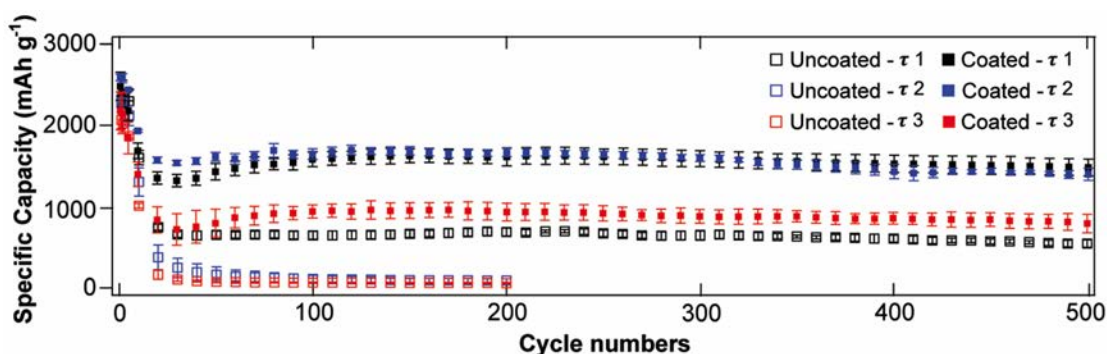


Figure IV-112: Specific capacity of uncoated and MLD coated electrodes (Si-C-PVDF, fabricated at NREL) versus cycle numbers. Specific charge (delithiation) capacity was considered for the comparison. Multiple cells have been tested in each condition to confirm the electrochemical cycling performance and plotted here by using the error bar

Electrochemical performances of Si-C-PVDF are remarkably improved by using MLD coating. In order to ensure the reproducibility of the electrochemical data, multiple cells have been tested for each electrochemical cycling condition. Therefore, all of electrochemical data include error bar for each condition. Both MLD coated thin and thick electrodes have shown highly reversible capacity for over 500 cycles, as shown in Figure IV-112. As expected, uncoated electrodes shows rapid capacity fade in its early cycles except for  $\tau$  1 thin electrode. For the thin electrode, the FEC additive has shown the great impact to stabilize the electrode, thereby leading to stable cycling performance. But the uncoated  $\tau$  1 electrode only delivers a specific capacity of  $\sim 550 \text{ mAh g}^{-1}$ . With AIGL-MLD coating, the remarkable improvement of cycling performances has been achieved for the coated electrodes. The coated electrode in  $\tau$  1 thickness delivers specific capacity of  $1,490 \text{ mAh g}^{-1}$  at 500 cycles that is much higher than the uncoated  $\tau$  1 electrode ( $\sim 550 \text{ mAh g}^{-1}$ ). Uncoated  $\tau$  2 and  $\tau$  3 electrodes lost all of capacity in the first couple cycles. In contrast, the coated  $\tau$  2 electrode delivers specific capacity of  $1,410 \text{ mAh g}^{-1}$  at 500 cycles. The coated  $\tau$  3 delivers specific capacity of  $810 \text{ mAh g}^{-1}$  at 500 cycles. Amount of Si particles utilized in electrochemical reaction is much lower for the  $\tau$  3 electrode than others. Simply, high areal capacity can be achieved by the combination of high specific capacity and mass loading. Not surprisingly all the uncoated electrodes deliver negligible amount of areal capacity during cycling. It is obvious that MLD coating has greatly increased the areal capacity of the electrodes. Although AIGL-MLD coating can accommodate the volume changes and stabilize the surface of silicon particles, using the PVDF binder limit the use of the high-mass-loading electrodes. Basically, PVDF fails to maintain the conductive matrix in the high-mass-loading Si electrodes. Considering the great improvement by using AIGL-MLD coating, we are working on other binder materials within the team to improve the performance for the thicker electrodes.

### Impact of MLD coating on the Mechanical properties of Si-C-PVDF electrodes.

Mechanical failure of Si-based electrodes caused by large volumetric changes is one of major reasons for fast capacity decay of Si-based electrodes. Here, nano-indentation and scratch tests have been used to investigate the effect of MLD coatings on mechanical properties of Si electrodes. 10 trimethyl aluminum-glycerol (AIGL) MLD cycles, which form the AIGL coating with a thickness of ~2.5nm, have been used to coat the electrodes in this work. Both elastic modulus and hardness increase in the MLD coated electrodes, as shown in Figure IV-113a. To be more comprehensible, we introduced the ratio of hardness to elastic modulus ( $H/E$ ). Higher  $H/E$  values results in higher elastic deformation than plastic deformation under loading. Figure IV-113b shows increased  $H/E$  values for the AIGL-coated electrodes. The elastic deformation enabled by MLD coating better accommodates the large volume changes during repeated lithiation and delithiation, which ensures the sustainable cycling performance for the coated electrodes.

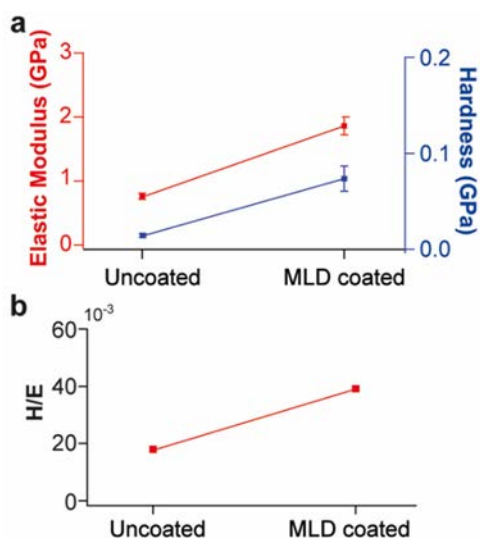


Figure IV-113: (a) Elastic modulus and hardness of uncoated and MLD coated electrodes. (b) The ratio of  $H/E$  of uncoated and MLD coated electrodes

Scratch tests have been further performed on both uncoated and coated electrodes to investigate the integrity of electrode and the adhesion of electrode to the Cu current collector. Maximum load of 50 mN was applied with the loading rate of 0.4 mN S<sup>-1</sup>. The optical images after scratch tests for both uncoated and MLD coated electrodes are shown in Figure IV-114a-d. Arrows in the optical images indicate the scratch directions. Delamination from Cu current collector is only observed in the uncoated electrode at the scratch distance 900 to 1,050  $\mu\text{m}$ . MLD coated electrodes do not show any delamination from the Cu current collector along the scratch test. Figure IV-114e exhibits the scratch depth profiles versus scratch distances. The uncoated electrode shows the higher scratch depth, as compared to the MLD coated electrode. It indicates that the MLD coating has greatly improved the adhesion among particles and to the Cu current collector.

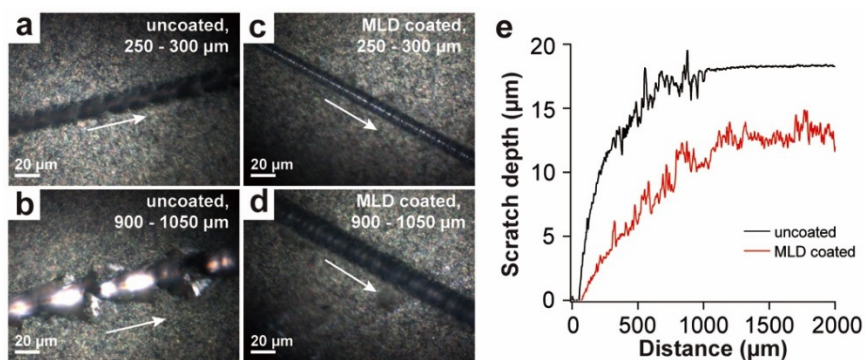


Figure IV-114: Optical image of scratch test for (a) bare electrode from 250 - 300  $\mu\text{m}$ ; (b) bare electrode from 900 - 1,050  $\mu\text{m}$ ; (c) MLD coated electrode from 250 - 300  $\mu\text{m}$ ; (d) MLD coated electrode from 900 - 1,050  $\mu\text{m}$ . (e) Depth profiles of uncoated and MLD coated electrodes versus scratch distance

## Interfacial Modification of Si Anode – Electrochemical/Chemical Approach through Electrolyte/Additive (ANL)

The chemical and electrochemical reaction of the lithiated silicon with the organic electrolyte plays a significant role in the electrochemical performance of the silicon anode. The non-volatile reaction products deposited on the surface of the silicon particle form the so-called SEI. The exclusively  $\text{Li}^+$ -conductive SEI layer prevents the further chemical/electrochemical reaction with electrolyte and enables the reversible lithiation and delithiation operation of lithium-ion battery with Si anode. However, this process is irreversible and consumes cyclable lithium-ions from the positive electrode leading to the huge initial capacity loss and low Coulombic efficiency. The instability of this SEI results in continuous reaction and thus consumption of active lithium cycle by cycle leading to rapid capacity loss.

The objective of this electrolyte research is to fundamentally understand the SEI formation mechanism and how the electrolyte reactivity and the chemical composition impact the SEI and electrochemical performance of the Si anode to shed deep insight for electrolyte design and synthesis capable of effective passivation through formation of the chemically and mechanically stable SEI layer to afford far extended cycle life.

The reactivity and the nature of the decomposition products are closely related to the surface area per unit mass, particle size, and morphology of the Si anode, which dictates the cycle and calendar life of Si anode, therefore, model silicon electrode was used early stage of the project.

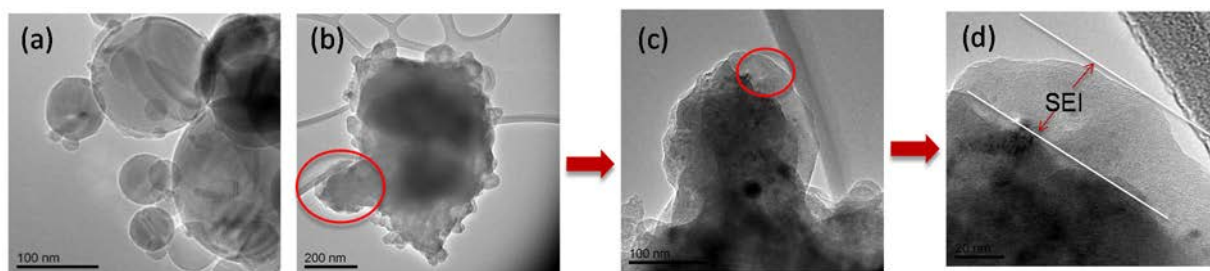


Figure IV-115: TEM images of (a) pristine silicon particles, (b) silicon particle after 1<sup>st</sup> formation (at delithiation state), (c, d) expanded surface area of the cycled silicon particle

Figure IV-115 shows the bright-field TEM images of the pristine (Figure IV-115a) and cycled Si nanospheres. Anisotropic expansion of the Si spheres (Figure IV-115b) and phase transition (Figure IV-115c, Figure IV-115d) from the surface to the bulk were observed. The striking feature from the images is the contrast between the darker cores and the lighter shell (Figure IV-115d) of the particle at the end of the initial lithiation process. Organic-dominated SEI surface layer was confirmed since the lighter elements scatter incident electrons less effectively, leading to brighter regions in the bright-field TEM images. SEI formation for the SOA electrolyte (Carbonate+10% FEC) was also confirmed by the  $dQ/dV$  profiles provided in Figure IV-116. FEC molecule reduces on the surface of medium lithiated silicon particle ( $\sim 0.95$  V vs  $\text{Li}^+/\text{Li}$ ) (Figure IV-116b) in contrast for LiBOB, which reduces at much shallow lithiation degree (Figure IV-116c). It is not clear how the reduction potential of the additives will impact the SEI morphology and structure, but how the additive decomposes and the nature of the final products dictates the property of the SEI. FEC proceeds reductive decomposition generating inorganic lithium fluoride (LiF) and initial radical anions in the inner layer of the SEI. The organic radical anions went through additional 2e-reduction process leading to the polymerized species with itself and/or adjacent solvent molecules. The proposed 2e reduction and additional 2e-decomposition pathway was proposed for FEC as shown in Figure IV-116d.

The non-passivating feature of FEC additive was evidenced by the designed *in situ* electrochemical impedance spectroscopy (EIS) experiment. During the repeated electrochemical lithiation/delithiation process (Figure IV-117a), EIS was recorded (Figure IV-117b) and the interfacial impedance data was extracted and plotted in Figure IV-117c. Clearly, the interfacial impedance fluctuates with lithiation and delithiation process indicating the reactive nature of the electrolyte/additives with various lithiation depth of Si. For three studied cells, SOA electrolyte without additive (Figure IV-117a) showed huge impedance at every stage compared with the additive cells. Silazane additive cell showed the mostly desired impedance evolution with lithiation as indicated in Figure IV-117c. For this cell, the SEI is relatively stabilized after the 2<sup>nd</sup> cycle and the impedance value is minimized and maintained at a very low level.

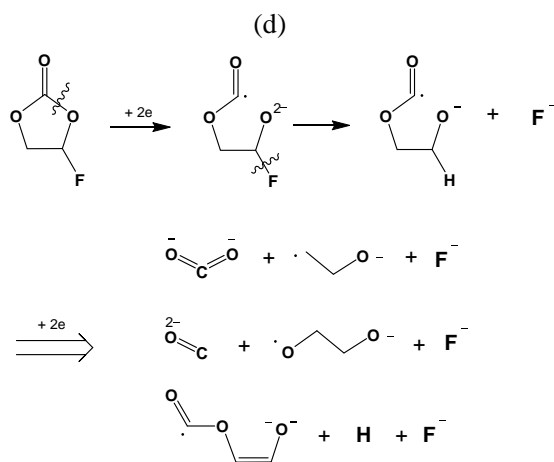
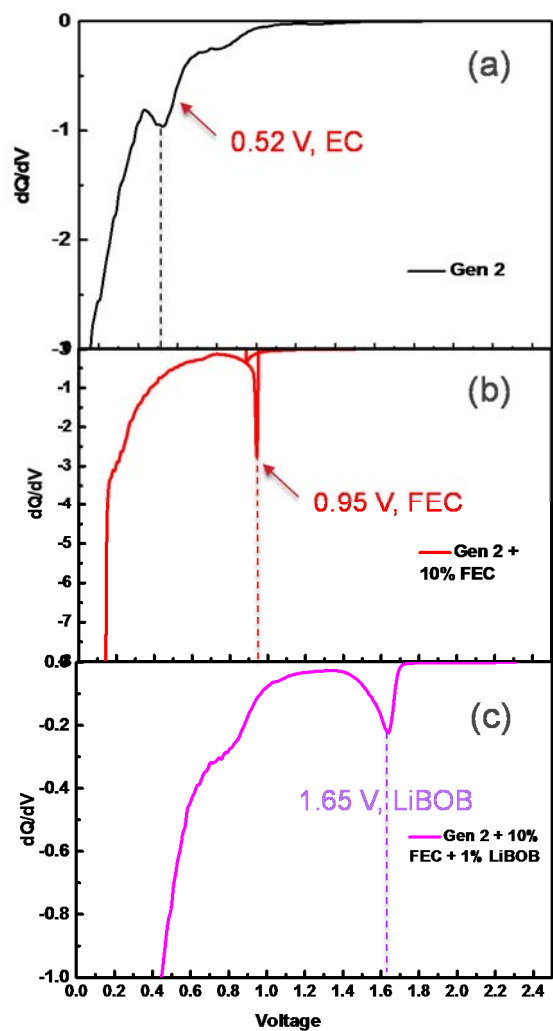


Figure IV-116: Differential capacity/voltage profiles (dQ/dV) of SOA electrolyte containing (a) no additive, (b) 10% FEC additive and (c) 2% LiBOB, and (d) proposed reductive decomposition pathway for FEC additive forming LiF-rich SEI

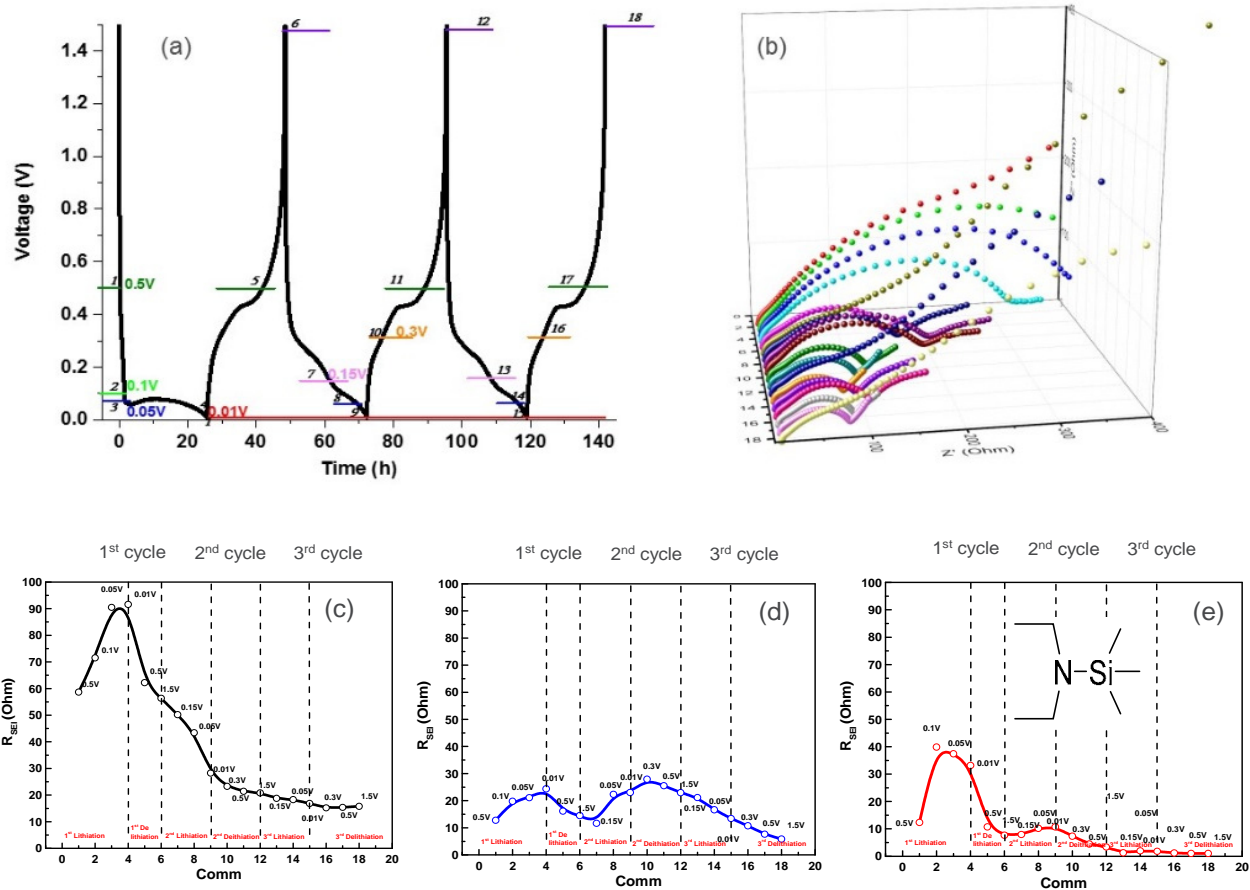


Figure IV-117: (a) Initial lithiation and delithiation voltage profiles of Si/Li half cells, (b) impedance spectra measured *in situ* during the lithiation/delithiation process, and extracted SEI interfacial impedance and its evolution with cycling with (c) no additive, (d) 10% FEC additive, (e) 10% FEC + 2% Silazane additive. (SOA electrolyte is 1.2 M LiPF<sub>6</sub> EC/EMC with 3/7 weight ratio.)

The impact of the stable SEI formed by the mixture additive FEC + Silazane was demonstrated by the extended charge/discharge cycling stability of the Si-C/Li cells. Figure IV-118a and b showed the capacity retention and coulombic efficiency profiles of the two studied additives hexamethyldisilazane (Figure IV-118a) and 1,1,1-trimethyl-2,2-diethylsilazane (Figure IV-118b).

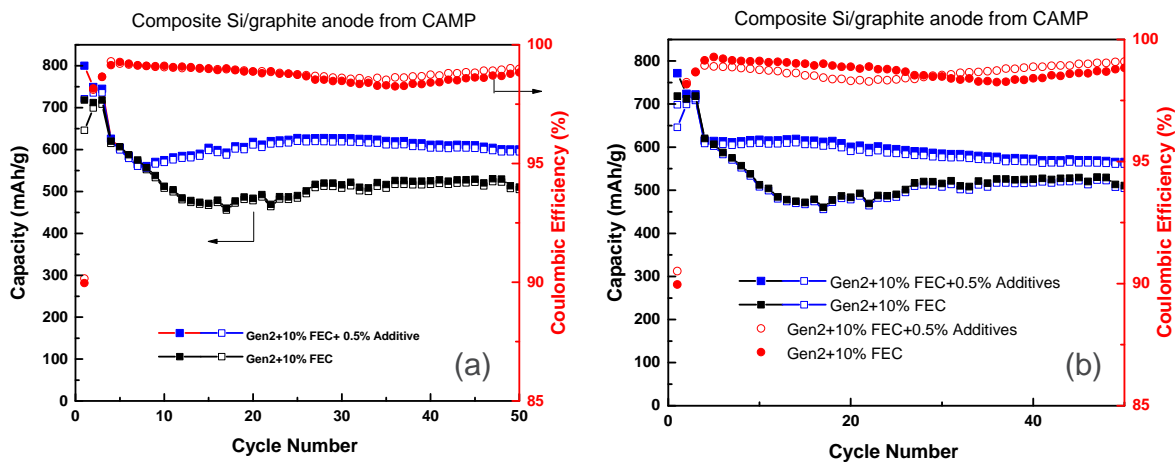


Figure IV-118: Capacity retention of Si-C composite anode half cells with silazane+FEC mixture additive. (a) Hexamethyldisilazane+10% FEC and (b) 1,1,1-trimethyl-2,2-diethylsilazane+10% FEC

Future research plan is to use synchrotron radiation based X-ray photoelectron spectroscopy with various photo energies for depth profiling to understand the synergistic effect of the mixture additive, including the chemical composition of the SEI at different depth and other *in situ* techniques (AFM, TEM) to investigate the robustness of the SEI and surface morphology formed by the mixture additive.

### Exploring Lithium Inventory Strategies (ANL)

Silicon containing anodes employed in lithium-ion cells are known to drastically boost the energy density of a full lithium-ion battery by providing a high intrinsic capacity via  $\text{Li}_x\text{Si}$  intermetallic alloy formation/utilization compared to capacity-limited graphite anodes. However, because a greater than 300% volume change occurs between (de)lithiated  $\text{Li}_x\text{Si}$  states, an irreversible trapping of cyclable Li in the full cell negatively impacts performance, potentially by lowering cycle life. Therefore, lithium inventory control and stabilization is an issue with silicon containing lithium-ion cells. Si/graphite blended electrodes require careful cell-capacity balancing to begin to enable the technology. Typically this requires much thicker (and heavier) cathodes to account for first cycle irreversible capacity losses (ICL). Also, because of electrode voltage slippage, where different portions of the positive and negative electrodes SOC are altered that leads to capacity limitation is a problem. The usable capacity begins to shrink in the cell, and eventually Li-trapping in the Si material wins out, and lifetime is exhausted.

New lithium inventory strategies are being explored to enable new high-energy Si-containing lithium-ion full cell systems with NMC cathodes by supplementing the lithium content in the cell from the cathode side via co-blending NMC powder with the anti-fluorite compound,  $\text{Li}_5\text{FeO}_4$  (LFO) that contains a tremendously high gravimetric capacity. This material is thus designed to firstly eliminate much of the ICL on the first cycle. As a consequence less cathode material is required for cell balancing, and a lighter electrode is possible. For example, in a Li/LFO half-cell, we observe a huge gravimetric capacity on the first charge (Figure IV-119, [25]). The LFO can release upwards of 730 mAh/g useable capacity on this sacrificial first charge, without increasing the impedance of the overall cathode. Note the LFO on discharge is electrochemically inactive above 2.5 V (vs Li metal), and thus will not contribute reversible capacity in a typical Si/C/NMC(LFO) cell cycled in a voltage range above about 2.5 V. If the testing protocol is optimized for full cells, then the LFO may also provide small aliquots of Li during long-term cycling in Si cells that spares NMC from overcharge, and also slows down electrode slippage.

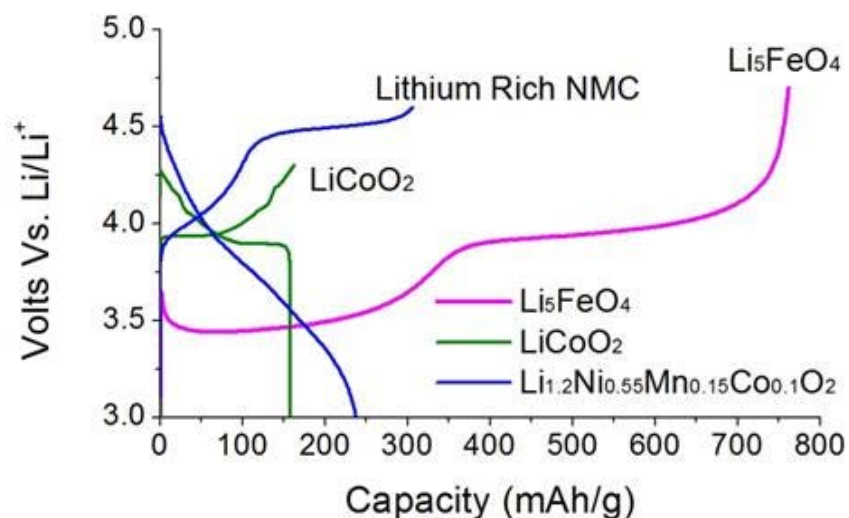


**Figure IV-119: Voltage profiles of various cathode materials**

*Li<sub>5</sub>FeO<sub>4</sub> LFO is shown in voltage profiles against common active material cathodes of LCO and LMR-NMC. Note the large capacity of LFO on first charge, and the proper voltage of electrochemical oxidation which will serve its purpose of lithium inventory control as pre-lithiation cathode additive.*

While the addition of LFO to the cathode should be ideal as a lithium inventory strategy for silicon containing anodes, there are a number of lithium-ion battery technologies where this concept can be applied. As an initial proof-of-concept LFO was added to an LCO cathode paired with a hard carbon (HC) anode. HC is known to have a higher ICL than graphite, but is not plagued with the stability issues of silicon. The HC//LCO(LFO) cell study is part of an integrated effort with the CAMP facility and MERF. The MERF was able to provide a

larger batch size of the LFO to enable a number of studies. The electrochemical results are detailed in section IV.B.2 (Materials Benchmarking Activities for CAMP Facility) of this annual report. In brief, the sacrificial Li provided by the LFO on the first charge is clearly visible and the effective capacity of the LCO is significantly improved by the addition of the LFO, with no new obvious signs of degradation.

With the success of the HC//LCO(LFO) cell studies, half-cell blended NMC(LFO) were initiated. The goal of the NMC532(LFO) half-cells studies is to show that the LFO, blended at 4.5 wt.% does not adversely affect the NMC532 cycle life, voltage profile, discharge capacity and electrode impedance. Figure IV-120 shows the first charge-discharge profile between 4.5 to 3.0 V vs. Li. Note that the black curve is with LFO and the blue curve is without LFO. It can be seen that (1) the black hump at 4.02 V (roughly) is due to LFO electrochemical activity, and (2) the discharge curves with and without (blue) LFO lie on top of each other, indicating no real change in discharge behavior for NMC532 with LFO addition. We are currently assessing the initial coulombic efficiency data as a function of content of LFO blended into the NMC532. Table IV-12 shows a few different cells (4.5%LFO/95.5%NMC532) that were made with different protocols (heat-treated, vacuum-dried, etc.) and at different times.

**Table IV-12: Capacities and Initial Coulombic Efficiencies of 4.5%LFO/95.5%NMC532 Cells**

Sample	Specific Charge capacity (mAh/g)	Specific Discharge capacity (mAh/g)	Columbic efficiency
Sx457	231.4	184.7	79.8%
Sx458	236.9	186.8	78.8%
Sx459	232.3	184.7	79.5%

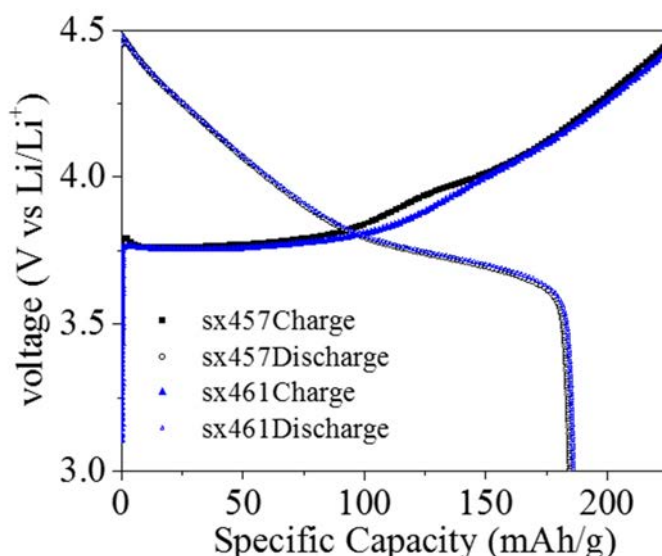


**Figure IV-120: Charge-discharge voltage profile plot**

*Initial charge-discharge voltage profile comparing LFO (4.5%) NMC 532 (95.5%) blend (black) and non-blended NMC532 only cell (in blue).*

Table IV-12 gives the specific charge capacity (1st cycle), specific discharge capacity (1st cycle), and the coulombic efficiency. Since we have 4.5% LFO, we calculate an initial charge capacity associated with LFO as 33 mAh/g (theoretical). NMC532 is expected to be about 197 mAh/g (1st charge to 4.5). Consequently summation to observed ~ 235 mAh/g capacity is self-consistent, and we identify LFO as being electrochemically active in LFO/NMC532 co-physical blend. In addition it doesn't seem to affect adversely the behavior of NMC532 in the cell. In Figure IV-121, we show the rate capability which is extremely similar for cells with and without LFO addition. The SX462 cell is the one without the LFO addition (again 4.5% wt.). Thus the capacity is slightly higher since LFO after first charge is not electrochemically active on discharge above about 2.3 V [25].

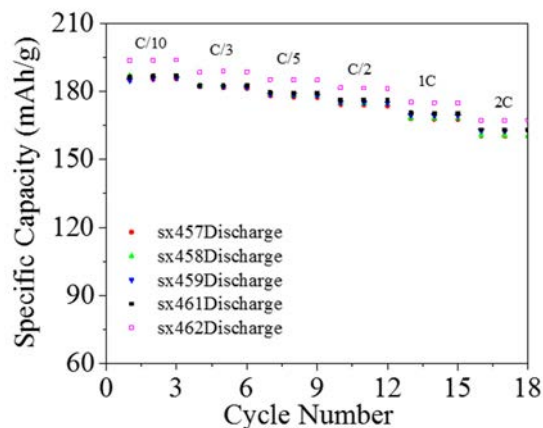


**Figure IV-121: C rates with cycle number plot**

Rate capability test of various LFO/NMC532 cells (4.5/95.5), and one non-LFO blended NMC532 cell – SX462.

### Polymer Binder for Silicon Anode (ANL, LBNL, and ORNL)

A critical issue for Si anodes mainly stems from the loss of electrode integrity and excessive side reactions caused by severe pulverization of Si particles during lithiation and delithiation. In parallel to the effort in developing Si-based anode materials for practical applications, equally important is identifying an effective polymer binder that can ensure the mechanical integrity of the bulk electrode during extended charge-discharge cycles. A variety of functional polymers have been studied as Si binders. However, the research is scattered and no systematic study of how the critical characteristics of a polymer including molecular weight, molecular weight distribution, adhesion, polymer topology, and ionic/electronic conduction impact the property and cell performance of the Si anode.

This joint effort from ANL, LBNL, and ORNL benefits from a diversity of expertise in polymer science that leads to several parallel approaches to investigate the fundamental sciences dictating the binder properties including polymer molecular weight, molecular weight distribution, adhesion, polymer topology and ionic/electronic conduction. Meanwhile, new binder design and synthesis will be pursued based on the fundamental understanding of the binder chemistry. Our final goal is to develop a practically deployable polymer binder system for the Si anode.

To facilitate the binder research, siloxane-based (Si-O-Si) and acrylate-based ( $\text{CH}_2=\text{CH}(\text{CH}_3)\text{-COR}$ ) polymer backbones or side chains were selected as platforms to study the impact of the substituents, the architecture of the copolymer, phase separation, molecular weight and the chemical/electrochemical stability in contact with lithiated silicon. 3D-network-forming polymer binders with strong adhesion to silicon particle and current collector will be synthesized to maintain the electrode integrity affording the extended cycling performance of Si anode.

### Molecular Weight Optimization for PAA Binder

The molecular weight is one of the most important factors that can impact the binder property. It is of practical interest and fundamental importance to understand how the molecular weight of polymer binders will affect the electrochemical performance of silicon anode. Five commercially available PAA polymers were purchased and their molecular weight was characterized by gel permeation chromatography (GPC) after methylation reaction with trimethylsilyldiazomethane. Narrow-dispersed polystyrene standards were used to calibrate the system and the data were processed using Cirrus GPC/SEC software. Table IV-13 listed the molecular weight as well as polydispersity index (PDI) values for five PAA polymers.

**Table IV-13: Molecular Weight Data of PAA Polymers Characterized by GPC**

Entry	Vendor	Mn	Mw	Mv	PDI
PAA-1	Aldrich	175.1 K	851.7 K	702.4 K	4.86
PAA-2	Aldrich	43.1 K	147.7 K	125.6 K	3.43
PAA-3	Aldrich	199.4 K	1151.8 K	937.8 K	5.78
PAA-4	Polysciences	29.1 K	90.6 K	78.3 K	3.11
PAA-5	Acros	3.6 K	6.8 K	6.2 K	1.89

To facilitate the slurry preparation process, all PAAs were titrated by LiOH aqueous solution to a final pH of 6-7 before making lamination. The electrode comprises of Hitachi MagE (73%), Si nanoparticles (70-130 nm, 15%), Timcal C45 (2%) and lithiated PAA (10%). The dried electrode was punched into disks of 1.6 cm<sup>2</sup> with a loading 2.7-3.8 mg/cm<sup>2</sup> and further dried at 80°C in vacuum prior cell assembly. Figure IV-122a shows the cycling performance of the Si/Li half cells. The cells with higher molecular weight PAA-1 to 3 showed much better initial capacity and capacity retention in 100 cycles (PAA-1, the second-high molecular weight polymer, showed the best performance) than the low molecular weight PAA-4 and 5. The high molecular weight PAA binder helps integrate the active particles and adhere strongly to the current collector. Figure IV-122b shows the Coulombic efficiency and no significant difference was observed. It is still too early to conclude, but there is definitely room to further optimize PAA binders solely based on the molecular weight. More work will be conducted to better understand this molecular weight impact, including binder material characterizations and post analysis.

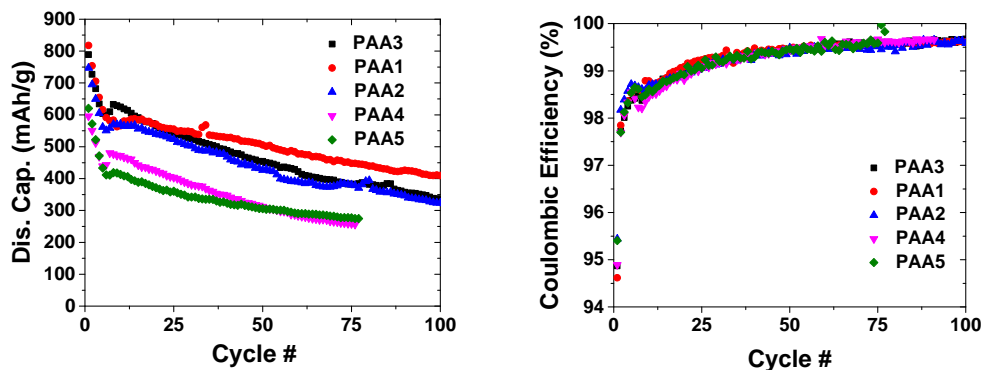


Figure IV-122: (a, left) PAA binder performance in Si-C/Li cells and (b, right) Coulombic efficiency of PAA binder cells

### Nature Derivative Polymer Binders with PAA as Side Chains

A multiphase graft copolymer with Chitosan as backbone and lithium polyacrylate as side chains was synthesized via a controlled radical polymerization (RAFT polymerization) as shown in Figure IV-123. A macro RAFT-CTA was synthesized by amidation reaction of carboxylic acid terminated RAFT-CTA with primary amine on chitosan in aqueous solution, and the following RAFT polymerization of acrylic acid allows the synthesis of well-defined comb-like copolymers, i.e., chitosan-graft-PAA. Further titration of the chitosan-graft-PAA with lithium hydroxide results in the comb-like copolymer with chitosan as a backbone with lithium polyacrylate as the side chains. The molecular weight of the multi-grafting polymer with different DP<sub>n</sub> (62, 27, and 17) of the side chain was synthesized, whereas the molecular weight of the polymer with DP<sub>n</sub> of 62 was calculated to be 710 kDa.

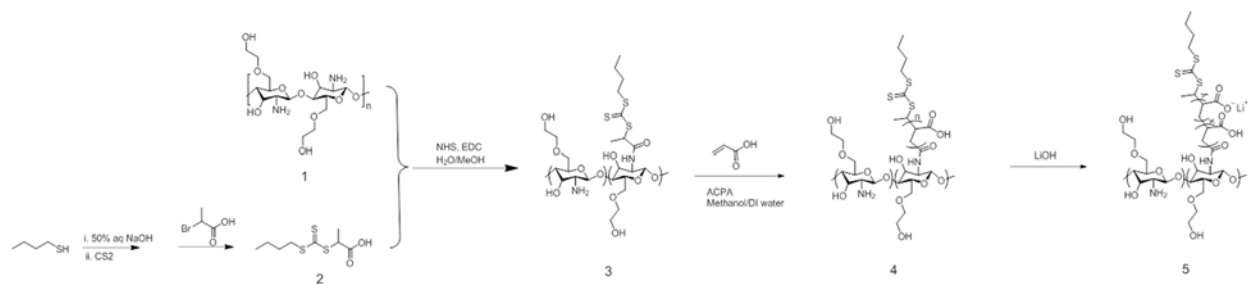


Figure IV-123: Design and synthesis of chitosan-graft-PAA binder

A silicon/graphite anode was prepared by casting the composite solution on copper foil with controlled viscosity. Coin-type half-cells with the prepared polymer-binder containing silicon/graphite film as the active electrode and Li metal as both of the reference and counter electrode were assembled. The effect of the polymer binder on the electrochemical performance of the Si-NP cells was assessed by galvanostatic cycling (specific capacity and coulombic efficiency) and the data is shown in Figure IV-124.

Initial results using the 15% silicon showed that linear polyacrylic acid and lithium polyacrylate exhibited much better cycling performance than the conventional PVDF. The coin-cell fabricated with the novel comb-like lithium polyacrylate binder showed higher specific capacity, and comparable long-term stability and coulombic efficiency compared to its linear analog, lithium polyacrylate. This is most likely due to the good mechanical property of the chitosan backbone and high density of lithium polyacrylate side chains, which provide better contact with the active material as shown in the scheme. Present work is focusing on tuning the architecture parameters (length (molecular weight) and density) of the comb-like copolymers on the binder performance in the silicon/graphite anode.

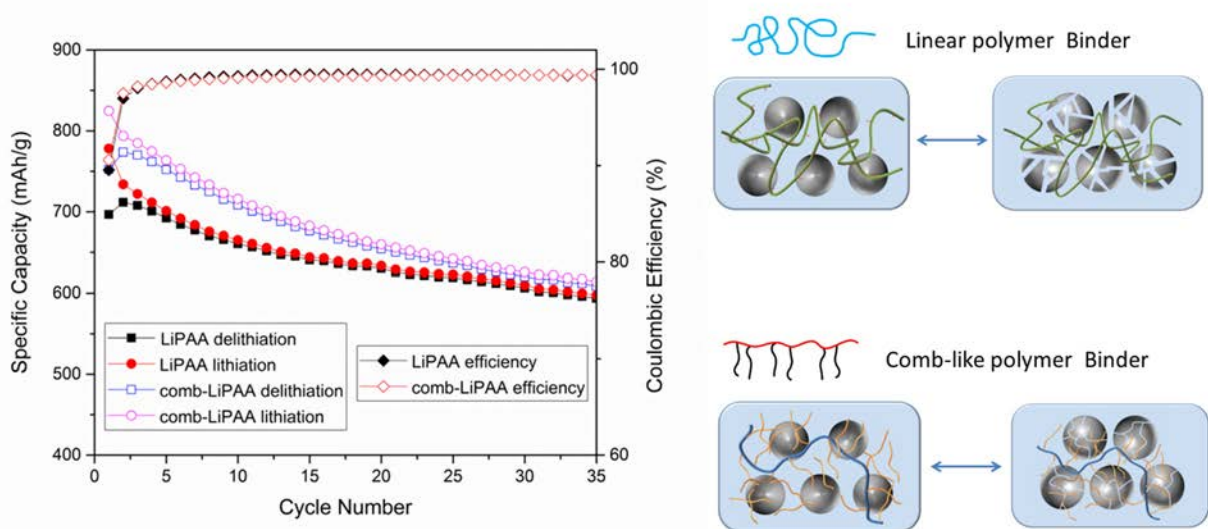


Figure IV-124: Comparative cycling performance of baseline binder lithium acrylate (LiPAA) and new synthesized multi-grafting lithium acrylate (comb-LiPAA) binder

### Polysiloxane-Based Binder

Polysiloxanes (PSs) polymers were chosen as the polymer backbone that allows us to precisely incorporate various functionalities and properties into the binder. PSs can afford some desirable properties as silicon anode compatible binders, such as elasticity and durability, which were evidenced by our previous studies in graphite anodes. On the other hand, PSs do possess several weak spots as a binder material, such as low molecular weight, lack of adhesion to the Si particles, and non-conductivity. Hydrosilylation reaction was utilized to introduce desirable properties into the PS polymer backbones.

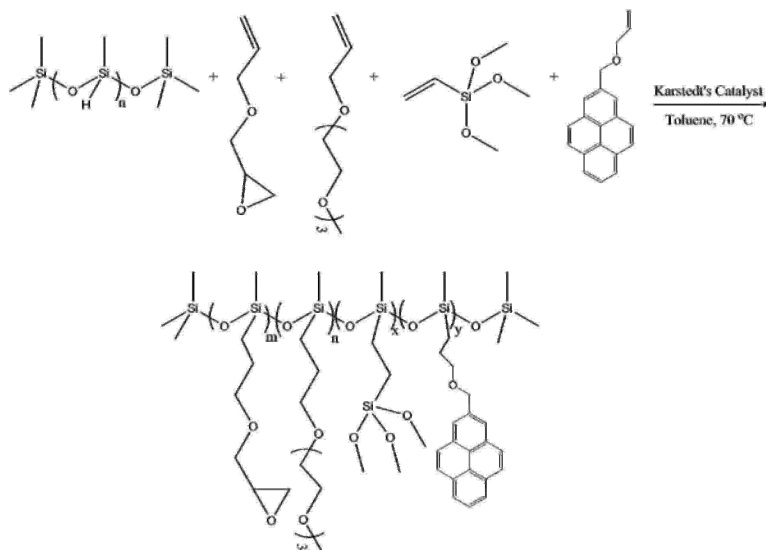


Figure IV-125: Hydrosilylation reaction to prepare polysiloxane based binders

A couple of polymethylhydrosiloxane (PMHS) with various substituents have been synthesized by Pt-catalyzed hydrosilylation reaction, as outlined in Figure IV-125. Table IV-14 listed all the synthesized polysiloxanes with the composition of different functional groups and the molecular weight data obtained from GPC. Note that all the molecular weight data from GPC were much higher than the calculated molecular weight, based on the DP of PMHS provided by vendor. However, most of the trend is still correct, especially for the AGE and AMPEO3 functionalized PMHS. For PMHS-3, the high PDI value is probably due to the self-crosslinking of the polymer during the purification and drying process.

**Table IV-14: Functionalized PMHS with the Composition of Different Functional Groups and their Molecular Weights**

Entry	AGE	AMPEO3	VTMS	Mn	PDI	Cal. MW
PMHS-0	0%	0%	0%	4.9 K	2.78	2.2 K
PMHS-1	100%	0%	0%	13.6 K	2.70	6.2 K
PMHS-2	0%	100%	0%	19.0 K	2.33	9.3 K
PMHS-3	0%	0%	100%	19.9 K	8.12	7.4 K
PMHS-4	50%	50%	0%	17.1 K	2.56	7.8 K
PMHS-5	50%	0%	50%	18.6 K	1.86	6.8 K
PMHS-6	10%	0%	90%	15.4 K	2.67	7.3 K

$^1\text{H}$  NMR and FT-IR were used to monitor the reaction. The disappearance of the Si-H peak at  $\sim 2200\text{ cm}^{-1}$  in FTIR indicates the complete consumption of Si-H bonds. Figure IV-126 shows the  $^1\text{H}$  NMR spectra of PMHS-1 and PMHS-3. All the peaks are assigned to the proposed structure and the disappearance of the Si-H peak (4.72 ppm) peak of PMHS and the double bond (5-6 ppm) of the AGE monomer indicates the full completion of the reaction and the high purity of the synthesized polymer.

For PMHS-3 and PMHS-6, since the polymer cannot be precipitated in hexanes, the volatile solvent was removed first after the reaction, and the viscous liquid was further dried under high vacuum to remove the monomer directly.

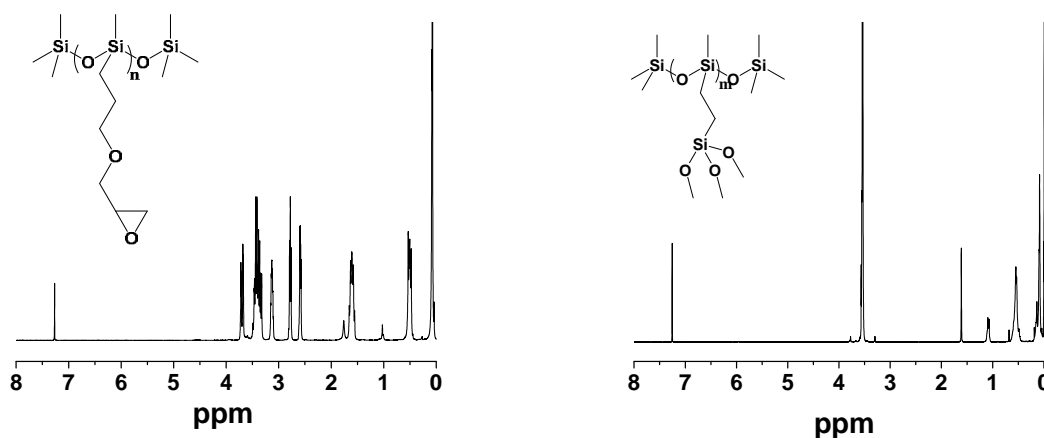


Figure IV-126: (a) 1H-NMR spectrum of PMHS-1 (PMHS-AGE) and (b) PMHS-3 (PMHS-VTMS)

The lamination process of the cross-linkable polymer binder is a big challenge. A traditional “dry” method was first used to prompt the crosslinking reactions. After mixing all the components including cross-linkers, the slurry was cast into a laminate and then dried under high vacuum oven directly at 80°C. The crosslinking reaction is supposed to occur during the drying. However, by using this method, the slurry was not homogeneous and it is also not convenient to monitor the crosslinking process. We then adapted a “wet method”, via which the electrode slurry was thrown into a reaction flask, and maintained at 80°C for five days. The crosslinking progress was monitored by GPC to make sure completion. The resultant slurry was then casted on copper foil as usual.

The half cells containing PMHS-1 and -2 have been cycled to investigate the cross-linking impact on the cell performance. JEFFAMINE T5000 polyamine was used in all the samples as the crosslinking agent. PMHS-2-“dry” also contained JEFFAMINE T5000 to serve as a control sample. As shown in Figure IV-127a, three formation cycles were first conducted at C/20 and then all cells were cycled at C/3 for 50 cycles (Figure IV-127b). From the first formation cycle, two cells using the “dry” method afforded relative higher discharge capacity (376 mAh/g), but all the numbers were far below the theoretical value (900 mAh/g). Such low capacities implied severe degradation of the silicon particles during lamination process. The cycling results were even worse. Two cells that were processed using “dry method” delivered no capacity at all. Only the PHMS-1-“wet” cell managed to provide some meaningful capacity, which was still far below the theoretical number. Even though the results were disappointing and of no practical interest, one thing we learned was that the traditional “cure” condition was not working well to prompt a well cross-linked network. The “wet” cross-linking condition showed much better results. PMHS-1-“wet” was also characterized by GPC, and the molecular weight was 75.7 K with PDI 2.03, indicating the crosslinking reaction indeed occurred. We are working on further optimization of the lamination process to protect silicon particles from degradation.

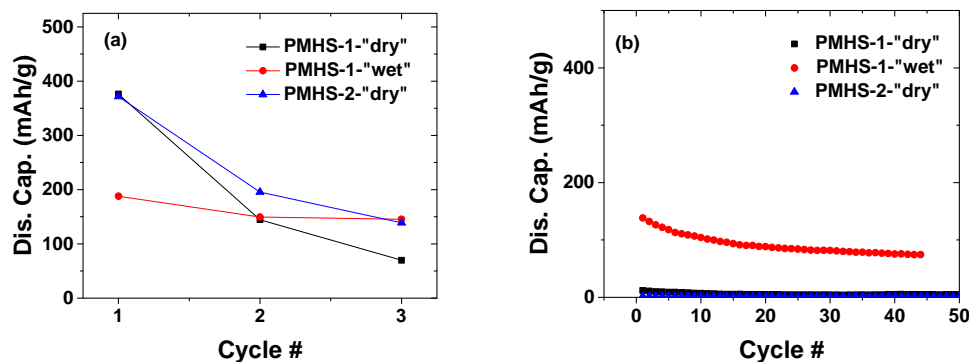


Figure IV-127: Specific discharge capacities of cells using PMHS-1 and PMHS-2 binders during the course of (a) three formation cycles under C/20 and (b) 50 cycles under C/3

## PPy Conductive Binders

Functional conductive polymer PPy binder was designed and synthesized by a radical initiated polymerization reaction of pyrene-substituted methacrylate. Other monomers with certain functions could also be incorporated to afford copolymers. The synthesis scheme is shown in Figure IV-128.

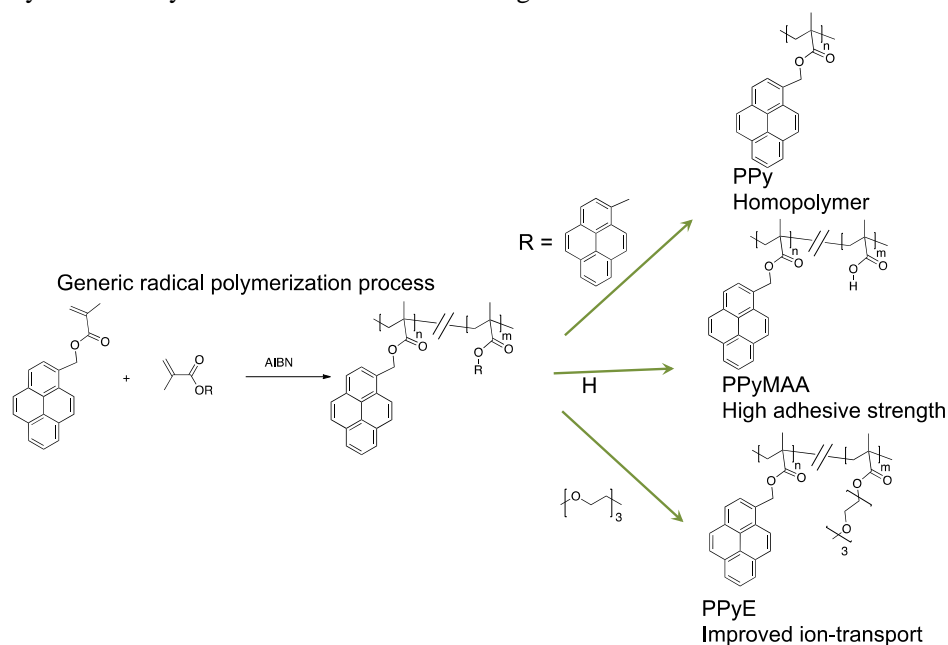


Figure IV-128: Synthesis of PPy polymer binder and copolymers

To calculate the lithiation into PPy, we compare the performance of PAALi with PPy, as PAALi has the same polymer backbone as PPy materials. This structure resemblance makes PAALi a good baseline materials. As the potential scans cathodically from the open circuit voltage of the Si anode at the first cycle, the solid electrolyte interface (SEI) starts to form at ca. 0.5 V to 0.8 V due to the electrolyte decomposition.[26-28] Ideally, the SEI blocks further electrolyte decomposition and only the lithium ion can pass through the SEI film and lithiate into Si anode. This electrochemical lithiation process is reflected by the cathodic current as shown in Figure IV-129. As the potential is scanned back to 1.0 V, the lithium ions are delithiated from Si anode. According to the cyclic voltammograms (CV) integration, the 1<sup>st</sup> cycle coulombic efficiency (CE) for PAALi and PPy based Si anode is 69.5% and 55.3%, respectively. This implies that more lithium is consumed by PPy than PAALi in the first cycles. To quantify the amount of lithium that is consumed before lithiation into Si, the quantity of electric charge (Q) is integrated from the open circuit voltage (OCV) to 0.8 V as shown in Figure IV-129b and d. The equivalent specific capacity based on PAALi/Si electrode is calculated to be 256 mAh/gSi, which is lower than that of the PPy/Si based electrode (279 mAh/gSi). The additional lithiation capacity is the lithiation into the pyrene group. To exclude the interference of lithiation into Si, the polymers are coated directly onto the copper foil to form a thin film with a thickness of around 1.0 micro-meter. The lithiation profile is presented in Figure IV-129e and f. There is a peak above 0.8 V which represents additional lithiation into pyrene in PPy polymer. The percentage of the total additional lithiation is calculated to be 4.7%.

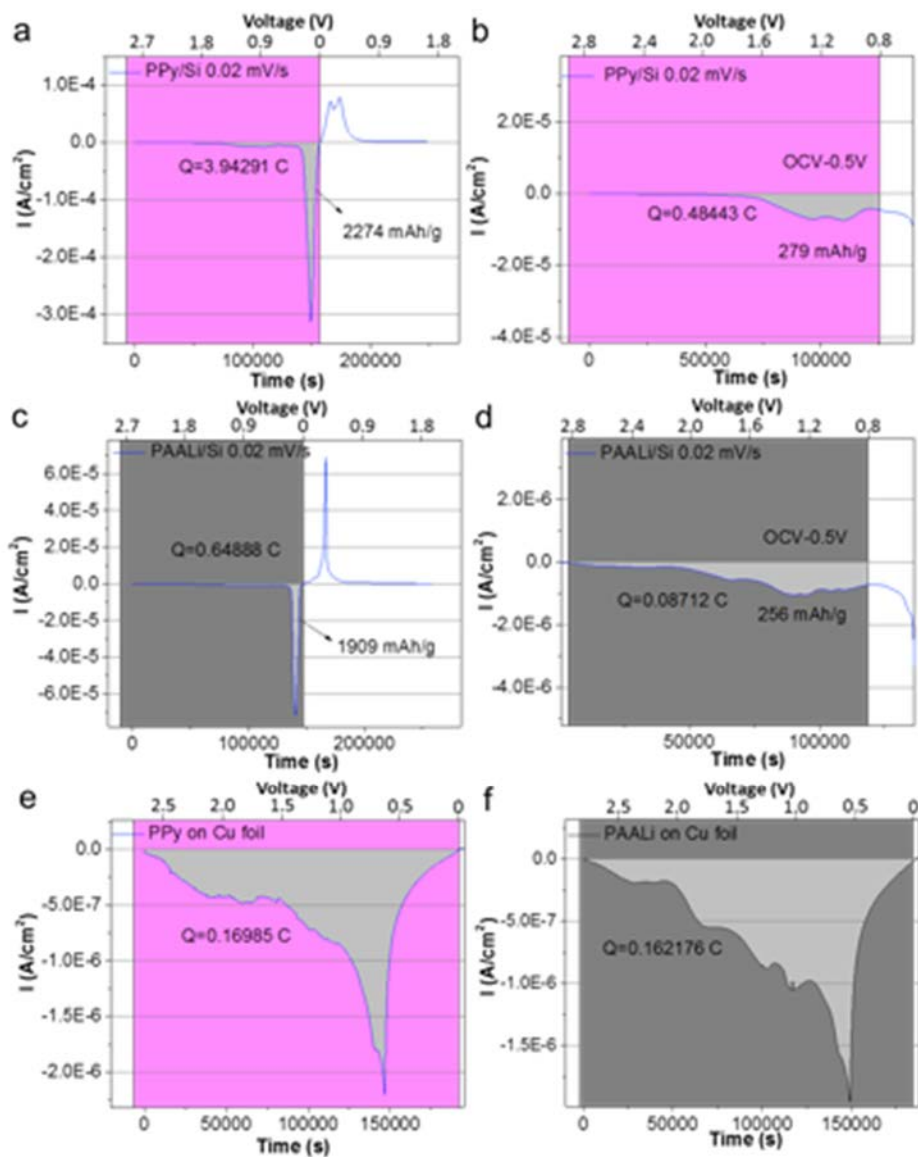


Figure IV-129: (a, b, c, d) Linear sweep voltammograms of the PPy/Si (1/2 wt%) and PAALi/Si (1/2 wt%) electrodes at 0.02 mV/s in 1.0 M LiPF<sub>6</sub> in ethylene carbonate, diethyl carbonate (EC/DEC=3/7 w/w) containing 30 wt% fluoroethylene carbonate (FEC) electrolyte. (e, f) Linear sweep voltammograms of the PPy and PAALi film on Cu foil at 0.02 mV/s in ethylene carbonate, diethyl carbonate (EC/DEC=3/7 w/w) containing 30 wt% fluoroethylene carbonate (FEC) electrolyte

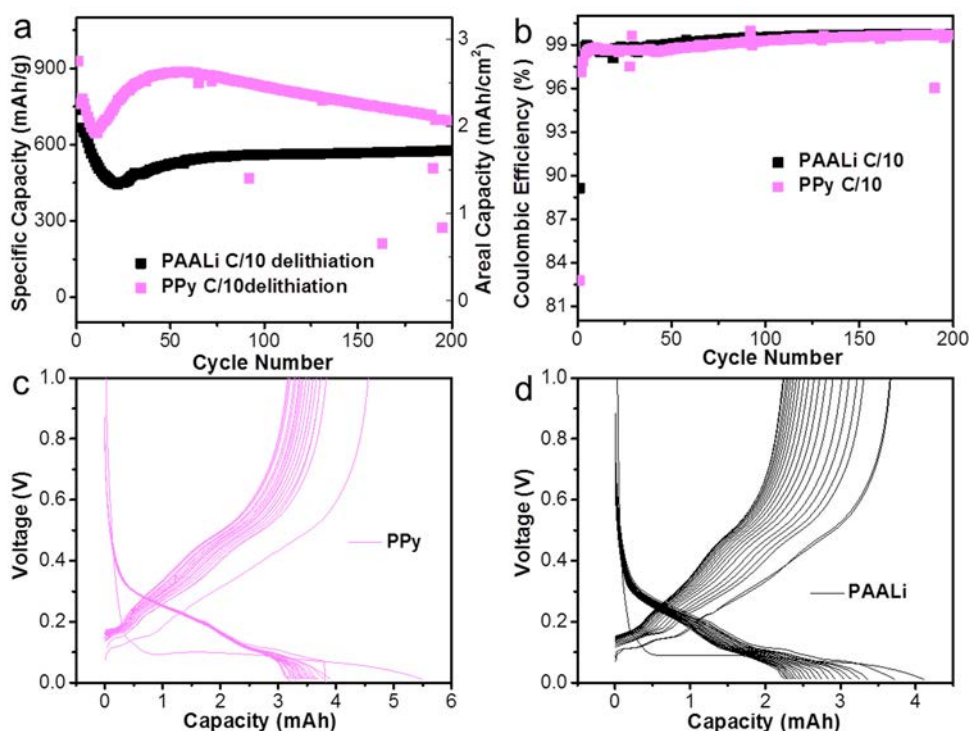


Figure IV-130: (a) Specific capacity (left Y axis) and areal capacity (right Y axis) vs. cycle number, (b) Coulombic efficiency vs. cycle number for electrodes based on PPy binder (PPy/Si/Graphite=12/15/73 wt%) and PAALi binder. (PAALi/Carbon black/Si/Graphite=10/2/15/73 wt%). The initial two cycles were at C/25, then C/10 for the long-term cycling. (c, d) Voltage profiles of PPy and PAALi based electrodes at the first 20 cycles, PPy shows much less capacity decay above 0.1 V, which implies the higher Si utilization for PPy based electrode

To *in situ* quantify the degree of lithium doping into the pyrene groups, PAALi and PPy are assembled into the graphite/Si composite electrode for their identical backbones except the pyrene side chain groups in PPy. Targeting at a commercial energy density, the relatively high loading electrodes are assembled and cycled. The PPy and PAALi based electrode contains 3.06 and 3.10 mg/cm<sup>2</sup> Si/graphite composite respectively. The left Y axis in Figure IV-130a is plotted as mAh per gram of graphite/Si, which exhibits capacity twice as high as conventional graphite anode even after 100 cycles. Also, a significant areal capacity of more than 2.5 mAh/cm<sup>2</sup> is achieved and maintained stable for more than 100 cycles. The corresponding coulombic efficiency (CE) is shown in Figure IV-130b. The CE of the first cycle for PPy and PAALi is 82.8% and 89.1%, respectively. Assuming the extra irreversible lithium ions are consumed by pyrene group, the calculated electron into pyrene structure is 0.22 C. Consequently, the ratio of lithium ions to pyrene group is 1, which is calculated based on the mass of PPy polymer (0.59 mg) in the electrode.

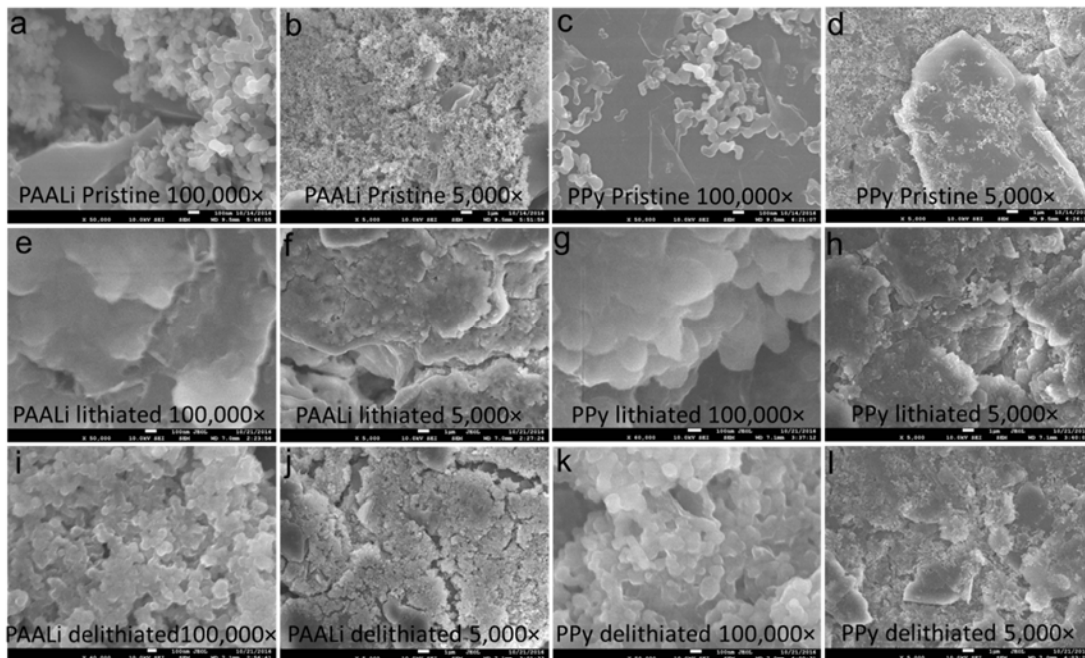


Figure IV-131: SEM images of PAALi and PPy based pristine, discharged charged Si/graphite electrodes with vary magnification

The effectiveness of functional PPy binder is further demonstrated by post analysis of the electrode. The cells are disassembled both in fully lithiated and delithiated states. The harvested electrodes are immersed in dimethyl carbonate (DMC) for 30 min and flushed three times prior to SEM image collection. When the cell is in fully lithiated state, as shown in Figure IV-131g, Si particles (50-70 nm) expand to more than 100 nm uniformly after lithiation, indicating the high utilization of Si particles. In contrast, the expansion is less uniform for PAALi based electrodes (Figure IV-131e), which is consistent with the cycle performances. This suggests that the PPy enhances the utilization of Si particles, critical to the success of Si/graphite composite anode. The mechanical uniformity of the PPy based electrode also improves, as cracks happen in PAALi based electrodes among the pristine, lithiated and delithiated electrodes, while there is no cracks in the PPy based electrodes in all cases as shown in Figure IV-131, indicating the better mechanical strength of PPy binder for the Si/graphite composite material.

### Self-Healing Polymer Binders

Polymers with dynamic hydrogen bonds are known to exhibit “self-healing” properties, and have previously been reported as superior binders for Si microparticle anodes. A series of copolymers of acrylamide (AAM) and N-[3-(Dimethylamino)propyl] acrylamide (DMAPA), **1**, were synthesized, in DMSO, using azobisisobutyronitrile (AIBN) as initiator (Figure IV-132a). An initial series of polymers, with a target average molecular weight of ~22 kDa, were synthesized; however, after precipitation of the reaction mixtures in acetone, the collected solids were found to be insoluble in most common solvents, including water. This insolubility meant that these polymers would not be useful as binders, as the laminate manufacturing process requires that the binder be soluble in either water or N-methylpyrrolidone (NMP).

In order to alleviate this issue, another series of polymers were synthesized, having a lower average molecular weight, and resulted in water soluble polymers. NMR spectroscopy confirms that there is good incorporation of both monomers into the copolymers, such that the feed ratio is very close to the monomer ratio found in the resulting copolymers.

Half-cell experiments indicate that these copolymers form anodes that can be lithiated and delithiated a number of times (Figure IV-132b), although the initial capacities are all lower than the baseline anode, and all of the half cells tested show a faster capacity fade than the baseline anode. Initial indications are that lower percentages of acrylamide in the copolymer results in half cells with higher initial capacities and slower capacity fade. This potential correlation will be studied further.

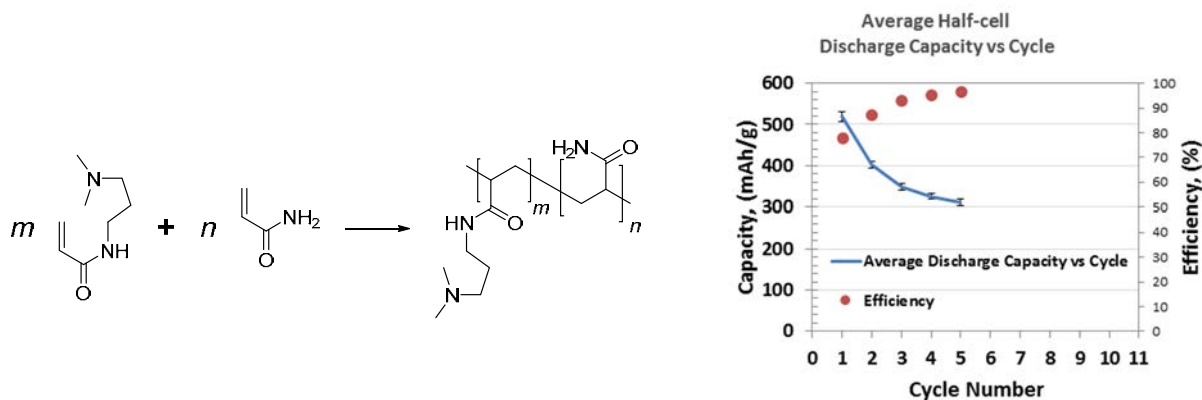


Figure IV-132: (a) Synthesis of poly(acrylamide-co-N-[N,N-dimethylpropylamine]acrylamide) and (b) Initial electrochemical performance

## Conclusions

Sandia National Laboratories (SNL), Oak Ridge National Laboratory (ORNL), National Renewable Energy laboratory (NREL), Lawrence Berkeley National Laboratory (LBNL), and Argonne National Laboratory (ANL) have teamed together to form an integrated program. Technical targets have been developed and regular communications have been established. BatPaC calculations indicate anode volumetric capacities greater than  $1000 \text{ mAh/cm}^3$  generally minimizes battery cost with an advanced NMC cathode. Further, a standard testing protocol for the program shown to work well for lithium-ion cells with silicon containing anodes has been adopted. Key to this integrated effort is the support of battery research facilities at the Labs, which include the Battery Abuse Testing Laboratory (BATLab), the Battery Manufacturing Facility (BMF), the Cell Analysis, Modeling, and Prototyping (CAMP), the Materials Engineering Research Facility (MERF), and the Post-Test Facility (PTF).

Support by the research facilities comprises the scale-up of materials, incorporation of materials advancements into baseline electrodes and prototype cells, and characterization and testing of cells, as well as evaluation of safety and abuse tolerance. Four electrodes were selected as the baseline anodes, which consisted of 0, 5, 10, and 15 wt. % silicon (50-70 nm from NanoAmor) balanced with Hitachi Mag-E graphite. A capacity-balanced NMC532 cathode was also selected as the baseline counter electrode. The physical and electrochemical properties of these electrodes have been examined. Clearly, increasing the amount of silicon dramatically improves the specific capacity of the total active material (graphite + silicon), and more effort is needed to improve the cycle life performance of silicon-based electrodes. Safety and abuse tolerance studies demonstrates that there is an impact on safety response with nanoscale silicon materials compared to graphite based anodes. Changes to material and cell level properties (particle size, electrolyte ratios, electrode composition) can have an impact on safety and thermal response characteristics. Thermal runaway properties of cells (coin cells and cylindrical cells) containing nanoscale silicon up to 15 percent by weight have been studied.

The fundamental understanding of silicon-based electrode active materials is based on extensive electrochemical and analytical diagnostic studies on components, electrodes, and cells conducted within the program. This effort includes *in situ* and *ex situ* studies, as well as the development and characterization of model systems. The model system studies (see IV.D.8 Next-Generation Anodes for Lithium-ion Batteries: Fundamental Studies of Si-C Model Systems) are generally thin-film well-defined active area electrodes on which it is easier to extract fundamental information on lithium-silicon phase formation, lithium transport, and interfacial phenomena (e.g. SEI formation and growth).

The blending of silicon with graphite increases the average potential of the negative electrode during delithiation from 0.15 V (for Gr) to 0.35 V (for SiGr). Hence, to maintain the same full cell voltage, the positive electrode needs to be cycled to a higher potential (by 0.2 V) for cells with SiGr electrodes. The SiGr electrode potential characteristics are a superposition of the Si and graphite materials. The addition of silicon also introduces a large potential hysteresis between the charge and discharge cycles, which is seen both in the presence and absence of the crystalline  $\text{Li}_{15}\text{Si}_4$  phase. This voltage hysteresis affects the full cell voltage

profiles and has a significant effect on impedance measurements, specifically at low cell voltages, leading to a large difference in measured impedance at a given voltage between charge and discharge.

Cycling of NCM523/SiGr cells using various electrolyte compositions containing VC and FEC compounds shows that the additive amount has a significant effect on capacity retention. After 100 cycles, capacity retention increases from 8% for the Gen2 cell, up to 20% for cells with 5 wt% additives, and up to 50% for cells with 10 and 20 wt% additives. Our results suggest that depletion of additives in the electrolyte during extended cycling leads to rapid capacity decline. Therefore, one could consider higher amounts of additives and even pure fluorinated carbonate solvents. However, for pure FEC, we noted a tendency towards the formation, aggregation, and phase separation of  $\text{Li}^+$  coordination polymers when the  $\text{LiPF}_6$  concentration exceeds  $\sim 0.8$  M in the electrolyte. These coordination polymers have the  $\text{Li}(\text{FEC})_3\text{PF}_6$  crystal structures as determined from X-ray diffraction and NMR spectroscopy data.

Comparing the electrochemical performance of silicon anodes fabricated with silicon before and after different oxidation treatments, showed that mild oxidation treatment exhibited both comparable initial performance and improved cycling performance. For a water-based laminate processing system, one needs to take into consideration both the reactivity of silicon with oxygen and water, as well as the insulation effect from  $\text{SiO}_2$ , in order to achieve optimized initial performance and cycle life.

A wide range of specialized characterization techniques being utilized within the program to understand operation and failure mechanisms in silicon-based anodes include neutrons, NMR, optical, acoustic, and X-ray techniques. Silicon NMR results suggest that small average particle sizes ( $<100\text{nm}$ ) result in large compositions of silicon oxide type order that could be significantly detrimental in electrochemical performance. Significant electrolyte decomposition and trapping have been observed on the anode, likely due to reactive lithiated silicide interaction with electrolyte and additives that leads to significant Li-loss and poor coulombic efficiency in the cell. Micro-Raman mapping of 100 X cycled 15 wt. % - Si composite electrodes showed presence of isolated crystalline Si along with regular amorphous Si. Cracking was observed and associated with Si for the first time in Si-graphite-NMC pouch cells using *in situ* electrochemical acoustic ToF measurements.

Supported by the diagnostic studies, materials development on silicon-based materials, electrodes, and cells is critical to enhance interfacial stability, accommodate intermetallic volume changes, and improve overall performance and life. Key to this effort is the development and testing of coatings and additives designed to modify and stabilize the dynamic silicon-electrolyte interface. Further, functional polymer binders designed to accommodate volume changes, increase conductivity, and improve adherence are being developed and analyzed. Finally, the program is exploring active material development. Alternative high-energy silicon-alloy/composite materials are being studied. Also, strategies for introducing additional lithium inventory into the cell are being developed.

Alucone MLD has been performed on the Si laminated electrodes made with different polymer binders. Significant improvements on the reversibility and the capacity retention have been achieved in PVDF-enabled electrodes, although no major impact was observed for the electrodes fabricated by using functional binders such as LiPAA and CMC. It is believed that the functional binders have the chemical interaction with the surface of Si particles, and behave like a surface coating. The MLD film acts as an extra coating layer beyond the polymer binder layer on the surface of Si particles. Therefore, the coating does not have major impact in the cycling performance.

The study of thickness effect on the cycling performance of Si electrodes has revealed that the MLD coating has greatly stabilized the cycling performance for the relatively thick Si-C-PVDF electrodes. Without MLD coating, a severe capacity loss was observed for the thick electrodes. The capacity degradation in the thick electrodes can be attributed to the high internal resistance, and the mechanical disintegration associated by volumetric changes of Si particles. Results from nanoindentation and scratch testing have confirmed the improved mechanical properties in the MLD coated electrodes. The ultrathin MLD coating has enhanced the adhesion of electrode to the substrate, and improved the deformation capability.

Electrolyte research initiated to fundamentally understand the SEI formation mechanism and how the electrolyte reactivity and the chemical composition impact the SEI and electrochemical performance of the Si anode in order to gain deep insight for electrolyte design and synthesis capable of effective passivation through formation of the chemically and mechanically stable SEI layer to afford long cycle life. TEM utilized to

conduct fundamental study of SEI formation on silicon anode particles. Also, detailed impedance and cycling studies were conducted to quantify impact of Silazane additive.

A variety of functional polymers have been designed and synthesized as new Si anode binders in order to understand the correlation of physiochemical property of the binder and the electrochemical property. Siloxane-based (Si-O-Si) and acrylate-based ( $\text{CH}_2=\text{CH}(\text{CH}_3)\text{-COR}$ ) polymer backbones or side chains were selected as platforms to study the impact of the substituents, the architecture of the copolymer, phase separation, molecular weight and the chemical/electrochemical stability in contact with lithiated silicon. 3D-network-forming polymer binder with strong adhesion to silicon particle and current collector was also synthesized to maintain the electrode integrity targeting the extended cycling performance of Si anode.

First, molecular weight and molecular weight distribution (PDI) of polymer binder plays a significant role in the electrochemical performance. Our research clearly indicated that the high molecular weight PAA is beneficial to the initial capacity and capacity retention of the Si anode. Second, the architecture of the polymer also impacts the Si anode performance. The new binder with Chitosan as backbone and lithiated PAA as side chains exhibited better cycling performance than that of lithiated PAA due to the good mechanical property of the chitosan backbone and high density of lithium polyacrylate side chains, which provide better contact with the active material. Another new binder with siloxane backbone was designed and synthesized with glycidyl ether (AGE) and oligo(ethylene glycol) (APEO3) side chains. Initial electrochemical testing was performed on the Si anode fabricated by a “wet” method. Comb-polymer with AGE was cross-linked at the presence of the diamine crosslinking agent and showed much better performance than its non-crosslinked counterpart.

Third, the binder reactivity during the lithiation process was quantified using poly(1-pyrenemethyl methacrylate) (PPy) binder at low potential. The higher utilization of Si for PPy based electrode has been proved through the voltage/capacity profiles, and lithiated electrode morphologies. The degree of lithium doping was further quantified to be 1  $\text{Li}^+$ /pyrene through the comparison of first cycle charge quantity between PAALi and PPy based electrode. The improved mechanical strength and stability of PPy to PAALi is demonstrated through SEM and post FTIR analyses. Lastly, “self-healing” co-polymer based on acrylamide (AAM) and N-[3-(Dimethylamino)propyl] acrylamide (DMAPA) were synthesized. Through a systematic variation of the monomer ratios and molecular weights, we are building a library of polymer binders which will then be tested in a number of ways to determine their effectiveness as binders for producing silicon anode laminates that are stable, have high capacities, and are stable to lithiation/delithiation cycling.

The synthesis of Si-Sn and Si-Sn-C nanocomposites and its electrochemistry via a facile mechanical milling method was explored. The as-prepared Si-Sn-C nanocomposites demonstrated the best electrochemical performance, evidenced by an initial discharge capacity of about 1000 mAh/g and 80% capacity retention at cycle 50. However, the challenge in the synthesis of homogeneous amorphous Si-Sn phase via mechanical milling process was revealed. Therefore, the scale up of this material was not pursued. Instead, this work suggests a potential avenue to search for high energy lithium-ion anodes within the phase diagrams containing Si and Sn. Based on the previous work on Si-Sn thin films, synthesis of mixed Si and Sn at an atomic level via different synthetic techniques (e.g., melt spinning, chemical reduction method, etc.) will be pursued.

Lithium inventory control in Si-graphite/NMC cells is critically important to the success of such advanced cells in EV transportation applications. Proof of concept experiments with LFO-LCO blends with hard carbon shows the efficacy of LFO to electrochemically oxidize and release additional lithium into a system at a very high mole% level. LFO works even with an anode of high irreversible capacity loss on the first cycle. While it is known that hard carbon is very reversible in lithium-ion cells, the problem for that material is the first ICL cycle. Now for Si, you have also the large ICL on the first cycles, but also cycle-over-cycle non-100% coulombic efficiency. In fact, in order to achieve 1000 cycles, it is calculated to get 1000 cycles with 20% capacity decline in Si-graphite cells (15% Si), you need a cycle-over-cycle coulombic efficiency of 99.98%. We aim to increase that value using pre-lithiation additive LFO. In the present report, we demonstrate that NMC/LFO blends do not adversely affect the NMC532 electrochemistry plus the LFO is electrochemically active with expected first cycle charge capacity as measured being close to theoretical. Furthermore, the rate capability of NMC532 is not lessened with the presence of LFO.

The challenge for this team is clearly defined. It involves solving a host of issues that span a broad range of length scales, from atomic to particle to electrode to cell and eventually to pack designs. This team brings a wide array of expertise and skills to address the issues and move the technology forward.

## Products

### Presentations/Publications/Patents

1. Eric Allcorn, Ganesan Nagasubramanian, Kyle Fenton. "Materials Safety Study of Practical Nano-Silicon + Graphite Anodes for Lithium-Ion Batteries." Prime 2016, Honolulu, HI, Oct. 2 - 7, 2016.
2. Kyle Fenton, Chris Orendorff, Ganesan Nagasubramanian, Josh Lamb, Eric Allcorn. "Impact of next Generation Electrode Materials on Abuse Response." Prime 2016, Honolulu, HI, Oct. 2 - 7, 2016.
3. M. Klett, J.A. Gilbert, K.Z. Pupek, S.E. Trask, D.P. Abraham, "Layered Oxide, Graphite and Silicon-Graphite Electrodes for Lithium-ion Cells: Effect of Electrolyte Composition and Cycling Windows", *J. Electrochem. Soc.* 164 (2017) A6095-6102.
4. C.D. Malliakas, K. Leung, K.Z. Pupek, I.A. Shkrob, D.P. Abraham, "Spontaneous aggregation of lithium ion coordination polymers in fluorinated electrolytes for high-voltage batteries", *Phys. Chem. Chem. Phys.* 18 (2016) 10846-10849.
5. D.P. Abraham, "A Closer Look at Silicon-Graphite (SiGr) Composite Electrodes During Cycling in NCM523/SiGr Full Cells", Advanced Automotive Battery Conference (AABC 2016), Detroit, MI, June 14-17 2016.
6. D.P. Abraham, "Designing high-energy lithium-ion cells with Si-containing electrodes", Gordon Research Conference on Batteries, Ventura, CA, February 21-26, 2016.
7. B. Key, "NMR Studies of Li-Si Chemistry", USDrive Electrochemical Energy Storage Tech Team Applied Battery Research for Transportation (ABR) Silicon Deep Dive Program Informational Meeting, Argonne National Laboratory, October 18th, 2016
8. L. Zhang, Y. Liu and W. Lu, "The effects of oxide layer on the electrochemical performance of silicon anodes", manuscript in prep.
9. C. Ban, S. M. George, "Molecular Layer Deposition for Surface Modification in Lithium-ion Batteries", Review, *Adv. Mater. Interface*, 2016, 1600762, DOI: 10.1002/admi.201600762
10. K. E. Hurst, J. M. Luther, C. Ban, S. T. Christensen, "Nanomaterials for Energy Applications" In Mansfield, E.; Kaiser, D. L.; Fujita, D.; Van de Voorde, M. (Ed). *Metrology and Standardization of Nanomaterials: Protocols and Industrial Innovations*; Wiley. 2016
11. D. M. Piper, Y. Lee, S-B. Son, T. Evans, F. Lin, D. Nordlund, X Xiao, S. M. George, S.H. Lee, C. Ban, "Cross-linked aluminum dioxybenzene coating for stabilization of silicon electrodes", *Nano Energy*, 2016, 22, pp 202–210, DOI: 10.1016/j.nanoen.2016.02.021.
12. Invited presentation in 51st American Chemical Society's Midwest Regional Meeting (ACS-MWRM), Manhattan, KS, 2016: Structural evolution of lithium-ion electrodes during battery cycling
13. Invited seminar in the department of Chemical and Biomolecular Engineering at University of Maryland, 2016: Surface modification for nanoscale silicon electrode materials
14. 11<sup>th</sup> U.S.-China Electric Vehicle and Battery Technology Meeting, Denver, Colorado, 2016: Development of silicon anode for high-energy Lithium-ion batteries
15. Invited seminar in the department of Chemical and Materials Engineering at University of Kentucky, 2016: Surface modification for Silicon-based alloy materials
16. C. S. Johnson, Li-rich  $\text{Li}_5\text{FeO}_4$  (LFO) Cathode Material as Pre-lithiation Additive for Enabling High-Energy Si/C/NMC Batteries, 2016 International Battery Association Conference (IBA), Nantes, France Mar.20-25, 2016
17. C. S. Johnson, Electrochemical Behavior of  $\text{Li}_5\text{FeO}_4$  in Energy Storage Applications, 18-IMLB (International Meeting on Lithium Batteries), Chicago, IL, June 24, 2016
18. Chi-Kai Lin, Xin Su, Xiaoping Wang, Wnequan Lu, C. S. Johnson,  $\text{Li}_5\text{FeO}_4$  Li Source Additive: Fixing Irreversibility in LIBs, 230th The Electrochemical Society Meeting/PRiME Conference, Honolulu, HI, October 2-8, 2016
19. A New Strategy to Mitigate the Initial Capacity Loss in Lithium-ion Batteries, Xin Su, Chi-Kai Lin, Xiaoping Wang, Victor Maroni, Yang Ren, Christopher Johnson, Wenquan Lu *J. Power Sources*, 324, 150-157, (2016)

20. Gao Liu, Zhengcheng Zhang, Lu Zhang, James Ciszewski, Tomonori Saito. Polymer Binders. USDrive Electrochemical Energy Storage Tech Team, Applied Battery Research for Transportation (ABR), Silicon Deep Dive Program Informational Meeting, Argonne National Laboratory, October 18, 2016.
21. Hui Zhao, Allen Du, Min Linga, Vincent Battaglia, Gao Liu Conductive polymer binder for nano-silicon/graphite composite electrode in lithium-ion batteries towards a practical application *Electrochimica Acta* 209 (2016) 159-162.
22. Hui Zhao, Qing Yang, Neslihan Yuca, Min Ling, Kenneth Higa, Vincent S. Battaglia, Dilworth Y. Parkinson, Venkat Srinivasan, and Gao Liu A Convenient and Versatile Method To Control the Electrode Microstructure toward High-Energy Lithium-Ion Batteries *Nano Lett.* 16 (2016) 4686-4690.

## References

1. *Alloy Negative Electrodes for Lithium-ion Batteries*. M.N. Obrovac and V.L. Chevrier, *Chem. Rev.* 2014, 114, 11444-11503.
2. Modeling the Performance and Cost of Lithium-Ion Batteries for Electric-Drive Vehicles. Second Edition, Argonne National Laboratory Report, ANL-12/55.
3. *Performance of Full Cells Containing Carbonate-Based LiFSI Electrolytes and Silicon-Graphite Negative Electrodes*. S.E. Trask, K.Z. Pupek, J.A. Gilbert, M. Klett, B.J. Polzin, A.N. Jansen, and D.P. Abraham, *Journal of The Electrochemical Society*, 163 (3) A345-A350 (2016)
4. B. Key, R. Bhattacharyya, M. Morcrette, V. Seznec, J-M. Tarascon, C. P. Grey, *J. Am. Chem. Soc.*, 2009, 131 (26), pp 9239–9249
5. B. Key, M. Morcrette, J-M. Tarascon, C. P. Grey, *J. Am. Chem. Soc.*, 2011, 133 (3), pp 503–512
6. A. L. Michan, M. Leskes, C. P. Grey, *Chem. Mater.*, 2016, 28 (1), pp 385–398
7. A. L. Michan, D. Divitini, A. J. Pell, M. Leskes, C. Ducati, C. P. Grey, *J. Am. Chem. Soc.* 2016, 138, 7918–7931
8. A. L. Michan, B. S. Parimalam, M. Leskes, R. N. Kerber, T. Yoon, C. P. Grey, B. L. Lucht, *Chem. Mater.*, 2016
9. S. Xun et al. “The effects of Native Oxide Surface Layer on the Electrochemical Performance of Si Nanoparticle-Based Electrodes”, *Journal of The Electrochemical Society*, 2011, 158 (12)
10. S. Xun et al. “Improved Initial Performance of Si Nanoparticles by Surface Oxide Reduction for lithium-Ion Battery Application”, *Electrochemical and Solid-State Letters*, 2011, 14(5)
11. A. Toudjine et al. “Partially Oxidized Silicon Particles for Stable Aqueous Slurries and Practical Large-Scale Making of Si-Based Electrodes”, *Journal of The Electrochemical Society*, 2015, 162(8)
12. T. D. Hatchard and J. R. Dahn, *Journal of The Electrochemical Society*, 2004, 151, A1628-A1635.
13. H.-J. Ahn, Y.-S. Kim, K.-W. Park and T.-Y. Seong, *Chemical Communications*, 2005, DOI: 10.1039/B407264B, 43-45.
14. X. Xiao, J. S. Wang, P. Liu, A. K. Sachdev, M. W. Verbrugge, D. Haddad and M. P. Balogh, *Journal of Power Sources*, 2012, 214, 258-265.
15. H. Wang, H. Huang, L. Chen, C. Wang, B. Yan, Y. Yu, Y. Yang and G. Yang, *ACS Sustainable Chemistry & Engineering*, 2014, 2, 2310-2317.
16. Y. Kwon and J. Cho, *Chemical Communications*, 2008, DOI: 10.1039/B716694J, 1109-1111.
17. M. N. Obrovac and V. L. Chevrier, *Chemical Reviews*, 2014, 114, 11444-11502.
18. N. L. Rock and P. N. Kumta, *Journal of Power Sources*, 2007, 164, 829-838.
19. Ban, C.; George S.M., Molecular Layer Deposition for Surface Modification of Lithium-ion Battery Electrodes, *Adv. Mater. Interfaces* 2016, 3(21), 1600762.
20. Son, S. B.; Kappes, B.; Ban, C. M., Surface Modification of Silicon Anodes for Durable and High-Energy Lithium-Ion Batteries. *Isr. J. Chem.* 2015, 55 (5), 558-569.
21. Jung, Y. S.; Cavanagh, A. S.; Riley, L. A.; Kang, S. H.; Dillon, A. C.; Groner, M. D.; George, S. M.; Lee, S. H., Ultrathin Direct Atomic Layer Deposition on Composite Electrodes for Highly Durable and Safe Lithium-ion Batteries. *Adv. Mater.* 2010, 22 (19), 2172-2176.

22. Piper, D. M.; Travis, J. J.; Young, M.; Son, S. B.; Kim, S. C.; Oh, K. H.; George, S. M.; Ban, C. M.; Lee, S. H., Reversible High-Capacity Si Nanocomposite Anodes for Lithium-ion Batteries Enabled by Molecular Layer Deposition. *Adv. Mater.* 2014, 26 (10), 1596-1601.
23. Piper, D. M.; Son, S.-B.; Travis, J. J.; Lee, Y.; Han, S. S.; Kim, S. C.; Oh, K. H.; George, S. M.; Lee, S.-H.; Ban, C., Mitigating irreversible capacity losses from carbon agents via surface modification. *J. Power Sources* 2015, 275, 605-611.
24. Piper, D. M.; Lee, Y.; Son, S. B.; Evans, T.; Lin, F.; Nordlund, D.; Xiao, X. C.; George, S. M.; Lee, S. H.; Ban, C. M., Cross-linked aluminum dioxybenzene coating for stabilization of silicon electrodes. *Nano Energy* 2016, 22, 202-210.
25. Li<sub>2</sub>O Removal from Li<sub>5</sub>FeO<sub>4</sub>: A Cathode Precursor for Lithium-Ion Batteries, C. S. Johnson, S.-H. Kang, J. T. Vaughey, S. V. Pol, M. Balasubramanian, M. M. Thackeray, *Chemistry of Materials*, 22, 1263-1270 (2010)
26. Vogl, U. S.; Lux, S. F.; Crumlin, E. J.; Liu, Z.; Terborg, L.; Winter, M.; Kostecki, R. J. *Electrochem. Soc.* 2015, 162, A603.
27. Cho, J.-H.; Picraux, S. T. *Nano Lett.* 2014, 14, 3088.
28. Jaumann, T.; Balach, J.; Klose, M.; Oswald, S.; Langklotz, U.; Michaelis, A.; Eckerta, J.; Giebelera, L. *Phys. Chem. Chem. Phys.* 2015, 17, 24956.

## IV.C.5. Next-Generation Anodes for Lithium-Ion Batteries: Fundamental Studies of Si-C Model Systems, Lawrence Berkeley National Laboratory (LBNL)

### **Robert Kostecki, Point-of-Contact, Dennis Dees, Program PI**

Lawrence Berkeley National Laboratory  
1 Cyclotron Road  
Berkeley, CA 94720  
Phone: 510-486-6002; Fax: 510-486-5454  
E-mail: [r\\_kostecki@lbl.gov](mailto:r_kostecki@lbl.gov)

### **Peter Faguy, DOE Program Manager**

U.S. Department of Energy  
Vehicle Technologies Office  
1000 Independence Avenue, SW  
Washington, DC 20585  
Phone: 202-586-1022  
E-mail: [Peter.Faguy@ee.doe.gov](mailto:Peter.Faguy@ee.doe.gov)

Start Date: October 1, 2015 (Kickoff: January 2016)

End Date: September 30, 2018

### **Abstract**

### **Objectives**

- The primary objective of this effort is to provide basic understanding and effective mitigation of key R&D barriers to implementation of silicon-based anodes in lithium-ion cells for PHEVs and EVs. Establish direct correlations between electrochemical performance, interfacial phenomena, surface chemistry, morphology, topology and degradation mechanisms of active materials i.e., silicon and graphite and passive components e.g., advanced binders.
- Develop and employ experimental model systems and advanced instrumental techniques to guide the development of novel Si-based electrodes and lithium-ion battery systems.
  - Obtain detailed insight into the dynamic behavior of molecules, atoms, and electrons at the Si/electrolyte interface at resolution that is adequate to the size and function of basic chemical or structural building blocks.
  - Establish electrochemical quartz crystal microbalance (EQCM) as a tool to study the evolution of the silicon-electrode SEI in standard thin film electrodes.
  - Establish the role of FEC additives in improving cycling performance in carbonate-based electrolytes.

### **Accomplishments**

- Formed collaborative multiple national lab team to study fundamental phenomena that control the performance of Silicon composite electrodes.
- Established new and unique experimental capabilities to produce Si, Si/binder, Si/C model electrodes. Initiated integrated electrochemical and analytical diagnostic studies on model systems.
  - Model Si/PPy electrodes consisting of 30 nm pin-hole free films on Si wafers or Cu foil show that the PPy binder is electrochemically stable during initial cycles (up to 8 cycles).
  - PPy binds very strongly to the Si. Under some conditions of drying, possibly forming chemical bonds to the native oxide surface.
  - Very strong bonding of the PPy to the Si surface, however, produces a ion-blocking interface that prevents lithiation of the Si at normal potentials (> 5 mV positive of Li/Li<sup>+</sup>). Electronic

- conduction through the interface may still occur, resulting in significant electrolyte reduction to mostly soluble products.
- PPY will be most effective as a binder in a composite electrode structure of the polymer film that does not encapsulate the Si particles, implying an optimal volume fraction of binder and application procedure.
- EQCM measurements showed that the SEI layer of a model thin film Si electrode in Gen2 electrolyte grows continuously over the lifetime of the experiment (10 cycles). Addition of FEC (> 10 wt%) to the electrolyte yielded a much denser and stable SEI layer on our Si electrodes.
- A potential path to make a more stable SEI through the formation of a more cross-linked, less soluble polymer SEI possibly through the design of more elaborate, large molecule, fluorinated carbonates was determined.

## Future Achievements

- Explore and study range of silicon and silicon-carbon model systems materials to establish correlations between properties of active and passive components and electrochemical performance of Si composite anode.
- Explore the SEI chemistry as a function of oxide surface termination and polymer binders, which likely also participate in the SEI passivation reaction and change the reaction mechanism(s).
- Assess failure modes in Si and Si-based materials and electrodes.
- Establish *general rules* of the surface-structure-composition-property relationships for Si-based materials and electrodes.
- Assess the impact of fluorinated electrolyte additives being developed in the ABR Silicon Deep Dive program on the stability of the SEI layer on a silicon-based electrode.
- Create model compounds to help the characterization team identify electrode components that contribute to irreversible capacity and cycling inefficiencies.
- Develop new and expand existing *in situ* and *ex situ* diagnostic approaches:
  - Far- and near-field optical micro-spectrometry of electrode/electrolyte interfaces at molecular resolution.
  - Advanced EELS to study lithium transport phenomena in bulk particles, across interfaces, and through grain boundaries.
  - Surface sensitive techniques such as synchrotron XPS, soft XAS, atom probe tomography (APT) and neutron reflectometry to study the composition of interfacial layers as a function of state-of-charge, electrolyte composition, etc.
  - $^1\text{H}$ ,  $^2\text{D}$ ,  $^6\text{Li}$ ,  $^7\text{Li}$ ,  $^{13}\text{C}$ ,  $^{19}\text{F}$ ,  $^{31}\text{P}$  Multinuclear Correlation NMR spectroscopy and new *in situ* MAS NMR techniques.

## Technical Discussion

### Background

This project addresses the key technical barriers related to the battery technology development effort of the DOE Office of Vehicle Technologies:

- Low lithium-ion battery energy density, and calendar/cycle lifetimes (related to cost) for PHV and EV applications.
- Need for Si-based anode materials and composite electrodes with high specific energy, durability, costs, and safety characteristics.

Silicon electrodes for LIB systems represent the next generation of anode material. The ten fold increase in capacity possible for silicon-based systems could have a significant impact on overall electrochemical cell storage market if issues related to their cycling stability can be addressed.

This collaborative work constitutes an integral part of the concerted R&D effort within the ABR Program, which involves a five national laboratory consortium (ANL, LBNL, NREL, ORNL, SNL) to tackle the barriers associated with the development of an advanced lithium ion negative electrode based on silicon as the active material (see IV.D.7. Next Generation Anodes for Lithium-ion Batteries: Overview).

The primary objective of this project is to understand and eliminate the fundamental scientific and technical barriers to implementation of silicon-based anodes in full lithium-ion cells. To accomplish this we address the key problems that have hindered practical applications of silicon and other silicon alloy anodes in commercial lithium-ion batteries. They include:

1. Large volume changes during cycling, which result in cracking and decrepitation of the active material, and loss of electronic connectivity and mechanical integrity in the composite electrode.
2. Inherent non-passivating behavior of silicon in organic electrolytes, which results in large irreversible capacity loss and gradual electrolyte consumption during the electrode operation. A better understanding of the underlying principles that govern these phenomena is inextricably linked with successful implementation of high energy density materials such as Si in lithium-ion cells for PHEVs and EVs.

The focus of this effort is on determining the interfacial properties of a charged silicon electrode, its interactions with the electrolyte and various active and passive components of the Si-C composite electrode. By combining detailed knowledge of the electrolyte degradation species present at the interface and their physical properties, this research effort provides a better understanding of the basic function and operation of system components and assists the ABR electrode and electrolyte development team on advantageous electrolyte compositions, including salts and additives, Si and C active material surface modification, and multifunctional binders and ion and/or electron conducting electrode additives.

## Introduction

Lithium-ion batteries utilizing Si negative electrodes are inherently complex and dynamic systems. Their successful operation relies heavily on a series of complex mechanisms, involving structural transformations of  $\text{Li}_x\text{Si}$  alloys, continuous side reactions at the Si/electrolyte interface, and mechanical instability of Si-based composite electrodes. This paradigm of such Si-based lithium-ion system operation usually drives the battery toward irreversible physical and chemical conditions that lead to rapid battery degradation and failure.

The requirements for a long-term stability of silicon-based anodes are extremely stringent and necessitate control of the chemistry at a wide variety of temporal and structural length scales. The design of the next generation of high-energy silicon anodes requires a fundamental understanding of the physical and chemical processes that govern these complex systems. Although some significant advances have been made to prepare and utilize new Si-based materials and electrodes, efforts towards the understanding of their operation mechanisms and degradation modes have been insufficient and/or unsuccessful. This in turn necessitates the development and use of new characterization strategies to probe and monitor these processes.

The silicon dioxide passivation layer of silicon is generally related to its handling during synthesis and manufacturing processes. The intrinsic  $\text{SiO}_2$  passivation layer is usually found to be approximately a 10 Å thick layer of silica. More aggressive passivation regimes can yield denser layers up to 30 Å thick. Theoretical work from the BATT/BMR program had indicated that this passivation silica layer reacts with electrolyte decomposition products around 900 mV to form  $\text{Li}_4\text{SiO}_4$ . Extensive spectroscopic work from Prof. K. Edstrom group confirmed these predictions. Preliminary work focused on the role of this modified silicon passivation layer on cycling and its reactivity as a function of state of charge where a side reaction driven condensation reaction that converted the good lithium-ion conducting  $\text{Li}_4\text{SiO}_4$  to the more condensed and poor lithium ion conducting  $\text{Li}_2\text{SiO}_3$  was identified by 29-Si NMR.

This project involves rigorous diagnostic studies of model silicon and composite electrode systems to enable deployment of Si in commercial high-energy lithium-ion cells. Advanced diagnostic tools are used to gain insight into why Si-based electrodes fail and to develop ways to mitigate that failure. An emphasis is placed on specially designed model experimental systems and *in situ* and *ex situ* methods that use multiple techniques at the same time e.g., imaging with spectroscopy. The diagnostic experimental strategies involve evaluations of silicon composite electrodes as well as studies of the properties of the individual components in model system

configurations and their interphases and interfaces. Using a combination of model compound synthesis,  $^{29}\text{Si}$  NMR and electrochemical studies, the evolution of the intrinsic silica surface layer during the SEI layer formation process can be followed and the role of silica thickness and electrolyte additives e.g., 4-fluoro-1,3-dioxolan-2-one; fluoroethylene carbonate (FEC) additive can be determined.

Results of these fundamental studies will supplement other characterization efforts within this ABR Project and ultimately will be used to help design and manufacture robust Si-graphite composite anodes that can cycle stably in a full cell configuration and deliver  $>1000$  mAh/g at a coulombic efficiency close to 100% i.e., meeting the targets for high-energy lithium-ion batteries for PHEV and EV applications.

## Approach

This collaborative task involves coordinated research efforts within a five laboratory consortium to tackle the barriers associated with development of an advanced silicon-based lithium ion negative electrode. This research project targets model Si electrodes and three advanced polymer binder systems (polysiloxane, polypyrene and polyacrylic). The primary objective of this project is to understand the fundamental phenomena that control function and operation of Si-based anodes in lithium-ion batteries, including inherent poor electronic conductivity of Si and non-passivating behavior of silicon surface in organic electrolytes.

Experiments that can help unveil structure and reactivity at interfaces are particularly important because these regions determine Si-based materials performance and failure modes. These interfaces include interactions between the electrolyte, solid electrolyte interphase (SEI), polymer binder and the electrode active material. Experimental approaches aimed at probing model and composite Si electrodes at an atom, molecular or nanoparticulate level include far- and near-field IR vibrational spectroscopy (FTIR, ATR-FTIR, IR aNSOM), scanning probe microscopy, spectroscopic ellipsometry, neutron reflectivity and x-ray absorption spectroscopy (XAS) at the C 1s edge. These studies are carried out both *in situ* (under potential control) and *ex situ* on model Si electrodes.

Utilizing thin film model silicon electrodes, the role of surface passivation, electrolyte additives, and electrolyte are investigated as a function of state of charge. The thin film electrode format is conducive to a variety of spectroscopic studies and utilizing a combination of  $^{29}\text{Si}$ ,  $^7\text{Li}$ , and  $^{19}\text{F}$  NMR combined with electrochemical quartz crystal microbalance (EQCM) the interfacial properties are correlated with the observed electrochemical performance.

*In situ* spectro-electrochemical measurements using thin-film and monocrystalline Si wafer electrodes to study a binding interaction with the polymer binder are to be carried out. A hypothesis of binding of the polymer binders to Si via an acid-base reaction between the  $\text{SiO}_x$  surface functionality with the carboxylate groups of the binder is studied via monitoring of the  $\nu_{\text{C}=\text{O}_{\text{sym}}}$  and  $\nu_{\text{C}=\text{O}_{\text{asym}}}$  stretching frequencies. The binding of polymers to the graphite may produce even more subtle shifts in the vibrational spectra e.g., strong  $\pi^*$  resonance at the C K-edge from the conjugation of the allylic bonds can be used to interrogate *in situ* the stability of electronically conducting polymer polymers. These hypotheses are evaluated in close collaboration with ANL, NREL, SNL and ORNL using the baseline polysiloxane, polypyrene and polyacrylic polymers, and determine the exact nature and stability of the binding under potential control and the durability during lithiation of the Si and graphite. Relevant mechanical properties of the binders i.e., swelling, adhesion and viscoelastic behavior are also characterized.

IR, NMR, and XAS spectroscopy and neutron reflectivity measurements are used to study solution chemistry, e.g. solvation or radical initiated reactions, induced by additives, which have not been studied as well as the film forming reaction of electrolyte additives but may be as important. Results of these studies will guide the development and selection of Si and Si-based electrodes, and define electrolyte formulations that yield effective SEI layers.

## Results

We have achieved the following progress:

### 1. Basic studies of advanced binders in model Si anodes

The model electrode chosen for this study was the candidate binder spin coated onto Si wafers with a thickness of 20 – 30 nm as determined by Atomic Force Microscopy (AFM). The Si wafers were boron doped p-type Si(100) polished on one side, 500  $\mu$  thickness with 0.001  $\Omega$ -cm resistivity purchased from MTI. However, only the polypyrrene (PPY) polymer could be spin coated successfully. The PPy polymer was synthesized at ANL as another part of this ABR program. The polyvinylidene difluoride (PVdF) and polyacrylic acid (PAA) could not be spin-coated and another method to produce uniformly pin-hole free coating of this thickness could not be found. The thickness of 20 – 30 nm is critical to model the thickness of the binder if it uniformly coats the nano-sized Si particles in a composite electrode.

For the purposes of measuring the relative adhesion of the polymers to the Si, polymer layers were simply sandwiched between Si wafers by drop casting. The results are summarized in Figure IV-133. Under the drying procedures used in making composite electrodes, the adhesion of PPy was significantly better than PVdF or PAA (Li-salt). Under certain conditions, PPy binding was so strong that chemical bonding to the native oxide film was implied. These observations would explain the superior performance of the PPY binder in Si composite electrodes reported by Gao Liu (LBNL) in the relevant effort in the ABR program.

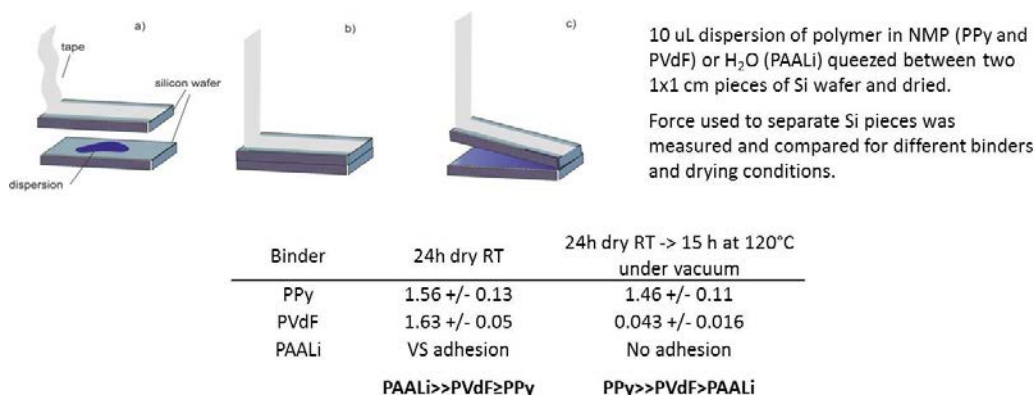


Figure IV-133: Adhesion tests of PPY, PAA and PVdF to Si following various drying procedures

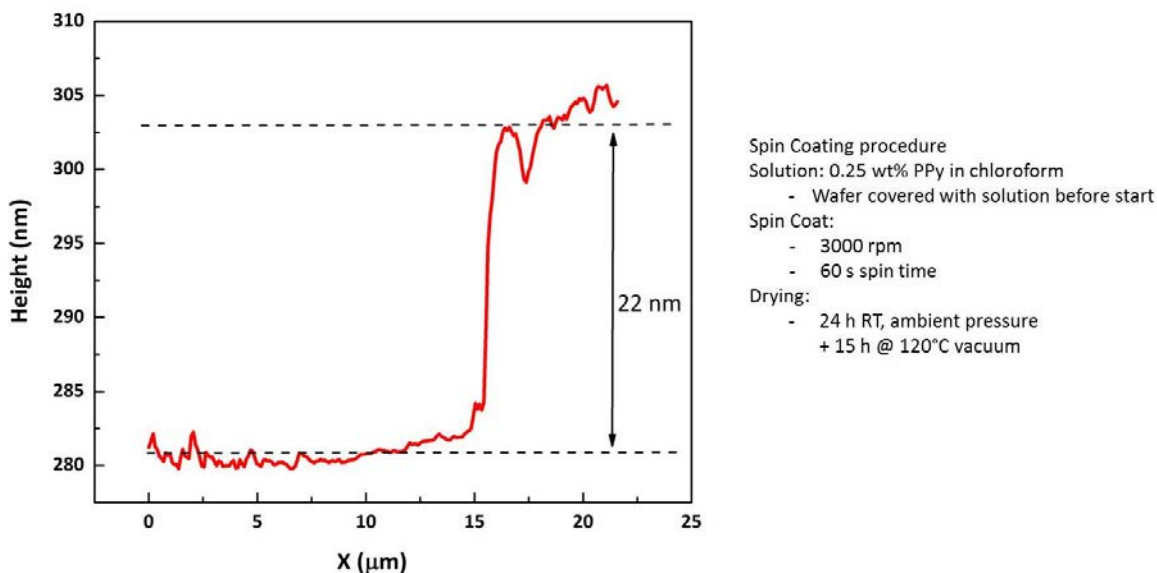


Figure IV-134: AFM profile of PPY spin-coating on Si wafer using scratch method

Further electrochemical testing and diagnostic analysis was done only using the PPY binder. Figure IV-134 shows the measurement of the spin-coated PPy film thickness on the Si(100) wafer substrate by AFM using the scratch method. In this method, a scratch made in the film using a razor blade is then examined with the AFM. For most samples, the PPy film is ~20 nm and the rms roughness of the film is ca. 2 – 3 nm. This degree of roughness makes it difficult for AFM to accurately evaluate the degree of polymer swelling upon exposure to the electrolyte as the expected film thickness increase from electrolyte sorption would be about the same as the rms roughness. A series of control SEM measurements showed that the film is homogenous and pin-hole free.

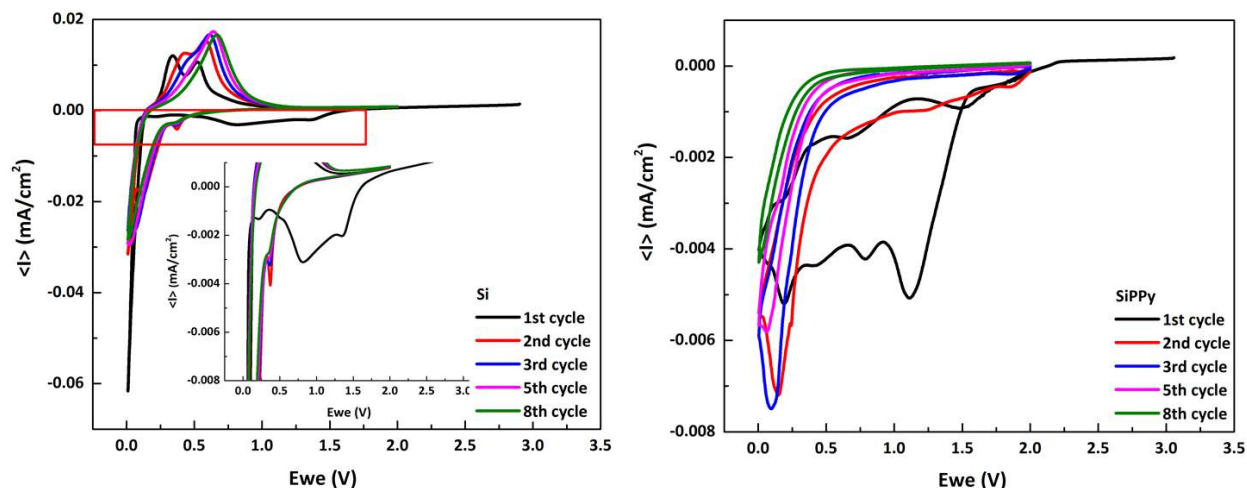


Figure IV-135: Cyclic voltammetry of (left) pristine Si wafer and (right) wafer with the PPY spin-coating

Electrochemical testing results of the Si(100) and Si(100)/PPy electrodes are shown in Figure IV-135. The electrolyte was the Gen2 baseline electrolyte used in this ABR program with 30% FEC additive. For the sake of clarity, the inset in the CVs of the pristine Si(100) wafer electrode shows the current within the same current range as the CVs of the Si(100)/PPy electrode. On the first scan, there is a cathodic process initiated at ca. 2.25 V on both electrodes and the current shows a similar pattern, which consist of four cathodic peaks as the potential is scanned to 0.05 V. However there are a few important observations that distinguish electrochemical behavior of these systems:

1. The relative intensities of the cathodic peaks, which correspond to reduction of the electrolyte components vary significantly between the two electrodes.
2. The overall charge consumed during the first cathodic scan that corresponds to the electrolyte reduction is significantly higher for the Si(100)/PPy electrode vs. the Si(100) electrode.
3. The cathodic current peaks for the Si(100)/PPy electrode are shifted toward lower potentials by ca. 0.25 V as compared to the corresponding peaks for the Si(100) electrode.
4. The Si(100) electrode surface passivates sooner than Si(100)/PPy electrode as the cycling continues.
5. There is no sign of lithiation of the underlying Si in the Si(100)/PPy even after 8 cycles.

In previous studies under the BMR program, we had identified these cathodic electrolyte reduction processes on the same pristine Si wafer lead to selective reduction of DEC to form mostly soluble products. Passivation of the surface was attributed to the lithiation of the native oxide layer, which poisons this reaction. Due to the similarity of the voltammery on the PPy/Si electrode to that of the pristine electrode in this region, we suggest the same reaction occurs at the PPy/Si interface. Below 0.05 V, the cathodic current becomes significantly higher on the pristine Si due to the onset of lithiation of the silicon as confirmed by the corresponding delithiation anodic peaks. No similar anodic behavior was observed for the PPy coated Si(100) electrode on the first and following cycles. However, electrode polarization due to charge and/or mass transport limitation through the PPy film can be responsible for this effect. The passivation of the DEC reduction reaction apparently takes two more cycles, but thereafter the surface remains active for continuous electrolyte reduction of some kind.

The electrode samples were removed from the test cell with residual electrolyte removed by rinsing with DMC (in the glovebox) and transferred (via sealed pouch) to a beamline at the Advanced Light Source (ALS) for analysis of the surface by x-ray absorption spectroscopy (XAS). The results are shown in Figure IV-136. As a control experiment, similar electrochemical tests and XAS analysis were conducted with Cu electrode spin-coated with PPy. With the Cu surface there was no electrochemical signature of the DEC reduction on the first sweep and no sign of lithiation or lithium deposition. Hence, only electrochemistry on the PPy film would be observed. The spectra showed clearly that the PPy film is not only still present but has not changed chemically by the electrochemical cycling (up to 8 cycles). The PPy film lost its adhesion to the Cu surface after 8 cycles, but otherwise there were no sign of change of PPy XAS spectral signature vs. the Si. It is also clear that there are no significant amounts of C and O containing species on the surface besides PPy, i.e. neither residual electrolyte nor organic reduction products of EC, DEC or FEC. These XAS spectra do not inform about possible inorganic species such as LiF. We conclude that for the most part the products of electrolyte reduction on the PPy/Si electrodes are soluble in the electrolyte and/or so weakly adherent to the surface that they are removed by rinsing in DMC.

The main conclusion from this study is that to be effective in a composite electrode, PPY needs to act as a “glue” between particles (Si or graphite) and not as a “coating” of the Si particles, and electrode preparation should be tailored to this function. As such, the strong adhesion of the PPY to the Si surface provides stronger and interparticle connection that lasts longer as compared to other binders.

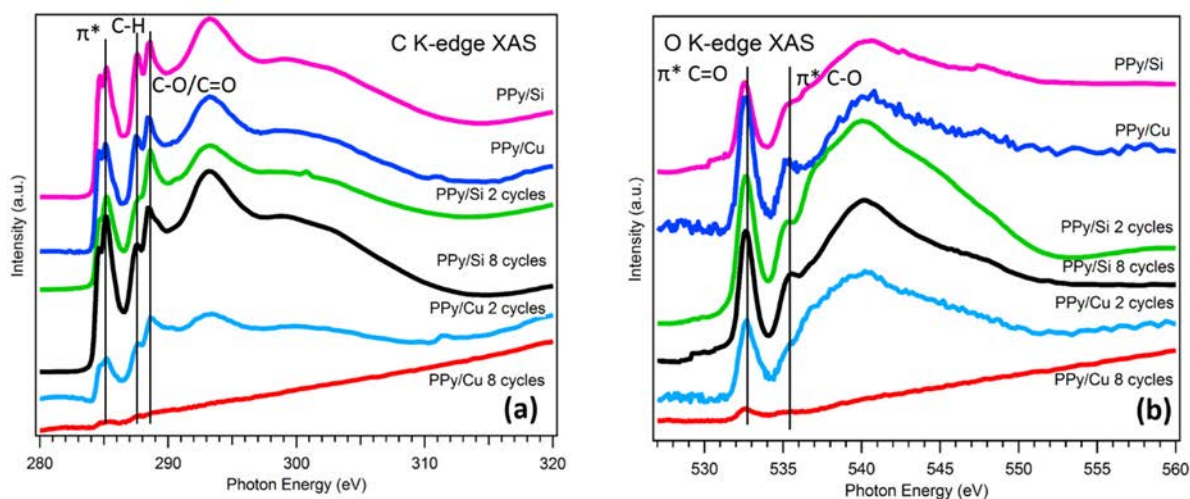


Figure IV-136: X-ray absorption spectra (XAS) from PPy films on Si and Cu before and after cycling in GEN2 electrolyte 0.005 – 2 V vs. Li/Li<sup>+</sup>

## 2. Interfacial Activity of Silicon Anodes

The interface between the silicon electrode and electrolyte is a key point of contact in the electrochemical cell. Silicon is well known to have an unstable SEI layer due in part to its reactivity at high states of charge and lack of dimensional stability on cycling, as opposed to graphitic carbon, which has exceptional dimensional stability [1,2]. The initial passivation layer of silicon is between 1-3 nm of silica. Previous work has shown that this layer is unstable in the cell environment and reacts to initially form Li<sub>4</sub>SiO<sub>4</sub> and eventually within the SEI layer reacts to form the stable end-member Li<sub>2</sub>SiO<sub>3</sub> [3-5].

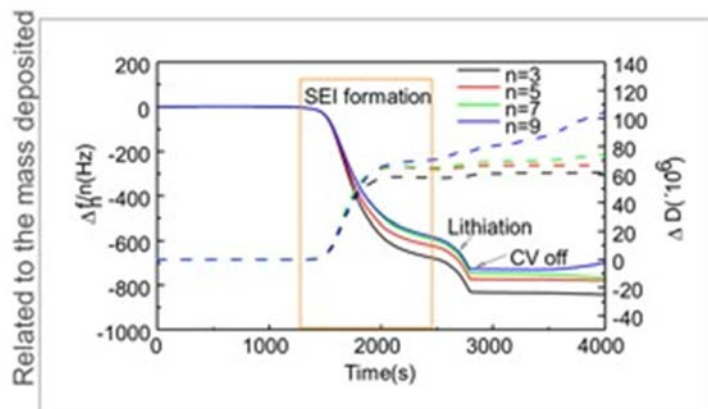


Figure IV-137: EQCM studies of the silicon model electrode. Solid line – relative mass changes during the cathodic scans. Dashed line – corresponding variations of the SEI layer density

EQCM studies of this system (Figure IV-137) were undertaken to establish how the passivation layer reactivity is affected by the addition of the common electrolyte additive FEC to the Gen2 electrolyte system. Without FEC, the system was found to form a relatively porous SEI layer that got thicker as a function of state of charge. This is in line with expectations based on previous interfacial models [6]. Addition of FEC (10 wt%) to the electrolyte was found to create a much denser SEI layer than the SEI formed in Gen2 electrolyte. Building a controlled amount of silicon dioxide into the silicon electrode (5 nm SiO<sub>2</sub>/150 nm Si) was also studied as a function of electrolyte. In these studies the silica layer, formed in as part of a post-deposition process in the PVD deposition system, was found to also make a dense SEI layer on the electrode, while addition of FEC to the Gen 2 was found to significantly inhibit any electrochemical activity. As the silica layer formed was 2-3X thicker and much denser than a native layer. On extended cycling, 29-Si NMR studies have shown that the signals attributable to the various lithium silicates (~1nm native oxide sample) diminish which may indicate dissolution or reactions with SEI components to bring any specific Si-containing species below detection limits. Further studies with the Veith group at ORNL are planned to assess the optimal silica thickness for these studies. In addition to evaluating the role of the silica passivation layer on the silicon electrode, we have initiated studies with the Zhang Group (ANL) to study the role of fluorinated electrolytes. Initial work has focused on a purified version of FEC mixed with Gen2 electrolyte. The Zhang group had previously shown that commercial FEC was in fact a mixture of ~90% FEC, ~8% 3,4 DFEC, and ~2% 4,4 DFEC. The difluoro-FEC compounds also have been investigated as additives but appear at this time to work by an alternative mechanism that is not as effective as FEC alone. It was found that at levels below 10 wt% the FEC appears to have minimal impact on the electrode performance. This is in agreement with the electrochemical cycling literature that amounts > 10 wt% are needed as the lifetime in the electrolyte is limited [6].

In this task, we also explored how an electrolyte additive (fluorinated ethylene carbonate – FEC) mediates the thickness and composition of the solid electrolyte interphase formed over a silicon anode *in situ* as a function of state-of-charge and cycle. To accomplish this we utilized neutron reflectivity to probe the growth and composition of the SEI. The use of neutrons is advantageous due to their sensitivity to Li and H species which make up the SEI layer. In NR, the specular reflection of neutrons from an interface is measured as a function of the wave vector transfer,  $Q = 4\pi\sin(\theta)/\lambda$ , perpendicular to the sample surface. The angle of incidence  $\theta$  is between the incoming neutron beam and the sample surface, and  $\lambda$  is the wavelength of the neutron. Analyzing the neutron reflectivity gives us information about the thickness and composition of the film layers.

Representative data are shown in Figure IV-138. The neutron measurements were coupled with traditional XPS and FTIR measurements to provide chemical specificity and link with prior studies. These studies were compared to electrochemical cells without FEC.

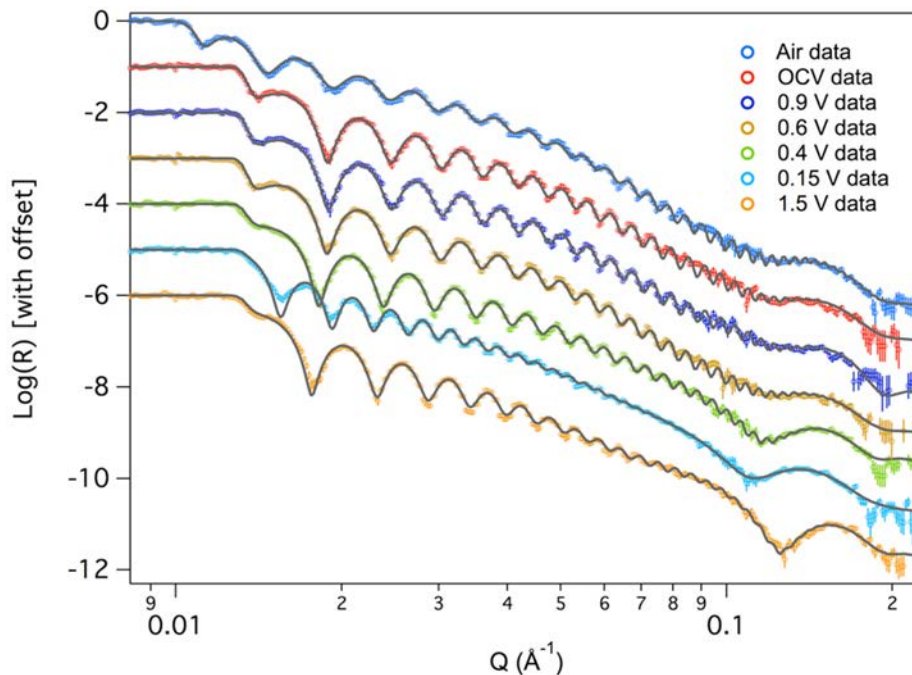


Figure IV-138: Neutron reflectometry data collected for silicon electrodes at various states of charge

We show the FEC condenses on the surface at open circuit voltage then is reduced to C-O containing polymeric species around 0.9 V (vs. Li/Li<sup>+</sup>). The resulting film is about 50 Å thick.

Upon further lithiation (0.4 V vs. Li/Li<sup>+</sup>) the chemistry evolves from a clear polymerization of the C=O functionality to more Li-O-C-D polymeric species with a low concentration of LiF (~14 at%). The FEC based SEI at 0.4 V increases to ~ 70 Å thick.

NR data collected for the silicon anode with extensive Li cycling between 0.15 and 1.5 V revealed significant and dynamic changes in the SEI thicknesses and composition. As demonstrated in Figure IV-139, the SEI layer increased in thickness by about 12-13 Å with lithiation, and its nuclear scattering length density (SLD – measure of the average nuclear potential of the films) decreased to about 2.3±0.3 (from 2.6±0.3) consistent with the addition of lithium. Upon delithiation the SEI shrunk to its prelithiation thickness and the SEI increased to 2.5±0.1. This swelling and contracting of the SEI layer thickness is consistent with the “breathing” reported for silicon anodes measured by previous NR studies as well as XPS, TOF-SIMS, and atomic force microscopy studies.

At this point, we will compare this data with previously reported NR data collected for electrolytes without FEC in the same electrochemical experiment. The OCV for both sets of data show a similar condensed layer with a thickness of about 50 Å, indicating a similar starting point to SEI formation. However, with cycling the previous non-FEC containing electrolyte, data showed the immediate formation of SEI layer with a thickness between 180 and 250 Å. This SEI layer shows a similar “breathing” as observed for the data in this work, however the magnitude of the breathing (60 Å) is significantly larger than the 13 Å measured for the FEC containing electrolyte. Comparing the SEI compositions of the two NR studies reveal that the non-FEC containing electrolyte SEI (at 0.12 V vs. Li/Li<sup>+</sup>) was comprised of similar functionality (i.e. C-C/C-H, C-O, C=O, O-C=O, -CO<sub>3</sub>, LiF, POF, etc.), but the organic content comprised about 4 at% carbon. There was a correspondingly larger increase in inorganic F-containing species (~ 80% LiF) in non-FEC electrolyte. This is significantly less organic components than the SEI produced from FEC containing electrolyte.

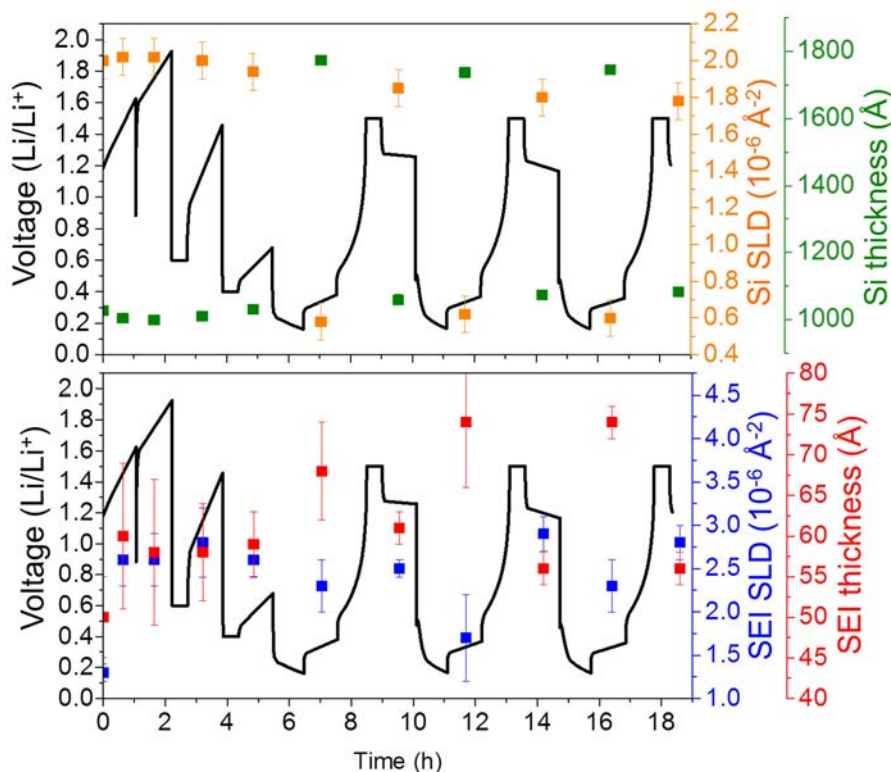


Figure IV-139: Plots of SLD values and layer thicknesses as a function of state of charge for silicon (top) and the SEI (bottom)

From the data described above, upon cycling the SEI layer becomes more organic at high states of lithiation and more inorganic at low states of lithiation due to dissolution of the polymer. This thin polymeric layer likely has the flexibility to bend and readjust in a manner that LiF-based SEI layers would not. This flexibility ensures a more stable SEI that would more effectively passivate the surface against further reactions. Despite the clear improvement in SEI chemistry with the use of FEC, there are still problems evident with the FEC containing cells. In both cases, the “breathing” measured for the SEI originates from the consumption of electrolyte. This consumption lowers the cycle life of the electrode by consuming the electrolyte needed to move lithium ions. The thinner FEC SEI and the much reduced “breathing” of the FEC SEI results in less electrolyte consumption resulting in the reported increase in cycle life of Si based electrodes. However, even these batteries fail with time as the FEC gets consumed. This points to a potential path to make a more stable SEI through the formation of a more cross-linked, less soluble polymer SEI possibly through the design of more elaborate, large molecule, fluorinated carbonates. It would be interesting to explore this chemistry as a function of oxide surface termination and polymer binders, which likely also participate in the SEI passivation reaction and change the reaction mechanism(s).

## Conclusions

- The primary objective of this effort is to provide basic understanding and effective mitigation of key R&D barriers to implementation of silicon-based anodes.
- The technical approach involves fundamental diagnostic studies of basic properties of the Si anode active and passive components (e.g. polymer binders) in model systems.
- Utilizing a combination of  $^{29}\text{Si}$  NMR and EQCM we were able to determine that the (1) thickness of the silicon oxide layer has a critical role in controlling the initial lithiation reactions, and (2) the oxides converted to lithium silicates appear to have a lifetime in the cell as they may be reactive with the SEI layer components to become soluble species.
- Gen2/FEC mixture forms a significantly denser SEI layer than the simple Gen2 baseline system (re)confirming the protective role of FEC. EQCM data indicates that since FEC has a lifetime in the electrolyte and reacts irreversibly to form a passivating film, amounts below 10 wt% may be ineffective in extending cycle life.

- To be effective in a composite electrode, PPY needs to act as a “glue” between particles (Si or graphite) and not as a “coating” of the Si particles, and electrode preparation should be tailored this function. As such, the strong adhesion of the PPY to the Si surface provides improved interparticle connection vs. other binders.

## Products

### Presentations/Publications/Patents

1. F. Dogan, L. D. Sanjeewa, S. –J. Hwu, J. T. Vaughey “Electrodeposited Copper Foams as Substrates for Thin Film Silicon Electrodes” *Sol. State Ionics*, 228, 204-207 (2016).
2. F. Dogan, J. T. Vaughey “Effect of Surface Termination on the Electrochemical Performance of Silicon Thin Films” *J. Electrochem Soc.* 163, A62-A66 (2016).
3. Aude A Hubaud, Zhen Zhen Yang, D.J. Schroeder, Fulya Dogan, Lynn Trahey, John T Vaughey “Interfacial Study of the Role of SiO<sub>2</sub> on Si Anodes using Electrochemical Quartz Crystal Microbalance” *J. Power Sources*, 282, 639 (2015).
4. L. Terborg, M. Ling, K. Nie, A. Dahi, C. Wu, J. Guo, P. N. Ross, G. Liu, and R. Kostecki, “The effect of Polymer Binder on the Electrochemical Performance of Si/C Anodes”, PRiME 2016, October, 2-7, 2016, Honolulu, HI, USA.
5. M. Ayache, D. Jang, and R. Kostecki, “Nanoscale IR Near-Field Imaging of the SEI Layer on an HOPG Electrode”, 227th ECS Meeting, Chicago, IL, May 24-28, 2015.
6. Robert Kostecki, “Battery Characterization and Diagnostics Across Length and Time Scales”, 10<sup>th</sup> China-U.S. Electric Vehicle and Battery Technology Workshop, Beijing P.R.China, March 29-30, 2015 (invited talk).
7. Robert Kostecki, Maurice Ayache, Simon Lux, Ivan Lucas, “Near-field optical imaging of the SEI layer on a Sn anode”, 249th ACS National Meeting & Exposition March 22-26, 2015, Denver, CO, USA (invited talk).
8. Robert Kostecki, Maurice Ayache, Angelique Jarry, Ivan Lucas, “Chemical Imaging of Interfaces and Interphases in Lithium-ion Anodes”, International Battery Association (IBA) and Pacific Power Source Symposium, January 5-9, 2015, Waikoloa Village, Hawaii, USA (invited talk).
9. M. Ayache, J. Syzdek, I. Lucas, N. Norberg and R. Kostecki, “Interfacial Studies of the SEI Layer on a Tin Electrode”, 2014 ECS and SMEQ Joint International Meeting Cancun, Mexico, October 5-9, 2014.
10. Maurice Ayache, Simon Lux, and Robert Kostecki, “Nanoscale Chemical Mapping of the Solid Electrolyte Interphase in Lithium-ion Systems”, SciX Conference, September 29, 2014, Reno, NV (invited talk).
11. Robert Kostecki, Maurice Ayache, Angelique Jarry, Ivan Lucas, Alexander McLeod, Richard Russo, Jaroslaw Syzdek, Vasileia Zormpa, “*In situ/in operando* characterization of electrical energy storage systems”, 65th Annual Meeting of the International Society of Electrochemistry, August 31 – September 5, 2014, Lausanne, Switzerland (keynote lecture).
12. F. Dogan, A. A. Hubaud, Zhen Zhen Yang, D. L. Proffit, D. J. Schroeder, J. Vaughey “Reactions at Silicon Electrode Surfaces” 20th International Conference on Solid State Ionics, Keystone, CO, 2015.
13. J. Vaughey, F. Dogan, A. Hubaud, D. Schroeder “Side Reactions and Cycling Efficiency with Silicon Electrode Surfaces” 228th Meeting of the Electrochemical Society, Phoenix, AZ, 2015.

### References

1. M. N. Obrovac, V. L. Chevrier *Chem. Rev.*, 114, 11444–11502 (2014).
2. X. Su, Q. Wu, J. Li, X. Xiao, A. Lott, W. Lu, B. W. Sheldon, *J. Wu Adv. Energy Mater.*, 4, 1300882 (2014).
3. A. A. Hubaud, Z.Z. Yang, D.J. Schroeder, F. Dogan, L. Trahey, J. Vaughey *J. Power Sources*, 282, 639 (2015).

4. B. Philippe, R. Dedryvère, M. Gorgoi, H. Rensmo, D. Gonbeau, K. Edström *Chem. Mater.*, 25, 394–404 (2013).
5. S. -Y. Kim, Yu Qi *Journal of the Electrochemical Society*, 161, F3137-F3143 (2014).
6. C. Xu, F. Lindgren, B. Philippe, M. Gorgoi, F. Björefors, K. Edström, T. Gustafsson *Chem. Mater.*, 27, 2591–2599 (2015).

## IV.D. Next-Generation Lithium-Ion Chemistries: “Improvements in Cell Chemistry, Composition, and Processing”

### IV.D.1. Advanced High Energy Lithium-Ion Cell for PHEV and EV (3M Company)

**Jagat D. Singh, Program Manager**

3M Center, Building 209-2C-26  
St. Paul, MN 55144  
Phone: 651-575-1230; Fax: 651-736-7478  
E-mail: [jdsingh@mmm.com](mailto:jdsingh@mmm.com)

**John Tabacchi, NETL Program Manager**

National Energy Technology Laboratory  
3610 Collins Ferry Road  
Morgantown, WV 26505  
Phone: 304-285-4764  
E-mail: [john.tabacchi@netl.doe.gov](mailto:john.tabacchi@netl.doe.gov)

Start Date: October 2013

End Date: March 2016

#### Abstract

#### Objectives

Leverage a cross-functional team to develop and demonstrate an advanced high energy lithium-ion cell with superior performance envelope. The specific deliverables include:

- Baseline cell, based on the advanced materials developed in 3M’s current contract number DE-EE0005499 titled, “High Energy Novel Cathode/Alloy Automotive Cell”.
- Advanced cell > 2Ah, achieved by cell level integration of high capacity Si anode with  $\geq 15\%$  improvement in lithiated volumetric capacity, high voltage cathode with 10% increase in Cathode Energy Factor (CEF), advanced electrolyte and advanced stable Si anode composite with novel conductive polymer binder.

#### Technical Barriers

The lithium-ion battery (LIB) shows a remarkable robustness as witnessed through its application in today’s world of portable consumer electronics, despite a quasi-stable chemistry. The operation at high voltages helps provide increase in the energy along with significant challenges in life performance. The development of advanced materials (anode, cathode and electrolyte) is important to address this challenge. The key technical barriers are:

- Short term cycle life and low rate capability
- High voltage electrolyte stability
- Si alloy volume expansion over life

#### Technical Targets

The technical targets are:

- Develop a >2Ah advanced high energy lithium-ion cell for EV and PHEV applications.
- Develop a high voltage NMC based cathode.

- Develop electrolyte for high voltage NMC and Si alloy anode.
- Develop a high capacity Si alloy anode.
- Develop advanced stable Si anode composite with novel conductive polymer binder.

## Accomplishments

The key accomplishments in this project are:

- Shipment of baseline and advanced cell (18650 format, >2 Ah to Argonne National Laboratory by 3M.
- Optimized cathode synthesis and scale up (100+ kg) of baseline and advanced high voltage NMC cathode material by Umicore.
- Optimized anode synthesis and scale up (100+kg) of baseline and advanced Silicon alloy anode by 3M.
- Research and development of advanced materials, i.e., high energy and high voltage (>4.5V) NMC based cathode and Silicon alloy anode.
- Identified electrolyte formulations after screening multiple formulation electrolyte additives, which synergistically work with high voltage cathode and Si alloy anodes.
- Gap analysis of baseline and advanced cells by General Motors (GM).
- Evaluation of pouch cells with advanced anode and cathode by GM.
- Multiple iteration of stack pouch cells assembly by Iontensity, demonstrating improvement in Wh/L and Wh/kg.
- Down selected advanced chemistry, i.e., Silicon alloy anode and high voltage NMC based cathode for manufacturing-ability study.
- Sampling of the same R2R electrode coating with advanced materials to collaborators, thereby, helping screen different electrolyte formulations and additives.
- Identified the voltage window to balance the cell energy to cycle life performance. More than 15 cells (18650 format) for Assembled 18650 cells with advanced chemistry and sampled to GM for evaluating the effect of full cell UCV to cycle life.
- Army Research Laboratory sampled electrolyte formulations and additives to help improve the long term performance of advanced chemistry in full cells such as 18650 and pouch cells.

## Technical Discussion

### Introduction

Lithium Ion Battery (LIB) technology's potential to enable a commercially viable high energy density is the key to a lower \$/Wh, i.e., a low cost battery. The design of a high energy LIB (HE-LIB) with high power, safety and long life is a challenge that requires cell design from the ground up and synergy between all components. 3M Company (3M), the Recipient, strongly believes that this challenge can be addressed by 'teaming' key commercial businesses [General Motors (GM), Umicore, and Leyden Energy (Leyden) which underwent a name change to Iontensity subsequently] as well as labs [Army Research Laboratory (ARL) and Lawrence Berkley National Laboratory (LBNL)]. The technology from each team member will be complementary and a close working relationship spanning the value chain will drive productivity. This HE-LIB would provide more energy efficient and environmentally friendly vehicles, meeting or exceeding performance expectations and goals, making America less dependent on imported oil.

## Approach

This project takes a team approach to address the project challenges. Each team member brings strong technical expertise to the table. The team consists of:

- 3M: Development of advanced cathode, anode and electrolyte. Sample 18650 cells.
- Iontensity: Design, test, diagnose and sample pouch cells.
- Army Research Laboratory: Development of advanced electrolytes.
- Lawrence Berkeley National Laboratory: Development of advanced conductive binder for Si alloy anode.
- General Motors: Evaluate cells and perform gap analysis vs. vehicle requirements.
- Umicore: Develop cathode synthesis and demonstrate pilot scale manufacturing.

The proposed work consists of two distinct phases. Phase I will focus on advanced materials development and baseline validation. Phase II will focus on iterative integration of advanced materials and testing in 18650/Pouch cells.

## Results

The deliverables of this program included integrating high-performance, commercially feasible materials, thereby allowing a transformative step change in energy density and cost reduction of LIB for automotive applications. Table IV-15 contains the results and accomplishments.

3M contribution to this project was the materials development of anode and cathode powders. 3M also showed the commercial scale manufacturing feasibility of Si alloy anode powder. The cathode powder was scaled to multiple kg levels for making 18650 cells and transferring the cathode synthesis knowhow to Umicore. Below are the key accomplishments from the 3M team.

3M Anode team made significant progress in improving the performance of Si alloy anode with improvement in the alloy microstructure. (See Figure IV-140, Figure IV-141.) The change was achieved by improving the alloy manufacturing process and changes to the composition.

**Table IV-15: Activity Summary and Accomplishments by 3M Company**

Goal & Objectives	Results and Accomplishment
Develop high capacity cathode performance	<ul style="list-style-type: none"> <li>a. Developed multiple advanced NMC based cathode candidates (core shell structure and particle coated structure).</li> <li>b. Demonstrated Lithiation capacity up to 250 mAh/g and &gt;95% capacity retention in half coin cells after 50 cycles at &gt;4.5V vs Li.</li> <li>c. Down selected final advanced cathode (particle coated structure) based on 1st cycle efficiency, energy, cycle life in full cells, lower gas generation and better rate capability.</li> </ul>
Develop high capacity Si alloy anode performance	<ul style="list-style-type: none"> <li>d. Developed multiple advanced Si alloy anode candidates with different formulations, surface treatments and particle morphology.</li> <li>e. Demonstrated capacity of &gt;1100 mAh/g of base Si Alloy anode material and &gt; 95% capacity retention in half coin cells after 50 cycles.</li> </ul>
Develop binder for high capacity Si anode performance	<ul style="list-style-type: none"> <li>f. Developed multiple candidates of binder for advanced Si anode.</li> <li>g. Evaluated performance of binder in full cells</li> <li>h. Improved the electrode areal capacity (3mAh/cm<sup>2</sup>)</li> </ul>
Advanced electrolyte performance	<ul style="list-style-type: none"> <li>i. Investigated multiple formulations to evaluate synergistic performance with a &gt;4.5V cathode and Si/graphite anode</li> <li>j. Down selected final electrolyte formulation for 18650 cells sampling to GM and ANL</li> </ul>
Demonstrate advanced material synthesis for large cell testing and commercial feasibility	<ul style="list-style-type: none"> <li>k. Successfully optimized materials synthesis parameters for both advanced anode and advanced cathode to establish a commercially scalable and viable process.</li> <li>l. Successfully scaled up advanced anode (Si alloy type) in &gt;100 kg quantities. Manufacturing scale up plan based on customer demand.</li> <li>m. Successfully scaled up advanced cathode in &gt;30 kg quantity. Manufacturing scale up plan based on customer demand.</li> </ul>
Demonstrate advanced materials performance in >2.0Ah cells	<ul style="list-style-type: none"> <li>n. Demonstrated advanced chemistry in an 18650 cell, &gt;2.0Ah, with energy improvement, rate capability at different temperatures, pulse characterization and life performance.</li> <li>o. Also demonstrated advanced chemistry in a pouch cells.</li> </ul>
Ship baseline cells for testing	<ul style="list-style-type: none"> <li>p. Successfully delivered 12, &gt;2.0 Ah, 18650 cells to Argonne National Laboratory.</li> </ul>
Ship advanced cells for testing	<ul style="list-style-type: none"> <li>q. Successfully delivered 12, &gt;2.0 Ah, 18650 cells to Argonne National Laboratory.</li> </ul>

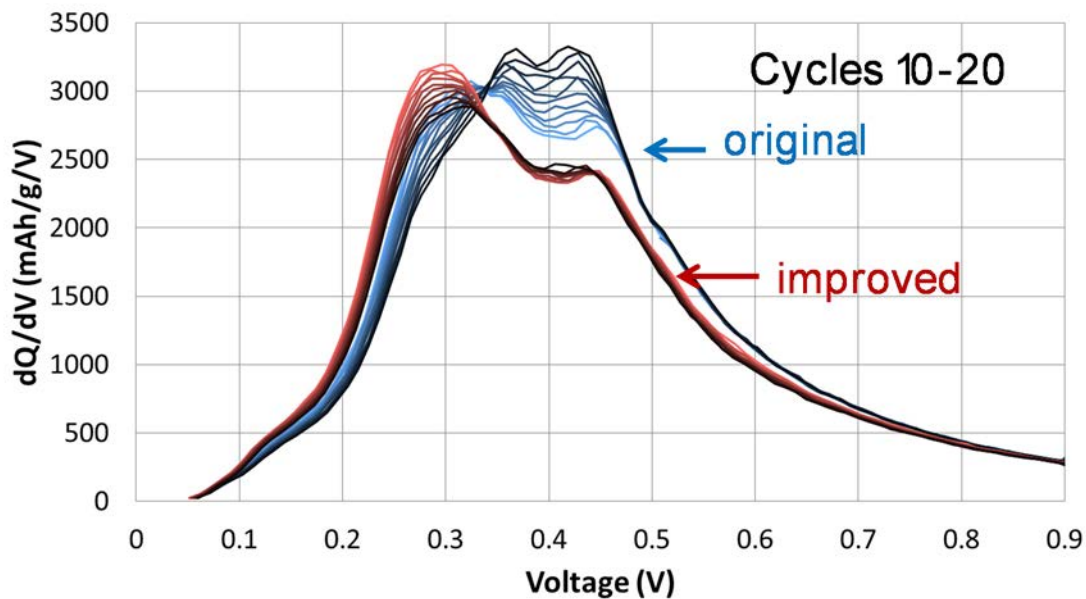


Figure IV-140: dQ/dV comparison of original Si alloy and the new version of Si alloy with improved microstructure

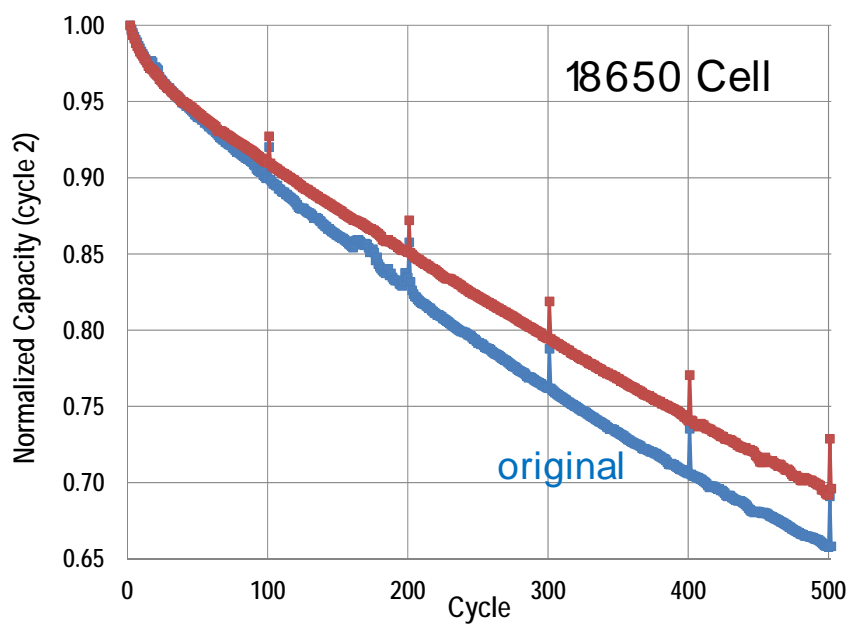


Figure IV-141: Cycle life comparison (accelerated testing) of original Si alloy and the new version of Si alloy with improved microstructure

18650 cells with improved microstructure show lower fade than the 18650 cells with the original Si alloy. Various techniques to study particle coating were also studied. Figure IV-142 shows the effect of pitch coating on the Si alloy anode particle.

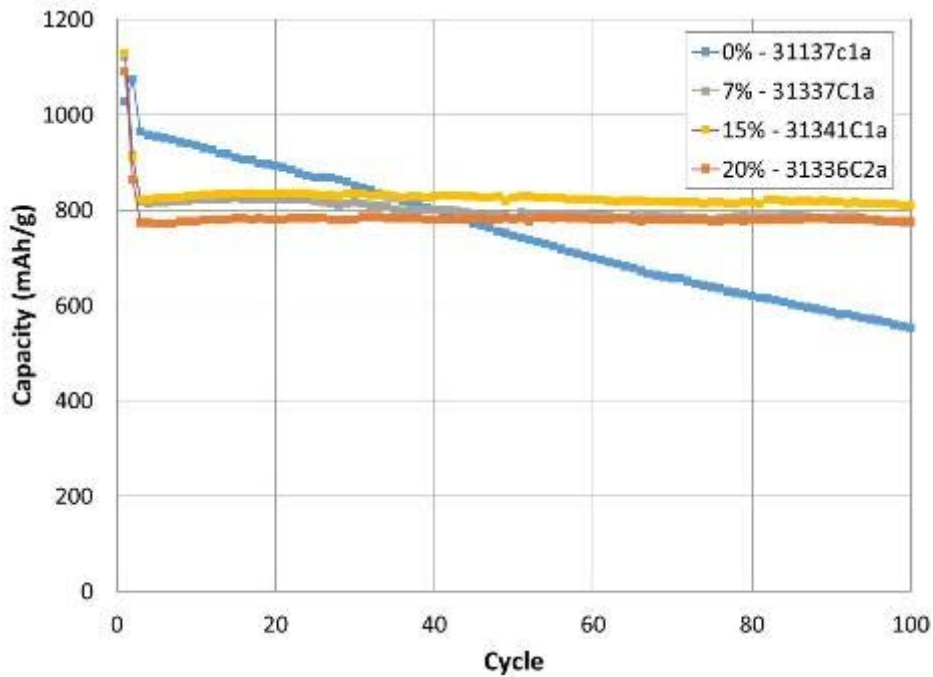


Figure IV-142: Half-cell cycling of pitch coated V11 annealed at 500 °C, pitch amounts are listed in the legend.

The final advanced Si anode chemistry was decided by appropriately selecting the material formulation, surface treatment and manufacturing scalability for reversible capacity and 1st cycle efficiency. Surface treatment was optimized for lower reactivity and better electrical network during life testing. Table IV-16 compares the properties of baseline and advanced anode materials.

**Table IV-16: Advanced and Baseline Anode Material Properties Comparison**

Si Alloy	BET (m <sup>2</sup> /g)	1st Lithiation (mAh/g)	1st Delithiation (mAh/g)	1st Delithiation (mAh/cc)	1st cycle Efficiency (%)	Manufacturability
Advanced Material	--	1170	1060	3370	90.4	✓
Baseline Material	3.5	1050	900	3280	85.7	✓

Two concepts were investigated for developing the advanced high voltage (>4.5V) NMC based cathode material. Concept 1 employed a core shell structure and concept two employed a particle coating structure. Concept two was selected for the advanced cathode material selection. Figure IV-143 shows the different cathode candidates. Finally New\_C622 was selected. Table IV-17 compares the properties of baseline and advanced cathode materials.

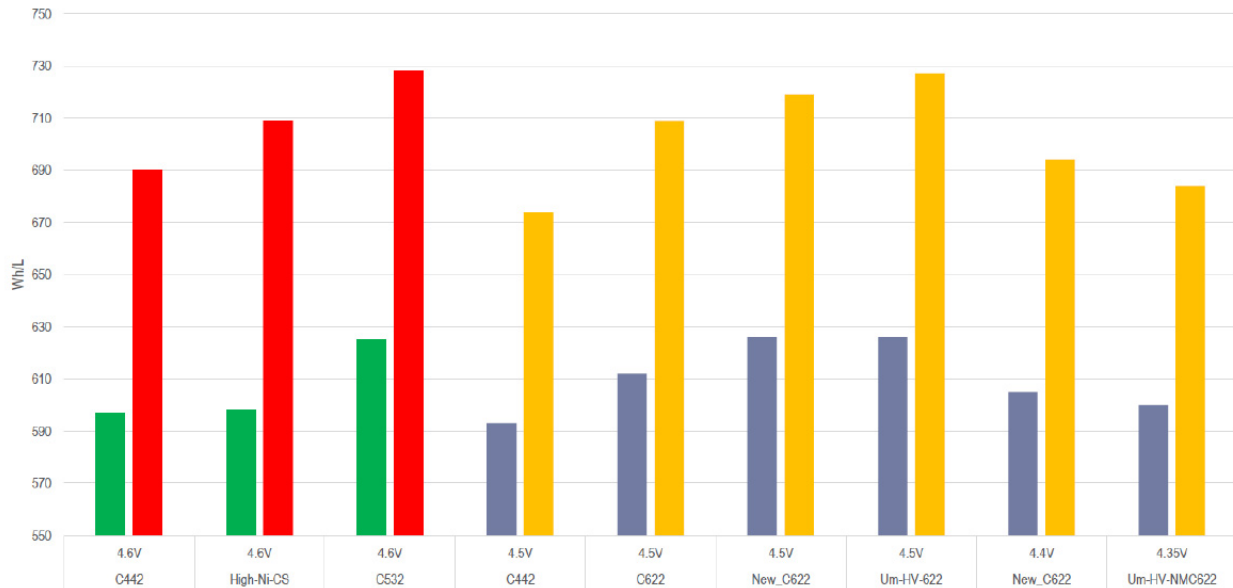


Figure IV-143: Compares the 18650 energy with different cathode candidates. The taller bar are with Si/graphite anode and the shorter bar is with graphite only anodes

**Table IV-17: Advanced and Baseline Cathode Material Properties Comparison**

Cathode	BET (m <sup>2</sup> /g)	1st Lithiation (mAh/g)	1st Delithiation (mAh/g)	1st cycle Efficiency (%)	Manufacturability
Advanced Material	0.31	230	211	91.9	✓
Baseline Material	--	273	227	83.3	✓

The above selected anode and cathode materials were scaled up in 10's to 100's of kg and then roll-to-roll coatings were made. The anode and cathode used coating runs are shown in Figure IV-144 (a and b). Over 40 of 18650 format cells were assembled for shipping to GM and DOE designated facility. The cells shipped to GM are summarized in Table IV-18

# Coating Run 743C

## Coating Request Information

Requestor	Singh
Request Date	11/2/2015
Ctg Type	Cathode
Project	Other
Type	Internal Data
Customer	
Format	18650
Foil	Al 15 micron
Reference #	Unique

	Description	Lot or NB Nbr	Ah/g	% Solids
Active Material 1	C622 (T2652)			94
Active Material 2				
Binder	PVDF			3.5
Conductive	Super P			1.25
Misc	KS6L conduct dilutar			1.25
Est. Amt of Active (kg)	6	Design 1st Lithiation mAh/cm2		
Coating Patch Length (cm)	61	Total mg/cm2 (side 1)		25.55
		Total mg/cm2 (side 2)		25.55

**Request Notes:** Advanced Cathode for DOE final cell deliverable. Cathode material available by 11/09/2015.

## Coating - Run Information and QC Summary

Scheduled	Yes	Tgt:	12/10/2015
Coating Number	743C		
Completed	Yes		12/10/2015
Total Length Coated (m)	45		
Electrode Format	18650		
Foil: Type	Al	Thickness	15
Dispersion Number			

### QC Summary Data

Thickness After Drying (microns)		
4 pt Probe Resistivity (ohm cm)		
GP Cycler File Name		
Coin Cell: Vs 'Li'		
<b>Total mg/cm<sup>2</sup></b>		
Min. #####	Max. #####	Avg. 25.27

Coating (Input in 'mm')	'S1'	'S2'		'S1'	'S2'
Coating Length: C1,C2	610	590	MFZ Length: U1,U2	60	80
Line Speed (m/min)	0.5	0.5	Tension (N)	14	14
'S2' Head Offset			'S2' B Roll-Sensor Length		
Comma Roll Gap (μ)			Comma Roll Min Gap (μ)		
<b>Roll Settings</b>					
Comma Roll Control	Fail	Fail	C Roll Control	Fail	Fail
Min Gap Length			Start Position		
Min Gap Position			Stop Position		
Roll Speed (m/min)	0.525	0.525	Roll Speed (m/min)		
<b>Dryer Settings</b>					
			Zone 2 Temp (°C)	130	130
Zone 1 Temp (°C)	110	110	Zone 2 Fan (Hz)	25	25
Zone 1 Fan (Hz)	45	45	Exhaust Fan (Hz)	35	35

# Coating Run 744A

## Coating Request Information

Requestor	Singh
Request Date	11/2/2015
Ctg Type	Anode
Project	Other
Type	Internal Data
Customer	
Format	18650
Foil	Cu 18 micron
Reference #	Unique

	Description	Lot or NB Nbr	Ah/g	% Solids
Active Material 1	CV7(lot9J49)			60
Active Material 2	BTR-918-II			18
Binder	LiPAA 250K ~7pH	2-20-13		8
Conductive	Super P			1
Misc	KS6L conduct dilutar			13
Est. Amt of Active (kg)	1.2	Design 1st Lithiation mAh/cm2		5.5
Coating Patch Length (cm)	80	Total mg/cm2 (side 1)		6.9
		Total mg/cm2 (side 2)		6.9

**Request Notes:** Advanced Anode for DOE final cell deliverable. Anode material available by 11/09/2015.

## Coating - Run Information and QC Summary

Scheduled	Yes	Tgt:	11/19/2015
Coating Number	744A		
Completed	Yes		11/19/2015
Total Length Coated (m)	37		
Electrode Format	18650		
Foil: Type	Cu	Thickness	18
Dispersion Number			

### QC Summary Data

Thickness After Drying (microns)		
4 pt Probe Resistivity (ohm cm)		
GP Cycler File Name		
Coin Cell: Vs 'Li'		
<b>Total mg/cm<sup>2</sup></b>		
Min. 7.11	Max. 7.26	Avg. 7.17

Coating (Input in 'mm')	'S1'	'S2'		'S1'	'S2'
Coating Length: C1,C2	800	750	MFZ Length: U1,U2	60	110
Line Speed (m/min)	0.6	0.6	Tension (N)	14	14
'S2' Head Offset			'S2' B Roll-Sensor Length		
Comma Roll Gap (μ)	186	186	Comma Roll Min Gap (μ)		
<b>Roll Settings</b>					
Comma Roll Control	Fail	Fail	C Roll Control	Fail	Fail
Min Gap Length			Start Position		
Min Gap Position			Stop Position		
Roll Speed (m/min)	0.6	0.6	Roll Speed (m/min)		
<b>Dryer Settings</b>					
			Zone 2 Temp (°C)	60	60
Zone 1 Temp (°C)	60	60	Zone 2 Fan (Hz)	14	20
Zone 1 Fan (Hz)	45	30	Exhaust Fan (Hz)	35	35

Figure IV-144: (a). Advanced cathode roll to roll coating details for final deliverable cells. (b). Advanced anode roll to roll coating details for final deliverable cells

**Table IV-18: Average and Standard Deviation Data for Final Deliverable Cells**

Rate	(mAh)		Irreversible % (After 1st cycle)	(mAh)		Irreversible % (after 3 cycles)	(mAh)					
	C/15	C/15		C/10	C/10		C/5	C/5	C/2	C/2	1C	1C
Cycle #	0	0		1	2		3	4	5	6	7	8
Avg	3390	2782	17.9%	2865	2881	15.0%	2864	2864	2823	2818	2759	2751
St Dev	52	57	0.5%	56	54	0.5%	53	53	53	52	56	56
Relative St Dev	1.5%	2.0%	3.0%	2.0%	1.9%	3.0%	1.9%	1.8%	1.9%	1.9%	2.0%	2.0%

Figure IV-145 shows the Wh/kg (wet laminate) performance of the cell. The gravimetric energy can be increased by approximately 24% by further cell design optimization. The key drivers for this energy improvement are thinner separator, wider cathode and anode electrodes, smaller number for N/P ratio, tighter winding, etc. Figure IV-146 shows the rate capability on energy basis.

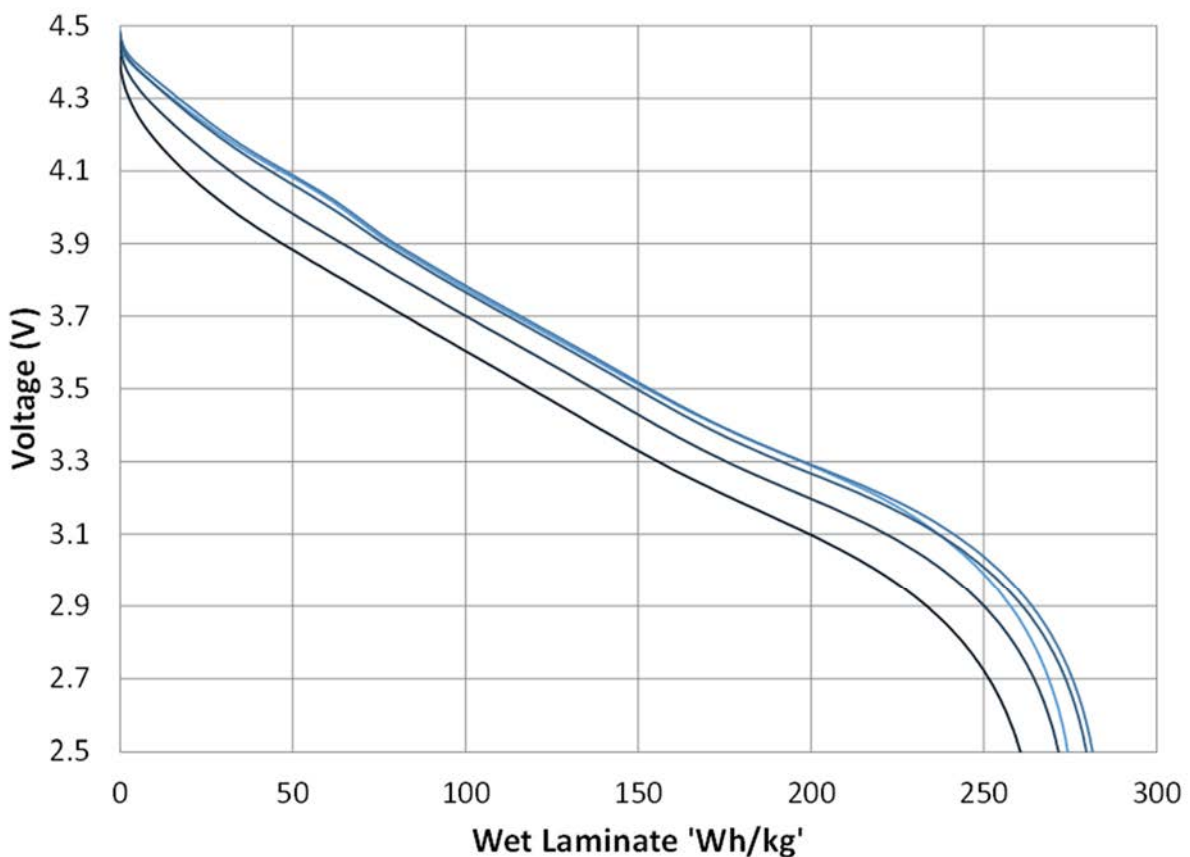


Figure IV-145: Gravimetric energy at different rates (C/15, C/10, C/5, C/2, 1C)

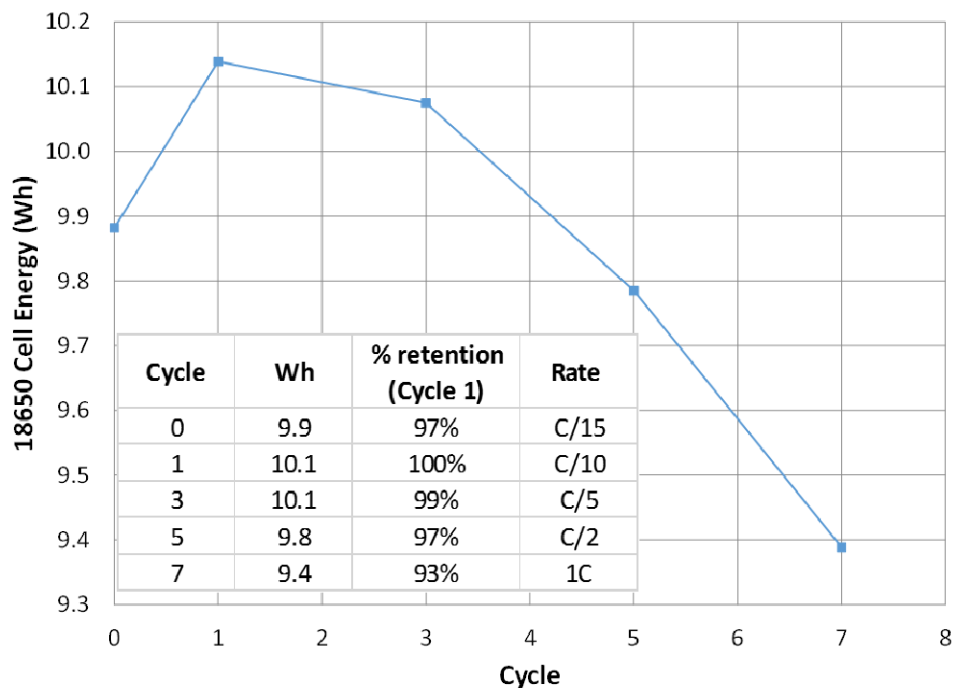


Figure IV-146: 18650 cell Wh and rate capability

### Work Summary and Accomplishments by General Motors

In this project, GM’s role was to perform testing of the 3M-fabricated 18650 cells using the protocols shown in Table IV-19, conduct gap analysis of the cell performance versus the performance targets which were based on USABC vehicle requirements, to carry out post-mortem analysis of the cells to understand the failure mechanisms, and finally to recommend material and cell design improvements to the project team. Three batches of 3M cells (using different cell chemistries) were delivered to GM. The detailed cell chemistry information is listed in Table IV-20. All of the cells showed 2.4-2.8 Ah capacity at C/3 depending on the upper cut-off voltage (4.4 vs. 4.6 V). The test results of the cells were compared to the battery requirements for electrical vehicles (EV) from the US Advanced Battery Consortium LLC (USABC) to determine the gap between the project cell technology and EV target. Several cells from each batch were selected for post-mortem analysis. The cells were torn down in an argon-filled glove box, and the electrodes were unwound and washed by DMC in preparation for various chemical and electrochemical analyses. The prepared electrodes were punched into small pellets and made into half cells to check the capacities of the individual cathode and anode. They were then studied by Scanning Electron Microscopy (SEM), X-ray Diffraction (XRD), and Electron Probe Micro-analysis (EPMA) to determine the chemical/structural changes in the electrode materials. The test results, gap analyses and post-mortem studies are discussed below.

**Table IV-19: Test Protocols for 18650 Cells.**

Test	No. of Cells	Temperature (°C)	DOD	Test Details
Cycle life	2	30	5-95%	C/3 (RPT at every 50 cycles)
Rate Capability	2	35, 25, 10, 0, -10, -20	100-0%	C/10, C/3, C/2, 1C, 2C, 3C, C/3 for 2 cycles at each rate
HPPC	2	35, 25, 10, 0, -10, -20	100-0%	C/3 CC/CV charge, 100% -C/3 discharge, 5% SOC -1C& 2.5C x20s pulse at 100% SOC, -1C&2.5Cx20s pulses every 5% SOC (C/3), Capacity check at 25°C, CCCV discharge to C/50

**Table IV-20: Cell Chemistry of Each Cell Batch**

Batch No.	Cell Chemistry
1	Core-shell structure HE-NMC vs. CV6/Graphite
2	Coated NMC (synthesized by 3M) vs. CV7/Graphite
3	Coated NMC (synthesized by Umicore) vs. CV7/Graphite

The Batch 1 cells used the core-shell structured HE-NMC cathode material and Si alloy/graphite mixture anode material and served as the baseline cell for performance in this project. Fourteen cells were delivered to GM in February 2014. They had been through a formation cycle followed by 2C, 1C, 0.3C, 0.2C and 0.1C rate tests at 3M. The same pre-conditioning protocols were used for Batches 2 and 3. The average C/3 capacity of the Batch 1 cells was 2.4 Ah, with 1.3% deviation. Six cells were arbitrarily chosen for cycle life, rate capability and HPPC tests, which followed the protocols listed in Table IV-19. The test results are compared to the USABC EV targets and are shown in Table IV-21. Because the weight of the 18650 cell casing is a large fraction of the whole cell weight, the data for cell level and wet laminate level are presented. The wet laminate energy content was the basis for the original project deliverable, which is 415 Wh/kg as proposed in the original funding application by 3M. The baseline (Batch 1) cell performance has large gaps relative to the project targets; especially the cell capacity, which decreased to 65% within 45 cycles. The failure mechanisms were studied by post-mortem analysis and will be discussed later. Another result to note is the poor low temperature performance of the baseline cells; no capacity was obtained when the temperature was below 0°C.

The Batch 2 cells used surface-coated NMC as the cathode and Si-alloy (CV7)/graphite mixture as the anode. The core-shell HE-NMC material in Batch 1 cell was set aside since it is unlikely to meet the project deliverables after initial gap analysis and post-mortem study which will be discussed later. There is 10-20% energy density increase from the Batch 1 to the Batch 2 cells, however there are still large gaps between the Batch 2 cells and the project target.

Three sets of cells were designed for different cutoff voltage windows: 4.4-2.0 V, 4.5-2.0 V and 4.6-2.0 V. The intention of using three voltage windows was to study the stability of the cathode material at different upper cut-off voltage. The cells showed average capacities of 2.46 Ah, 2.61 Ah, and 2.81 Ah for the 4.4-2.0 V, 4.5-2.0 V, and 4.6-2.0 V voltage windows, respectively. As shown in Table IV-21, the energy density increased with increased upper cutoff voltage, and the gain is from the extra capacity of cathode at higher voltage. There is no difference between the cycle life of the cells tested in the 4.4-2.0 V and 4.5-2.0 V voltage windows, but the cycle life at 4.6-2.0 V is much lower than both, indicating that the cathode and/or electrolyte material may have experienced significant damage at 4.6V. However, compared to Batch 1 cells, the cycle life of Batch 2 cells was greatly improved, and the cells could be operated at much lower temperatures.

**Table IV-21: Gap Analysis of the Batch 1 and 2 Cells vs. EV Targets. (1) End of Life Requirement for EV Application from USABC; (2) Data for Beginning of Life; (3) Including the Weight of Electrode, Separator, and Electrolyte; (4) Data from C/3; (5) Data Based on 40% SOC at 25°C Using Voltage Limit for Calculation; (6) 35% Capacity Loss at C/3 with 90% DOD Range.**

	Unit	Target	Batch 1 <sup>2</sup> (4.55-2V)		Batch 2 (4.4-2.5V)		Batch 2 (4.5-2.5V)		Batch 2 (4.6-2.5V)	
			Cell Level	Wet Laminate Level <sup>3</sup>	Cell Level	Wet Laminate Level <sup>3</sup>	Cell Level	Wet Laminate Level <sup>3</sup>	Cell Level	Wet Laminate Level <sup>3</sup>
Gravimetric Energy Density	Wh/kg	400	192 <sup>4</sup>	247 <sup>4</sup>	206	260	218	274	234	295
Volumetric Energy Density	Wh/L	600	490 <sup>4</sup>	490 <sup>4</sup>	556	556	596	596	633	633
Gravimetric Discharge Power Density	W/Kg	800	366 <sup>5</sup>	471 <sup>5</sup>	676	853	691	870	NA	NA
Volumetric Discharge Power Density	W/L	1200	933 <sup>5</sup>	933 <sup>5</sup>	1818	1818	1873	1873	NA	NA
Gravimetric Regen Power Density	W/Kg	400	690 <sup>5</sup>	888 <sup>5</sup>	1396	1761	1528	1926	NA	NA
Volumetric Regen Power Density	W/L	600	1757 <sup>5</sup>	1757 <sup>5</sup>	3756	3756	4146	4146	NA	NA
Cycle life	cycles <sup>6</sup>	1000	45	45	194	194	189	189	158	158
Operating Temperature Range	°C	-30~65	0~35	0~35	-20~35	-20~35	-20~35	-20~35	30	30

Whereas the Batches 2 cells cathode materials were synthesized by 3M, Umicore scaled up the cathode material for the Batch 3 cells. Otherwise the cells were identical to the Batch 2 cells; same cell design, anode formulation and electrolyte. The testing was done following the same protocols as listed in Table IV-19 except that the rate capability and HPPC tests were conducted only at room temperature. As plotted in Figure IV-147, the Batch 3 cells tested at 4.5-2.0V showed slightly better cycle life performance compared the Batch 2 cells cycled using the same voltage window. The rate capability and HPPC results were similar performance to those of the Batch 2 cells.

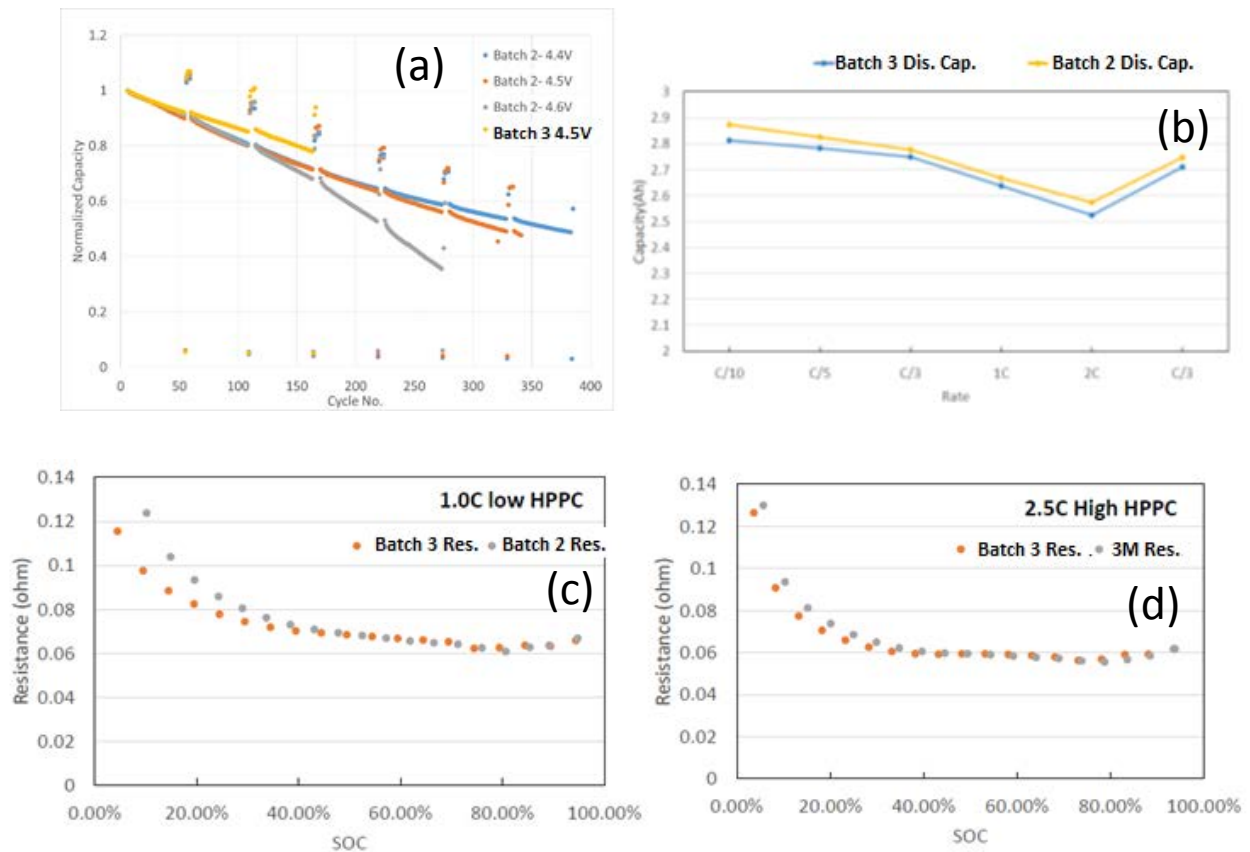


Figure IV-147: The electrochemical performance comparison between the Batch 2 & 3 cells, (a) cycle life test at C/3 at 30 °C, (b) rate capability test at 25 °C, (c) low HPPC test with 1C pulses at 25°C under the same voltage window (4.5-2.5 V), and (d) high HPPC test at 2.5C at 25 °C

## Post mortem analysis results

Two cells were selected from the Batch 1 cells for post-mortem analysis: one cell went only through the formation cycle followed by rate testing as mentioned above and was labeled as the “fresh” sample; the other cell was cycled to failure (no capacity left) and was labeled as the “cycled” sample. We drew two conclusions about the poor cycle life of the electrode materials. These are summarized in Figure IV-148. First, elemental mapping showed a large variation in the transition metal distribution, and no core-shell structure was observed in the cathode particles, as shown in Figure IV-148a. Second, the SEM pictures (Figure IV-148b) showed very different morphologies for the samples. The pristine sample (as-prepared cathode) and the powder showed clean surfaces. But, a thick passivation layer was observed on the cycle-aged cathode compared to the pristine and fresh samples, which could be due to electrolyte decomposition. The passivation layer could contribute to the internal resistance increase of the cycled cell as observed in the cycle life testing. Third, the fresh anode had a relatively homogeneous oxygen distribution which came from the oxygen in the binder material (LiPAA), but a concentrated oxygen layer was observed on the surface of the cycled anode with little oxygen signal inside the electrode in Figure IV-148c, indicating the binder decomposed during cycling, which may be the cause of the anode delamination. The oxygen signal on the surface came from the SEI layer as observed in the SEM image (Figure IV-148b). Fourth, as shown in Figure IV-148d, the fluorine signals representing the solid electrolyte interphase (SEI) were found on the surface of the anode to a thickness of ~5µm. A thin layer of Mn signal was also observed on the surface of the anode, which is due to the Mn dissolution from cathode material. In summary, we conclude that the core-shell structured HE-NMC wasn't made well and that a thick passivation layer was formed on the surfaces of both the cathodes and anodes during cycling leading to resistance increase in the cells, which caused quick capacity failure of the cells.

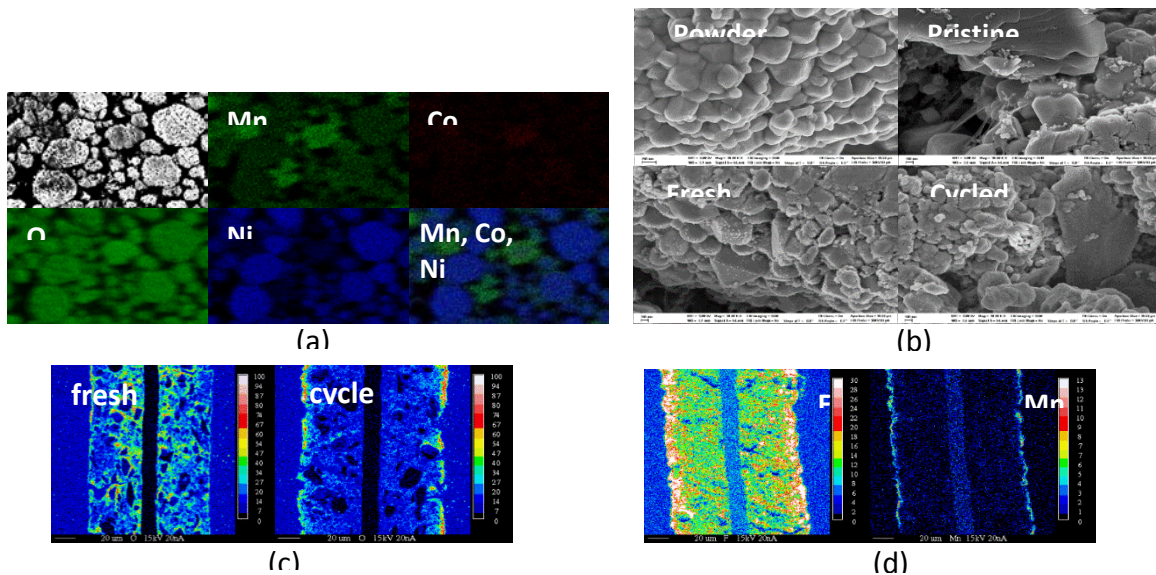


Figure IV-148: Post-mortem analysis results of Batch 1 cells. (a) SEM-EDS analysis of pristine cathode powder material, (b) SEM pictures of cathode materials, (c) EPMA oxygen maps of fresh and cycled anodes, and (d) EPMA fluorine and manganese maps of cycled anodes

**Table IV-22: Half-Cell Capacity Test Results of Post-Mortem Electrodes from Batch 2 Cells**

Sample Type	Voltage Window	Cathode Specific capacity (mAh/g)	Anode Specific capacity (mAh/g)
Fresh	4.4-2.5V	175.16	1210.46
	4.5-2.5V	172.87	1131.93
Rate Tested	4.4-2.5V	178.45	811.21
	4.5-2.5V	170.59	686.44
Cycled	4.4-2.5V	165.64	416.02
	4.5-2.5V	168.26	405

Based on the testing results and learnings from the post-mortem analysis, the team decided that the core-shell structure HE-NMC would not be a promising candidate to meet the project targets. Based on calculation of possible cell energy density, the surface coated NMC is proposed as the cathode for the final delivered cells.

Three cells from two voltage windows (4.4-2.5V and 4.5-2.5V) were disassembled for post-mortem analysis. The cells labeled as the “fresh” sample went only through the formation cycle followed by rate testing at room temperature, the “rate tested” cells were tested at different rates and temperatures following the protocols listed in Table IV-19, and the “cycled” cells were cycled to 40% of initial capacity at 30°C. All the cells were fully discharged to 2.5 V before disassembling in a glove box. The extracted electrodes were washed by DMC and punched into pellets for half-cell fabrication and chemical/structural analysis. As listed in Table IV-22, the cathodes from all the cells showed similar specific capacities. Although the cathodes from the cycled cells showed slightly less capacity (~6% decrease) than the fresh samples, the total capacity loss of the cycled cell was about 60%, indicating that the failure of the cell wasn’t from the cathode. This is consistent with our interpretation of the XRD patterns for these materials; no structural changes were observed. On the other hand, the specific anode capacity gradually decreased from that of the fresh to those of the rate tested and cycled samples, indicating that the capacity loss observed in the full cells was due to anode degradation.

Further analysis of the anodes was done to identify the failure mechanisms. Figure IV-149 shows the phosphorous intensity profile across the anodes and their current collector; tested using 4.4-2.5 V and 4.5-2.5 V voltage windows. The reason for the cycled samples showing only one electrode was because one side of the active material coating delaminated from the current collector during cell disassembly. By comparing the edges of the profiles, one notes that the thickness of the cycled sample increased  $\sim 10 \mu\text{m}$  from that of the fresh sample which is likely due to SEI formation and electrode swelling during cycling. The integrated phosphorous intensity of the cycled sample is 2.72 times of that in the fresh sample, in the case of 4.4-2.5 V, which is additional evidence of SEI growth during cycling since phosphorus is one of the main components of the SEI.

The Batch 3 (final) cells were considerably improved compared with the baseline cells; e.g., energy density, cycle life and low temperature performance. Nevertheless, the performance was far from the EV targets. To meet the EV's energy density target, a cathode with much higher capacity will have to be used. Post-mortem analysis results indicate that the anode stability is the biggest road block to meet the cycle life performance, and that a more stable anode material with a better binder will be required to achieve the cycle life. SEI formation is still an on-going problem for Si-enhanced anode materials. To reduce SEI formation and continuous electrolyte decomposition due to the volume change of Si particle, effective electrolyte additives need to be designed to stabilize the SEI layer, therefore, to improve cycle life and diminish cell internal resistance increase.

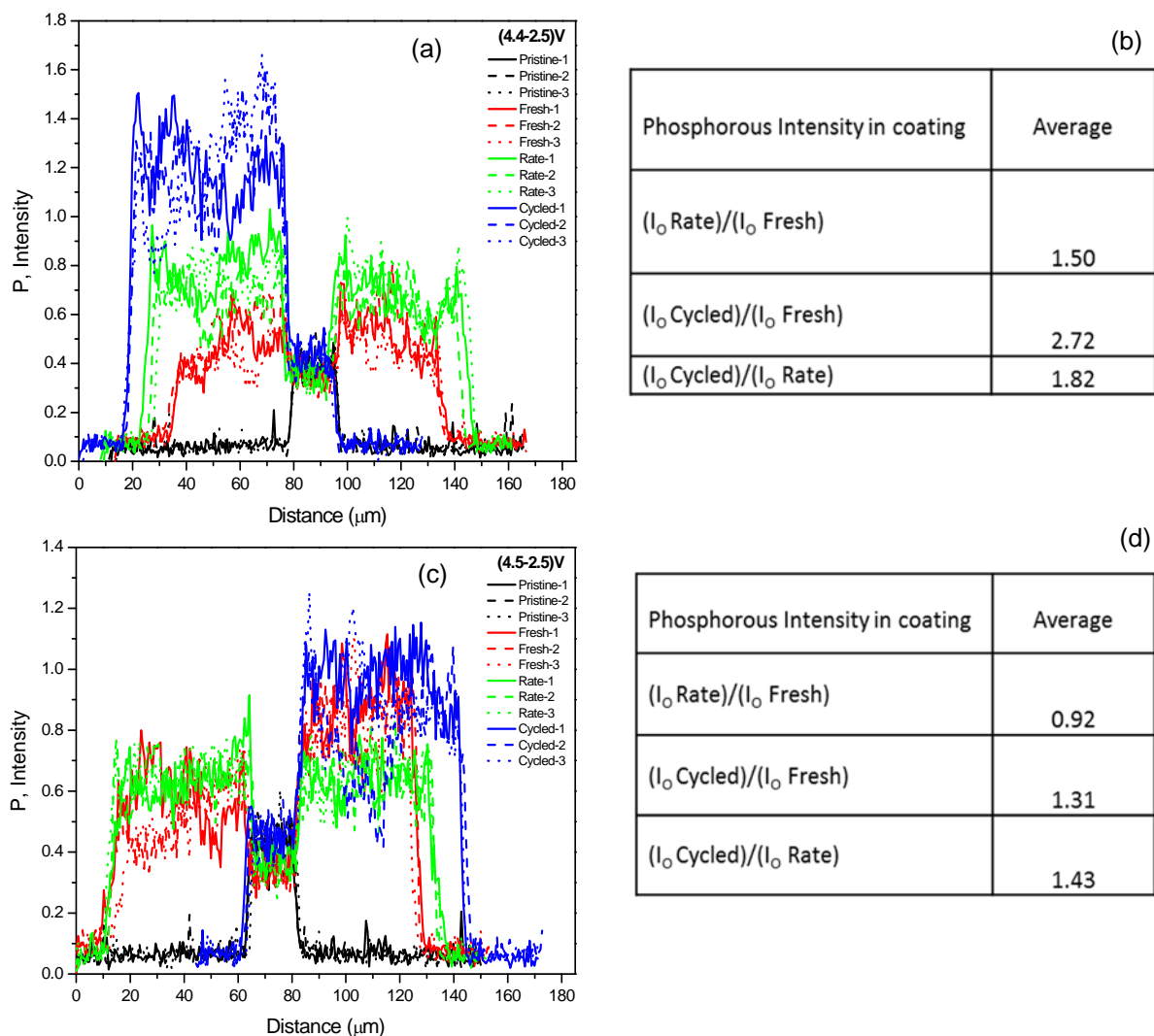


Figure IV-149: The phosphorous intensity profiles across the current collectors of anodes tested between (a) 4.4-2.5 V and (c) 4.5-2.5 V, and the integrated oxygen intensity ratios of different samples tested between (b) 4.4-2.5 V and (d) 4.5-2.5 V

## Activity Summary and Accomplishment by Umicore

### Scale-up process development for core-shell structured high energy density NMC materials

To increase driving distance of electrical vehicle, lithium-ion batteries has an important role to play when a vehicle company designs new vehicle model or when customer decides to purchase electrical vehicle. The design of high energy and power of LIB is mainly dependent on cathode materials' performance. Therefore, it is very important to develop cathode materials with high capacity and energy, long cycle life and low cost. In our project, Umicore will introduce scalable process for cathode materials with capacity around 250mAh/g by using core-shell structured NMC materials designed by 3M and Umicore will deliver the cathode materials on-time to our project partners.

Previous 3M recipe for core-shell high energy NMC (HE-NMC) has potential issues to scale-up to pilot-scale due to long processing time (double firing), complicated process and difficult handling of lithium source (Lithium Hydroxide, LiOH). To overcome those problems of piloting, Umicore decided to introduce scalable process using single firing and using a different lithium source as lithium carbonate (LiC) instead of LiOH.

Figure IV-150 shows scale-up steps for core-shell NMC materials. First, Umicore prepared cathode materials by double firing in furnace using precursor (P0332) which is prepared by Umicore group R&D based on 3M recommended process (Step 1). Then, Umicore modified scalable process using single firing (Step 2). Finally, Umicore introduced scalable process and prepared 50kg of product to deliver to project partners (Step 3).

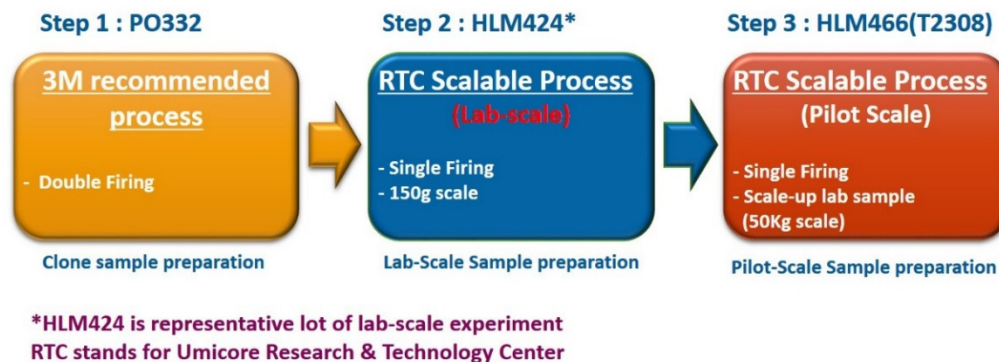


Figure IV-150: Scale-up steps for core-shell NMC materials at Umicore

Materials properties of prepared samples were fully analyzed by BET, PSD, XRD, TAP, Moisture, ICP and SEM. In addition, electrochemical properties were measured using CR2032 coin cell for capacity, cycle, and rate performance.

## Results and Discussion

Table IV-23 shows physical properties of final products prepared by each step. There were some differences of products but physical properties are almost the same.

Lithium to metal ratio were analyzed by ICP method and the result (calculated value) showed 1.157 mol% (Step 1), 1.142 mol% (Step 2) and 1.164 mol% (Step 3). Different Li/M ratio were mainly came from using different lithium sources and scale-up factor. (Not shown in the figure) Figure IV-151 shows SEM images of final products. As seen in the figure, all sample showed similar morphology and crystallite shape. Additionally, XRD patterns of final samples showed the same results (not shown in the figure).

**Table IV-23: Physical Properties of Final Products**

Sample ID	Sample Information	Comment	BET	TD	Moisture
			(m <sup>2</sup> /g)	(g/cm <sup>3</sup> )	(ppm)
P0332	Umicore Lithiation	UmGRD016-20	0.489	-	411
	(3M recipe)				
HLM424	Umicore Lithiation	Repeat of P0332	0.592	-	345
	(Umicore Recipe, Lab scale)				
HLM466 (T2308)	Umicore Lithiation	Scale-up of P0332	0.493	2.12	155
	(Umicore recipe, Pilot scale)				

Sample ID	< 1um	< 3um	Dmin	D10	D50	D90	D95	D99	Dmax
	(%)	(%)	(um)	(um)	(um)	(um)	(um)	(um)	(um)
P0332	0	0	3.476	5.33	8.43	13.2	14.8	17.8	22.73
HLM424	0	0.04	2.908	5.04	8	12.54	14.06	16.91	20.99
HLM466	0	0.17	2.908	4.79	7.92	12.89	14.54	17.58	21.17

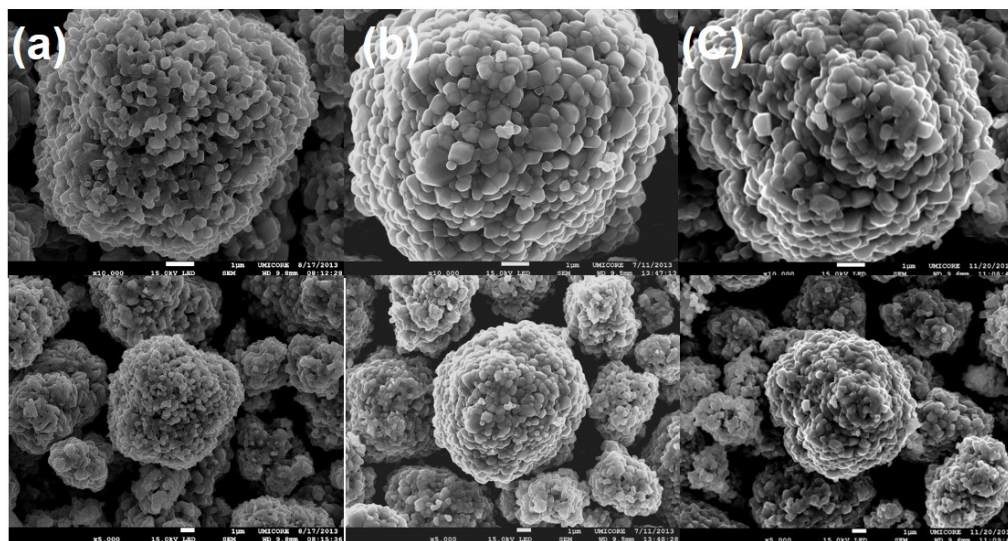


**Figure IV-151: SEM images for final products as (a) Step 1, (b) Step 2, and (c) Step 3**

Figure IV-152 and Table IV-24 show electrochemical properties of the final products. 3M designed sample (Lab scale) shows high electrochemical properties than other products, which are prepared for scalable process. However, if we consider it as a first scale-up sample, then this result also represents successful scale-up.

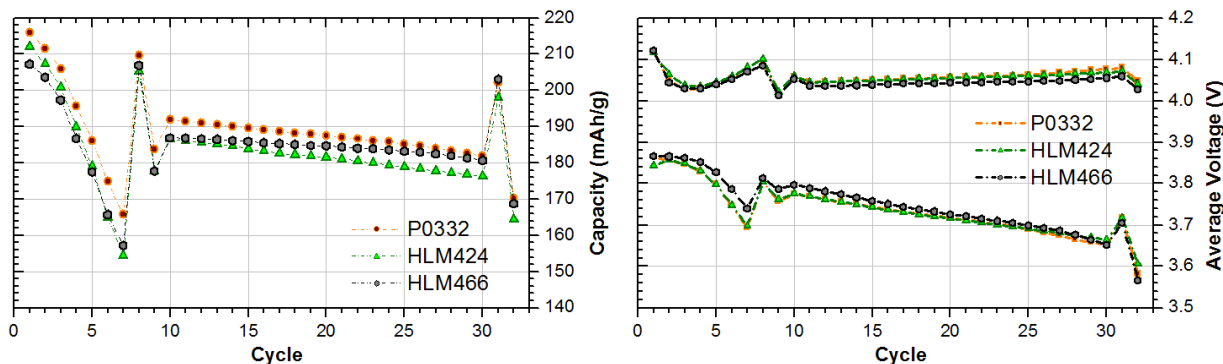


Figure IV-152: Cell performance of final products prepared by different steps. (P0332: Step1, HLM424: Step2, HLM466: Step 3). Rate performance were measured in C/20, C/10, C/5, 1/2C, 1, 2, and 3C at 4.6 V. Cycle was measured at 1 C

**Table IV-24: Electrochemical Properties of Final Products**

Sample ID	QD1 (4.6V)	Qirr (%)	Q 0.1C (mAh/g)	1C (%)	Rate	Rate	Rate	Fade	Fade
	(C/20)				(1C/0.1C)	(2C/0.1C)	(3C/0.1C)	(0.1C)	(1C)
	mAh/g				%	%	%	%/100	%/100
P0332	215.98	14.77%	209.6	87.63%	87.99%	82.60%	78.30%	16.32%	33.38%
HLM424	211.16	15.38%	204.98	86.73%	86.68%	80.09%	75.16%	15.99%	34.01%
HLM466	207.25	17.15%	206.84	85.92%	87.19%	81.37%	77.20%	8.16%	22.90%

Umicore introduced simple and scalable process to prepare core-shell structured high capacity NMC materials by single firing. The scale-up sample showed very similar physical and electrochemical properties compared to 3M designed process. Therefore, the first scale-up process was successful. In addition, Umicore already delivered 35Kg of scale-up core-shell NMC to 3M.

### Scalable process development for LaPO<sub>4</sub>-coated high Ni NMC materials

Surface modification by coating is an important method to achieve improved electrochemical properties and the coating layer prevents the direct contact with the electrolyte solution and as a result cycle stability could increase compared to bare cathode materials. Also, preliminary studies done by 3M to compare full cell (18650) properties of Umicore provided HV622 (High voltage NMC 622, without coating) and La-622 (LaPO<sub>4</sub> coated NMC 622) showed similar capacity and energy density. However, with 3M electrolyte formula, LaPO<sub>4</sub> coated NMC 622 showed better cycle ability at 30°C and 45°C.

From the preliminary results, 3M and Umicore agreed to prepare scale-up sample of LaPO<sub>4</sub> coated NMC 622 based on 3M provided coating recipe and Umicore did optimization of coating process. Therefore, in this report, we would like to provide scalable process based on wet-coating method and results for their physical and electrochemical tests.

For the preparation of coating solution, different wt% of Phosphoric acid (H<sub>3</sub>PO<sub>4</sub>) and Lanthanum Nitrate (La(NO<sub>3</sub>)<sub>3</sub>) were mixed together in deionized water and stirred it until white precipitates were created. Then, prepared coating solution were slowly dropped into NMC 622 powders with stirring. After physical mixing, slurries were dried in dry oven at 120°C for overnight in air. Finally, dried powders were fired at 500°C in dry air atmosphere muffle furnace. Detailed experiment conditions are shown in Figure IV-153.

After coating, samples were fully analyzed their physical and electrochemical properties by SEM, EDS, BET, PSD, coin cell, full cell and so on.

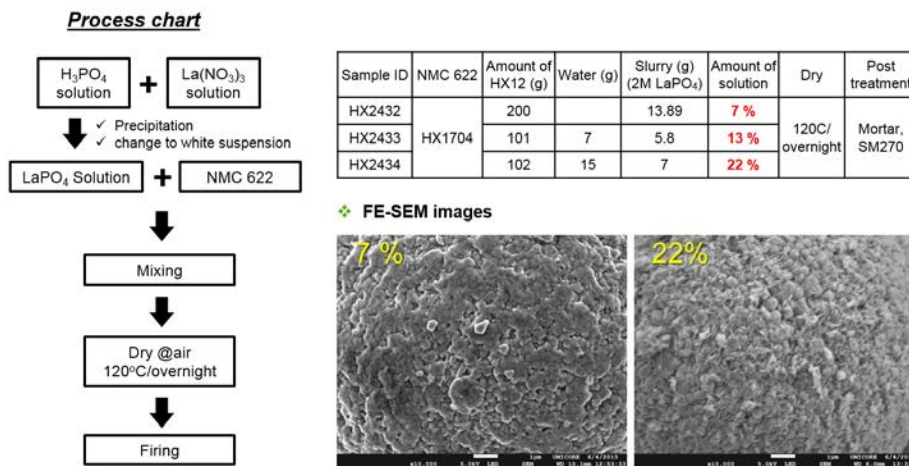


Figure IV-153: Experiments conditions and FE-SEM images of LaPO<sub>4</sub> coated NMC 622 (Lab-scale)

For the optimization of firing temperature after coating, 0.5 mol% LaPO<sub>4</sub> coating NMC 622 with various heating temperature were considered and XRD patterns did not show secondary phase until 800°C as shown in Figure IV-154(a). However, coin cell results showed slightly better performance of powders fired at 500°C compared to others (Figure IV-154(b)).

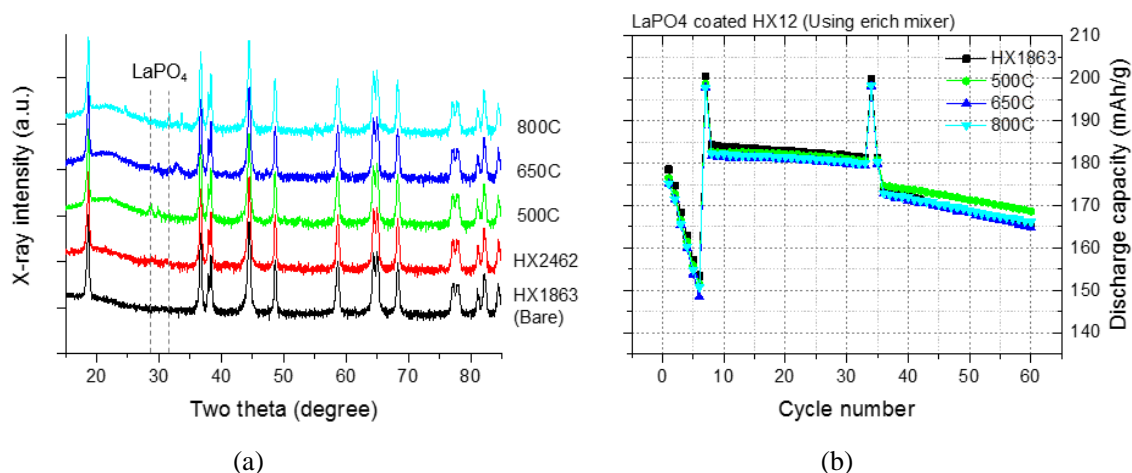


Figure IV-154: Firing temperature optimization results for 0.5 mol% LaPO<sub>4</sub> coating NMC 622

Also, it is important to adjust appropriate coating solution amount for the process point of view. To decide optimal solution amount to the powder mass, we prepared different solution concentration as 5%, 10% and 20%, respectively, and investigated their coat ability. For solution concentration as 5%, inhomogeneous coating on powders were observed and also this amount of coating solution was not enough to coat LaPO<sub>4</sub> on the powders (Figure IV-155).

Figure IV-156 shows the EDS mapping images of powders coated by 10% and 20% of coating solution amount to the sample mass. Still partial aggregation of LaPO<sub>4</sub> observed in both case of 10% and 20% of solution amount but with increasing coating solution amount, LaPO<sub>4</sub> was homogeneously coated on the powder surface than 10% coating solution. However, if we use more than 10% of solution amount, blend making was too difficult due to sticking of powder. Therefore, Umicore optimized coating solution amount as 10%.

Figure IV-157 shows the coin cell results of bare NMC 622 (HX1863), samples coated by 3M (P0357) and Umicore scale-up sample (HX2493). Compared to 3M coated sample, Umicore scale-up sample showed better electrochemical properties in capacity, cycle, and rate and this results was similar as bare HX materials. (Full cell test is on-going and data will be available in next report.)

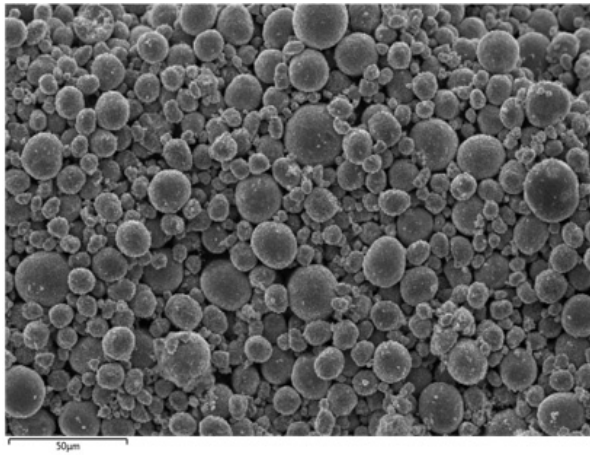


Figure IV-155: SEM and EDS mapping images of LaPO<sub>4</sub> coated NMC 622 with 5% coating solution amount to the sample mass

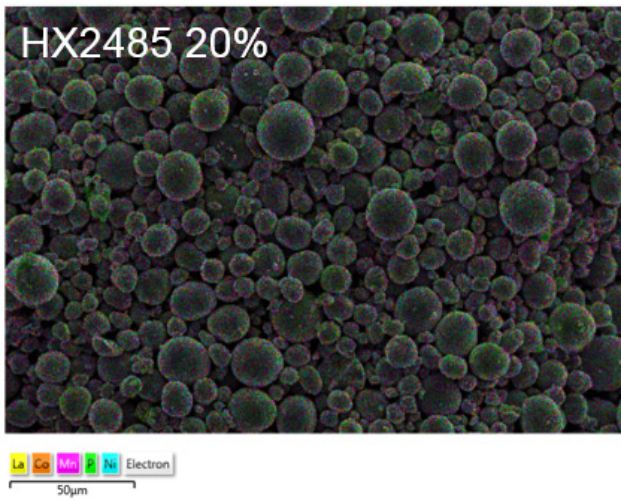
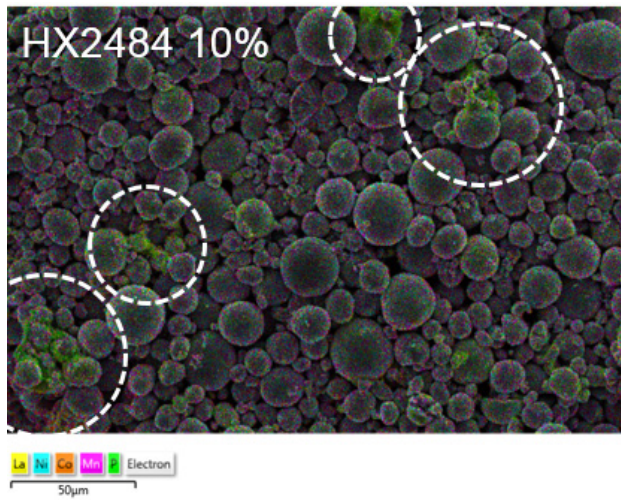


Figure IV-156: SEM and EDS mapping images of powders coated by 10% and 20% of coating solution amount to the sample mass

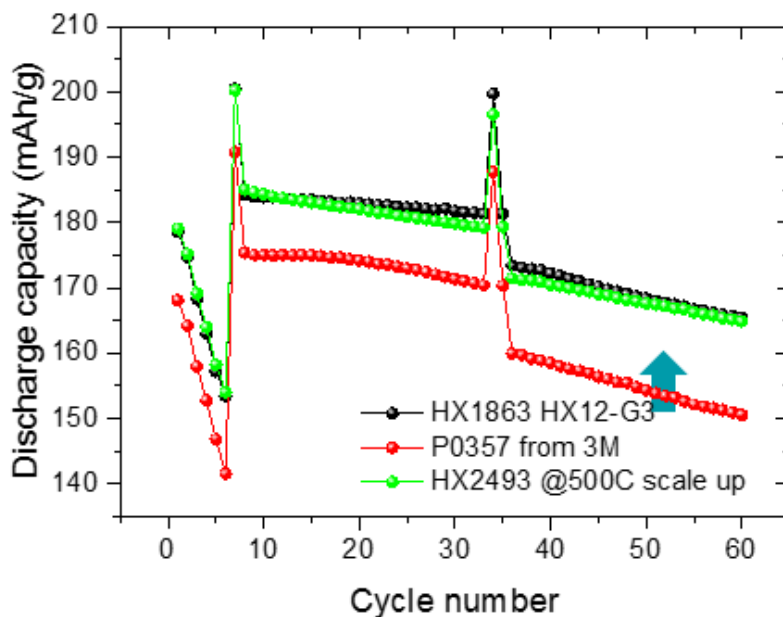


Figure IV-157: Coin cell comparison results for bare NMC 622 (HX1863), 3M coating NMC 622 (P0357) and Umicore scale-up sample (HX2493)

To optimize  $\text{LaPO}_4$  coating conditions, Umicore developed scalable coating process based on 3M recipe and 0.5 mol%  $\text{LaPO}_4$  in 10% of coating solution to the sample mass and 500°C firing temperature were selected. With those conditions, Umicore  $\text{LaPO}_4$  coated NMC622 sample showed better electrochemical properties than 3M coating sample.

### Optimization of scalable process for $\text{LaPO}_4$ -coated high Ni NMC materials

To optimize  $\text{LaPO}_4$  coating conditions, Umicore developed scalable coating process based on 3M recipe and 0.25 mol%  $\text{LaPO}_4$  coating solution to the sample mass and 700°C firing temperature were selected. With those conditions, Umicore prepared 20Kg of  $\text{LaPO}_4$  coated NMC622 sample to achieve final targets.

For the preparation of 0.25M  $\text{LaPO}_4$  coating solution, phosphoric acid ( $\text{H}_3\text{PO}_4$ ) and lanthanum nitrate ( $\text{La}(\text{NO}_3)_3$ ) were mixed together in 3000ml of deionized water and stirred it until white precipitates were created. Then, prepared coating solution were slowly injected by syringe pump into NMC 622 powders using pilot scale blender which was heated at 80°C. After physical mixing, slurries were dried in dry oven at 120°C for overnight in  $\text{N}_2$  atmosphere to prevent  $\text{CO}_2$  uptake. Finally, dried powders were fired at 700°C in dry air atmosphere muffle furnace and sieved using ASTM #270 screen. After coating, samples were fully analyzed their physical and electrochemical properties by SEM, EDS, BET, PSD, coin cell, and so on.

Table IV-25 shows the physical properties results of  $\text{LaPO}_4$ -coated NMC 622 (HX2652) powder. BET value shows  $0.395\text{m}^2/\text{g}$  and total base value was measured as  $209.33\ \mu\text{mol}$ . PSD results of prepared sample are shown in Figure IV-158. Compared to that with bare NMC 622 powder (HX1863), peak intensity decreased but no size changing was observed.

Coin cell results of 3M sample, lab scale sample (3Kg scale), and pilot scale sample (20Kg scale) are shown in Figure IV-159. Umicore scale-up sample showed better electrochemical properties in rate, cycle stability compared to 3M sample. Also, coin cell results of lab scale and pilot scale sample showed no big difference.

From the upscaling study on  $\text{LaPO}_4$  coated NMC 622 powder, pilot scale wet coating method showed exactly the same properties in physical and electrochemical test. Therefore, successful scale-up process was developed together with 3M and Umicore and it will be applicable for mass production scale.

**Table IV-25: Physical Properties of LaPO<sub>4</sub> Coated NMC 622 (HX2652) Sample**

Sample ID	BET	Carbon	pH titration 2.5 g				Cal. Carbon
	SSA (m <sup>2</sup> /g)	C (ppm)	LiOH(%)	Li <sub>2</sub> CO <sub>3</sub> (%)	Ratio CO <sub>3</sub> /Total Base	Total Base (umol/g)	
HX2652	0.3095	174.36	0.2749	0.3493	0.4516	209.33	582

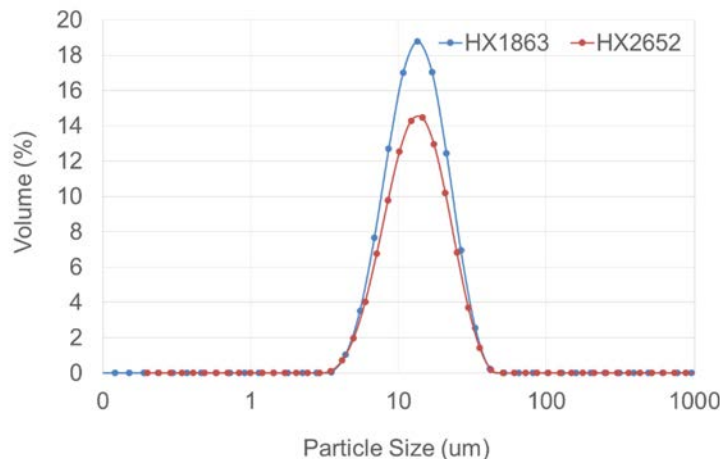


Figure IV-158: PSD results of bare NMC 622 (HX1863) and LaPO<sub>4</sub> coated NMC 622 (HX2652)

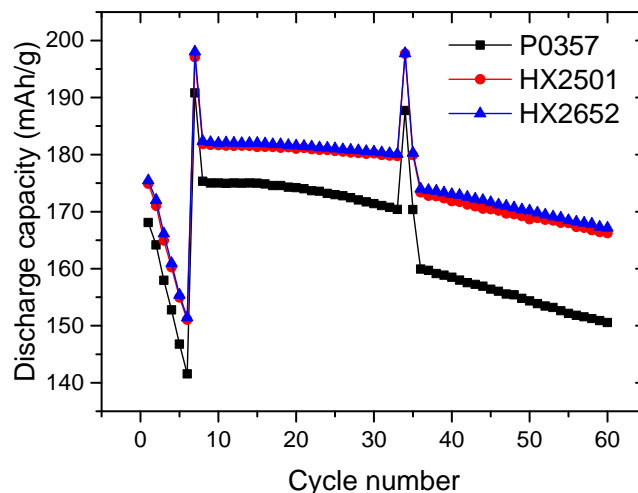


Figure IV-159: Coin cell test results of 3M sample (P0357), lab scale sample (HX 2501) and pilot scale sample (HX2652)

### Work Summary and Accomplishments by Iontensity

In addition to assembling dry and filled lithium-ion pouch cells for this program for testing by others in the consortium, Iontensity ran several test matrices to determine the “mechanical” effect on different current collectors using varying percentage Si alloy/graphite formulations.

#### First Matrix: 20% to 60% Si Alloy

Cells with a 42 x 61 mm footprint and 0.5Ah capacity were assembled and tested. A range of CV-7 formulations from 20% to 60% were tested against 3M’s NMC 622C formulated with 96.5% active material. Three current collectors were tested: (1) 10 μm Cu foil, (2) 18 μm Cu foil and (3) 15 μm Ni foil. (See Figure IV-160.) The high loadings of the Si alloy anode formulations made it difficult to process the thin 10 μm Cu foil on our roll-to-roll coater. The 15 μm Ni foil is lighter than the 18 μm Cu foil providing higher gravimetric

energy density in addition to higher volumetric energy density based on thickness. Ni foil also has a higher tensile strength than either of the Cu foils. The energy densities and cell expansion were quantified. Cells were cycled between 2.5 to 4.4V and 4.5V at a C/3 rate.

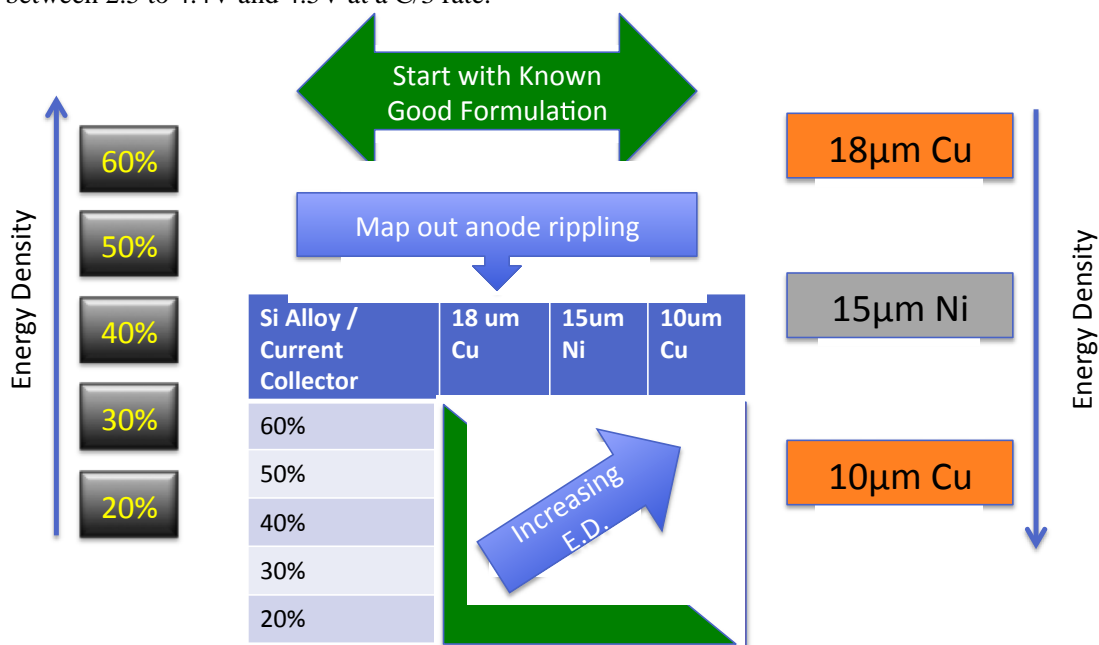


Figure IV-160: Si Alloy % / Current Collector Matrix

For a given Si anode there are two competing forces:

- Si particle expansion / contraction within anode matrix; and
- Tensile strength of current collector.

A great deal of the industry's R&D effort is going into Si particle expansion / contraction. In addition to studying the nature and structure of the Si particle or alloy, extensive work is in progress to better understand the role of binders and conductive additive components. Our focus in this test matrix was on the second force: the tensile strength of the current collector.

A major observation from this study was the occurrence of “rippling” seen on the surface of some of the pouch cells. We have previously found that the tensile strength of current collector is important as thinner Cu foil provides higher energy density but with lower tensile strength, expansion and contraction of the Si anode coating leads to rippling which results in a thicker cell and ultimately lower volumetric energy density. Substitution of Cu foil with Ni or alternate foil increases tensile strength but also the cost. Obviously, this rippling is not observed with 18650 cells and can go undetected. Autopsies revealed that the rippling originated at the anode current collector. Three factors were identified: (1) use of a stiff PAA binder, (2) the % Si alloy in the formulation and (3) the tensile strength of the current collector.

The cells with the 10  $\mu\text{m}$  Cu foil rippled even at the low 20% Si alloy formulation. The cells with the 18  $\mu\text{m}$  Cu foil showed minor rippling with 40% Si alloy and major rippling at 50% and 60%. In the 18  $\mu\text{m}$  copper cells, excessive rippling seen in the higher Si alloy formulations resulted in lower volumetric energy densities even though the capacities were higher. Maximum energy density in the 18  $\mu\text{m}$  Cu foil cells was seen at 30% Si alloy. The cells with the Ni foil did not ripple and their energy densities were not as affected. (See Table IV-26.)

**Table IV-26: Rippling of Lithium-Ion Pouch Cell Anodes  
(Green = No Rippling; Red = Rippling)**

Si Alloy/Current Collector	10 μm Cu	18 μm Cu	15 μm Cu
60%	Red	Red	Green
50%	Red	Red	Green
40%	Red	Red	Green
30%	Red	Green	Green
20%	Red	Green	Green

Energy density measurements at 2.5V to 4.4, 4.5 and 4.6V are shown in Table IV-27 and Figure IV-161 and Figure IV-162. The gravimetric energy densities at each temperature are shown in Figure IV-161 with 50% Si having the highest gravimetric energy density at 282 Wh/kg at 4.5V. Figure IV-162 shows the energy density for the full 2 mm x 42 mm x 61 mm cell. At 4.5V, the 30% Si alloy cell reached 604 Wh/L (625 Wh/L at 4.6V). Note that assembling a larger lithium-ion pouch cell, 58 mm x 145 mm for example, will have a higher energy density than the 42 mm x 61 mm test vehicles we used, due to the volumetric efficiencies gained primarily by a smaller top seal area; thickness is also an important factor.

**Table IV-27: Si % Energy Data for 2.5 V to 4.4 V, 4.5 V, 4.6 V in 42 mm x 61 mm Pouch Cells**

204261			Mass and Dimensions					Discharge Energy to 2.5V					
Lot-			Stack only		4.35V,4.5V	Volume	Expansion	(Wh/kg)			(Wh/L)		
Cell ID	Si%	Foil	Mass(g)	Thick(mm)	Thick(mm)	(cc)	(%)	4.4V	4.5V	4.6V	4.4V	4.5V	4.6V
131-B04	20	18um Cu	11.902	1.40	2.04	5.2	30	234	251	256	533	571	583
142-A01	20	10um Cu	9.5110	1.21	1.78	4.6	28	219	230	243	479	502	517
142-B01	20	18um Cu	10.0072	1.23	1.76	4.5	25	207	222	227	477	492	518
142-E02	20	15um Ni	9.8174	1.19	1.71	4.4	25	217	228	237	490	515	534
132-B03	30	18um Cu	12.079	1.44	2.04	5.2	26	242	258	267	558	596	618
132-C03	30	15um Ni	11.703	1.40	2.01	5.1	27	249	266	275	567	604	625
133-B04	40	18um Cu	11.911	1.40	2.11	5.4	35	227	240	229	500	528	505
133-C04	40	15um Ni	11.591	1.38	1.98	5.1	27	250	263	266	571	601	609
142-C02	40	18um Cu	12.5845	1.56	2.44	6.3	42	259	273		519	547	
142-D03	40	15um Ni	12.2093	1.56	2.23	5.7	28	261	274	286	565	594	
134-B05	50	18um Cu	11.709	1.32	1.95	5.0	31	236	253	246	554	593	576
134-C03	50	15um Ni	12.019	1.49	2.22	5.7	34	271	282	293	533	556	577
135-B03	60	18um Cu	11.517	1.31	2.20	5.6	51	245	258	263	501	527	537
135-C03	60	15um Ni	11.309	1.33	1.96	5.0	30	222	239	239	500	538	537

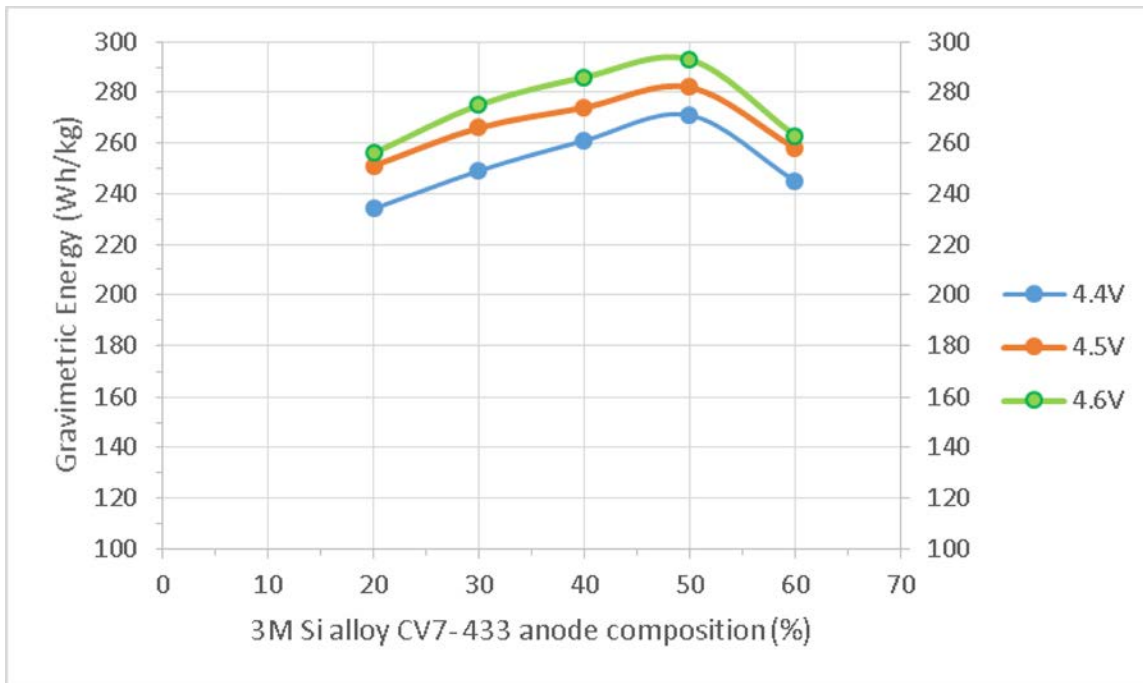


Figure IV-161: Gravimetric Energy Density in Pouch Cells

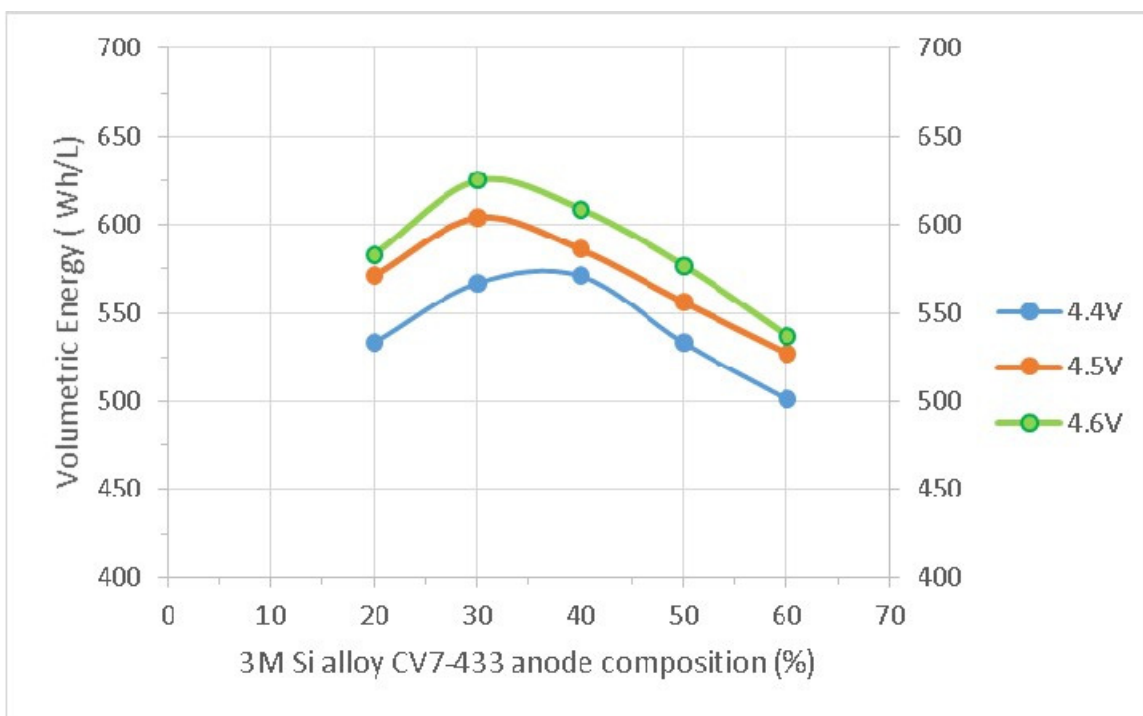


Figure IV-162: Volumetric Energy Density in Pouch Cells

Cycle life of the lithium-ion pouch cells was higher for (1) lower % Si alloy content and (2) lower charge voltage of 4.35V versus 4.4V or 4.5V. A greater amount of Si expansion and particle isolation in the higher % Si alloy and higher upper charge voltages is believed to lower the cycle life. Higher charge voltage is also known for increased electrolyte degradation, also leading to lower cycle life. Note that optimizing the electrolyte formulation for high voltages was not part of this program.

**Table IV-28: Legend for Cell Numbering for % Si Alloy/Current Collector Matrix**

Cell Lot #	% Si Alloy	Sub Lot	Current Collector
131	20%	A	10 μm Cu foil
132	30%	B	18 μm Cu foil
133	40%	C	15 μm Cu foil
134	50%		
135	60%		

Cycling to 4.35V provided good cycle life albeit at low energy as shown in Figure IV-163. Best cycling was with 20% Si alloy (131). All of the other cells were cycled to 4.5V @ C/4 as shown in Figure IV-164. The 18 μm Cu foil series is shown in Figure IV-165. The 20% Si alloy (131) outperformed the higher concentration cells. In Figure IV-166 the 15 μm Ni foil cells were cycled. The 30% Si alloy (132) had the best cycle life but note that there were no 20% cells available in the testing. (The legend for identifying those cells appears in Table IV-28.)

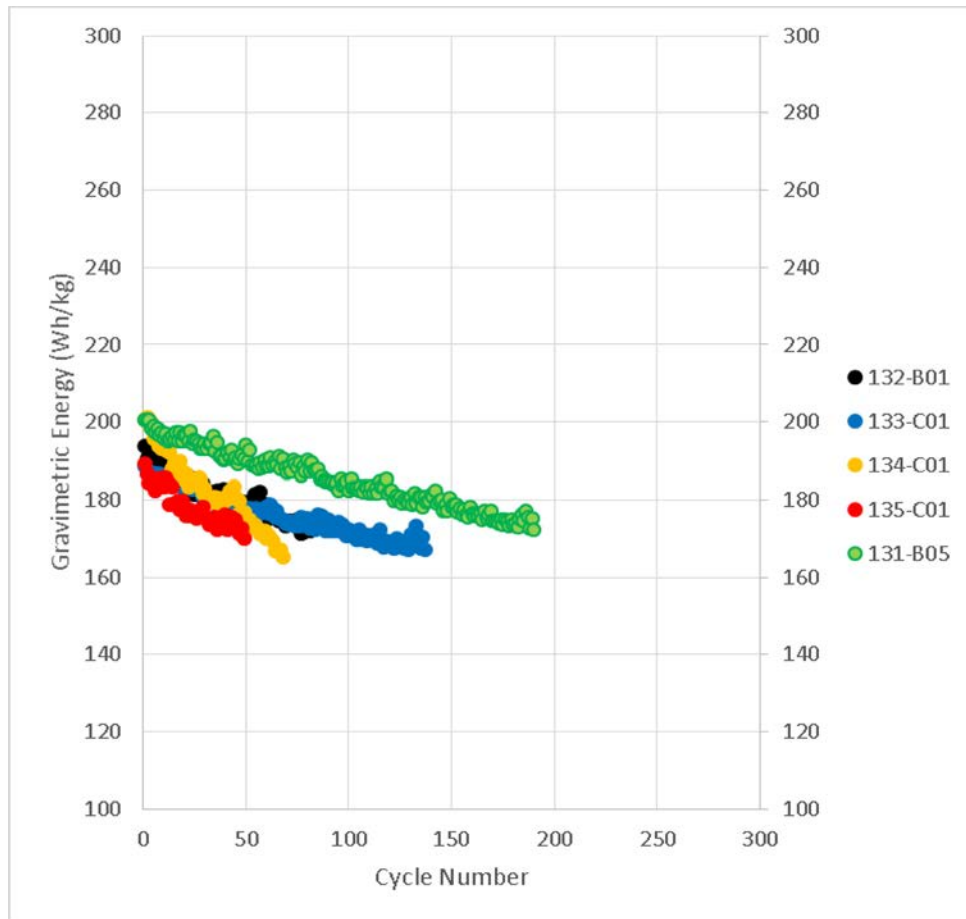


Figure IV-163: Cycle Life: 20% to 60% Si Alloy; 3 to 4.35 V @ C/4

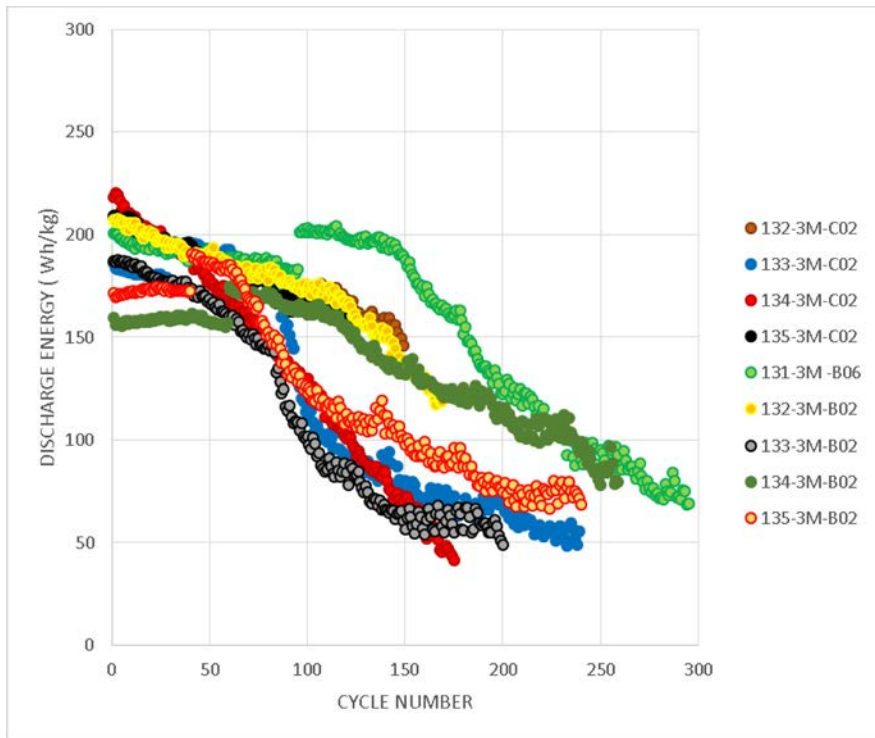


Figure IV-164: Cycle Life: 20% to 60% Si Alloy; 3 Current Collectors; 3 to 4.5 V @ C/4

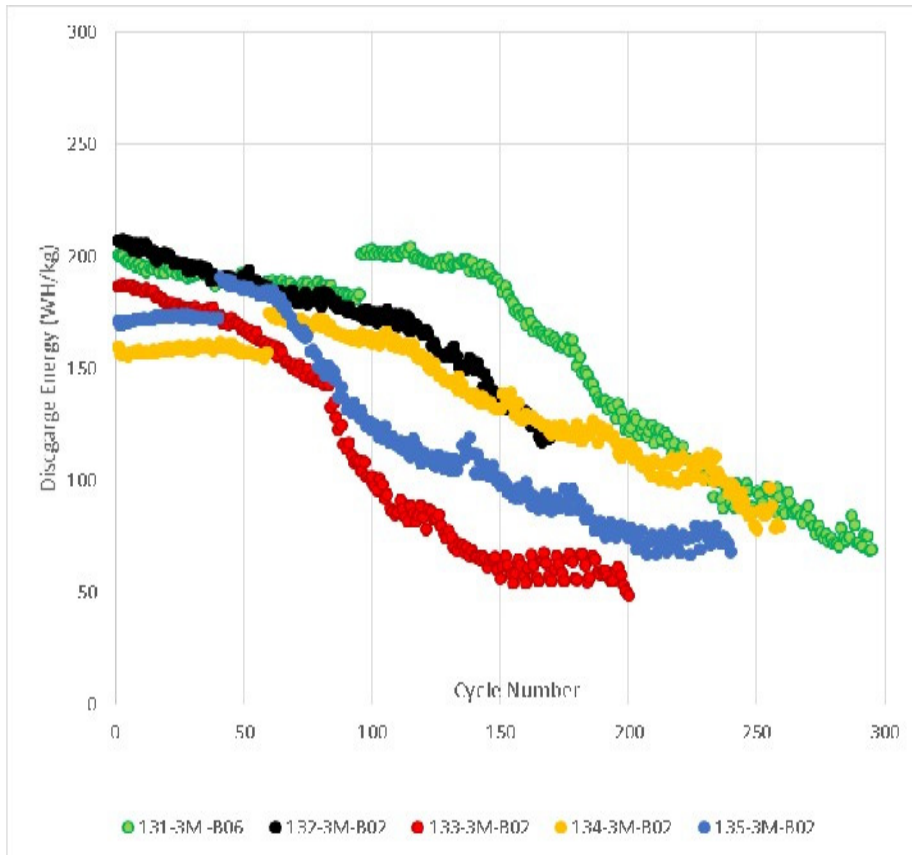


Figure IV-165: Cycle Life: 20% to 60% Si Alloy; 18 um Cu Foil; 3 to 4.5 V @ C/4

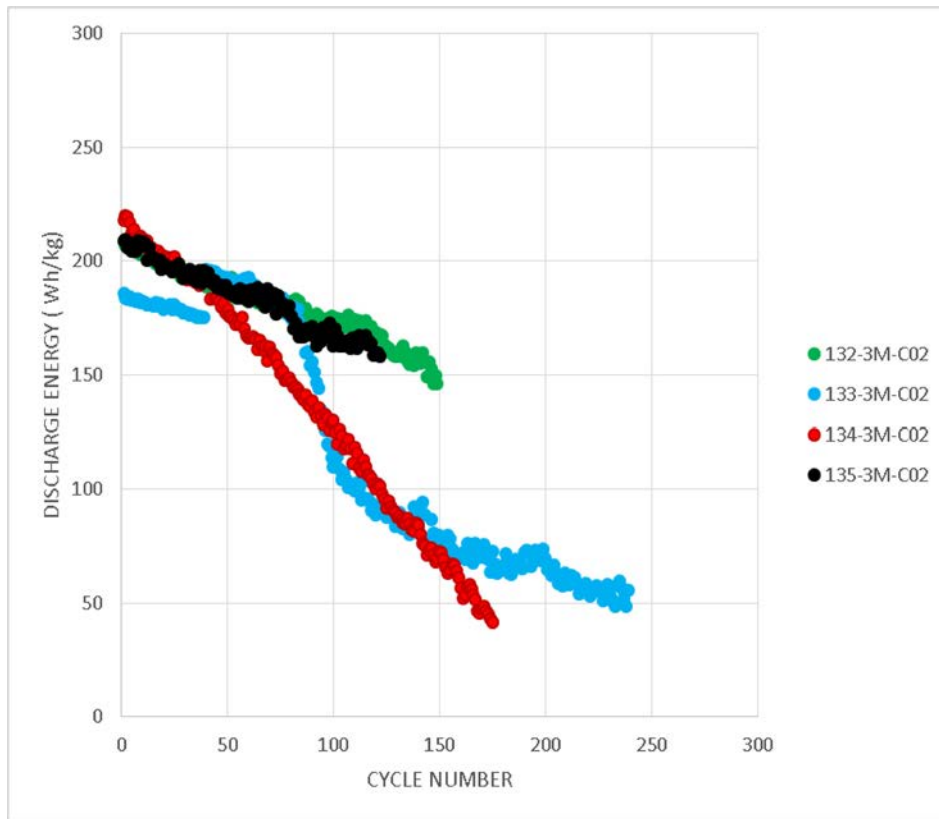


Figure IV-166: Cycle Life: 20% to 60% Si Alloy; 15 um Ni Foil 3 to 4.5 V @ C/4

Our measurements for the increase in thickness from a fresh (as assembled) cell, to a fully charged cell during the formation process are shown in Figure IV-167. It is clear that the percentage in cell thickness increase is a function of the percentage of Si alloy in the formulation for the 18  $\mu\text{m}$  Cu foil to a greater extent than the higher tensile strength 15  $\mu\text{m}$  Ni foil.

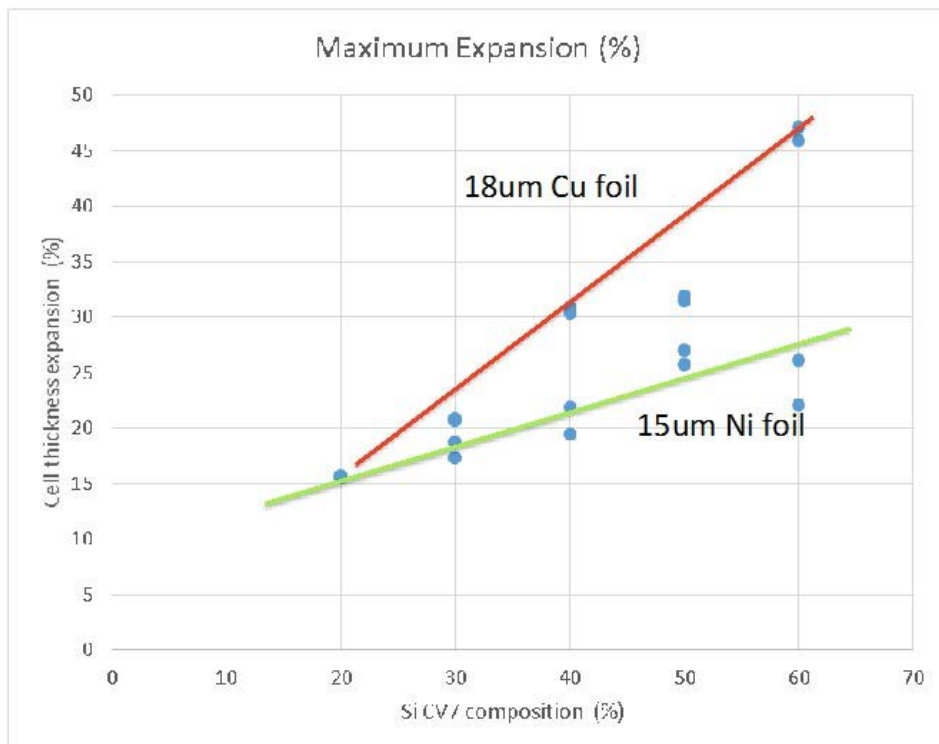


Figure IV-167: Cell Thickness Expansion vs. % CV7 Si Alloy in Anode

## Second Matrix: 20% to 40% Si Alloy

Following the complete Si alloy % / current collector matrix, five new cell lots were assembled. A 20% Si alloy formulation was coated onto 10  $\mu\text{m}$  and 18  $\mu\text{m}$  Cu foil and 15  $\mu\text{m}$  Ni foil. A 40% Si alloy formulation was coated onto 18  $\mu\text{m}$  Cu foil and 15  $\mu\text{m}$  Ni foil. Energy density, cell thickness expansion and cycle life were measured.

Energy density measurements at 2.5V to 4.4, 4.5 and 4.6V are shown in Table IV-29 and Figure IV-168, Figure IV-169 and Figure IV-170. In Figure IV-168 the gravimetric energy densities follow the mass of the current collectors with the 10  $\mu\text{m}$  Cu foil, providing the highest energy and the 18  $\mu\text{m}$  Cu foil the lowest with the 20% Si alloy. At 40% Si alloy the cells reached 275 Wh/kg at 4.5V.

Figure IV-169 shows the energy density for the full 2 mm x 42 mm x 61 mm cell. At 4.5V, the 40% Si alloy cell reached 600 Wh/L and exceeded 600 Wh/L at 4.6V. Figure IV-170 was calculated for “chemistry only” by extracting all volume outside of the cell stack. Note that by assembling a larger lithium-ion pouch cell, EV size: 225 mm x 225 mm for example, will have a higher energy density than the 42 mm x 61 mm test vehicles we used, due to the volumetric efficiencies gained primarily by a smaller top seal area; thickness is also an important factor. At 4.5V, the 40% Si alloy chemistry achieved over 1000 Wh/L.

**Table IV-29: Energy Density for 20% and 40% Si Alloy (42x61 mm) Lithium-Ion Pouch Cells**

LOT	Si%	Foil	Cell Mass(g)	Max. Thick(mm)	Vol. (cc)	Grav. Energy(Wh/kg)			Vol. Energy(Wh/L)		
						4.4V	4.5V	4.6V	4.4V	4.5V	4.6V
142-3M											
CELL Series											
A	20%	10um Cu	9.5104	1.70	4.36	219	230	243	479	502	517
B	20%	18um Cu	10.3523	1.75	4.48	207	218	227	477	502	518
E	20%	15um Ni	9.8215	1.70	4.36	217	228	237	490	515	534
C	40%	18um Cu	12.5845	2.44	6.25	259	273	284	519	547	569
D	40%	15um Ni	12.4819	2.21	5.66	261	274	285	565	594	614

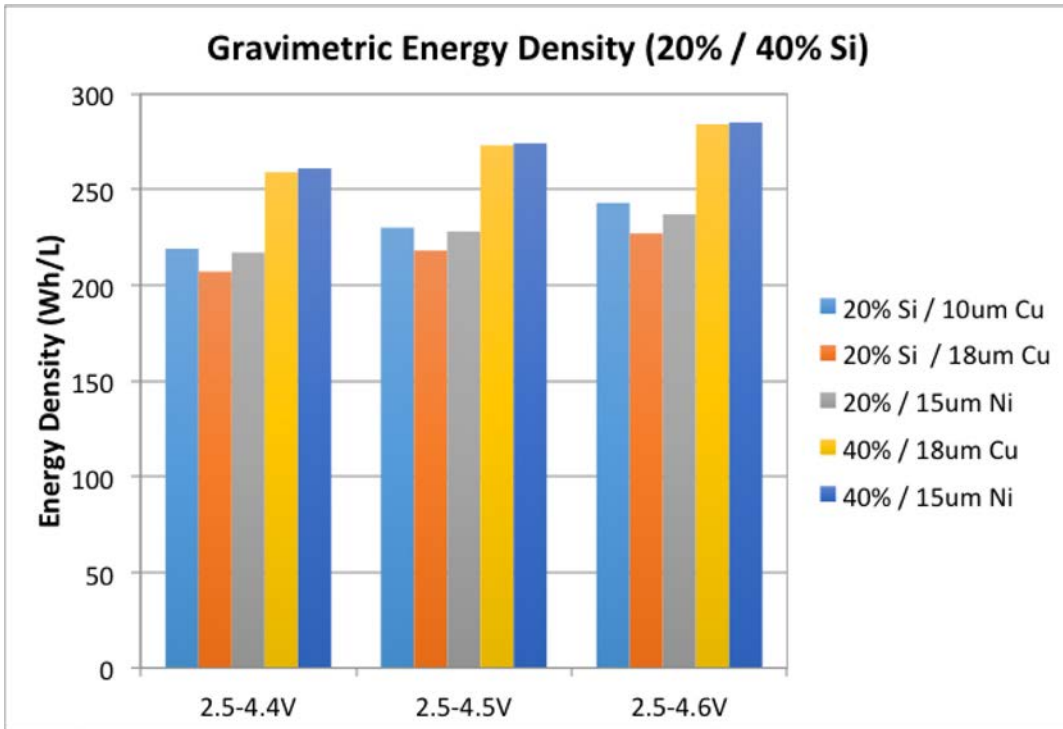


Figure IV-168: Gravimetric Energy Density for 20% and 40% Si Alloy

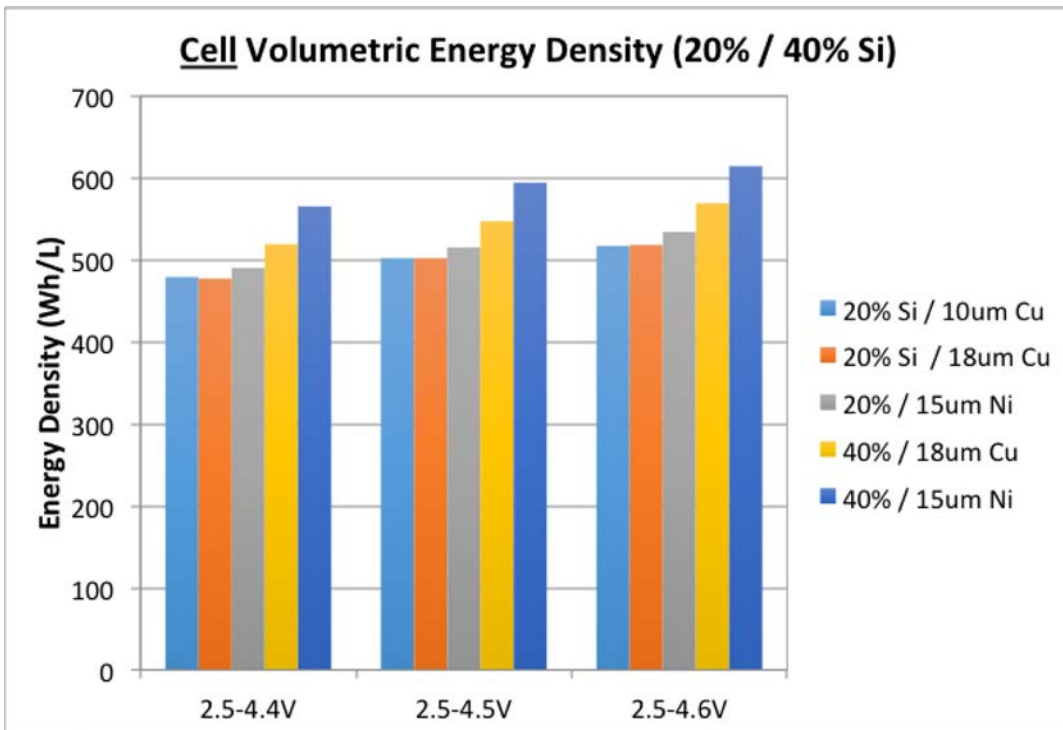


Figure IV-169: Volumetric Energy Density for 20% and 40% Si Alloy (Cell Level)

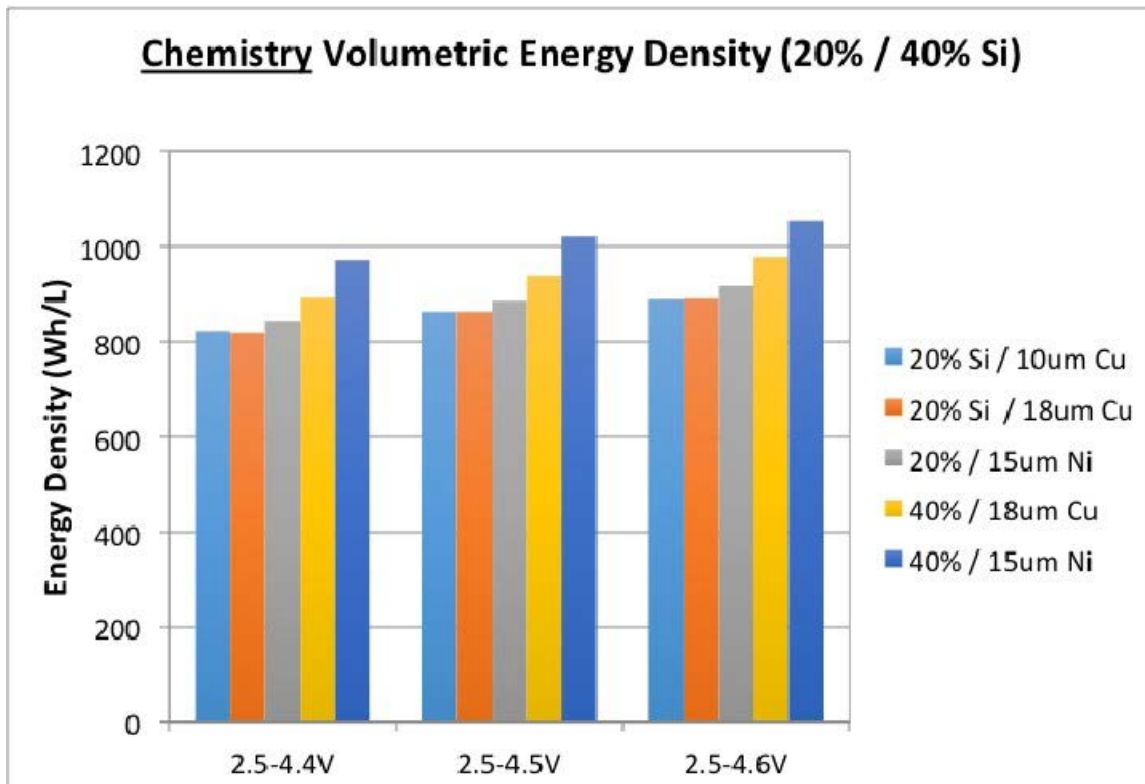


Figure IV-170: Volumetric Energy Density for 20% and 40% Si Alloy (Chemistry Level)

Our measurements for the increase in thickness from a fresh (as assembled) cell, to a fully charged cell during the formation process were similar to the previous test matrix. It is clear that the percentage in cell thickness increase is a function of the percentage of Si alloy in the formulation for the 18  $\mu\text{m}$  Cu foil to a greater extent than the higher tensile strength 15  $\mu\text{m}$  Ni foil.

The cells were cycled from 2.5V to 4.4V @ C/3 at room temperature as shown in Figure IV-171 and 2.5V to 4.5V @C/3 in Figure IV-172. During cycling, the higher energy 40% Si alloy cell capacity dropped off at a lower cycle number than the lower energy 20% Si alloy. Overall the cycle life was poor.

One of the first cells assembled in this program in August 2014 is shown for comparison in purple. This cell used an LCO cathode. The cell had higher energy density and cycled well before dropping precipitously.

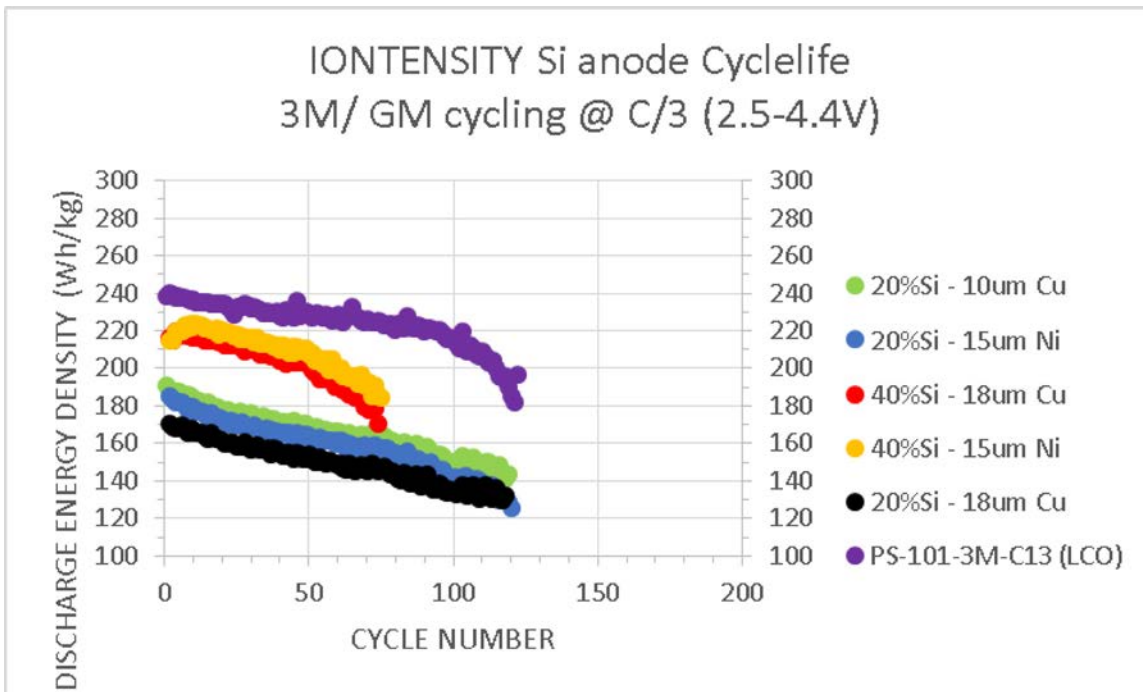


Figure IV-171: Cycle Life for 20% and 40% Si Alloy vs. 3M NCM622C (2.5 V to 4.4 V)

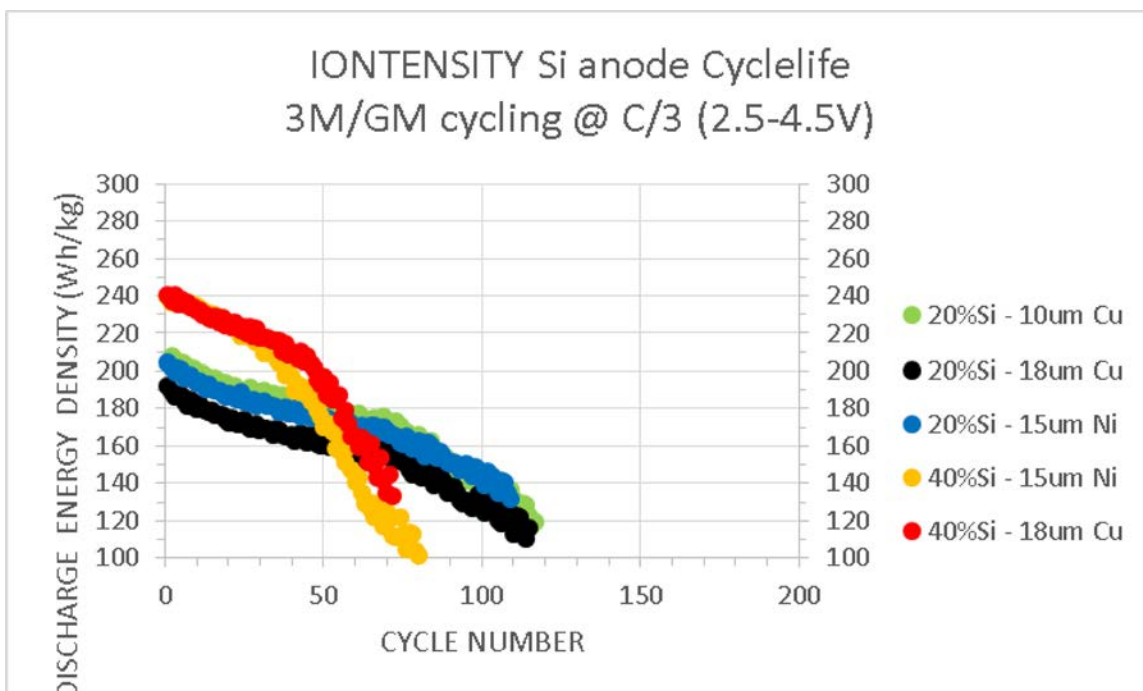


Figure IV-172: Cycle Life for 20% and 40% Si Alloy vs. 3M NCM622C (2.5 V to 4.5 V)

The new cells were inspected visually to determine if rippling occurred and reported in Table IV-30. As expected the Cu foils all rippled to an extent but no rippling was seen with the Ni foil cells.

**Table IV-30: Visual Inspection of Lithium-Ion Pouch Cells Following Cycle Life**

Si Alloy Content	Current Collector	Visual Inspection
20%	10 $\mu\text{m}$ Cu	Minor rippling
20%	18 $\mu\text{m}$ Cu	Very minor rippling
20%	15 $\mu\text{m}$ Ni	No rippling
40%	18 $\mu\text{m}$ Cu	Rippled
40%	15 $\mu\text{m}$ Ni	No rippling

Test matrices with different Si alloy % and various current collectors were completed. In these matrices, we found that the least cell thickness expansion (15%) was with only 20% Si alloy and independent of current collector. Cell thickness expansion was found to be proportional to Si alloy %. Not surprising, but the best cycling was also found for the 20% Si Alloy cells. When tested at different voltages, 4.35V cycled better than 4.4V and 4.5V, respectively; also not surprising with greater Li insertion at higher voltages and increased electrolyte degradation at higher voltages. To achieve high energy density, cycling to  $\geq 4.5\text{V}$  is critical as opposed to 4.35V or 4.4V. At 4.5V the 20% Si alloy cells cycled better than the higher % Si alloys. The highest gravimetric energy density at 4.5V was achieved with 50% Si alloy at 280 Wh/kg. The highest volumetric energy density at 4.5V was achieved with 30% Si alloy at 600 Wh/L. This is presumably due to the greater thickness increase in the higher Si alloy content.

In some test cells, we observed rippling of the surface of the cells. This rippling leads to increased cell thickness and lower energy density. After disassembly, it was clear that the anode was rippling and the ripples on the anode could be seen through the outer package. In our study, we found that Ni foil, even when thinner than Cu foil, will not ripple due to its higher tensile strength. 10  $\mu\text{m}$  Cu foil easily ripples with any Si content. 18  $\mu\text{m}$  Cu foil ripples at 40% and higher Si alloy content. Although not seen due to the metal 18650 cans, we believe the anode current collector, if rippled, could have detrimental effects on the performance of the cells.

### Work Summary AND Accomplishment by Army Research Laboratory

The baseline electrolyte contained 1M LiPF<sub>6</sub> in a solution of 3:7 wt% ratio of ethylene carbonate:ethyl methyl carbonate. Electrolyte additives were initially investigated in coin cells in full cell configuration using core-shell NCM cathode material and CV6 Si-carbon alloy. Of the various different additives tested, six additives showed potential in the initial cycles for improving the fade rate of the cells. However, these tests were carried out in electrolyte flooded coin cells such that the amount of electrolyte additive per unit active electrode materials might be too high. In pouch or 18650 prototype cells, the amount of electrolyte per cell is limited. The results obtained in flooded coin cells may not translate well into real cells with limited amount of electrolyte. The electrolyte additives were then tested using a limited amount of electrolyte in the coin cells. To compare to the pouch cells formulated by Iontensity, 2.2 g electrolyte per Ah, resulting in 12  $\mu\text{g}$  electrolyte for 6.4 mAh coin cells, was tested. However, the results were not reproducible and displayed erratic cycling behavior. It was concluded that the limited electrolyte introduced wettability issues due to the spread of electrolyte to the void space in the coin cells. When the electrolyte amount was increased to 25  $\mu\text{g}$ , the coin cells showed reproducible cycling with excellent efficiency (as high as 99.95%).

Next, the upper and lower voltage cutoff potentials were examined using the same electrode materials. Two lower voltage cutoffs (2.5 and 3.0V) and 5 upper voltage cutoffs (4.35, 4.40, 4.45, 4.50 and 4.55V) were examined (Figure IV-173). Raising the lower cutoff voltage has a much more dramatic effect on the cell performance than lowering the upper cutoff voltage. While the cells cycled to 2.5V have a higher initial capacity, the fade rate begins to increase dramatically after around 60 cycles. The cells cycled to 4.55V have higher initial capacity than those cycled to 4.50 and 4.45V but the fade rate is higher. We have determined that a voltage range of 3.0-4.45V is ideal for this system for improved cycle life while maintaining a high capacity.

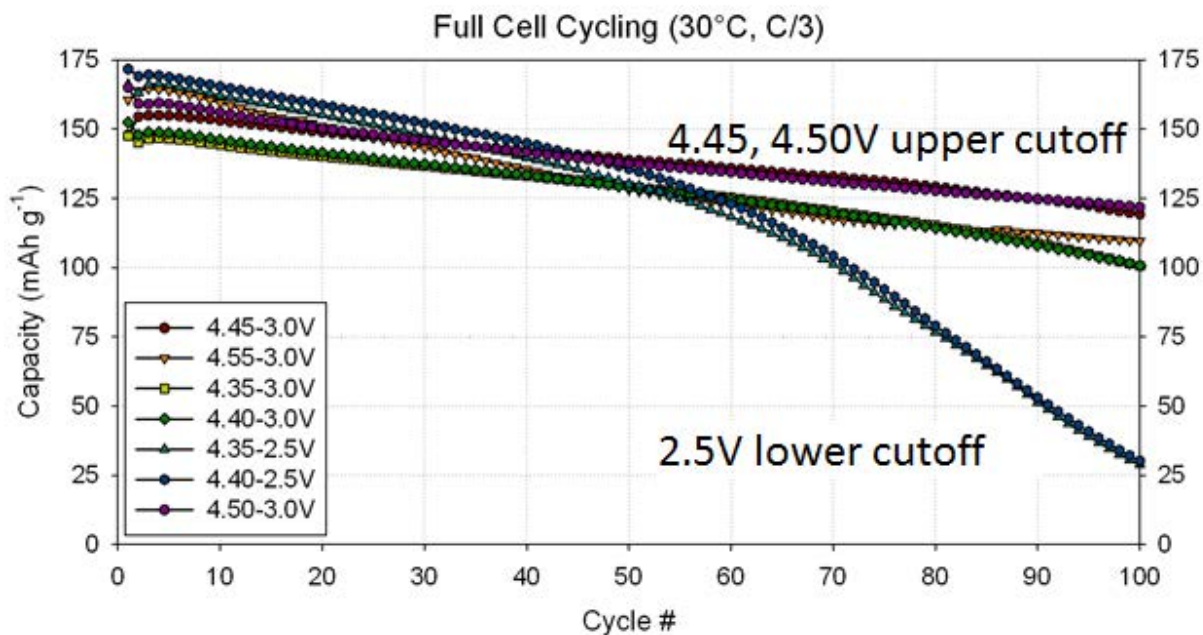


Figure IV-173: Cycle life performance under different voltage windows

Several different electrolyte formulations were cycled in full coin cells with coated NCM-622 cathode material (683C-2) and CV7 anode material (684A-1). The cells were cycled from 4.45-3V at 30°C at C/3 rate (baseline, baseline + 1% succinic anhydride, baseline + 1% Fluoroethylene carbonate (FEC), baseline + 10% FEC, and 1M LiPF<sub>6</sub> in a solution of 1:4 wt% FEC:dimethyl carbonate). The electrolyte containing 10% FEC suffered from gassing in pouch cell testing leading to the formulation of electrolytes without FEC or with decreased FEC. For comparison, an electrolyte containing only FEC and DMC in a 1:4 ratio was also tested to see if more gas was produced (there appeared to be more gas by comparing the amount the pouch cell expanded to the other pouch cells). Decreasing the FEC content to 1% also produced similar cycling results to the 10% FEC electrolyte. An electrolyte containing 1% succinic anhydride (SAH) was tested and it maintained capacity as well as the FEC containing electrolytes for the first 300 cycles (Figure IV-174). The concentration of SAH needs to be optimized to determine if the results can be improved.

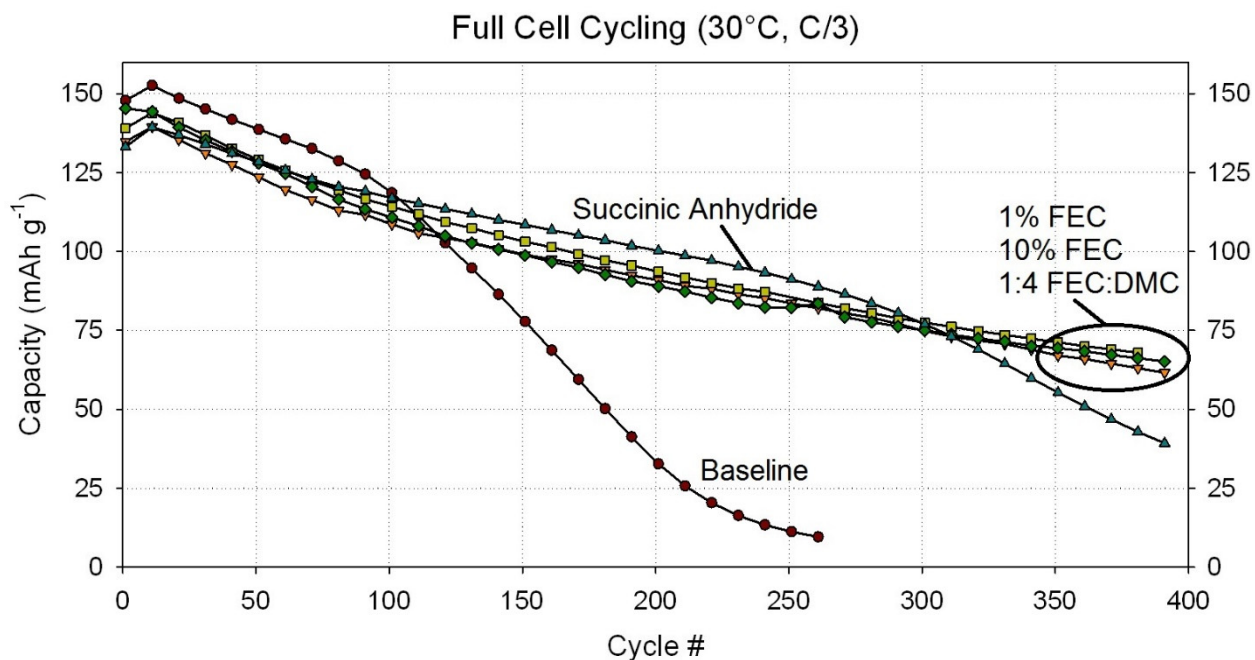


Figure IV-174: Effect of different electrolyte formulations baseline and advanced chemistry

Various additives were screened for cycle life using coin cells in a full cell configuration with coated NCM-622 cathode material (683C-2) and CV7 anode material (684A-1). The electrolytes tested were baseline, baseline + 1% tris(trimethylsilyl) phosphate (TMSP), baseline + 1% SAH, baseline + 1% lithium difluoro(oxalate)borate, baseline + 0.5% TMSP + 0.5% SAH, baseline + 10% FEC, baseline + 10% FEC + 1% TMSP and baseline + 10% FEC + 1% SAH. The use of the additives TMSP, SAH or LiDFOB increased the cycle life compared to the baseline. The addition of 10% FEC also increased the cycle life over that of the baseline. However, the addition of other additives such as TMSP or SAH to the 10% FEC electrolyte did not increase the cycle life. The use of two additives (TMSP + SAH) in the baseline provided the longest cycle life (Figure IV-175).

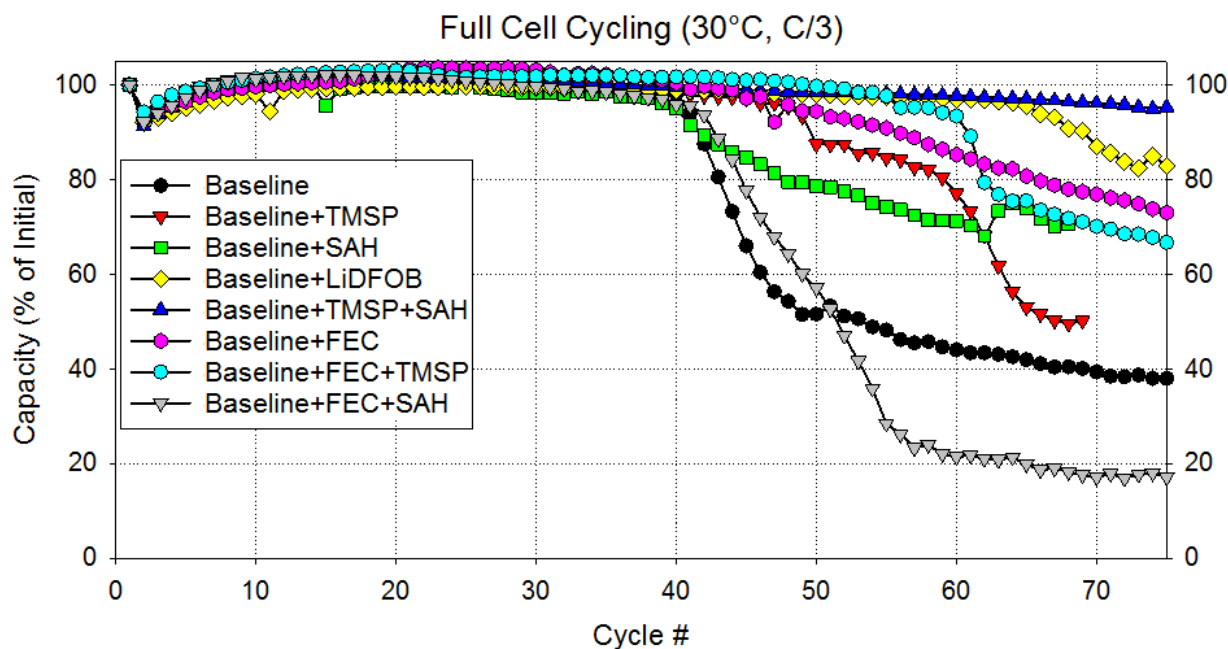


Figure IV-175: Cycle life of different electrolyte formulations with advanced chemistry

## Work Summary and Accomplishments by Lawrence Berkeley National Laboratory

The lithium-ion battery (LIB) has enabled the development of portable computers, cell phones, and digital cameras, long-driving-range electric vehicles and the storage of renewable energy in the utility grids are also experiencing revolutionary changes by LIB. High-capacity active materials and components are key to the next generation of high-power LIB. The most popular graphite anode only has a gravimetric specific capacity of 372 mAh/g, while the alternative alloy anode materials such as tin (Sn, 994 mAh/g) or Si (Si, 4200 mAh/g) have much higher gravimetric specific capacities. However, almost 300% volume expansion occurs as the material transitions from Si to its fully lithiated phase. Because of this large volume change, the electronic integrity of the composite electrode is disrupted, and high and continuous surface side reactions are induced, leading to a drastic capacity decay. Polymeric binders have shown their unique role in addressing this problem. Incorporating the hydrogen bonding structure to a low T<sub>g</sub> polymer, the binder with a self-healing property was shown to heal the electrode crack and enabled a satisfactory cycling performance of a Si micro-particles. Cross-linking systems using dual binder with carboxylic acid and hydroxyl groups was shown to effectively accommodate the large volume change during cycling, resulting good cycling stability. An intrinsically-conductive polymer eliminates the use of brittle acetylene black conductive additives, electronic conductive channel of the electrode rely on the ductile polymer binder and the integrity is perfectly maintained during cycling. These previous work demonstrate the modification of binder as a viable path to drive the application of high-capacity Si-based anodes.

In spite of different novel concepts toward a better polymer binder, the imperative property still lies on its original function and also suggested by its name, binding. The electrode laminate adheres onto the current collector as a whole, active materials particles need good cohesion to ensure the flow of ions and electrons. A perfect adhesion property by the binder is a prerequisite to endure the drastic volume changes in the Si-based system. Numerous material developments are inspired by the observation and investigation of phenomena in

the natural world. Mussels rely on byssal threads to attach to a firm substrate for essential activities. The long-lasting adhesion in the wet environment comes from 3,4-dihydroxy-L-phenylalanine (DOPA) in the specialized adhesive proteins. Inspection of mussel adhesive protein gave insight into the rational design of mussel-mimetic polymeric binders for Si-based lithium-ion batteries. This work systematically studied the catechol content in a conductive polymer binder for a Si-alloy anode. Perfect stable cycling performance is achieved by the dual strategy of mussel-inspired adhesion and conductive polymer, with this strong adhesion supported by comparing the AFM unbinding force measurements of pulling single catechol-containing conductive polymer chain on a silica substrate to single chain of other conventional polymer binders on the same surfaces. To ensure the real single molecule event, a screen protocol was applied here as well to filter the force data based on several criteria (see supporting information) established to reject curves that exhibit the stretching of multiple chains in parallel or from bundles.

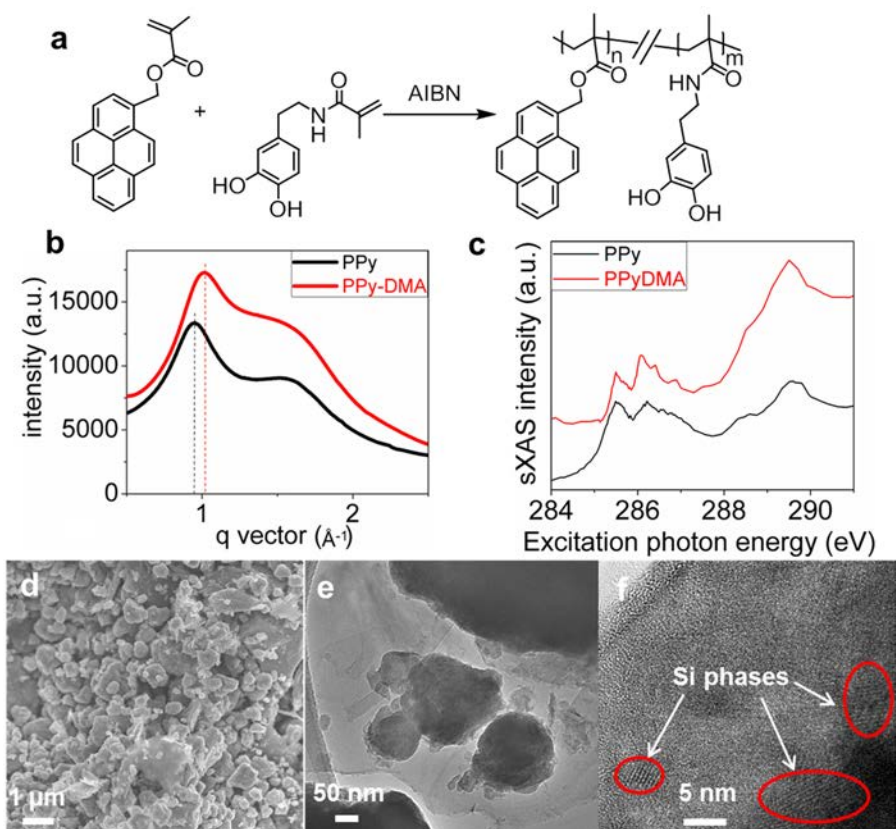


Figure IV-176: (a) Generic synthesis of Poly(1-pyrenemethyl methacrylate-co-dopamine methacrylamide) (PPyDMA). (b) Wide angle X-ray scattering (WAXS) of PPy and PPyDMA polymers. (c) Carbon K-edge sXAS of PPy and PPyDMA shows that the LUMO energy is intact in PPyDMA, although non-conductive DMA groups are introduced. (d) SEM and (e) (f) High resolution TEM (HRTEM) of the CV7 Si alloy pristine particle

Pyrene-based polymers, poly(1-pyrenemethyl methacrylate) (PPy), were established as an excellent electric-conducting polymers. Pyrene molecules are connected to the flexible backbone along the chain, they are close in position to be easily self-assembled into ordered structures, realizing electron conductivity via the side chain  $\pi$ - $\pi$  stacking force of the aromatic moieties. A versatile radical-based polymerization is used to synthesize this type of polymer, which facilitate the incorporation of different functional groups. Dopamine methacrylamide (DMA) was synthesized based on a literature procedure, Poly(1-pyrenemethyl methacrylate-co-dopamine methacrylamide) (PPyDMA) was synthesized through free-radical polymerization where the adhesive monomer, DMA, accounts for 36% of this copolymer by mole (1H- nuclear magnetic resonance spectroscopy). PPyDMA has a high number-average molecular weight of 28,672 Dalton and a polydispersity index of 1.9, typical value for a free-radical process, while being soluble in solvents such as tetrahydrofuran (THF) and N-Methylpyrrolidone (NMP). Wide-angle X-ray scattering (WAXS) results show the ordered phase characteristic of the pyrene in both PPY and PPyDMA (Figure IV-176a). Diffraction peaks are located at  $\sim 0.95 \text{ \AA}^{-1}$  and  $\sim 1.02 \text{ \AA}^{-1}$ , respectively. This corresponds to a lattice spacing of  $\sim 0.6$  nanometers (nm). The broadening of the diffraction peak for the PPyDMA sample indicates that the crystal grain size is smaller when copolymerized with DMA moieties (Figure IV-176b).

To ensure that the newly-designed PPyDMA binder still maintains the electronic conductivity, the study looked at the electronic structure of both the PPy and PPyDMA polymers using synchrotron-based x-ray absorption spectroscopy (sXAS). sXAS is a direct probe of the excitations of core level electrons to the unoccupied valence states. Previous results of this work demonstrated that sXAS could be employed to study the electric properties of polymer materials efficiently. The methodology is based on the fact that the lowest-energy sXAS feature directly corresponds to the state of the lowest unoccupied molecular orbital (LUMO), which is very sensitive to the electric properties of the polymers. Figure IV-176c shows the sXAS spectra of PPy and PPyDMA. The splitting peaks around 285-286 eV correspond to the  $\pi^*C=C$  bonds with conjugation, and the features around 288 eV are from  $\pi^*C=O$ . The study focused on the low-energy sXAS features corresponding to the LUMO states. It is obvious that incorporating the DMA group does not change the lowest-energy features in sXAS, indicating the LUMO of the PPy polymer is intact in PPyDMA. The consistency of the overall lineshape also implies that the electron states close to the Fermi level are dominated by the pyrene-based PPy states. This comparison is thus reliable without core-hole potential concerns.

A CV7 Si-alloy is used as an anode to evaluate the electrochemical performance of the PPyDMA polymer as a binder (Figure IV-176c, d). The pristine particles have a diameter of typically less than 1  $\mu\text{m}$ . Alloying the active Si elements with inactive elements can reduce volume expansion, an improved cycle life is obtained while still maintaining a specific capacity much higher than the graphite anode. Si is present in nano-size domains (Figure IV-176e) within a matrix of other elements, such as Al and Fe. Not only the volume expansion of the active Si phase is buffered by the matrix, the existence of the nano-Si domain could also suppress the formation of the crystalline  $\text{Li}_{15}\text{Si}_4$ . A typical specific capacity of 800~1000 mAh/g is expected for this anode, resulting only 100% volume change during cycling.

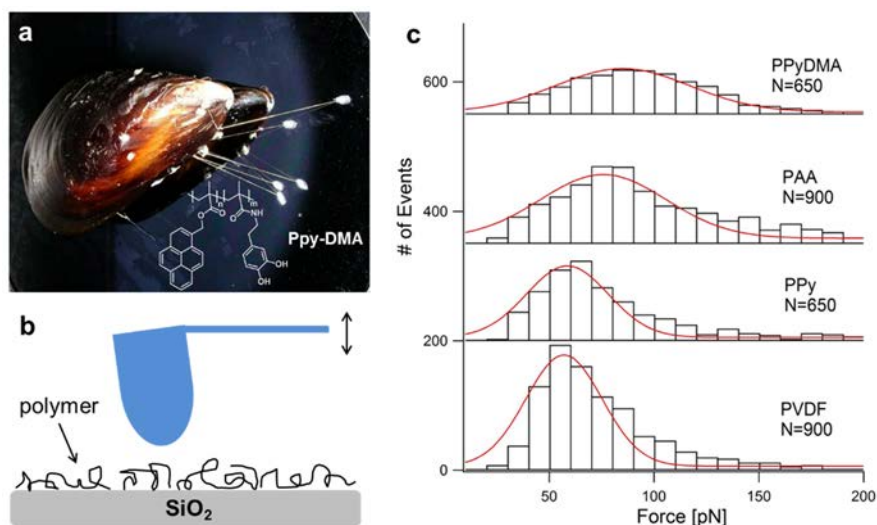


Figure IV-177: AFM tapping mode on the adhesion test of PPy-DMA polymer binder. (b) A schematic illustration of how the characterization of adhesion force is performed. (c) Histograms of AFM rupture force distribution corresponding to pulling a single polymer chain from a silica substrate. N=900 for PVDF, N=650 for PPy, N=900 for PAA, and N=650 for PPyDMA. N is number of observations

The high volume changes of the Si-based anode during cell cycling may cause particle isolation from the polymer during delithiation/shrinkage of the active material particles, which is one of the major electrode failure mechanisms for these high-capacity anodes. To characterize the binding affinity between polymer binders and the Si-alloy anode particles, we have investigated the unbinding forces originated from pulling a single polymer chain of different binders from silica substrate, with the consideration that the higher unbinding force of a single attached polymer chain, the stronger its affinity to substrate. To enable a strict comparison of the unbinding force resulting from different polymers, it is important to isolate and detect a single molecular rupture force. Otherwise, it would be meaningless if the comparison of unbinding force is no single molecular event since the strong unbinding force may come from multiple chains involved at the same time, which is not due to the intrinsic adhesion. To ensure that the observed force was originated from a single molecular event, a novel and complete screening protocol was employed. Figure IV-177c thus shows the histogram of unbinding event of pulling a single PPyDMA, PPy, and PVDF binders on silica substrate at a constant speed. As shown, a single PPyDMA was strongly attached to the silica substrate with the averaged unbinding force value on this

surface being higher than that of a single PPy and PVDF chain on the same surface while the averaged unbinding forces involved were actually very similar between the last two binders, thus suggesting the strongest binding affinity between polymer binders containing DOPA moiety and the Si-alloy anode particles. Taking into consideration that the improved adhesion of binders on silica surface could stabilize the cycling performance toward the Si-alloy anode, it is apparent that from AFM unbinding force measurements the PPyDMA is an ideal binder for Si-alloy anode in lithium-ion batteries, as expected.

The dual functionality of intrinsic electronic conductivity and strong adhesion property of the PPyDMA polymer makes it a promising binder in the use of Si-based high-capacity anode. The electrode was fabricated by dissolving PPyDMA polymer into N-methylpyrrolidone (NMP) solvent, active material particles are then dispersed into the polymer solution by high-speed homogenizer for 1 hour before coating the slurry onto Cu current collector using doctor blade. PPyDMA is determined to be a good binder for either graphite or pure Si nanoparticles, without any need of the conductive additives. The good cycling performance indicates that by randomly incorporating catechol structure into the polymer backbone, pyrene moieties still form good  $\pi$ - $\pi$  stacking, enabling a good electric conductivity of the polymer binder and cycling performance of active materials.

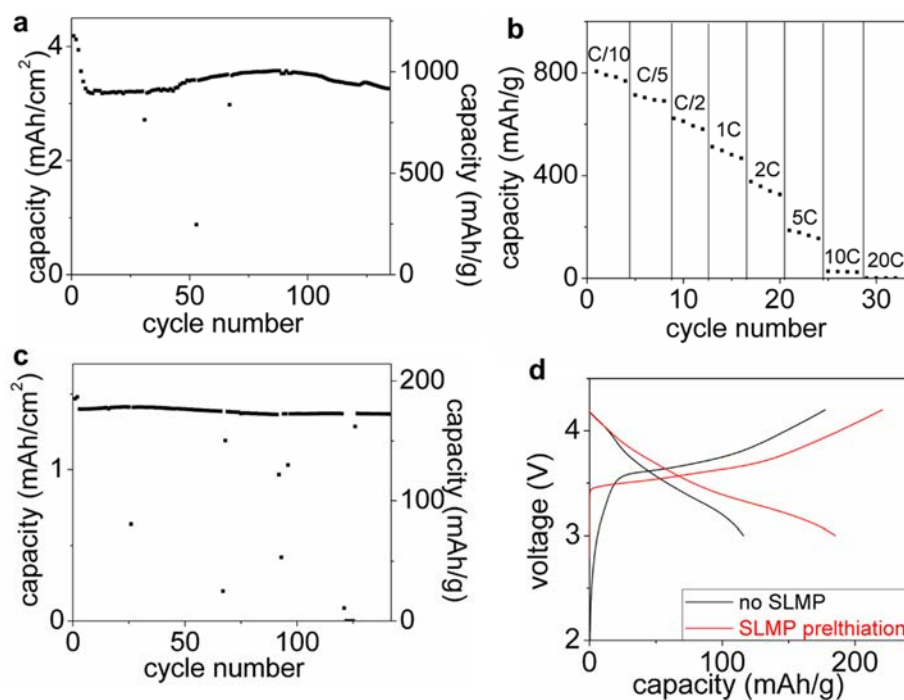


Figure IV-178: Electrochemical performance of PPy-DMA/CV7 Si alloy anode. (a) Specific capacity vs. cycle number of the PPy-DMA/Si alloy anode with different binder contents at C/10. (b) Specific capacity vs. cycle number of Si alloy anode with different types binders (10 wt% binder content) at C/10. (c) Galvanostatic voltage curves and (d) rate performance of the PPyDMA/Si alloy anode laminate. (e) cycling performance and (f) 1st cycle voltage curves of full cells using PPyDMA/Si alloy anode, with or without SLMP prelithiation

When used for the Si alloy anode, as shown in Figure IV-178a, 10 wt% PPyDMA content is determined to be the best composition, which maintains a stable cycling of the CV7 Si alloy anode for more than 100 cycles with a specific capacity of 800 mAh/g. Compared to conventional binders such as polyvinylidene difluoride (PVDF) and carboxymethyl cellulose (CMC), which are intrinsically non-conductive, PPyDMA exhibits an obvious advantage (Figure IV-178b). The homo-PPy polymer is also synthesized and used as a binder. However, PPy does not furnish a good adhesion strength between the binder and the Si alloy particles. Although PPy is established as a conductive polymer binder for Si-based anode, PPy/Si-alloy electrode still suffers capacity decay. The minimum capacity fade from PPyDMA binder is also shown in the voltage curves in Figure IV-178d, the voltage curves at 10th and 100th cycles almost overlap with each other. The rate performance of the PPyDMA/Si alloy anode is shown in Figure IV-178d. Without any conductive additives, the specific capacity enabled by only PPyDMA binder could still retain a specific capacity of above 500 mAh/g at 1C.

**Table IV-31: Electrochemical Data of the Si Alloy Anode Based on Different Binders at C/10. (a Charge (Delithiation) Capacity b Coulombic Efficiency)**

		10%PPyDMA	5%PPyDMA	10% CMC
1st cycle	Qca(mAh/g)	845.2	1006.9	918.6
	Hb (%)	64.64	77.95	82.69
10th cycle	Qca (mAh/g)	780.2	710.1	686.4
	Hb (%)	99.38	98.27	97.86
70th cycle	Qca (mAh/g)	741.1	439.7	94.6
	Hb (%)	99.85	99.20	98.22

Table IV-31 summarizes the electrochemical results of Si alloy with different binders at a C/10 rate. The excellent capacity retention based on 10 wt% PPyDMA binder is directly correlated to the good coulombic efficiency (CE) of the cell, which has a high value of 99.85% at 70th cycle, compared to 98.22% for the CMC binder. Note that the typical 1st CEs for the Si alloy is in the range of 70%, an prelithiation method should be able to address issue toward a lithium-ion full cell application, which was demonstrated recently in a SiO anode. A nickel-cobalt-manganese (NCM 6/2/2) cathode is used to assemble full cell for the PPyDMA/Si alloy anode. A 48-hour rest period was used to allow the crushed SLMP to fully prelithiate the Si alloy anode before current-driven charging of the cells. Both full cells were put in a formation process consisting of two cycles at C/10 prior to C/3 cycling. Apparent improvement was shown for the SLMP-loaded full cells. The first cycle CE increased from 65.41% to ~84% with the SLMP. Compared to the regular cell without SLMP, the voltage profile at both ends (start of charge and end of discharge) are distinctly different, indicating different lithiation and delithiation of Si alloy anode during these two stages. In the first cycle charge process, SLMP eliminated the needs for SEI formation and activation of the anode, so the curve goes directly to the anode lithiation voltage region. When SLMP is not used, this charging curve shows a long multi-plateau curvature accounting for a capacity of ~30 mAh/g, which is typical for irreversible processes of Si alloy anode activation and SEI formation.

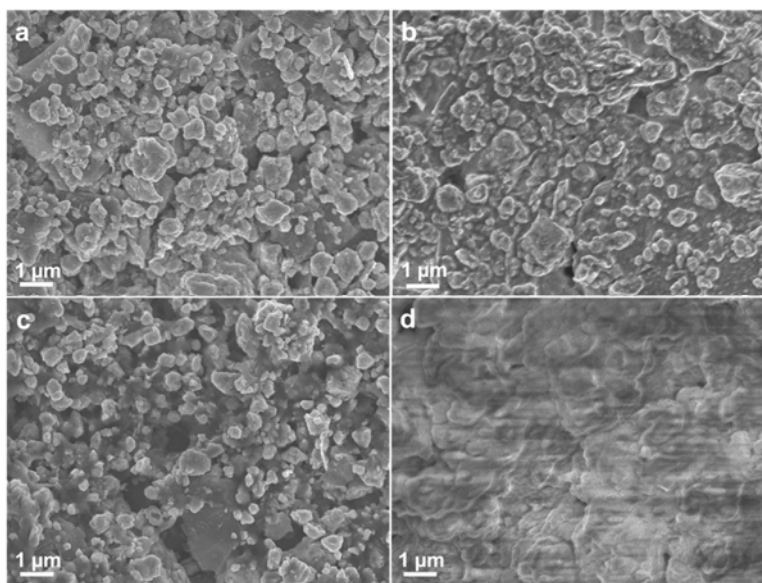


**Figure IV-179: SEM images of the Si-alloy anode-based electrodes. (a) pristine and (b) after 10 cycles at C/10 of the PPy-DMA-based electrode. (c) pristine and (d) after 10 cycles at C/10 of the PVDF-based electrode**

The SEM images of the Si electrodes after long-term cycling are shown in Figure IV-179. Compared to the conventional electrode with a nonconductive binder (PVDF), the decomposition layer on the PPyDMA-based electrode was much thinner. The Si alloy particles were still individually visible after 10 cycles of deep charge and discharge. In a conventional electrode with PVDF binder, the continuous volume change of active material particles makes the stable SEI formation impossible. The volume expansion of Si alloy during lithiation

exposes new surfaces, leading to additional SEI formation and more side reaction products. However during delithiation, the Si particles shrink, and the SEI crumbles from the Si surface. These processes cause the formation of a thick layer of organic species due to the continuous decomposition of the electrolyte (Figure IV-179d). In contrast, the PPyDMA conductive binder-based electrode has a much thinner SEI layer after repeated cycles, and SEI growth is very minimal. The edges of Si alloy particles are clearly visible with very minimum size changes after 10 cycles (Figure IV-179b). The PPyDMA-based electrode has 10% binder to entirely cover the Si alloy particle surfaces. Due to the electric conductivity of the pyrene and the strong adhesion force of the catechol moiety, the intimate binding between binder and Si alloy particle is consistently maintained during cell cycling. The strong adhesion between PPyDMA and Si-alloy particles ensures that the particle surface is completely covered by the binder to form an artificial SEI. The real SEI is formed on the surface of the PPyDMA binder instead of on the active material particle surface directly. Since the polymer tends to have higher free volume, the PPyDMA binder provides volume stability during Si volume expansion and contraction. PPyDMA polymers completely cover the particle surface during the volume change, which reduces the contact between the Si alloy particles and the electrolyte, and continuous consumption of the electrolyte is hindered. Therefore, the SEI on the PPyDMA/Si alloy electrode is much more stable compared to the SEI on the conventional composite. This is also confirmed by the high coulombic efficiency of 99.8% during long-term cycling.

Inspired by the mussel holdfast foot protein, combined with the established side-chain conductive polymer, a DOPA-containing conductive polymer was developed and characterized as an effective binder for a Si-alloy anode in lithium-ion batteries. The facile synthetic route of the side-chain conductive polymer relaxes the requirement for synthesis and allows easy incorporation of the functional adhesion moieties such as DOPA. A quantitative analysis of the adhesion between polymer and silica confirms the strong adhesion force, which contribute significantly to improving the capacities and cycle lives of the Si alloy anode. The commercial Si-alloy anodes reaches a high specific capacity of 800 mAh/g, a much higher value compared to the state-of-the-art graphite anode. Combined with a prelithiation method, the lithium ion full cell based on this novel binder-enabled high capacity anode delivers a high 1st cycle efficiency (84%) and a stable cycling at high material loadings. The mussel-inspired functional conductive polymer binder solves the volume expansion and low first-cycle coulombic efficiency problems, leading to a high-energy lithium-ion chemistry.

## Conclusions

The team has completed the project and is very appreciative of the support provided by the Department of Energy. The final project report was successfully submitted. 18650 format cells with advanced chemistry were also shipped to the DOE-designated facility, ANL.

## Products

## Presentations/Publications/Patents

1. "Silicon Alloy Anode: Sudden Fade Challenge", ES256\_Singh\_2015\_p, US DOE Vehicle Technologies AMR, 2015.
2. "Advanced high energy Lithium-ion Cell for PHEV and EV", ES210\_Singh\_2015\_p, US DOE Vehicle Technologies AMR, 2015.
3. "Advanced high energy Lithium-ion Cell for PHEV and EV", ES210\_Singh\_2015\_p, US DOE Vehicle Technologies AMR, 2016.

## IV.D.2. New High Energy Electrochemical Couple for Automotive Applications (ANL)

### **Khalil Amine, Principal Investigator**

Argonne National Laboratory  
9700 South Cass Avenue  
Argonne, IL 60439-4837  
Phone: 630-252-3838; Fax: 630-972-4520  
E-mail: [amine@anl.gov](mailto:amine@anl.gov)

### **Peter Faguy, DOE Program Manager**

U.S. Department of Energy  
Vehicle Technologies Office  
1000 Independence Avenue, SW  
Washington, DC 20585  
Phone: 202-586-1022  
E-mail: [Peter.Faguy@ee.doe.gov](mailto:Peter.Faguy@ee.doe.gov)

Start Date: October 2013

End Date: September 2015

### **Abstract**

### **Objectives**

The main objective of the project is to develop a new redox couple that meets and exceeds the DOE targeted energy density of 200 Wh/kg and exhibits outstanding cycle and calendar life, low cost, and excellent abuse tolerance.

### **Accomplishments**

- Optimize the process of making FCG material and demonstrate capacity as high as 210 mAh/g with 2.7 g/cc tap density.
- Confirm thermal stability and safety of FCG material using soft and hard X-ray analysis in collaboration with Brookhaven.
- Scale up FCG cathode to 1-kg level for electrode making using the Cell Analysis, Modeling, and Prototyping (CAMP) facility at Argonne.
- Demonstrate that capacity, cycle life, and safety of the FCG (6:2:2) cathode outperform those of the NMC (6:2:2) baseline cathode.
- Improve the efficiency of the  $\text{SiO-Sn}_{30}\text{Co}_{30}\text{C}_{40}$  anode to 81% by developing  $\text{SiO-Sn}_{30}\text{Co}_{30}\text{C}_{40}$ -MAG graphite composite and scale up the new composite to 1-kg level.
- Develop a suitable binder that works well with the new composite anode for Gen 1 cell fabrication.
- Develop a new prelithiation process to eliminate the large irreversible loss on  $\text{SiO-Sn}_{30}\text{Co}_{30}\text{C}_{40}$  anode
- Build prototype cell and test.

### **Future Achievements**

A redox couple that provides specific energy in excess of 200 Wh/kg with cycle life of at least 500 cycles can be developed

- A high-voltage (~4.5 V) and high-capacity cathode composed of lithium manganese, cobalt, and nickel metal oxide (~210 mAh/g) with full concentration gradient across each particle (FCG) to stabilize the material at high voltage.
- A high-capacity and high-density composite anode composed of  $\text{SiO-Sn}_x\text{Co}_y\text{Fe}_{1-y}\text{C}_z$  with conductive binder to enhance cycle life.

## Technical Discussion

### Background

Lithium-ion batteries exhibit the highest power and energy density of any existing commercial battery system and offer many advantages for applications in the transportation sector.<sup>1</sup> Among existing cathode chemistries used in lithium batteries,  $\text{LiMn}_2\text{O}_4$  spinel (LMO)<sup>2</sup> and  $\text{LiFePO}_4$  olivine (LFP)<sup>3</sup> show considerable promise for high-power applications such as hybrid electric vehicles (HEVs), where power is more important than energy. However, these cathodes offer very limited capacity, and thus are not suitable for plug-in hybrid vehicles (PHEVs) and full electric vehicles (EVs). The layered oxide materials such as  $\text{LiNi}_{0.8}\text{Co}_{0.1}\text{Mn}_{0.1}\text{O}_2$  or  $\text{LiNi}_{0.8}\text{Co}_{0.15}\text{Al}_{0.05}\text{O}_2$  (NCA) and  $\text{Li}_{1.1}[\text{Ni}_{1/3}\text{Mn}_{1/3}\text{Co}_{1/3}]_{0.9}\text{O}_2$  (NMC) offer higher capacity than LMO and LFP, but the capacity is not high enough to meet the PHEV (with 40-mile electric range) and full EV demands within a required volume and weight that does not compromise the trunk volume and vehicle performance.<sup>4</sup> Therefore, cathodes possessing very high capacity (over 200 mAh/g), good cycle and calendar life, and outstanding safety are urgently needed for use in EVs and PHEVs-40, which require thousands of charge-depleting cycles and 15 years of calendar life.

### Introduction

Among the cathode materials that have the potential of providing either very high capacity or high voltage are the layered lithium mixed metal oxides such as Argonne's layered composite oxide  $x\text{Li}_2\text{MnO}_3 \cdot (1-x)\text{LiMO}_2$  (M=Ni, Co),<sup>5</sup> and  $\text{LiNi}_{1-x}\text{Mn}_y\text{Co}_z\text{O}_2$ <sup>6,7</sup> for high energy, and  $\text{LiNi}_{0.5}\text{Mn}_{1.5}\text{O}_4$  (4.8 V),<sup>8</sup>  $\text{LiMnPO}_4$  (4.1 V),<sup>9</sup> and  $\text{LiCoPO}_4$  (5.1 V)<sup>10</sup> for high voltage.

The practical capacity of layered lithium mixed metal oxides, such as  $\text{LiNi}_{0.8}\text{Co}_{0.1}\text{Mn}_{0.1}\text{O}_2$ , NCA, and NMC, is only 50% of the theoretical maximum (275 mAh/g) under the operating potential window of 4.2 V~3 V. Operating at voltages higher than 4.3 V can lead to a significant increase in the specific capacity up to 220 mAh/g. However, at high potential, the cycle life of this material is very poor. This fast capacity decay with cycling is caused by the high interfacial reactivity of the fully charged electrode with the electrolyte, which leads to film growth at the surface of the cathode and an increase in the cell interfacial impedance with cycling. The high reactivity with the electrolyte is caused by the high concentration of unstable tetravalent Ni during high voltage charge, which reduces to stable divalent Ni and leads to  $\text{O}_2$  release from the particle surface, oxidation of the electrolyte, and formation of a polymeric film at the surface of the cathode. Similar characteristics, mainly a capacity increase at high voltage accompanied by capacity fade during cycling, were also observed for NCA and NMC.

### Approach

Argonne (ANL) is working closely with Brookhaven (BNL) and Lawrence Berkeley National Laboratory (LBNL) to develop an advanced electrochemical couple. The cathode is a high-voltage, high-capacity, and dense material with FCG across each particle, and the anode is a high-capacity and high-density  $\text{SiO-Sn}_x\text{Co}_y\text{Fe}_{1-y}\text{C}_z$  composite that offers capacities higher than 600 mAh/g. This system will be investigated in cell tests using a conventional electrolyte with additives that stabilize the interface of both the cathode and anode.

### Results

#### Optimization of full concentration gradient (FCG) cathodes

The second (and last) year of the project was focused on optimizing the synthesis conditions needed to obtain the FCG cathode material with high capacity, good cycle life at high voltage, high tap density that leads to high active material loading at the electrode level, and spherical morphology with sharp particle distribution. The focus was on an average composition  $\text{LiNi}_{0.6}\text{Mn}_{0.2}\text{Co}_{0.2}\text{O}_2$  cathode (6:2:2) but with gradient concentration across the particle.

After a significant effort in optimizing the co-precipitation condition (including the speed of the precursor feed to the reactor, the stirring angle and condition, the pH of the solution, the chelating agent nature, and the co-precipitation agent concentration), we focused our attention on the calcination temperature, as it can impact the

gradient concentration across the particle. Very high calcination temperature can lead to significant displacement of the metals within the particle, affecting the concentration gradient of Ni, Co, and Mn across the particle.

Figure IV-180 shows the first charge and discharge capacity of different cells made with FCG (6:2:2) cathode calcined at different temperatures and the effect of the calcination condition on the rate capability. In this case, the material was pre-calcined at 500°C at different times and further calcined at elevated temperatures (between 700°C and 850°C).

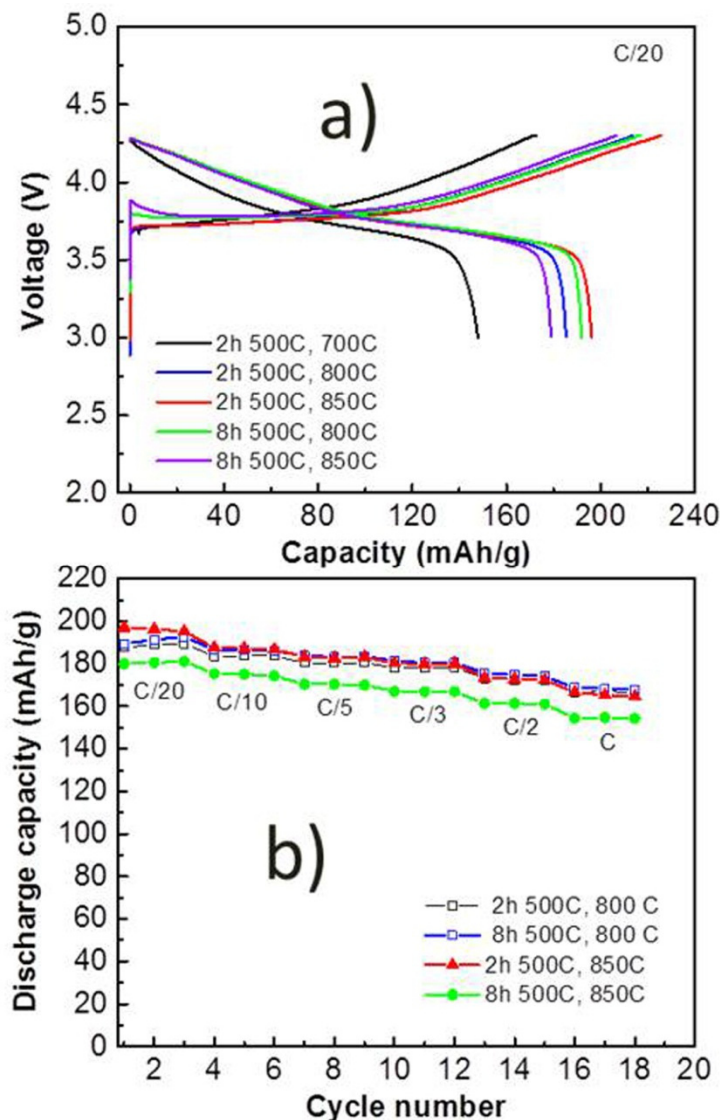


Figure IV-180: (a) Initial charge and discharge capacities with different calcination temperature and (b) capacity vs. rate at different calcination temperatures of FCG  $\text{LiNi}_{0.6}\text{Mn}_{0.2}\text{Co}_{0.2}\text{O}_2$  cathode

Figure IV-181a shows the initial charge and discharge curve of the FCG (6:2:2) cathode at different cut off voltage. The cell that cycled up to 4.5 V shows a capacity of 210 mAh/g. The rate capability and the cycling performance of the cell cycled to 4.5 V are similar to those cycled at lower cut off voltage (Figure IV-181b and Figure IV-181c). This result clearly indicate that the full concentration gradient approach significantly enhances the interfacial stability of the cathode with the electrolyte. This conclusion is reinforced by the excellent cycling performance of the FCG (6:2:2) cathode when operating at 55°C (see Figure IV-182).

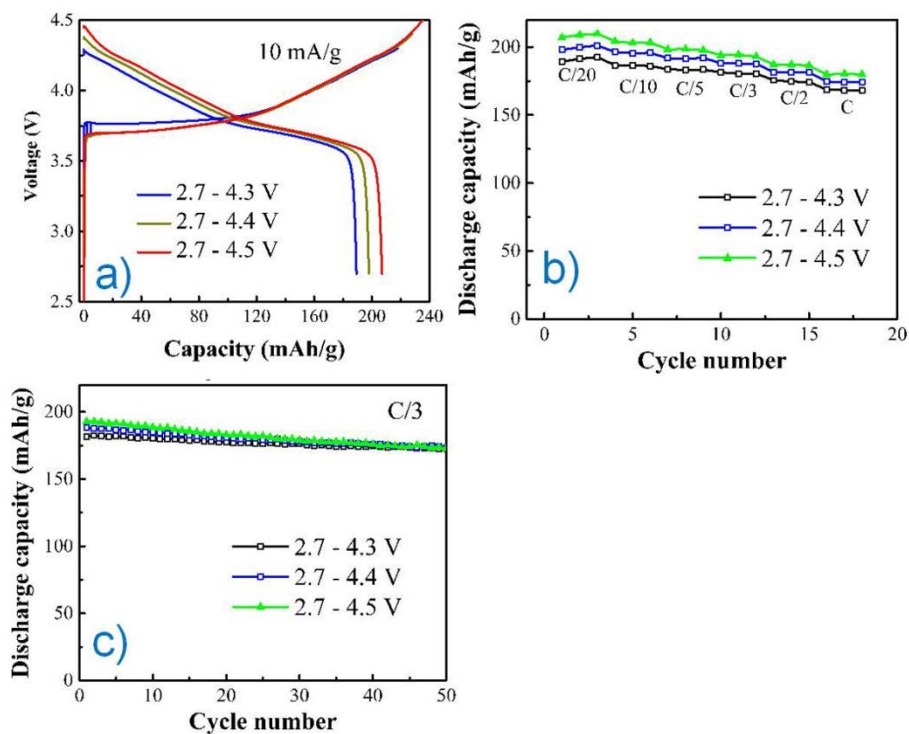


Figure IV-181: (a) Initial charge and discharge capacities of FCG (6:2:2) cathode at different cut-off voltages and (b) rate capability of cells cycled at different cut of voltages and c) capacity vs. cycle number of FCG cycled at different cut of voltages

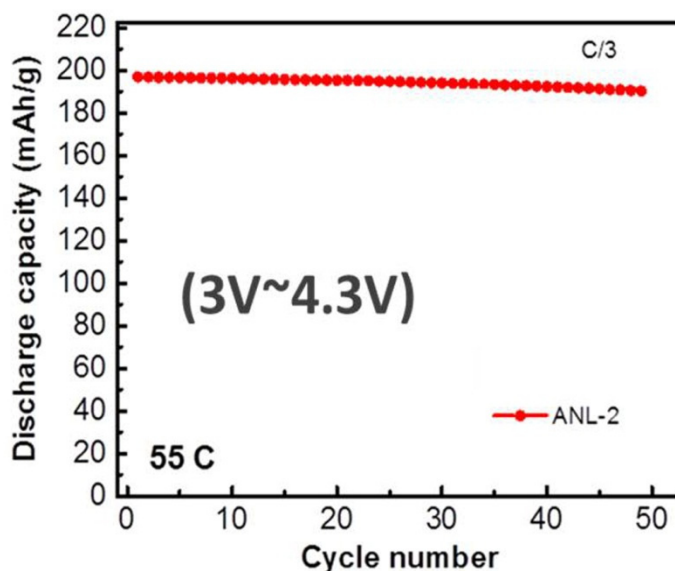


Figure IV-182: Cycling performance of FCG cathode at 55 °C

### Anode material development

In the first year of this project, our focus was on scaling up the anode material to 1-kg level and using 90% of it as active material in the electrode. However, the irreversible loss during the initial cycling was extremely high (charge, 1600 mAh/g, and discharge, 900 mAh/g). As a result, the energy density of the cell based on FCG and  $\text{SiO-Sn}_x\text{Co}_y\text{C}_z$  composite becomes low since a large amount of lithium from the cathode was used to compensate for the large irreversible loss of the anode.

In the second and last year, the focus was on optimizing a blend of  $\text{SiO-Sn}_x\text{Co}_y\text{C}_z$  composite with graphite to reduce the irreversible loss. In this case, both the graphite and  $\text{SiO-Sn}_x\text{Co}_y\text{C}_z$  composite are active. Adding a

large amount of graphite will provide the conductive network needed to prevent the  $\text{SiO-Sn}_x\text{Co}_y\text{C}_z$  composite from particle isolation during the cycling process. The other focus was on selecting a binder that works well with this new anode and the final focus was on developing a pre-lithiation concept to reduce significantly the first irreversible capacity loss of  $\text{SiO-Sn}_x\text{Co}_y\text{C}_z$  composite.

Since the cell performance using conductive binder in the anode was not satisfactory, we extensively investigated numerous other binders, such as polyimide binder (PI), polyacrylic binder (PAA), polyvinylidene fluoride (PVDF) binder mixed with PI, PVDF mixed with PAA, and lithiated polyacrylic binder (LiPAA). The cells with PAA and LiPAA show very good performance (Figure IV-183): a capacity of 550 mAh/g and an initial coulombic efficiency of 81%, which are much better than those obtained with PVDF, PI, and the LBNL conductive binder that was originally selected. The best cell performance was obtained with 5% LiPAA: a capacity of 670 mAh/g and 81% efficiency. The cell with LiPAA binder showed no capacity loss after numerous cycles (Figure IV-183 and Figure IV-184).

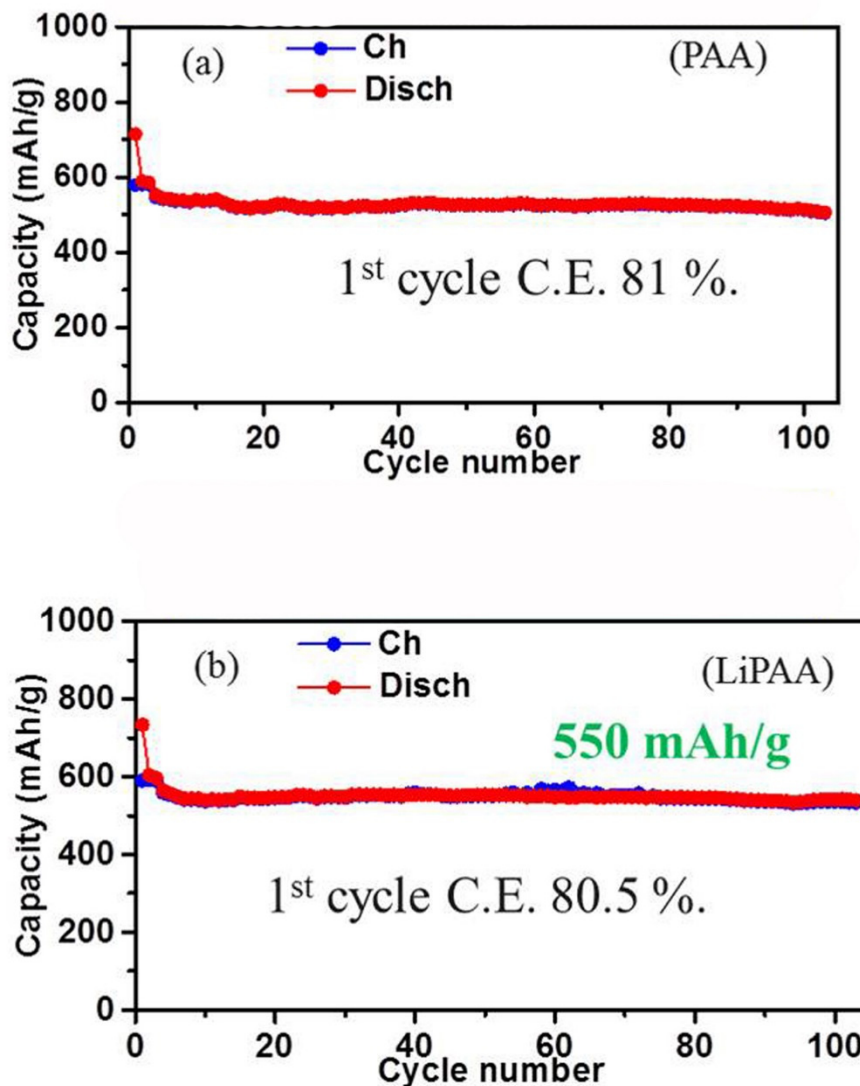


Figure IV-183: Cycling performance of cells based on  $\text{SiO-Sn}_x\text{Co}_y\text{C}_z$  and MAG anode using (a) 5% PAA binder and (b) 4% LiPAA binder

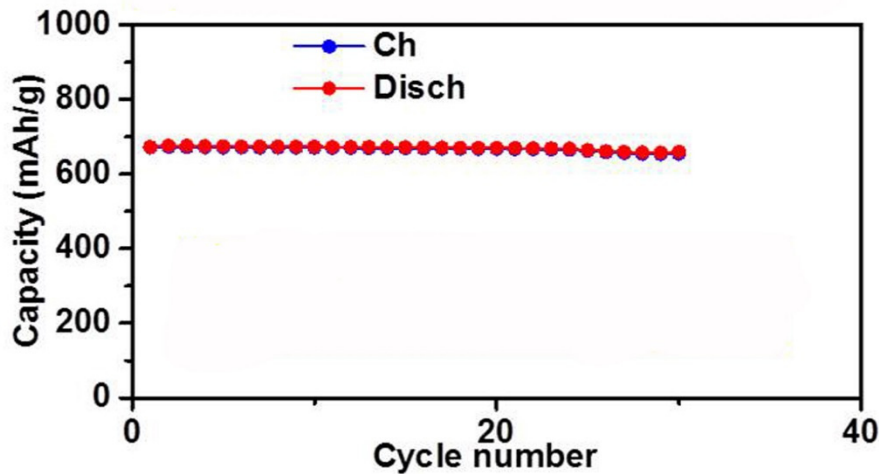


Figure IV-184: Cycling performance of a cell based on SiO-Sn<sub>x</sub>Co<sub>y</sub>C<sub>z</sub> and MAG anode using 5% LiPAA binder

The optimum composition of the composite anode was provided to the CAMP facility for making cells based on the FCG (6:2:2) cathode and SiO-Sn<sub>x</sub>Co<sub>y</sub>C<sub>z</sub>/MAG graphite composite anode with LiPAA binder. However, because the active material loading of the anodes made at the CAMP facility shows a different distribution within the same electrode, the decision was made to build a cell based on the FCG cathode and graphite anode as an intermediate cell build until the issue of electrode coating at the CAMP facility is addressed. These intermediate cells were built at the CAMP facility and were shipped to Idaho National Laboratory for testing. Some of these cells were also tested at Argonne National Laboratory. Figure IV-185 shows the cycling performance of a full cell having an initial capacity of 460 mAh. The cell was cycled up to 4.3 V at 1C rate. The cell lost only 12% capacity at this high operating voltage after 280 cycles.

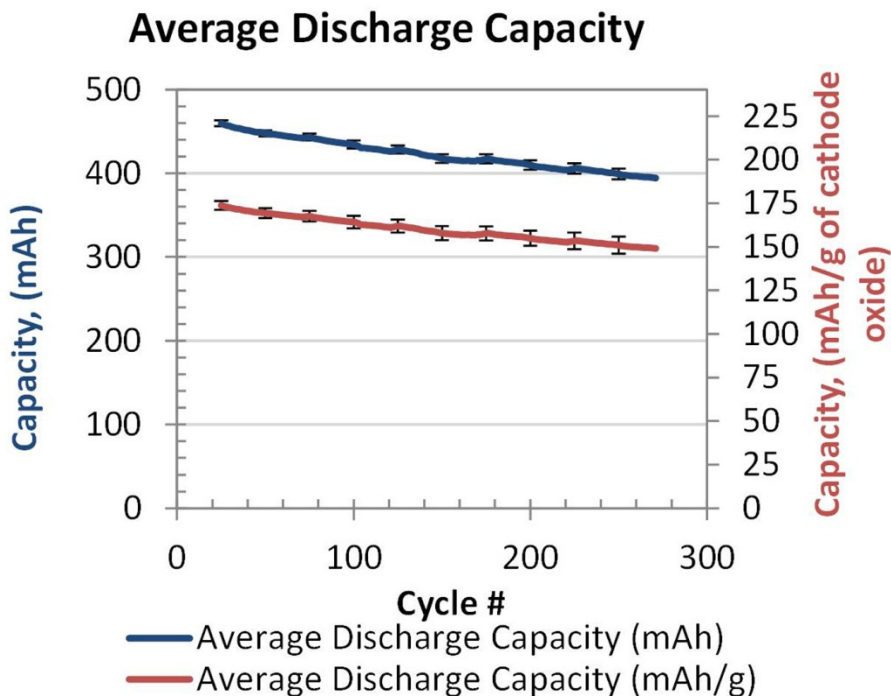


Figure IV-185: Cycling performance of a full cell having FCG (6:2:2) cathode and graphite (MAG anode)

### New prelithiation concept

Despite the existence of high-capacity anodes such as silicon composites, the use of these materials in commercial batteries is limited due to their large first-cycle irreversibility. In a full cell, a large excess of cathode material has been added to compensate for the irreversible capacity loss at the anode, but the energy

density of the cell has only been increased slightly. One possibility is to use a small amount of lithium to partially pre-lithiate these anodes, but this causes a safety concern because of the potential fire hazard. Recently, a new stabilized lithium metal powder (SLMP) was introduced to overcome the first-cycle irreversibility in full cells.<sup>11</sup> This lithium powder, which is coated with lithium carbonate, can be mixed with anode materials such as silicon or graphite in a dry condition. The main drawback of SLMP is its incompatibility with the N-methylpyrrolidone or water solvent used to prepare electrodes, and the need of calendaring the electrode to fracture the  $\text{Li}_2\text{CO}_3$  coating shell and thereby activate the lithium powder. Shanmukaraj et al. proposed the use of  $\text{Li}_3\text{N}$  as a source of lithium in the cathode; unfortunately, this material cannot be used for large battery applications due to its high reactivity.<sup>12</sup>

In this work, we demonstrate that  $\text{Li}_2\text{O}$  can be electrochemically activated in LIBs when it is mixed with a high-capacity composite cathode material, such as  $\text{Li}_2\text{MnO}_3\text{-LiMO}_2$  ( $\text{M}=\text{Mn, Ni, Co}$ ), and can work as a lithium source to compensate for the first-cycle irreversibility of full cells having high capacity anodes such as silicon composites and alloys.

$\text{Li}_2\text{O}$  was mixed with a  $\text{Li}_2\text{MnO}_3\text{-LiMO}_2$  composite material, named thereafter HEM (“high energy material”). This HEM- $\text{Li}_2\text{O}$  electrode was charged to 4.7 V with a lithium anode and the Gen I electrolyte [1M  $\text{LiClO}_4$  in EC: EMC (3:7 ratio by weight)]. Interestingly, a large plateau at ~4.45 V was observed during the initial charge of the HEM- $\text{Li}_2\text{O}$  electrode as shown in Figure IV-186. The first charge capacity of ~600 mAh/g of HEM is close to twice the charge capacity of the HEM cathode material by itself (300 mAh/g). The large observed charging capacity is due to  $\text{Li}_2\text{O}$  being activated at high voltage. The influence of the electrolyte and anode was then investigated. To understand the role of the electrolyte in the  $\text{Li}_2\text{O}$  activation, we conducted coin cell tests with electrolytes (Gen I) and Gen II [1.2 M  $\text{LiPF}_6$  in EC: EMC (3:7 ratio by weight)]. The carbonate electrolytes were selected because of their relative stability at high voltage and the need to activate HEM at 4.7 V. Similar capacities were obtained using either the Gen I or Gen II electrolytes in half-cell tests at the 10 mA/g rate as shown in Figure IV-186.

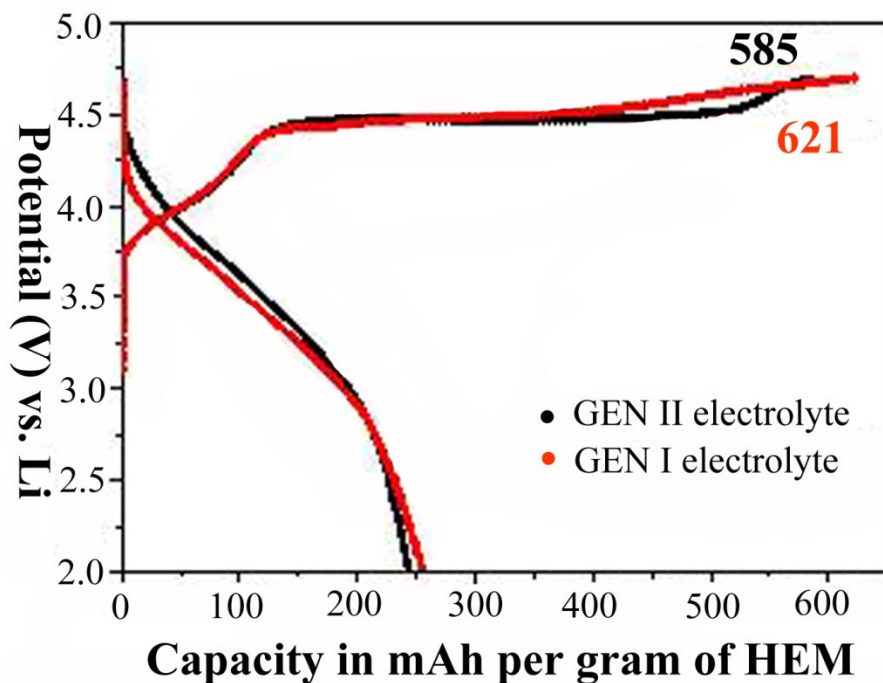


Figure IV-186: Voltage profile versus capacity of HEM- $\text{Li}_2\text{O}/\text{Li}$  half-cell with Gen I and Gen II electrolytes ( $I = 10 \text{ mA/g}$ )

Based on this new concept of prelithiation, we fabricated and tested HEM- $\text{Li}_2\text{O}/\text{SiO-SnCoC}$  and HEM/ $\text{SiO-SnCo}$  full cells. The oxide-alloy anode provided good cycling performance but suffered from a high initial irreversible capacity of ~35%. The capacity obtained based on the HEM cathode weight is higher than 250 mAh/g with the presence of  $\text{Li}_2\text{O}$ , while it is less than 180 mAh/g without the  $\text{Li}_2\text{O}$  as shown in Figure IV-187.

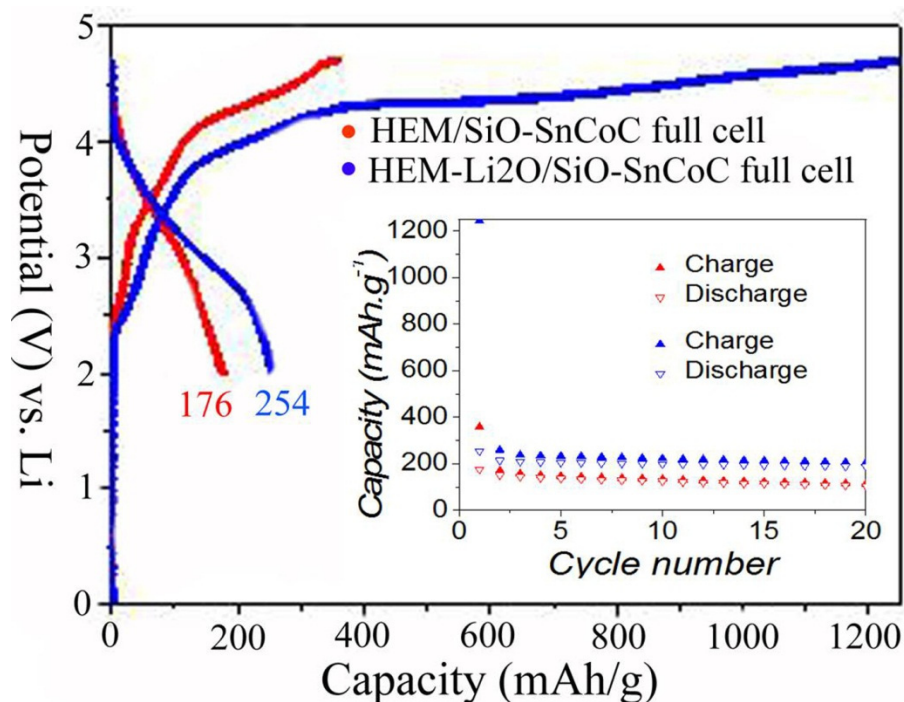


Figure IV-187: First-cycle voltage profile versus capacity and cycling performance (inset) of HEM-Li<sub>2</sub>O/SiO-SnCoC and HEM/SiO-SnCoC full cells (GEN I electrolyte)

The degree of activation depends on the current rate, electrolyte salt, and anode type. In full-cell tests, the Li<sub>2</sub>O was used as a lithium source to counter the first-cycle irreversibility of high-capacity composite alloy anodes. When Li<sub>2</sub>O is mixed with the HEM to serve as a cathode, the electrochemical performance was significantly improved in a full cell having a SiO-SnCoC composite as an anode. These results points to the likelihood of the role of Li<sub>2</sub>O, present as traces in the pristine HEM type materials or formed during the charge process, in significantly extending the first charge plateau through redox shuttle reaction. It is true that in our example, 20% of Li<sub>2</sub>O added in the electrode is a high amount because it is not yet optimized. Nevertheless, based on our ICP/X-ray measurements we found that the amount of activated Li<sub>2</sub>O could reach as high as 68% of its 1675 mAh theoretical capacity (=1139 mAh/g). As example, in a cathode electrode 1.75 mg of Li<sub>2</sub>O per cm<sup>2</sup> can generate a capacity of  $1.75 \times 1675 \times 68\% = 2 \text{ mAh/cm}^2$ . This capacity is needed to accommodate the 40% first cycle irreversibility of silicon based material. For example, if we have a silicon based anode with a reversible capacity of 3 mAh/cm<sup>2</sup> (first cycle irreversibility of 40%) and a cathode material with a capacity of  $3/0.6 = 5 \text{ mAh/cm}^2$  is needed to produce a full cell of 3 mAh/cm<sup>2</sup>. This capacity is obtained with the use of 25 mg/cm<sup>2</sup> of HEM (Li<sub>2</sub>MnO<sub>3</sub>-LiMO<sub>2</sub> (M=Mn, Ni, Co), with practical capacity of 200 mAh/g). However, 40% of this 25 mg/cm<sup>2</sup> HEM (10 mg/cm<sup>2</sup>) is consumed by providing lithium to form SEI on the silicon based material. As only Li from HEM is used, the other elements (nickel, cobalt, manganese and oxygen) are inactive elements and only adding dead weight to the cathode weight. We conclude that 1.75 mg of Li<sub>2</sub>O can possibly replace 10 mg of HEM. Instead of using 2/5 weight ratio of Li<sub>2</sub>O on HEM (in our first attempt), a 1.75/25 weight ratio could solve the first irreversibility of silicon based material. This Li<sub>2</sub>O/HEM weight ratio did not depend on the nature of the used anode material.

## Conclusions

The effect of co-precipitation condition and calcination process on the tap density, morphology and electrochemical properties of full concentration gradient cathodes were investigated. The optimum FCG cathode can deliver a high reversible capacity of 210 mAh/g and maintain excellent cycle and rate performance even when operating at high temperature. SiO-Sn<sub>x</sub>Co<sub>y</sub>C<sub>z</sub> based anode with high reversible capacity of over 600 mAh/g and excellent cycle performance was developed by blending with graphite and LiPAA binder. The optimum FCG/SiO-Sn<sub>x</sub>Co<sub>y</sub>C<sub>z</sub> full cell has only 12% capacity loss in 280 cycles even cycled up to 4.3 V at 1C rate, demonstrating superior cycle performance. Moreover, a new prelithiation process to eliminate the large irreversible capacity loss of conventional anode materials was proposed. We expect that the new redox couple developed here could meet the DOE targeted energy density of 200 Wh/kg for EVs and PHEVs-40 application.

### Presentations/Publications/Patents

1. Liu, B.; Abouimrane, A.; Ren, Y.; Balasubramanian, M.; Wang, D.P.; Fang, Z.G.; Amine, K., *Chem. Mater.* 2012, 24, 4653-4661.
2. Liu, B.; Abouimrane, A.; Balasubramanian, M.; Ren, Y.; Fang, Z.G.; Amine, K., GeO<sub>2</sub>-Snoc Composite Anode Material for Lithium Batteries: Li Insertion and De-Insertion Study, 224th ECS meeting, 2013.
3. Liu, B.; Abouimrane, A.; Ren, Y.; Neufeind, J.; Fang, Z.G.; Amine, K., *J. Electrochem. Soc.* 2013, 160, A882-A887.
4. Liu, B.; Abouimrane, A.; Brown, D.; Zhang, X.F.; Ren, Y.; Fang, Z.G.; Amine, K., *J. Mater. Chem. A* 2013, 1, 4376-4382.
5. Liu, B.; Abouimrane, A.; Balasubramanian, M.; Ren, Y.; Amine, K., *J. Phys. Chem. C* 2014, 118, 3960-3967.
6. Lee, E.J.; Chen, Z.H.; Noh, H.J.; Nam, S.C.; Kang, S.; Kim, D.H.; Amine, K.; Sun, Y.K., *Nano Lett.* 2014, 14, 4873-4880.
7. Abouimrane, A.; Cui, Y.; Chen, Z.H.; Belharouak, I.; Yahia, H.B.; Wu, H.M.; Assary, R.; Cuitiss, L.A.; Amine, K., *Nano Energy* 2016, 27, 196-201.
8. Li, Y.; Xu, R.; Ren, Y.; Lu, J.; Wu, H.M.; Wang, L.F.; Miller, D.J.; Sun, Y.K.; Amine, K.; Chen, Z.H., *Nano Energy* 2016, 19, 522-531.
9. Zhao, H.; Fu, Y.B.; Ling, M.; Jia, Z.; Song, X.Y.; Chen, Z.H.; Lu, J.; Amine, K.; Liu, G., *ACS Appl. Mater. Interf.* 2016, 8, 13373-13377.
10. Abouimrane, A.; Amine, K., Anode materials for lithium-ion batteries, U.S. Patent, US9054373 & US20150255785.
11. Wu, H.M.; Amine, K.; Abouimrane, A., Electroactive materials for rechargeable batteries, U.S. Patent, US9012091 & US20150228964.

### References

1. Armand, M.; Tarascon, J. M. *Nature* **2008**, 451, 652-657.
2. Belharouak, I.; Sun, Y. K.; Lu, W.; Amine, K. *J. Electrochem. Soc.* **2007**, 154, A1083-A1087.
3. Kang, B.; Ceder, G. *Nature* **2009**, 458, 190-193.
4. Yu, H. J.; Zhou, H. S. *J. Phys. Chem. Lett.* **2013**, 4, 1268-1280.
5. Yu, X. Q.; Lyu, Y. C.; Gu, L.; Wu, H. M.; Bak, S. M.; Zhou, Y. N.; Amine, K.; Ehrlich, S. N.; Li, H.; Nam, K. W.; Yang, X. Q. *Adv. Energy Mater.* **2014**, 4, 1300950.
6. Sun, Y. K.; Chen, Z. H.; Noh, H. J.; Lee, D. J.; Jung, H. G.; Ren, Y.; Wang, S.; Yoon, C. S.; Myung, S. T.; Amine, K. *Nat. Mater.* **2012**, 11, 942-947.
7. Sun, Y. K.; Myung, S. T.; Park, B. C.; Prakash, J.; Belharouak, I.; Amine, K. *Nat. Mater.* **2009**, 8, 320-324.
8. Belharouak, I.; Koenig, G. M.; Ma, J. W.; Wang, D. P.; Amine, K. *Electrochem. Commun.* **2011**, 13, 232-236.
9. Delacourt, C.; Poizot, P.; Morcrette, M.; Tarascon, J. M.; Masquelier, C. *Chem. Mater.* **2004**, 16, 93-99.
10. Amine, K.; Yasuda, H.; Yamachi, M. *Electrochem. Solid State Lett.* **2000**, 3, 178-179.
11. Li, Y. X.; Fitch, B. *Electrochem. Commun.* **2011**, 13, 664-667.
12. Shanmukaraj, D.; Grugeon, S.; Laruelle, S.; Douglade, G.; Tarascon, J.-M.; Armand, M. *Electrochem. Commun.* **2010**, 12, 1344-1347.

## IV.D.3. High Energy Lithium Batteries for PHEV Applications (Envia Systems, LBNL, ORNL, GM)

### Subramanian Venkatachalam, Principal Investigator

Envia Systems  
7979 Gateway Boulevard, Suite 101  
Newark, CA 94560  
Phone: 510-962-3688; Fax: 510-790-7012  
E-mail: [mani@enviasystems.com](mailto:mani@enviasystems.com)

### Peter Faguy, DOE Program Manager

U.S. Department of Energy  
Vehicle Technologies Office  
1000 Independence Avenue, SW  
Washington, DC 20585  
Phone: 202-586-1022  
E-mail: [Peter.Faguy@ee.doe.gov](mailto:Peter.Faguy@ee.doe.gov)

Start Date: October 2013  
End Date: March 2016

### Abstract

Lithium-rich NMC cathodes offer high capacity, making this class of materials a perfect choice for automotive applications. However, the inherent material characteristics which show high DC-resistance (DC-R) and voltage-fade which further increases DC-R with each cycle, makes this material less attractive. Additionally, in order to achieve more economic, high energy density batteries, utilization of Si-based anode is also imperative. Si-based anodes show very high capacity, however plagued by a variety of challenges such as poor cycle-life and volume expansion. In this project, Envia Systems in collaboration with LBNL, ORNL and General Motors worked together to understand and mitigate the aforementioned problems so as to enable economically feasible, long-range PHEV's.

### Objectives

- Understand the root-cause of cathodes' DC-R issues via spectroscopic, microscopic, and electrochemical analytical techniques.
- Mitigate High Capacity Manganese Rich (HCMR™) cathodes' DC-R issues via four different surface coating strategies: (a) Plasma Enhanced Chemical Vapor Deposition (PE-CVD) carbon coating (b) Physical Vapor Deposition (PVD) of LiPON, (c) Atomic Layer Deposition (ALD) and solution-based coatings (AlF<sub>3</sub>, Al<sub>2</sub>O<sub>3</sub>, TiN, etc.) and (d) conducting polymer-based coatings.
- Develop atomistic models for HCMR™ cathodes' DC-R rise, phase change, and voltage sag.
- Apply theoretical solutions from atomistic models to mitigate phase change, voltage sag, and DC-R issues for HCMR™ cathodes.
- Develop cell-level models to understand cell behaviors that contribute to DC-R issues.
- Develop suitable conducting polymeric binders for Si-anodes to enhance cycle life and meet the PHEV targets.
- Develop high capacity HCMR™ cathodes, and Si-SiO-C based anodes and integrate them to build high capacity (0.25-40 Ah) pouch-cells that exceed the ABR minimum target goals for PHEVs shown in Table IV-32.

**Table IV-32: Cell Specifications for ABR Target Goals**

Characteristics	Unit	PHEV40
Specific Discharge Pulse Power	W/kg	800
Discharge Pulse Power Density	W/L	1600
Specific Regen Pulse Power	W/kg	430
Regen Pulse Power Density	W/L	860
Recharge Rate	NA	C/3
Specific Energy	Wh/kg	200
Energy Density	Wh/L	400
Calendar Life	Years	10+
Cycle Life (at 30° C with C/3 Charge and 1C Discharge Rates)	Cycles	5000
Operating Temperature Range	°C	-30 to +52

### Accomplishments

- A Li-rich NMC cathode material (HCMR™ XE) which meets the requirements to fabricate PHEV grade automotive cells has been developed.
- Various surface coating studies on HCMR™-XLE and XE cathode materials were performed to mitigate the DC-resistance (DC-R) and voltage fade challenges, however, none showed any significant benefits with respect to DC-R growth mitigation.
- Different SiO-based anode materials were employed to achieve the ABR-PHEV goals mentioned in Table IV.D.4 1.
- 26 Ah cells with 200 Wh/kg and 400 Wh/l (BoL) have been fabricated utilizing HCMR™-XE and SiO based anode system and delivered for independent validation at INL.

### Future Achievements

- Validation of specific energy and energy density from INL
- Cycle life and calendar life performance of the 25 Ah cells from INL

### Technical Discussion

#### Background

In order to reduce the demand of fossil-fuels as the main energy source for automotive vehicles, Plug-in Hybrid Electric Vehicles (PHEVs) that surpass the performance standards for commercially available automobiles are required. Successful development of such PHEVs depends on the development of batteries constructed with cathode and anode materials that provide high capacity, energy, power, and safety. The goal of this project is to develop these advanced cathode and anode materials to construct batteries that can enable the use of next-generation cost-efficient PHEVs.

#### Introduction

With regards to cathode materials for PHEV applications, currently, some of the most attractive materials take on the chemical composition of  $x Li_2MnO_3 \cdot (1-x) LiMO_2$ , where  $x$  represents the molecular fraction and  $M$  represents any such elemental blend of Ni, Co, and Mn. This nomenclature system also reflects the hypothesized two-layered nature of this material, the  $Li_2MnO_3$  Mn-rich layer responsible for the high capacity

of the material and the transition-metal  $LiMO_2$  layer responsible for the cycling stability. This class of materials, also known as High Capacity Manganese Rich (HCMR™) cathodes are known to provide higher capacity, higher safety, and lower material cost than alternative cathode technologies. However, key issues with HCMR™ materials include high DC-Resistance (DC-R), fading of voltage upon cycling, and poor durability, all of which are accentuated after several cycles. Altogether, increasing the content of Mn in the composition of the cathode results in higher capacity and higher safety at the cost of growing DC-R, and worsening voltage retention. For this reason, Envia Systems has developed a family of HCMR™ materials with ranging Mn-content in order to study and identify the optimal chemical composition for HCMR™ materials.

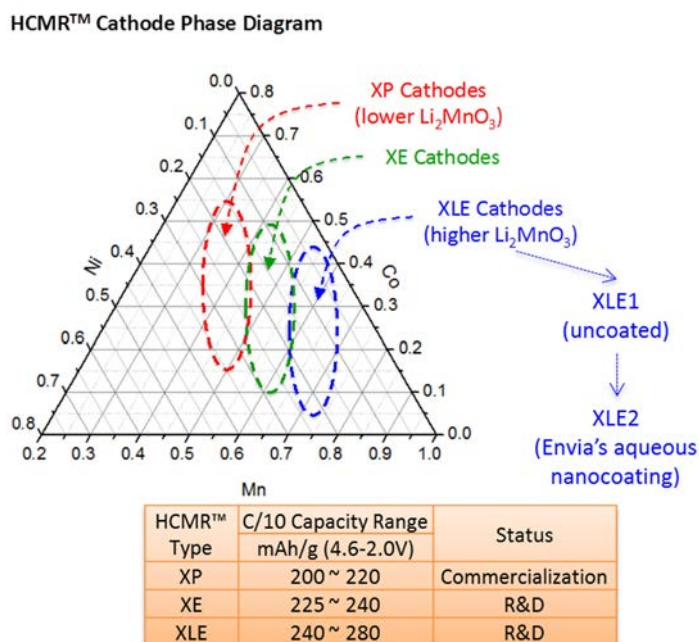


**Figure IV-188: Ternary-phase diagram for Envia Systems' HCMR™ class of cathode materials**  
Envia Systems

Figure IV-188 identifies Envia Systems' HCMR™ cathode material library in the ternary diagram as well as the listing basic electrochemical characteristics of such materials.

It is important to note that in this nomenclature, HCMR™-XLE1 refers to the cathode material as synthesized, while the XLE2 is the further processing of XLE1 material with an Al-halide nm-sized surface coating (nanocoating) deposited onto the material via an aqueous reaction. Usually, the nanocoated analog of the material, which shows improved cycle-life over the uncoated, is the baseline onto which further coatings such as LiPON,  $Al_2O_3$ , or TiN among others, are applied. The same nomenclature applies to HCMR™-XP and XE materials.

At the beginning of this ABR program, the HCMR™-XLE class of materials (higher Mn content) was investigated in order to take advantage of the material's high capacity while preventing the growth of DC-R and loss of cycle ability. Preliminary studies showed that by adding a thin layer of conductive carbon on the surface of the of HCMR™-XLE2 particle, the resistance of the material as a function of SOC at the BoL (Beginning of Life) was severely improved. For instance, the baseline HCMR™-XLE2 shows 75% usable energy, while the Carbon-coated analog showed and improved 82% usable energy. This was obtained by measuring the percentage of energy obtained at a resistance lower than  $75 \Omega/cm^2$  (as measured by an HPPC test between 4.4-2.0V with 10 sec 1C Ch/Dis pulses) from an HCMR™//Graphite cell. However, the HCMR™-XLE2 cathode showed a drastic increase in DC-R and drop in average voltage with each cycle, which could not be addressed by any type of surface modifications. A combination of electrochemical tests and analytical techniques revealed that the HCMR™-XLE material's main degradation process took place in the bulk of the material by irreversible reactions which deteriorate the Mn-rich layer and poison the transition metal layer in addition to surface side-reactions.

Consequently, a second class of materials was introduced in Q5 of this program, the HCMR™-XE, which contains lower content of Mn and shows both higher usable energy (>88%) and energy retention with cycling than the HCMR™-XLE2 (75% usable energy BoL). Figure IV-189 highlights the BoL DC-R improvement for the HCMR™-XE2 when compared the HCMR™-XLE2 analogs. Therefore, in the second year of the program, the development of HCMR™-XE2 cathode materials with surface coatings and the engineering of large capacity cells for cycle-life using this cathode became the main focus.

As the program approaches its conclusion, the material development, diagnostics, and cell modeling efforts have been completed. Nevertheless, important ongoing efforts focus on (i) continuing microscopic investigations on the structural integrity and degradation of HCMR™-XE2 cathode materials and (ii) delivery of 26 Ah final delivery cells for testing at INL.

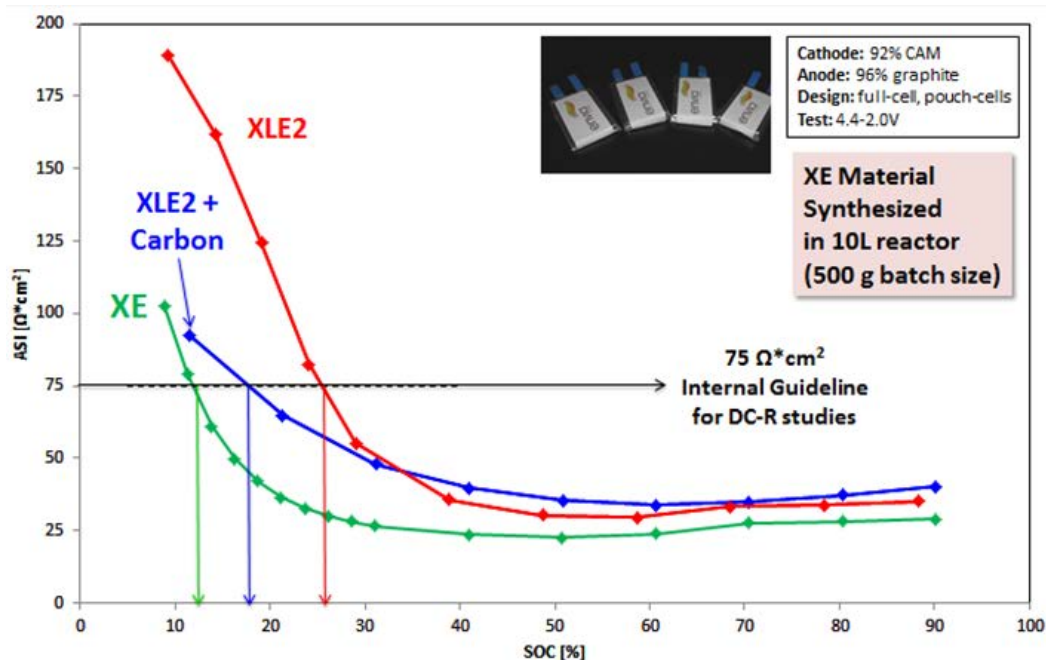


Figure IV-189: DC-R profiles for HCMR™-XE, HCMR™-XLE and Carbon-coated HCMR™-XLE materials in pouch-cell vs graphite anode

Envia Systems

## Approach

**Material development.** Under this approach, cathode materials with varying compositions, and surface coatings were synthesized with the intention to minimize the (1) electronic, (2) ionic, and (3) charge-transfer contributions to DC-R. Figure IV-190 summarizes the approach taken with respect to material development, and the collaboration with each partner institution.

**Analytical studies.** Utilize spectroscopic and microscopic techniques to identify the root-cause for material failure and areas of improvement. Such studies include:

1. Electrochemical Impedance Spectroscopy (EIS), which provides information regarding the various modes that cause the increase in resistance, specifically determining whether the resistance is ionic or electronic in nature.
2. Raman spectroscopy, which helps observe the change in oxidation state of transition metals and the corresponding change in crystal structures specially when the cathode is approaching full discharge.
3. XAS, which provides in-depth knowledge regarding the change of transition metal oxidation state and chemical/structural origins for voltage fade.
4. STEM/HAADF, in which the various forms of such spectroscopy can be used to identify the crystal structure in the bulk and the surface of the primary particle of the material, with focus on studying the hypothesized layered nature of the structure of the cathode.

**Silicon-based anode development.** The development of robust silicon-based electrodes with enhanced binders and surface coatings extends the cycle-life of large capacity cells.

**Modeling and large cell performance.** Cell-level modeling allows for engineering the optimal electrodes, cell size, and voltage window of operation to maximize usable energy and cycle-life.

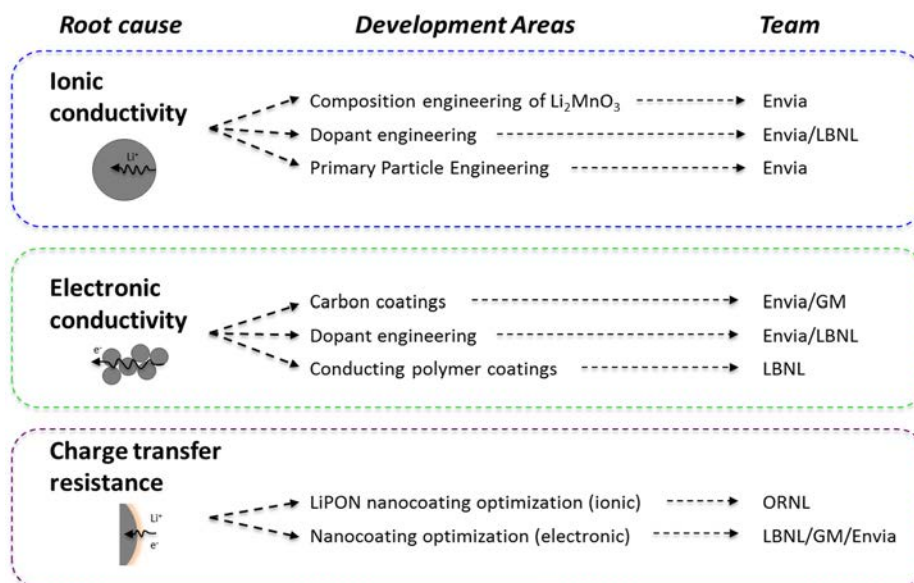


Figure IV-190: Overview for HCMR™ material development and surface modifications by addressing root causes for DC-R Envia Systems

## Results

### 25 Ah Cell Development

Throughout this program, multiple advances on material, electrode, and cell-level have been incorporated into large-format (25 Ah) cell designs. Cell Designs #1 and #2 have been reported, Design #3 was provisional (not tested in 25 Ah cell), and Design #4 was introduced in last year's report via preliminary coin-cell data. In this report, data from Design #4 25 Ah cells tested at Envia Systems is shown. To showcase the improvement on cell development, a comparison of Cell Design #1 (bench-mark) and Cell Design #4 is presented. Figure IV-191 shows the cycle-life measured at Envia at a C/3-1C Ch/Dis rate for Cell Designs #1 and #4 with their respective cell characteristics shown in Table IV-33.

As observed from Figure IV-191, the cycle-life of Cell Design #4 is far superior to that of Design #1. Furthermore, Design #4 exceeds many of the PHEV40 ABR Targets for the cells. In terms of capacity retention, after 270 cycles, Design #4 shows 94% retention whereas Design #1, at the same cycle number, showed an 86% capacity retention. This demonstrates that many of the advances at the material, electrode, and cell-level have contributed to a clear improvement in cycle-life retention by Envia throughout this program. Similar cells have been submitted to INL and they are being currently validated and tested.

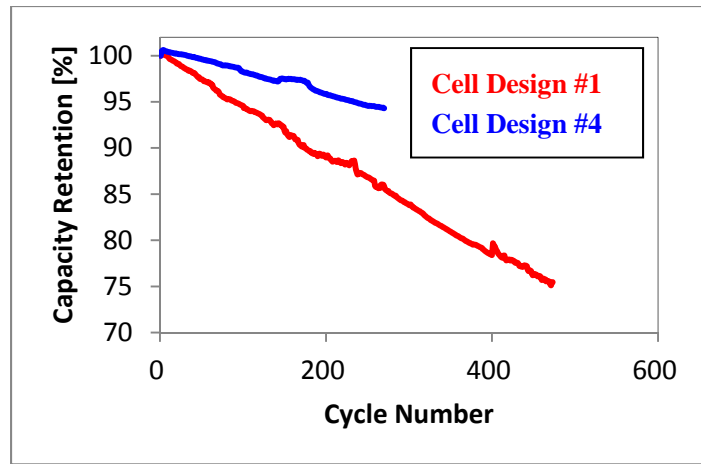


Figure IV-191: Cycle-life capacity retention for C/3 Ch and 1 C Dis for 25 Ah Cell Designs #1 and #4 measured at Envia Envia Systems

Table IV-33: Cell Specifications for ABR Target Goals

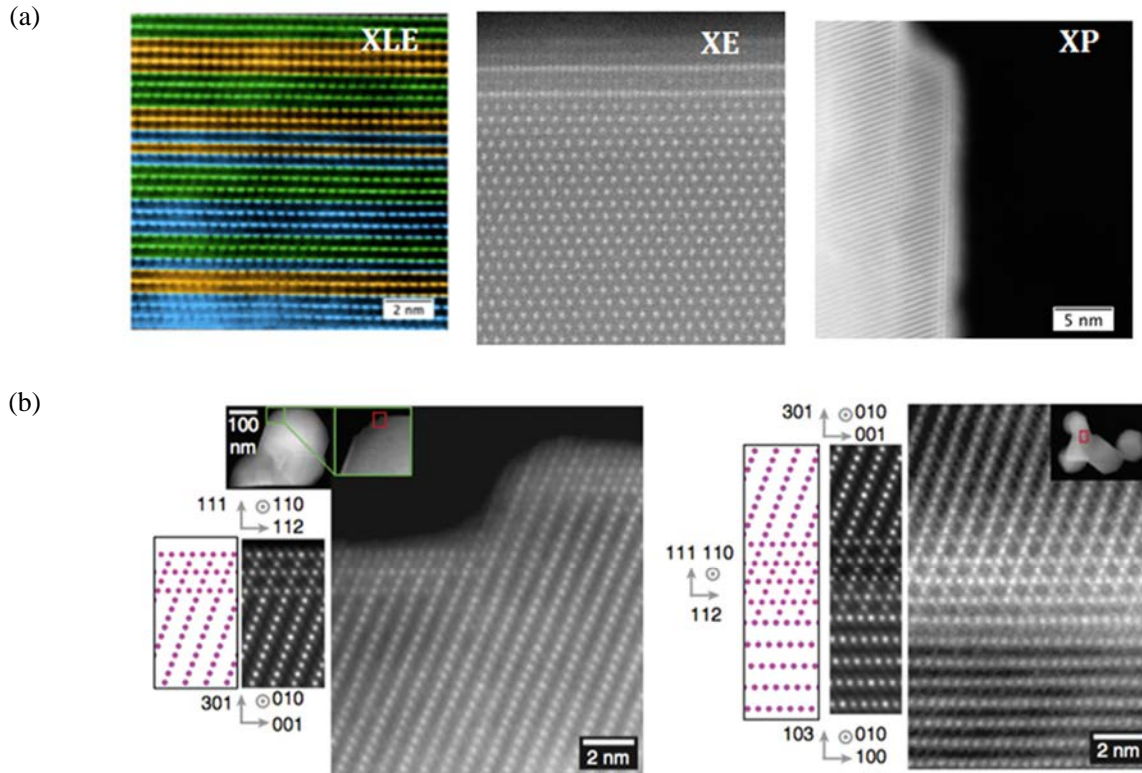
Characteristics	Unit	PHEV40 Targets	XE Blend : Si-Gr Cells	
			Design #1	Design #4
Specific Discharge Pulse Power	W/kg	800	1718	2699
Discharge Pulse Power Density	W/L	1600	3693	6701
Specific Regen Pulse Power	W/kg	430	2103	1739
Regen Pulse Power Density	W/L	860	4523	3930
Specific Energy @ 1C	W/kg	200	203	210
Energy Density @ 1C	W/L	400	436	474
Calendar Life	Years	10+	TBD	TBD
Cycle Life (C/3-1C)	# of cycles	5000	350	TBD
Operating Temperature	°C	-30 to +52	25	25

### STEM/HAADF Analysis of HCMR™ Materials

STEM-HAADF imaging studies for understanding the intricacies of varying the Li/M ratio (composition) were continued this year. Materials with three different lithium-metal-ion ratios were synthesized using a co-precipitation method and the effect of composition on the bulk and surface structure of pristine material has been studied using advanced electron microscopy techniques such as aberration-corrected STEM imaging, EELS, 4D STEM (diffraction mapping) and XEDS. The HAADF- STEM images for the three different HCMR™ compositions, XLE, XE and XP are shown in Figure IV-192. Following are the results obtained from the XLE1, XE1 and XP1 (uncoated) samples:

- Bulk structure: Preliminary results obtained from HAADF STEM analysis of XLE, XE and XP materials suggests that as the Li and Mn content is decreased, there is an increase in variation of lithium content in the shared column present in monoclinic domains as observed from [100] monoclinic zone axis.
- Surface structure: All three materials exhibited the presence of spinel surface having the same orientation relationship with the bulk structure and also with similar thickness (~2 nm).

- The results indicate that the composition does not have an effect on the thickness of this spinel layer, indicating that the bulk structure might be more responsible in the reduction of DC-R with decrease in Li/M ratio.
- All compositions (XLE, XE, and XP) are single phase and consist of monoclinic domains. Order (within a domain) decreases with a decrease in lithium content.
- The above results are summarized and in preparation for publication<sup>4</sup>



A. K. Shukla et al. Nat Commun, vol. 6, p. 8711, Oct. 2015

Figure IV-192: (a) HAADF-STEM images for the different HCMR™ compositions in [100]supercell zone axis. (b) HAADF-STEM images for the different HCMR™-XLE in different zone axis  
 Envia Systems; A.K. Shukla et al. Nat Comm, vol. 6, p. 8711, Oct. 2015

## Conclusions

One of the major findings from this project is that the DC-R affecting the usable energy of the Li-rich NMC cathode material is more dependent on the bulk composition rather than the surface modification. Envia has developed a composition from the HCMR™-XE family to meet the DC-R goals employing its conventional solution-based metal fluoride nanocoating. Different surface modifications such as ionic conductors (via PVD), electronic conductors (via solid state process) and insulators/semi-conductors (via ALD) have been shown to have almost no impact on the DC-R characteristics of Li-rich NMC materials. Development of new polymeric binders for Envia's anode material did not lead to favorable results. 25 Ah cells employing HCMR™ cathode and Si-based anode met all the ABR target metrics except the cycle life. A variety of cell engineering approaches have been applied to deliver an optimal design towards achieving all of the ABR project goals. 25 Ah cells from the final build for this program have been submitted to INL for testing and evaluation.

## Products

### Presentations/Publications/Patents

1. “High Energy Lithium Batteries for PHEV Applications”, ES211\_venkatachala\_2016\_o, US DOE Vehicle Technologies Program Annual Merit Review, AMR, 2014.
2. “High Energy Lithium Batteries for PHEV Applications”, ES211\_venkatachala\_2016\_p, US DOE Vehicle Technologies Program Annual Merit Review, AMR, 2015.
3. “High Energy Lithium Batteries for PHEV Applications”, ES211\_venkatachala\_2016\_o, US DOE Vehicle Technologies Program Annual Merit Review, AMR, 2016.
4. Effect on composition on the structure and electrochemical properties of lithium- and manganese-rich transition metal oxides, Alpesh Khushalchand Shukla, Quentin M. Ramasse, Colin Ophus, Despoina Maria Kepaptsoglou, Fredrik Hage, Christoph Gammer, Charles Bowling, Pedro Alejandro Hernández Gallegos, Subramanian Venkatachalam (*In preparation*).

## IV.D.4. High Energy Density Lithium-Ion Cells for EVs Based on Novel, High Voltage Cathode Material Systems (Farasis Energy, Inc.)

### Keith Kepler, Principal Investigator

Farasis Energy, Inc.  
21363 Cabot Blvd.  
Hayward, CA 94545  
Phone: 510-732-6600 x203  
E-mail: [kkepler@farasis.com](mailto:kkepler@farasis.com)

### Peter Faguy, DOE Program Manager

U.S. Department of Energy  
Vehicle Technologies Office  
1000 Independence Avenue, SW  
Washington, DC 20585  
Phone: 202-586-1022  
E-mail: [Peter.Faguy@ee.doe.gov](mailto:Peter.Faguy@ee.doe.gov)

Start Date: October 2013  
End Date: June 2017

### Abstract

#### Objectives

- Develop advanced electrode materials and cell components to enable stable high-voltage operation.
- Design and demonstrate a lithium-ion cell using those materials meeting the PHEV40 performance targets.
- Design and demonstrate a lithium-ion cell using those materials meeting the EV performance targets.

#### Accomplishments

- Improved capacity retention of NCM materials for 4.4+ V operation, through both surface treatment and bulk-doping approaches.
- Improved rate capability of HE-NCM materials through novel synthesis approach, doubling the relative capacity at 1C over materials synthesized using standard methods.
- Manufactured cells with intermediate energy density and long cycle life under high voltage operation for PHEV applications.
- Manufactured cells with high energy density for EV applications.

### Technical Discussion

#### Background

Current lithium-ion cell technology for automotive applications provides an energy density of ca. 150 - 200 Wh/kg using a voltage window defined to ensure sufficient cell life and safety. Increased energy density and power density are critical to lower costs and to enable the widespread adoption of electric vehicles. In order to meet these goals, Farasis proposed a comprehensive effort to develop high voltage capable lithium-ion technology designed around new positive electrode materials systems, with the potential to enable a PHEV40 cell with a >25% increase in energy density with a corresponding 2x increase in cycle life and a EV light duty cell with a 2x increase in energy density relative to comparable commercial lithium-ion cells. The project builds on Farasis Energy's development and production expertise, leveraging our commercial, high performance lithium-ion cell technology and incorporating advanced active materials.

## Introduction

The overall goal of this project is to develop and demonstrate a new class of high energy, high power lithium-ion cells based on novel high voltage, high capacity active materials. In collaboration with our partners, multiple material classes are being developed simultaneously: on the positive electrode side, layered NCM materials are being developed and stabilized for high voltage operation using various coating technologies. Simultaneously, high capacity layered-layered-spinel composites are being explored using novel synthetic approaches based on ion-exchange reactions. High capacity negative electrode development is focused on silicon-carbon composites. Tying the cell together are electrolyte/separator systems optimized for high-voltage performance.

This project addresses three specific limitations to the development of better performing lithium-ion batteries: low cathode specific energy, electrolyte stability during high voltage operation, and capacity retention during deep discharge for Si-containing anodes. The major challenge to creating stable high energy cells with long cycle life is system integration. Although materials that can give high energy cells are known, stabilizing them towards long-term cycling in the presence of other novel cell components is a major challenge.

## Approach

The approach taken by Farasis in this project is to develop multiple materials in parallel, with periodic integration of materials in design of experiment studies to evaluate higher-order interactions between components. This approach relies on close collaboration with our partners, leveraging the strengths of each organization to accelerate development.

## Results

In the final year of this project, Farasis focused on manufacturing the deliverable cells. There were two sets of performance targets to meet and two different cell designs accordingly. The PHEV cells have a lower specific energy, higher power density, and higher cycle life requirements compared to the EV cells. The cells designed to meet PHEV performance targets utilized a stabilized NCM as the positive electrode active material and can utilize graphite as the negative electrode active material due to the lower specific energy demands. With these parameters fixed, electrolyte optimization was performed using a variety of fluorinated and nonfluorinated solvents and several additives.

Fluorinated solvent electrolytes are frequently reported to exhibit an increase in gas generation compared to conventional carbonate ester systems. This was also observed using the advanced fluorinated solvents in our study (Figure IV-193). The use of appropriate additives can significantly diminish the amount of gas generated with the fluorosolvent systems, but gas generation in these systems is still above a baseline carbonate ester electrolyte (with the same additives).

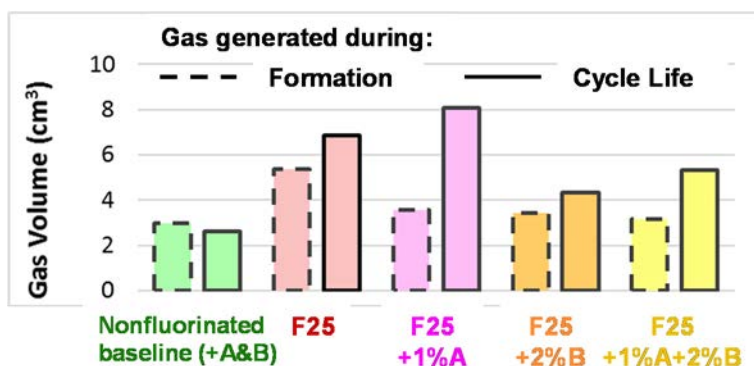


Figure IV-193: Gas generation measurements in PHEV cells for novel fluorinated solvent F25. Formation gas volume and gas generated during cycling are reported separately

The cycle life retention of the same set of cells under accelerated conditions showed that the longest cycle life was achieved for the cells that utilized additive B in a fluorinated solvent system (Figure IV-194). Additive A gave unusual results: decreased gas generation was observed during formation, but increased gassing occurred during cycling, which led to a short cycle life for F25+1%A cells. After one of these cells reached end-of-life due to gas buildup (at approximately 150 cycles), it was vented and resealed (no additional electrolyte was added), thereby restoring much of the apparently lost capacity.

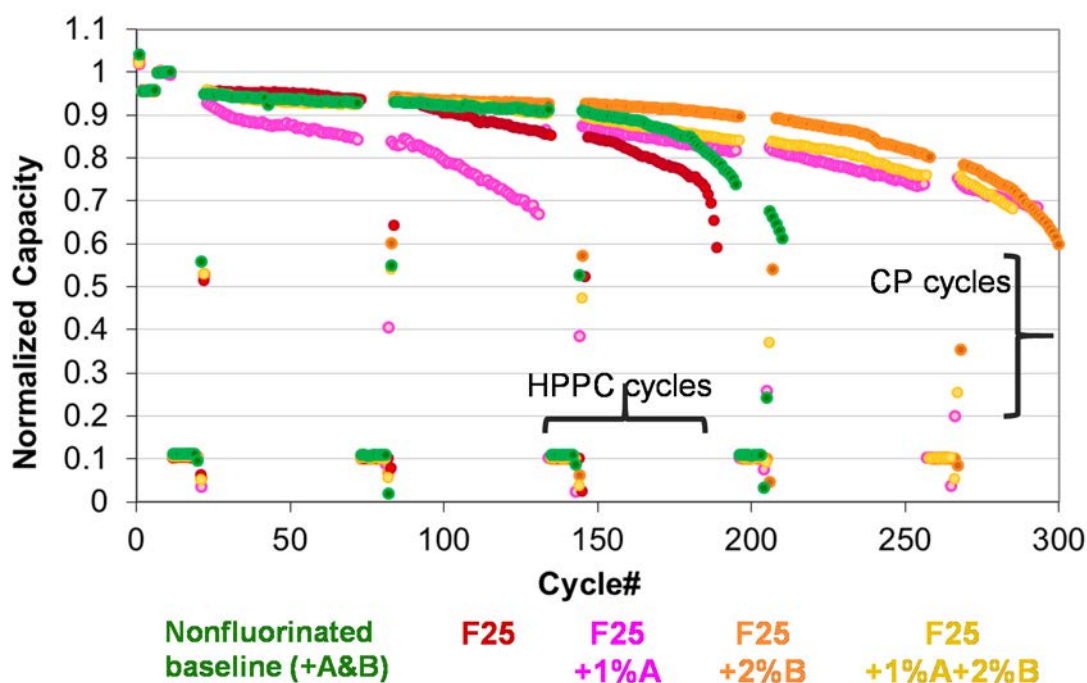


Figure IV-194: Gen2 PHEV accelerated testing cell performance: Small pouch cells (ca. 2 Ah); two cells for each test condition. Test conditions: C/2 CCCV charge to 4.5 V, C/100 cutoff, 1 C discharge to 3.0 V; 30 °C. RPT consists of HPPC & CP measurements every 50 cycles

The EV design cells have higher specific energy, lower power density, and lower cycle life requirements compared to the PHEV cells. The cells designed to meet EV performance targets utilized an advanced high-capacity NCM system as the positive electrode active material and require a high capacity intermetallic component in the negative electrode active material in order to achieve the high specific energy target; given the other constraints on the cell design, a minimum Si content in the negative electrode of ca. 20-25% w/w is necessary to achieve specific energies around 400 Wh/kg. To date, electrode formulations in this compositional range have exhibited a poor cycle life.

Initial design optimizations for the EV cells evaluated several silicon composite negative electrode active materials with differing Si/C ratios and morphologies/topologies. Based on these results, lower Si content formulations of 8 or 16% w/w in two distinct morphologies were selected for further development since the higher wt% Si materials exhibited rather poor cycle life; two leading high-voltage stable electrolytes were tested for each (Figure IV-195). The 16% Si cells, which exhibit approximately 5% greater specific energy than the 8% cells, have a much higher rate of capacity fade, a phenomenon which is mostly attributed to the Si morphology of this particular material rather than the higher Si content alone. In the voltage window / cycle life section of the testing, the widening voltage window accounts for the increasing capacity for the 8% Si cells, while the 16% Si cells maintain capacity in the face of rapid fade.

A second round of 8% Si cells was evaluated under different test conditions using the same two high voltage stable electrolytes (Figure IV-196). The cells using electrolyte F43 show increased capacity fade in the early cycles and an overall lower relative rate performance compared to cells using electrolyte F02. On this basis, electrolyte F02 was used in the final deliverable cells.

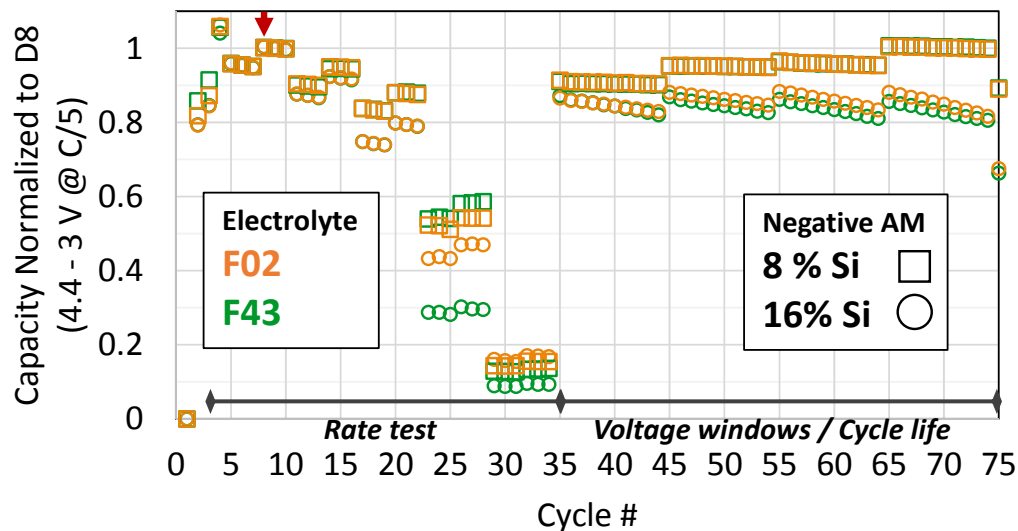


Figure IV-195: Gen2 EV testing cell performance: Small pouch cells (ca. 1 Ah); two cells for each test condition. Test conditions: C/5 CCCV charge to 4.4 or 4.5 V, C/100 cutoff, variable discharge rate in the range 0.2 - 4 C to 3.0 or 2.7 V; 30 °C

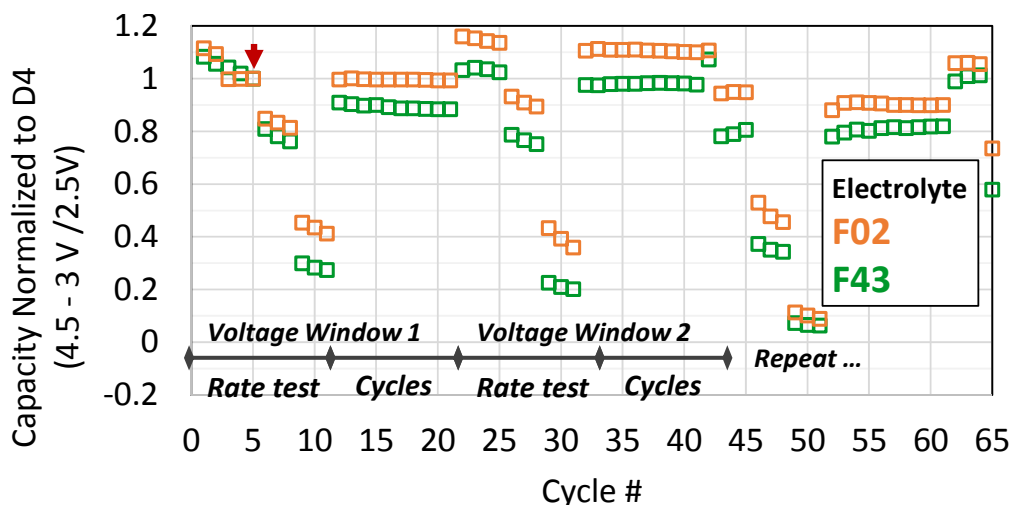


Figure IV-196: Gen3 EV testing cell performance: Small pouch cells (ca. 1 Ah); two cells for each test condition. Test conditions: C/5 CCCV charge to 4.5 V, C/100 cutoff, variable discharge rate in the range 0.2 - 2 C to 3.0 or 2.7 V; 30 °C

## Conclusions

In the final year of this project, Farasis integrated advanced materials developed through the course of the project in the final deliverable cells builds. Results from the Gen2 cell build provided input for final refinements of deliverable cell designs. Different versions of high voltage positive electrode and electrolyte technologies were implemented in the PHEV and EV cell designs. While the final PHEV cells used a standard graphite negative electrode, the EV cells essentially require Si (or a related intermetallic material system) to meet specific energy and energy density targets. While the EV cell performance is still limited by the poor cycle life of Si anodes, the final design aimed to balance energy density and cycle life.

## Products

## Presentations/Publications/Patents

1. "High Energy Density Lithium-ion Cells for EVs Based on Novel, High Voltage Cathode Material Systems," ES213\_Slater\_2016\_o, US DOE Vehicle Technologies AMR, 2016.

## IV.D.5. High Energy, Long Cycle Life Lithium-Ion Batteries for PHEV Application (PSU)

### **Donghai Wang, Principal Investigator**

Pennsylvania State University  
328 Reber Building  
University Park, PA 16802  
Phone: 814-863-1287; Fax: 814-863-4848  
E-mail: [dwang@psu.edu](mailto:dwang@psu.edu)

### **Adrienne Riggi, DOE Project Manager**

National Energy Technology Laboratory  
3610 Collins Ferry Road  
Morgantown, WV 26507  
Phone: 304-285-5223  
E-mail: [adrienne.riggi@netl.doe.gov](mailto:adrienne.riggi@netl.doe.gov)

Start Date: October 1 2013  
End Date: September 30 2016

### **Abstract**

#### **Objectives**

Demonstrate a 2.5 Ah prismatic lithium-ion cell capable of 1) an energy density of 330 Wh/kg (770 Wh/L) at C/3 rate; 2) a power density of 1600 W/L while maintaining an energy density above the DOE PHEV goal of 200 Wh/kg; 3) a long cycle life with 95% capacity retention in 500 cycles at C/3 and 1C rate at 80% depth of discharge (DOD).

#### **Technical barriers**

The development of the proposed lithium-ion battery presents technical barriers for each of the system's components: anode, cathode, binder, and electrolyte. Although silicon-alloy anode materials have shown remarkable capacities above 2000 Ah/g, the silicon will undergo large volume change (~400%) upon lithiation/delithiation. In effect, other issues arise including unstable SEI, pulverization and aggregation of the Si particle, and low coulombic efficiency (less than 99.8%) compared with graphite (higher than 99.9%). Furthermore, layered oxide cathode materials will need to overcome a relatively low practical capacity (~170 mAh/g), along with other issues such as chemical and structural instability, transition metal dissolution, and transition metal redox potential changes. The technical barriers for the anode and cathode may partially be addressed with an appropriate binder/electrolyte, however the chemical composition of these components must be optimized to ensure compatibility.

#### **Accomplishments**

- The optimization of structure, particle size and surface coating of PSU Si-graphite anode material have been completed.
- Optimized PSU Si-graphite material has been scaled up (~500 g).
- The high-loading (6.5 mg/cm<sup>2</sup>) electrode using a cross-linked binder with great quality has been fabricated.
- The specific capacity, mass loading and binder content of PSU Si-graphite anode has been optimized.
- The areal capacity, cyclability, electrolyte additives, voltage window of PSU Si-graphite anode have been optimized using the full pouch cell for the full cell construction.

- The surface electrochemical degradation processes of Ni-rich cathode material  $\text{LiNi}_{0.7}\text{Co}_{0.15}\text{Mn}_{0.15}\text{O}_2$  have been demonstrated by time-of-flight secondary ion mass spectrometry (TOF-SIMS) and high-angle annular dark-field scanning transmission electron microscopy (HAADF-STEM).
- Diverse performance modification strategies have been utilized to suppress the degradation of Ni-rich cathode materials and to improve their overall electrochemical performance.
- One kilogram of the optimized concentration-gradient (CG) cathode material  $\text{LiNi}_{0.76}\text{Co}_{0.10}\text{Mn}_{0.14}\text{O}_2$  has been prepared with good control of composition, morphology, and electrochemical performance, which delivered an initial specific capacity close to  $190 \text{ mA h g}^{-1}$  at C/10 and  $180 \text{ mA h g}^{-1}$  at C/3 as well as good cyclability in pouch-type graphite full cells with a 4.4 upper voltage cut-off.
- Scalable SLMP coating method on electrodes is developed through a polymer solution system. The system is optimized through the selection of solvent, polymer binder and polymer concentration. The optimized binder solution is 1% concentration of polymer binder in xylene, and the polymer binder is chosen as the mixture of poly(styrene-co-butadiene) rubber (SBR) and polystyrene (PS).
- The scalable SLMP method is applied on Graphite anode materials.
- The scalable SLMP method is applied on Si derived anode materials.
- The effect of SLMP is demonstrated through both half coin cells and full pouch cells.
- Electrolyte additive with Si-N skeleton forms a less resistant SEI on the surface of silicon anode (from PSU) as evidenced by the evolution of the impedance at various lithiation/de-lithiation stages and the cycling data.
- New fluorinated additive was investigated to stabilize the interphase of the NCM523/electrolyte.
- New fluorinated linear cosolvents were designed and synthesized for a high cut off voltage NCM523-Graphite system.
- New batch Anode from PSU were tested
- New FSI based ionic liquid synthesized and purified at ANL.
- Continued the additive research based on EC/EMC/FEC system.
- Focused on the optimization of the electrolyte formulation that is compatible with both NCM cathode and Si anode in contingent with material development teams at PennState and UT-Austin.
- Continued verification of the impact of the additives on the NCM523 cathode at higher cut-off voltages.
- Co-solvent has been studied to future improve the ionic liquid performance.
- New fluorinated cyclic carbonate shows good anodic stability.
- A series of electrolyte containing fluorinated cyclic carbonates as the anode SEI former with trifluoroethyl methyl carbonate (F-EMC) and  $\text{LiPF}_6$  has been designed, synthesized and evaluated.
- Linear sweep voltammetry have been used as an evaluation tool for the voltage stability of the fluorinated cyclic carbonate. Of the cyclic carbonates screened, DFEC is the most stable solvent and the HFEEC is the worst due to involve the ether bond in to the molecular structure.
- The conductivity test result shows a long chain fluorinated substituent may leads to a high resistant and viscosity.
- Full cells fabrication, activation and pre-test have been carried out. Three kinds of cells have been prepared as follow: unlithiated PSU Si-graphite anode | NCM523 cathode, unlithiated PSU Si-graphite anode | UTA cathode and lithiated PSU Si-graphite anode | NCM523 cathode.

## Future Achievements

- Further optimization of the full pouch cell using PSU Si-graphite anode and UTA Ni-rich oxide cathode.

- Further improvements of the first cycle efficiencies of high-loading and high-capacity PSU Si-graphite anode and UTA Ni-rich oxide cathode.
- Further enhancement of the uniformity and effect of SLMP prelithiation for high-loading and multilayered full pouch cell.

## Technical Discussion

### Background

With a relatively high energy density and long lifespan, lithium-ion batteries have become the state-of-the-art and widely-adopted power technology for plug-in hybrid electric vehicle (PHEV), electric vehicle (EV), and other portable electronic devices. However, the potential of the current PHEVs and EVs in our daily lives is seriously hindered by their high cost, limited travelling distance, and restrained vehicle size, mainly due to the lack of high-performance and cost-effective lithium-ion batteries.

### Introduction

In effect, research in the field of battery chemistry has focused on the development of advanced battery components that will significantly improve the practical performance of lithium-ion batteries. Within the last decade, the performances of the primary components - cathode, anode, binder, and polymer - have been enhanced through careful modification in chemical composition, although often independent of each other. In this regard, a collaborative effort is needed to improve the overall performance of lithium-ion batteries by enhancing individual battery components simultaneously, so that a high-performance, cost-effective lithium-ion battery able to satisfy diverse demands, especially transportation, can be achieved.

### Approach

The development of a high energy/power lithium-ion battery suitable for PHEV and EV applications can be accomplished through the expertise and experience of a multi-organizational team with facilities and collaboration including Pennsylvania State University (PSU), University of Texas at Austin (UT-Austin), Lawrence Berkley National Laboratory (LBNL), Argonne National Laboratory (ANL), and the industrial partner EC Power (ECP). PSU and UT-Austin will use their extensive knowledge in the state-of-the-art anode and cathode materials, respectively, to develop optimized and compatible electrodes in the lithium-ion battery. Innovative polymer binders/ anode prelithiation and electrolytes solutions will be developed by LBNL and ANL, respectively, based on their well-established expertise in this area. Finally, the culmination of these state-of-the-art battery components will be realized through the intelligent cell design and fabrication techniques of ECP.

### Results

We have achieved the following progress:

## Anode

1. PSU cross-linked binders have been developed, enabling fabrication of high quality Si anodes with good performance.

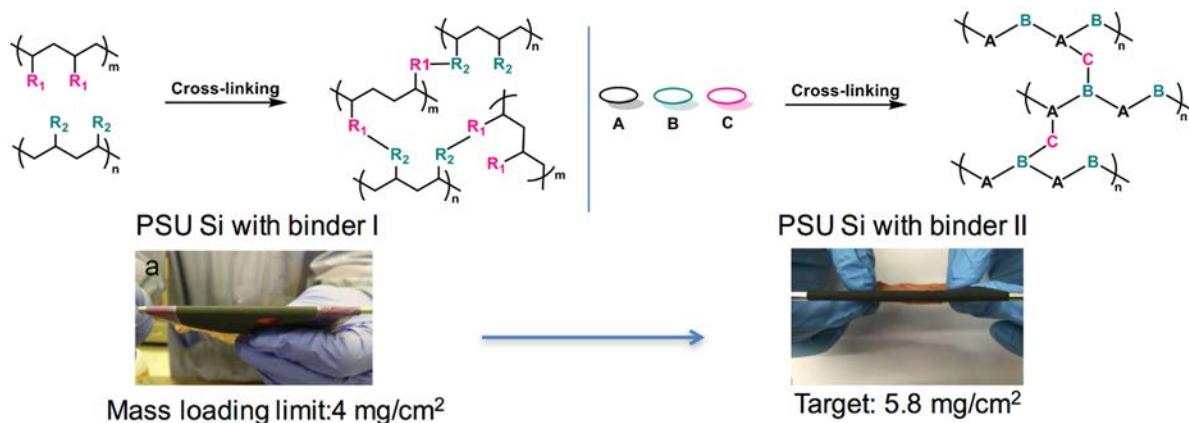


Figure IV-197: PSU cross-linked binders for high-loading PSU Si-graphite anodes. The left binary cross-linked binder enables good electrode quality with the active material mass loading of 4 mg/cm<sup>2</sup> and the right ternary cross-linked binder pushes the mass loading to 5.8 mg/cm<sup>2</sup> with great quality

To develop the PSU Si-graphite anode with a high areal capacity, we need to push the mass loading of active material of the electrode to a very high level (~5.8 mg/cm<sup>2</sup>) and the electrode quality should be good enough for the full cell operation. As shown in Figure IV-197, we have developed two kinds of cross-linked binders: binary and ternary cross-linking polymers. The mass loading of the PSU Si-graphite anode using the binary binder I can be pushed up to 4 mg/cm<sup>2</sup>, while the one of ternary binder II shows great quality with the mass loading of 5.8 mg/cm<sup>2</sup>. This is adequate for our full cell operation design. The Si-graphite anode using the ternary binder II exhibits good cyclability in half-cell system (Figure IV-198). The area capacity has been reached to 4.9 mAh/cm<sup>2</sup>.

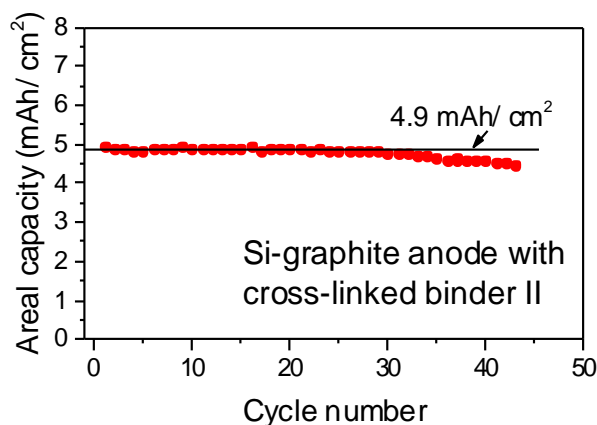


Figure IV-198: Half-cell performance of Si-graphite anode with ternary binder II. The mass loading is 5.8 mg/cm<sup>2</sup>

## 2. PSU Si-graphite material scale-up and electrode fabrication.

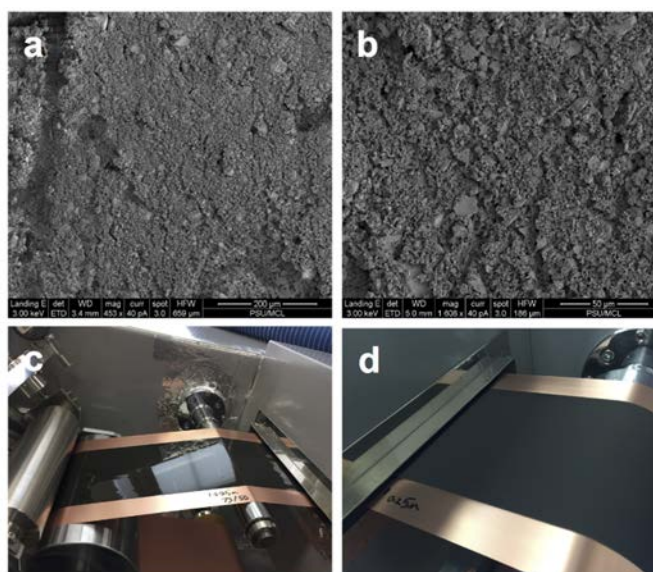


Figure IV-199: Material fabrication and electrode fabrication of PSU Si-graphite. a,b, SEM images of Si materials with uniform particle size. c,d, High-quality electrode using Si-graphite material and ternary binder II

After optimizing the Si structure and surface layer, we have completed the material scale-up and are able to prepare 500 g Si material every single batch. The Si particle size has also been screened to ensure the uniform particle size. The electrode also presents very good quality before and after heat treatment. (See Figure IV-199.)

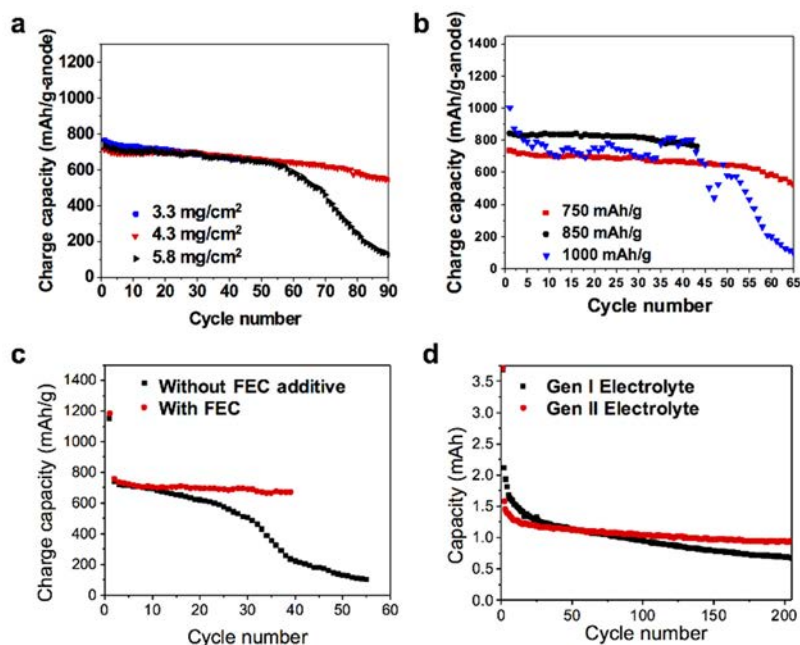


Figure IV-200: PSU Si-graphite anode optimization including a) mass loading of active material, b) specific capacity, c) electrode with FEC additives and d) electrode with different electrolyte systems

## 3. Electrochemical optimization of the PSU Si-graphite anode in half- cell and full- cell systems

The electrochemical performances of PSU Si-graphite including mass loading, specific capacity, electrolyte and additives have been optimized in the half-cell systems. As shown in Figure IV-200, PSU Si-graphite electrodes with mass loading of 5.8 mg/cm<sup>2</sup> shows similar capacity with the ones of low loadings, indicating good electrode structure and conductivity. By tuning the ratio of Si and graphite, we demonstrate that the

electrode which delivers a charge capacity of 850 mAh/g, presents the best cyclability. Moreover, the compatibility of the material with electrolyte and additives has also been studied. The Gen II electrolyte with FEC additive exhibits the optimized cell performance and is used for the full cell operation. The FEC has been proved to be very important for the Si-graphite electrode with high mass loading.

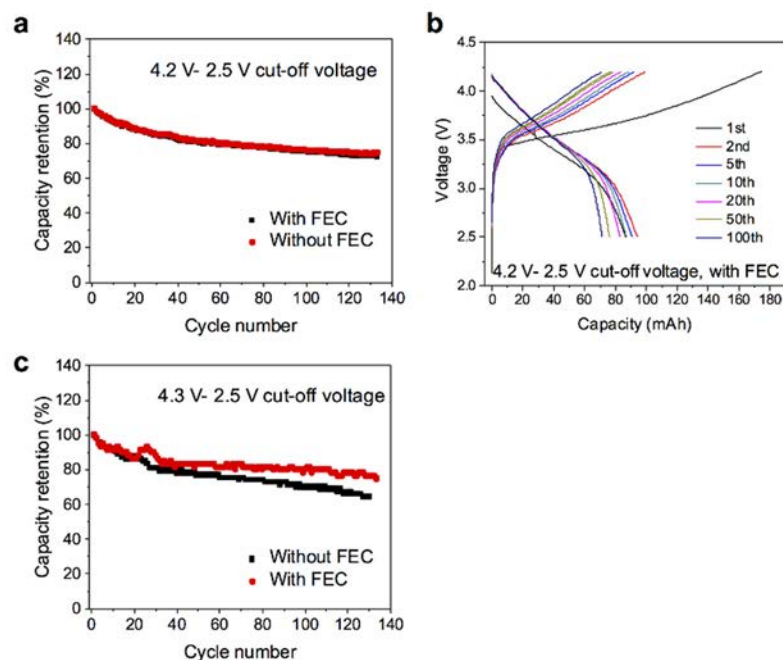


Figure IV-201: Full-cell performance optimization including additives and voltage window with the double-layer pouch cell system

Using the optimized electrode structure and electrolyte, the full-cell performance has been optimized with the double-layer pouch cell system. PSU Si-graphite anode is paired with commercial NCM523 cathode with a 1:1 N/P ratio. As shown in Figure IV-201a, both cells with/ without FEC additive show good performance under the voltage window of 4.2 –2.5V. However, when changing the voltage window to 4.3 –2.5V, the one with FEC additive shows much better performance with a 73% capacity retention after 130 cycles.

## Cathode

### 1. Understanding the degradation processes of Ni-rich $\text{LiNi}_{0.7}\text{Co}_{0.15}\text{Mn}_{0.15}\text{O}_2$ during cycling

As a very promising high-performance cathode material, Ni-rich materials attract great attention from both academia and industry. However, the Ni-rich compositions generally show poor cyclability, hindering widespread applications. Therefore, it is of great importance to understand the various degradation processes of nickel-rich materials, so that more specific and effective methods can be adopted to improve their overall performance. We prepared a baseline material  $\text{LiNi}_{0.7}\text{Co}_{0.15}\text{Mn}_{0.15}\text{O}_2$  (denoted as NCM 71515) and its electrochemical performance in lithium half-cells was obtained at room temperature with a cut-off voltage of 4.5 V vs.  $\text{Li}/\text{Li}^+$ . The sample delivered a discharge capacity close to  $190 \text{ mA h g}^{-1}$  and also showed notable voltage and capacity fade during cycling. It is generally believed that the capacity fading mechanism of Ni-rich layered oxides is linked to the rapid degradation of electrode/electrolyte interface that induces large overpotentials during both charge-discharge processes as cycling proceeds and to the structural instability at the highly charged state during cycling, while the bulk remains largely intact and undamaged.

Figure IV-202a illustrates the TOF-SIMS depth profiles of the baseline sample after 100 charge-discharge cycles. These profiles of the secondary ions of interest, such as  $\text{LiF}_2^-$ , are referenced to those obtained from the pristine electrode, and they reveal the complex multi-layer characteristics of the surface chemistry of Ni-rich layered oxide electrodes during high-voltage electrochemical operation, as proposed theoretically in the literature. Importantly, we notice degradation products including: (i)  $\text{LiF}$ , represented by  $\text{LiF}_2^-$ , appearing mostly localized at the very surface of the electrode, the first layer, and also rich in the subsequent second layer; (ii)  $\text{MnF}_2$ , signified by  $\text{MnF}_2^-$ , showing the highest concentration in the second layer; and (iii)  $\text{NiO}$ ,

indicated here by the  $\text{NiO}^-$  to  $\text{Ni}^-$  ratio, emerging in the third layer. These three “layers” correspond to the various aspects of electrochemical degradation at the surface of Ni-rich layered oxide electrodes in the common EC-DEC/LiPF<sub>6</sub> solutions: (i) deposition of various solvent and salt decomposition products from the electrolyte, (ii) active mass dissolution aggravated by acidic species attack (*e.g.*, HF – generated in the presence of a trace amount of electrolyte impurities such as H<sub>2</sub>O), and (iii) intrinsic surface structural reconstruction from the layered to ‘rock-salt’ phase due to destabilized Ni-ion migration towards neighboring Li layers in the highly delithiated state.

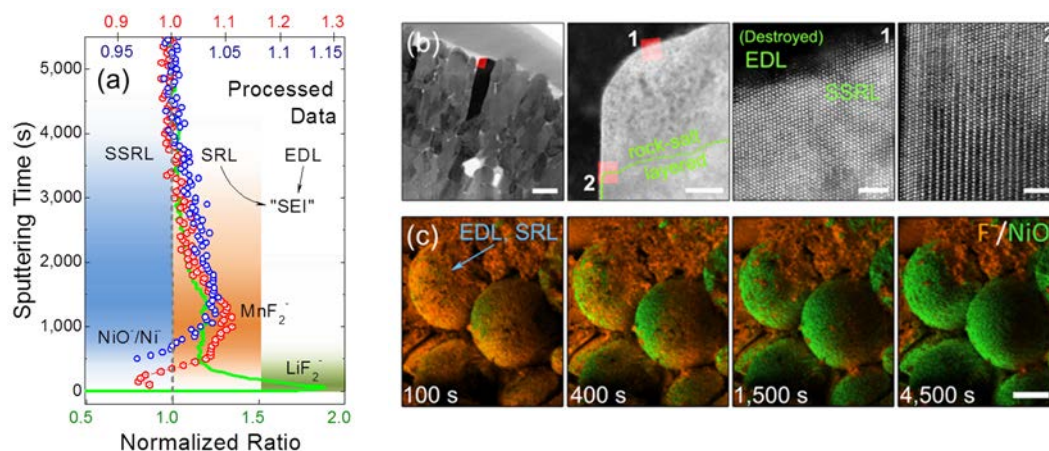


Figure IV-202: (a) TOF-SIMS depth profiles of various chemical species from the surface of the baseline NCM 71515 composite electrodes after 100 cycles at room temperature, referenced with the pristine electrode (not shown here) as a function of sputtering time; and visualization of the surface degradation of NCM 71515 electrodes after 100 cycles. (b) HAADF-STEM images showing the local structure at the primary particle surface; the scale bars are 400, 20, 2, and 2 nm from left to right; (c) TOF-SIMS mappings showing the composite electrode surface with cathode secondary particles, additive carbon, and binder; the scale bar is 10  $\mu\text{m}$

In this work, we refer to the aforementioned three ‘layers’ as an electrolyte deposition layer (EDL), a surface reaction layer (SRL), and a surface structural reconstruction layer (SSRL), respectively, as shown in Figure IV-202a. In Figure IV-202b, HAADF-STEM images reveal the local structure of the cycled NCM 71515 primary particle surface. A clear boundary is shown between the pristine layered  $R\bar{3}m$  structure and the irreversibly formed rock-salt  $Fm\bar{3}m$  phase (SSRL) during cycling, with distinctly differing thickness along different crystal orientations. It is expected that the SSRL formation is promoted along the lithium diffusion pathway in the layered matrix of Ni-rich layered oxides. Of particular note, the surface organic deposits due to electrode-electrolyte reactivity are largely nonexistent in the HAADF-STEM images due to their highly sensitive nature towards the high-energy electron-beam irradiation. Important also is a considerable difficulty in the elimination of ambient air-exposure-induced artifacts during the sample preparation for high-resolution STEM. Consequently, illustrative TOF-SIMS high-resolution mappings were collected on the same sample as a function of etching depth, as seen in Figure IV-202c. In the figure, maps of the electrode along the  $x$ - $y$  planes demonstrate that the surface of the particles (represented by the  $\text{NiO}^-$  fragment), initially entirely covered by the degradation-induced chemical functional groups (represented by  $\text{F}^-$ ), gradually emerges upon  $\text{Cs}^+$  etching.

For further detailed and comprehensive visualization in three dimensions of the chemical alterations occurring on the electrode surface, a series of TOF-SIMS maps of various organic and inorganic species were collected on the cycled baseline NCM 71515 sample (Figure IV-203). In the upper two rows of Figure IV-203, complex surface deposits in EDL, represented by cumulative signals of  $\text{C}_2^-$ ,  $\text{POF}_2^-$ , and  $\text{LiF}_2^-$  fragments projected along the  $x$ - $y$  planes prior to and after intensive sputtering, are unequivocally visualized. Not surprisingly, signal counts of most of these fragments are reduced nearly uniformly on the entire electrode during etching. Also shown are the surface corrosion products in SRL evidenced by  $\text{LiF}_2^-$ ,  $\text{Ni}^-$ , and  $\text{MnF}_2^-$  ions. In contrast to the EDL species, these fragments show substantial decrease in intensity at the cathode particles, since the additive carbon and binder in the composite electrode do not react with HF. Apparently, the degradation products are mostly located at the surface of the secondary particles, although electrolyte penetration along with further attack through micro-cracks towards the interior of particles is possible. Notably, several maps of  $\text{O}^-$ ,  $\text{Ni}^-$ ,  $\text{Li}^-$ ,  $\text{MnF}_2^-$ , etc. in the bottom row of Figure IV-203 reveal the complex surface chemistry on carbon additives, which is believed to be mostly the result of the active mass dissolution. During migration within the electrolyte, these dissolved compounds make their ways to the conductive carbon surface and eventually

through the separator to the anode. The precipitation of the dissolved products from the common cathode materials on the graphite anode as well as conductive carbon additives at the cathode side are recognized as a key limiting factor for the cycle life in existing lithium-ion batteries. Upon closer inspection, it was also noticed that the NiO phase ( $\text{NiO}^+$ ) appears rich at the exterior of a secondary particle whereas Li ( $\text{Li}^-$ ) is more concentrated at the core (Figure IV-203, bottom). This further corroborates that the electrochemical degradation for Ni-rich layered oxides tends to be more localized at the secondary particle's surface.

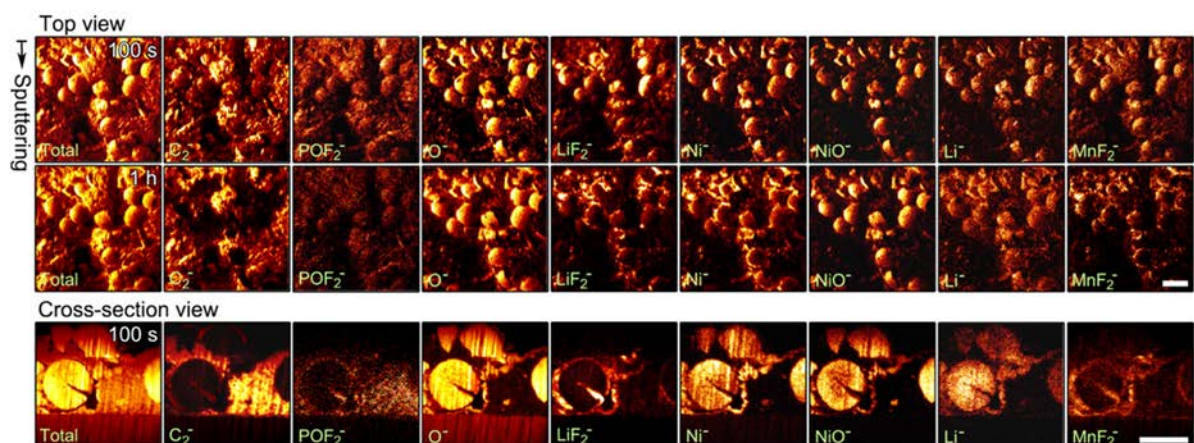


Figure IV-203: Two-dimensional TOF-SIMS mapping of baseline NCM 71515 composite electrodes after 100 cycles, revealing various surface degradation products at the secondary particle surface as well as additive carbon and polymeric binder. Upper two rows are top views collected after 100 s- and 1 h- $\text{Cs}^+$  etching, while the bottom row is taken from the cross-sectional perspective (100 s- $\text{Cs}^+$  etching). From left to right, the secondary ions of interest are total,  $\text{C}^-$ ,  $\text{C}_2\text{P}^-$ ,  $\text{POF}_2^-$ ,  $\text{O}^-$ ,  $\text{LiF}_2^-$ ,  $\text{Ni}^-$ ,  $\text{NiO}^-$ ,  $\text{Li}^-$ , and  $\text{MnF}_2^-$ , respectively. The scale bars are both 20  $\mu\text{m}$

## 2. Performance enhancement of Ni-rich materials

The degradation mechanism research above indicates that the performance improvement of Ni-rich materials primarily lies in the enhancement of their surface chemical and structural stability. On the basis of this, several strategies were used to achieve this goal, including compositional alteration, element doping, surface coating, and the combination of materials.

### 2.1 Effect of Mn substitution for Ni in $\text{LiNi}_{0.8-x}\text{Co}_{0.10}\text{Mn}_{0.1+x}\text{O}_2$

Rate performance of the  $\text{LiNi}_{0.8-x}\text{Co}_{0.10}\text{Mn}_{0.1+x}\text{O}_2$  cathodes with different Mn contents is presented in Figure IV-204. The  $\text{LiNi}_{0.76}\text{Co}_{0.10}\text{Mn}_{0.14}\text{O}_2$  sample shows higher discharge capacities at various C rates.  $\text{LiNi}_{0.72}\text{Co}_{0.10}\text{Mn}_{0.18}\text{O}_2$  shows slightly poor rate capability as compared to  $\text{LiNi}_{0.76}\text{Co}_{0.10}\text{Mn}_{0.14}\text{O}_2$ , probably due to the reduced conductivity of the electrode caused by the increase in Mn content. From the charge/discharge voltage profiles at different C rates, it can be found that the  $\text{LiNi}_{0.80}\text{Co}_{0.10}\text{Mn}_{0.10}\text{O}_2$  sample shows discharge voltage profiles with dramatically reduced working voltage at high C rates Figure IV-204b, indicating a significant increase in internal resistance and an obvious energy fade when operating at increased current densities, which is undesired for practical applications. In contrast, both  $\text{LiNi}_{0.72}\text{Co}_{0.10}\text{Mn}_{0.18}\text{O}_2$  and  $\text{LiNi}_{0.76}\text{Co}_{0.10}\text{Mn}_{0.14}\text{O}_2$  exhibit limited decay in the working voltage even at 5 C discharge rate, demonstrating the improved structural stability and rate capability of materials with relatively higher Mn contents.

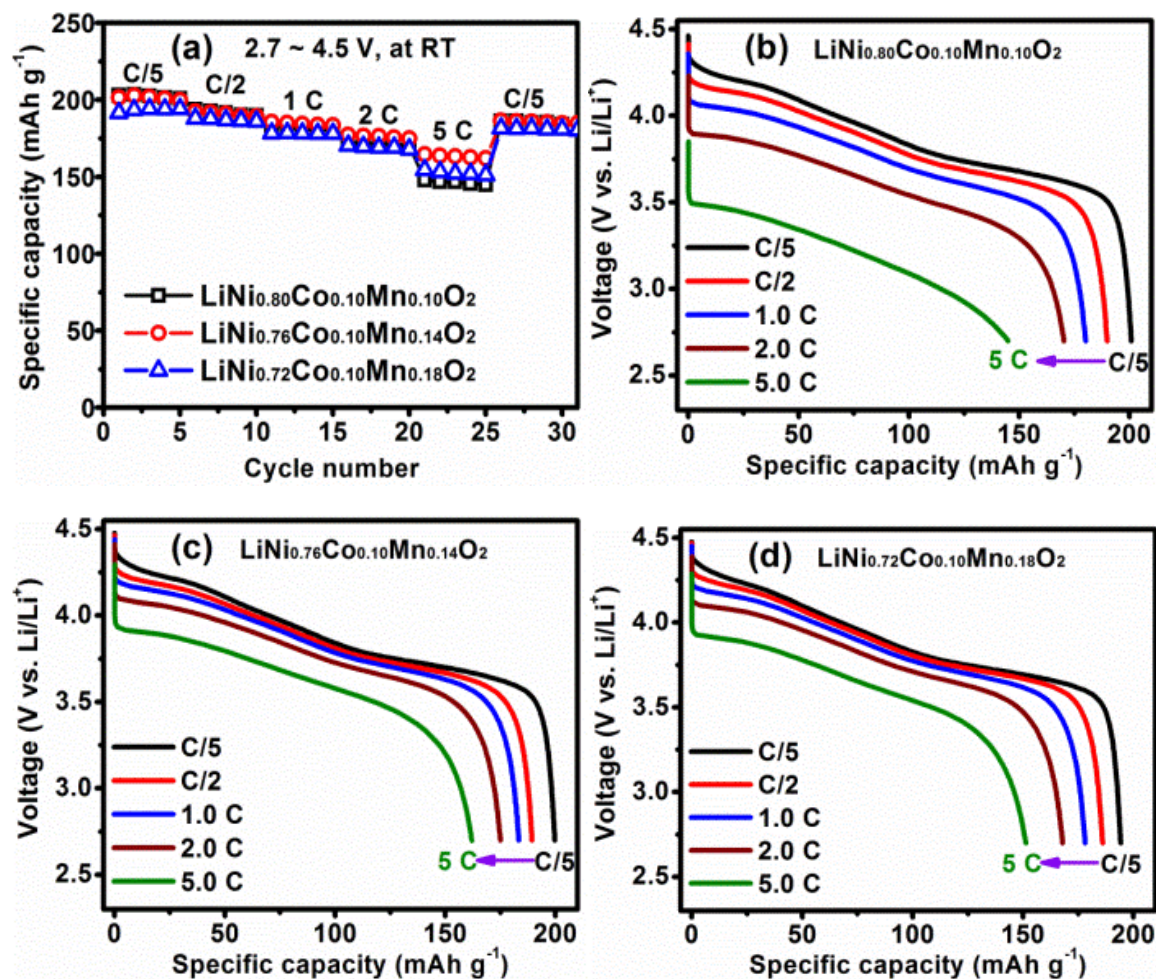


Figure IV-204: (a) Rate performance of the  $\text{LiNi}_{0.8-x}\text{Co}_{0.10}\text{Mn}_{0.1+x}\text{O}_2$  materials at room temperature and the corresponding discharge profiles of (b)  $\text{LiNi}_{0.80}\text{Co}_{0.10}\text{Mn}_{0.10}\text{O}_2$ , (c)  $\text{LiNi}_{0.76}\text{Co}_{0.10}\text{Mn}_{0.14}\text{O}_2$ , and (d)  $\text{LiNi}_{0.72}\text{Co}_{0.10}\text{Mn}_{0.18}\text{O}_2$  at different C rates in the range of 2.7 - 4.5 V

To get insight into the good structural stability of the material with high Mn content, electrochemical impedance spectroscopy (EIS) analysis was carried out to study the interfacial electrochemistry and reaction kinetics of the  $\text{LiNi}_{0.8-x}\text{Co}_{0.10}\text{Mn}_{0.1+x}\text{O}_2$  cathode materials at the charged state of 4.3 V (Figure IV-205 (Left)). Upon cycling, the passivation surface-film resistance and the charge-transfer resistance of the high-Mn-content cathode is considerably lower than those of the low-Mn-content cathode, ascribed to the stabilization of the  $\text{LiNi}_{0.72}\text{Co}_{0.10}\text{Mn}_{0.18}\text{O}_2$  electrode surface in the presence of higher Mn contents. After 50 cycles,  $\text{LiNi}_{0.72}\text{Co}_{0.10}\text{Mn}_{0.18}\text{O}_2$  exhibits a low surface layer resistance, indicating a thinner passivation film accumulated on the electrode surface. Meanwhile, the charge-transfer resistance of the  $\text{LiNi}_{0.72}\text{Co}_{0.10}\text{Mn}_{0.18}\text{O}_2$  electrode is also much smaller than that observed for the  $\text{LiNi}_{0.8}\text{Co}_{0.10}\text{Mn}_{0.1}\text{O}_2$  electrode over the same period of cycling. The stable interfacial resistances in the  $\text{LiNi}_{0.72}\text{Co}_{0.10}\text{Mn}_{0.18}\text{O}_2$  electrode reflect an improved quality of electrode/electrolyte interface. The high Mn content at the particle surface stabilizes the interface during cycling, resulting in better electrochemical performance. The  $\text{Li}_{1-\delta}\text{Ni}_{0.72}\text{Co}_{0.10}\text{Mn}_{0.18}\text{O}_2$  electrode exhibits an exothermic reaction with the peak located at a higher temperature of 229°C compared to that of  $\text{Li}_{1-\delta}\text{Ni}_{0.8}\text{Co}_{0.10}\text{Mn}_{0.1}\text{O}_2$  (221°C) (Figure IV-205 (Right)). Also, the exothermic heat generated with  $\text{Li}_{1-\delta}\text{Ni}_{0.72}\text{Co}_{0.10}\text{Mn}_{0.18}\text{O}_2$  is lower ( $527 \text{ J g}^{-1}$ ) than that with  $\text{Li}_{1-\delta}\text{Ni}_{0.8}\text{Co}_{0.10}\text{Mn}_{0.1}\text{O}_2$  ( $721 \text{ J g}^{-1}$ ), indicating that higher Mn content, especially in the particle outer layer, significantly enhances the thermal stability of the Ni-rich cathodes.

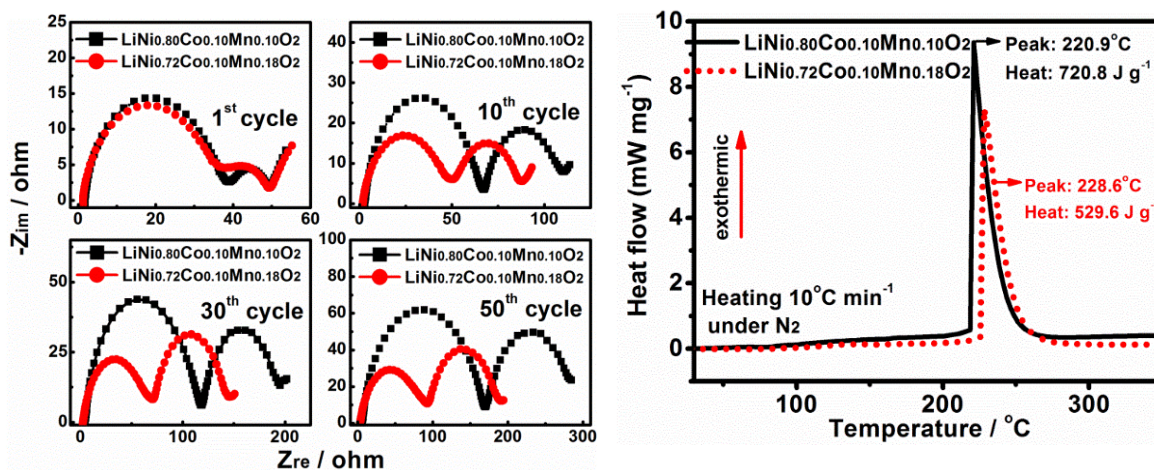


Figure IV-205: Left, Nyquist Plots of the  $\text{LiNi}_{0.8-x}\text{Co}_{0.10}\text{Mn}_{0.1+x}\text{O}_2$  materials in thick electrodes at the charged state of 4.3 V during cycling at C/3 rate after 3 formation cycles at C/5 rate, Right, DSC profiles of the  $\text{Li}_{1-x}\text{Ni}_{0.8-x}\text{Co}_{0.10}\text{Mn}_{0.1+x}\text{O}_2$  electrodes at the charged state of 4.5 V

## 2.2 Effect of Al doping on the performance of Ni-rich material

Improving the cycling stability of Ni-rich cathode materials is one of the major goals in this project. One of the effective strategies is elemental doping. Thus, Al-doped  $\text{LiNi}_{0.81}\text{Co}_{0.14}\text{Al}_{0.05}\text{O}_2$  (NCA) was prepared via a two-step method: transition-metal co-precipitation of  $\text{Ni}_{0.85}\text{Co}_{0.15}(\text{OH})_2$  and subsequently 5 mol. % Al doping during the lithiation heat treatment. Also,  $\text{LiNi}_{0.85}\text{Co}_{0.15}\text{O}_2$  was prepared for a comparison.

The electrochemical performance of NCA was first recorded in coin-type Li half cells at room temperature and then in pouch full cells. Figure IV-206a compares the cycling stability of the two samples in the voltage window of 3.0–4.5 V at C/5 using the standard 1.0 M  $\text{LiPF}_6/\text{EC-DEC}$  electrolyte. As shown, both samples delivered high initial specific discharge capacities of slightly above 200  $\text{mAhg}^{-1}$  (203  $\text{mAhg}^{-1}$  for NCA, 201  $\text{mAhg}^{-1}$  for NC8515), common for Ni-rich layered oxides with Ni incorporation above 0.8. Not surprisingly, the  $\text{LiNi}_{0.85}\text{Co}_{0.15}\text{O}_2$  sample demonstrates rather poor cycling performance under high-voltage cell operation, with capacity rapidly decreasing to around 50% after 100 charge-discharge cycles. The Al-doped NCA cathode, on the other hand, demonstrates notable improvement in the cycling stability, and a capacity retention of 93.6% was achieved after 100 cycles, much higher than that of  $\text{LiNi}_{0.85}\text{Co}_{0.15}\text{O}_2$ . Further evidence of the voltage stability of NCA cathode is shown in Figure IV-206b. It can be seen that charge-discharge overpotentials remain relatively stable over the course of 200 cycles. Also, the capacity retention of the sample is still ~88% after 200 cycles. The full-cell testing of NCA cycled between 2.5 and 4.4 V under C/3 in Figure IV-206c, clearly shows the desired cyclability, with a capacity retention of 92.0% after 250 cycles. These results indicate that Al doping is very effective in prolonging the cycle life of Ni-rich layered oxide cathode materials.

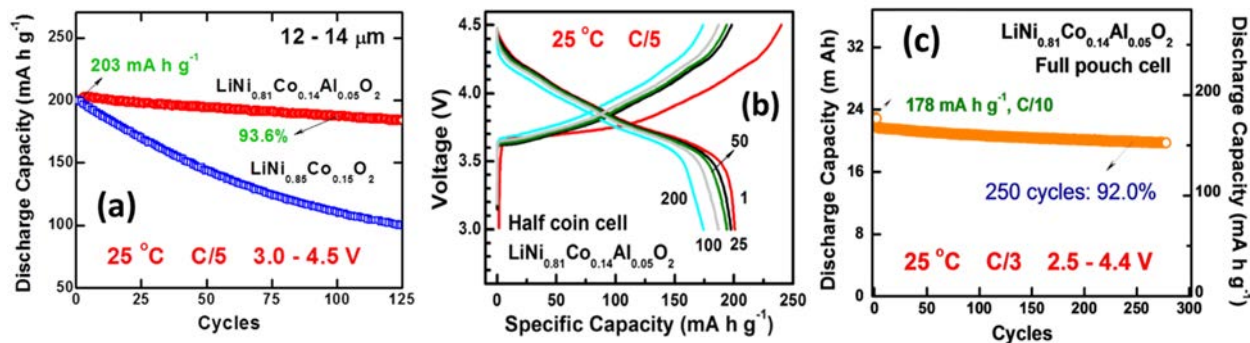


Figure IV-206: (a) Evolution of discharge capacities of the two samples as a function of cycles in coin-type Li half cells, (b) galvanostatic electrochemical profiles, and (c) cycling test of  $\text{LiNi}_{0.81}\text{Co}_{0.14}\text{Al}_{0.05}\text{O}_2$  in pouch-type full cells

### 2.3 Effect of surface coating on the performance of Ni-rich material

Surface coating is regarded as an effective method of enhancing the surface stability of cathode materials. Investigated is the effect of several coating materials and coating structure on the performance of Ni-rich cathode material. All of them have proven effective in improving the performance of Ni-rich materials.

To enhance the surface stability of the Ni-rich  $\text{LiNi}_{0.7}\text{Co}_{0.15}\text{Mn}_{0.15}\text{O}_2$  cathode,  $\text{Li}_2\text{ZrO}_3$  has been coated on the particles' surfaces as a protective agent by two methods: sol-gel and precipitation. Inspired by the thermodynamic mechanisms of solid-state diffusion of transition-metal ions at high temperatures, two sintering temperatures of 650 and 800°C were chosen to investigate the possible bi-functional effects of doping and coating under different sintering conditions. Figure IV-207 presents a comparative cross-sectional SEM-EDX mapping of the Zr element of all samples. Two observations are to be noted as important. First, the most uniform distribution of Zr at one secondary particle's surface was achieved by the precipitation method, followed by sintering at 650°C. Second, the most uniform doping of  $\text{Zr}^{4+}$  into the local lattice at one secondary particle was achieved by sol-gel method, followed by sintering at 800°C. Besides, the other two preparation conditions cause an aggregation of Zr to a certain extent at one secondary particle's surface. The reason for such variations in Zr distribution could be understood as follows: first, sol-gel leads to surface coating of  $\text{Li}^+$  and  $\text{Zr}^{4+}$  agents on primary particles while precipitation leads to the secondary particle's coating; second, 650 and 800°C sintering temperatures result in different levels of elemental diffusion across the particles.

Figure IV-207 also shows the capacity retention during 100 cycles of all the samples. Apparently, the  $\text{Li}_2\text{ZrO}_3$ -coated  $\text{LiNi}_{0.7}\text{Co}_{0.15}\text{Mn}_{0.15}\text{O}_2$  cathodes prepared by precipitation and after sintering at 650°C provide the best cyclability compared to others, *i.e.*, 92.2, 92.8, and 97.7% capacity retention with respect to 1, 3, and 5 wt.% of coating agent. This observation agrees well with the conclusion from SEM-EDX mapping that the most uniform coating of Zr on one secondary particle could provide the most efficient protection from corrosive electrolyte. The results indicate that  $\text{Li}_2\text{ZrO}_3$  can improve the cyclability of Ni-rich material effectively.

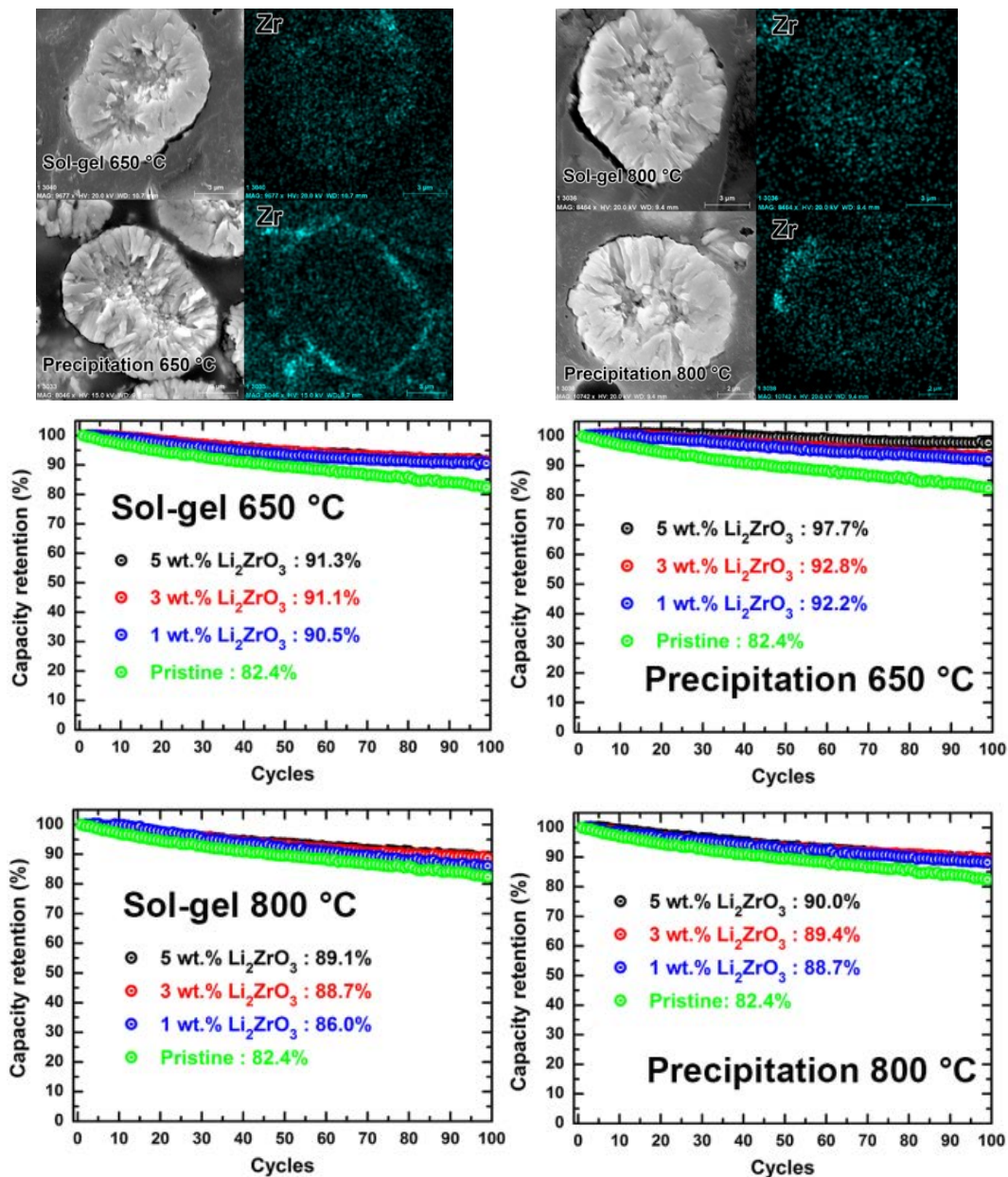


Figure IV-207: Cross sectional SEM-EDX mapping of the Zr element in the  $\text{Li}_2\text{ZrO}_3$ -coated  $\text{LiNi}_{0.7}\text{Co}_{0.15}\text{Mn}_{0.15}\text{O}_2$  samples prepared by sol-gel and precipitation methods and capacity retention of the  $\text{Li}_2\text{ZrO}_3$ -coated  $\text{LiNi}_{0.7}\text{Co}_{0.15}\text{Mn}_{0.15}\text{O}_2$  cathodes prepared by sol-gel and precipitation methods with a cycling condition of 3.0 – 4.5 V, C/3 rate, and 25 °C

Besides the single coating, a double coating strategy was also adopted, aiming to enhance the surface stability of Ni-rich materials without the expense of specific capacity. To stabilize the surface of the Ni-rich material, we pursued Li-rich material coating on Ni-rich oxides. Note that, in general, Li-rich materials show more stable cycle performance compared to Ni-rich materials when they are cycled at above 4.5V. In this regard, Li-rich material is a good coating material for Ni-rich materials, which can reduce the surface instability of Ni-rich materials. Figure IV-208 highlights the stabilization effect of Li-rich material coating ( $\text{Li}_{1.2}\text{Ni}_{0.2}\text{Mn}_{0.6}\text{O}_2$ ) on  $\text{LiNi}_{0.7}\text{Co}_{0.15}\text{Mn}_{0.15}\text{O}_2$ . The coated sample with 20 wt. % of  $\text{Li}_{1.2}\text{Ni}_{0.2}\text{Mn}_{0.6}\text{O}_2$  (yellow line) shows improved cyclability with a capacity retention of 93% during 100 cycles, while the bare material ( $\text{LiNi}_{0.7}\text{Mn}_{0.15}\text{Co}_{0.15}\text{O}_2$ , yellow line) has a capacity retention of 80%. However, Li-rich materials need a high charge voltage (at least 4.6 V) to activate their  $\text{Li}_2\text{MnO}_3$  phase that plays a key role in realizing high capacity. As a result, the coated sample with 20 wt. % of  $\text{Li}_{1.2}\text{Ni}_{0.2}\text{Mn}_{0.6}\text{O}_2$  has a lower discharge capacity than the bare sample Figure IV-208. Therefore, to prevent the decrease in the capacity of the coated material, we need to activate the  $\text{Li}_2\text{MnO}_3$  phase before utilization. To do so, we applied chemical activation to activate the surface  $\text{Li}_2\text{MnO}_3$  phase instead of electrochemical activation with the charge process of above 4.6V, because Ni-rich material

undergoes severe phase degradation from layered to NiO rock salt structure at above 4.6V. (Chemical activation method denotes Li extraction using acidic or basic chemical solvent.) In this experiment, we conducted chemical activation on Li-rich coated Ni-rich materials using  $\text{AlF}_3$  sub-coating, which is a well-known coating material as both a stabilizing and activation agent for Li-rich materials. As a result of the  $\text{AlF}_3$  treatment, the double-coated sample with 20 wt. % of  $\text{Li}_{1.2}\text{Ni}_{0.2}\text{Mn}_{0.6}\text{O}_2$  and 1 wt. % of  $\text{AlF}_3$  (red line) shows a high discharge capacity of  $210 \text{ mA h g}^{-1}$  with good cycle performance of 94% retention during 100 cycles.

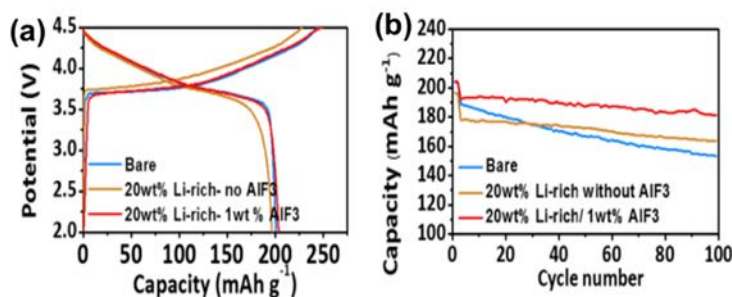


Figure IV-208: (a) Voltage profiles of bare and coated samples between 2.0 and 4.5 V at C/10 rate ( $= 20 \text{ mA g}^{-1}$ ) at  $25^\circ\text{C}$ . (b) Cycle performance during 2 initial cycles at C/10 rate and further 98 cycles at C/3 rate

Furthermore, the double coating with  $\text{Li}_{1.2}\text{Ni}_{0.2}\text{Mn}_{0.6}\text{O}_2$  and  $\text{AlF}_3$  results in superior cycle performance at elevated temperatures and rate capability. The rate and cycle results are shown in Figure IV-209, respectively. The double-coated sample shows a higher discharge capacity of  $145 \text{ mAhg}^{-1}$  at 10C rate compared to a lower discharge capacity of  $112 \text{ mAhg}^{-1}$  for the bare, uncoated sample. The superior rate property of the coated sample is due to the surface electrochemical stability that comes from the protecting effect of the surface coating layer. The double coating layer alleviates the surface instability of the Ni-rich material by reducing the unstable side reaction with electrolyte, which is the main reason for thick SEI layer formation and structural degradation of Ni-rich materials.

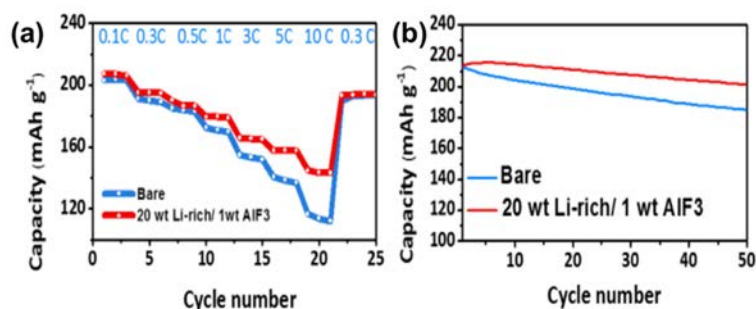


Figure IV-209: (a) Rate capabilities of bare and coated samples with increasing C-rates from C/10 to 10C rate between 2.0 and 4.5 V at  $25^\circ\text{C}$ , and (b) cycle performance during 100 cycles at 1 C rate and  $55^\circ\text{C}$

Li-rich layered  $\text{Li}_2\text{MnO}_3$  is more stable towards carbonate-based nonaqueous electrolytes than the Ni-rich layered phase with a high cut-off voltage, such as 4.8 V vs.  $\text{Li/Li}^+$ . This is due to the less oxidizing surface  $\text{Mn}^{4+}$  ions (than  $\text{Ni}^{4+}$ ) at highly delithiated states. Thus, a strategy based on a chemical formula of  $x\text{Li}_2\text{MnO}_3 \cdot (1-x)\text{LiNi}_{0.7}\text{Co}_{0.15}\text{Mn}_{0.15}\text{O}_2$  is proposed to stabilize the local structure aiming for enhanced cyclability. A typical preparation procedure is quite simple, involving mixing the as-prepared  $\text{LiNi}_{0.7}\text{Co}_{0.15}\text{Mn}_{0.15}\text{O}_2$  precursor with a stoichiometric amount of  $\text{MnCO}_3$  and  $\text{LiOH} \cdot \text{H}_2\text{O}$  according to various  $x$  values, followed by heat treatment at  $500$  and  $800^\circ\text{C}$ . For the obtained  $0.07\text{Li}_2\text{MnO}_3 \cdot 0.93\text{LiNi}_{0.7}\text{Co}_{0.15}\text{Mn}_{0.15}\text{O}_2$ , we conducted long-term cycling tests in both coin half cell and laminated pouch full cell under C/3. As shown in Figure IV-210, at  $25$  and  $55^\circ\text{C}$ , 90.3 and 81.3% of capacity retention, respectively, after 400 and 200 cycles cycled have been obtained, by taking advantages of the stabilized surface by  $\text{Li}_2\text{MnO}_3$  formation. Additionally, 87.7% capacity retention after 170 cycles for laminated pouch full cell fabricated with graphite anode was also achieved. All the results show that the combination of  $\text{Li}_2\text{MnO}_3$  and Ni-rich material can improve the stability of Ni-rich material.

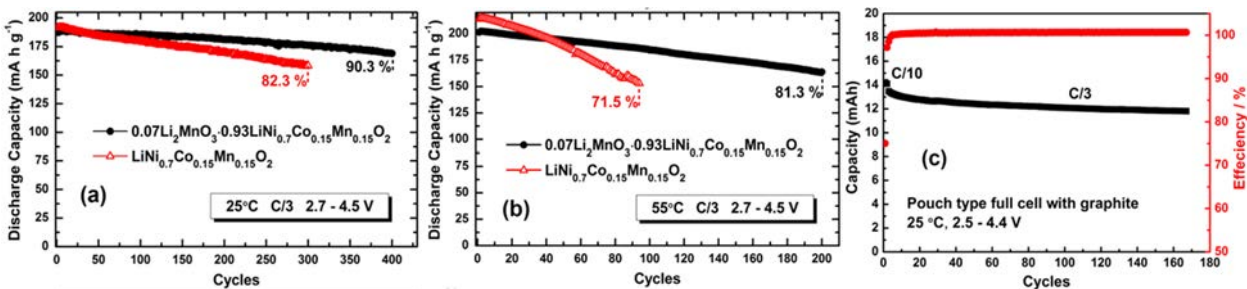


Figure IV-210: Cycling performance of the pristine  $\text{LiNi}_{0.7}\text{Co}_{0.15}\text{Mn}_{0.15}\text{O}_2$  and surface-modified  $0.07\text{Li}_2\text{MnO}_3\cdot 0.93\text{LiNi}_{0.7}\text{Co}_{0.15}\text{Mn}_{0.15}\text{O}_2$  samples in 1.2 M  $\text{LiPF}_6$  in a 3 : 7 mixture of ethylene carbonate (EC) and ethylmethyl carbonate (EMC) electrolyte at (a) 25 °C and (b) 55 °C, and (c) cycling test of  $0.07\text{Li}_2\text{MnO}_3\cdot 0.93\text{LiNi}_{0.7}\text{Co}_{0.15}\text{Mn}_{0.15}\text{O}_2$  in laminated-type pouch graphite full cells at 25 °C

### 3. Development of optimized concentration-gradient $\text{LiNi}_{0.76}\text{Co}_{0.10}\text{Mn}_{0.14}\text{O}_2$ (CG) cathode material

In order to further improve the performance and reach the project goal of cathode materials, concentration-gradient (CG) nickel-rich materials were investigated systematically. The research focused on the effect of different parameters on the performance, including element ratio, element distribution, particle size, base agent, and pH value. The research results showed that the best CG material is  $\text{LiNi}_{0.76}\text{Co}_{0.1}\text{Mn}_{0.14}\text{O}_2$  prepared at a pH value of  $\sim 11.2$ , having a diameter of  $\sim 13 \mu\text{m}$ , and a composition distribution of continuously decreasing Ni content, increasing Mn, and constant Co content from the interior to the surface.

We have delivered one kilogram of the optimized concentration-gradient  $\text{LiNi}_{0.76}\text{Co}_{0.1}\text{Mn}_{0.14}\text{O}_2$  (CG) cathode material for the project through transition-metal co-precipitation with precise composition and morphology control. In Figure IV-211a, it can be seen that the sample consists of uniform spherical particles of around  $13 \mu\text{m}$ . The electrochemical performance of the CG material was evaluated in pouch full cells at room temperature with a  $\sim 4 \text{ mg cm}^{-2}$  mass loading. Figure IV-211b, and Figure IV-211c show the evolution of galvanostatic charge-discharge profiles and specific discharge capacity, respectively, as a function of cycles. It can be seen that the sample delivered a discharge capacity of  $186 \text{ mAh g}^{-1}$  at C/10 ( $C = 180 \text{ mA g}^{-1}$ ) and retained  $\sim 89\%$  of its initial discharge capacity after 400 cycles within the voltage window of 2.5 – 4.4 V vs.  $\text{Li/Li}^+$ . The over-potentials during cell operation, as demonstrated by the charge-discharge curves in Figure IV-211b, are noticeable, although the sample has been surface-modified to suppress various interfacial side reactions.

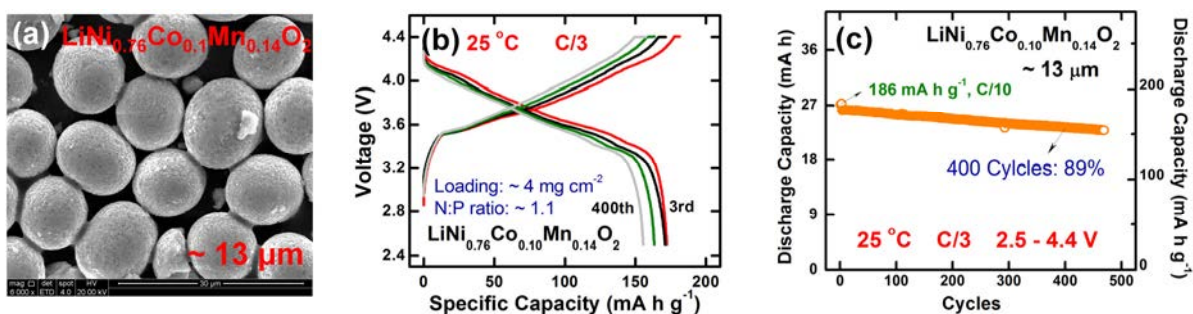


Figure IV-211: (a) SEM image of  $\text{LiNi}_{0.76}\text{Co}_{0.1}\text{Mn}_{0.14}\text{O}_2$  (CG). (b) Galvanostatic charge-discharge curves and (c) capacity evolution of the sample as a function of cycles in pouch-type full cells with  $\sim 4 \text{ mg cm}^{-2}$  mass loading

### Electrolyte

With the new batch of anode from PSU, PSU\_1000\_30, we investigated the performance of 10% FEC as an additive in the EC and EMC based electrolyte (1.2M  $\text{LiPF}_6$  in EC/EMC=3/7 in weight ratio). The anode half cell using that electrolyte was tested. The voltage window was set from 0.005V to 1.5V at room temperature. The first formation cycle was under the rate of 0.1C and the rest of cycling life was tested under 0.2C. SEM image of the pristine anode electrodes are shown in Figure IV-212 and no morphology difference with pervious batch was observed.

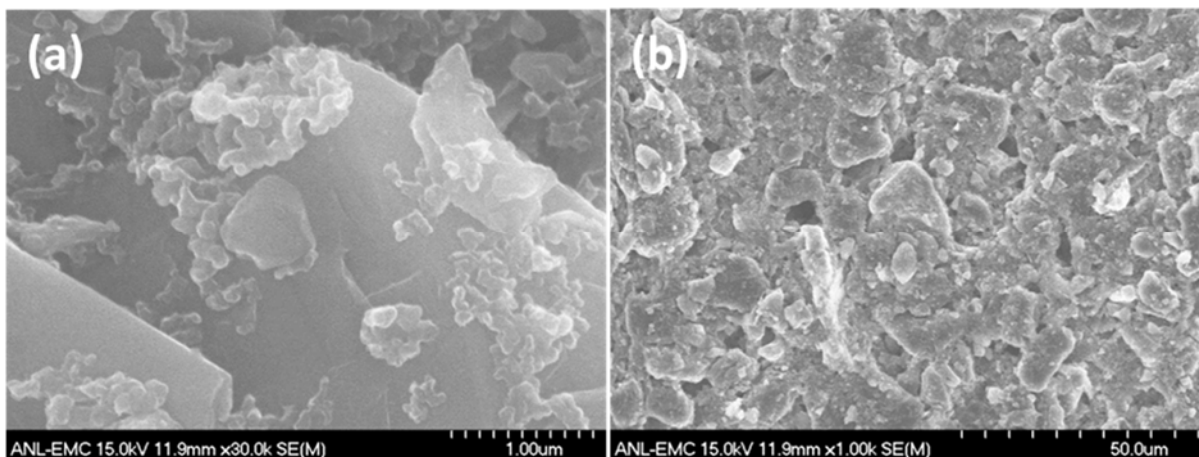


Figure IV-212: SEM characterization of pristine Si anode from PSU in different magnification. (a). High magnification (b). Low magnification

The cycling performance of PSU\_1000\_30 is shown in Figure IV-213a and Figure IV-213b. Two electrodes showed good capacity retention. The first cycle's Coulombic efficiency of the first sample is 72.68% and 72.67% of the second sample. Both of them are higher than the last batch PSU600 and PSU800 sample half cells. After the first few cycles, the Coulombic efficiency for both electrodes was stabilized on 99.5%. The area capacity of the first sample was stabilized on 5mAh/cm<sup>2</sup> and for the second sample, on 4.2mAh/cm<sup>2</sup>.

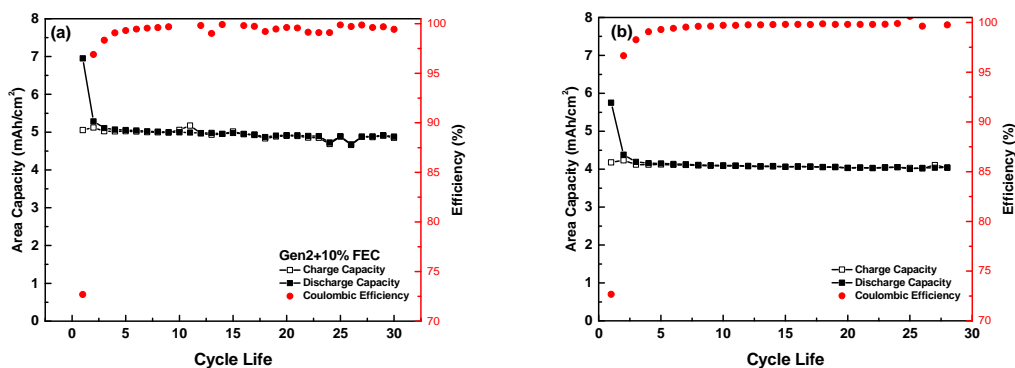


Figure IV-213: Capacity retention and Coulombic efficiency of PSU anode /Li half cells with baseline electrolyte (a) PSU\_1000\_30 sample 1. (b) PSU\_1000\_30 sample 2

Due to the PSU\_1000\_30 sample shows a good capacity retention on the half cell, we try to assemble the PSU\_100\_30/LiNi<sub>0.5</sub>Mn<sub>0.3</sub>Co<sub>0.2</sub>O<sub>2</sub> full cell in Argonne to further investigate the performance of the anode. The LiNi<sub>0.5</sub>Mn<sub>0.3</sub>Co<sub>0.2</sub>O<sub>2</sub> electrode (AC013 batch) was fabricated in Argonne national lab by CAMP facility. The cycling data of AC013/Li half cells in different cut off voltage with Gen 2 electrolyte are shown in Figure IV-214. Under a 4.4V cutoff voltage, the cell shows a good capacity retention and the area capacity was stabilized on 2.0mAh/cm<sup>2</sup>. When we increased the cutoff voltage from 4.4V to 4.6V, a higher area capacity, 2.4 mAh/cm<sup>2</sup>, can be reached. However, the capacity retention was not comparable with the 4.4V data.

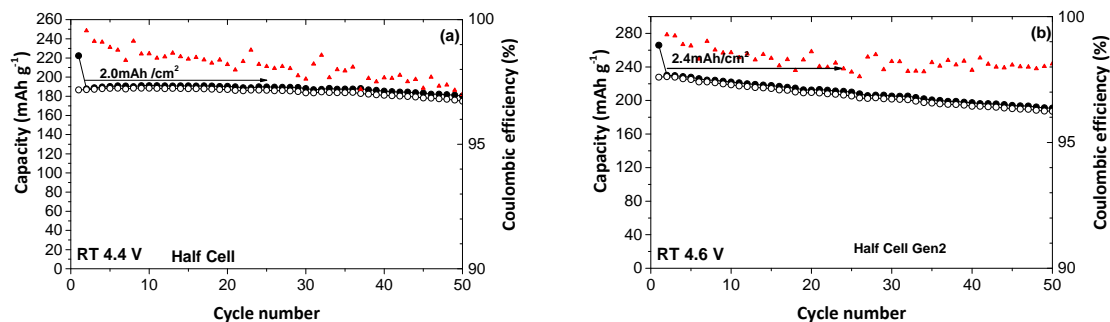


Figure IV-214: Capacity retention and Coulombic efficiency of AC013/Li half cells with Gen 2 electrolyte in different cutoff voltage. (a). 3.0 V-4.4 V, (b). 3.0 V-4.6 V

Based on the half cell data we have, we begin testing the full cell with PSU100\_30 anode and AC013 cathode under 4.5V cut off voltage in different electrolyte. Figure IV-215a and b show the capacity retention and Coulombic efficiency of the full cell in Gen2 and Gen2+10% FEC electrolyte. Both of the two cells shows a low first cycle Coulombic efficiency, 42.9% for the Gen2 one and 41.8% for the Gen2+10% FEC one. The low first cycle's Coulombic efficiency would result from a high areal capacity ratio of negative to positive electrodes (N/P ratio). The N/P ratio is one of the most important factors to design the lithium-ion batteries with high performance in the consideration of balanced electrochemical reactions. Based on our previous study, the cell with 1.1 to 1.2 of N/P ratio shows the enhanced cycle performance in comparison with other cells. A low N/P ratio may cause the lithium plating on the anode side and a high N/P ratio will lead to a low first cycle's Coulombic efficiency due to the loss of lithium ion on the formation of SEI step.

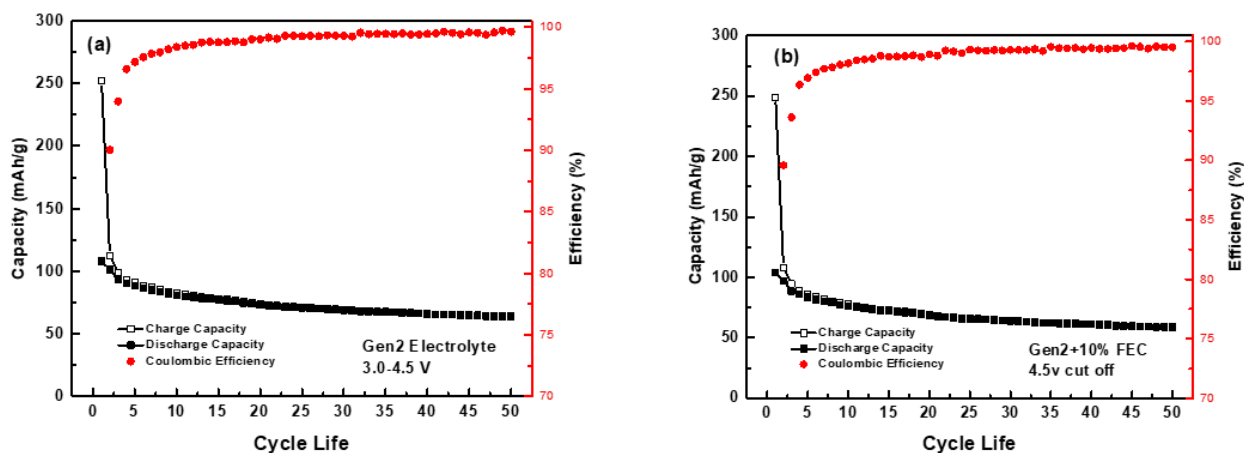


Figure IV-215: Capacity retention and Coulombic efficiency of PSU\_1000\_30/ AC013 full cell under 4.5 V cutoff voltage in different electrolyte (a) Gen2 electrolyte (b) Gen2+10% FEC electrolyte

Three new FSI based ionic liquid electrolytes were also synthesized and purified at ANL for Si/ NCM523 full cell. Their structures are shown in Figure IV-216. All the products are viscous and colorless liquid.

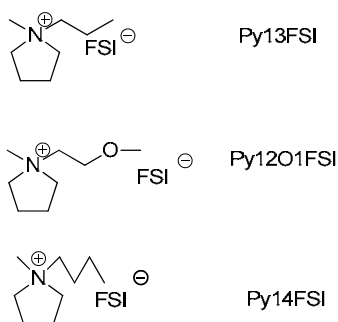


Figure IV-216: Chemical structure and name of the synthesized ionic liquid

Scheme 1 depicts the synthesis of the FSI-based ionic liquids (See Figure IV-217). N-methylpyrrolidine was first reacted with the corresponding alkyl bromide to generate the pyrrolidinium bromide salt. The bromide ion in the pyrrolidinium bromide salt was then exchanged with bis (fluorosulfonyl) imide ion through the anion exchange reaction with lithium bis (fluorosulfonyl) imide in water to produce the corresponding ionic liquid.

Scheme 1

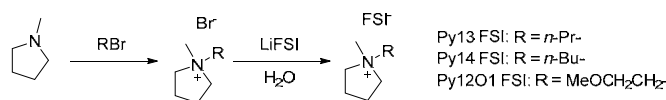


Figure IV-217: Scheme 1: Scheme 1. Synthetic step of the ionic liquid electrolyte

Si-Graphite anode from CAMP facility was used to test the new ionic liquid. The half cell performance in EC and EMC based electrolyte with or without 10% FEC additive are shown in Figure IV-218a and Figure IV-218b. 2 cycles under 0.1C were used as formation step and 0.2C was used as the cycling rate. The voltage window was from 0.05V to 1.5V. It shows with 10% FEC as the additive, both the capacity retention and Coulombic efficiency were improved. And it's similar with our previous results.

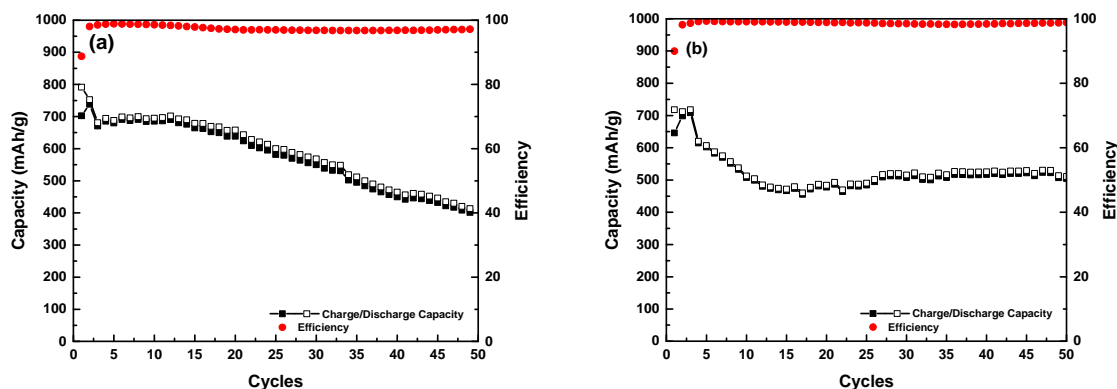


Figure IV-218: Capacity retention and Coulombic efficiency of Si-Graphite/Li half cells with (a) Gen 2; (b) Gen 2+10% FEC electrolyte in different cutoff voltage from 0.05 V to 1.5 V

The capacity retention and Coulombic efficiency data of the CAMP Anode half cell with 1M LiFSI in Py13FSI with or without 10 wt % FEC as additive are given in Figure IV-219. 2 cycles under 0.1C were used as formation step and 0.2C was used as cycling rate. The voltage window was from 0.05V to 1.5V. It shows that unlike the EC and EMC based electrolyte, adding of FEC brings no impressive improvement in the electrochemical performance of the ionic liquid based half cell. Both cells have a capacity stabilized on 550mAh/g, based on the whole electrode, and Coulombic efficiency is stabilized on 99.6%.

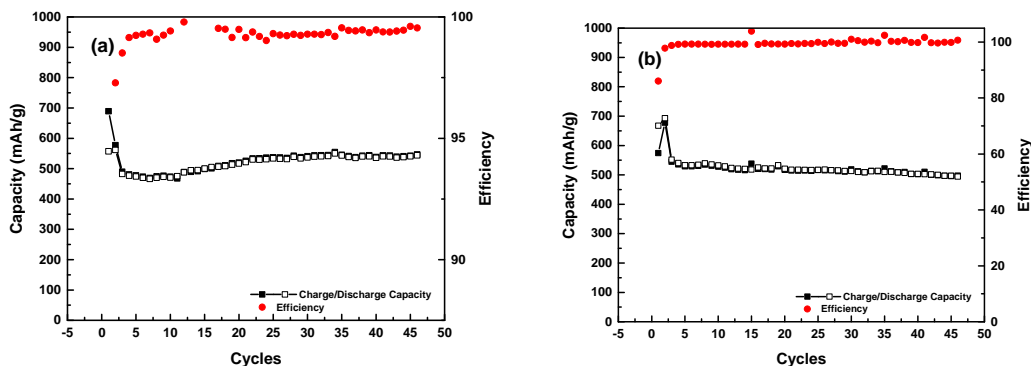


Figure IV-219: Capacity retention and Coulombic efficiency of Si-Graphite/Li half cells with (a) 1M LiFSI in Py13FSI; (b) 1M LiFSI in Py13FSI +10% FEC electrolyte in cutoff voltage from 0.05 V to 1.5 V

The capacity retention and Coulombic efficiency data of the CAMP Anode half cell with 1M LiFSI in Py1312O1 with or without 10 wt % FEC as the additive are given in Figure IV-220. 2 cycles under 0.1C were used as formation step and 0.2C was used as the cycling rate. The voltage window was from 0.05V to 1.5V. The results show that interestingly unlike the Py13 based ionic liquid, adding of FEC even decreased the capacity of the half cell from 550mAh/g to 480mAh/g.

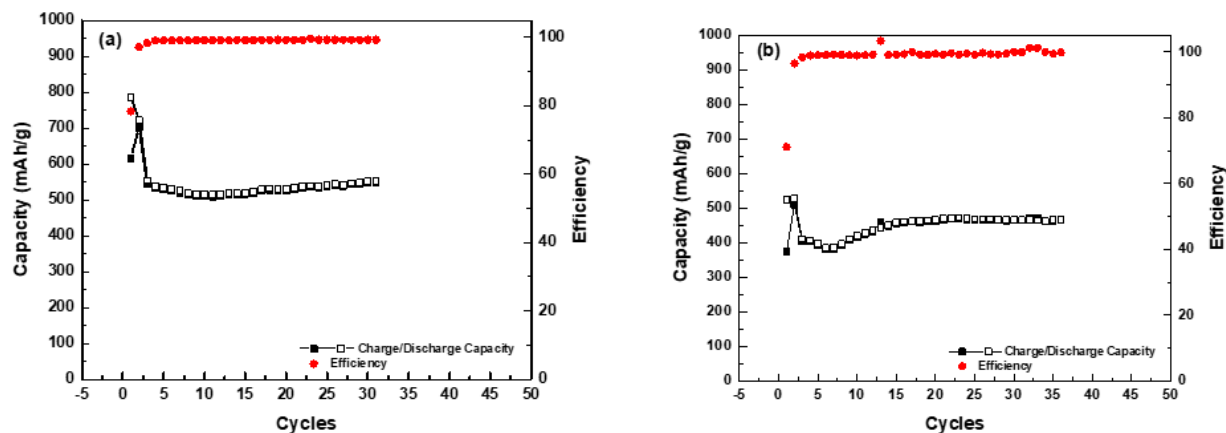


Figure IV-220: Capacity retention and Coulombic efficiency of Si-Graphite/Li half cells with (a) 1M LiFSI in Py12O1FSI; (b) 1M LiFSI in Py12O1FSI +10% FEC electrolyte in cutoff voltage from 0.05 V to 1.5 V

In phase 2, we studied the substitutional group effect on the cyclic carbonate. Ethylene carbonate (EC) was used for the SEI former in the conventional electrolyte for decade years. However, both EC and other linear carbonates in the commercial electrolyte suffered from the low oxidation potential and severe capacity decay during cycling under high voltage operation. As a result, finding a viable electrolyte with a good SEI former and high anodic stability for next-generation high voltage lithium-ion batteries is of primary importance. In this quarter, a series of electrolytes containing fluorinated cyclic carbonates as the anode SEI former with trifluoroethyl methyl carbonate (F-EMC) and LiPF<sub>6</sub> has been designed, synthesized and evaluated. The effects of fluorine substitution on the cyclic carbonate on the electrolyte oxidation stability were examined by the 3 electrodes cell with Pt as the working electrode. And the cycling performance were investigated by the LiNi<sub>0.5</sub>Co<sub>0.2</sub>Mn<sub>0.3</sub>O<sub>2</sub> (NCM523)/ graphite 4.6V full cell. Based on this study, the electrolyte with DFEC/FEMC (1.0M LiPF<sub>6</sub>) inhibits the oxidation side reaction on the cathode and forms a good SEI on the anode. It realizes the high voltage NCM532/Graphite battery that exhibits excellent cycling durability under both room and high (55 °C) temperature.

To determine the oxidation stability of different fluorinated cyclic carbonates shown in Figure IV-221, linear sweep voltammetry measurements were performed under room temperature and the results are shown in Figure IV-222. To begin, we selected the linear carbonate F-EMC as the fixed component and mixed it with different fluorinated cyclic carbonates (FEC, DFEC, TFPC, HFEEC and NFPEC) to evaluate the oxidation potential of the resulting mixtures. The solvent F-EMC was chosen since it has shown relatively good stability against the high voltage cathode. For the baseline EC/EMC electrolyte, the anodic current increases drastically at 6.5 V, indicating the onset of solvent decomposition. Except of HFEEC, most of fluorinated cyclic carbonate showed higher voltage stability than the baseline electrolyte. And the anodic stability follows the order NFPEC > DFEC > FEC > TFPC > EC > HFEEC, the same order as predicted from the quantum chemistry calculations considering the anion effect of PF<sub>6</sub><sup>-</sup> we proposed before. For HFEEC, although there is an electron-withdrawing tetrafluoroethyl group at the far end of the molecule, a -CH<sub>2</sub>-O-CH<sub>2</sub>- link separates the F-alkyl from the carbonate ring; therefore, the electron-withdrawing effect is minimized. The -CH<sub>2</sub>-O-CH<sub>2</sub>- group actually acts as an electron-donating group, which lowers the oxidation potential of the carbonate ring. Moreover, the ether linkage -CH<sub>2</sub>-O-CH<sub>2</sub>- itself is vulnerable to oxidation as well.

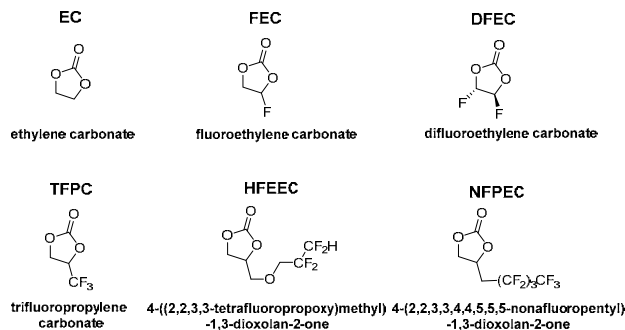


Figure IV-221: Structural formulas for different cyclic carbonate

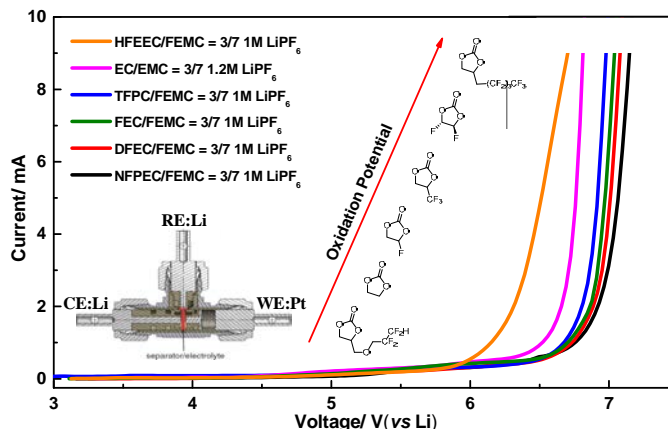


Figure IV-222: Linear oxidation sweep voltammograms of baseline electrolyte and fluorinated electrolyte containing different carbonate

Conductivity is one of the most important properties of electrolytes because it affects the rate performance of the cell. Together with the liquid range, conductivity also affects the high temperature performance. Compared with the SOA electrolyte, fluorinated electrolytes generally have a lower conductivity depending on the degree of fluorination. Even with the negative effect, the conductivity of most fluorinated electrolytes is still the within the same order of magnitude of the conductivity of SOA electrolyte. Figure IV-223 shows the ionic conductivity of the cyclic fluorinated formulations as a function of temperature. The conductivity increased monotonically with increasing temperature in the whole investigated temperature range. The fluorinated electrolytes contain FEC shows the highest ionic conductivity and the electrolytes contain HFEEC or NFPEC shows comparable low ionic conductivity due to a long fluorinated substituent. Meanwhile, the electrolytes contain DFEC or TFPC shows intermedia conductivity.

The temperature dependence of the conductivity also shows a typical non-Arrhenius behavior of liquid electrolytes well described by the VTF (Vogel–Tamman–Fulcher) function. The applicability of the VTF function to the conductivity data also illustrates the close relationship between the conductivity and the viscosity of electrolytes.

$$\ln \sigma = \ln \sigma_0 + \frac{-B}{T - T_0}$$

In the VTF equation,  $\sigma_0$  is the pre-exponential factor,  $T_0$  represent the glass transition temperature, and T is the absolute temperature. B is related to the activation energy of ion transport associated with the configurational entropy of the electrolyte. The fitted VTF equation results are shown in Table IV-34. The electrolyte contains the TFPC shown the highest viscosity and the HFEEC shown the lowest.

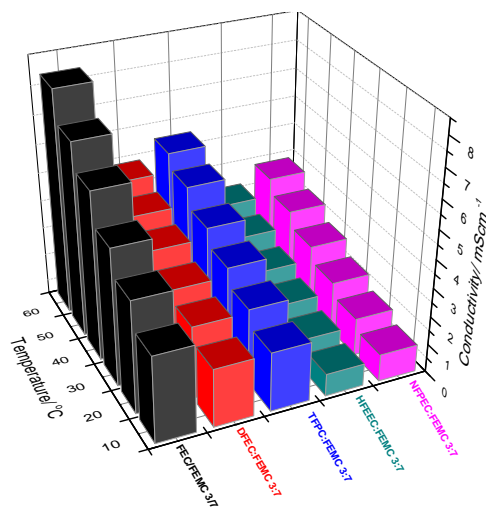


Figure IV-223: Conductivity measurement of different fluorinated formulations (1.0 M LiPF<sub>6</sub>)

Table IV-34: Fitted VTF Empirical Equation Results

Electrolyte (1M LiPF <sub>6</sub> )	B (K)	$\sigma_0$ (mS/cm)	T <sub>0</sub> (K)
FEC:FEMC 3:7	317	59.7	177
DFEC:FEMC 3:7	226	19.5	183
TFPC:FEMC 3:7	251	27.8	186
HFEEC:FEMC 3:7	517	54.4	161
NFPEC:FEMC 3:7	388	42.8	181

### NCM523/graphite cell performance

LiNi<sub>0.5</sub>Co<sub>0.2</sub>Mn<sub>0.3</sub>O<sub>2</sub>/graphite cells were subjected to charge-discharge cycling at a rate of C/3 with the cutoff voltage between 4.6 V and 3.0 V. The first 25 cycles were tested under room temperature. To test the thermostability of the different electrolyte, from the 26 to 50 cycle, the cells were removed into a 55 °C oven. Figure IV-224a and b show the cycling performance of these cells. For the baseline cell under room temperature, the initial charge and discharge capacities are 246 and 211 mAh/g, respectively (corresponding to 85.7% coulombic efficiency). The capacity retention is 84.5% after 25 room temperature cycles, and the coulombic efficiency (CE) is maintained at 99.4% over 25 cycles. All of the cells cycled in the fluorinated electrolyte showed a lower 1st CE compared with the baseline electrolyte, which follows the order HFEEC > NFPC > DFEC > FEC > TFPC. It is well known that SEI formation on graphite electrode leads to loss of Li<sup>+</sup> inventory causing the decrease in capacity. For the fluorinated cyclic carbonate, more active Li<sup>+</sup> ion might be consumed to form the SEI layer on the graphite surface during the first cycle because of the reductive reaction of the C-F bond. As a result, a long fluorinated substituents as NFPC and HFEEC may cause a low 1st CE, furthermore. Furthermore, the formation of LiF on the electrode surface may increase the anode impedance in the same time. Under room temperatures, TFPC, FEC and DFEC shows similar capacity retention. Moreover, due to superior anodic stability, FEC and DFEC show higher CE than the baseline electrolyte. For the cell cycled with HFEEC, a low 1st CE and high resistance surface lead to the dramatically capacity fade under even room temperature. And for the cell cycled with NFPEC, due to the electrolyte suffer from a low anodic, shows a poor capacity retention and CE stability.

It is well known that the oxidative decomposition of organic solvent on the cathode surface causes further side reaction to consume the active Li<sup>+</sup> in the closed circuit. This process depletes the lithium salt and changes the bulk properties of the electrolyte and will be accelerated under high temperature. As a result, both the coulombic efficiency and capacity retention under high temperature cycling are always worse than for room

temperature cycling. However, the LIBs high temperature performance is extremely important for the hybrid vehicles application. Unlike the room temperature performance, when the temperature was raised to 55°C, the difference between fluorinated electrolytes contain TFPC, FEC or DFEC and baseline electrolyte carbonates became clearly differentiated. The cell containing DFEC as the SEI former exhibits the highest Coulombic efficiency and the best capacity retention. It is thought to result from the electrolyte decomposition is suppressed due to the high oxidation potential of DFEC. Meanwhile, the DFEC also can form a good passivation SEI on the graphite anode.

### **Extended cycling performance and EIS Results**

To further investigate the stability of the DFEC/FEMC electrolyte system, full cells were also cycled for longevity, 100 cycles, under both room temperature and 55°C. Figure IV-224c depicts comparison of the performance of NCM523/Graphite full cells assembled with conventional EC/EMC (1.2 M LiPF<sub>6</sub>) and DFEC/FEMC (1.0 M LiPF<sub>6</sub>) electrolytes. Both cells presented in Figure IV-224c were operated and controlled under the same parameters, C/10 formation and C/3 cycling between 3.0-4.6V, for fair comparison. The cell cycled in the baseline electrolyte deliver 249 mAh/ g charge capacity and 84.9% 1st CE. The cell cycled in DFEC/FEMC electrolyte shows similar 1st charge capacity, however a lower 79.8% 1st CE. Again, the difference in 1st CE is attributed to the reduction of C-F and consumption of active Li<sup>+</sup> of the DFEC specie. But this limitation is countered by unparalleled cycling stability. After 50 room temperature cycles, the cell cycled in carbon-based electrolyte degrades and show 79.6% capacity retention with the CE stabilized on 99.4%. In contrast, the cell cycled in DFEC/FEMC (1.0 M LiPF<sub>6</sub>) electrolyte shows remarkable stability, attributed to the high CEs around 99.7%, with the capacity retention of 90.2% for the first 50 room temperature cycles. Difference between the two electrolytes becomes dramatic under high temperature cycling followed by the room temperature cycling. Under 55°C cycling, the cell with baseline electrolyte suffers from the non-negligible Li consumption and the charge capacity drops from 186mAh/g to 115mAh/g with the CE around 98.5%. On the other hand, the cell with DFEC/FEMC (1.0 M LiPF<sub>6</sub>) electrolyte represents better capacity retention, from 184mAh/g to 155mAh/g and higher average CE, 99.2%.

Impedance spectroscopy was also used to probe the nature of the stability of electrode surface layer. The impedance spectra of the cells after the 50 room temperature cycles and the subsequent high temperature cycling as shown in Figure IV-224c were obtained. These impedance spectra also consist of two semi-cycles and one straight line. These resistances were estimated by fitting of the impedance spectra using the equivalent circuits shown in the insets and are given in Table IV-35. After the 50 room temperature cycles, the cells with baseline electrolyte showed lower interfacial and resistance higher charge transfer resistance compare with the cell cycled in DFEC/FEMC electrolyte. After the subsequent 50 high temperature cycles, DFEC/FEMC cells displayed significantly lower surface and charge transfer resistances, suggesting that DFEC/FEMC derived SEI efficiently suppressed electrolyte breakdown (that ordinarily results in the formation of thick, insulating deposits with large resistance). In contrast, the cells containing baseline electrolyte exhibited higher charge transfer resistance already after the initial cycling, and this resistance became still greater upon the subsequent cycling, suggesting that baseline derived interphase acted as an insulator for Li<sup>+</sup> ions.

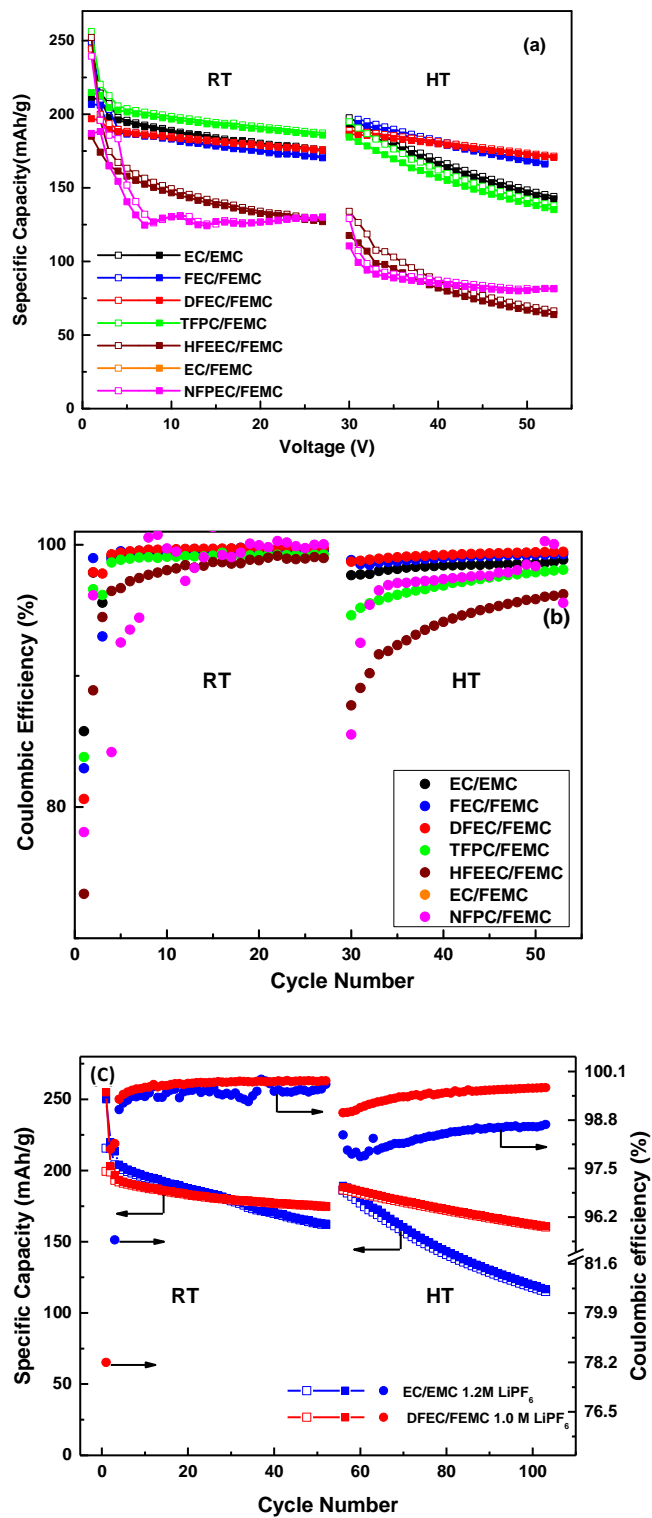


Figure IV-224: Electrochemical performance of  $\text{LiNi}_{0.5}\text{Mn}_{0.3}\text{Co}_{0.2}\text{O}_2/\text{graphite}$  cells containing different electrolyte under room/high temperature. Panel (a) capacity retention and (b)Coulombic efficiency for these cells as a function of the cycle number and (c) performance comparison for two electrolytes at both room and high temperatures

**Table IV-35: Estimates for Interfacial and Charge Transfer Resistance for the Cell Cycled in Different Electrolyte**

Electrolyte	After room temperature cycling (Ohm)			After 55°C high temperature cycling (Ohm)		
	Rbulk	Rsei	Rct	Rbulk	Rsei	Rct
EC/EMC	4.83	9.3	54.8	8.15	57.63	363.68
DFEC/FEMC	7.3	15.6	29.5	10.48	21.858	183.61

## Prelithiation

### 1. Choice of Solvent for Solution Processing Method

In the solution processing method, the compatibility between solvent and SLMP is important. Investigation of the SLMP stability in different solvents has been done in previous work(28). According to previous reports, SLMP is not compatible with some polar solvent such as 1-Methyl-2-pyrrolidinone (NMP) (28). Only hydrocarbon solvents are stable towards lithium metal such as hexane, toluene and xylene. As for the selection of binders for the SLMP slurry, poly(styrene-co-butadiene) (SBR) has already been successfully used in the previous SLMP work. Therefore, we selected SBR as binder for the SLMP slurry first. Both polymer binders can dissolve in the toluene and xylene to form uniform solution. The ability of binder solution to maintain uniformity of SLMP suspension for long periods of time is very important. Therefore, a solvent with higher viscosity is preferred. The viscosity of toluene and xylene are 0.55cP and 0.61cP at 25°C, respectively (39, 40). This indicates that xylene should be better at sustaining SLMP slurry than that of toluene. However, both pure toluene and xylene are not viscous enough to maintain the SLMP dispersion in the slurry. As indicated in Figure IV-225, all the particles tend to float onto the surface of the solvent because of the extremely small density of SLMP and low viscosity of the solution. What's more, the SLMP will fly away after the solvent is evaporated because no attachment force exists between the SLMP and the laminate surface if no polymer binder is included. Therefore, polymer binder is introduced into the solution processing method and its effect on the SLMP coating is further investigated.

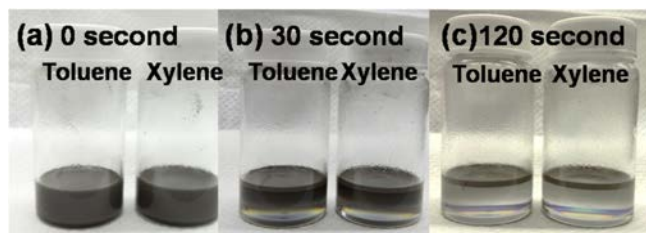


Figure IV-225: Photo images of SLMP suspension in toluene and xylene without addition of polymer, rested for 0 s (a), 30 s (b), and 120 s (c)

## 2. Concentration and Viscosity of Binder Solution for Sustain SLMP Suspension

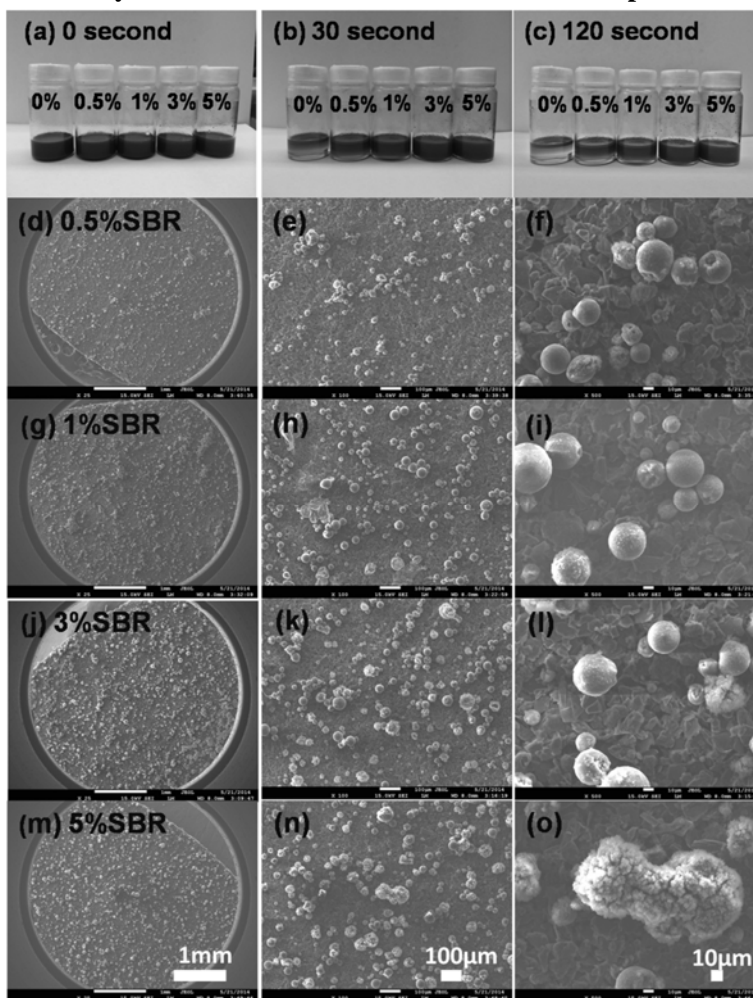


Figure IV-226: Photo images of SLMP suspension in 0%, 0.5%, 1%, 3%, and 5% SBR binder solution, rested for 0 s (a), 30 s (b) and 120 s (c). The SEM images of SLMP loading on a graphite surface with 0% (a, b, c), 0.5% (d, e, f), 1% (g, h, i), 3% (j, k, l), and 5% (m, n, o) SBR binder solution. The scale bar for each row of SEM is the same and shown at the bottom

By introduction of the polymer into the solution processing method of SLMP coating, the viscosity of the solution can be greatly increased. Therefore, a well dispersed SLMP suspension can maintain uniform dispersion for long handling times. The introduced polymers can act as binders to fix the SLMP on the anode surface after the solvent is evaporated. SBR and PS are selected as the binders in this work. SBR has a strong cohesive ability that can provide good attachment between the SLMP and anode surface(37). The characteristics of the polymer solution with different SBR concentration (0%, 0.5%, 1%, 3% and 5%) on SLMP coating are studied. The viscosity is tested to be 1.02cP, 2.52cP, 15.00cP and 36.90cP for 0.5%, 1%, 3% and 5% SBR solution, respectively. The same amounts of SLMP are dispersed in each SBR solution to demonstrate the sustain ability of each binder solution for SLMP slurry. Photo images are taken after the slurries are well mixed and rested for different time duration, 0 second, 30 seconds and 120 seconds, respectively. As shown in Figure IV-226, the addition of polymer binder can effectively increase the viscosity of the solution and maintain the uniform distribution of the SLMP in the slurry. It also indicates that the higher concentration of polymer binder solution, the better sustainability of SLMP distribution in the slurry.

The morphology and distribution of SLMP coating with different SBR concentrations are studied with SEM, Figure IV-226(d-o). Significant difference is observed among them both at low and high magnification images. For the coating with 0.5% SBR, very few SLMP is coated on the anode surface, Figure IV-226(d-f). This is because, the viscosity for the 0.5% SBR solution is too low (1.02 cP) and the difference in density between lithium and xylene is large (the density for lithium is 0.534 gcm<sup>-3</sup>, while the density for xylene is 0.87 gcm<sup>-3</sup>). So most of the SLMP tend to float on the surface of the coating suspension during the coating process and are mostly removed by the doctor blade. When the SBR concentration increases to 1%, the viscosity increases to 2.52 cP, the SLMP distribution can be well sustained in the slurry for 120 seconds Figure IV-226(a-c) and

uniform SLMP coating can be achieved on the anode surface, Figure IV-226(g-i). With further increase of the SBR concentration to 3% and 5%, the SLMP coating can be as uniform, but the number of SLMP coated on the laminate surface doesn't seem to increase much compared to the coating performed with 1% SBR solution, Figure IV-226(j-o). From the above discussion, we can conclude that the ability to sustain SLMP slurry increase with higher viscosity and uniform SLMP coating can be achieved when the viscosity of the binder solution is above 2.5cP. So the binder concentration is set to be 1% in the following discussion with the above optimization. Further efforts will be focused on achieving the uniform coating and easy pressure activation. Minor adjustment could be made when other polymer binders are used.

### 3. Choices of Binder Species for High Efficient Pressure/Calendar Activation

Another important issue that needs to be addressed for application SLMP is the activation process. Easy pressure activation method has been developed in our previous work(32). But when the polymer binder is introduced in the processing method, the activation feasibility and efficiency have to be re-evaluated. When we take a closer look at the SEM images of the SLMP with 5% SBR binder, a polymer shell is observed on the SLMP surface, Figure IV-226(l). In comparison, none of the polymer shell is observed at 1% binder solution, Figure IV-226(f, i) and very few shells are observed on SLMP coated with 3% SBR, Figure IV-226(k, l). The main concern for the process development is: will this thin polymer shell have any negative effect on the pressure activation process? Therefore, the SEM morphology of SLMP coated anode before and after adding electrolyte is studied in Figure IV-227, and 3% concentration of the polymer binder is used to demonstrate the effect of this polymer shell.

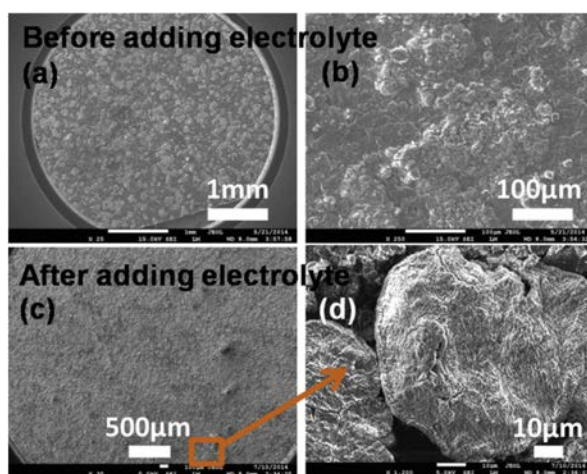


Figure IV-227: The SEM morphology of an SLMP-coated anode surface after pressure activation (a) (b) and after immersing in electrolyte for 48 h (c) (d)

By applying adequate pressure to the SLMP coated anode, most of the  $\text{Li}_2\text{CO}_3$  coating of SLMP can be smashed, as shown in SEM images in Figure IV-227(a, b). After immersing the pressure activated, SLMP coated anode in the electrolyte for 48 hours, the prelithiated anode is observed via SEM again. All the smashed SLMP disappear from view in Figure IV-227(c). But when taking a closer look through high magnification SEM image, a few un-reacted SLMP particles can be found, as showed Figure IV-227(d). From the oblate morphology, we can suggest that these particles have been exposed to pressure, but the lithium is not directly in electric contact with the electrode, so didnot react with the anode and electrolyte. Because SBR is well known for high elasticity, the shell is not efficiently broken under pressure. This SBR shell on the SLMP surface prevents electrical contact between lithium core, anode and electrolyte and leads to insufficient pressure SLMP activation.

There are two ways to eliminate the inefficient activation caused by the polymer binder shell. First, there is less chance to form a complete shell when the binder concentration is lower. But lower concentration may result into other issues, such as non-uniform SLMP dispersion; poor sustainability and poor attachment on the anode surface, etc. Second, polymer binder with less elasticity should be chosen as alternative for this application. The commercially available polystyrene (PS) is introduced. The transition temperature ( $T_g$ ) is  $95^\circ\text{C}$  for PS and  $-65^\circ\text{C}$  for SBR, which indicates that PS is more brittle and easier to break compared to SBR, which can largely help the pressure activation process. Additional, PS with high molecular weight was easily obtained, so a higher viscosity PS solution can be obtained than SBR when the concentration is the same.

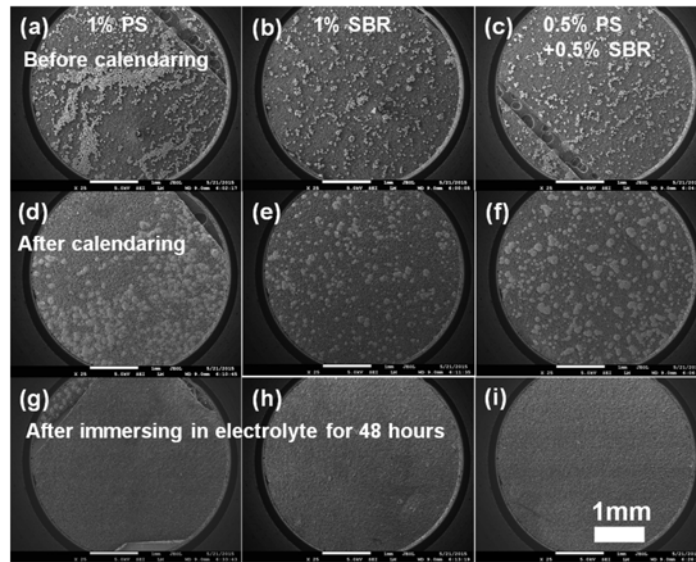


Figure IV-228: The SEM images of SLMP loading on graphite surface before, after calendaring, and after immersing in electrolyte for 48 h with 1% PS (a, d, g), 1% SBR (b, e, h), and 0.5% PS with 0.5% SBR (c, f, i) binder solution

Three sets of binder solutions (1% PS, 1% SBR and 0.5% PS with 0.5% SBR) are introduced to optimize the binder composition for easier pressure activation. The SEM images of SLMP loading on graphite surface before, after calendaring and after immersing in electrolyte for 48 hours with 1% PS, 1% SBR and 0.5% PS with 0.5% SBR binder solutions are shown in Figure IV-228. Uniform SLMP coating is observed for SLMP coating with 1% SBR and 0.5% PS with 0.5% SBR binder solutions, Figure IV-228(b, c). The uniformity of SLMP coating will be discussed in the next section. The SLMP are smashed on the graphite surface after calendaring and the anodes have similar morphology with different binder solutions (Figure IV-228). After the calendared electrodes are immersed in the electrolyte for 48 hours, all the smashed SLMP particles disappear from SEM view. Almost none of the residual SLMP similar to Figure IV-228(d) is observed under the high magnification SEM observation for SLMP coating with 1% PS solution and 0.5% PS with 0.5% SBR solution, Figure IV-228(g, i). Only two residual SLMP are observed in Figure IV-228(h). This indicates that the optimized binder solutions, which partially or totally use PS as polymer binder, have a positive effect in achieving high pressure activation efficiency.

#### 4. The Uniformity of SLMP Coating with Optimized Binder Solution

To investigate the sustainability of the three binder solutions, SLMP slurries are made with the 1% PS, 1% SBR and 0.5% PS with 0.5% SBR solutions, respectively. The viscosity of the binder solutions with 1% PS, 1% SBR and 0.5% PS with 0.5% SBR is 4.83cP, 2.52 cP and 3.60 cP, respectively. This further gives evidence that PS with high molecular weight can lead to higher viscosity. Photo images of the SLMP suspension are taken after different time durations for 0 second, 30 seconds and 120 seconds, Figure IV-229(a, b and c). It showed that in all three solvents, SLMP are in uniform distribution for longer than 120 seconds. The phase separation of SLMP slurry begin to be observable after 5-6 minutes. Since this work is aimed at designing a slurry composition for continuous coating procedure performed right after the slurry is mixed, it can indicates that this composition of this polymer binder can give us enough time to process the homogenously dispersed SLMP suspension with the continuous coating procedure.

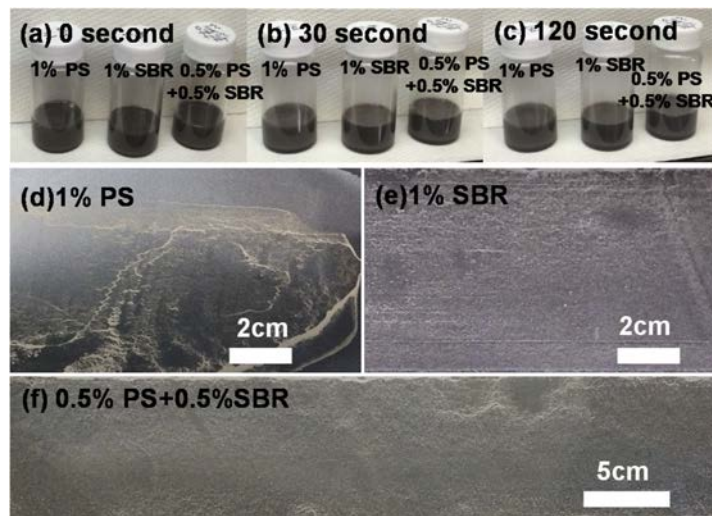


Figure IV-229: Photo images of SLMP suspension in 1% PS, 1% SBR, and 0.5% PS with 0.5% SBR binder solution, rested for 0 s (a), 30 s (b), and 120 s (c). The photo images of SLMP loading on a large piece of graphite anode surface with 1% PS (d), 1% SBR (e), and 0.5% PS with 0.5% SBR (f) binder solution

Doctor blade method is performed for the coating with SLMP slurries in binder solution (1% PS, 1% SBR and 0.5% PS with 0.5% SBR in xylene). Photo images of SLMP coated graphite anodes with different binder solutions are used to exhibit their abilities in achieving uniform SLMP coating and good SLMP attachment. Although with three binder solutions, the sustainability of SLMP slurries is comparable and the appearances of SLMP coatings are similar to those before solvent evaporation. The SLMP coating with 1% PS binder solution exhibits poor attachment on the electrode surface. Most of SLMP particles tend to float to the edge instead of attaching on the anode surface after the solvent evaporates, Figure IV-229(d). But with the 1% SBR and 0.5% PS with 0.5% SBR binder solutions, a uniform SLMP coating and good attachment of SLMP on the anode surface can be achieved after the solvent evaporates. The reason for this difference is that the transition temperature ( $T_g$ ) is  $95^\circ\text{C}$  for PS and  $-65^\circ\text{C}$  for SBR. The glass transition temperature is the temperature below which the polymers are in glass phase and the polymer structure is rigid. Therefore, at room temperature ( $25^\circ\text{C}$ ), the PS is in a brittle glassy state, and cannot act as soft glue; but the SBR is in soft, flexible rubbery state, and can act as good glue to fix SLMP on anode surface. The good attachment of SLMP with SBR binder benefits from the high flexibility of SBR chemical structure. In the case of 1% PS without SBR, the poor SLMP attachment is caused by the rigid PS structure. With this concern, we can take advantage of both polymers and combine the PS and SBR into a mixed binder solution. The flexible SBR can help achieve a good SLMP attachment, while the rigid PS can help achieve much easier pressure activation. Therefore, with the overall consideration of achieving long sustained SLMP slurry, uniform SLMP coating, good SLMP adhesion and easy activation, the best composition of binders and solvent combination is 0.5% PS with 0.5% SBR binder in xylene solution for the processing method, its superb coating effect shown in Figure IV-229(f).

## 5. Prelithiation Effect in Graphite/NMC Full Cell

Two types of cell chemistry have been used to demonstrate the prelithiation effect of SLMP coated with this solution processing method: Graphite/NMC full cell and high energy density SiO/NMC full cell. The prelithiation effects of SLMP on graphite/NMC full cell and graphite half-cell are plotted in Figure IV-230. Figure IV-230(a) is the first cycle voltage profile for the graphite/NMC full cells with and without SLMP prelithiation. In the voltage region below 3.5 V, the cell without SLMP prelithiation shows charge capacity which corresponds to the lithiation of graphite anode with the SEI formation in the first cycle. While for cells with SLMP prelithiation, SEI has been formed in the prelithiation process before cycling and the graphite has already been partially lithiated, so the open circuit voltage starts from 3.5 V and almost no capacity is shown below 3.5 V. The lithium ion loss in the full cell during SEI formation can be compensated by the addition of SLMP so the first cycle coulombic efficiency is increased up to 87.8%, which is higher than the 82.35% for graphite/NMC cells without SLMP prelithiation, as calculated from Figure IV-230(b). Also, the cycle stability of graphite/NMC full cell can be greatly improved with the SLMP prelithiation. This indicates that the failure mechanism of irreversible lithium loss in the full cell can be partially compensated by the addition of the extra lithium ion from SLMP. The prelithiation effect of SLMP on anode can also be observed in voltage profile of the graphite half-cell, Figure IV-230(c). The voltage plateau at 0.7-0.8 V in the half-cell without SLMP

prelithiation indicates the SEI formation at the beginning of lithiation process. While the start voltage of SLMP prelithiated half-cell has already reached lower than 0.3 V, Figure IV-230(c), which further proves that the SEI formation has been achieved in the SLMP prelithiation process. The cycle performances of graphite and the NMC half-cells are shown in Figure IV-230(d) and (f), respectively, along with the voltage profile of NMC half-cell for reference, Figure IV-230(e).

## 6. Prelithiation Effect in SiO/NMC Full Cell

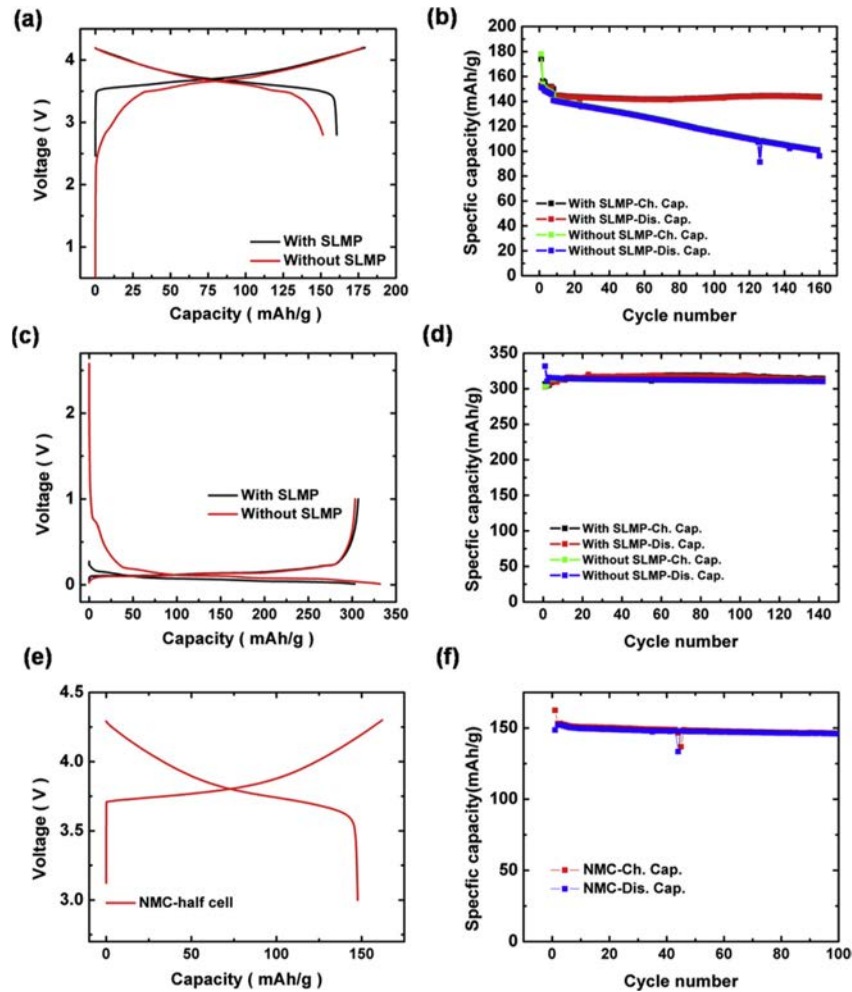


Figure IV-230: The voltage profile for the first cycle (a), and cycling performance (b) for a graphite/NMC full cell, the first-cycle voltage (c), and cycling performance (d) for graphite half cell and the first-cycle voltage (e), and cycling performance (f) NMC half cell. The performance of each cell both with and without SLMP prelithiation is plotted (in red)

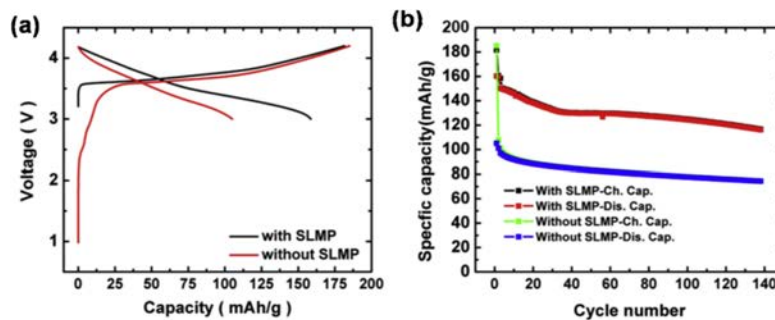


Figure IV-231: The voltage profile for the first-cycle (a) and cycling performance (b) for SiO/NMC full cell

The prelithiation of SLMP becomes crucially important in high energy density anode, such as Si or SiO, etc., because of up to 40%-50% first cycle coulombic loss. The prelithiation effect of SLMP is demonstrated by SiO/NMC full cell with the solution processing method of SLMP coating, Figure IV-231. The SiO anode is composed of SiO nanoparticle (95 wt.%) with conductive binder (PFM, 5 wt.%). Significant improvement is observed in the SLMP prelithiated full cells, Figure IV-231 (b). The first cycle CE increases from 56.78% (without SLMP prelithiation) to 88.12% (with SLMP prelithiation) with this solution processing method. This is because in the full cell design, the lithium ion in the cathode is accurately calculated to match the capacity of the anode and not much excess lithium ion exists. The formation of SEI in the first few cycles will consume most of the excess lithium ion and the long term cycle ability will suffer due to the lithium ion loss. What's more, the lithium ion consumption during the SEI formation is a lot higher in the SiO anode than in graphite anode. So without the prelithiation of SLMP, the SiO/NMC full cell can only start with a capacity of ~110 mAhg<sup>-1</sup> and dropped to ~80 mAhg<sup>-1</sup> after 100 cycles (based on cathode weight). While with the prelithiation of SLMP, the SiO/NMC full cell can maintain a reversible capacity of 130 mAhg<sup>-1</sup> for over one hundred cycles. Therefore, with the coating of SLMP onto the anode of the full cell, well calculated amount of lithium ion is added into the system and compensates the lithium ion loss during SEI formation. In this way, a much prominent improvement in cycle ability can be observed in SiO/NMC full cell.

### 7. Baseline for Si/Graphite composite anode.

The above work established a polymer solution dispersion method to coat SLMP onto the SiO electrode surface to improve Coulombic efficiency. The morphology of the SLMP coated electrodes were collected through SEM observation. The morphology study showed that SBR solution enables a uniform distribution of SLMP coating, polystyrene (PS) helps the activation of SLMP after electrolyte addition. Based on configuration of SiO electrode, Si based electrode is scheduled here. Prior the integration of SLMP, Si/graphite composite half cells were evaluated as control as below:

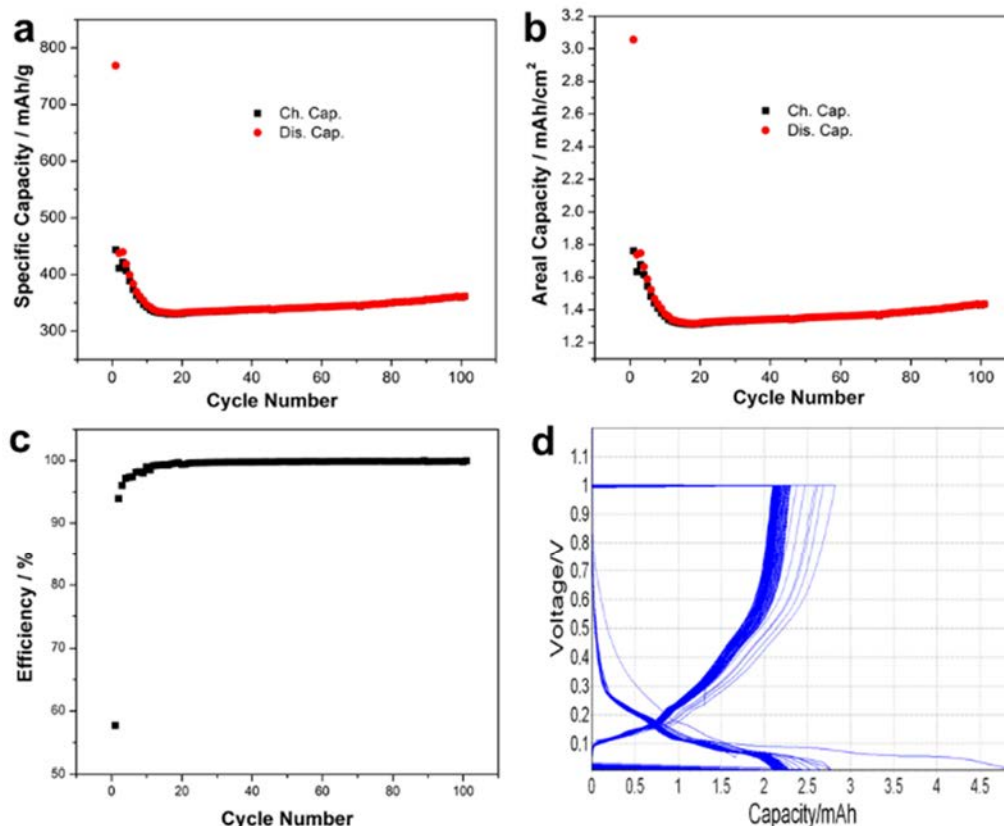


Figure IV-232: Cycling performance of Si-graphite composite between 1 V and 0.01 V. The calculated theoretical capacity is 600 mAh/g with a coating thickness of 80  $\mu\text{m}$

As shown in Figure IV-232, charge-discharge cycling performed of Si/graphite anode with Li insertion theoretical capacity of 600 mAh/g showed stable performance for more than 100 cycles. At a current density of 0.1C, the reversible Li extraction specific capacity is in the range of 320 to 450 mAh/g. The corresponding

areal capacity can reach between 1.3 and 1.8 mAh/cm<sup>2</sup>. The initial CE is around 58% and charge-discharge takes place around 0.5 and 0.4V.

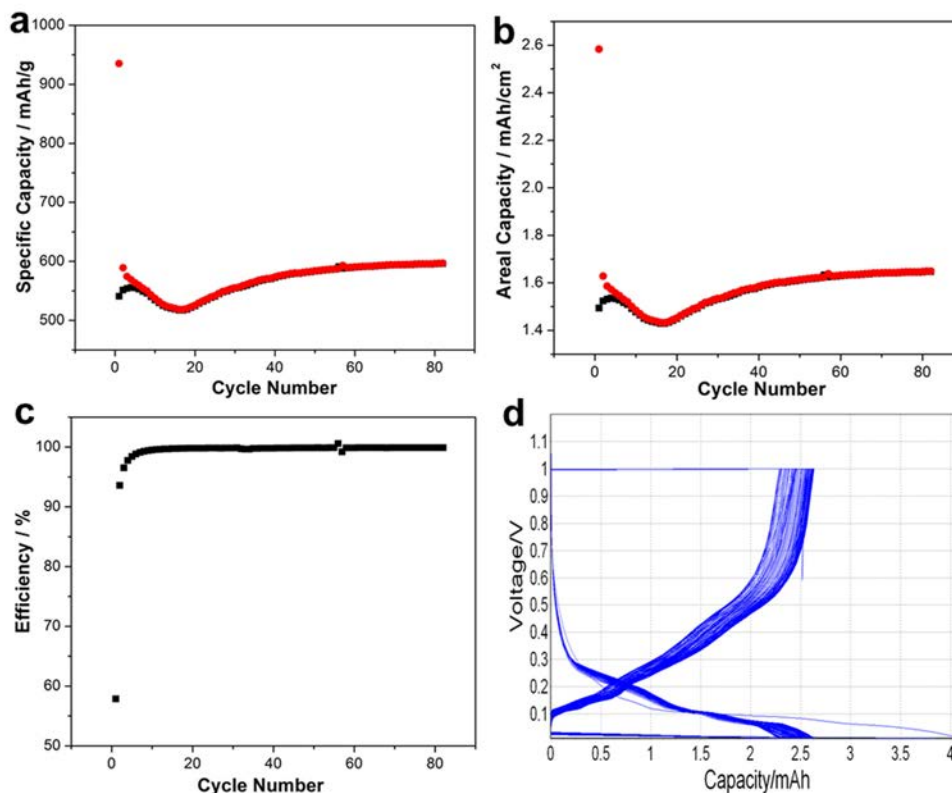


Figure IV-233: Cycling performance of Si-graphite composite between 1 V and 0.01 V. The calculated theoretical capacity is 800 mAh/g with a coating thickness of 60  $\mu\text{m}$

To optimize the energy density, the ratio of Si was increased to possess a theoretical capacity of 800 mAh/g. The thickness of the electrode was controlled to 60  $\mu\text{m}$ . Figure IV-233 shows the galvanostatic measurements for this composite at 0.1 C. As displayed in Figure IV-233a, over the whole range of 80 cycles, the composite shows 500 to 600 mAh/g capacities, which is higher than the composite with less Si. However, the areal capacity is similar, which is ascribed to a relatively low mass loading. Hence, a higher loading performance is presented in Figure IV-234 with the same Si-graphite ratio to reach higher areal capacity. As expected, the areal loading in Figure IV-234 b increased to around 2.1 mAh/cm<sup>2</sup> when the coating thickness was increased to 80  $\mu\text{m}$ . The initial CE for these two composites is both around 55%. Afterwards, the CE increases rapidly to more than 99.9% as shown in Figure IV-233c and Figure IV-234c.

To reach a higher energy density, a composite anode with a higher Si content and a lower loading is fabricated. Within 100 cycles, the composite anode approaches an areal capacity of around 3.5 mAh/cm<sup>2</sup> at a rate of 0.1. (Figure IV-235 b) Although the coulombic efficiency slightly increases to more than 60%, it is still not adequate to fabricate a full cell. The non-ideal coulombic efficiencies likely result from repetitive SEI cracking and regeneration during cycling caused by huge volumetric changes in the Si.

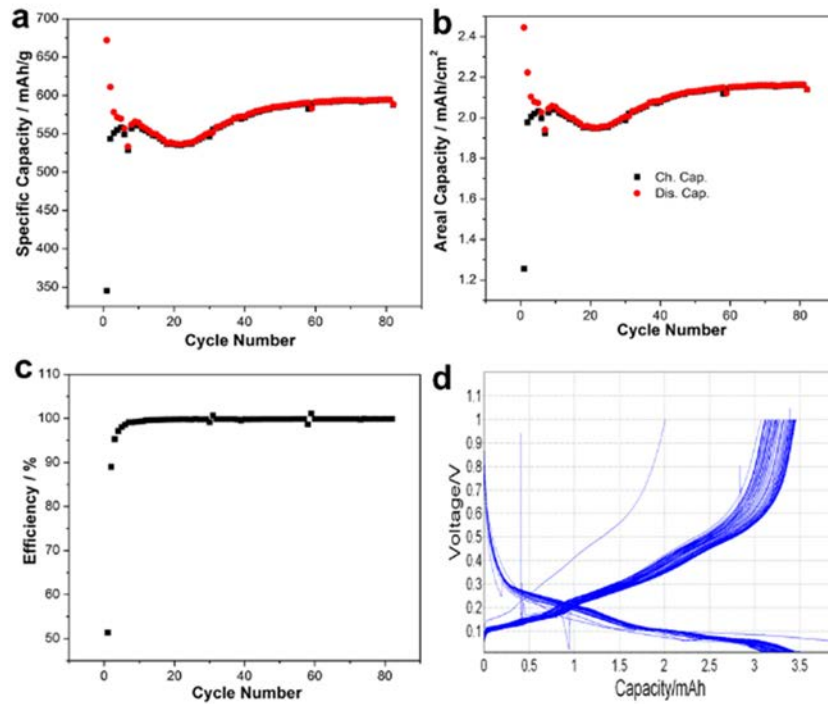


Figure IV-234: Cycling performance of Si-graphite composite between 1 V and 0.01 V. The calculated theoretical capacity is 800 mAh/g with a coating thickness of 80 μm

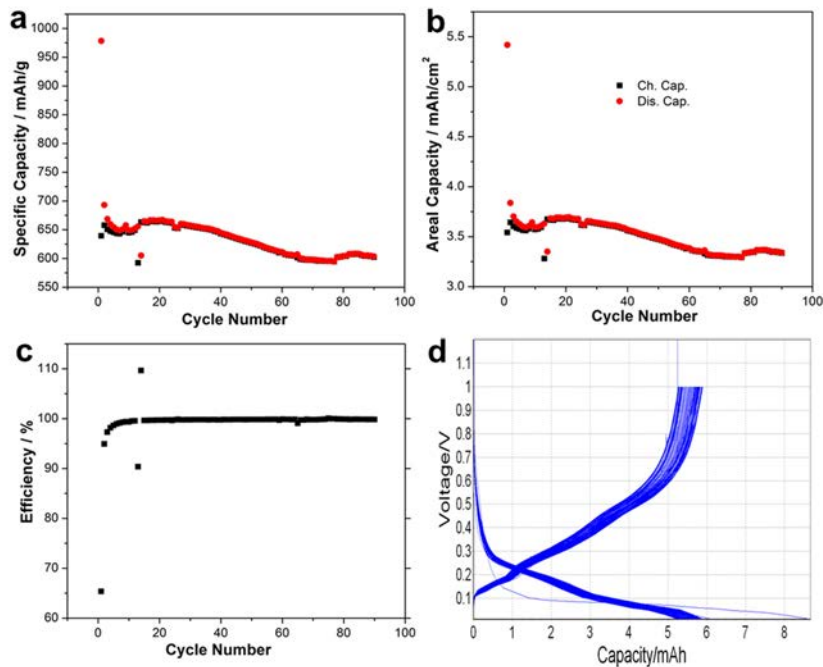


Figure IV-235: Cycling performance of Si-graphite composite between 1 V and 0.01 V. The calculated theoretical capacity is 1000 mAh/g with a coating thickness of 30 μm

Considering all of the above, the study showed that excellent cycle performance can be achieved through the optimization of the ratio between Si and graphite and the electrode thickness modification. The performance makes the optimized Si-graphite composite a good candidate for lithium-ion batteries. However, the low CE issue should be addressed before the full cell test. Hence, a series of full cells with SLMP modified Si-graphite composite anode will be assembled in pouch cells with improved initial coulombic efficiencies.

## 8. Application of SLMP in NMC/Si-C full pouch cell

Based on the Si/graphite half cell investigation, the Si-C ABR 1000 anode material is adopted to integrate with NMC to test in full pouch cell. The cell built up information is specified in Table IV-36. The image of SLMP coating on anode electrode is shown in Figure IV-236.

**Table IV-36: Full Pouch Cell Bultup Information**

	Mass loading (mg/cm <sup>2</sup> )	Theoretical capacity (mAh/g)
NMC	30.6	150
Si-C ABR 1000	8.8	1000



Figure IV-236: SLMP coating on 12 cm<sup>2</sup> pouch cell with the optimized disperse agent, i.e.m 0.5 wt% SBR and 0.5 wt% PST in xylene solution

The first cycle coulombic efficiency of Si-graphite composite half cell is 65.3% without SLMP. The irreversible capacity for the first cycle is 338.9 mAh/g, equals to 35.9 mAh based on the loading in Table IV-36. Hence, the calculated weight of SLMP is 12 mg. The composite anode after 12 mg SLMP coating is shown in Figure IV-237.

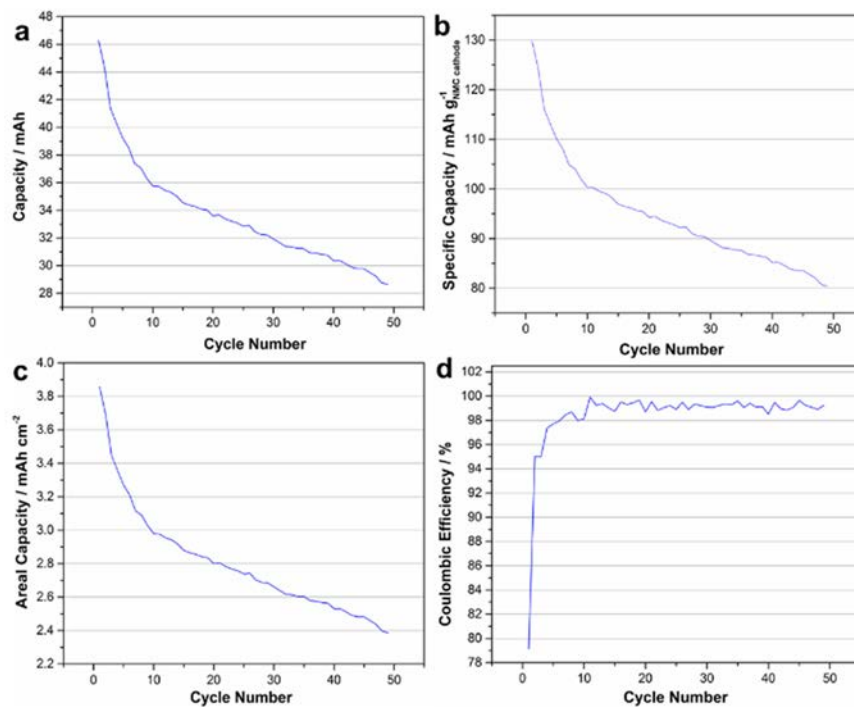


Figure IV-237: Cycle performance of the NMC and Si-C ABR-1000 pouch full cell in 1.2 M LiPF<sub>6</sub> in EC/DEC (30% FEC) electrolyte

The cycle performance is shown in Figure IV-238. The current of the first two cycles are C/20 then C/10 for the later cycles. The first cycle charge capacity could reach ca. 130 mAh/gNMC and the capacity decreased 80 mAh/gNMC after 50 cycles. The first cycle coulombic efficiency of the full pouch cell with SLMP is ca. 79%,

which is around 14% higher than the half cell without SLMP. The capacity voltage profiles of the pouch cell is shown in Figure IV-238. Through the observation of the first charge curve, the open circle voltage is around 3.45 V, which is higher than the cells without SLMP due to the prelithiation of SLMP into Si-C composite anode.

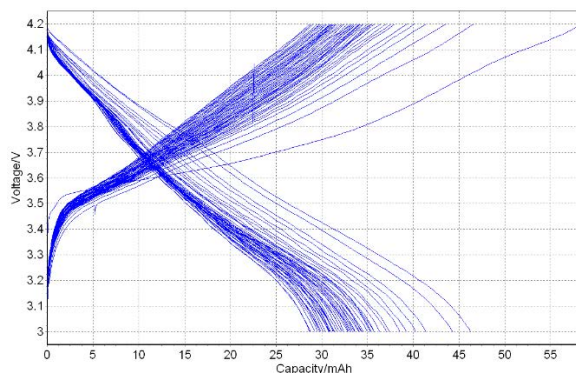


Figure IV-238: Voltage-capacity profiles of the NMC and Si-C ABR-1000 pouch full cell in 1.2 M LiPF<sub>6</sub> in EC/DEC (30% FEC) electrolyte

Although the coulombic efficiency was improved from 65.3% to 79%, there is still potential for it to be increased to an even higher value through more additive of SLMP. The optimization of the application of SLMP in NMC/Si-C ABR1000 full pouch cell will be further investigated.

## 9. Scale up of NMC/Si-C full pouch cell

The CE and cycle stability of SLMP prelithiated Si/graphite anode were certified through coin cells and single layer punch cells. Based on that, 80 pieces of double coated Si/graphite anode were prelithiated using SLMP to scale up its application. The SLMP powder was dispersed on the Si/graphite electrode (Size: 4.4 cm x 5.6 cm) uniformly in Ar filled glove box. Afterwards, the dispersed electrodes were packed and vacuum sealed in Laminated Crystal Clear Bags (Size: 4 3/4" x 6 1/8", SKU: LB4X6WNF) separately. Then the sealed bags, SLMP prelithiated electrodes inside, were calendared to activate the lithium powders.

The single side mass loading for the Si/graphite is 6.5 mg/cm<sup>2</sup>. The first lithiation/delithiation capacity is 1300 and 850 mAh/g, respectively. Accordingly, the prelithiation capacity is calculated to be 450 mAh/g. Considering the loading of 6.5 mg/cm<sup>2</sup>, the prelithiated SLMP amount is calculated to be 0.76 mg/cm<sup>2</sup>. Hence, the weight of prelithiated SLMP is 18.7 mg per single side.

## Final cell

### 1. Cell design

The cell design for Lithiated Si/C-Graphite / Ni Rich NCM Pouch Cell was developed. Since silicon has a very high irreversible capacity, pre-lithiation is necessary to achieve high energy density of pouch cells. We had three types of cells fabricated in EC Power. Type 1 (Cells #1-18) uses Si anode and NCM523 cathode. Type 2 (UT-1 and UT-2) uses Si anode and Ni rich NCM cathode made by UT Austin. Type 3 (LiSi series) uses lithium powder coated Si anode and NCM523 cathode.

### 2. Cell fabrication

EC power fabricated 3 types of cells. Type 1 (Cells #1-18) uses Si anode and NCM523 cathode. Type 2 (UT-1 and UT-2) uses Si anode and Ni rich NCM cathode made by UT Austin. Type 3 (LiSi series) uses lithium powder coated Si anode and NCM523 cathode.

Totally, 24 cells were fabricated. Table IV-37 lists the initial performance of these cells. Because anode has ~ 1.8 Ah irreversible capacity, all the Si/NCM523 and Si/Ni rich cells shows low capacity. Li coating can increase cell capacity a lot, but Li powder coating increase electrode thickness a lot. The weight of pouch cell using Li coated Si anode increases ~3 g and the cell thickness increases from 6.2 mm to 7.2 mm.

The specific energy of LiSi series cells can reach 190 Wh/kg. The specific energy of Si-Graphite / NCM523 cells are about 120 Wh/kg. Ni Rich NCM made by UT-Austin shows higher capacity than commercial NCM523. But particle size of UT-Austin NCM is not uniform. Roll to roll electrode coating using this material is very difficult.

**Table IV-37: Initial Performance of ABR Cells\***

Cell No.	HFR after filling, mΩ	1 <sup>st</sup> charge capacity @ current= 0.22 A, Ah	1 <sup>st</sup> discharge capacity @ current= 0.22 A, Ah	2 <sup>nd</sup> charge capacity @ current= 0.16 A, Ah	2 <sup>nd</sup> discharge capacity @ current= 0.16 A, Ah	Pouch cell weight, g	Pouch cell thickness, mm
1	64.53	2.946	1.247	1.439	1.328	40.83	6.2
2	57.23	2.877	1.220	1.392	1.287	41.17	
3	52.35	2.917	1.200	1.37	1.306	41.16	
4	54.73	2.835	1.189	1.921	1.19	40.29	
5	56.87	2.837	1.129	1.254	1.358	41.32	
6	62.21	2.798	1.180	1.384	1.291	40.65	
7	68.34	2.914	1.194	1.32	1.257	39.83	
8	60.33	2.926	1.233	1.454	1.365	40.81	
9	60.03	2.944	1.264	1.446	1.369	41.16	
10	60.48	2.912	1.304	1.512	1.429	40.72	
11	57.03	2.921	1.214	2.851	1.233	41.3	
12	66.38	2.825	1.247	1.465	1.384	40.68	
13	53.51	2.844	1.165	1.399	1.267	40.83	
14	47.98	2.913	1.265	1.418	1.278	41.53	
15	57.89	2.937	1.245	1.443	1.317	41.11	
16	63.57	2.959	1.239	1.403	1.278	41.18	
17	55.39	2.864	1.231	1.418	1.327	40.5	
18	51.95	2.884	1.235	1.427	1.31	40.83	
UT-1	42.77	3.231	1.388	1.929	1.447	41.13	6.3
UT-2	42.77	3.310	1.520	1.724	1.543	41.23	
LiSi-1	71.89	1.800	1.086	2.34	2.221	43.4	7.2
LiSi-2	70.80	2.819	2.079	2.239	2.294	43.81	
LiSi-3	64.10	2.696	2.033	2.197	2.236	44.06	
LiSi-4	59.26	2.820	1.870	2.3	2.321	44.01	

\* Charge/Discharge window: 4.2V/2.7V.



Figure IV-239: Photos of the final delivered full cell

Figure IV-239 shows the stacking package, top view and side view of the full cell, just before top sealing and the front view of pouch cells produced by EC Power. The sealing is perfect and the surface is very smooth. The cell is very hard. 14 pieces of double-side coating anode and 15 pieces of cathode (13 double side coating and 2 single-side coating cathode) was assembled. Nickel tab was welded with copper current collector. Aluminum tab was welded with aluminum current collector. The cell thickness is very uniform.

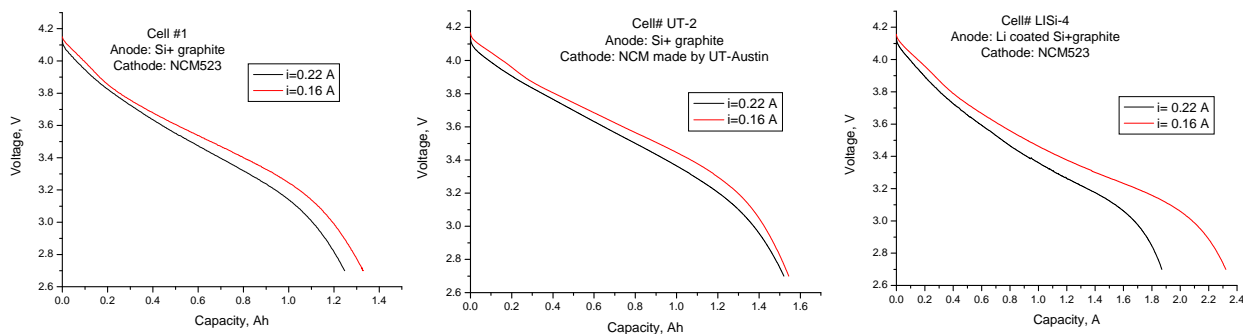


Figure IV-240: Voltage profile of the first cycles of cell #1, cell# UT-2 and cell# LiSi-4 at discharged states

### 3. Cycle performance

Figure IV-240a shows the capacity of cell #1 at different discharge currents. The cell capacity is 1.328 Ah at a discharge current of 0.16 A. Figure IV-240b shows the capacity of cell# UT-2. Nickel rich NCM made by UT-Austin is used as the cathode active material. The cell capacity using UT-Austin NCM is higher than that using commercial NCM523. Figure IV-240c shows the capacity of cell# LiSi-4. Because there was some Li power peeled off, the anode has ~ 0.8 Ah irreversible capacity (designed irreversible capacity: 0.4 Ah), the cell capacity still a little lower than designed value.

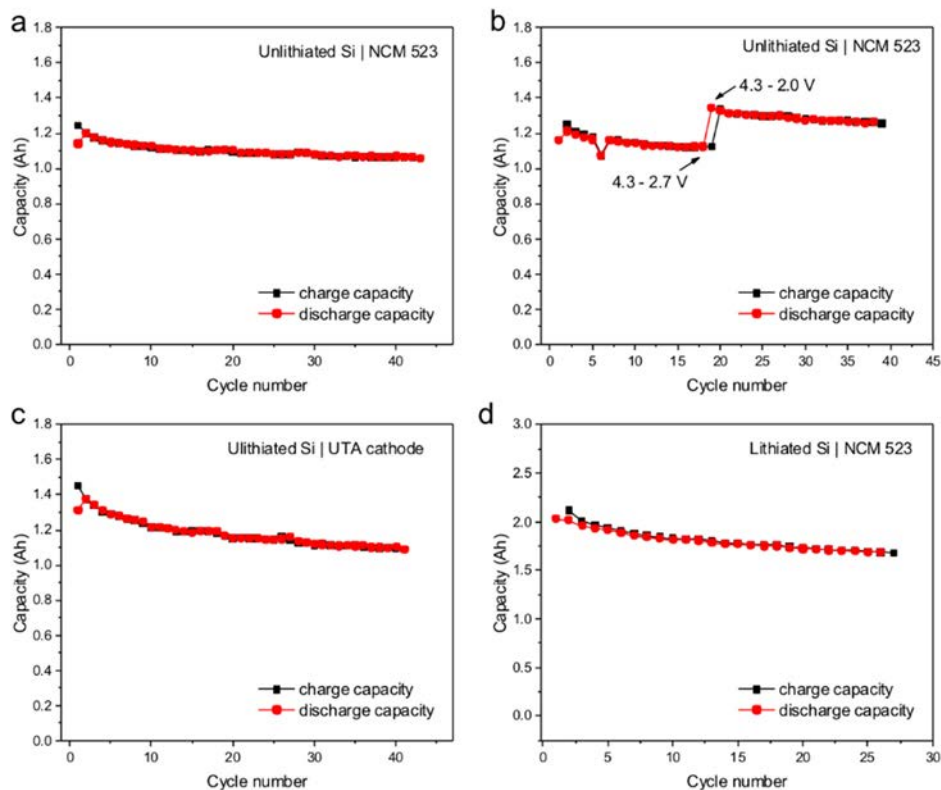


Figure IV-241: Cycling performances of three types of full cell systems: a,b) Unlithiated Si | NCM523 with two kinds of voltage window, c) unlithiated Si | UTA cathode and d) Lithiated Si | NCM523

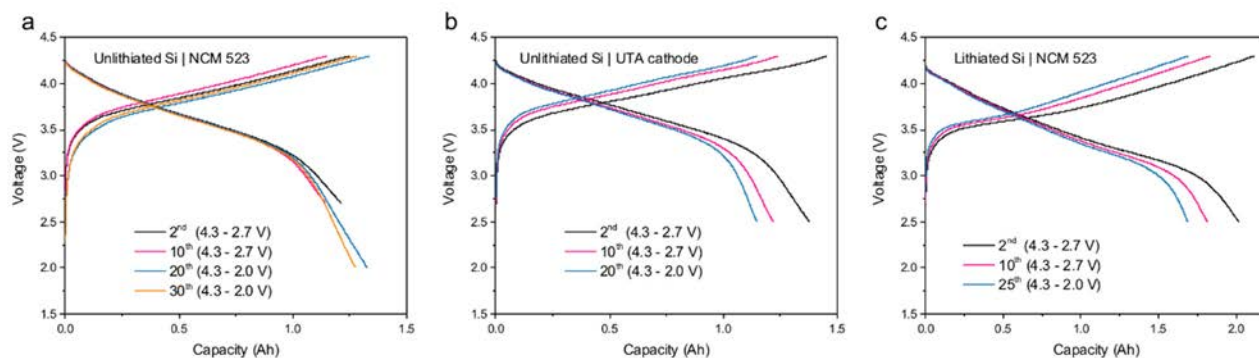


Figure IV-242: Voltage profiles of three types of full cell systems: a) Unlithiated Si | NCM523, b) unlithiated Si | UTA cathode and c) Lithiated Si | NCM523

As shown in Figure IV-241 and Figure IV-242, unlithiated Si | NCM523 cell and unlithiated Si | UTA cathode show the capacity of 1.3 Ah and 1.5 Ah. The lithiated cell presents 2.2 Ah due to the prelithiation. All cells exhibit good cyclability under 4.3- 2.7 V voltage window and 4.3 – 2.0V voltage window.

## Conclusions

High-loading and high quality PSU Si anode has been optimized and fabricated. The electrochemical performance has been utilized. The PSU Si-graphite anode exhibits the mass loading of 5.8 mg/cm<sup>2</sup>, charge capacity of 850 mAh/ g and good cycling performance. This optimized electrode has been used for full-cell fabrication.

TOF-SIMS and HAADF-STEM have been used to characterize the surface electrochemical degradation of Ni-rich LiNi<sub>0.7</sub>Co<sub>0.15</sub>Mn<sub>0.15</sub>O<sub>2</sub> cathode material during cycling. Various degradation products originating from (i)

parasitic electrolyte oxidative decomposition, (ii) active mass dissolution, and (iii) surface irreversible structural reconstruction have been demonstrated. The performance enhancement of Ni-rich materials can be achieved by diverse strategies. Higher Mn content and a small amount of Al doping can improve the electrochemical performance by suppressing interfacial side reactions with electrolytes, thus greatly benefiting the cyclability of the samples. Also, surface coatings of Li-rich materials and  $\text{AlF}_3$  are able to improve the performance stability of Ni-rich cathodes. One kilogram of optimized concentration-gradient  $\text{LiNi}_{0.76}\text{Co}_{0.10}\text{Mn}_{0.14}\text{O}_2$  (CG) with careful control of composition, morphology and electrochemical performance was delivered to our collaborators. The sample achieved an initial specific capacity close to  $190 \text{ mA h g}^{-1}$  at C/10 rate and  $180 \text{ mA h g}^{-1}$  at C/3 rate as well as good cyclability in pouch full cells with a 4.4 V upper cut-off voltage at room temperature.

Electrolyte additive with Si-N skeleton forms a less resistant SEI on the surface of silicon anode (from PSU) as evidenced by the evolution of impedance at various lithiation/de-lithiation stages and the cycling data. A new fluorinated additive was investigated to stabilize the interphase of the NCM523/electrolyte. New fluorinated linear cosolvents were designed and synthesized for a high cut-off voltage NCM523-Graphite system. New fluorinated cyclic carbonate shows good anodic Linear sweep voltammetry has been used as an evaluation tool for the voltage stability of the fluorinated cyclic carbonate. Of the cyclic carbonates screened, DFEC is the most stable solvent and the HFEEC is least so due to involving the ether bond into the molecular structure. The conductivity test results show a long chain fluorinated substituent may lead to a high resistance and viscosity.

The prelithiation results demonstrate a solution processing method to achieve large area, uniform SLMP coating on well-made anode surface for the prelithiation of lithium-ion batteries. By well optimizing the composition of the binder solution, the SLMP can sustain uniform distribution in the slurry to carry out the coating process. Additionally, with the addition of polymer binders, the SLMP can be fixed on the anode surface for easy transportation before activation. Considering the sustainability and coating performance, the SLMP adhesion and the ease of activation, the best composition of binders and solvent combination is 0.5% PS with 0.5% SBR binder in xylene solution for the processing method, and the super coating effect can be obtained. The prelithiation effect with this method is applied both in graphite half cells, graphite/NMC full cells, SiO half cells, SiO/NMC full cells, Si-Graphite half cells and Si-Graphite/NMC full cells with improvements in cycle performance and higher first cycle coulombic efficiency than their corresponding cells without SLMP prelithiation.

As to the full cell fabrication and test, full pouch cells with high capacity of 2.2 Ah and 1.2 Ah have been fabricated and delivered. The cells show great uniformity and good cycling performance. The prelithiation method effectively compensate the loss in the first cycle. The cell with high energy density and long-cycle life has been achieved.

## Products

## Presentations/Publications/Patents

### Publications

1. J.-Y. Liao and A. Manthiram, "Surface-modified Concentration-gradient Ni-rich Layered Oxide Cathodes for High-energy Lithium-ion Batteries," *Journal of Power Sources* **282**, 429-436 (2015).
2. J. Zheng, W. H. Kan, and A. Manthiram, "Role of Mn Content on the Electrochemical Properties of Nickel-rich Layered  $\text{LiNi}_{0.8-x}\text{Co}_{0.1}\text{Mn}_{0.1+x}\text{O}_2$  ( $0.1 \leq x \leq 0.18$ ) Cathodes for Lithium-ion Batteries," *ACS Applied Materials & Interfaces* **7**, 6926-6934 (2015).
3. A. Manthiram, J. C. Knight, S.-T. Myung, S.-M. Oh, and Y.-K. Sun, "Nickel-rich and Lithium-rich Layered Oxide Cathodes: Progress and Perspectives," *Advanced Energy Materials* **1501010**, 1-23 (2015).
4. J. Zheng, P. Yan, W. H. Kan, C. Wang, and A. Manthiram, "A Spinel-integrated P2-type Layered Composite: High-rate Cathode for Sodium-ion Batteries," *Journal of the Electrochemical Society* **163**, A584-A591 (2016).

5. P. Oh, B. Song, W. Li, and A. Manthiram, "Overcoming the Chemical Instability on Exposure to Air of Ni-rich Layered Oxide Cathodes by Coating with Spinel  $\text{LiMn}_{1.9}\text{Al}_{0.1}\text{O}_4$ ," *Journal of Materials Chemistry A* **4**, 5839-5841 (2016).
6. P. Oh, S.-M. Oh, W. Li, S. Myeong, J. Cho, and A. Manthiram, "High-performance Heterostructured Cathodes for Lithium-ion Batteries with a Ni-rich Layered Oxide Core and a Li-rich Layered Oxide Shell," *Advanced Science* **1600184**, 1-8 (2016).
7. B. Song, W. Li, P. Yan, S.-M. Oh, C.-M. Wang, and A. Manthiram, "A Facile Cathode Design Combining Ni-rich Layered Oxides with Li-rich Layered Oxides for Lithium-ion Batteries," *Journal of Power Sources* **325**, 620-629 (2016).
8. J.-Y. Liao, S.-M. Oh, and A. Manthiram, "A Core/double-shell Type Gradient Ni-rich  $\text{LiNi}_{0.76}\text{Co}_{0.10}\text{Mn}_{0.14}\text{O}_2$  with High Capacity and Long Cycle Life for Lithium-ion Batteries," *ACS Applied Materials and Interfaces* **8**, 24543-24549 (2016).
9. W. Li, A. Dolocan, P. Oh, H. Celio, S. Park, J. Cho, and A. Manthiram, "Revealing the Interphases and Their Implications on High-energy-density Cathode Materials in Lithium-ion Batteries," *Nature Communications* (submitted).
10. Xiaodong Yan, Zhihui Wang, Min He, Zhaohui Hou, Ting Xia, Gao Liu, and Xiaobo Chen.  $\text{TiO}_2$  nanomaterials as anode materials for lithium-ion rechargeable batteries. *Energy Technology*, **2015**, 3, 801-814.
11. Hui Zhao, Zhe Jia(**co-first author**), Wen Yuan, Heyi Hu, Yanbao Fu, Gregory Baker, and Gao Liu. Fumed silica based single-ion nanocomposite electrolyte for lithium batteries. *ACS Applied Materials & Interfaces*, **2015**, 7, 19335-19341.
12. Kehua Dai, Zhihui Wang(**co-first author**), Guo Ai, Hui Zhao, Wen Yuan, Xiangyun Song, Vincent Battaglia, Chengdong Sun, Kai Wu, and Gao Liu. The transformation of graphite electrode materials in lithium-ion batteries after cycling. *J. Power Sources*, **2015**, 298, 349-354.
13. Hui Zhao, Fadi Asfour(**co-first author**), Yanbao Fu, Zhe Jia, Wen Yuan, Ying Bai, Min Ling, Heyi Hu, Gregory Baker, and Gao Liu. Plasticized polymer composite single-ion conductors for lithium batteries. *ACS Applied Materials & Interfaces*, **2015**, 7, 19494-19499.
14. Ying Bai, Xingzhen Zhou, Zhe Jia, Chuan Wu, Liwei Yang, Mizi Chen, Hui Zhao, Feng Wu, and Gao Liu. Understanding the combined effects of microcrystal growth and band gap reduction of  $\text{Fe}_{(1-x)}\text{TixF}_3$  nanocomposites as cathode materials for lithium-ion batteries. *Nano Energy*, **2015**, 17, 140-151.
15. Zhe Jia, Hui Zhao, Ying Bai, Ting Zhang, Amanda Siemens, Andrew Minor, and Gao Liu. Solvent processed conductive polymer with single-walled carbon nanotube composites. *Journal of Materials Research*, **2015**, Accepted.
16. Hui Zhao, Wei Yang, Ruimin Qiao, Chenhui Zhu, Ziyang Zheng, Min Ling, Zhe Jia, Ying Bai, Yanbao Fu, Jinglei Lei, Xiangyun Song, Vincent Battaglia, Wanli Yang, Phillip Messersmith, and Gao Liu. Conductive polymer binder for high-tap-density nano-silicon material for lithium-ion battery negative electrode application. *Nano Letters*. **2015**, 15, 7927-7932.
17. Guo Ai, Zhihui Wang, Hui Zhao, Wenfeng Mao, Yanbao Fu, Vincent Battaglia, Sergey Lopatin, and Gao Liu. Scalable process for application of stabilized lithium metal powder in Lithium-ion batteries. *Journal of Power Sources* 309 (2016) 33-41.
18. He, Meinan, et al. "Mechanistic Insight in the Function of Phosphite Additives for Protection of  $\text{LiNi}_{0.5}\text{Co}_{0.2}\text{Mn}_{0.3}\text{O}_2$  Cathode in High Voltage Lithium-ion Cells." *ACS applied materials & interfaces* 8.18 (2016): 11450-11458.
19. He, Meinan, et al. "Fluorinated Electrolytes for 5-V Lithium-ion Chemistry: Probing Voltage Stability of Electrolytes with Electrochemical Floating Test." *Journal of the Electrochemical Society* 162.9 (2015): A1725-A1729.

## Presentations

1. A. Manthiram, "Materials for Next-Generation Rechargeable Batteries," *5<sup>th</sup> Association of East Asian Research Universities (AEARU) Advanced Materials Workshop*, Hong Kong, June 4, 2014 (invited).

2. A. Manthiram, "Electrochemical Energy Storage: Challenges and Prospects," *International Conference on Electrochemical Science & Technology (ICONEST-2014)*, Bangalore, India, August 7 – 9, 2014 (invited plenary talk).
3. A. Manthiram, "From Insertion-compound Electrodes to Conversion-reaction Electrodes for Energy Storage," Battery Division Research Award Presentation, *226<sup>th</sup> Electrochemical Society Meeting*, Cancun, Mexico, October 5 – 10, 2014 (invited).
4. A. Manthiram, "Next Generation Rechargeable Battery Chemistries," *XII International Congress of the Mexican Hydrogen Society*, Cancun, Mexico, September 30 – October 4, 2014 (invited keynote talk).
5. A. Manthiram, "Next Generation Rechargeable Battery Chemistries," 2014 Global Innovation Festival, Daegu Gyeongbuk Institute of Science and Technology, Daegu, South Korea, November 20 – 21, 2014 (invited).
6. A. Manthiram, "Rechargeable Batteries: Transitioning from Insertion-compound Electrodes to Conversion-reaction Electrodes," *International Symposium on Energy Conversion and Storage*, Beijing, China, May 31 – June 1, 2015 (invited).
7. A. Manthiram, "Prospects and Challenges of Nickel-rich Layered Oxide Cathodes," *2015 Annual Merit Review Meeting of the Office of Vehicle Technologies*, U.S. Department of Energy, Washington, D.C, June 8 – 12, 2015 (invited).
8. A. Manthiram, "Transitioning from Insertion-reaction Electrodes to Conversion-reaction Electrodes for Energy Storage," Lawrence Berkeley National Laboratory, Berkeley, CA, July 13, 2015 (invited).
9. A. Manthiram, "Structural and Electronic Stabilities of Oxide Cathodes for Lithium-ion Batteries," *5<sup>th</sup> Polish Forum on Smart Energy Conversion and Storage*, Bialka Tatrzenska, Poland, September 22 – 25, 2015 (invited).
10. A. Manthiram, "Electrical Energy Storage: Next Generation Battery Chemistries," *2015 International Conference on Innovative Electrochemical Energy Materials and Technologies (EEMT2015)*, Nanning, China, November 8 – 11, 2015 (invited plenary talk).
11. A. Manthiram, "Electrical Energy Storage: Materials Challenges and Prospects," *2015 Fall Meeting of the Materials Research Society*, Boston, MA, November 29 – December 4, 2015 (invited talk at Symposium X: Frontiers of Materials Research).
12. A. Manthiram, "Tutorial on Electrode Materials and Electrolytes for Next Generation Rechargeable Batteries," *2016 Spring Meeting of the Materials Research Society*, Phoenix, AZ, March 28, 2016.
13. A. Manthiram, Wangda Li, Jin-yun Liao, Jianming Zheng, "Advanced Surface Characterization and Surface-controlled Compositional Design of Nickel-rich Layered Oxide Cathodes for Lithium-ion Batteries," *2016 Spring Meeting of the Materials Research Society*, Phoenix, AZ, March 28 – April 1, 2016 (invited).
14. A. Manthiram, "Next Generation Battery Chemistries: Materials Challenges and Prospects," *Materials Challenges in Alternative and Renewable Energy (MCARE) Meeting*, Clearwater, FL, April 17 – 21, 2016 (invited plenary talk).
15. D. Wang and A. Manthiram, "High Energy, Long Cycle Life Lithium-ion Batteries for Vehicle Applications," *2016 Annual Merit Review Meeting of the Office of Vehicle Technologies*, U.S. Department of Energy, Washington, D.C, June 6 – 10, 2016.
16. A. Manthiram, "Materials for Electrochemical Energy Conversion and Storage Technologies," Indian Institute of Technology Madras, Chennai, India, August 16, 2016 (invited).
17. A. Manthiram, "Electrical Energy Storage: Next Generation Battery Chemistries," *4<sup>th</sup> International Workshop on Nanotechnology, Renewable Energy, and Sustainability*, Xi'an Jiaotong University, Xi'an, China, September 19, 2016 (invited keynote talk).
18. N, N-Diethyltrimethylsilylamine (DETMSA) As Electrolyte Additive for Si Based High Energy Lithium-Ion Batteries. Meinan He, Libo Hu, Yan Wang, Kang Xu and Zhengcheng Zhang. 227<sup>th</sup> ECS meeting, Chicago, May 24-28.
19. Donghai Wang, "Development of Stable Intermetallic Alloy Anodes for Lithium-ion/Na-ion Batteries," ACS National Spring Meeting, San Diego, March, 2016.
20. Donghai Wang, "Development of Functional Nanocomposite Materials for Energy Storage Applications" 11<sup>th</sup> Sino-US Nano Forum, Nanjing, China, 18-20 June, 2016.

## Patents

1. Scalable process for application of Stabilized Lithium Metal Powder in Lithium-ion Batteries, patent filed by Applied Materials Inc. on 2015.
2. Wang, D. H., Song, J., Electroactive Polymer Binders with In situ Formation of Artificial Solid-Electrolyte-Interphase Layer for Si Anodes, U.S. Provisional Application (61/934,171), 2014

## References

1. J.B. Goodenough, Y. Kim, *Chemistry of Materials*, 22 (2010) 587-603.
2. F.T. Wagner, B. Lakshmanan, M.F. Mathias, *The Journal of Physical Chemistry Letters*, 1 (2010) 2204-2219.
3. J.M. Tarascon, M. Armand, *Nature*, 414 (2001) 359-367.
4. Y. Dai, L. Cai, R.E. White, *Journal of The Electrochemical Society*, 160 (2013) A182-A190.
5. Y. Dai, L. Cai, R.E. White, *Journal of The Electrochemical Society*, 161 (2014) E3348-E3356.
6. Y. Dai, L. Cai, R.E. White, *Journal of Power Sources*, 247 (2014) 365-376.
7. W.-f. Mao, Y. Ma, S.-k. Liu, Z.-y. Tang, Y.-b. Fu, *Electrochimica Acta*, 147 (2014) 498-505.
8. W.-f. Mao, J. Yan, H. Xie, Z.-y. Tang, Q. Xu, *Journal of Power Sources*, 237 (2013) 167-171.
9. G. Ai, Y. Dai, Y. Ye, W. Mao, Z. Wang, H. Zhao, Y. Chen, J. Zhu, Y. Fu, V. Battaglia, J. Guo, V. Srinivasan, G. Liu, *Nano Energy*, 16 (2015) 28-37.
10. W.-f. Mao, Y.-b. Fu, H. Zhao, G. Ai, Y.-l. Dai, D. Meng, X.-h. Zhang, D. Qu, G. Liu, V.S. Battaglia, Z.-y. Tang, *ACS Applied Materials & Interfaces*, 7 (2015) 12057-12066.
11. L. Ji, Z. Lin, M. Alcoutlabi, X. Zhang, *Energy & Environmental Science*, 4 (2011) 2682-2699.
12. X.-L. Wu, Y.-G. Guo, L.-J. Wan, *Chemistry – An Asian Journal*, 8 (2013) 1948-1958.
13. U. Kasavajjula, C. Wang, A.J. Appleby, *Journal of Power Sources*, 163 (2007) 1003-1039.
14. Y. Bai, Y. Tang, Z. Wang, Z. Jia, F. Wu, C. Wu, G. Liu, *Solid State Ionics*, 272 (2015) 24-29.
15. G. Liu, S. Xun, N. Vukmirovic, X. Song, P. Olalde-Velasco, H. Zheng, V.S. Battaglia, L. Wang, W. Yang, *Advanced Materials*, 23 (2011) 4679-4683.
16. S.-J. Park, H. Zhao, G. Ai, C. Wang, X. Song, N. Yuca, V.S. Battaglia, W. Yang, G. Liu, *Journal of the American Chemical Society*, 137 (2015) 2565-2571.
17. H. Zhao, Z. Wang, P. Lu, M. Jiang, F. Shi, X. Song, Z. Zheng, X. Zhou, Y. Fu, G. Abdelbast, X. Xiao, Z. Liu, V.S. Battaglia, K. Zaghbi, G. Liu, *Nano Letters*, 14 (2014) 6704-6710.
18. D.D. Vaughn, R.E. Schaak, *Chemical Society Reviews*, 42 (2013) 2861-2879.
19. M.W. Forney, M.J. Ganter, J.W. Staub, R.D. Ridgley, B.J. Landi, *Nano Letters*, 13 (2013) 4158-4163.
20. V.A. Agubra, J.W. Fergus, *Journal of Power Sources*, 268 (2014) 153-162.
21. X. Su, Q. Wu, J. Li, X. Xiao, A. Lott, W. Lu, B.W. Sheldon, J. Wu, *Advanced Energy Materials*, 4 (2014) 1300882.
22. Y. Wang, H. Li, P. He, E. Hosono, H. Zhou, *Nanoscale*, 2 (2010) 1294-1305.
23. J. Christensen, J. Newman, *Journal of The Electrochemical Society*, 152 (2005) A818-A829.
24. D. Shanmukaraj, S. Grugeon, S. Laruelle, G. Douglade, J.M. Tarascon, M. Armand, *Electrochemistry Communications*, 12 (2010) 1344-1347.
25. A. Ito, D. Li, Y. Sato, M. Arai, M. Watanabe, M. Hatano, H. Horie, Y. Ohsawa, *Journal of Power Sources*, 195 (2010) 567-573.
26. C.R. Jarvis, M.J. Lain, Y. Gao, M. Yakovleva, *Journal of Power Sources*, 146 (2005) 331-334.
27. C.R. Jarvis, M.J. Lain, M.V. Yakovleva, Y. Gao, *Journal of Power Sources*, 162 (2006) 800-802.
28. B.B. Fitch, M. Yakovleva, Y. Li, I. Plitz, A. Skrzypczak, F. Badway, G.G. Amatucci, Y. Gao, *ECS Transactions*, 3 (2007) 15-22.
29. J.T. Vaughey, G. Liu, J.-G. Zhang, *MRS Bulletin*, 39 (2014) 429-435.
30. Y. Li, B. Fitch, *Electrochemistry Communications*, 13 (2011) 664-667.
31. H. Zhao, N. Yuca, Z. Zheng, Y. Fu, V.S. Battaglia, G. Abdelbast, K. Zaghbi, G. Liu, *ACS Applied Materials & Interfaces*, 7 (2015) 862-866.

32. Z. Wang, Y. Fu, Z. Zhang, S. Yuan, K. Amine, V. Battaglia, G. Liu, *Journal of Power Sources*, 260 (2014) 57-61.
33. X. Zhu, Y. Zhu, S. Murali, M.D. Stoller, R.S. Ruoff, *ACS Nano*, 5 (2011) 3333-3338.
34. D.W. Murphy, P.A. Christian, F.J. DiSalvo, J.N. Carides, J.V. Waszczak, *Journal of The Electrochemical Society*, 128 (1981) 2053-2060.
35. K.-W. Nam, S.-B. Ma, W.-S. Yoon, X.-Q. Yang, K.-B. Kim, *Electrochemistry Communications*, 11 (2009) 1166-1169.
36. W.J. Cao, J. Shih, J.P. Zheng, T. Doung, *Journal of Power Sources*, 257 (2014) 388-393.
37. L. Wang, Y. Fu, V.S. Battaglia, G. Liu, *RSC Advances*, 3 (2013) 15022–15027.
38. F. Cassel, D. Chua, M. Lane, M. Yakovleva, Y. Gao, G. Au, *ECS Transactions*, 11 (2008) 157-166.
39. F.J.V. Santos, C.A. Nieto de Castro, J.H. Dymond, N.K. Dalaouti, M.J. Assael, A. Nagashima, *Journal of Physical and Chemical Reference Data*, 35 (2006) 1-8.
40. S. Singh, B.P.S. Sethi, R.C. Katyal, V.K. Rattan, *Journal of Chemical & Engineering Data*, 50 (2005) 125-127.

## IV.D.6. High Energy High Power Battery Exceeding PHEV40 Requirements (TIAX LLC)

### Dr. Jane Rempel, Principal Investigator

TIAX LLC  
35 Hartwell Avenue  
Lexington, MA 02421  
Phone: 781-879-1238; Fax: 781-879-1202  
E-mail: [rempel.jane@tiaxllc.com](mailto:rempel.jane@tiaxllc.com)

### Dr. Kimberly Nuhfer, DOE Program Manager

National Energy Technology Laboratory  
3610 Collins Ferry Road  
Morgantown, WV 26507  
Phone: 304-285-6544  
E-mail: [kimberly.nuhfer@netl.doe.gov](mailto:kimberly.nuhfer@netl.doe.gov)

Start Date: October 2013  
End Date: March 2016

## Abstract

### Objectives

- Implement CAM-7<sup>®</sup> cathode material, Si-based anode chemistry in lithium-ion cells designed to achieve >200Wh/kg specific energy, >400Wh/L energy density, and >800W/kg and >1600W/L 10s pulse power targets under USABC PHEV battery testing procedures.
- Demonstrate that these lithium-ion cells have higher energy and power capability than CAM-7/graphite baseline cells, and deliver these cells to DOE for independent performance verification.
- Demonstrate that these lithium-ion cells have a cycle life and a calendar life that is projected to meet PHEV40 targets.

### Accomplishments

- Demonstrated CAM-7/Si-based blended anode cell chemistry in prototype 18650 cells that deliver 198Wh/kg total energy and >845W/kg down to 10% SOC (projected to have 220Wh/kg in state-of-the-art 18650 cell hardware and 250Wh/kg in 15Ah pouch cells).
- Showed that we will exceed the 800W/kg PHEV40 power target and meet the 200Wh/kg available energy target, when CAM-7/Si-based anode cell chemistry and electrode design is implemented in mass production 18650 cells. Easily exceeded volumetric energy and power targets even in prototype 18650 cells.
- Achieved 85% capacity retention after 1000 cycles in on-going cycle life testing of the CAM-7 cathode and Si-based blended anode in program demonstration 18650 cells.
- Demonstrated baseline CAM-7/Graphite chemistry in 18650 cells with 70% capacity retention after ~4000 cycles at room temperature. Validated baseline cell performance and life in independent testing by ANL (78% retention after 2400 cycles at 30°C).

### Future Achievements

This project has demonstrated high specific energy and long life of the CAM-7/Si-based lithium-ion battery chemistry, ideally suited for PHEV, EV, and consumer electronics applications. While the program has concluded, we are investigating further ways of optimizing and scaling this CAM-7/Si-based lithium-ion battery chemistry to accelerate its adoption and commercialization for electric vehicles.

## Technical Discussion

### Introduction

State-of-the-art PHEV battery systems are currently limited to only 50-80Wh/kg specific energy and 100-150Wh/l energy density (David Howell, Presentation at the 30th International Battery Seminar & Exhibit, March 2013). Even if the specific energy and energy density for the cells in these battery systems are approximately twice the battery-level values, these cells cannot meet the PHEV40 200Wh/kg specific energy target for cells. These limitations are due to the cells' utilization of low energy density LMO-based cathodes, or blends of LMO with higher capacity but lower power NCM cathode material. The energy density of PHEV cells is also limited by the graphite anodes they employ. In addition, for a given set of active materials, power delivery capability is also limited by the inactive components employed (e.g. separators), potentially resulting in cells with a large contribution from inactive components to the final cell weight, volume, and cost. In order to improve cell specific energy and power, a system-level approach is needed that combines novel high energy cathode and anode active materials in optimized electrode and cell designs to simultaneously achieve the high energy, power and life of the DOE's PHEV40 targets.

### Approach

Our overall approach to meet the energy and power targets was to combine cathodes based on TIAX's high-energy and high-power cathode material, CAM-7, with silicon-based anodes in electrode designs optimized for PHEV40 application in cells using high-performance inactive components:

- **CAM-7® high energy, high power cathode material.** CAM-7 is a family of stabilized high-nickel-content cathode materials developed, patented, and recently licensed by TIAX that combines both high-energy and high-power capabilities. The CAM-7 version employed in baseline cells delivers over 210mAh/g at C/20 and 150mAh/g at 50C, with excellent cycle and calendar life. During this project, we selected and scaled-up a CAM-7.x grade with higher capacity for use in program demonstration cells (detailed below). With over a decade of research and development effort and direct sampling evaluations by major battery companies, CAM-7 is now in transition to commercial production, currently being scaled-up from ~30kg/week in a lab-scale facility to ~50 ton/year in our powder production plant located in Rowley, Massachusetts. CAM-7 cathode material was recently licensed to two leading battery materials manufacturers for scaled-up production.
- **Blended Si/Carbon anode.** During the program, we worked with multiple leading silicon anode materials developers on implementing their anode materials in blended electrodes formulated specifically for high energy and power delivery capability. We sourced anode active materials from those suppliers under a non-disclosure agreement (NDA), which were then engineered into electrodes in TIAX labs.
- **System approach to cell design.** Along with the selection of the anode and cathode active materials, we also selected inactive components, electrolytes, and electrode formulations to meet the energy and power targets while maintaining long life. TIAX has developed methodologies for high throughput testing of materials, electrode components, and electrode designs that are predictive of performance in scaled-up cells. Combining electrochemical data with engineering cell design models allowed us to rapidly assess the impact that design factors can have towards enabling high cell energy while delivering PHEV-scaled power levels, before implementing these changes in 18650 cells. Using these methods, we optimized electrode designs and integrated high performance inactive components and cell hardware to maximize cell power and energy delivery capability.

### Results

#### Baseline CAM-7/Graphite 18650 Cell Performance

Baseline 18650 cells containing CAM-7 cathode material and graphite-based anode were fabricated at TIAX in 2014 (soon after the program began) and delivered to Argonne National Laboratory (ANL) for independent evaluation. Several cells from this cell build were retained at TIAX for performance, cycle and calendar life

testing. (Performance of these baseline cells is summarized later in Table IV-39.) We have previously reported on extensive life testing of these cells in the 2015 Annual Progress Report, including full DOD and reduced DOD cycling at room temperature along with storage at 45°C. Briefly, in TIAX testing, the baseline 18650 cells with CAM-7/Graphite achieved 70% capacity retention after 4000 cycles at room temperature for 2.7 - 4.1V operation (Figure IV-243).

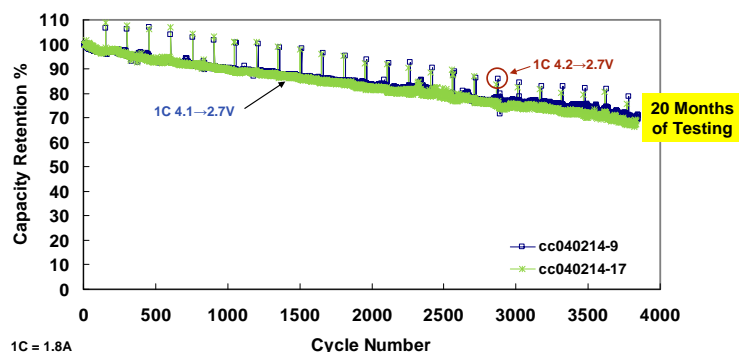


Figure IV-243: Room temperature cycling of baseline CAM-7/Graphite 18650 cells between 2.7 and 4.1 V. C/2 charge - 1C discharge; 1 C discharge from 4.2 V every 150 cycles. Note that cycling between 2.7 and 4.1 V corresponds to 90% SOC swing. Cells fabricated at TIAX

### Cathode Material Optimization and Electrode Engineering

During the program we have selected and scaled-up a higher capacity CAM-7 cathode material that exhibits good cycle life for use in the program deliverable cells. Discharge capacity of the baseline and the higher capacity material along with cycle life testing in 18650 cells are shown in Figure IV-244. To determine the optimum cathode design, experiments were carried out in coin cells with a graphite counter electrode varying electrode loading, formulation, porosity, separator type, and electrolyte formulation. Based on results of those experiments (presented previously in the 2015 Annual Progress Report) final cathode design was selected for use in the program demonstration cells.

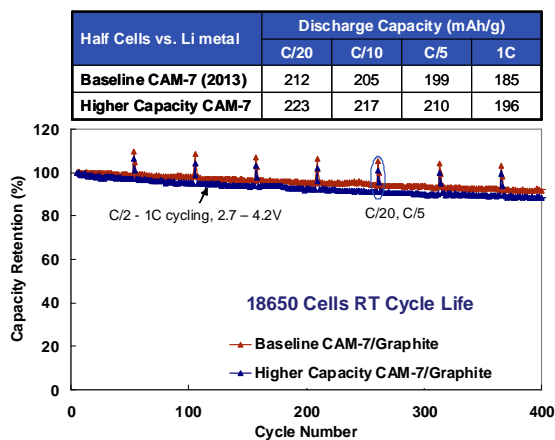


Figure IV-244: The table above shows the discharge capacity of the baseline and higher capacity CAM-7 cathode materials measured in half cells with Li metal anode (3.0-4.3 V) at room temperature. The bottom figure shows the full DoD cycle life of the higher capacity CAM-7 at room temperature with graphite anode in 18650 cells. 18650 cell design with equal electrode lengths, ~2 mAh/cm<sup>2</sup> cathode active material loading, graphite anode, and carbonate electrolyte

### Anode Material Selection and Electrode Optimization

During the course of the program, we sourced many state-of-the-art silicon anode materials from leading materials suppliers worldwide under non-disclosure agreements. Specifically, we focused on materials that are available in the multi-kg quantities essential for coating roll-to-roll electrodes and 18650 cell fabrication. These anode materials were initially fabricated into small-scale electrodes at TIAX and evaluated for capacity, first cycle efficiency, cycle life and cycle-to-cycle coulombic efficiency vs. Li-metal in coin cells (Table IV-38,

materials designated S1 through S8). A range of experiments evaluating different strategies for improving cycle life of Si-based anodes were carried with the results presented in the 2015 Annual Progress Report. The best-performing Si-based materials were evaluated in blends with graphite, leading to increased first cycle efficiency, capacity retention, and coulombic efficiency (Figure IV-245). Based on these results, we down-selected Si-based active material and blend formulation for use in the program demonstration cells.

**Table IV-38: Range of Si-Based Anode Materials Evaluated in the Program**

Material	Capacity (mAh/g)	1 <sup>st</sup> Cycle Efficiency	Cycle Life	Coulombic Efficiency
S1	500	82%	Good	OK
S2	600	84%	Good	OK
S3	1650	86%	OK	OK
S4	1850	86%	OK	OK
S5	3800	90%	Poor then good	Good
S6	3400	89%	Poor then good	Good
S7	1400	71%	Good	Good
S8	3100	88%	Good	Poor

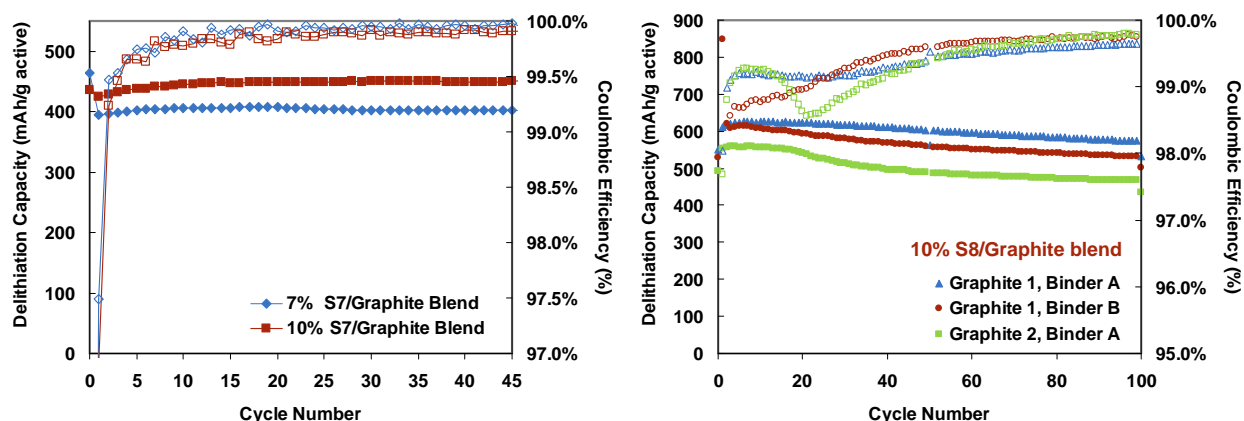


Figure IV-245: Capacity retention and coulombic efficiency for blended graphite/Si-based electrodes evaluated in lithium metal half cells. 1M LiPF<sub>6</sub> in EC:DMC:EMC 1:1:1 + 1%VC + 10%FEC electrolyte (EDEV1FEC10) and polymer separator. C/2 CC-CV lithiation to 50mV; C/2 delithiation to 1.2 V; 1 C = 600 mAh/g

During the program we also investigated the impact of binder selection in combination with blend composition on cycle life. In that work, we found that in addition to impacting cycle life, binders play an important role in resistance of the Si-containing electrodes. For example, the typical binder used in the academic literature for Si-based anodes to achieve good cycle life actually has poor adhesion with high loading blended electrodes, leading to higher impedance in HPPC testing (Binder 1 in Figure IV-246). Moreover, poor adhesion can result in cracking of the electrode coating during winding. We tested several alternative binders and identified one that combined good adhesion and low ASI for high loading S7-graphite blended anodes (Figure IV-246).

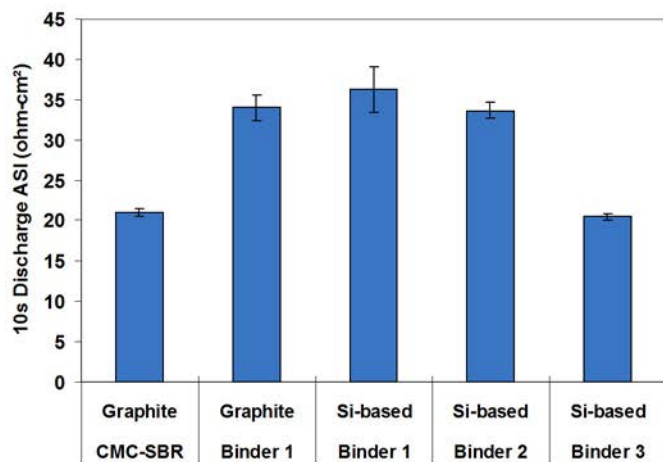


Figure IV-246: Impact of electrode adhesion on full cell ASI at 50% SOC of blended S7 Si-based anode with various binders. Blended anodes were formulated with 95:0:5 (active material:conductive carbon:binder), ~1.5-1.6 g/cc density matching a CAM-7 cathode with ~3 mAh/cm<sup>2</sup> active cathode loading. EDEV1FEC10 electrolyte and polymer separator. HPPC test with 3 C 10 s discharge and 2 C 10 s charge pulse

### Small Scale Full Cell Evaluation

The most promising Si-based anodes and their blends were evaluated in coin cells with CAM-7 based cathode for capacity, energy, rate capability during continuous discharge and during pulse power testing, along with cycle life. Strategies for improving cycle life with different blended Si-based anodes in full cells were tested (see the 2015 Annual Progress Report). Based on these scoping experiments, we selected a final blend and electrode formulation and binder/solvent system for scaling-up the blended S7/graphite electrodes for 18650 cells. Anodes were coated on our pilot coater and first tested in coin cells using a matching high capacity CAM-7 based cathode. Full cell capacity and cycle life of the pilot anode coating with a matching CAM-7 based cathode are shown in Figure IV-247 along with a comparison to a graphite control. We obtained excellent cathode utilization and high rate capability for these cells with comparable capacity retention to graphite containing cells indicating that our blending approach had successfully overcome the inherently low first cycle efficiency of S7 Si-based anode material.

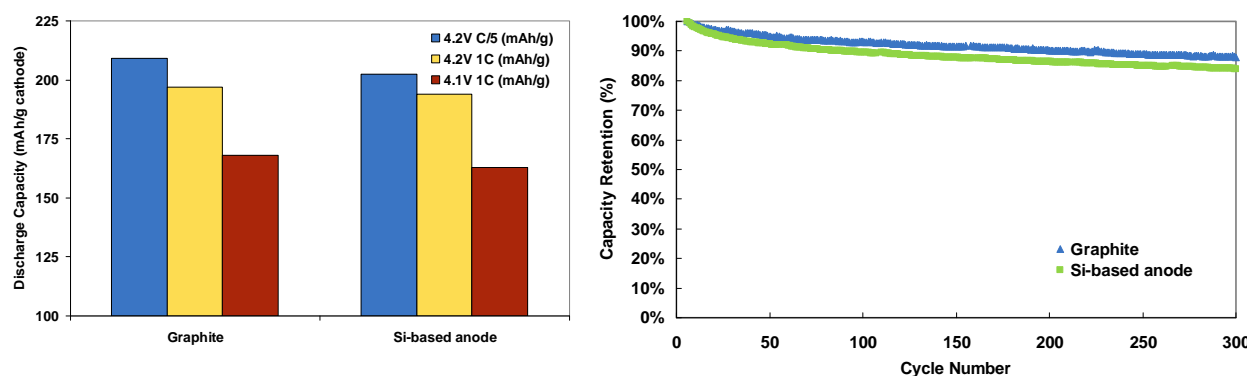


Figure IV-247: Comparison of full cell capacity and cycle life of CAM-7 cathode paired with graphite or with a S7-graphite blended anode. Blended anode was formulated with 95:0:5 (active material:conductive carbon:binder), ~1.6 g/cc density matching a CAM-7 based cathode with ~3 mAh/cm<sup>2</sup> active loading. EDEV1FEC10 electrolyte and polymer separator were used. Cycling with C/2 charge and 1 C discharge between 2.7 and 4.1 V

## Program Demonstration Si-based 18650 Cells

Several iterations of Si-containing 18650 cells with a CAM-7 based cathode were prepared at the TIAX cell-prototyping facility and tested for ability to deliver high specific energy and power along with cycle life. For the final program demonstration cells, blended S7 Si-based electrodes were paired with a higher capacity CAM-7 cathode material in an 18650 cell design utilizing improved cell hardware. In addition to high specific power and energy (Figure IV-249 and Table IV-39), the final CAM-7/Si-based anode program demonstration cells also achieved excellent cycle life, as shown in Figure IV-248, with 90% capacity retention after 500 cycles at full DOD and 85% after 1000 cycles at reduced DOD.

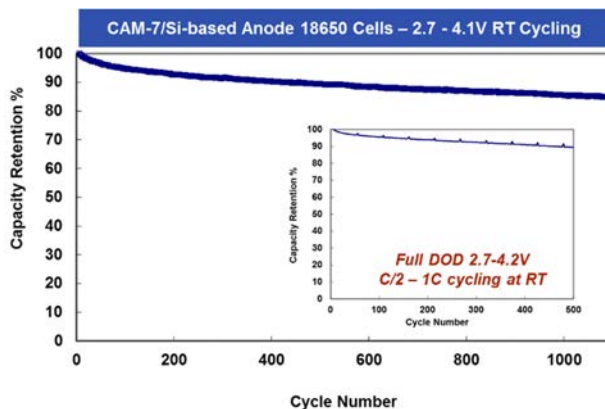


Figure IV-248: Cycle life of the final program demonstration cells combining higher capacity CAM-7 cathode material with a graphite blended S7 Si-based anode in 18650 cells during 2.7-4.1 V and 2.7-4.2 V (inset) cycling at room temperature. C/2 charge and 1 C discharge. Intermittent full DOD capacity and HPPC testing

## Comparison to Program Objectives

Direct comparison of performance between the baseline and program demonstration cells for both continuous discharge and in HPPC testing under PHEV relevant conditions is shown in Figure IV-249 and Table IV-39. By implementing a higher capacity CAM-7 cathode material with a blended Si-based anode, we were able to substantially increase both cell specific energy and power. Moreover, the CAM-7/Si-based chemistry and electrode design developed in this program can meet and exceed the 200Wh/kg (available) and 800W/kg targets in state-of-the-art 18650 hardware. Furthermore, by scaling the cell size to 15Ah pouch cells, we project 250Wh/kg total and 225Wh/kg available energy for these electrodes, demonstrating cell chemistry that can exceed DOE cell-level targets for PHEV40 lithium-ion batteries.

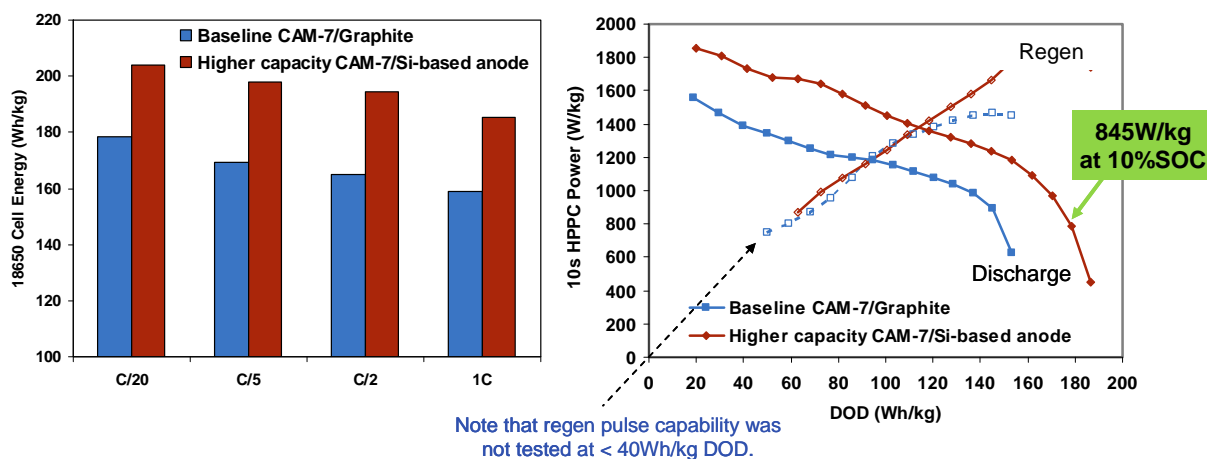


Figure IV-249: Comparison of rate capability during continuous discharge (left) and in HPPC power delivery capability (right) between the baseline and program deliverable 18650 cells. Note that heavier/smaller diameter 18650 cell hardware (circa 2004) was used for prototype cells. ~5-10% higher specific energy and power can be achieved with current mass production 18650 hardware

**Table IV-39: Comparison of Cell Capacity, Energy, and Power Capability between the Baseline and Program Demonstration 18650 Cells**

Measured Cell Performance	Baseline CAM-7/Graphite	Higher capacity CAM-7 Blended Si-based Anode	PHEV40 Target
C/5 Discharge Capacity (Ah)	1.83	2.29	
C/5 Discharge Energy (Wh)	6.70	8.38	
Total Specific Energy (Wh/kg*) <i>(Wh/kg electrode stack only**)</i>	167* <i>(235)**</i>	198* <i>(273)**</i>	200 <i>(available)</i>
10s Discharge Power at 10% SOC (W/kg*) <i>(W/kg electrode stack only**)</i>	800* <i>(1110)**</i>	845* <i>(1165)**</i>	800
Total Energy Density (Wh/L) <i>(Wh/L electrode stack only**)</i>	412 <i>(535)**</i>	530 <i>(670)**</i>	400
10s Discharge Power at 10% SOC (W/L) <i>(W/L electrode stack only**)</i>	1,945 <i>(2530)**</i>	2,188 <i>(2845)**</i>	1600

\* 18650 hardware circa 2004, ~5-10% higher specific energy and power can be achieved with current 18650 hardware.

\*\* *Electrode stack includes cathode and anode electrode coatings, current collector foils, separator, and electrolyte filling the electrode and separator pores. It does not include any cell packaging.*

## Conclusions

TIAX has developed long-life lithium-ion cells that can meet and exceed the energy and power targets (200Wh/kg and 800W/kg pulse power) set out by DOE for PHEV40 battery cells. To achieve these targets, we selected and scaled-up a high capacity version of our proprietary high energy and high power CAM-7<sup>®</sup> cathode material. We paired the cathode with a blended anode containing Si-based anode material capable of delivering high capacity and long life. Furthermore, we optimized the anode blend composition, cathode and anode design, and selected binder and electrolyte compositions to achieve not only the best performance, but also long life. By implementing CAM-7 with a Si-based blended anode, we built and tested prototype 18650 cells that delivered measured specific energy of 198Wh/kg and specific power of 845W/kg at 10% SOC (projected to 220Wh/kg in state-of-the-art 18650 cell hardware and 250Wh/kg in 15Ah pouch cells). These program demonstration cells achieved 85% capacity retention after 1000 cycles in on-going cycle life testing. Moreover, we also tested the baseline CAM-7/graphite system in 18650 cells showing that 70% capacity retention can be achieved after ~4000 cycles (20 months of on-going testing).

Ultimately, by simultaneously meeting the PHEV40 power and energy targets and providing long life, we have developed a lithium-ion battery system that is smaller, lighter, and less expensive than current state-of-the-art lithium-ion batteries. Although the program period is complete, we are investigating further ways of optimizing and scaling this CAM-7/Si-based lithium-ion battery chemistry to accelerate its adoption and commercialization for electric vehicles. Specifically, we are looking to further optimize electrolyte composition to improve cycle life, scale-up to larger cylindrical and prismatic cell size, and demonstrate scale-up cells in small modules.

## Products

### Presentations/Publications/Patents

Some of the results from this program were presented at various conferences:

1. J. Rempel, High Energy High Power Battery Exceeding PHEV40 Requirements, U.S. Department of Energy Vehicle Technology Office Annual Merit Review, Washington D.C., June 2014 (presentation).

2. J. Rempel, D. Ofer, A. Pullen, S. Dalton-Castor, M. Menard, D. Kaplan, B. Barnett, and S. Sriramulu, Implementation of High Capacity Cathode Material in High Power and in High Energy Lithium-ion Cells, 32nd International Battery Seminar & Exhibit, March 2015 (presentation).
3. J. Rempel, High Energy High Power Battery Exceeding PHEV40 Requirements, U.S. Department of Energy Vehicle Technology Office Annual Merit Review, Washington D.C., June 2015 (poster).
4. J. Rempel, Materials Development for High Energy High Power Battery Exceeding PHEV40 Requirements, U.S. Department of Energy Vehicle Technology Office Annual Merit Review, 2015 Washington D.C., June 2015 (poster).
5. Pullen, J. Rempel, D. Ofer, S. Dalton-Castor, M. Menard, D. Kaplan, B. Barnett, and S. Sriramulu, High-performance nickel-based cathode material for a wide range of automotive applications, AABC 2015, Detroit, MI, June 2015 (poster).
6. J. Rempel, High Energy High Power Battery Exceeding PHEV40 Requirements, U.S. Department of Energy Vehicle Technology Office Annual Merit Review, Washington D.C., June 2016 (presentation).
7. J. Rempel, D. Ofer, A. Pullen, D. Kaplan, B. Barnett, and S. Sriramulu, High Energy Lithium-ion Cells Based on CAM-7 Cathode Material, 47th Power Sources Conference, June 2016 (presentation).